Spring 1-1-2011

OH Masers from Andromeda to the Peak of Cosmic Star Formation

Kyle William Willett
University of Colorado at Boulder, willettk@gmail.com

OH Masers from Andromeda to the Peak of Cosmic Star Formation

by

Kyle William Willett

B.A., Carleton College, 2005

M.S., University of Colorado, 2007

A thesis submitted to the

Faculty of the Graduate School of the

University of Colorado in partial fulfillment

of the requirements for the degree of

Doctor of Philosophy

Department of Astrophysical and Planetary Sciences

2011

This thesis entitled:
OH Masers from Andromeda to the Peak of Cosmic Star Formation
written by Kyle William Willett
has been approved for the Department of Astrophysical and Planetary Sciences

Prof. Jeremy Darling

Prof. John Bally

Prof. Heather Lewandowski

Prof. J. Michael Shull

Prof. John Stocke

Date

The final copy of this thesis has been examined by the signatories, and we find that both the content and the form meet acceptable presentation standards of scholarly work in the above mentioned discipline.

Willett, Kyle William (Ph.D., Astrophysics)

OH Masers from Andromeda to the Peak of Cosmic Star Formation

Thesis directed by Prof. Jeremy Darling

OH masers are naturally-occurring phenomena powered by stimulated emission, existing in a variety of astrophysical environments. The presence of powerful OH megamasers (OHMs) is associated with merging galaxies and extreme star formation, while the high luminosities and narrow beams of masers make them powerful probes of local physical conditions. I present research on three projects concentrating on observations of extragalactic OH masers.

The first project analyzes mid-infrared spectroscopy of OHM host galaxies with data from the *Spitzer Space Telescope*. I identify several mid-infrared spectral features that signal the presence of an OHM, including deep silicate absorption and steep continuum emission, indicating the presence of large amounts of warm dust. Mid-infrared data are also used to test new OH pumping models, demonstrating that OHM hosts favor a smooth, highly embedded dust geometry. Secondly, I describe results of a radio-wavelength survey using the Green Bank Telescope for new OHMs at redshift $z \sim 1$. Detections of two new OHMs are included, while statistics of galaxies in which OH was not detected constrain the OHM fraction and overall galaxy merger rate. Finally, I present data from the first OH survey of M31 (the Andromeda galaxy) using the Very Large Array. We found no OH masers above a $5\sigma = 10$ mJy limit in the galaxy. I discuss our results in the context of ongoing efforts to use masers as tools for measuring M31's proper motion with respect to the Milky Way.

Dedication

To my parents, Dr. Diane Pike and Dr. Stephen Willett. I'm excited to join you both at the big kids' table.

Acknowledgements

First and foremost credit for this thesis must go to my advisor, Jeremy Darling. Over the last five years, I've been fortunate to benefit from his scientific insight, financial support, career advice, and his never-ending reservoir of interesting ideas. He has treated me as a colleague from day one, and it's been an honor to have been his first thesis student.

My colleagues at Colorado have helped me maintain sanity both within the office and outside. Thanks to Phil Oakley for the months of studying that got me through Comps 1; Ben Zeiger and Ting Yan for help with GBT and VLA data reduction; and to Devin Silvia and Adam Ginsburg for rescuing my AAS thesis talk. Heather Beasley provided extensive feedback on various drafts of this thesis. Charles Danforth has been an officemate extraordinaire, and counteracted my descents into bitterness with ever-increasing affability.

Observational astronomers are dependent on an enormous group of people who provide us with data. Particular thanks goes to the staff at NRAO and the Spitzer Science Center, which provided the bulk of the observations used in this thesis. Henrik Spoon, Lee Armus, and Vassilis Charmandaris shared their knowledge, scientific support, and hospitality in Pasadena and Crete. Socorro-based thanks go to Jürgen Ott, Walter Brisken, Chris Carilli, Nissim Kanekar, Kumar Golap, Adam Deller, Joan Wrobel, and Mark Claussen, in addition to the VLA operators. Green Bank staff who have been of great help include Toney Minter, Dan Perera, Dave Rose, Dave Curry, Donna Stricklin, Barry Sharp, Greg Monk, Kevin Gum, Daryl Shinaberry, and Max Gum. I am also grateful to Phil Lockett, Jeyhan Kartaltepe, Lihwai Lin, Karina Caputi, Brian Kent, Jim Braatz, Rainer Beck, and James McBride for sharing their data with me.

Finally, thank you to Susannah, who has uncomplainingly made it through six years of erratic sleep schedules and weird conversations about astrophysics. I'll keep trying to do better.

Contents

Chapter

Tables

Table

Figures

Figure

mss′@mss mss″@mss

Chapter 1

Physics of OH masers

1.1 Introduction

Since the early days of radio astronomy, the study of molecules and their behavior at radio wavelengths has been of extreme interest. The hydroxyl radical, OH, was the first molecule detected in interstellar space by radio telescopes and was the first example discovered of an astrophysical maser. Over the last 45 years, OH masers have been observed in a wide variety of environments, including comets, stellar envelopes, star-forming regions, and out to cosmic distances in the nuclei of merging galaxies. OH masers have been of enormous importance to astrophysics in several areas: they serve as examples of the details of radiative transfer and molecular physics, signposts for the astrophysical conditions necessary to create masers, and as tracers of their environments, measuring redshifts, kinematics, gas content, and magnetic field strengths. This dissertation describes results of three projects involving OH masers: a mid-infrared study of the host galaxies of OH megamasers (OHMs), a survey for new OHMs in galaxies at $z \sim 1$, and a search for OH masers in M31 (the Andromeda galaxy) with the eventual goal of using masers to measure M31's proper motion.

The remainder of this chapter will give a brief overview of the physics of astronomical masers. This summary draws heavily on the excellent reviews by Reid & Moran (1981); Elitzur (1992a); Lonsdale (2002); Lo (2005), and the indispensable textbook by Elitzur (1992b); further details can be found in these sources. Section 1.2 covers the basics of stimulated emission, with Section 1.3 focusing on the particular structure of the OH molecule. Sections 1.4 and 1.5 describe the known environments and properties of Galactic OH masers and extragalactic OH megamasers, respectively.

A short summary of some open questions relating to maser astrophysics are given in Section 1.6, while Section 1.7 describes the specific research presented in this thesis.

As an important note, there are two main types of stimulated emission are discussed in this dissertation: OH masers and OH megamasers (OHMs). The abbreviation "OHM" is intended to refer **only** to the classes of OH megamasers and gigamasers discussed in Chapters 2-4. The phrase "OH maser" typically refers to lower-luminosity masers ($L_{OH} < 1\ L_{\odot}$) associated with HII regions – these objects are targeted in the survey in Chapter 5. I will endeavor to clearly distinguish between the two whenever possible.

1.2 Stimulated emission

Stimulated emission is one of the three basic radiative processes, in addition to absorption and spontaneous emission. The characteristics of the radiation measured by the observer will depend on its interaction with matter, including its source and propagation along the line of sight. Here, I review the basic equations of radiative transfer, focusing specifically on applications to masers.

1.2.1 Radiative transfer

A radiation field in space (excluding for the moment the time-varying nature and polarization properties of the EM field) can be treated as the amount of energy carried by the rays of radiation though a specific location. The specific intensity I_ν is defined as (Rybicki & Lightman, 1979):

$$\frac{dE}{dA\ dt\ d\Omega\ d\nu} = I_\nu, \tag{1.1}$$

where dE is the energy passing through an area dA with solid angle $d\Omega$ in time interval dt and frequency interval $d\nu$. If there is no interaction with matter along the line of sight (either adding or removing energy from the beam), the specific intensity is constant at all points. To account for the interaction of matter with the radiation, the monochromatic emission (j_ν) coefficient is defined:

$$\frac{dE}{dA\ ds\ dt\ d\Omega\ d\nu} = j_\nu. \tag{1.2}$$

This is equivalent to the amount of energy added to the beam per unit volume ($dV = dAds$, where ds is an interval along the beam's path). Substitution into Equation 1.1 gives the differential equation for pure emission:

$$\frac{dI_\nu}{ds} = j_\nu. \tag{1.3}$$

The case for absorption is slightly more complicated, since the amount of energy removed from the beam will depend on the intensity at that particular point. The absorption coefficient (α_ν) is defined as:

$$dI_\nu = -\alpha_\nu I_\nu ds, \tag{1.4}$$

where α_ν represents the differential amount of absorption taking place over path length ds. The sign in Equation 1.4 is negative, indicating absorption; if $\alpha_\nu < 0$ (shown later to be the case for masers), the net effect adds energy to the beam at each step.

Combining Equations 1.2 and 1.4 gives the differential equation for radiative transfer:

$$\frac{dI_\nu}{ds} = -\alpha_\nu I_\nu + j_\nu. \tag{1.5}$$

This can be rewritten in terms of the monochromatic optical depth τ_ν, defined as $d\tau_\nu \equiv \alpha_\nu \, ds$. We also define the source function $S_\nu \equiv j_\nu/\alpha_\nu$. Substituting τ_ν and S_ν into Equation 1.5 gives:

$$\frac{dI_\nu}{d\tau_\nu} = -I_\nu + S_\nu. \tag{1.6}$$

This can be formally solved to express the intensity at any point as a function of S_ν and the optical depth:

$$I_\nu[\tau_\nu] = I_\nu[0]e^{-\tau_\nu} + \int_0^{\tau_\nu} S_\nu[\tau'_\nu]e^{-(\tau_\nu - \tau'_\nu)}d\tau'_\nu. \tag{1.7}$$

If the source function is constant ($\frac{dS_\nu}{d\tau_\nu} = 0$), then the integral can be simplified:

$$I_\nu[\tau_\nu] = I_\nu[0]e^{-\tau_\nu} + S_\nu(1 - e^{-\tau_\nu}). \tag{1.8}$$

This relation can be interpreted as absorption of the initial intensity diminished by the e-folding factor of the absorption, plus the change in the source function diminished by the e-folding factor. For thermal radiation, the intensity is described by the Planck function $I_\nu = B_\nu$, where $B_\nu = \frac{2h\nu^3/c^2}{e^{h\nu/kT}-1}$. Using the Planck function to derive the Einstein coefficients for a two-level atom, the monochromatic absorption coefficient for stimulated emission can be written as:

$$\alpha_\nu = \frac{h\nu}{4\pi}\phi[\nu](n_1 B_{12} - n_2 B_{21}). \tag{1.9}$$

Here, $\phi[\nu]$ is the normalized frequency profile of the line emission and B_{12}, B_{21} are the Einstein coefficients for absorption and stimulated emission, respectively. If the upper level becomes overpopulated with respect to the lower level (such that $\frac{n_1}{g_1} < \frac{n_2}{g_2}$), then the absorption coefficient in Equation 1.9 will be **negative** and the intensity will **increase** along the ray by a factor of $\exp[\int_0^s -\alpha_\nu[s']ds']$. Since the gain is exponential, this has the potential to increase the brightness by many orders of magnitude if coherence is maintained over a sufficiently long path.

Finally, it is often useful to characterize emission in the Rayleigh-Jeans approximation in terms of temperature. For masers, two commonly used definitions are the *brightness temperature* T_b:

$$T_b = \frac{B_\nu c^2}{2k\nu^2}, \tag{1.10}$$

which is the temperature of a source that would result in a given observed brightness; and the *excitation temperature* T_{ex}:

$$\frac{n_2}{n_1} = e^{-h\nu/kT_{ex}}. \tag{1.11}$$

For masers, $T_{ex} < 0$ and T_b can be very high due to the nature of the non-thermal emission. Masing allows an area that is physically small (or that subtends a narrow angle within the telescope

beam) to produce extremely bright emission; for Galactic OH masers in star forming regions, T_b can exceed 10^{12} K. This is impossible to achieve with thermal emission, since the OH molecule would dissociate at these temperatures.

Equation 1.8 can be rewritten in terms of T_b and T_{ex}:

$$T_b[s] = T_b[0]e^{-\tau_\nu[s]} + T_{ex}(1 - e^{-\tau_\nu[s]}), \tag{1.12}$$

where s is the path length traveled along the ray. For a maser, $e^{-\tau_\nu[s]} > 0$ and is akin to a gain factor. This shows the relative importance of the two input signals: the background emission is governed by T_b and the spontaneous emission from the maser by T_{ex}.

1.2.2 Population inversion

A fundamental requirement for masing is a population inversion of the energy levels. As an example, take a two-level population whose number densities are given by N_1, N_2 with an energy separation of ΔE. If isolated levels can only exchange populations between themselves in the absence of external radiation, then the principle of detailed balance means that the level populations will approach a Boltzmann distribution (Elitzur, 1992a):

$$\frac{N_2}{N_1} = e^{-\Delta E/kT}\left(\frac{g_2}{g_1}\right)\frac{C_{21}}{A_{21} + C_{21}}, \tag{1.13}$$

where A_{21} and C_{21} are the rates of spontaneous and collisional decay, respectively. To create a steady state of population inversion, additional levels must be introduced such that detailed balance is not the only principle acting on the level populations. In this case, for each level we introduce a loss rate Γ_i and pump rate per unit volume P_i. The steady-state equation for the two levels (now labeled $N_{1\nu}, N_{2\nu}$ to account for explicit frequency dependence of the line profile) becomes:

$$\frac{\partial N_{2\nu}}{\partial t} = 0 = P_{2\nu} - \Gamma_2 N_{2\nu} - A_{21}N_{2\nu} - J_\nu(N_{2\nu}B_{21} - N_{1\nu}B_{12}) - (N_{2\nu}C_{21} - N_{1\nu}C_{12}). \tag{1.14}$$

To simplify the calculation, it can be assumed that statistical weights ($g_1 = g_2$) and loss rates ($\Gamma_1 = \Gamma_2$) are equal for the level populations, and that the spontaneous emission and collisional exchanges can be neglected. Here, $J_\nu \equiv \frac{1}{4\pi}\int I_\nu d\Omega$ is the specific intensity integrated over all angles. Equation 1.14 can then be solved via linear algebra to give the population difference:

$$n_2 - n_1 = (n_2 + n_1)\left(\frac{p_2 - p_1}{p_2 + p_1}\right)\frac{\Gamma}{\Gamma + 2B_{21}J_\nu}, \tag{1.15}$$

where $p_i = P_i/g_i$ is the pumping rate per sub-level and $n_i = N_i/g_i$ the number density per sub-level. This shows that population inversion ($n_2 > n_1$) will occur if the pumping rate per sub-level of the upper state exceeds that of the lower state.

The amplification of the maser is determined by the relative populations of the two levels, using the definition of the absorption coefficient α_ν (Equation 1.9):

$$\alpha_\nu = \frac{(p_1 - p_2)g_2 B_{21} h\nu}{4\pi\Gamma(1 + 2B_{21}J_\nu/\Gamma)}\phi[\nu]. \tag{1.16}$$

Thus, for a molecule in which the upper level rate of pumping is greater than that in the lower state, the gain factor will increase in proportion to the excess pump rate. The volume emission rate of radiation is given by the excess of stimulated emission over absorption events, $g_2 B_{21} J_\nu (n_2 - n_1)$. Substituting the derived population inversion from Equation 1.15 gives:

$$g_2 B_{21} J_\nu (n_2 - n_1) = g_2(\Gamma/2)(n_2 - n_1)\phi[\nu]\frac{J_\nu}{J_\nu + \Gamma/(2B_{21})}. \tag{1.17}$$

The exponential gain of the maser is ultimately limited by the factor of $J_\nu/(J_\nu + \Gamma/(2B_{21}))$; when J_ν exceeds $\Gamma/(2B_{21})$, the conversion efficiency of inversions to maser photons approaches unity and the maser *saturates*. Physically, this means that every pumping event is now producing a maser photon; increased gain at this point can only be achieved by a larger difference in pumping levels.

1.2.3 Maser pumping models and additional considerations

The model described above is a simplified version of the physics necessary to model maser line emission. In reality, all possible radiative connections between levels must be simultaneously considered to solve the radiative transfer equation, as well as tracking population changes from spontaneous emission and collision. For example, Lockett & Elitzur (2008) solved for the populations of 24 levels of the OH molecule, including all hyperfine levels with direct radiative connections to the ground state. Reliable estimates of the radiation field J_ν and local collision rates are also necessary, as is the dependence of the gas and radiation field on the local geometry.

Finally, measurements of maser line ratios show that the line width due to turbulent motions is also a key component in determining the relative level populations. Broadening of transitions in the radiative decay ladder means that a photon emitted in one transition may be Doppler-shifted and absorbed in a different one - numerical calculations show that this is necessary, for example, to explain the relative strength of the 1667 MHz feature in OHMs (Lockett & Elitzur, 2008).

For further details on general maser theory, Elitzur (1992b) provides a set of thorough derivations.

1.3 OH molecule

OH is a diatomic molecule consisting of one atom of oxygen and one of hydrogen, connected with a covalent bond. The molecule is electrically neutral and the outer electron shell is unfilled, with a single unpaired electron. The interaction of the unpaired electron with the various rotational and nuclear spins lead to many of the OH transitions that are observed in astrophysical environments. The unfilled electron shell also distinguishes OH (the hydroxyl radical) from the hydroxide ion OH^-. OH is a relatively common molecule in the interstellar medium of galaxies, with an average abundance of 10^{-8} with respect to HI gas (Liszt & Lucas, 1996). The molecule can be formed through multiple chemical pathways via its progenitors O and ionized H^+, H_2^+ (Lequeux, 2005).

1.3.1 Rotational ladders

Since the moment of inertia of a diatomic molecule is dominated by the masses and relative distances of the nuclei, such molecules are symmetric along the inter-nuclei axis. This means that projections of the angular momentum along this axis (referred to as $\hat{\mathbf{z}}$) are conserved quantities. The nuclear spin is a small contributor to the total angular momentum as a result of the small magnetic moment of the unpaired proton in the hydrogen nucleus. The total angular momentum for the orbital ($\mathbf{J}$) can therefore be approximated as:

$$\mathbf{J} = \mathbf{K} + \mathbf{L} + \mathbf{S} \tag{1.18}$$

where $\mathbf{K}$ is the end-over-end rotational angular momentum, $\mathbf{L}$ is the total electronic orbital angular momentum, and $\mathbf{S}$ is the total electronic spin.

For projections along $\hat{\mathbf{z}}$, $K_z = 0$ since the molecule is symmetric about this axis. The ground electronic state of OH has $L_z = 1$ (in units of $\hbar$), referred to as a Π orbital. Finally, since the molecule has a single unpaired electron, the magnitude of $\mathbf{S}$ is $S = 1/2$. The total magnitude of the angular momentum component is thus $J_z = 1 \pm (1/2)$ in the rotational ground state.

The interaction of the electronic orbital and spin angular momenta gives rise to two rotational energy ladders, denoted as the ${}^2\Pi_{1/2}$ and ${}^2\Pi_{3/2}$ ladders. The superscript refers to the two possible electron spin orientations, while the subscript refers to the total J_z. Each ladder is split into energy levels separated by $\Delta J = n\hbar$ (where $n = 0, 1, 2\ldots$), beginning at the ground state J_z. Both intra- and inter-ladder electric dipole transitions are permitted, following the selection rules discussed in §1.3.3.

1.3.2 Λ-doubling

The energy levels of the rotation ladders are perturbed by quantum mechanical interactions with other nearby electronic configurations. Because the internuclear component of the electronic orbital angular momentum is represented by $\mathbf{L}$, the phenomenon is known as Λ-doubling. In the

case of the ground state of the OH molecule, the primary perturbations come from a Σ state ($L_z = 0$; Hougens, 1970).

Since L_z can have two possible orientations with respect to the Σ state, this perturbation splits the rotational level into two nearly degenerate levels. The two Λ-split levels for each rotational level will have opposite parity (the even/oddness of the total electronic orbital angular momentum, $\sum l_i$). Since parity must change for a dipole transition, this permits transitions within a single rotational state even if $\Delta K = 0$.

For the OH $^2\Pi_{3/2}$ ladder ground state ($J = 3/2$), the lower energy transition has odd parity; the ground state of the $^2\Pi_{1/2}$ ladder has even parity for the lower energy transition. The order of the even-odd parity transitions reverses for several of the lowest rotational sets on both ladders, but changes order between $J = 7/2$ and $J = 9/2$ on the $^2\Pi_{1/2}$ ladder due to spin uncoupling effects (Brown et al., 1978).

1.3.3 Hyperfine splitting

A final splitting of the rotational levels occurs due to the interaction of the nuclear spin and its associated magnetic moment. The total spin angular momentum of the nucleus is given by **I**; for the OH molecule, the spin of the unpaired proton in the hydrogen nucleus is $I = 1/2$. This angular momentum couples with the previous angular momentum vector **J** (Equation 1.18), defining the total angular momentum vector:

$$\mathbf{F} = \mathbf{J} + \mathbf{I}. \tag{1.19}$$

These states are known as hyperfine splitting, since the differences in energy levels are typically orders of magnitude smaller (by a factor of $m_e/m_p \simeq 1800$) than fine-structure splittings. The 21-cm emission from HI is one of the most prominent examples of hyperfine transitions in astronomy.

1.3.4 Observed radio-wavelength OH transitions

For the OH molecule, each rotational state is split twice by Λ-doubling and twice again by hyperfine splitting, resulting in four levels per J defined by a quantum number F. The standard dipole selection rules apply, in which parity must change between transitions and $\Delta F = 0, \pm 1$ (but $F = 0 \rightarrow 0$ is forbidden). The hyperfine splitting in the ground state of OH is unequal (by ~ 2 MHz) between the upper and lower states, resulting in four distinct fine-structure transitions with wavelengths near 18 cm. The two "main lines" are F-conserving, with measured laboratory rest frequencies of 1665.401803 (12) MHz for the $F = 1 \rightarrow 1$ transition and 1667.358996 (4) MHz for the $F = 2 \rightarrow 2$ transition (Hudson et al., 2006). The F-changing transitions are known as satellite lines, with measured frequencies of 1612.230825 (15) MHz for the $F = 1 \rightarrow 2$ transition and 1720.529887 (10) MHz for the $F = 2 \rightarrow 1$ transition (Lev et al., 2006).

Hyperfine splitting and Λ-doubling also occurs in the excited rotational states of OH. Transitions as high as 23.8 GHz ($^2\Pi_{3/2}, J = 9/2$) have been observed in the interstellar medium, with several excited states also showing maser action (e.g., Knowles et al., 1973; Baudry et al., 1981; Pihlström et al., 2008). Figure 1.1 shows the energy levels and allowed transitions for the bottom 24 hyperfine transitions of OH. Note that the 23.8 GHz ($^2\Pi_{3/2}, J = 9/2$) levels are not shown in this diagram.

For optically thin lines, the brightness temperatures and relative intensities of fine-structure $\Delta J = 0$ transitions are a function of the quantum numbers of the projected angular momentum vectors I, J, F and the rotational constant A_r (Townes & Schawlow, 1955):

$$\begin{aligned} F - 1 \rightarrow F; \quad & -A_r \tfrac{(J+F+I+1)(J+F-I)(J-F+I+1)(J-F-I)}{F} \\ F \rightarrow F; \quad & A_r \tfrac{(J(J+1)+F(F+1)-I(I+1))^2(2F+1)}{F(F+1)} \\ F + 1 \rightarrow F; \quad & -A_r \tfrac{(J+F+I+2)(J+F-I+1)(J-F+I)(J-F-I-1)}{F+1} \end{aligned} \tag{1.20}$$

In the ground state of OH ($J = 3/2$, $I = 1/2$), the thermal ratios are $1 : 5 : 9 : 1$ for the $1612 : 1665 : 1667 : 1720$ MHz transitions. Deviations from these predicted ratios are a strong sign

that that non-thermal processes (such as masing) are occurring.

1.4 Galactic-analog OH masers

1.4.1 History

OH was the first molecule to be observed in astrophysical environments at radio frequencies. Weinreb (1963) observed both the 1665 and 1667 MHz transitions in absorption toward the supernova remnant Cassiopeia A using the 84-ft. Millstone Hill telescope. Weaver et al. (1965) published the first detections of OH emission lines arising from the W3 region in Orion at 1665 MHz; since the measured brightness temperatures were far in excess of what would be expected for thermally excited OH, the unidentified line was initially referred to as "mysterium". Main-line 1665/1667 MHz OH emission had been detected in W49 earlier that year by Gundermann (1965), followed by several detections toward the Galactic center from the Southern Hemisphere (McGee et al., 1965). Weinreb et al. (1965) measured the polarization of the "mysterium" in W3 and suggested that the lines could (among other possibilities) be a result of maser-amplified OH transitions. Theoretical models (Litvak et al., 1966; Perkins et al., 1966; Litvak, 1969; Goldreich & Keeley, 1972) later established plausible pumping models for stimulated emission of the OH molecule.

The first extragalactic detection of OH was made in absorption by Weliachew (1971) toward the galaxies NGC 253 and M82, with main line absorption in NGC 253 confirmed by Whiteoak & Gardner (1973). OH was also detected in the Large Magellanic Cloud both in absorption at 1667 MHz (Whiteoak & Gardner, 1976) and in emission at 1665 MHz (Caswell & Haynes, 1981). The detections of OH emission in both NGC 253 and M82 were both an order of magnitude brighter than known Galactic OH masers. The 1667 MHz line was observed to be stronger than the 1665 MHz line, in contrast to the line ratios previously seen in OH masers associated with HII regions in the Milky Way.

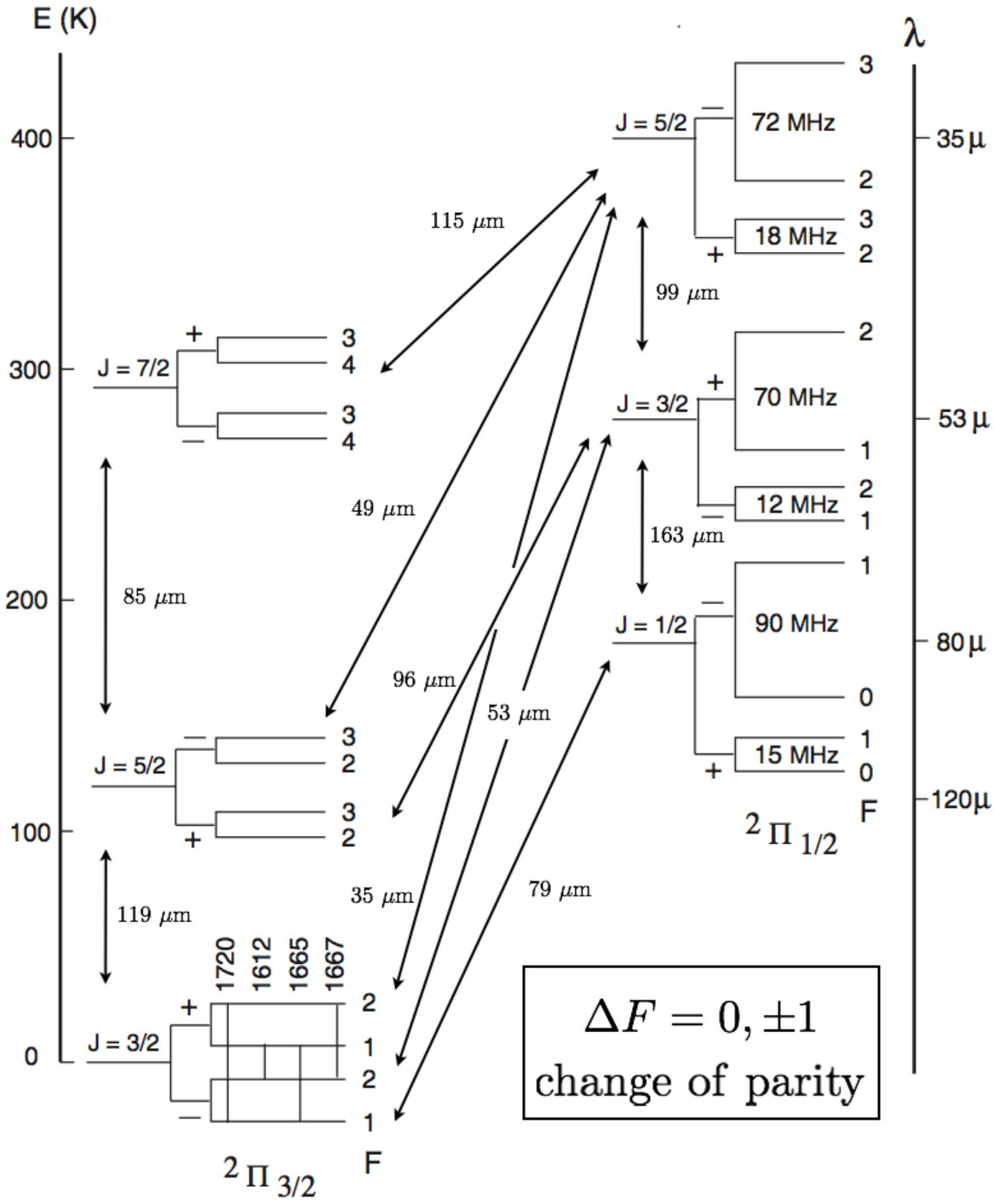

Figure 1.1 Diagram of the lowest 24 hyperfine OH energy levels, adapted from Lockett & Elitzur (2008). The left axis indicates the energy of rotational transitions above the ground state (E/k_b), and the right axis gives the wavelength of the transitions in μm. Relative sizes of the energy level splittings are not to scale.

1.4.2 OH masers in HII regions

The strongest OH maser radiation in the Milky Way is observed in the main line 1665 MHz transition from regions of active star formation (Elitzur, 1992a; Fish, 2007). The brightest masers observed in Galactic HII regions have peak flux densities of a few hundred Jy, although OH masers do show significant variability and can flare as bright as 1000 Jy (Alakoz et al., 2005). In addition to the four ground state transitions, many Galactic HII regions mase in rotationally-excited states of OH ($\lambda = 2,\ 5$, and 6 cm). Typical Galactic OH maser spectra have multiple narrow components that span a range in radial velocity of up to 10 km s^{-1}. Individual OH components tend to show high degrees of circular polarization. The masing action in star-forming regions is likely caused by a combination of collisional and far-infrared radiative pumping (Cesaroni & Walmsley, 1991).

VLBI observations of OH masers in HII regions demonstrate that masers can occur in a variety of environments, although they are primarily found expanding outward between the shock and ionization fronts. Physical sizes of the maser spots are of order $(1-10)$ AU, which is similar to the typical separation between adjacent maser spots. OH masers have also been observed tracing out molecular disks and in extended filamentary emission. Typical conditions in the HII regions hosting OH masers are molecular hydrogen densities between $10^5 - 10^8$ cm^{-3}, dust temperatures of roughly 300 K, and magnetic field strengths of $2-10$ mG (Reid & Moran, 1981).

The OH masers associated with (ultra)compact HII regions are among the brightest radio sources in the sky at centimeter wavelengths; the peak flux densities are high-enough that Galactic-analog OH masers could be detected in galaxies within 1 Mpc of the Milky Way. Our search for OH masers associated with star-forming regions in the Andromeda galaxy is described in Chapter 5 of this thesis.

1.4.3 Other OH maser environments

The other main environment for OH maser emission in the Milky Way comes from the outer regions of late-type stars known as OH/IR stars. Molecular gas in the outer stellar envelope is

blown outward by radiation pressure, with H_2O photodissociating and forming OH at stellar radii of $\sim 10^{16}$ cm from the star. Type I OH/IR stars have thin dust shells at temperatures of 150–180 K and show only main line 1665 and 1667 MHz OH emission. Type II OH/IR stars have higher mass loss rates than Type I, and also show 1612 MHz OH maser emission from cooler dust shell radii exterior to the main line-emitting regions (Elitzur, 1992b). 1720 MHz OH masers have been observed both in star-forming regions and in shocked regions where a supernova remnant interacts with a molecular cloud (Frail et al., 1994). Finally, weak OH maser emission has also been detected in cometary envelopes (e.g., Biraud et al., 1974).

Both cometary and late-type stellar OH masers are too dim to be detected at extragalactic distances, and as a result are not discussed further in this thesis.

1.5 Extragalactic OH megamasers

1.5.1 History

Baan et al. (1982) discovered the first OH megamaser in Arp 220 (IC 4553) using the Arecibo telescope in a search for main line 18-cm OH absorption. The integrated isotropic emission from the 1667 MHz line in the galaxy was an unexpected $L_{OH} = 10^3\ L_\odot$, six orders of magnitude more powerful than the brightest known Galactic OH maser. The Arp 220 OH emission is unpolarized, with a much broader linewidth ($\Delta v \simeq 100$ km s^{-1}) than Galactic masers and with the strongest emission in the 1667 MHz transition. The OH luminosity difference between Arp 220 and Galactic masers led to the use of the term "megamaser" to describe extragalactic masers with $L_{OH} = 10^{1-4}\ L_\odot$. This lower limit still mostly distinguishes OH megamasers from OH kilomasers ($L_{OH} \sim 10^{0-1}\ L_\odot$), which show mixed OH absorption and emission features and may be governed by different physical processes than OHMs.

Early surveys for OHMs initially focused on galaxies that possessed bright radio continuum near 1.6 GHz and HI absorption, with OH detection rates of a few percent or less (Baan et al., 1985; Schmelz et al., 1986). The number of OHM candidate galaxies was greatly increased by observations

from the all-sky Infrared Astronomical Satellite (IRAS), which identified infrared-bright galaxies in bands centered near 12, 25, 60, and 100 μm. Radio surveys of IRAS targets concentrated on galaxies with steep spectral indices in mid-infrared wavelengths ($f_{25\mu m}/f_{12\mu m} \geq 4$) and flat spectral indices in far-infrared wavelengths ($f_{100\mu m}/f_{60\mu m} = 0.7 - 1.5$; Staveley-Smith et al., 1987, 1992; Norris et al., 1989). Further selections of OHM candidates were made using far-infrared colors, based both on empirical results [Henkel et al. (1986) showed that OHMs have color excesses near 25 and 60 μm compared with non-masing galaxies] and theoretical predictions: if mid-infrared transitions are responsible for pumping the upper levels that drive the population inversion, then galaxies with SEDs peaking in this range will provide a stronger radiation field for maser pumping. A survey with the Green Bank 300-ft. telescope by Baan et al. (1992a) showed that the probability of detecting an OHM increased by applying both color and luminosity selections (galaxies with $L_{IR} > 10^{11.5}\ L_{\odot}$ have increased OHM fractions). The overall detection rate, however, was still less than 10% and resulted in ~ 50 known OHMs by the 1990s.

An upgrade to the Arecibo telescope that increased its L-band sensitivity by a factor of ~ 5 allowed Darling & Giovanelli (2000, 2001, 2002a) to carry out a much deeper survey for OHMs. Candidate galaxies for this survey were chosen from the flux-limited IRAS catalog ($f_{60\mu m} > 0.6$ Jy) and were confined to the redshift range $0.1 < z < 0.45$, based on the receiver bandwidth and local RFI. With no color or flux selection made for the IRAS galaxies, the survey detected 52 OHMs in 311 total galaxies, roughly doubling the total number of known OHMs. The results showed a slight tendency for OHMs to have smaller $f_{100\mu m}/f_{60\mu m}$ ratios than in non-masing galaxies. The OHM detection rate was shown to be a stronger function of the total infrared luminosity; 30% of galaxies with $L_{FIR} > 10^{12}\ L_{\odot}$ displayed OHM emission.

Detections of $\sim$ 113 OHMs have been published in the literature to date, with the most distant at a redshift of $z = 0.265$ (Figure 1.2). The majority of the known OHMs are compiled in Darling & Giovanelli (2002a), excepting recent additions from Kent et al. (2002) and this thesis (Chapter 4).

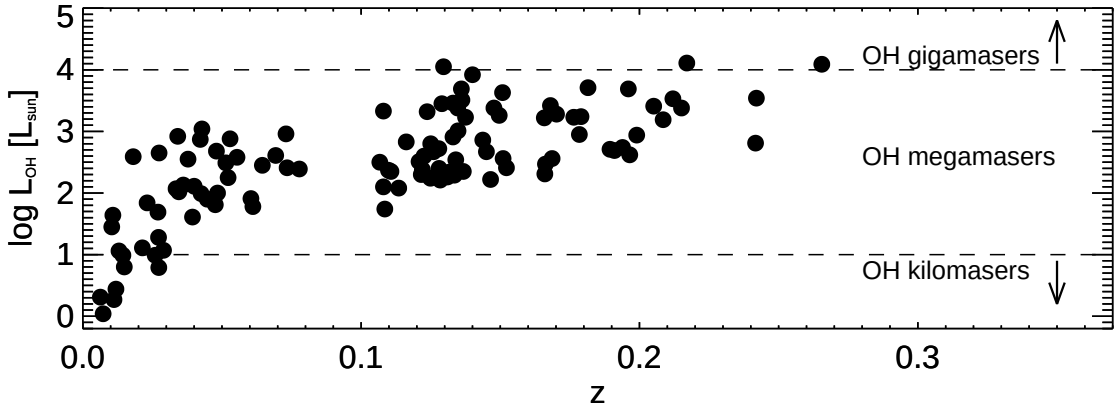

Figure 1.2 Integrated isotropic line luminosities of all published OHMs as a function of redshift. The dashed lines indicate the nominal luminosity cutoffs for OH gigamasers ($L_{OH} > 10^4\ L_\odot$) and OH kilomasers ($L_{OH} < 10\ L_\odot$).

1.5.2 Host galaxies

The host galaxies of OH megamasers are without exception (ultra)luminous infrared galaxies ([U]LIRGs). The two classes of galaxies are distinguished by their infrared luminosities, with LIRGs having $L_{IR} = 10^{11-12} L_{\odot}$, and ULIRGs having $L_{IR} = 10^{12-13} L_{\odot}$. [U]LIRGs are among the most infrared-luminous objects in the universe, and are thought to be responsible for the majority of the cosmic infrared background and the population of sub-millimeter galaxies at $z > 2$ (Le Floc'h et al., 2005; Soifer et al., 2008). The primary source of the far-infrared radiation is thought to be dust heated by either star formation or an embedded AGN to temperatures of $\sim 50 - 100$ K. The star formation rates in such galaxies can be as high as hundreds of $M_{\odot}$/yr. All OHM host galaxies have far-infrared luminosities in excess of 10^{10} $L_{\odot}$, with 90% of known OHMs having $L_{FIR} > 10^{11}$ $L_{\odot}$ and 20% greater than 10^{12} $L_{\odot}$.

Figure 1.3 shows an example of the properties of a typical OHM: IRAS 14059+2000. The galaxy is a ULIRG with $L_{FIR} = 10^{11.66}$ $L_{\odot}$, lying at redshift $z = 0.1237$. Imaging in near-infrared and optical bands shows a disturbed host galaxy with a bright central nucleus and extended tails that are likely a sign of recent interaction. The megamaser in this galaxy was discovered by the Arecibo survey (Darling & Giovanelli, 2002a) and has a luminosity of $L_{OH} = 10^{3.32}$ $L_{\odot}$, with a rest-frame full-width half-maximum (FWHM) of 161 km s^{-1}. Maps of the radio emission of IRAS 14059+2000 with the VLA (which have an angular resolution of $\sim 1''$) show single peaks for both the continuum and integrated OH line emission that are spatially coincident. Both radio peaks may be slightly offset from the optical/near-IR nucleus.

Among known OHMs, optical and infrared imaging have revealed morphologies similar to that shown in Figure 1.3, often with multiple nuclei and extended tidal features. There are no currently identified optical/near-IR morphological features, however, that conclusively distinguish OHMs from non-masing ULIRGs. The location of the peak radio emission within the galaxy can vary considerably; maps at arcsecond resolution have revealed examples of OHMs in which neither the radio continuum nor the OH line emission is coincident with the optical/near-IR nucleus.

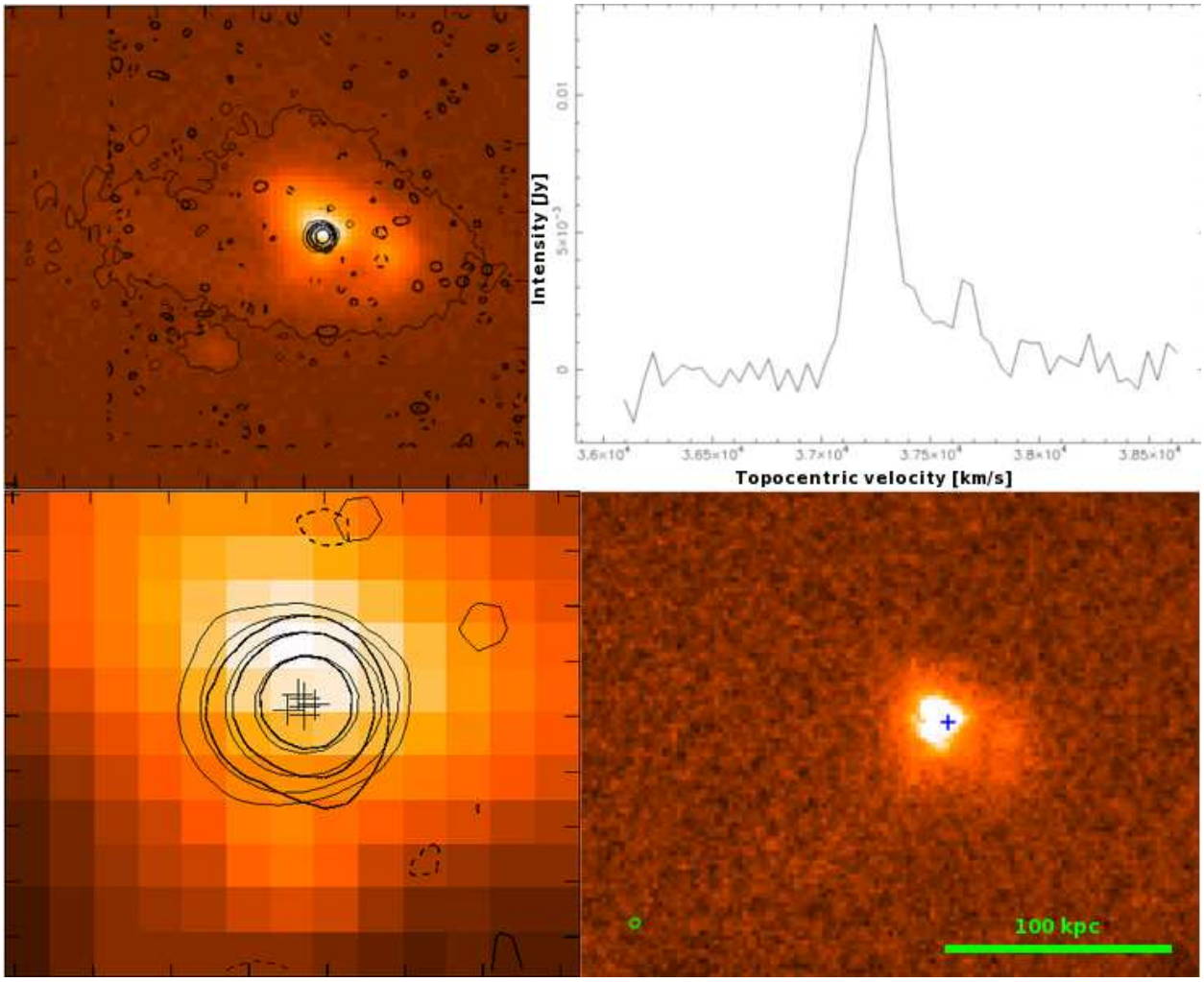

Figure 1.3 Examples of the properties of a "typical" OHM (IRAS 14059+2000). **Top left**: optical i-band image from the Magellan telescope. Dark and light contours show emission from 18-cm continuum and OH line emission, respectively, taken with the VLA. **Bottom left**: a zoomed-in image of the optical/radio emission from the top left. The emission from both the OH line and radio continuum is unresolved in this image, with no significant offset between the two beams. The crosses indicate the location of the peak OH line channel-by-channel, demonstrating no significant velocity gradient in the plane of the sky. **Top right**: spectrum of the integrated OH emission. **Bottom right**: near-infrared (K_s-band) image from the ARC 3.5m telescope. The blue cross indicates the location of the peak integrated OH emission, while the green ellipse represents the VLA beam size ($1.01'' \times 0.92''$). All Magellan and VLA data courtesy J. Darling.

Furthermore, the continuum peak is not always coincident with the OH line emission (J. Darling, priv. comm).

1.5.3 Properties of the OH emission

The luminosity distribution of the OH emission itself is largely a function of the total linewidth ($\Delta\nu$), rather than the peak intensity. The isotropic line luminosity ranges from $L_{OH} = 10\ L_{\odot}$ (the nominal dividing line between OH kilomasers and megamasers) to the brightest known OHM at $L_{OH} = 10^{4.11}\ L_{\odot}$ (Darling & Giovanelli, 2001). The relationship between the OH luminosity and that of its host galaxy is interpreted as a natural result of the pumping models. The strength of any maser will be proportional to the product of the maser pumping mechanism and the stimulated emission rate. In OH masers, the dominant pumping lines are thought to be the radiative transitions at 35 and 53 μm; the stimulated emission rate will be proportional to the number of background radio continuum photons being amplified. The product of the two factors yields:

$$L_{OH} \propto (L_{pump} \times L_{1.6\ GHz}). \tag{1.21}$$

Since the peak energy density of OHM host galaxies peaks in the 50–100 μm range, the total (far)-infrared luminosity of the galaxy is a good proxy for L_{pump}. Furthermore, the radio and infrared luminosities of galaxies show a linear correlation in star-forming galaxies (Condon et al., 1991; Murphy et al., 2009) and thus Equation 1.21 can be simplified to $L_{OH} \propto L_{IR}^2$.

The quadratic relationship between L_{OH} and L_{IR} was assumed for many years to describe the general population of OHMs, and was supposedly supported by empirical observations. However, a quadratic relationship rests on the assumption that the pumping rate is high enough such that each and every background photon undergoes stimulated emission – this is known as *unsaturated* masing. If the pumping rate is much lower than the stimulated emission rate, then the second term drops out and $L_{OH} \propto L_{IR}$. Intermediate levels of saturation would result in $L_{OH} \propto L_{IR}^{\gamma}$, where $1 < \gamma < 2$. Kandalian (1996) demonstrated that previous empirical measurements of the OH-IR luminosity relationship had also not properly accounted for the Malmquist effect, in which

observations of more distant galaxies select preferentially brighter targets in a flux-limited survey. Darling & Giovanelli (2002a) used a larger sample of $\sim$ 100 OHMs to measure an exponent of $\gamma = 1.2 \pm 0.1$, implying a mix of saturated and unsaturated masing. These results were supported by high-resolution VLBI observations of OH megamasers, which showed that the OH emission is a combination of diffuse, unsaturated emission and compact, saturated emission (e.g., Diamond et al., 1999; Pihlström et al., 2001; Rovilos et al., 2003; Klöckner & Baan, 2004).

Linewidths of individual maser spots in OHMs range from several tens of km s^{-1} up to 150 km s^{-1} (Lonsdale, 2002); however, the total velocity widths associated with merging galaxies can exceed 1000 km s^{-1} due to the superposition of many individual maser spots within the telescope beam. Almost all single-dish OHM spectra exhibit multiple components that cannot be fit with a simple one- or two-profile model (e.g., Figure 1.3). For galaxies in which the OH emission has been mapped with VLBI, the angular size of the clouds (< 1 pc) imply internal velocity dispersions on the order of 20 km s^{-1} (Pihlström et al., 2001). This means that individual masing clouds typically have large transverse velocity gradients, as well as local supersonic turbulence which contributes to line overlap (Downes & Solomon, 1998). This is another sign of the violent mergers with which OHMs are associated.

Polarization measurements of OHMs are challenging; although OH is a paramagnetic molecule and displays Zeeman splitting in circular polarization, the fact that single-dish spectra are generally a superposition of many maser spots (each with its own local magnetic field strength and direction) means that the Stokes V components are often blended in observations. Robishaw et al. (2008) succeeded in measuring Zeeman splitting in the 1667 MHz transition of five OHMs, inferring line-of-sight magnetic field strengths of $B_{||} = 0.5 - 18$ mG. These field strengths are similar to those measured in star-forming regions from Galactic OH masers. The number of OHMs with polarization measurements is currently being expanded to all megamasers observable from the declination range of Arecibo (J. McBride & C. Heiles, priv. comm).

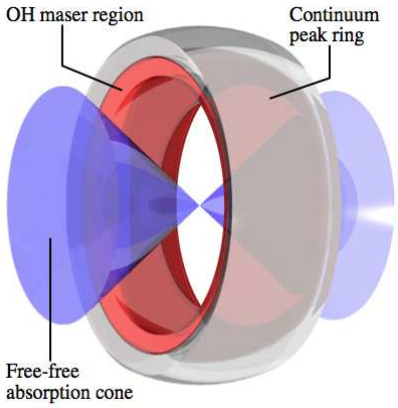

Figure 1.4 Model of the source geometry for the OHM III Zw 35, from Parra et al. (2005). The inner red ring indicates the region in which many OH masing clouds of size < 0.7 pc and with internal velocity dispersions of 60 km s^{-1} are confined. The grey shows an outer ring of smoothly distributed gas emitting in the radio continuum, while the blue represents a bi-cone of free-free absorption. The masing ring has an inner radius of 22 pc, a radial thickness of 3 pc, and rotates at a velocity of 57 km s^{-1}.

1.5.4 Geometry of masing regions

Early theoretical models of OHMs assumed that the megamaser was produced by low-gain ($|\tau| < 2$), unsaturated amplification of background radio continuum by a diffuse foreground. The background continuum is assumed to arise either from the host galaxy nucleus or dispersed areas of star formation, while the foreground screen was composed of many diffuse OH clouds (Baan, 1989; Henkel & Wilson, 1990). These models were later challenged by VLBI observations that showed both compact and diffuse OH emission (Diamond et al., 1999); compact emission spots were was shown to not be spatially coincident with compact radio continuum, as would be expected in a diffuse foreground model. A two-phase model was then proposed in which the compact and diffuse OH spots had separate origins. The diffuse emission was suggested to be unsaturated amplification of the background pumped by infrared radiation, while the compact components were collisionally pumped OH masers associated with shock fronts (Lonsdale et al., 1998).

The current unified model for the OHM emission was initially proposed by Pihlström et al. (2001) and fully developed by Parra et al. (2005). Using VLBI observations of the OHM III Zw 35, they showed that the observed OH distribution and linewidths were consistent with a single phase

of low-opacity clouds arranged in a molecular ring (Figure 1.4). The brighter compact OH emission was shown to arise from points tangent to the observer's line of sight along the ring. Extreme line-to-continuum ratios in these spots are a result of cloud-cloud overlap, which was neglected in the earlier diffuse models. Multiple parsec-scale clouds overlapping along a particular line of sight will rapidly increase the gain. The total OH emission observed will be a function of both small-scale (individual overlapping OH clouds) and large-scale structure (organization of clouds relative to a line of sight) in the host galaxy. The emission is also highly beamed, with the overlap causing $\tau > 5$ sightlines to be visible only within a solid angle of $\Omega \sim 10^{-4}$ sr.

The overlapping clump model currently explains the existence of both compact and diffuse components, the distribution of VLBI-mapped OHM spots, and the observed OH line-to-continuum ratios, hyperfine ratios, and linewidths. However, it does not explain the physical basis for a ring geometry or the ranges in sizes and shapes for individual masing clouds. This model has also only been tested for a handful of galaxies, since VLBI mapping is currently limited to nearby OHMs. There is also no definitive prediction from this model why a particular ULIRG would be predicted to mase, although the viewing angle may play a key role.

1.6 Current research

Although a great deal of progress has been made in understanding maser astrophysics, the field is rapidly growing and many areas of research remain open. Here, I discuss several active areas relevant to the research presented in this dissertation.

While models of the pumping mechanisms have made vast improvements recently, it is still difficult to test direct predictions for these models. For example, the pumping calculations of Lockett & Elitzur (2008) predict specific flux ratios for the 1667/1665 MHz and 1667/1720 MHz transitions in OHMs. However, only five OHMs have published flux densities of the satellite 1720 MHz OH transition, and as a result this flux ratio is not well-constrained. Sensitive measurements of the 18-cm satellite frequencies in large numbers of OHMs would test the accuracy of the pumping model; such data could also be used to potentially constrain the parameters used to generate the model,

including the OH gas density and temperature, the overlapping line widths, and the temperature and distribution of the dust. This would also test whether these parameters are consistent for the population of OHMs as a whole, or whether there is significant variation from galaxy to galaxy.

The nature of the pumping mechanism is related to the question of what distinguishes an OHM from a ULIRG that does not display OH megamaser emission. Recent work by Darling (2007) has shown that OHM host galaxies have the highest mean molecular gas densities among starbursts, suggesting that a possible trigger for OHMs may be related to their ISM gas density. This may be associated to a temporal spike in tidal gas density associated with specific stages in galactic mergers. Ongoing work in this area will involve constraining the OHM lifetime, as well as comparing images of OHMs to numerical simulations in order to identify the specific stage of the density enhancement.

Little is currently known about the population of Galactic-analog masers outside the Milky Way. Isolated cases of H_2O and OH maser emission have been detected for a few galaxies near the Milky Way, including the Large Magellanic Cloud, NGC 253, M82, IC 10, and M33. The current detections, however, are likely to be among the brightest maser sources in their respective galaxies and provide few constraints on the maser population as a whole. It is not known, for example, how the various maser populations scale (if at all) as a function of global star formation rates, metallicity, galaxy mass, or age. The current expectation is that this is only an issue of sensitivity, and that such questions can be answered with the development of more sensitive telescopes. Deep censuses of the maser population, even at the distances of M31 or M33, may require the large collecting area of future observatories such as the Square Kilometer Array.

Finally, the surface is just being scratched in employing masers as astronomical tools. The bright, spatially compact emission from masers makes them excellent candidates for parallax measurements; an extensive series of papers by Reid et al. (2009b) and collaborators have measured geometric distances to multiple star-forming regions in the Milky Way using masers in a variety of species. Their work has revised models of the Milky Way and measurements of its fundamental kinematic parameters, such as the Sun's Galactocentric radius R_0, its circular rotation speed Θ_0,

and the galaxy's enclosed mass. Measurements of Zeeman splitting in maser lines can act as a sensitive astrophysical magnetometer, probing strengths and orientations of magnetic fields from stars to HII regions to nuclear conditions in merging galaxies. Finally, the increasing number of detections of extragalactic masers is answering new questions - OH megamasers trace the gas density and merger fractions in the early Universe, while distances measured to galaxies with H_2O megamasers are being used to make precise measurements of the Hubble constant and constrain the parameters of dark energy. Reid (2007) summarizes these and many other results from the most recent international meeting on astrophysical megamasers - clearly, there is a great deal left to do.

1.7 This work

The topics covered in this thesis address three basic issues within the context of extragalactic maser research: investigating the environments and local physics of masers; using masers as tools to measure other astrophysical quantities; and discovering new masers that can be added to our overall knowledge base.

Chapters 2 and 3 are concerned with OH megamaser environments. I attempt to answer questions such as: What are the physical conditions local to OHM production? What is the difference between an OHM and a non-masing galaxy of similar mass and luminosity? Can the presence of an OHM be inferred from the global properties of its host? Are current theoretical models of OHMs supported by the observational evidence? To address these issues, I used mid-infrared spectroscopic data from the *Spitzer Space Telescope* for a large sample of OHMs and non-masing galaxies. Chapter 2 describes the observations and reduction of the *Spitzer* data. Chapter 3 presents analysis and interpretation of the *Spitzer* data. I identify several spectral features that signal the presence of an OHM and use the mid-infrared data to test new OH pumping models. I also show that OHMs favor a smooth, embedding dust geometry and suggest methods in which these results can be applied for efficient surveys of OHMs in the future.

In Chapter 4, I describe results of a new survey for OHMs at $z \sim 1$, probing distances out to ten times that of the previous OHM record-holder. This is the first systematic survey for OHMs

at these redshifts. The properties of two new OHM discoveries are described, and I discuss the statistics of the many non-detections as well as the measured OHM detection fraction. Finally, I use these results to construct a new OHM luminosity function and show that even non-detections of OHMs are sufficient to place some constraints on the evolution of the overall galaxy merger rate at $z \sim 1$.

The final section of this thesis (Chapter 5) focuses on the utility of masers as precise kinematic probes. Discovery of masers in Local Group galaxies M33 and IC 10 led to the first-ever measurements of their proper motions; however, the proper motion of M31 (Andromeda), the Milky Way's nearest massive neighbor, is still an unknown quantity. Measurements of M31's proper motion and three-dimensional velocity have tremendous implications for the dynamical history of the Local Group (eg, van der Marel & Guhathakurta, 2008). However, no masers that could be used to make a proper motion measurement were known to exist in M31 when I began this thesis. I describe results of a complete OH survey of M31, provide upper limits on the non-detection of any OH masers, and interpret our results in the context of parallel searches for H_2O and CH_3OH masers.

Several appendices are attached to the end of this thesis. Appendix A provides a glossary for abbreviations and terms used. Appendix B gives the calibrated *Spitzer* spectra and additional data tables from Chapters 2 and 3. Finally, Appendix C presents the Green Bank Telescope spectra of all galaxies from Chapter 4 in which no OH was detected. The reduced spectra are provided here as a possible resource for future researchers.

Since the topics covered in this thesis are fairly distinct from each other, discussions of future work and upcoming observations are given separately for Chapters 3, 4, and 5. Results from Chapters 2 and 3 have already been published (Willett et al., 2011a,b); Chapters 4 and 5 are expected to be separately submitted for publication during the summer of 2011.

Chapter 2

Mid-infrared observations of OH megamaser host galaxies

OH megamasers (OHMs) are 18-cm masers with integrated line luminosities on the order of $10^1 - 10^4$ $L_\odot$. They are an extremely rare phenomenon in the local universe, with roughly one hundred currently known out to a redshift of $z = 0.265$ (Baan et al., 1992b). All OHMs, including the more powerful "gigamasers" ($L_{OH} > 10^4$ $L_\odot$) are associated with starburst nuclei in merging galaxies. OHMs have been identified in many different types of nuclear environments as classified by optical spectra, but the merging galaxies are without exception (ultra)luminous infrared galaxies ([U]LIRGs). Since OHMs are signposts of gas-rich merging galaxies, their presence can also indicate the existence of associated phenomena including massive black hole mergers and highly obscured circumnuclear starbursts (Darling, 2007). OHMs are a powerful tool in this respect due in large part to their ability to be seen at cosmic distances. In order to employ OHMs as tracers, however, the assumption must be made that the OH line properties remain constant as a function of cosmic time and host environment. An explanation of the physical mechanisms and conditions responsible for distinguishing OHMs from non-masing ULIRGs is thus vital for understanding both the megamaser phenomenon and the associated merger characteristics.

Spectroscopic studies of the mid-infrared emission in the host galaxies offer multiple diagnostics which can provide clues to the nature of the maser pumping mechanism and the associated OH emission. We used the Infrared Spectrograph (IRS) aboard the *Spitzer Space Telescope* (Werner et al., 2004) to study merging ULIRGs. Since the dusty nuclear regions are typically obscured at optical wavelengths, mid-infrared observations can yield valuable information specific to the loca-

tions in which the OHMs are generated. These include measurements of the dust temperature and optical depth (from broadband photometry and absorption features), the excitation and temperature of the gas (molecular and fine-structure atomic lines), and high-ionization lines that can signal the presence of an active galactic nucleus (AGN), a possible heating source for the dust.

This data chapter presents full low- and high-resolution IRS spectra for 51 OHMs and 15 non-masing ULIRGs, along with measurements of their mid-infrared properties. §2.1 describes the sample selection. §2.2 gives details of the IRS observations and §2.3 describes the data reduction process. §2.4 gives the results of the observations, along with example spectra and full data tables of the measured mid-infrared features. §2.5 gives a summary of the findings. The full analysis of the data, including statistical comparisons between the two samples and discussion of the results in the context of theoretical models, is given in Chapter 3.

The majority of this research in this chapter has been published in the *Astrophysical Journal Supplement Series* as Willett et al. (2011a).

2.1 The sample

The OHM host galaxies selected for IRS observations were primarily drawn from the Arecibo OHM survey (Darling & Giovanelli, 2002a,b). We selected well-studied OHMs with unambiguous maser detections and large amounts of ancillary data (including OH line and radio continuum maps, near-infrared imaging, and optical imaging and spectroscopy) to maximize scientific return on the sample. A lower threshold of $L_{OH} > 10^{1.6}\ L_{\odot}$ also eliminated extragalactic "kilomasers" from the sample, which are likely powered by different radiative processes than megamasers (Henkel & Wilson, 1990).

In order to be detected in reasonable integration times using the IRS, we required that all potential targets have $S(60\ \mu\mathrm{m}) > 0.8$ Jy as measured by the IRAS satellite. After removing objects already observed by the IRS (largely through the GTO ULIRG program; *e.g.,* Armus et al., 2007), we observed 24 galaxies in the redshift range $0.1 < z < 0.2$.

We supplemented these galaxies with additional spectra of OHM hosts publicly available

through the *Spitzer* archive. To ensure uniformity of the data, we selected only galaxies from the archive that had full coverage with both the IRS low- and high-resolution modules. As of March 2008, the publicly available data from the archive yielded an additional 27 OHM galaxies (Table 2.1).

Table 2.1. Radio, optical, and far-infrared properties of OHMs and non-masing galaxies

	IRAS FSC	RA J2000.0	Dec J2000.0	$z_\odot$ [a]	D_L [h_{70}^{-1} Mpc]	log L_{FIR} [b] [$h_{70}^{-2} L_\odot$]	log L_{OH} [c] [$h_{70}^{-2} L_\odot$]	$f_{1.4\ GHz}$ [d] [mJy]
OHMs	IRAS 01355−1814	01 37 57.4	−17 59 21	0.191	929	12.49	2.75	< 5.0
	IRAS 01418+1651	01 44 30.5	+17 06 05	0.0274	115	11.63	2.71	40.6
	IRAS 01562+2528	01 59 02.6	+25 42 37	0.1658	788	12.19	3.31	6.3
	IRAS 02524+2046	02 55 17.1	+20 58 43	0.1815	873	12.07−12.54	3.80	2.9
	IRAS 03521+0028	03 54 42.2	+00 37 03	0.1522	718	12.59	2.49	6.7
	IRAS 04121+0223	04 14 47.1	+02 30 36	0.1216	568	11.69−11.96	2.39	3.1
	IRAS 04454−4838	04 46 49.5	−48 33 33	0.0529	235	11.89	2.95	< 5.0
	IRAS 06487+2208	06 51 45.8	+22 04 27	0.1437	678	12.34	2.87	10.8
	IRAS 07163+0817	07 19 05.5	+08 12 07	0.1107	515	11.79	2.43	3.5
	IRAS 07572+0533	07 59 57.2	+05 25 00	0.1894	926	12.31	2.80	5.0
	IRAS 08201+2801	08 23 12.6	+27 51 40	0.1680	808	12.26	3.51	16.7
	IRAS 08449+2332	08 47 51.0	+23 21 06	0.1510	723	12.05	2.65	6.1
	IRAS 08474+1813	08 50 18.3	+18 02 01	0.1450	692	12.19	2.76	4.2
	IRAS 09039+0503	09 06 34.2	+04 51 25	0.1250	589	12.16	2.88	6.6
	IRAS 09539+0857	09 56 34.3	+08 43 06	0.1290	608	12.09	3.53	9.5
	IRAS 10035+2740	10 06 26.3	+27 25 46	0.1662	794	12.26	2.55	6.3
	IRAS 10039−3338	10 06 04.8	−33 53 15	0.0341	154	11.74	2.98	24.7
	IRAS 10173+0828	10 20 00.2	+08 13 34	0.0480	222	11.86	2.77	10.8
	IRAS 10339+1548	10 36 37.9	+15 32 42	0.1965	969	12.35	2.71	5.1
	IRAS 10378+1109	10 40 29.2	+10 53 18	0.1362	646	12.35	3.35	8.9
	IRAS 10485−1447	10 51 03.1	−15 03 22	0.1330	629	12.23	2.99	4.4
	IRAS 11028+3130	11 05 37.5	+31 14 32	0.1990	975	12.39	3.03	5.0
	IRAS 11180+1623	11 20 41.7	+16 06 57	0.1660	801	12.27	2.40	4.2
	IRAS 11524+1058	11 55 02.8	+10 41 44	0.1784	868	12.19	3.04	5.0
	IRAS 12018+1941	12 04 24.5	+19 25 10	0.1687	814	12.48	2.96	6.5
	IRAS 12032+1707	12 05 47.7	+16 51 08	0.2170	1082	12.64	4.21	28.7
	IRAS 12112+0305	12 13 46.0	+02 48 38	0.0730	335	12.38	3.04	23.8
	IRAS 12540+5708	12 56 14.2	+56 52 25	0.0422	188	12.42	2.94	309.9
	IRAS 13218+0552	13 24 19.9	+05 37 05	0.2051	1011	12.44	3.50	5.3
	IRAS 13428+5608	13 44 42.1	+55 53 13	0.0378	167	12.18	2.61	145.4
	IRAS 13451+1232	13 47 33.3	+12 17 24	0.1220	571	12.21	2.46	5398.0

Table 2.1 (cont'd)

	IRAS FSC	RA J2000.0	Dec J2000.0	$z_\odot$ [a]	D_L [h_{70}^{-1} Mpc]	log L_{FIR} [b] [$h_{70}^{-2} L_\odot$]	log L_{OH} [c] [$h_{70}^{-2} L_\odot$]	$f_{1.4\ GHz}$ [d] [mJy]
	IRAS 14059+2000	14 08 18.7	+19 46 23	0.1237	580	11.94	3.40	7.5
	IRAS 14070+0525	14 09 31.2	+05 11 32	0.2644	1346	12.87	4.50	5.2
	IRAS 14553+1245	14 57 43.4	+12 33 16	0.1249	585	11.87	2.33	3.8
	IRAS 15327+2340	15 34 57.1	+23 30 11	0.0181	80	12.22	2.65	326.8
	IRAS 16090−0139	16 11 40.5	−01 47 06	0.1339	628	12.57	3.52	20.9
	IRAS 16255+2801	16 27 38.1	+27 54 52	0.1340	627	11.94	2.62	5.0
	IRAS 16300+1558	16 32 21.4	+15 51 45	0.2417	1212	12.80	2.91	7.9
	IRAS 17207−0014	17 23 21.9	−00 17 01	0.0428	188	12.45	3.10	82.4
	IRAS 18368+3549	18 38 35.4	+35 52 20	0.1162	536	12.24	2.91	21.0
	IRAS 18588+3517	19 00 41.2	+35 21 27	0.1067	489	11.92	2.58	5.9
	IRAS 20100−4156	20 13 29.5	−41 47 35	0.1296	603	12.68	4.13	< 5.0
	IRAS 20286+1846	20 30 55.5	+18 56 46	0.1347	633	12.06	3.47	5.0
	IRAS 21077+3358	21 09 49.0	+34 10 20	0.1764	846	12.10−12.24	3.32	9.4
	IRAS 21272+2514	21 29 29.4	+25 27 50	0.1508	709	11.99−12.14	3.71	4.4
	IRAS 22055+3024	22 07 49.7	+30 39 40	0.1269	587	12.19	2.79	6.4
	IRAS 22116+0437	22 14 09.9	+04 52 24	0.1939	937	12.12−12.32	2.83	8.4
	IRAS 22491−1808	22 51 49.2	−17 52 23	0.0778	346	12.19	2.46	5.9
	IRAS 23028+0725	23 05 20.4	+07 41 44	0.1496	701	11.86−12.06	3.34	19.5
	IRAS 23233+0946	23 25 56.2	+10 02 49	0.1279	591	12.18	2.80	11.6
	IRAS 23365+3604	23 39 01.3	+36 21 09	0.0645	283	12.19	2.52	28.7
Non-masing	IRAS 00164−1039	00 18 50.4	−10 22 08	0.0272	113	11.36	< 1.25	< 5.0
	IRAS 01572+0009	01 59 50.2	+00 23 41	0.1630	774	12.47	< 2.12	26.7
	IRAS 05083+7936	05 16 46.4	+79 40 13	0.0537	237	11.93	< 1.94	41.4
	IRAS 06538+4628	06 57 34.4	+46 24 11	0.0214	93.6	11.24	< 0.89	64.3
	IRAS 08559+1053	08 58 41.8	+10 41 22	0.1480	705	12.18	< 1.72	< 5.0
	IRAS 09437+0317	09 46 20.6	+03 03 30	0.0205	93.5	11.15	< 1.01	< 5.0
	IRAS 10565+2448	10 59 18.1	+24 32 34	0.0431	194	12.04	< 1.66	57.0
	IRAS 11119+3257	11 14 38.9	+32 41 33	0.1890	923	12.48	< 2.07	110.4
	IRAS 13349+2438	13 37 18.7	+24 23 03	0.1076	500	11.39	< 1.72	20.0
	IRAS 15001+1433	15 02 31.9	+14 21 35	0.1627	781	12.42	< 2.04	16.9

Table 2.1 (cont'd)

IRAS FSC	RA J2000.0	Dec J2000.0	$z_{\odot}$ [a]	D_L [h_{70}^{-1} Mpc]	log L_{FIR} [b] [$h_{70}^{-2} L_{\odot}$]	log L_{OH} [c] [$h_{70}^{-2} L_{\odot}$]	$f_{1.4\ GHz}$ [d] [mJy]
IRAS 15206+3342	15 22 38.0	+33 31 36	0.1244	582	12.13	< 1.75	11.2
IRAS 20460+1925	20 48 17.3	+19 36 54	0.1807	868	12.03	< 2.15	18.9
IRAS 23007+0836	23 03 15.6	+08 52 26	0.0163	64.9	11.43	< 0.63	181.0
IRAS 23394−0353	23 42 00.8	−03 36 55	0.0232	95.4	11.11	< 1.18	< 5.0
IRAS 23498+2423	23 52 26.0	+24 40 17	0.2120	1037	12.44	< 2.25	6.8

[a]Heliocentric optical redshift (Darling & Giovanelli, 2002a).

[b]Computed according to the prescription of Sanders & Mirabel (1996), with a scale factor of $C = 1.6$. IRAS photometry is from Sanders et al. (2003); a range in L_{FIR} means that the object was not detected by IRAS at 100 μm.

[c]OH fluxes are from Darling & Giovanelli (2002a,b); limits are computed according to Equation 2.1.

[d]Flux densities at 1.4 GHz are from the NRAO VLA Sky Survey (Condon et al., 1998).

In order to provide a baseline for analysis of the OHMs, we also identified a control sample of ULIRGs that showed no megamaser emission above a firm limit. To identify these galaxies, we drew on non-detections from OH surveys by Baan et al. (1992a); Staveley-Smith et al. (1992); Darling & Giovanelli (2000, 2001, 2002a) and Kent et al. (2002). The upper limit for OH emission is conservatively derived from the rms noise in the spectrum at 1667 MHz, assuming a boxcar line profile with a linewidth $\Delta v = 150$ km s^{-1} and a 1.5σ detection at a luminosity distance D_L:

$$L_{OH}^{max} = 4\pi D_L^2 (1.5\sigma) \left(\frac{\Delta v}{c}\right) \left(\frac{\nu_0}{1+z}\right) \tag{2.1}$$

For this control sample, we set an upper limit of $L_{OH}^{max} < 10^{2.3}\ L_{\odot}$; this limit compromises between ensuring that all but the faintest megamaser emission is excluded and yielding a reasonable number of objects in the control sample for statistical analysis. All 51 OHMs in our IRS sample have L_{OH} above this limit.

In addition to selecting galaxies based on OH non-detection, we imposed two additional criteria to ensure that the control sample was as similar as possible to the OHM hosts. Firstly, we set a lower limit on the far-infrared luminosity (Sanders & Mirabel, 1996) of the non-masing galaxies as measured by their IRAS fluxes. OHMs occur exclusively in IR-bright galaxies, due to the fact that the maser is pumped primarily by rotational transitions of a few hundred K above

the ground state (Baan et al., 1982; Henkel et al., 1987). Darling & Giovanelli (2002a) show that the relationship between the OH and infrared luminosities is a power law with $L_{OH} \propto L_{FIR}^{1.2}$. Since no OHM observed with the IRS has $L_{FIR} < 10^{11} L_{\odot}$, we established this as the lower limit for inclusion in the non-masing sample.

Secondly, a cutoff in redshift space is applied to sample a sufficiently large volume ($V \sim 1\,\mathrm{Gpc}^3$) in order to avoid systematic effects such as the Malmquist bias. The available data in the archive contained many more galaxies at lower redshifts ($z < 0.05$) than those further away. To avoid over-weighting the control sample towards galaxies at low redshifts, we sorted galaxies that met the L_{OH}^{max} and L_{IR} criteria into bins of $\Delta z = 0.02$. For bins where the number of non-masing galaxies exceeded those of OHMs, we randomly removed objects from the non-masing bins until the numbers were equal. This reduced the control sample to 1 galaxy at $0 < z < 0.02$ and 4 galaxies at $0.02 < z < 0.04$; for all other redshift bins, no such adjustments were necessary. As of March 2008, there existed 15 suitable candidates in the *Spitzer* archive qualifying for the non-masing control sample (Table 2.1). Figure 2.1 shows the distribution of OH luminosity for all objects as a function of redshift; for the non-masing galaxies, we display upper limits as computed in Equation 2.1.

Throughout this chapter, we assume the WMAP5 cosmology with $H_0 = 70.5$ km s^{-1} Mpc^{-1}, $\Omega_M = 0.274$, and $\Omega_\Lambda = 0.726$ (Hinshaw et al., 2009).

2.2 *Spitzer* IRS observations

We observed 24 OHMs with the IRS from August 2006 through December 2007. The IRS contains four modules in two different spectroscopic resolutions: low- (LR) and high-resolution (HR) (Houck et al., 2004). The short-high (SH) and long-high (LH) modules operate at a resolution of $R \sim 600$; the short-low (SL1 & SL2) and long-low (LL1 & LL2) modules operate at resolutions ranging from $R \sim 56-127$, depending on the observing wavelength. Two orders, SL3 ($7.3-8.7$ μm) and LL3 ($19.4-21.7$ μm), cover the overlapping range between the first and second orders in both SL and LL. We used these only as checks for the absolute flux calibration between the different orders.

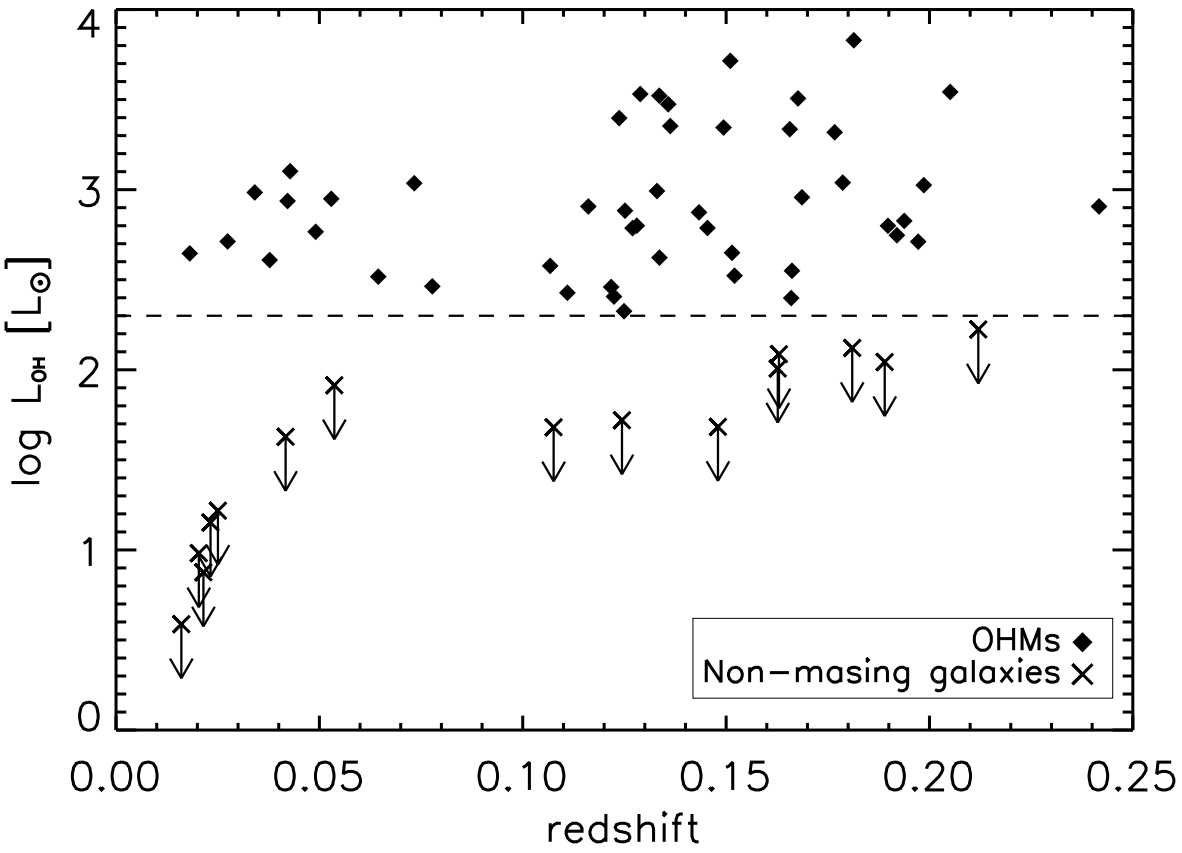

Figure 2.1 Distribution of integrated OH luminosity for the IRS samples as a function of redshift. For non-masing galaxies, the OH luminosity is an upper limit calculated from Equation 2.1. The dashed line at $L_{OH} = 10^{2.3}\ L_\odot$ is the upper limit on possible OH emission for the non-masing control sample.

All targets used the Staring Mode Astronomical Observing Template (AOT) with the galaxies placed at two nod positions approximately one-third and two-thirds the length of the slit. We observed targets in all six modules as well as an equal-time, off-target exposure in the LH module to be used for sky subtraction.

Although the majority of our sources had no previous IRAS detections in either the 12 or 25 μm bands, we extrapolated the likely flux based on the colors of ULIRGs at similar redshifts and the measured fluxes at 60 μm. We chose cycle times intended to yield signal-to-noise ratios of $S/N = 50 - 100$ for the low-resolution modules and $S/N \geq 10$ for the high-resolution modules, allowing for accurate measurement of faint emission and absorption features, as well as accurate spectral decomposition.

For the 24 objects in the dedicated OHM program, we took dedicated sample-up-the-ramp (SUR) peakup observations in both the blue (16 μm) and red (22 μm) filters in sample-up-the-ramp (SUR) mode for photometric calibration of the spectra. The SUR peakups did not coincide in time with the spectroscopy for the majority of targets. None of the galaxies selected from the *Spitzer* archive possessed SUR peakup data; 16 archived galaxies have double correlated sampling (DCS) peakups with slightly worse photometric accuracy than those with SUR data. Only one galaxy, IRAS 10173+0828, had no peakup observations of any kind. Measured peakup fluxes are given in Table 2.3.

The *Spitzer* beam is diffraction limited past 6 μm, with slit widths for the spectral modules between $3 - 11''$. The vast majority of the nuclei in merging ULIRGs have angular separations less than the instrument PSF, and thus can be treated as point sources. For the few galaxies close enough to be resolved, we chose staring mode observations centered on the IR-dominant nuclear region of the galaxy. The only available observations of the double nucleus in IRAS 10485−1447 were centered on the western nucleus. Details of the IRS observations are given in Table 2.2.

Five galaxies with confirmed OHM emission (IRAS 09320+6134, IRAS 16399−0937, IRAS 17540+2935, IRAS 20550+1656, IRAS 23019+3405) had IRS observations that were analyzed in our original program. However, the OH luminosity for these five targets lies below our eventual

cutoff for the L_{OH}^{max} in the sample of non-masing galaxies. We therefore removed these galaxies from our sample, and results from these targets are not used in this analysis. Mid-infrared data for these galaxies is available from the author upon request.

Table 2.2. IRS observation log

Object	Date	Peakup type	SL1	SL2	LL1	LL2	SH	LH	Program
IRAS 01355−1814		BPU-offset	60 × 2	60 × 2	30 × 2	30 × 2	120 × 4	240 × 5	4,6
IRAS 01418+1651		BPU	14 × 2	14 × 2	14 × 4	14 × 4	120 × 5	60 × 7	2,3
IRAS 01562+2528	2007 Sep 09	BPU-offset	14 × 7	14 × 7	30 × 3	30 × 3	120 × 2	60 × 2	1
IRAS 02524+2046	2007 Sep 09	BPU	14 × 7	14 × 7	30 × 3	30 × 3	120 × 2	60 × 2	1
IRAS 03521+0028		BPU-offset	60 × 2	60 × 2	30 × 3	30 × 3	120 × 3	60 × 4	4
IRAS 04121+0223	2007 Oct 05	BPU-offset	60 × 2	60 × 2	30 × 3	30 × 3	120 × 2	60 × 2	1
IRAS 04454−4838		BPU	60 × 2	60 × 2	30 × 3	30 × 3	120 × 3	240 × 2	3
IRAS 06487+2208	2007 May 04	BPU-offset	14 × 7	14 × 7	30 × 3	30 × 3	120 × 2	60 × 2	1
IRAS 07163+0817	2007 May 03	BPU	14 × 6	14 × 6	30 × 3	30 × 3	120 × 2	60 × 2	1
IRAS 07572+0533	2007 May 04	BPU	14 × 6	14 × 6	30 × 3	30 × 3	120 × 2	60 × 2	1
IRAS 08201+2801	2007 May 03	BPU-offset	14 × 7	14 × 7	30 × 3	30 × 3	120 × 2	60 × 2	1
IRAS 08449+2332	2007 May 04	BPU-offset	14 × 6	14 × 6	30 × 3	30 × 3	120 × 2	60 × 2	1
IRAS 08474+1813	2007 Dec 05	BPU	14 × 6	14 × 6	30 × 3	30 × 3	120 × 2	60 × 2	1
IRAS 09039+0503		BPU	60 × 2	60 × 2	30 × 4	30 × 4	120 × 4	240 × 3	5,6
IRAS 09539+0857		BPU	60 × 2	60 × 7	30 × 4	30 × 4	120 × 3	240 × 3	5,6
IRAS 10035+2740	2007 Jun 09	BPU-offset	14 × 7	14 × 7	30 × 3	30 × 3	120 × 2	60 × 2	1
IRAS 10039−3338		BPU	14 × 6	14 × 6	14 × 4	14 × 4	30 × 6	60 × 2	3
IRAS 10173+0828		none	60 × 1	60 × 1	14 × 4	14 × 4	120 × 4	60 × 12	3,7,8
IRAS 10339+1548	2007 Jun 08	BPU-offset	14 × 7	14 × 7	30 × 3	30 × 3	120 × 2	60 × 2	1
IRAS 10378+1109		BPU-offset	60 × 2	60 × 2	30 × 3	30 × 3	120 × 3	60 × 4	4
IRAS 10485−1447		BPU	60 × 2	60 × 2	30 × 4	30 × 4	120 × 2	240 × 2	5,6
IRAS 11028+3130	2007 Jun 09	BPU-offset	60 × 2	60 × 2	30 × 3	30 × 3	120 × 2	60 × 2	1
IRAS 11180+1623	2007 Jun 08	BPU-offset	14 × 7	14 × 7	30 × 3	30 × 3	120 × 2	60 × 2	1
IRAS 11524+1058	2007 Jun 12	BPU-offset	14 × 7	14 × 7	30 × 3	30 × 3	120 × 2	60 × 2	1
IRAS 12018+1941		BPU-offset	60 × 1	60 × 1	30 × 3	30 × 3	120 × 3	60 × 4	4
IRAS 12032+1707		BPU-offset	60 × 2	60 × 2	30 × 2	30 × 2	120 × 3	240 × 3	4,6
IRAS 12112+0305		BPU-offset	14 × 3	14 × 3	30 × 2	30 × 2	120 × 2	60 × 4	4
IRAS 12540+5708		BPU	14 × 2	14 × 2	6 × 5	6 × 5	30 × 6	60 × 4	9
IRAS 13218+0552		BPU-offset	60 × 1	60 × 1	30 × 3	30 × 3	120 × 3	60 × 4	4
IRAS 13428+5608		BPU	14 × 2	14 × 2	14 × 2	14 × 2	30 × 6	60 × 4	4
IRAS 13451+1232		BPU	14 × 3	14 × 3	30 × 2	30 × 2	30 × 6	60 × 4	4
IRAS 14059+2000	2007 Jul 31	BPU-offset	60 × 2	60 × 2	30 × 3	30 × 3	120 × 2	60 × 2	1

Table 2.2 (cont'd)

Object	Date	Peakup type	SL1	SL2	LL1	LL2	SH	LH	Program
IRAS 14070+0525		BPU-offset	60 × 2	60 × 2	30 × 2	30 × 2	120 × 3	240 × 2	4
IRAS 14553+1245	2007 Jul 31	BPU	60 × 2	60 × 2	30 × 3	30 × 3	120 × 2	60 × 2	1
IRAS 15327+2340		BPU	14 × 3	14 × 3	6 × 5	6 × 5	30 × 6	60 × 4	10
IRAS 16090−0139		BPU-offset	60 × 1	60 × 1	30 × 3	30 × 3	120 × 2	60 × 4	4
IRAS 16255+2801	2006 Sep 17	BPU	60 × 2	60 × 2	30 × 3	30 × 3	120 × 2	60 × 2	1
IRAS 16300+1558		BPU-offset	60 × 2	60 × 2	30 × 5	30 × 5	120 × 4	240 × 4	4,6
IRAS 17207−0014		BPU	14 × 3	14 × 3	14 × 3	30 × 2	30 × 6	60 × 4	4
IRAS 18368+3549	2007 May 01	BPU	60 × 2	60 × 2	30 × 3	30 × 3	120 × 2	60 × 2	1
IRAS 18588+3517	2006 Nov 20	BPU	60 × 2	60 × 2	30 × 3	30 × 3	120 × 2	60 × 2	1
IRAS 20100−4156		BPU-offset	60 × 1	60 × 1	30 × 2	30 × 2	120 × 2	60 × 4	4
IRAS 20286+1846	2006 Nov 20	BPU	60 × 2	60 × 2	30 × 3	30 × 3	120 × 2	60 × 2	1
IRAS 21077+3358	2007 Jun 13	BPU	60 × 2	60 × 2	30 × 3	30 × 3	120 × 2	60 × 2	1
IRAS 21272+2514		BPU-offset	60 × 2	60 × 2	30 × 3	30 × 3	120 × 2	240 × 1	4,11
IRAS 22055+3024	2007 Jun 27	BPU	60 × 2	60 × 2	30 × 3	30 × 3	120 × 2	60 × 2	1
IRAS 22116+0437	2006 Dec 21	BPU-offset	60 × 2	60 × 2	30 × 3	30 × 3	120 × 2	60 × 2	1
IRAS 22491−1808		BPU-offset	60 × 1	60 × 1	30 × 2	30 × 2	120 × 2	60 × 4	4
IRAS 23028+0725	2006 Dec 20	BPU	14 × 7	14 × 7	30 × 3	30 × 3	120 × 2	60 × 2	1
IRAS 23233+0946		BPU	60 × 2	60 × 2	30 × 4	30 × 4	120 × 5	240 × 4	5,6
IRAS 23365+3604		BPU	14 × 3	14 × 3	30 × 2	30 × 2	30 × 6	60 × 4	4
IRAS 00163−1039		BPU	14 × 3	14 × 3	14 × 2	14 × 2	30 × 3	60 × 2	3
IRAS 01572+0009		BPU	14 × 3	14 × 3	30 × 2	30 × 2	30 × 6	60 × 4	4
IRAS 05083+7936		BPU	14 × 6	14 × 6	14 × 4	14 × 4	30 × 6	60 × 2	3
IRAS 06538+4628		BPU	14 × 3	14 × 3	14 × 2	14 × 2	30 × 3	60 × 2	3
IRAS 08559+1053		BPU-offset	60 × 2	60 × 2	30 × 3	30 × 3	120 × 3	60 × 4	12
IRAS 09437+0317		BPU	60 × 2	60 × 2	30 × 3	30 × 3	120 × 3	240 × 2	3
IRAS 10565+2448		BPU	14 × 3	14 × 3	30 × 2	30 × 2	30 × 6	60 × 4	4
IRAS 11119+3257		BPU	60 × 1	60 × 1	30 × 3	30 × 3	120 × 3	60 × 4	4
IRAS 13349+2438		BPU	14 × 5	14 × 5	14 × 5	14 × 5	120 × 5	60 × 10	13
IRAS 15001+1433		BPU-offset	60 × 2	60 × 2	30 × 3	30 × 3	120 × 3	60 × 4	4
IRAS 15206+3342		BPU-offset	60 × 1	60 × 1	30 × 3	30 × 3	120 × 3	60 × 4	4
IRAS 20460+1925		BPU	14 × 5	14 × 5	14 × 5	14 × 5	120 × 5	60 × 10	13
IRAS 23007+0836		BPU	14 × 2	14 × 2	6 × 5	6 × 5	30 × 4	60 × 2	14

Table 2.2 (cont'd)

Object	Date	Peakup type	SL1	SL2	LL1	LL2	SH	LH	Program
IRAS 23394−0353		BPU	30 × 6	30 × 6	60 × 2	60 × 2	14 × 6	14 × 4	3
IRAS 23498+2423		BPU-offset	60 × 2	60 × 2	30 × 2	30 × 2	120 × 3	240 × 2	4

Note. — *Spitzer* archival data are from programs: (1) 30407 (PI: J. Darling); (2) - 3237 (PI: E. Sturm); (3) - 30323 (PI: L. Armus); (4) - 105 (PI: J. Houck); (5) - 2306 (PI: M. Imanishi); (6) - 3187 (PI: S. Veilleux); (7) - 3605 (PI: C. Bradford); (8) - 20549 (PI: R. Joseph); (9) - 1442 (PI: L. Armus); (10) - 1444 (PI: L. Armus); (11) - 20375 (PI: L. Armus); (12) - 666 (PI: J. Houck); (13) - 61 (PI: G. Rieke); (14) - 14 (PI: J. Houck). Exposure times for all modules are given as seconds per cycle × number of cycles.

Table 2.3. IRS photometry and continuum measurements

Object	16 μm PU [mJy]	22 μm PU [mJy]	PU type	α_{15-6}	α_{30-20}	S/N
IRAS 01355−1814	...	45.5	DCS	2.8 ± 0.3	5.2 ± 0.8	75
IRAS 01418+1651	...	...	...	2.2 ± 0.3	5.2 ± 0.8	18
IRAS 01562+2528	6.1	13.0	SUR	1.8 ± 0.3	5.1 ± 0.8	11
IRAS 02524+2046	10.6	21.7	SUR	2.0 ± 0.4	5.7 ± 1.0	25
IRAS 03521+0028	25.6	...	DCS	2.3 ± 0.4	5.5 ± 0.8	63
IRAS 04121+0223	10.5	22.6	SUR	2.6 ± 0.1	5.9 ± 0.5	21
IRAS 04454−4838	...	...	...	2.7 ± 0.4	6.1 ± 0.9	37
IRAS 06487+2208	85.0	177.5	SUR	2.4 ± 0.2	3.6 ± 0.8	48
IRAS 07163+0817	12.3	28.8	SUR	2.5 ± 0.3	4.8 ± 1.0	26
IRAS 07572+0533	52.1	103.0	SUR	2.6 ± 0.3	3.0 ± 0.7	55
IRAS 08201+2801	61.8	74.3	SUR	2.2 ± 0.2	4.5 ± 0.7	37
IRAS 08449+2332	26.6	48.2	SUR	2.2 ± 0.2	4.4 ± 0.4	52
IRAS 08474+1813	9.5	28.7	SUR	2.2 ± 0.5	6.5 ± 0.6	30
IRAS 09039+0503	86.7	...	DCS	1.8 ± 0.5	5.5 ± 0.7	41
IRAS 09539+0857	...	...	...	2.2 ± 0.1	6.0 ± 0.3	36
IRAS 10035+2740	9.2	22.8	SUR	2.1 ± 0.2	6.0 ± 0.5	23
IRAS 10039−3338	...	...	...	-0.1 ± 0.1	5.4 ± 0.3	17
IRAS 10173+0828	...	...	...	2.6 ± 0.4	6.4 ± 1.0	48
IRAS 10339+1548	10.7	28.1	SUR	2.5 ± 0.3	5.1 ± 0.7	22
IRAS 10378+1109	...	114.8	DCS	2.0 ± 0.3	4.5 ± 0.7	35
IRAS 10485−1447	...	...	...	2.5 ± 0.3	4.8 ± 0.8	75
IRAS 11028+3130	4.8	13.0	SUR	2.4 ± 0.2	7.0 ± 0.6	26
IRAS 11180+1623	14.8	33.6	SUR	2.2 ± 0.3	5.6 ± 0.9	15
IRAS 11524+1058	8.2	14.8	SUR	1.5 ± 0.4	6.1 ± 0.8	20
IRAS 12018+1941	121.7	...	DCS	3.0 ± 0.3	2.9 ± 0.4	63
IRAS 12032+1707	...	73.9	DCS	2.2 ± 0.3	4.2 ± 0.7	42
IRAS 12112+0305	91.9	...	DCS	2.3 ± 0.3	5.3 ± 0.7	42
IRAS 12540+5708	...	...	...	1.6 ± 0.3	2.4 ± 0.7	30
IRAS 13218+0552	212.9	...	DCS	0.6 ± 0.3	2.4 ± 0.7	100
IRAS 13428+5608	...	...	...	1.9 ± 1.3	4.6 ± 0.6	12
IRAS 13451+1232	...	...	...	2.3 ± 0.4	1.9 ± 0.7	50

Table 2.3 (cont'd)

Object	16 μm PU [mJy]	22 μm PU [mJy]	PU type	α_{15-6}	α_{30-20}	S/N
IRAS 14059+2000	12.2	26.3	SUR	1.1 ± 0.6	4.9 ± 0.8	20
IRAS 14070+0525	...	30.1	DCS	1.6 ± 0.3	5.6 ± 0.5	33
IRAS 14553+1245	28.7	61.2	SUR	2.0 ± 0.7	4.3 ± 0.7	22
IRAS 15327+2340	...	...	...	2.4 ± 0.2	5.5 ± 0.4	17
IRAS 16090−0139	71.4	...	DCS	1.3 ± 0.4	4.6 ± 0.6	59
IRAS 16255+2801	16.0	36.7	SUR	1.4 ± 0.3	4.7 ± 0.6	22
IRAS 16300+1558	...	35.0	DCS	1.7 ± 0.5	5.6 ± 0.9	31
IRAS 17207−0014	...	...	...	1.8 ± 0.6	6.2 ± 0.6	28
IRAS 18368+3549	26.6	49.8	SUR	1.7 ± 0.5	5.4 ± 0.8	29
IRAS 18588+3517	43.6	92.1	SUR	1.5 ± 0.3	4.8 ± 0.8	28
IRAS 20100−4156	86.7	...	DCS	1.9 ± 0.2	5.2 ± 0.7	73
IRAS 20286+1846	11.4	22.0	SUR	2.3 ± 0.3	5.8 ± 0.6	20
IRAS 21077+3358	31.1	62.1	SUR	2.8 ± 0.3	4.2 ± 0.6	52
IRAS 21272+2514	...	39.0	DCS	2.0 ± 0.3	5.0 ± 0.7	36
IRAS 22055+3024	54.5	132.4	SUR	2.7 ± 0.3	4.0 ± 0.7	30
IRAS 22116+0437	46.6	68.2	SUR	2.3 ± 0.5	4.5 ± 0.9	35
IRAS 22491−1808	87.5	...	DCS	2.8 ± 0.3	5.1 ± 0.6	28
IRAS 23028+0725	56.4	140.7	SUR	...	3.2 ± 0.7	25
IRAS 23233+0946	...	...	...	2.1 ± 0.3	4.7 ± 0.5	33
IRAS 23365+3604	...	...	...	2.5 ± 3.1	4.6 ± 0.5	15
IRAS 00163−1039	...	...	...	2.3 ± 0.4	2.1 ± 0.4	34
IRAS 01572+0009	...	...	...	1.8 ± 0.2	2.2 ± 0.3	81
IRAS 05083+7936	...	...	...	2.0 ± 0.4	2.8 ± 0.4	48
IRAS 06538+4628	...	...	...	2.9 ± 0.3	2.5 ± 0.4	37
IRAS 08559+1053	...	90.7	DCS	1.3 ± 0.1	2.8 ± 0.4	64
IRAS 09437+0317	...	...	...	1.7 ± 0.3	2.2 ± 0.4	19
IRAS 10565+2448	...	...	...	2.1 ± 0.4	3.2 ± 0.5	19
IRAS 11119+3257	...	...	...	1.2 ± 0.1	2.5 ± 0.3	79
IRAS 13349+2438	...	...	...	0.8 ± 0.1	0.1 ± 0.1	110
IRAS 15001+1433	...	135.3	DCS	1.9 ± 0.2	3.4 ± 0.5	58
IRAS 15206+3342	110.7	...	DCS	2.3 ± 0.4	2.6 ± 0.4	65

Table 2.3 (cont'd)

Object	16 μm PU [mJy]	22 μm PU [mJy]	PU type	α_{15-6}	α_{30-20}	S/N
IRAS 20460+1925	...	...	...	...	1.1 ± 0.3	16
IRAS 23007+0836	...	...	...	1.7 ± 0.1	1.8 ± 0.4	19
IRAS 23394−0353	...	...	...	1.8 ± 0.3	2.9 ± 0.4	37
IRAS 23498+2423	46.5	...	DCS	1.0 ± 0.1	3.1 ± 0.4	87

Note. — Errors in the peakup (PU) fluxes are at the 15% level.

2.3 Data reduction

2.3.1 Dedicated observations of OHM galaxies

The data were processed using the *Spitzer* Science Center S17.0 data pipeline. We used basic calibrated data (BCD) products for our analysis, having already been corrected for flat-fielding, stray light contributions, non-linear responsivity in the pixels, and "drooping" (an increase in detector pixel voltage that occurs during non-destructive readouts). The 2-D BCD images were first medianed over the data cycles at each nod position to remove transient effects such as cosmic rays. For the SL and LL modules, we subtracted the sky contribution by differencing the BCD images for each nod position with the adjacent position in the same module.

The slit sizes of the SH and LH modules are too small to permit extraction of a sky background during the same observation. The continuum levels in the high-resolution modules, however, contain strong contributions from scattered zodiacal light. Estimations of the flux at 15 μm using SPOT predict contributions from zodiacal light within the *Spitzer* beam ranging from 20–80 mJy, which in many cases is of comparable magnitude to the expected signal from the galaxies themselves. The wavelength-dependent brightness of the sky contribution means that it cannot be corrected using a simple scaling, and so we did not attempt to further calibrate either HR module. The calibrated low-resolution spectra were thus used for absolute fluxes and the high-resolution spectra for line ratio diagnostics (which are unaffected by continuum levels).

To obtain more accurate measurements of faint lines at longer wavelengths, we took dedicated

off-source sky observations in the LH module for all 24 OHMs in our program. Subtraction of the wavelength-dependent background, however, significantly affected the measured line fluxes. For galaxies with background subtraction in only the LH module, this changes the line ratios measured between different HR modules (e.g., [S III]λ33 μm/[S IV]λ10.5 μm). We reduced the data both with and without subtraction of the sky backgrounds; background-subtracted LH data are attached in Appendix B.

Following the initial cleaning of the 2-D BCD products, we eliminated rogue pixels using the IDL package IRSCLEAN_MASK[1] . We used rogue pixel masks provided by the SSC for each IRS campaign, and supplemented the standard masks with manual cleaning of each nod and module. The 1-D spectra were then extracted using the Spitzer IRS Custom Extractor (SPICE) v.2.0. For all modules we used the optimal extraction routine with the standard aperture to improve the S/N ratio in faint galaxies.

The low-resolution modules were stitched together to match continuum levels by using a multiplicative scaling. We fixed the LL1 module and then scaled LL2 to LL1, SL1 to LL2, and SL2 to SL1. The mean scaling factors were 1.03 ± 0.08 for LL2 to LL1, 1.49 ± 0.69 for SL1 to LL2, and 1.37 ± 0.78 for SL2 to SL1. We then calibrated the entire low-resolution spectra as a single unit by scaling to the IRS 22 μm sample-up-the-ramp (SUR) peakups. The required scaling in the majority of cases was quite small, indicating that the sky subtraction and spectral extraction techniques are robust; the mean scaling factor was 0.94 ± 0.08. The accuracy of the overall continuum flux calibration is $\sim 5\%$ (Houck et al., 2004).

Noisy areas on both ends of the SH and LH orders were trimmed from the 1-D spectra. These areas typically encompass a range of 10–30 pixels on the edges of the orders and correspond to areas of decreased sensitivity on the detector. We deliberately trimmed only pixels with an overlapping wavelength range in adjacent orders so that a maximum amount of information is preserved. In isolated cases, we also removed obvious rogue pixels by hand from spectra in which exceptional

[1] IRSCLEAN_MASK is available at `http://ssc.spitzer.caltech.edu/archanaly/contributed/irsclean/IRSCLEAN_MASK.html`

1-channel features appear in only a single nod.

We calculated a simple figure of merit to measure the signal-to-noise ratio in the low-resolution data. The data near $\lambda_{rest} = 21$ μm (a feature-free area near the center of most spectra) are fit with a low-order polynomial; the median flux in that region is then divided by the rms noise to yield the S/N (Table 2.3). We note that this parameter is a function of wavelength, as well as the performance and integration time in each spectral module; this is intended to give only a rough estimate for each object. The S/N for the samples ranges from $\sim 10 - 110$, with a median of 35.

2.3.2 Archival data

Since the archival OHM and non-masing galaxies did not come from a unified observing program, the version of the *Spitzer* data pipeline and the level of processing varied slightly from object to object - we used the most recent versions available in the archive (v15.3.0 or later). The reduction process was identical to that for the OHM galaxies in our program, with the exception of the LR photometric scaling; since observations in the archive varied in availability of peakup data, we used a variety of sources to calibrate the spectra. In order of priority, we used the IRS dedicated 22 μm SUR peakups, IRS acquisition 16 and 22 μm DCS peakups, or IRAS 25 μm observations (all lying within the coverage of the LL modules). For galaxies from the archive, 17 are calibrated with DCS peakups, 21 with IRAS 25 μm photometry, and 4 are left uncalibrated. The mean scaling factor for the objects without SUR photometry was 1.05 ± 0.25, slightly higher than the mean scaling for galaxies in the dedicated OHM program.

Five OHMs and five non-masing galaxies from the archive had both SH and LH sky backgrounds taken simultaneously with the spectroscopic observations; the remainder had no high-resolution sky backgrounds in either module. Since we emphasize uniformity of the observations to the fullest extent possible, all data used for statistical comparisons between the samples use data **without** HR sky subtraction; line measurements for the background-subtracted objects are given in the Appendix.

The IRS spectra for IRAS 20460+1925 and IRAS 23028+0725 had no flux in the SL modules,

most likely due to a pointing error during observations. No SL data from either galaxy are used in our analyses here or in Chapter 3.

2.3.3 High-resolution data with background sky subtraction

As discussed in §2.2, the reduction process for the overall sample is slightly different for some archival galaxies that did not have separate IRS sky backgrounds in the high-resolution modules. Since much of our subsequent analysis (Chapter 3) depends on statistical comparisons between the two samples, we chose to minimize possible systematic errors and reduced all galaxies in a uniform manner **without** HR sky subtraction. These data are, however, likely to be a more reliable indicator of the absolute flux levels due to subtraction of the zodiacal background; therefore, we present atomic and molecular line fluxes for these galaxies in Appendix B.

2.4 Results

We show examples of the peakup-scaled low-resolution spectra for the OHMs in Figure 2.2, with the individual modules stitched together and bonus orders removed. Examples of the high-resolution SH and LH data are shown in Figures 2.3 and 2.4; full spectra for all galaxies are in Appendix B. While individual orders within the high-resolution modules are typically well-aligned in flux, the differences in calibration between the SH and LH modules are clearly apparent when matching the spectra; this is due to a combination of different slit sizes for the SH and LH modules (a factor of ~ 4) and the lack of separate sky subtraction for the SH modules. For this reason, as well as emphasizing the narrow atomic and molecular features visible in the high-resolution spectra, we display separate plots for the SH and LH modules.

A small amount of the archival objects have previously published full IRS spectra (Armus et al., 2004; Weedman et al., 2005; Armus et al., 2007), mainly consisting of bright, nearby galaxies. Farrah et al. (2007) published HR spectra for roughly half of our archival OHM hosts. While many papers use the available data from the GTO programs, however, the majority of objects extracted from the archive have **no** published spectra, although some data are used in larger studies of ULIRG

properties (*e.g.*,, Higdon et al., 2006; Desai et al., 2007; Hao et al., 2007). The spectra for many of the archival galaxies are thus presented here for the first time.

Comparison of our data with the few spectra of objects previously published (*e.g.*,, Mrk 1014, Arp 220, NGC 7469) revealed no significant differences in spectral shape or detection of individual features. Measurements of line flux and equivalent widths, however, may be affected by the photometric scaling and/or line-fitting routines used; for this reason, we chose to reduce **all** data in a uniform matter.

For many of our high-resolution spectra, especially those with low S/N, there exist individual spikes that do not correspond to any identified feature (see IRAS 01562+2528 for a prominent example). These features are typically 1–2 channels wide, much narrower than the expected linewidth for an unresolved feature. We regard such features as spurious, possibly caused by hot pixels or other instrumental conditions that are not corrected by our cleaning routines. All features we regard as valid detections are listed in the data tables, with the locations of the most common features marked on the spectra themselves.

2.4.1 Mid-infrared continuum

The continuum emission for all objects in the OHM sample has a relatively homogeneous spectral shape over the range of the IRS, although differences in spectral shape between the two samples do appear and are explored in Chapter 3. Figure 2.5 shows the individual objects overlaid with a template generated by medianing the flux in each wavelength bin from **all** galaxies. The template bears a close resemblance to starburst ULIRG spectra seen in previous surveys (Hao et al., 2007; Weedman & Houck, 2009). The LR spectrum clearly shows silicate absorption at 9.7 and 18 μm and water ice absorption at 6 μm. Low-resolution emission features are dominated by the broad PAH features from 6–13 μm, with weaker contributions from neon, sulfur, and molecular hydrogen also visible.

The continuum data from $\lambda_{rest} = 20 - 30$ μm is in most cases well-characterized by a power-law fit, with the short wavelength break occurring near the 18 μm silicate feature and the long

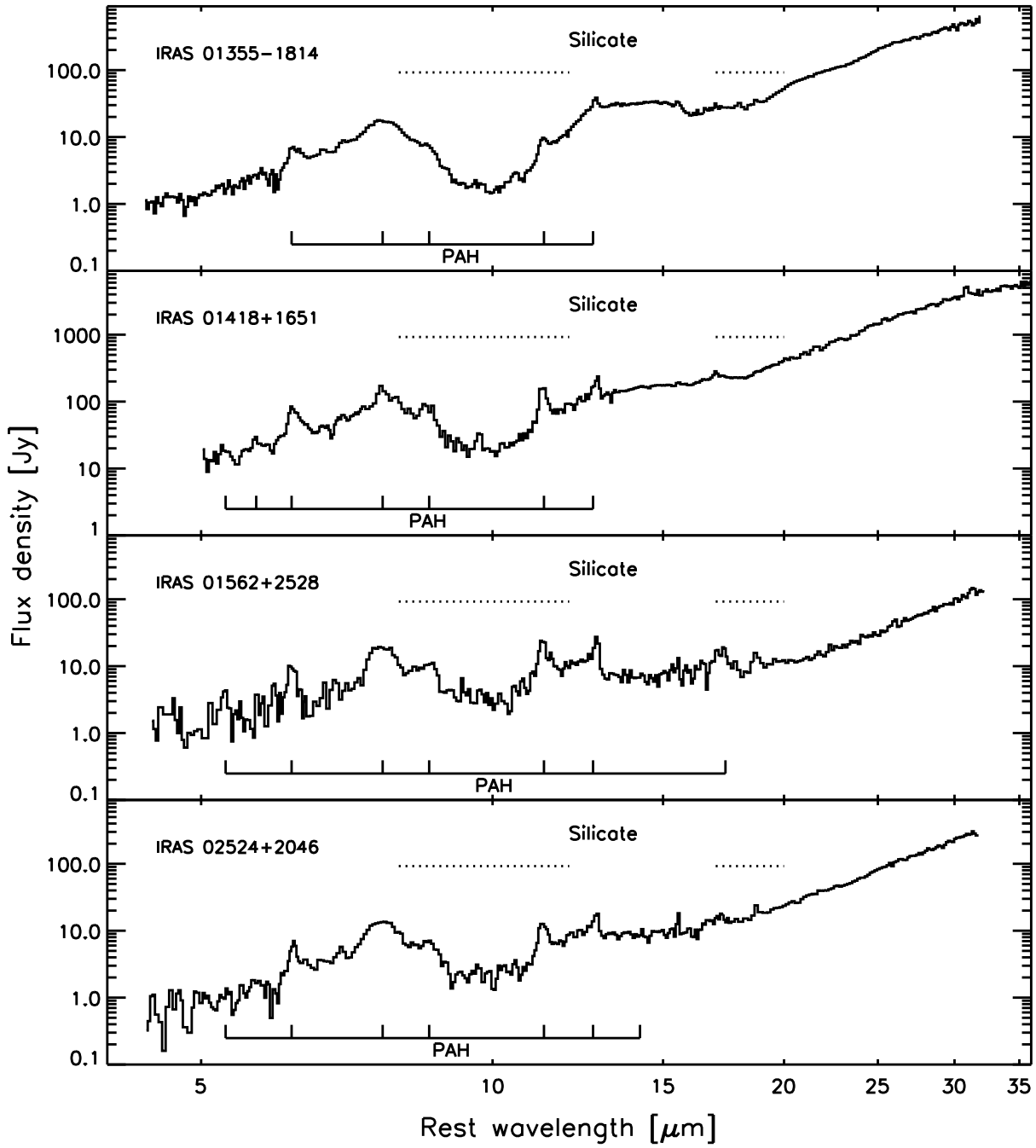

Figure 2.2 IRS spectra from the low-resolution modules (LR) for OHMs. Spectra for all OHMs and non-masing galaxies are in Appendix B; portions are shown here for guidance on form and style. All detected PAH emission and absorption features from water ice and silicates are marked.

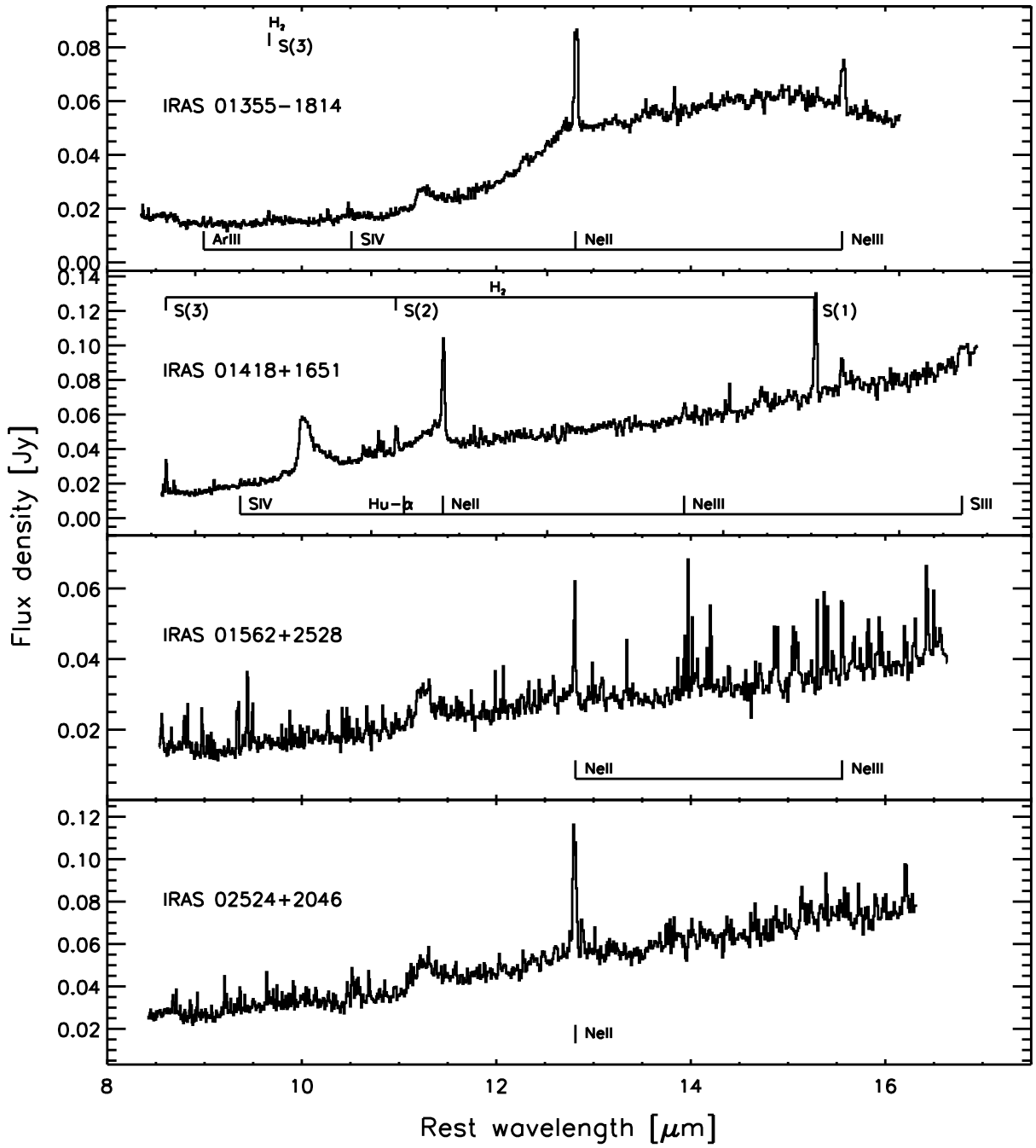

Figure 2.3 IRS spectra from the short-high module (SH) for OHMs. Spectra for all OHMs and non-masing galaxies are in Appendix B; portions are shown here for guidance on form and style. All detected atomic and H_2 features in each spectra are marked.

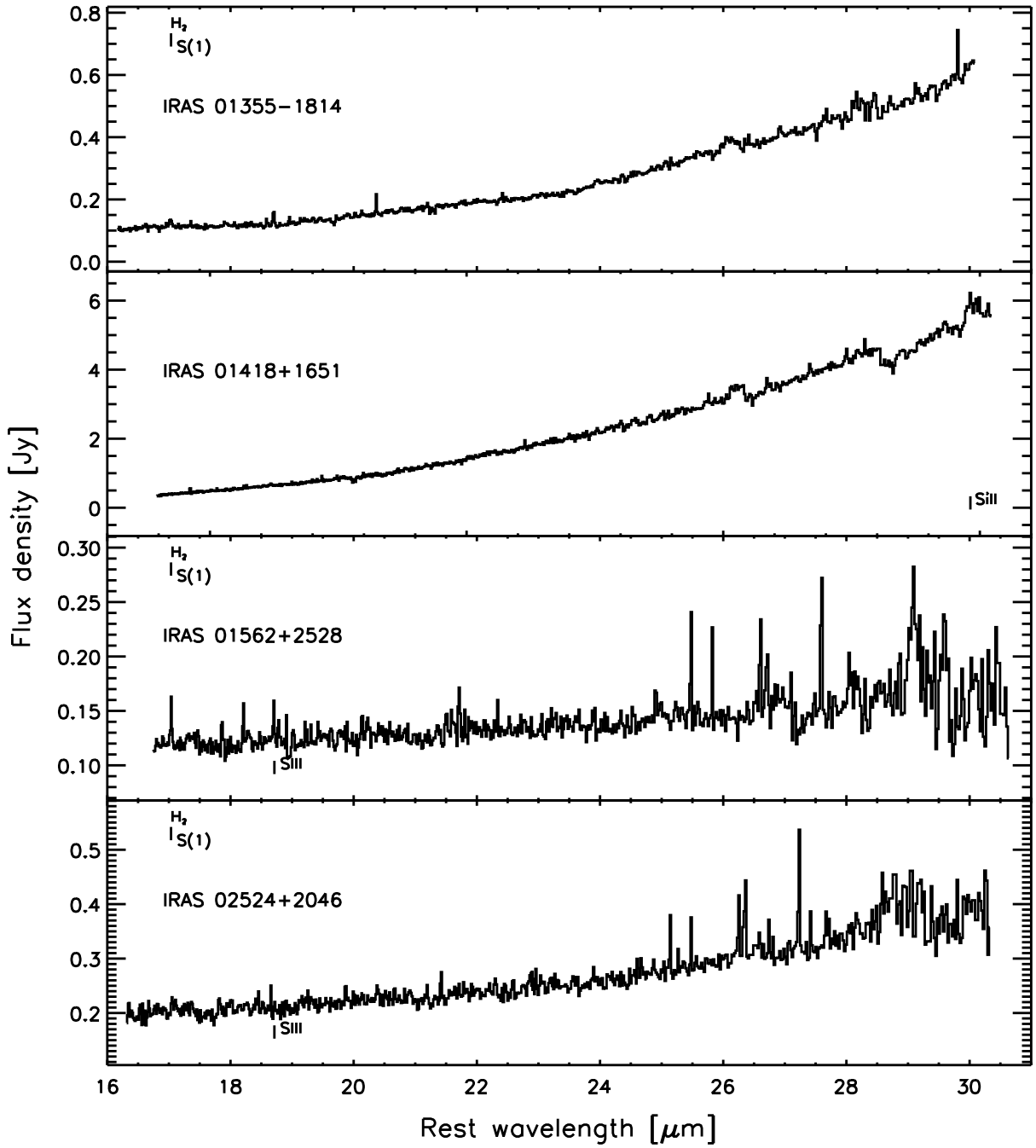

Figure 2.4 IRS spectra from the long-high module (LH) for OHMs. Spectra for all OHMs and non-masing galaxies are in Appendix B; portions are shown here for guidance on form and style. All detected atomic and H_2 emission features are marked.

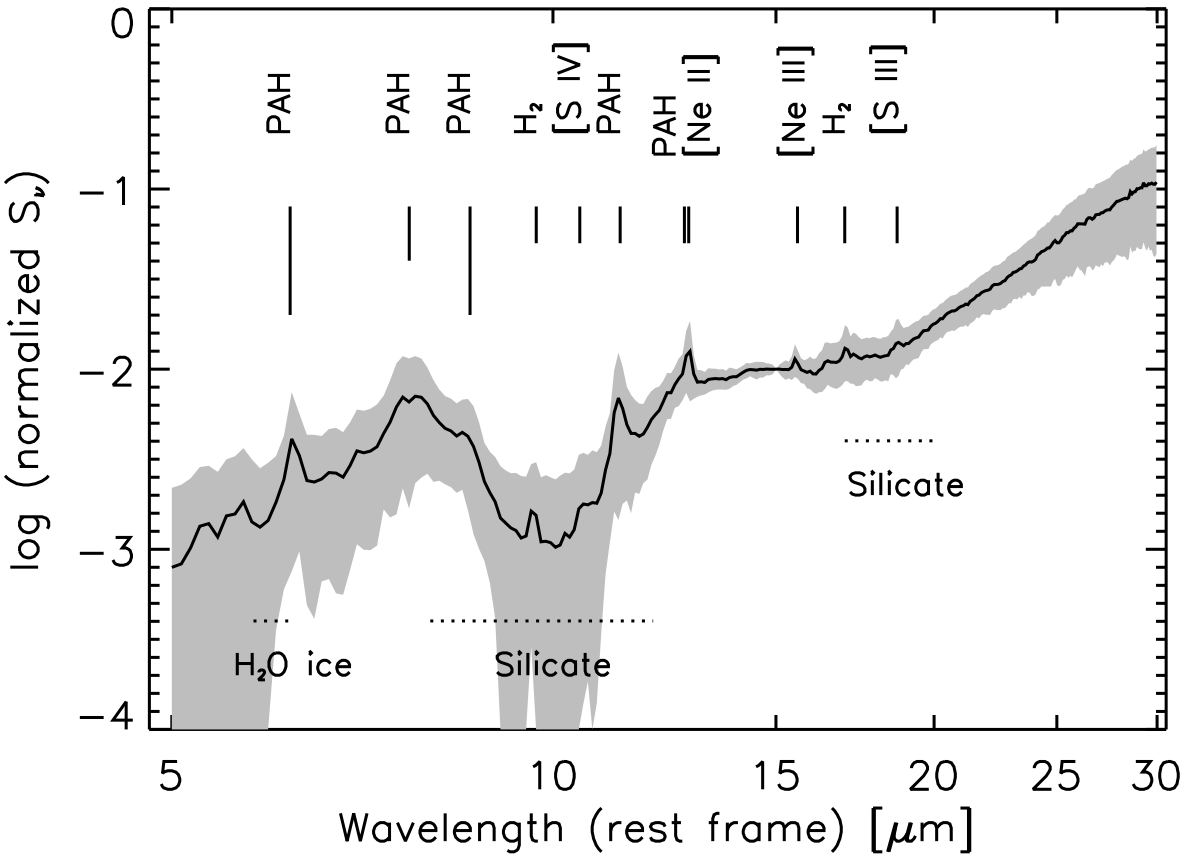

Figure 2.5 Low-resolution spectrum of all galaxies in our sample normalized at $S_\lambda = 15$ μm. The black spectrum is the composite template made from an error-weighted median of the individual galaxies; the grey shaded area shows the 1-σ envelope for each resolution element (exaggerated toward negative values in log space).

wavelength end cut off by the spectral range of the IRS. Shortward of 15 μm, the continuum becomes increasingly contaminated by individual absorption and emission features, especially from PAH emission and the deep silicate absorption at 9.7 μm. Following Brandl et al. (2006), we fit a spectral index to the continuum in two components, with α_{30-20} measuring the relatively feature-free flux from $20 - 30$ μm and α_{15-6} measuring the contribution from $5.3 - 14.8$ μm; the wavelengths are slightly shifted to avoid contamination from water ice at 6 μm and [Ne III] at 15.6 μm (Table 2.3).

The mean $15-6$ μm spectral index for the entire OHM sample is $\alpha_{15-6} = 2.1 \pm 0.6$; the mean 30-20 slope is $\alpha_{30-20} = 4.8 \pm 1.1$. The shallowest slope occurs for IRAS 10039−3338 ($\alpha_{15-6} = -0.1$), an object with weak PAH features and very strong silicate absorption; the steepest index occurs for IRAS 12018+1941 ($\alpha_{15-6} = 3.0$), which has moderate PAH and line emission features and a nearly constant spectral index over the entire mid-infrared range. Steeper $15 - 6$ μm indices are likely due to a combination of smaller relative quantities of warm dust (thermal blackbodies of ~ 300 K peaking near 10 μm) and larger quantities of cooler dust.

The shallowest $30 - 20$ μm slope occurs for IRAS 13451+1232 ($\alpha_{30-20} = 1.9$); the low-resolution spectrum for this object more closely resembles that seen in Seyfert galaxies and PG quasars (Schweitzer et al., 2006; Hao et al., 2007), with weak PAH emission and shallower silicate absorption. The continuum emission for this object is also much closer to being uniform over the entire range of the IRS; the difference between the two spectral indices is only $\Delta\alpha = -0.4$, compared to an average of $\Delta\alpha = 2.7$ for the entire sample. This behavior is more typical of non-thermal emission that can extend over many decades with the same index. The steepest 30-20 emission measured is from IRAS 11028+3130 ($\alpha_{30-20} = 7.0$); the galaxy shows moderate PAH and line emission features, but a flat continuum between 12 and 20 μm.

The non-masing galaxies have average spectral indices of $\alpha_{15-6} = 1.8 \pm 0.6$ and $\alpha_{30-20} = 2.5 \pm 0.9$. A full statistical analysis of the values for the two samples (particularly α_{30-20}) is presented in Chapter 3.

2.4.2 Atomic emission lines

We measured emission from atomic and molecular lines using the standard packages in the Spectroscopic Modeling Analysis and Reduction Tool (SMART) v6.2.4 (Higdon et al., 2004). A simple Gaussian is a good fit for virtually all high-resolution lines in the sample; in cases where lines are blended (such as the [Ne V]/[Cl II] and [O IV]/[Fe II] complexes), we used a multi-Gaussian fit centered at the redshifted rest wavelengths of the expected transitions. To compute upper limits for non-detections, we use the 3-σ noise measured from the surrounding continuum and a Gaussian shape with an FWHM estimated from detected lines. Accuracy for all measured line fluxes is on the order of $\sim 10\%$. References to wavelengths of specific lines are quoted in microns unless designated otherwise.

Table 2.4. Atomic line fluxes for high-resolution spectra

Object λ_{rest} [μm]	[Ar III] 8.991	[S IV] 10.511	H I 7-6 12.368	[Ne II] 12.814	[Ne V] 14.322	[Cl II] 14.369	[Ne III] 15.555	[Fe II] 17.936	[S III] 18.713	[Ne V] 24.318	[O IV] 25.890	[Fe II] 25.988	[S III] 33.481	[Si II] 34.815
IRAS 01355−1814	0.15	0.10	< 0.20	2.45	< 0.27	< 0.25	0.89	< 0.51	< 1.52	< 0.78	< 1.28	< 0.82	–	–
IRAS 01418+1651	–	0.15	0.13	4.17	< 0.46	< 0.29	0.41	< 0.67	0.94	< 3.84	< 3.52	< 4.05	< 24.62	19.43
IRAS 01562+2528	< 0.77	< 1.93	< 0.30	1.07	< 0.91	< 0.75	0.77	< 0.77	0.67	< 0.73	< 2.06	< 1.29	–	–
IRAS 02524+2046	< 0.63	< 1.01	< 0.36	2.39	< 0.68	< 0.56	< 0.97	< 1.11	0.47	< 1.04	< 0.96	< 0.59	–	–
IRAS 03521+0028	< 0.34	< 0.40	< 0.41	2.72	< 0.36	< 0.24	1.11	1.70	1.18	< 1.02	< 0.93	< 0.59	–	–
IRAS 04121+0223	0.35	< 0.84	< 0.41	1.81	< 1.01	< 0.99	< 0.87	< 0.92	0.93	< 1.06	0.97	< 1.34	–	–
IRAS 04454−4838	–	0.47	< 0.74	2.04	< 0.75	< 0.61	0.39	< 0.27	< 1.00	< 7.75	< 9.59	< 6.29	0.90	< 87.49
IRAS 06487+2208	1.71	1.78	< 0.81	11.75	< 1.44	< 1.19	9.45	< 0.87	4.89	< 1.36	0.48	1.31	–	–
IRAS 07163+0817	0.44	< 1.05	< 0.22	3.19	< 0.46	< 0.39	0.33	< 1.04	0.81	< 1.73	< 0.78	< 0.71	–	–
IRAS 07572+0533	< 1.69	< 0.87	< 0.40	1.74	< 0.79	< 0.65	< 0.89	< 0.61	< 1.15	< 1.37	< 1.53	< 1.03	–	–
IRAS 08201+2801	< 0.70	< 2.74	< 0.64	2.23	< 0.60	< 0.41	0.88	< 0.84	0.41	< 0.50	< 0.66	< 0.50	–	–
IRAS 08449+2332	< 0.94	< 0.71	< 0.64	3.60	< 2.03	< 1.64	1.57	< 0.60	1.62	< 0.73	< 0.69	< 0.40	–	–
IRAS 08474+1813	< 0.76	< 0.64	< 0.36	1.26	< 1.10	< 0.89	< 1.10	< 1.09	0.86	< 1.27	< 3.04	< 1.86	–	–
IRAS 09039+0503	0.11	< 0.27	< 0.85	3.68	< 0.46	< 0.38	1.17	< 0.85	0.88	< 0.55	< 1.11	0.48	–	–
IRAS 09539+0857	< 0.63	< 0.43	< 0.30	1.25	< 0.86	< 0.69	< 1.88	< 1.82	< 1.02	< 1.41	< 2.05	< 1.36	–	–
IRAS 10035+2740	< 0.89	< 0.75	< 0.48	1.82	< 0.42	< 0.31	0.57	< 0.97	0.78	< 0.95	< 2.11	< 1.37	–	–
IRAS 10039−3338	–	0.93	< 1.25	16.69	< 1.21	< 1.10	3.93	< 0.81	6.57	< 14.49	< 11.09	< 7.54	< 10.49	101.40
IRAS 10173+0828	–	< 0.29	< 0.34	1.71	< 0.33	< 0.32	0.46	< 0.42	< 1.36	< 1.33	< 2.42	< 1.61	2.55	81.70
IRAS 10339+1548	1.00	0.55	< 0.34	1.25	1.24	< 1.13	2.03	0.49	1.17	0.52	2.85	0.89	–	–
IRAS 10378+1109	0.34	< 0.25	< 0.35	3.95	< 0.61	< 0.63	0.68	< 0.95	1.82	< 0.87	< 1.99	< 1.30	–	–
IRAS 10485−1447	< 1.14	< 0.20	< 0.23	1.99	< 0.44	< 0.48	0.36	< 0.87	< 1.08	< 0.91	< 1.08	< 0.66	–	–

Table 2.4 (cont'd)

Object λ_{rest} [μm]	[Ar III] 8.991	[S IV] 10.511	HI 7-6 12.368	[Ne II] 12.814	[Ne V] 14.322	[Cl II] 14.369	[Ne III] 15.555	[Fe II] 17.936	[S III] 18.713	[Ne V] 24.318	[O IV] 25.890	[Fe II] 25.988	[S III] 33.481	[Si II] 34.815
IRAS 11028+3130	< 1.06	< 0.70	< 0.28	< 0.63	< 0.44	< 0.38	< 0.74	< 0.47	< 0.71	< 3.07	< 4.45	< 3.14	–	–
IRAS 11180+1623	< 0.80	< 0.70	< 0.36	1.98	< 0.50	< 0.39	0.62	< 0.71	0.89	< 0.85	< 1.00	< 0.69	–	–
IRAS 11524+1058	< 0.78	< 0.56	< 0.35	7.82	< 0.43	< 0.37	< 0.77	< 0.52	< 1.61	< 1.49	< 0.93	< 0.70	–	–
IRAS 12018+1941	< 0.27	< 0.28	< 0.59	2.73	< 0.52	< 0.38	0.64	< 1.01	< 1.32	< 1.22	< 1.71	< 1.30	–	–
IRAS 12032+1707	< 1.33	0.13	< 0.48	4.98	1.39:	< 1.51	1.57	< 1.22	1.18	0.66	< 1.50	< 1.00	–	–
IRAS 12112+0305	–	0.43	< 0.88	13.06	< 0.76	< 0.55	3.37	0.68	4.32	< 1.50	< 7.56	< 4.65	8.77	–
IRAS 12540+5708	–	< 11.45	< 4.40	17.95	< 8.05	< 6.86	9.36	< 4.40	< 5.05	< 22.99	< 18.84	< 14.43	< 49.65	< 163.66
IRAS 13218+0552	< 0.66	< 0.54	< 0.46	0.84	< 0.71	< 1.23	< 1.24	< 0.78	< 2.27	< 1.85	< 2.93	< 1.76	–	–
IRAS 13428+5608	–	7.69	< 2.42	41.21	10.62	< 5.37	29.05	< 1.32	16.67	9.28	75.13	< 29.79	28.14	< 134.61
IRAS 13451+1232	0.57	1.57	< 0.70	4.71	0.71	< 0.88	4.73	< 1.19	1.15	< 2.50	< 5.17	< 1.85	–	–
IRAS 14059+2000	< 0.64	0.35	< 0.53	2.83	< 0.88	< 1.00	2.65	< 0.97	1.68	< 1.04	< 1.70	< 1.11	–	–
IRAS 14070+0525	< 0.19	< 0.18	< 0.27	1.33	< 0.42	< 0.33	2.01	< 0.53	< 0.77	< 1.25	< 1.98	< 1.37	–	–
IRAS 14553+1245	0.47	0.71	< 0.25	3.24	< 1.55	< 1.29	3.10	< 0.89	1.58	< 0.89	< 2.38	< 1.49	–	–
IRAS 15327+2340	–	< 0.79	< 3.60	61.13	< 6.29	< 5.29	6.89	< 1.04	5.19	< 24.96	< 24.33	< 15.22	< 151.68	< 202.18
IRAS 16090−0139	0.49	0.10	< 0.49	6.72	< 0.65	< 0.76	2.26	1.03	3.07	< 3.95	1.12	< 2.23	–	–
IRAS 16255+2801	0.18	0.20	< 0.27	1.73	< 0.82	< 0.68	1.18	< 5.36	1.54	< 12.06	< 7.16	< 4.83	–	–
IRAS 16300+1558	0.13	< 0.15	< 0.28	2.27	< 0.33	< 0.25	0.42	< 1.20	0.50	< 1.23	< 0.88	< 0.70	–	–
IRAS 17207−0014	–	0.40	< 2.12	38.84	< 0.93	< 0.69	8.42	< 0.51	6.39	< 6.40	< 11.27	< 7.70	12.24	46.91
IRAS 18368+3549	< 0.42	< 0.81	0.11	6.91	< 0.34	< 0.43	1.07	< 0.49	1.18	< 1.07	< 0.91	< 0.59	–	–
IRAS 18588+3517	0.57	0.37	0.24	5.12	< 0.40	< 0.43	1.87	< 3.75	7.96	< 4.91	< 4.13	< 4.05	–	–
IRAS 20100−4156	0.33	0.23	< 0.31	6.73	< 0.65	< 0.49	1.71	< 0.69	2.86	< 3.58	1.20	1.34	–	–

Table 2.4 (cont'd)

Object λ_{rest} [μm]	[Ar III] 8.991	[S IV] 10.511	HI 7-6 12.368	[Ne II] 12.814	[Ne V] 14.322	[Cl II] 14.369	[Ne III] 15.555	[Fe II] 17.936	[S III] 18.713	[Ne V] 24.318	[O IV] 25.890	[Fe II] 25.988	[S III] 33.481	[Si II] 34.815
IRAS 20286+1846	< 0.56	< 0.50	< 0.27	1.67	< 0.72	< 0.65	0.37	< 0.30	0.44	< 0.58	< 0.73	< 0.70	–	–
IRAS 21077+3358	< 0.67	< 0.63	< 0.39	3.06	< 0.45	< 0.36	1.09	< 0.50	0.77	< 0.80	< 0.60	< 0.47	–	–
IRAS 21272+2514	< 0.18	< 0.16	0.16	2.29	< 0.31	< 0.22	0.35	< 0.21	0.45	< 0.50	< 0.68	< 0.46	–	–
IRAS 22055+3024	0.12	< 0.67	< 0.71	4.55	< 0.76	< 0.74	1.05	< 0.51	1.04	< 2.12	< 2.30	< 1.34	–	–
IRAS 22116+0437	< 0.47	< 0.73	< 0.37	2.25	< 0.82	< 0.68	1.33	< 1.07	1.04	< 2.16	< 2.54	< 2.35	–	–
IRAS 22491−1808	–	0.41	< 0.54	4.88	< 0.55	< 0.43	1.70	< 0.72	1.86	< 3.40	< 7.11	< 3.35	13.72	–
IRAS 23028+0725	< 0.55	< 0.61	< 0.39	1.81	< 0.90	< 0.72	1.04	< 1.05	< 1.15	< 1.72	< 2.70	< 1.72	–	–
IRAS 23233+0946	0.37	0.33	< 0.43	4.93	< 0.43	< 0.38	1.06	< 0.89	3.13	< 1.06	1.20	0.66	–	–
IRAS 23365+3604	–	< 0.36	< 0.51	8.51	< 0.63	< 0.52	1.12	< 0.44	4.29	< 4.74	< 11.96	< 7.97	6.81	–
IRAS 00163−1039	–	3.40	0.43	80.95	< 1.96	< 0.92	14.53	< 1.70	30.85	< 7.59	1.42	3.35	34.70	73.84
IRAS 01572+0009	0.73	3.06	< 0.72	6.15	5.51	< 3.23	10.34	< 0.89	1.66	4.76	9.82	< 6.12	–	–
IRAS 05083+7936	–	< 1.19	< 1.57	49.40	0.60	0.48	7.63	< 1.19	18.67	< 1.89	1.28	1.33	28.00	71.27
IRAS 06538+4628	–	0.80	1.09	47.39	0.69	< 1.16	6.07	1.17	19.11	< 2.33	< 6.97	2.70	37.60	57.37
IRAS 08559+1053	< 0.37	0.56	< 0.43	8.38	0.51	0.35	1.87	< 0.93	1.35	< 1.34	2.54	0.45	–	–
IRAS 09437+0317	–	< 1.04	< 0.61	8.74	< 0.64	< 0.51	1.22	< 0.70	3.33	< 0.99	0.47	0.68	9.45	23.27
IRAS 10565+2448	–	< 0.76	< 1.34	57.60	< 1.29	0.67	7.65	< 1.02	12.42	< 3.07	< 5.13	< 2.35	20.89	51.37
IRAS 11119+3257	< 0.83	0.31	< 0.78	2.19	< 0.71	< 0.58	1.89	< 2.30	< 1.75	< 2.40	< 3.08	< 1.95	–	–
IRAS 13349+2438	2.76	1.66	< 0.45	1.43	0.81	< 0.99	3.50	< 4.54	1.68	3.46	7.28	< 5.11	–	–
IRAS 15001+1433	0.39	0.28	< 0.30	6.61	1.08	< 0.98	2.62	< 0.78	2.36	0.67	1.21	0.56	–	–
IRAS 15206+3342	2.01	3.82	0.23	10.96	< 0.34	< 0.41	19.87	< 1.03	8.58	1.36	0.74	1.21	–	–
IRAS 20460+1925	< 0.39	< 0.66	< 0.42	< 0.44	< 0.60	< 0.51	< 0.69	< 0.72	< 0.79	< 3.68	1.95	< 1.01	–	–

Table 2.4 (cont'd)

Object λ_{rest} [μm]	[Ar III] 8.991	[S IV] 10.511	H I 7-6 12.368	[Ne II] 12.814	[Ne V] 14.322	[Cl II] 14.369	[Ne III] 15.555	[Fe II] 17.936	[S III] 18.713	[Ne V] 24.318	[O IV] 25.890	[Fe II] 25.988	[S III] 33.481	[Si II] 34.815
IRAS 23007+0836	–	8.67	< 1.84	179.04	8.36	< 4.23	33.69	< 3.28	70.16	15.51	30.98	9.47	97.56	188.36
IRAS 23394−0353	–	0.72	0.57	46.75	< 1.45	< 1.08	7.71	< 1.10	17.16	< 1.92	1.27	2.43	44.29	53.48
IRAS 23498+2423	0.23	1.27	< 0.23	3.10	0.92	< 0.91	7.79	< 0.55	1.13	1.26	4.61	< 3.77	–	–

Note. — Line fluxes are given in 10^{-21} W cm^{-2}. – indicates that the redshifted line wavelength lay outside the range of the IRS.

The most common lines detected are the forbidden [Ne II] λ12.814 and [Ne III] λ15.555 transitions (Table 2.4). [Ne II] is observed in nearly the entire sample, with detections in 50/51 OHMs and 14/15 non-masing galaxies. The only exceptions are the OHM IRAS 11028+3130 and the non-maser IRAS 20460+1925. [Ne III] is also common, detected in 43/51 OHMs and 14/15 non-masing galaxies. Other common lines are the [S III] λ18.713 (detected in $\sim$ 80% of galaxies) and [S IV] λ10.511 ($\sim$ 50%). [Ar III] λ8.991 is detected in 15 OHMs and 5 non-masing galaxies, but the redshifted line is not visible in the SH module for archived objects at $z < 0.1$.

We detect "rarer" line transitions that appear in less than 15% of our sample, including [Ne V] λ14.322 and λ24.318, [Fe II] λ17.936 and λ25.988, and [O IV] λ25.890. IRAS 10339+1548 is the only galaxy in the sample with detections for all atomic transitions listed above. Eight galaxies also show the non-forbidden HI 7-6 transition (Humphreys-α) at 12.368 μm.

[S III]λ33.481 and [Si II]λ34.815 are commonly observed in ULIRGs for which the redshifted transitions appear within the red edge of the LH module. Farrah et al. (2007) detected [S III]λ33.481 in roughly half of all ULIRGs with $z < 0.06$, all of which show the stronger [S III]λ18.713 associated transition. For our sample, however, many galaxies have the lines redshifted beyond the range of the IRS; when visible, the lines lie at the far red edge of the 11^{th} order in the LH module, an area with high noise and decreased sensitivity with respect to neighboring orders.

For galaxies taken from the *Spitzer* archive, we compared our high-resolution measurements with those appearing in the sample of Farrah et al. (2007). The agreement between detected lines is good for nearly all objects; however, Farrah et al. (2007) report detections of [Ne V] in IRAS 11119+3257, [O IV] in IRAS 13451+1232, and H_2 S(0) and S(2) lines in IRAS 01572+0009 and IRAS 23498+2423 which we fail to confirm. Limits for the measured fluxes are given in Tables 2.4 and 2.5.

The IRS is designed to make accurate measurements of narrow atomic transitions in the SH and LH modules; however, several lines are also detected in the LR modules, most often the powerful neon, sulfur, and H_2 transitions. The only emission lines visible in the low-resolution

modules without a corresponding detection in high-resolution are the H_2 S(7) line at 5.5 μm and the H_2 S(5)/[Ar II] complex near 6.7 μm; this is due to the SH low-wavelength cutoff at $\lambda_{rest} = 8.2-9.0$ μm, depending on the redshift of the galaxy. All other atomic emission features observed in the low-resolution modules have corresponding detections in high-resolution; furthermore, blending of narrow lines makes accurate measurements of flux difficult in the LR modules. For isolated lines with well-defined surrounding continuum, our fluxes are consistent for measurements in both low- and high-resolution.

We note the presence of two features which have no obvious identifications occurring in the LH spectra for multiple objects: one is an emission feature seen near 29 μm (a prominent example occurs for IRAS 17539+2935) and the second is an absorption feature near 30 μm. The two are often paired and are seen in $\sim 50\%$ of the galaxies observed. The **rest** wavelengths of the transitions, however, vary significantly from object to object (with a standard deviation of $\sigma_\lambda \simeq 0.7$ μm), while the **observed** wavelengths are nearly fixed ($\sigma_\lambda \lesssim 0.05$ μm). This implies that the features are either artifacts of the extraction process or that both the emission and absorption come from unidentified foreground features with little to no Doppler shift. Given that we see no evidence for these unidentified lines in any of the LR spectra (which should be detectable, given the high S/N for many of the features), we consider both to be spurious.

2.4.3 Molecular hydrogen

We detected multiple emission lines from the pure rotational series of molecular hydrogen in both OHMs and non-masing galaxies. At redshifts of $z \lesssim 0.1$, transitions from H_2 S(0) at 28.22 μm to H_2 S(3) at 9.67 μm are visible in the HR modules; in addition, the LR module is capable of detecting lines as far out as the S(7) transition at 5.51 μm. In each case, the line number [*e.g.*,, 0 for H_2 S(0)] indicates the rotational quantum number of the lower state ($J = 2 \rightarrow 0$) for the quadrupole S-branch transition. $\Delta J = 2$ results in two separate branches: ortho (parallel nuclear spin, odd J) and para (anti-parallel nuclear spin, even J).

We detected at least one H_2 line in 49/51 OHMs and 13/15 non-masing galaxies, with S(1)

seen in all objects for which at least one molecular hydrogen transition is reported. The higher-order S(2) and S(3) lines are seen in roughly 2/3 of the sample, while the para ground state S(0) transition is detected in only $\sim 15\%$ of the sample. Our line detection rate is consistent with results from the SINGS galaxies examined in Roussel et al. (2007) and the ULIRG sample of Higdon et al. (2006). Lower detection rates of S(0) and S(2) are likely due to a combination of the intrinsic ortho-para ratio as well as rising continuum levels near 28 μm that can obscure weak line emission by S(0). Higdon et al. (2006) find that the S(2)/S(3) ratios are consistent with no significant differential extinction for the two lines, which is supported by numerous detections in our sample of S(3) line emission superimposed on optically deep silicate absorption near 9.7 μm. We thus applied no extinction or reddening corrections to the line fluxes (Table 2.5).

Table 2.5. Molecular H_2 gas properties

Object λ_{rest} [μm]	H_2 S(7) 5.51 μm	H_2 S(5) 6.91 μm	H_2 S(4) 8.03 μm	H_2 S(3) 9.67 μm	H_2 S(2) 12.28 μm	H_2 S(1) 17.04 μm	H_2 S(0) 28.22 μm	T_{warm} [K]	T_{hot} [K]	M_{warm} [10^7 M$_\odot$]	M_{hot} [10^7 M$_\odot$]
IRAS 01355−1814	< 1.52	< 3.25	–	0.22	0.63	1.13	< 1.63	262		4.74	
IRAS 01418+1651	< 5.29	6.96:	–	1.16	0.94	2.15	< 5.40	320		0.14	
IRAS 01562+2528	< 3.25	< 7.06	–	< 0.52	< 0.39	0.94	< 0.92				
IRAS 02524+2046	< 1.52	0.88:	–	< 2.51	< 0.46	0.88	< 1.03				
IRAS 03521+0028	< 2.89	0.58:	–	0.63	0.47	1.69	< 0.55	292		4.24	
IRAS 04121+0223	< 3.54	1.03:	–	< 1.62	< 0.43	< 0.73	< 1.06				
IRAS 04454−4838	< 3.31	< 13.24	–	1.04	1.27	3.05	0.76	222		0.82	
IRAS 06487+2208	< 5.99	0.97:	–	2.10	1.02	1.80	< 1.52	381		4.13	
IRAS 07163+0817	< 1.84	< 4.58	–	< 0.77	0.04	0.47	1.68	110		0.60	
IRAS 07572+0533	< 1.03	< 2.62	–	< 0.90	< 0.50	< 0.99	< 3.41				
IRAS 08201+2801	< 3.41	< 10.84	–	0.28	< 0.90	0.56	< 0.91	313		1.79	
IRAS 08449+2332	< 3.67	1.22:	–	0.63	0.33	1.36	< 0.70	301		3.48	
IRAS 08474+1813	< 1.07	0.61:	–	0.75	< 0.46	0.27	< 1.33	493		0.68	
IRAS 09039+0503	1.13	2.69:	–	2.21	1.46	2.91	1.27	198	978	4.88	0.42
IRAS 09539+0857	< 2.40	< 6.29	–	0.53	0.26	1.07	< 0.95	308		1.93	
IRAS 10035+2740	< 0.98	0.81:	–	0.70	< 0.63	1.06	< 2.31	334		3.29	
IRAS 10039−3338	< 28.84	< 46.95	–	3.27	1.71	3.95	< 7.46	348		0.46	
IRAS 10173+0828	< 5.73	3.00:	–	0.58	0.49	1.38	< 1.67	302		0.33	
IRAS 10339+1548	< 1.09	< 2.88	–	< 0.58	< 0.42	0.42	< 1.94				
IRAS 10378+1109	0.53	1.42:	–	1.82	0.55	2.25	< 0.61	315	876	4.59	0.46
IRAS 10485−1447	0.52	< 5.57	–	0.18	0.14	0.28	< 0.76	307	1540	0.55	0.03

Table 2.5 (cont'd)

Object λ_{rest} [μm]	H_2 S(7) 5.51 μm	H_2 S(5) 6.91 μm	H_2 S(4) 8.03 μm	H_2 S(3) 9.67 μm	H_2 S(2) 12.28 μm	H_2 S(1) 17.04 μm	H_2 S(0) 28.22 μm	T_{warm} [K]	T_{hot} [K]	M_{warm} [10^7 $M_\odot$]	M_{hot} [10^7 $M_\odot$]
IRAS 11028+3130	< 0.44	< 1.83	–	< 0.61	< 0.36	0.39	< 1.75				
IRAS 11180+1623	< 2.25	0.51:	–	0.39	0.61	1.06	< 1.88	302		3.32	
IRAS 11524+1058	< 1.99	< 4.35	–	< 0.43	< 0.42	0.66	< 2.14				
IRAS 12018+1941	< 3.27	< 8.84	–	0.47	0.36	1.28	2.21	165		4.10	
IRAS 12032+1707	< 2.78	4.93:	< 0.27	0.81	0.58	1.61	< 3.34	312		9.24	
IRAS 12112+0305	7.03	5.89:	–	1.87	1.66	3.71	1.30	195	1680	2.01	0.08
IRAS 12540+5708	< 32.27	< 49.24	–	2.42	3.21	6.23	< 17.62	301		1.07	
IRAS 13218+0552	< 4.32	< 7.55	–	0.32	0.42	0.97	< 2.91	292		4.83	
IRAS 13428+5608	< 13.14	8.96:	–	7.77	4.83	8.63	< 9.82	360		1.19	
IRAS 13451+1232	< 8.46	3.26:	–	1.65	1.10	2.61	< 0.79	329		4.18	
IRAS 14059+2000	0.91	1.55:	–	2.12	0.73	2.36	< 0.88	319	944	3.90	0.40
IRAS 14070+0525	< 2.54	< 5.85	< 0.41	0.28	0.22	1.30	< 0.85	260		11.42	
IRAS 14553+1245	0.32	< 9.92	–	0.92	0.19	1.05	< 0.82	317	906	1.76	0.19
IRAS 15327+2340	22.70	41.6:	–	< 0.56	7.66	13.68	14.53	159		0.42	
IRAS 16090−0139	1.20	< 15.12	–	1.10	< 0.28	2.12	< 2.93	299	1160	4.09	0.20
IRAS 16255+2801	< 1.82	0.21:	–	< 0.59	0.28	0.55	< 4.18	348		1.07	
IRAS 16300+1558	< 1.77	< 5.63	0.31	0.56	0.42	1.58	< 1.31	287		11.33	
IRAS 17207−0014	6.12	10.2:	–	4.56	4.44	7.51	< 3.60	311	1230	1.30	0.07
IRAS 18368+3549	< 6.98	4.22:	–	1.11	0.70	1.38	< 0.81	349		1.95	
IRAS 18588+3517	< 7.44	< 15.54	–	0.92	0.76	1.61	< 5.12	324		1.89	
IRAS 20100−4156	< 9.04	< 15.77	–	0.78	0.35	0.92	0.94	195		1.61	

Table 2.5 (cont'd)

Object λ_{rest} [μm]	H_2 S(7) 5.51 μm	H_2 S(5) 6.91 μm	H_2 S(4) 8.03 μm	H_2 S(3) 9.67 μm	H_2 S(2) 12.28 μm	H_2 S(1) 17.04 μm	H_2 S(0) 28.22 μm	T_{warm} [K]	T_{hot} [K]	M_{warm} [10^7 $M_\odot$]	M_{hot} [10^7 $M_\odot$]
IRAS 20286+1846	< 1.74	0.35:	–	< 0.78	0.30	0.92	< 0.51	282		1.80	
IRAS 21077+3358	< 2.13	1.59:	–	0.67	0.34	1.16	< 1.29	319		4.05	
IRAS 21272+2514	0.39	0.51:	–	0.36	0.28	0.91	< 0.46	287	1160	2.22	0.09
IRAS 22055+3024	0.65	2.52:	–	1.30	1.09	1.61	< 1.39	320	976	2.72	0.24
IRAS 22116+0437	< 2.45	< 6.21	–	0.74	0.64	1.09	< 1.82	340		4.70	
IRAS 22491−1808	< 7.01	< 14.81	–	0.76	0.92	2.10	< 8.22	298		1.23	
IRAS 23028+0725	–	–	–	0.48	0.45	0.77	< 1.67	333		1.86	
IRAS 23233+0946	< 3.20	1.60:	–	1.03	0.80	1.47	< 0.73	340		2.53	
IRAS 23365+3604	< 7.02	6.98:	–	1.26	0.73	2.14	< 5.75	321		0.84	
IRAS 00163−1039	< 9.00	24.46:	–	2.79	2.87	5.13	< 2.63	326		0.32	
IRAS 01572+0009	2.15	1.21:	–	0.60	< 0.71	2.15	< 1.36	268	1650	6.26	0.15
IRAS 05083+7936	< 8.11	27.31:	–	2.34	2.73	3.59	< 2.75	341		0.99	
IRAS 06538+4628	< 3.69	14.56:	–	< 0.63	3.28	8.86	2.63	189		0.38	
IRAS 08559+1053	< 5.91	1.76:	–	0.72	0.64	1.83	< 0.74	298		4.44	
IRAS 09437+0317	< 9.39	22.60:	–	< 0.36	0.68	2.68	2.20	153		0.11	
IRAS 10565+2448	< 12.33	32.87:	–	3.34	1.95	5.73	< 3.77	320		1.06	
IRAS 11119+3257	< 6.58	< 7.87	–	0.42	< 1.02	2.47	< 2.23	256		10.21	
IRAS 13349+2438	< 23.79	< 20.52	–	< 1.67	< 0.83	< 1.05	< 1.62				
IRAS 15001+1433	< 4.21	1.72:	–	0.44	0.24	1.25	< 0.84	283		3.72	
IRAS 15206+3342	< 8.31	1.61:	–	0.65	0.46	0.94	1.02	196		1.54	
IRAS 20460+1925	–	–	–	< 0.48	< 0.43	< 0.88	< 4.24				

Table 2.5 (cont'd)

Object λ_{rest} [μm]	H_2 S(7) 5.51 μm	H_2 S(5) 6.91 μm	H_2 S(4) 8.03 μm	H_2 S(3) 9.67 μm	H_2 S(2) 12.28 μm	H_2 S(1) 17.04 μm	H_2 S(0) 28.22 μm	T_{warm} [K]	T_{hot} [K]	M_{warm} [10^7 M$_\odot$]	M_{hot} [10^7 M$_\odot$]
IRAS 23007+0836	< 23.20	77.35:	–	< 3.53	6.30	12.90	< 6.28	342		0.27	
IRAS 23394−0353	< 14.60	32.52:	–	3.15	2.44	5.24	1.79	226		0.23	
IRAS 23498+2423	< 1.25	0.49:	–	0.34	< 0.29	0.89	< 1.50	298		4.66	

Note. — Line fluxes are given in 10^{-21} W cm^{-2}. – indicates that the redshifted line lay outside of the IRS spectral range. Fluxes for H_2 S(7) and S(5) are measured in the SL module; all other lines are measured in the SH and LH modules. S(5) lines are tentative upper limits (indicated by a :) due to possible blending with [Ar II] at 6.99 μm; see §2.4.3.

We did not detect the S(6) line in any galaxy, while S(4) showed a single detection in IRAS 16300+1558. Since these lines are excited by hotter gas ($T \sim 1000$ K), they are typically weaker than the lower states which probe the larger reservoir of cool gas. In addition, both lines are only visible in the low-resolution modules at $z \sim 0.1$. This means that deblending is a significant issue, since both lines lie near broad PAH emission complexes. Eleven OHMs and one non-masing galaxy show the unresolved S(7) ortho line at 5.51 μm in the SL module.

Measurement of the S(5) line presents a particular problem due to its location in a crowded section of the spectra. Its rest wavelength of 6.91 μm lies near the [Ar II] feature at 6.99 μm; in addition, both features are bracketed by possible hydrocarbon absorption at 6.85 and 7.25 μm. This not only creates difficulties in establishing a reliable continuum, but also in deblending the [Ar II] and the S(5) emission (see §2.4.5.2). Emission in the [Ar II]/H_2 S(5) complex is seen in more than half of our sample, however, and so we present measurements for the **entire** feature, including blended emission from both lines. We caution that these fluxes should be viewed as upper limits for either [Ar II] or H_2 S(5) emission, since the SL module does not have sufficient resolution to separate the two features.

For galaxies in which multiple H_2 lines are observed, we fit excitation temperatures (T_{ex}) to the molecular gas following the methods of Rigopoulou et al. (2002) and Higdon et al. (2006). We assume that the emission is optically thin (so that the lines are unsaturated), populations are in local thermodynamic equilibrium (LTE), and that the sources are unresolved in the *Spitzer* beam. The luminosity of a molecular emission line for the transition from $(J+2) \rightarrow J$ is then $L_J = A_J \times \Delta E_J \times N_{J+2}$, where A_J is the Einstein-A coefficient, ΔE_J is the energy of the transition, and N_{J+2} is the number of molecules in the $J+2$ state. The partition function for a given symmetry branch is:

$$Z_{J_{o/p}} = \sum_{J_{o/p}} g_J \, \exp[-E_J/kT_{ex}] \tag{2.2}$$

where T_{ex} is the excitation temperature and we sum only over a single symmetry branch (ortho or

para). The statistical weights are $g_J = (2J+1) \times J_s$, where $J_s = 1$ for the para branch (even J) and $J_s = 3$ for ortho (odd J).

Assuming that the lines are in LTE, the ratio of level populations follows a Boltzmann distribution such that $N_J \propto \ g_J \ \exp[-E_J/k \ T_{ex}]$. The inverse slope of the best-fit line of an excitation diagram yields T_{ex} - Figure 2.6 shows examples of temperature fits to the data. The total warm H_2 mass can be then calculated from T_{ex} and the flux (F_J) from any transition as:

$$M_{tot} = m_{H_2} \times \phi_{o/p} \times \frac{(4\pi D_L^2) F_J Z_{J_{o/p}}}{A_J \Delta E_J g_J \ \exp[-E_J/kT_{ex}]} \tag{2.3}$$

where $\phi_{o/p}$ is a numerical factor accounting for the ortho-to-para ratio (assumed to be 3:1), m_{H_2} is the mass of the hydrogen molecule, and D_L is the luminosity distance.

For cases where the S(7) line was detected, a single excitation temperature gives a poor fit to the full set of transitions. In these cases, we first fit T_{ex} between S(3) and S(7), measuring hotter gas. We then subtracted this component from the S(0) to S(3) fluxes, and fit a second T_{ex} to the warm gas component. This decreased the mean warm T_{ex} by ~ 20 K, with a negligible effect on the gas mass. We calculated the warm H_2 mass using the flux in the S(1) transition and the hot gas mass using the S(3) flux (Table 2.5).

Both Higdon et al. (2006) and Roussel et al. (2007) suggest that the H_2 emission arises from far-ultraviolet photons from massive stars powering photodissociation regions (PDRs). Detections of the H_2 S(3) transition in nearly all objects implies that the silicate absorption at 9.7 μm must be partially background to the warm molecular gas seen in emission. Since the dust is very optically thick in almost all ULIRGs, this means that at least some molecular gas (and possibly other atomic transitions) actually come from superficial layers at the edge of the merging system. Given that the OHM is typically formed within the central kiloparsec of the host galaxy, a link between the observed warm H_2 gas and the OHM is uncertain.

11 objects in the OHM sample and 2 non-masing galaxies have CO detections published in the literature (Solomon et al., 1997; Gao & Solomon, 2004a). The beam width used for CO

observations is several times that of the HR slits; since most ULIRGs are unresolved in the *Spitzer* beam, we consider the gas mass estimates to be comparable. The cold gas masses derived using a ULIRG-calibrated M_{H_2}/L_{CO} ratio of $\sim 1.4 M_{\odot}/(\mathrm{K\ km\ s^{-1}\ pc^2})$ give a warm gas mass fraction for the OHMs ranging from $0.04 - 0.8\%$, with the gas fraction of the non-masing galaxies lying in a similar range ($0.06 - 0.1\%$). This is comparable to warm gas fractions in ULIRGs from Higdon et al. (2006), implying that the mid-infrared H_2 lines probe only a small amount of the total gas mass in these galaxies. The bulk of the remaining portion is likely cold gas without sufficient energy to excite rotational transitions in the mid-infrared.

2.4.4 PAH emission

In addition to the atomic and simple molecular emission lines, we also observed multiple features attributed to polycyclic aromatic hydrocarbons (PAHs); the broad-line emission comes from vibrational modes of C-C and C-H bonds (Draine, 2003). PAH features are ubiquitous in the mid-infrared emission of starburst galaxies and ULIRGs (Lutz et al., 1998; Genzel et al., 1998; Sturm et al., 2000; Peeters et al., 2004; Desai et al., 2007; Imanishi et al., 2007), and dominate the low-resolution spectra of most galaxies in our sample. Multiple PAH features are seen for all OHMs, encompassing galaxies with very wide ranges in continuum shape and line emission. We detect strong PAH transitions centered at 6.2, 7.7, 8.6, 11.3, and 12.7 μm, several of which are also visible in the high-resolution spectra. Weaker emission features at 13.5, 14.2, 16.4, 17.1, and 17.4 μm are also visible in many galaxies.

We measured the PAH emission via two methods: the first defines a local continuum around the PAH feature using a spline fit, and then integrates the total flux after baseline subtraction. The default continuum pivots are located at 5.15, 5.55, 5.95, 6.55, and 7.10 μm for the 6.2 μm feature, and at 10.1, 10.9, 11.8, and 12.4 μm for the 11.3 μm feature. These are shifted slightly for each object to avoid both broad absorption features (including water ice and hydrocarbons) and narrow atomic emission lines. We quantify the emission from the two cleanest PAH features appearing in our spectra: the 6.2 and 11.3 μm complexes (Table 2.6).

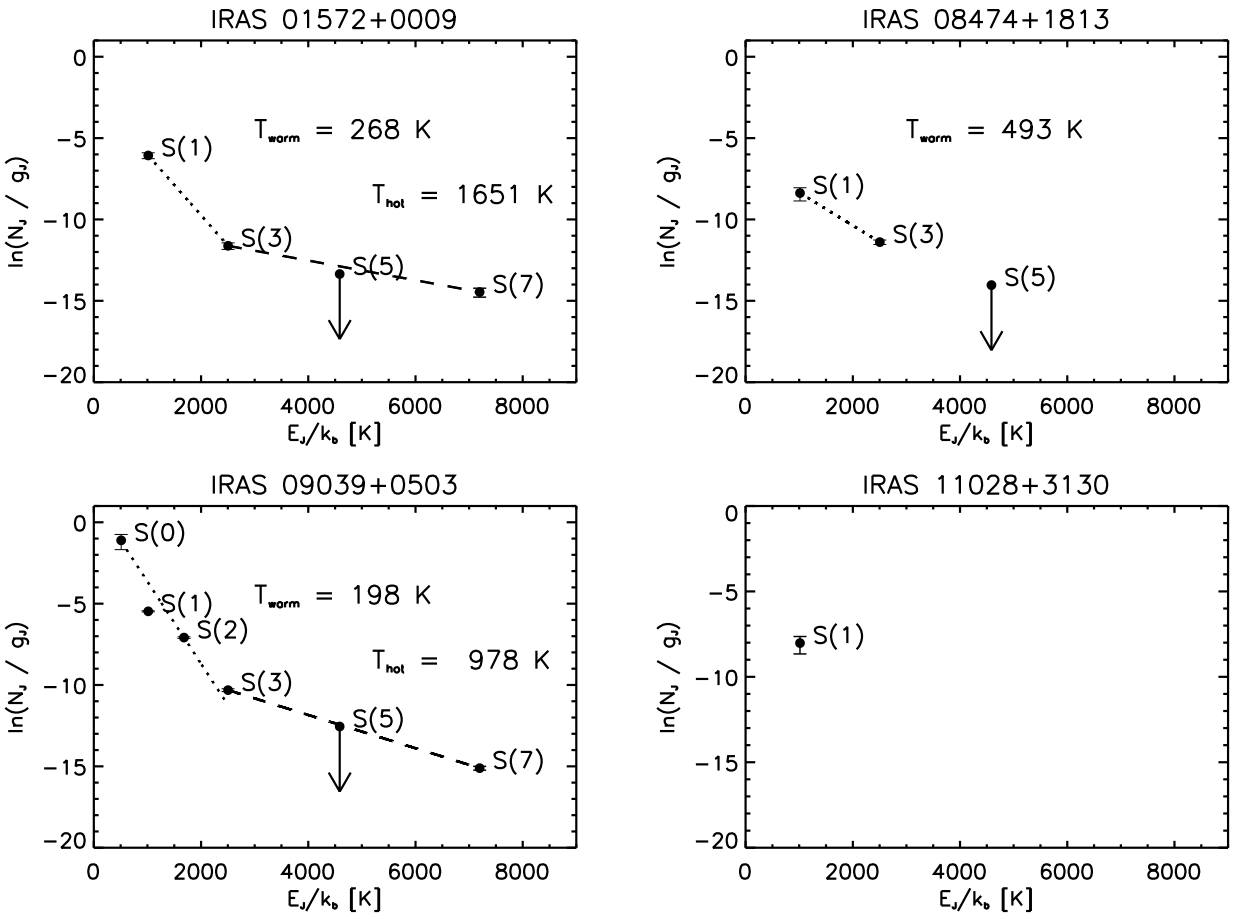

Figure 2.6 Example H_2 excitation diagrams for both non-masing (IRAS 01572+0009) and OHM galaxies (all others). Two galaxies (*left*) are fit with both warm and hot excitation temperatures; IRAS 08474+1813 fits only a warm component since the higher J lines are not detected. IRAS 11028+3130 shows an example of a galaxy with only a single H_2 detection (for which no T_{ex} can be determined). Dotted lines are fit to the warm gas for all detections from S(0) to S(3); dashed lines are fit to the hotter gas using detections of S(3), S(4) and S(7). The S(5) line is always an upper limit due to possible blending from [Ar II] and is not used in the temperature fits.

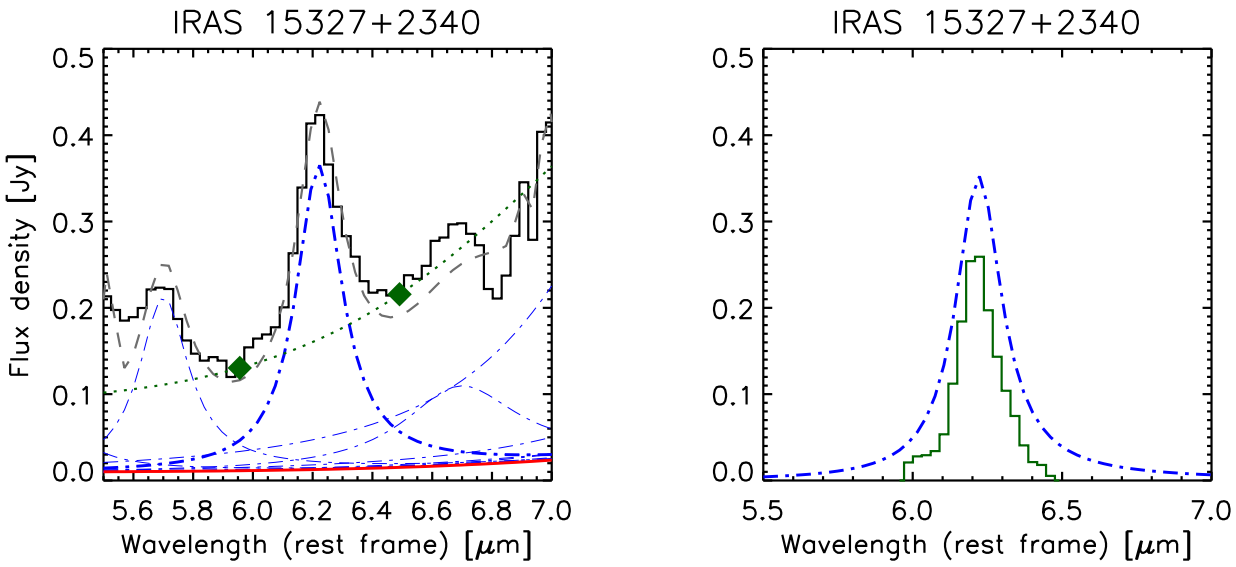

Figure 2.7 Differences between two methods used to measure PAH fluxes in IRS spectra, illustrated on the spectrum of IRAS 15327+2340 (Arp 220). (*left*): The observed spectrum centered on the 6.2 μm PAH feature is shown in black. The minimum at 5.9 μm is the result of absorption by water ice. For the spline method, the PAH feature is defined as the integrated flux above a spline-interpolated continuum (*green dotted line*) between 5.95 and 6.5 μm. The dot-dashed blue lines represent individual Drude fit components from PAHFIT, while the red line is the continuum emission (blackbody dust + starlight). The dashed grey line shows PAHFIT's global fit to the data. (*right*): PAHFIT (*blue*) and spline-fit (*green*) results with the continuum subtracted; the feature as measured by PAHFIT has significantly more flux than with the spline continuum, typical of nearly all galaxies in our sample.

Table 2.6. PAH emission features in low-resolution spectra

Object	PAHFIT luminosity		PAHFIT EW			Spline-fit luminosity		Spline-fit EW		
	6.2 [log $L/L_\odot$]	11.3 [log $L/L_\odot$]	6.2 [μm]	6.2 ice [μm]	11.3 [μm]	6.2 [log $L/L_\odot$]	11.3 [log $L/L_\odot$]	6.2 [μm]	6.2 ice [μm]	11.3 [μm]
IRAS 01355−1814	9.81	9.42	2.25		0.49	9.07	8.97	0.14		0.26
IRAS 01418+1651	8.98	9.07	1.81		1.86	8.60	8.48	0.44		0.61
IRAS 01562+2528	9.59	9.71	2.07		2.22	9.23	9.43	0.37		0.86
IRAS 02524+2046	9.37	9.62	0.54		1.85	9.19	9.13	0.49		0.53
IRAS 03521+0028	9.78	9.60	1.67	0.36	0.81	9.41	9.29	0.43	0.36	0.60
IRAS 04121+0223	9.48	9.42	1.82	0.89	2.01	9.11	9.02	0.44	0.38	0.78
IRAS 04454−4838	10.07	9.90	23.53	0.05	1.31	8.26	8.42	0.07	0.05	1.07
IRAS 06487+2208	9.89	9.75	0.55		0.36	9.60	9.47	0.26		0.26
IRAS 07163+0817	9.21	9.12	12.82		1.30	8.93	8.84	0.58		0.77
IRAS 07572+0533	–	8.95	–		0.04	$<$ 8.95	8.88	$<$ 0.10		0.04
IRAS 08201+2801	10.03	9.52	2.83	0.39	0.57	9.41	9.33	0.19	0.09	0.71
IRAS 08449+2332	9.78	9.63	2.79		1.09	9.38	9.25	0.43		0.59
IRAS 08474+1813	9.37	9.20	2.33		1.41	8.72	8.82	0.23		1.40
IRAS 09039+0503	9.65	9.73	1.59	0.19	2.58	9.13	9.09	0.30	0.19	0.76
IRAS 09539+0857	10.2	10.06	6.38		6.50	8.91	8.96	0.11		1.09
IRAS 10035+2740	9.21	9.33	2.10		1.03	8.77	8.72	0.27		0.25
IRAS 10039−3338	10.96	10.32	2.90	0.01	8.28	8.72	8.94	0.01	0.01	0.72
IRAS 10173+0828	9.37	9.51	2.50		5.13	8.65	8.64	0.35		0.95
IRAS 10339+1548	9.30	9.63	0.71		0.85	9.14	9.23	0.42		0.44
IRAS 10378+1109	9.30	9.36	0.45	0.04	0.64	8.62	9.02	0.07	0.04	0.49

Table 2.6 (cont'd)

Object	PAHFIT luminosity		PAHFIT EW			Spline-fit luminosity		Spline-fit EW		
	6.2 [log $L/L_\odot$]	11.3 [log $L/L_\odot$]	6.2 [μm]	6.2 ice [μm]	11.3 [μm]	6.2 [log $L/L_\odot$]	11.3 [log $L/L_\odot$]	6.2 [μm]	6.2 ice [μm]	11.3 [μm]
IRAS 10485−1447	9.73	9.19	1.64		0.47	8.73	8.84	0.09	0.08	0.36
IRAS 11028+3130	9.11	9.54	1.13		2.33	8.41	8.85	0.14		0.64
IRAS 11180+1623	9.69	9.44	5.87	0.97	0.95	9.02	9.07	0.24	0.26	0.57
IRAS 11524+1058	9.55	9.85	1.09		3.07	8.87	9.17	0.12		0.69
IRAS 12018+1941	9.85	9.44	0.25		0.08	9.58	9.06	0.17		0.05
IRAS 12032+1707	10.33	10.20	3.54	0.06	1.33	9.40	9.64	0.07	0.06	0.61
IRAS 12112+0305	9.62	9.35	4.39	0.37	0.76	9.27	9.02	0.61	0.37	0.52
IRAS 12540+5708	9.59	8.66	0.03		0.01	8.94	9.29	0.01		0.04
IRAS 13218+0552	–	–	–	–	–	$<$ 9.79	9.50	$<$ 0.01		$<$ 0.03
IRAS 13428+5608	9.55	9.45	0.52	0.09	0.76	9.03	8.98	0.14	0.09	0.37
IRAS 13451+1232	9.34	9.34	0.06		0.04	8.23	8.76	0.01		0.01
IRAS 14059+2000	9.16	9.06	0.25		0.48	8.93	8.89	0.23		0.43
IRAS 14070+0525	10.37	10.31	1.86	0.01	2.41	8.92	9.63	0.02	0.01	0.83
IRAS 14553+1245	9.57	9.47	0.63		0.65	9.37	9.22	0.44		0.60
IRAS 15327+2340	10.45	10.03	91.96	0.16	8.23	8.89	8.67	0.30	0.17	0.64
IRAS 16090−0139	10.17	9.99	1.14	0.07	1.45	9.34	9.38	0.09	0.07	0.51
IRAS 16255+2801	9.54	9.14	0.94	0.50	1.02	8.95	8.58	0.16	0.13	0.37
IRAS 16300+1558	10.31	9.97	1.66	0.04	1.09	9.28	9.48	0.07	0.04	0.60
IRAS 17207−0014	10.01	9.86	3.58	0.45	2.75	9.52	9.24	0.50	0.45	0.76
IRAS 18368+3549	9.82	9.74	2.43		2.62	9.50	9.26	0.61		0.74

Table 2.6 (cont'd)

Object	PAHFIT luminosity		PAHFIT EW			Spline-fit luminosity		Spline-fit EW		
	6.2 [log $L/L_\odot$]	11.3 [log $L/L_\odot$]	6.2 [μm]	6.2 ice [μm]	11.3 [μm]	6.2 [log $L/L_\odot$]	11.3 [log $L/L_\odot$]	6.2 [μm]	6.2 ice [μm]	11.3 [μm]
IRAS 18588+3517	9.84	9.67	1.85	0.56	1.65	9.45	9.25	0.41	0.23	0.82
IRAS 20100−4156	9.96	9.83	1.52	0.06	1.23	9.32	9.38	0.19	0.06	0.77
IRAS 20286+1846	9.44	9.45	1.58	0.63	2.26	8.93	8.86	0.41	0.20	0.91
IRAS 21077+3358	9.86	9.85	2.88		1.15	9.23	9.28	0.21		0.40
IRAS 21272+2514	9.66	9.60	1.97	0.15	1.73	9.11	8.97	0.34	0.15	0.56
IRAS 22055+3024	9.22	9.27	0.28		0.26	8.88	9.10	0.15		0.22
IRAS 22116+0437	10.27	9.85	3.16		0.75	9.34	9.38	0.08		0.40
IRAS 22491−1808	9.47	9.33	1.38	0.45	0.98	9.07	8.94	0.43	0.45	0.57
IRAS 23028+0725	...	...	...	...	...	...	...	...	...	...
IRAS 23233+0946	9.68	9.59	1.74	0.36	1.45	9.30	9.17	0.47	0.36	0.76
IRAS 23365+3604	9.80	9.63	2.37	0.27	0.92	9.31	9.18	0.35	0.27	0.43
IRAS 00163−1039	9.30	9.16	3.32		0.95	9.00	8.83	0.52		0.43
IRAS 01572+0009	9.86	9.47	0.10		0.04	9.60	9.55	0.07		0.06
IRAS 05083+7936	9.93	9.95	4.45		2.10	9.68	9.57	0.62		0.66
IRAS 06538+4628	8.75	8.77	1.00		0.60	8.51	8.50	0.45		0.36
IRAS 08559+1053	9.89	9.86	0.31	0.19	0.55	9.63	9.52	0.21	0.19	0.29
IRAS 09437+0317	9.10	9.16	1.47		1.99	8.89	8.82	0.62		0.77
IRAS 10565+2448	9.90	9.80	1.53		1.43	9.55	9.31	0.51		0.51
IRAS 11119+3257	9.92	9.68	0.04	0.05	0.04	9.93	8.36	0.06	0.05	0.003
IRAS 13349+2438	–	–	–	–	–	< 9.39	< 9.10	< 0.01		< 0.01

Table 2.6 (cont'd)

Object	PAHFIT luminosity		PAHFIT EW			Spline-fit luminosity		Spline-fit EW		
	6.2 [log $L/L_\odot$]	11.3 [log $L/L_\odot$]	6.2 [μm]	6.2 ice [μm]	11.3 [μm]	6.2 [log $L/L_\odot$]	11.3 [log $L/L_\odot$]	6.2 [μm]	6.2 ice [μm]	11.3 [μm]
IRAS 15001+1433	9.86	9.86	0.30	0.14	0.43	9.54	9.44	0.16	0.14	0.20
IRAS 15206+3342	9.81	9.75	0.38		0.41	9.56	9.47	0.25		0.27
IRAS 20460+1925	...	...	...	...	...	...	...	...	...	...
IRAS 23007+0836	9.23	9.19	0.33		0.34	8.99	8.89	0.19		0.20
IRAS 23394−0353	9.26	9.16	2.24		2.47	8.94	8.72	0.53		0.64
IRAS 23498+2423	9.52	9.53	0.06		0.13	9.25	9.05	0.04		0.06

Note. — The "ice" 6.2 μm PAH columns use a continuum that is corrected for water ice absorption (where present) at 6 μm. – indicates that PAHFIT fit no significant flux for a particular dust component.

A second method uses PAHFIT (Smith et al., 2007), a public IDL package, to fit global mid-infrared spectral templates and simultaneously measure the relative effects of overlapping features. The routine decomposes the low-resolution IRS spectra into emission from stellar continuum, dust features (including PAHs), atomic and molecular lines, and blackbodies from thermally heated dust at a variety of temperatures; this is simultaneously fit with an extinction curve including silicate features at 9.7 and 18 μm. Due to the large number of parameters being fit, however, even strong features may overlap sufficiently to affect the accuracy of the fit (Spoon et al., 2002). In addition, PAHFIT does not fit for several features commonly found in ULIRGs, such as absorption features from ice, hydrocarbons, and gas-phase molecules.

PAHFIT fits the dust emission features (including PAHs) with a Drude profile, which has the form:

$$I_\lambda[\lambda] = \frac{b\gamma^2}{(\lambda/\lambda_c - \lambda_c/\lambda)^2 + \gamma^2}, \tag{2.4}$$

where λ_c is the central wavelength, γ is the fractional FWHM, and b is the (peak) central intensity. The Drude profile is typically broader than a Gaussian, with significant amounts of power in the extended wings. Several dust emission features (*e.g.*, the 7.7 and 12.7 μm PAHs) require more than one component for a reasonable fit. PAHFIT returned positive detections for both the 6.2 and 11.3 μm PAH features for nearly all galaxies; the fit for OHM IRAS 07572+0533 showed no emission at 6.2 μm, while the fits to OHM IRAS 13218+0552 and the non-masing galaxy IRAS 13349+2438 show no emission in either dust feature.

We compared the flux measured in the 6.2 and 11.3 μm PAH features from our baseline-subtracted spline fits to the PAHFIT values; results from PAHFIT are consistently higher than those from the spline fit, indicating significant mixing between the PAH emission and what was previously designated as "continuum" (Figure 2.7). Fluxes of the 6.2 μm complex measured with PAHFIT are a factor of $\sim 3-4$ greater than the spline-fit fluxes, while the 11.3 μm feature is an average of $\sim 2-3$ times larger. The relative strengths of the two features are consistent using both

methods; the mean value of the (6.2 μm PAH/11.3 μm PAH) ratio is identical to within 15% for OHMs.

Galliano et al. (2008) also use both spline and multi-component profile fitting approaches to measure the PAH variations within galaxies; they show that both methods yield the same overall trends, although each have their own underlying biases depending on the property being measured. Given the large contributions of overlapping dust emission features to the 5–10 μm spectrum, which are not possible to separate from the underlying blackbody emission using spline fits (Marshall et al., 2007), we consider the PAHFIT results to be the more robust method. Measurements of PAH features in the literature, however, typically use a spline-fit method (*e.g.*, Brandl et al., 2006; Desai et al., 2007; Spoon et al., 2007; Zakamska et al., 2008). In particular, comparisons of PAH data from the OHM galaxies to other samples (*e.g.*, the "fork diagram" from Spoon et al., 2007) must use the same method to return physically meaningful results. While PAHFIT fluxes may thus better represent the absolute PAH luminosity, the spline-fit data are used when comparing the OHMs to objects from the literature (Table 2.6).

Water ice absorption at 6 μm can have significant effects on the measurement of the 6.2 μm PAH equivalent width (EW); following the method of Spoon et al. (2007), we correct for this by substituting the continuum inferred while measuring the 9.7 μm silicate strength for the measured 6.2 μm continuum (see §2.4.5). In total, 24 OHMs and three non-masing galaxies with SL data showed absorption strong enough to affect the measured EW; the spline fit with the new continuum decreased the EW for all objects except IRAS 11180+1623, for which the continuum levels as measured by the PAH fit and the silicate depth are nearly identical (within error). Since PAHFIT does not fit for ice absorption, we also calculate ice-corrected EW for objects showing absorption at 6 μm by using the flux from PAHFIT and the inferred continuum from silicate measurements.

The 11.3 μm PAH is seated atop the edge of the deep silicate absorption at 9.7 μm; determining an extinction-corrected continuum level for EW measurements is thus also difficult. Spectral mapping of AGN galaxies with ISOCAM has shown that PAH emission can be spatially extended and suppressed near the nucleus (Le Floc'h et al., 2001; Díaz-Santos et al., 2010); this means that

the PAH emission in AGN may be largely unaffected by dust absorption. Starburst galaxies, however, can show strong PAH emission in both the 6.2 and 11.3 μm bands in the nuclear regions where the silicate optical depth is at its highest (Galliano et al., 2008), and is likely to affect continuum levels for PAH features. The measured 11.3 μm PAH data using the spline-fit method are therefore likely to underestimate the luminosities.

2.4.5 Absorption features

2.4.5.1 Silicates

The LR spectra show near-ubiquitous absorption from amorphous silicate dust, with a strong feature caused by a Si-O stretching mode near 9.7 μm and a weaker feature caused by an Si-O-Si bending mode near 18 μm (Knacke & Thomson, 1973). The presence of dust is unsurprising, as the characteristic extreme infrared luminosities of ULIRGs are caused by large amounts of heated dust being thermally re-radiated. Hao et al. (2007) found that ULIRGs nearly uniformly show absorption in the two silicate features, in contrast to QSOs and some Seyfert galaxies which typically show the feature in emission (Siebenmorgen et al., 2005; Hao et al., 2005; Sturm et al., 2005; Schweitzer et al., 2008).

We measure the strength of the silicate absorption at both 9.7 and 18 μm using the method of Spoon et al. (2007):

$$S_\lambda = \ln\left(\frac{f_\lambda}{f_{cont}}\right), \tag{2.5}$$

where f_λ is the measured flux and f_{cont} the interpolated continuum at the feature extremum. More negative values of S_{sil} represent deeper absorption. The expected continuum is calculated using a combination of spline and power-law fits, depending on the strength of the PAH and water ice features in the spectrum (Spoon et al., 2007).

All OHMs and $\sim 95\%$ of the non-masing galaxies showed absorption at both 9.7 and 18 μm (Table 2.7); the average depth for the OHMs is $S_{9.7} = -1.8 \pm 0.8$, while the average depth of the

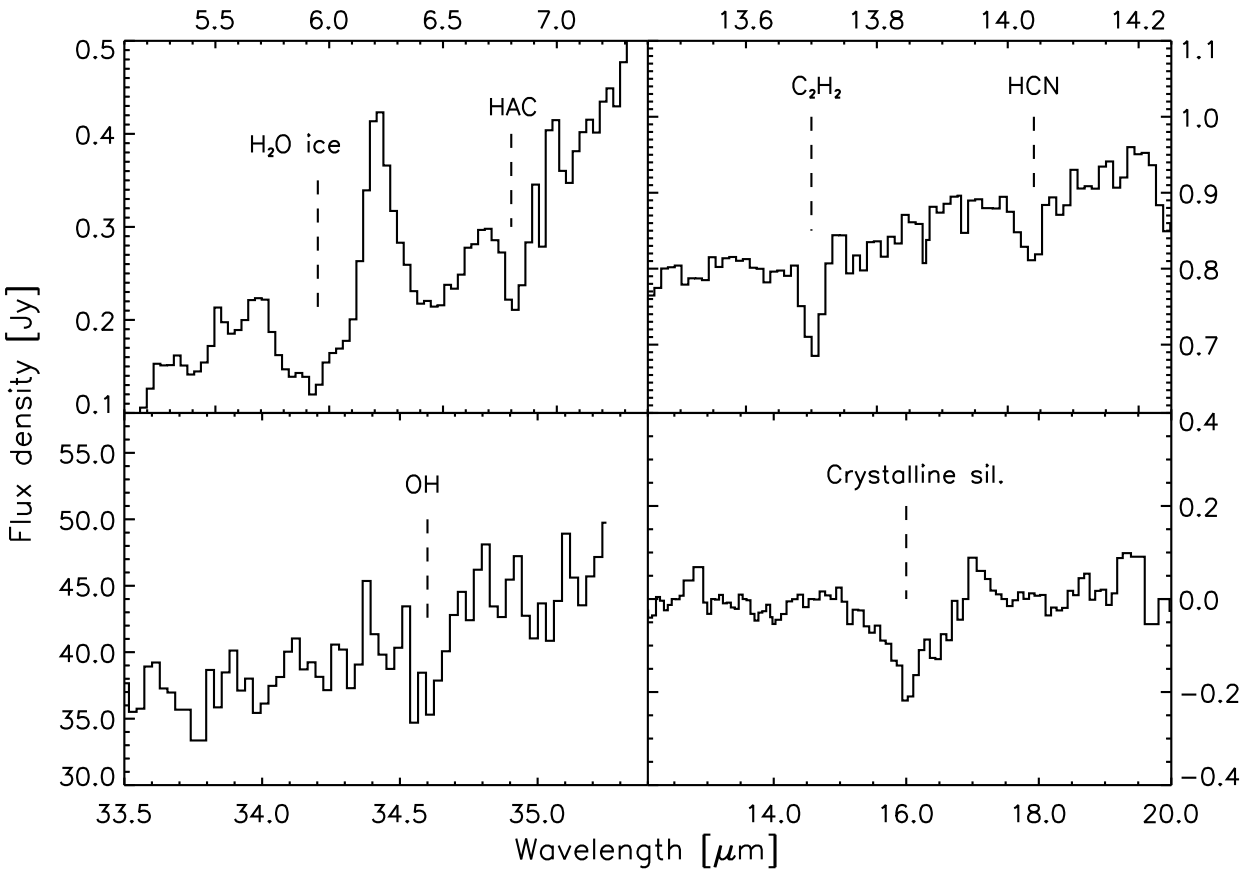

Figure 2.8 Examples of mid-infrared absorption features for the OHM IRAS 15327+2340 (Arp 220). *Top left*: The 6.0 μm H_2O ice and 6.85 μm HAC absorption features. *Top right*: Gas-phase C_2H_2 13.7 μm and HCN 14.0 μm absorption. *Bottom left*: Gas-phase OH 34.6 μm absorption. *Bottom right*: Residual optical depth of the 16 μm crystalline silicate feature. Measurements for all labeled features are in Tables 2.7 and 2.8.

non-masing galaxies is $S_{9.7} = -0.6 \pm 0.4$. The deepest absorption is in the OHM IRAS 04454-0838 ($S_{9.7} = -3.7$), while only one object (the non-masing galaxy IRAS 13349+2438) shows emission in both amorphous silicate features.

Table 2.7. Solid-phase absorption features

Object	6.0 μm H_2O ice	6.85 μm HAC		7.25 μm HAC		9.7 μm	18 μm	16 μm	23 μm
	τ	τ	flux	τ	flux	S_{sil}	S_{sil}	S_{sil}^{resid}	S_{sil}^{resid}
IRAS 01355−1814						−2.4	−0.9	−0.3	−0.2
IRAS 01418+1651		0.49	−8.3			−1.3	−0.4		
IRAS 01562+2528						−0.7	−0.3		
IRAS 02524+2046		0.20	−0.4			−0.9	−0.3		
IRAS 03521+0028	0.42	0.13	−0.4			−1.4	−0.2	−0.1	−0.1
IRAS 04121+0223	1.61					−1.0	−0.2		
IRAS 04454−4838	0.42	0.35	−9.0	0.10	−1.5	−3.7	−1.0	−0.3	−0.2
IRAS 06487+2208		0.23	−4.6			−1.2	−0.3		
IRAS 07163+0817						−1.2	−0.1		
IRAS 07572+0533						−0.6	−0.3		
IRAS 08201+2801	1.06	0.37	−4.0	0.22	−1.5	−2.2	−0.6	−0.2	−0.1
IRAS 08449+2332						−1.2	−0.5	−0.1	−0.1
IRAS 08474+1813		0.36	−0.2			−1.9	−1.2		
IRAS 09039+0503	0.98	0.15	−0.5			−2.0	−0.6		
IRAS 09539+0857		0.24	−2.5			−3.1	−1.2	−0.4	−0.2
IRAS 10035+2740						−1.5	−0.8		
IRAS 10039−3338	0.23	0.23	−166.3			−3.1	−1.0	−0.4	−0.3
IRAS 10173+0828						−1.9	−0.8	−0.3	−0.2
IRAS 10339+1548						−1.1	−0.05		
IRAS 10378+1109	0.72	0.18	−0.6			−2.0	−0.3		
IRAS 10485−1447		0.25	−0.4			−2.9	−0.9		
IRAS 11028+3130						−2.6	−1.0		
IRAS 11180+1623	0.54					−1.7	−0.5		
IRAS 11524+1058		0.27	−1.5	0.2:	−0.3:	−1.5	−0.8		
IRAS 12018+1941		0.16	−2.6			−1.4	−0.4		
IRAS 12032+1707	0.71	0.55	−6.6	0.30	−3.9	−2.7	−0.8		
IRAS 12112+0305	0.59	0.41	−3.5			−1.8	−0.3	−0.2	−0.1
IRAS 12540+5708						−0.7	−0.2		
IRAS 13218+0552						−0.5	−0.4		
IRAS 13428+5608	0.50	0.40	−28.5			−2.0	−0.5		
IRAS 13451+1232						−0.5	−0.1		

Table 2.7 (cont'd)

Object	6.0 μm H_2O ice	6.85 μm HAC		7.25 μm HAC		9.7 μm	18 μm	16 μm	23 μm
	τ	τ	flux	τ	flux	S_{sil}	S_{sil}	S_{sil}^{resid}	S_{sil}^{resid}
IRAS 14059+2000						−0.8	−0.1		
IRAS 14070+0525	0.90	0.24	−1.8	0.15	−1.8	−2.7	−0.9		
IRAS 14553+1245						−1.3	−0.5		
IRAS 15327+2340	0.68	0.35	−50.1			−3.1	−0.4	−0.2	−0.1
IRAS 16090−0139	0.56	0.45	−10.5	0.24	−5.6	−2.4	−0.6		
IRAS 16255+2801	0.54					−2.2	−0.6		
IRAS 16300+1558	0.61	0.38	−2.2	0.21	−1.1	−2.7	−0.7	−0.3	−0.1
IRAS 17207−0014	0.31	0.23	−17.4			−1.9	−0.6	−0.2	−0.1
IRAS 18368+3549						−1.8	−0.2	−0.3	−0.2
IRAS 18588+3517	0.72					−2.2	−0.6	−0.3	–
IRAS 20100−4156	1.45	0.23	−2.9	0.23	−4.5	−2.4	−0.7	−0.2	−0.1
IRAS 20286+1846	1.08					−1.6	−0.6		
IRAS 21077+3358						−1.9	−0.7		
IRAS 21272+2514	1.66	0.21	−0.7			−2.8	−0.7		
IRAS 22055+3024						−1.3	−0.3		
IRAS 22116+0437		0.04:	−0.1:			−2.6	−0.9	−0.2	−0.2
IRAS 22491−1808	0.43	0.19	−0.2			−1.5	−0.5	−0.2	–
IRAS 23028+0725	...	...	...	...	...	...	−0.6		
IRAS 23233+0946	0.44					−1.9	−0.4		
IRAS 23365+3604	0.66					−2.0	−0.5		
IRAS 00163−1039						−0.5	−0.1		
IRAS 01572+0009						−0.2	−0.2		
IRAS 05083+7936						−1.1	−0.3		
IRAS 06538+4628						−0.5	−0.2		
IRAS 08559+1053	0.18					−0.6	−0.2		
IRAS 09437+0317						−1.1	−0.3		
IRAS 10565+2448						−1.2	−0.3		
IRAS 11119+3257	0.19					−0.7	−0.3	−0.2	–
IRAS 13349+2438						0.1	0.07		
IRAS 15001+1433	0.30					−0.9	−0.4		
IRAS 15206+3342						−0.4	−0.2		

Table 2.7 (cont'd)

Object	6.0 μm H_2O ice	6.85 μm HAC		7.25 μm HAC		9.7 μm	18 μm	16 μm	23 μm
	τ	τ	flux	τ	flux	S_{sil}	S_{sil}	S_{sil}^{resid}	S_{sil}^{resid}
IRAS 20460+1925	...	...	...	...	...	...	−0.4		
IRAS 23007+0836						−0.3	−0.1		
IRAS 23394−0353						−0.7	−0.3		
IRAS 23498+2423						−0.6	−0.3		

Note. — Silicate strength is defined in Equation 2.5; the 9.7 and 18 μm features are depths for amorphous silicates, while the 16 and 23 μm crystalline features are residual depths measured after the 18 μm feature was subtracted. Fluxes are given in 10^{-21} W cm^{-2}; objects marked with a : represent uncertain detections.

In addition to the amorphous silicate, we detect weaker features from crystalline silicate absorption in 19 OHMs, including bands at 11, 16, 19, 23, and 28 μm (see Figure 2.8 for an example). We use the method of Spoon et al. (2006) to subtract off both the dust continuum and amorphous component to measure the residual optical depth at 16 and 23 μm, typically the strongest crystalline features (Table 2.7). The deepest S_{16} occurs for IRAS 10039−3338, at −0.4; however, the S/N ratio means we are only sensitive to an absorption limit of $S_{16} \simeq -0.1$ and $S_{18} \simeq -0.05$. Only one detection of crystalline silicates is made in a non-masing galaxy, in IRAS 11119+3257. Since all detections of crystalline silicates in OHMs have $S_{9.7} < -1.4$, the lower total dust column in non-masing galaxies is a likely contributor to the detection rate.

2.4.5.2 Aliphatic hydrocarbons

Absorption bands arising from hydrogenated amorphous carbon grains (HACs) can also be significant contributors to diffuse dust in the galactic ISM (Chiar et al., 2000). ISO (Spoon et al., 2001, 2002) and *Spitzer* (Dartois et al., 2007; Dartois & Muñoz-Caro, 2007) observations have identified HAC absorption features due to bending modes at 6.85 μm (CH_2/CH_3) and 7.25 μm (CH_3) in ULIRGs. These aliphatic features represent a counterpart to the aromatic hydrocarbons responsible for PAH emission and are an abundant component of the ISM in luminous galaxies.

We detect absorption from the 6.85 μm HAC transition in 27/51 galaxies in the OHM sample (Figure 2.8), with zero detections in the non-masing sample. The accompanying 7.25 μm feature

is detected in eight of the galaxies in which the 6.85 μm feature is seen. The strength of the HAC is measured using a spline fit with pivots at 5.2, 5.6, 7.8, 14.0, and 26.0 μm to determine the local continuum in the 6–8 μm region (Spoon et al., 2007) and integrate the total flux within the absorption feature (Table 2.7). The average optical depth of the 6.85 μm feature is $\tau_{6.85} = 0.23 \pm 0.11$, and the average depth of the 7.25 μm feature is $\tau_{7.25} = 0.20 \pm 0.06$. Many of the galaxies with no detection of HACs, however, have limits from noise that are consistent with the absorption depths measured in brighter galaxies.

2.4.5.3 Ices

Absorption from ices in a variety of molecular species (including H_2O, CO, CO_2, and CH_3OH) has been detected in spectroscopy of IR-bright galaxies (Spoon et al., 2000, 2001; Sturm et al., 2000). The band from water ice absorption stretching from 6–8 μm is prominent (Figure 2.8) and was detected in $\sim 10\%$ of a sample of bright galaxies using ISO (Spoon et al., 2002) and the IRS (Armus et al., 2004; Spoon et al., 2005; Armus et al., 2007).

We detected water ice absorption at 6 μm in 24 OHMs and three non-masing galaxies. We use the spline continuum from fitting the 9.7 μm silicate feature as the local 5.5–7 μm continuum in order to obtain an optical depth spectrum for the 6 μm absorption complex. The resulting water ice optical depths are tabulated in Table 2.7. We note that contamination by 6.2 μm PAH emission and absorption by other species than water ice (Spoon et al., 2005) may add confusion in properly measuring optical depths.

2.4.5.4 C_2H_2, HCN, and CO_2

Previous mid-infrared surveys have also identified bands of molecular gas absorption in ULIRGs (Spoon et al., 2006; Armus et al., 2007; Lahuis et al., 2007), including the vibration-rotation bands of acetylene (C_2H_2; 13.7 μm), hydrogen cyanide (HCN; 14.02 μm), and carbon dioxide (CO_2; 15.0 μm). Lahuis et al. (2007) reported the detection of both C_2H_2 and HCN in fifteen (U)LIRG nuclei, with detections of CO_2 in four objects. Eight of the objects in the Lahuis

Table 2.8. Gas-phase absorption features

Object	13.7 μm C_2H_2		14.02 μm HCN		15.0 μm CO_2	
	f_{norm}	flux	f_{norm}	flux	f_{norm}	flux
IRAS 10039−3338	0.93	−0.9	0.86	−4.0		
IRAS 12018+1941	0.95	−0.7	0.94	−0.8		
IRAS 12540+5708	0.95	−9.5				
IRAS 13218+0552	0.82	−1.1				
IRAS 13428+5608	0.93	−0.8				
IRAS 14070+0525	0.79	−0.4				
IRAS 15327+2340	0.84	−5.8	0.90	−5.6	0.94	−2.0
IRAS 16090−0139	0.86	−1.1				
IRAS 17207−0014	0.93	−0.7				
IRAS 20100−4156	0.82	−1.4	0.84	−1.1		
IRAS 22491−1808	0.92	−0.7				

Note. — f_{norm} gives the peak depth of absorption features plotted in normalized flux units. Fluxes are measured in 10^{-21} W cm^{-2}.

sample are OHMs in our sample; we confirm detections of C_2H_2 in all eight galaxies, in addition to the OHMs IRAS 10039-3338 and IRAS 12018+1941 (Figure 2.8). HCN is detected in only 4/10 archival galaxies, meaning that we cannot confirm the HCN detection of four galaxies; since the optical depth of HCN is typically much weaker than that of C_2H_2, however, it is possible that our lower detection rate is a result of improved S/N in their reduction process. We also confirm the detection of CO_2 in IRAS 15327+2340 (Arp 220). No galaxies in the non-masing control sample showed absorption in any molecular band, nor did any of the OHMs observed in our dedicated program.

Since these gas-phase absorption features are actually a blend of multiple absorption lines, the peak optical depth measured is a function of the velocity resolution of the spectrograph. We therefore report the integrated flux and the peak depth in normalized flux units (f_{norm}, where the spectrum has been divided by the adopted continuum; Spoon et al., 2004) in Table 2.8.

Lahuis et al. (2007) model abundances for ULIRGs with detections of C_2H_2, HCN, and CO_2, and suggest that they are associated with a phase of deeply embedded star formation, excluding the possibility of the features arising from an X-ray dominated region (XDR) powered by AGN. Darling (2007) has also shown that OHMs have the highest mean molecular gas densities among

starburst galaxies (traced by the $J = 1 \rightarrow 0$ rotational HCN transition) and also possess high dense molecular gas fractions, comprising a distinct population in the IR-CO relation. The results of Lahuis et al. (2007) show that 9/15 ULIRGs with absorption in both C_2H_2 and HCN are known OHMs in our *Spitzer* sample; this dense gas fraction ($\sim 50\%$) is nearly identical to the observed OHM fraction in starbursts with dense (ULIRGs with $L_{HCN}/L_{CO} > 0.07$) fractions of molecular gas (Gao & Solomon, 2004b; Darling, 2007; Baan et al., 2008).

Given that the S/N ratio for the OHM and non-masing galaxies are of comparable magnitude, the lack of detection of any gas-phase species in the non-masing galaxies is a striking difference compared to the OHMs. Figure 2.9 shows the median stack of both samples near the regions of gas-phase absorption; while the C_2H_2 feature at 13.7 μm can be clearly seen in the median OHM spectrum, neither the HCN nor the CO_2 transition is prominent. Since the data have been median stacked (as opposed to a mean, which can be dominated by a few deep absorbers), this suggests low-levels of C_2H_2 present in a significant fraction of the OHM host galaxies. No molecular absorption appears in the medianed spectrum for the non-masing galaxies.

While a connection between OHMs and dense molecular gas is known to exist, the lack of detected molecular absorption in the mid-infrared for the majority of OHMs is not entirely unexpected. OHMs occur in merging galaxies where different populations of gas may be kinematically and thermally distinct, yet are observed as a single unresolved region within the *Spitzer* beam. Lahuis et al. (2007) suggest that high abundances of warm, dense gas are associated with deeply-embedded star formation, where HII regions are prevented from expanding by large pressure gradients and extend the lifetime of the star formation process.

Baan et al. (2008) interpret dense gas abundances as excluding very hard radiation fields (such as those found in XDRs) that dissociate the molecules; they suggest that the molecular emission arises from PDRs surrounding HII regions. Although few OHMs show absorption from dense molecular gas, the OHM sample also has few identified AGN or XDRs (only 4/51 OHMs show [Ne V] at 14 μm). The connection between dense molecular gas and the presence of an AGN is thus unclear based on this data alone.

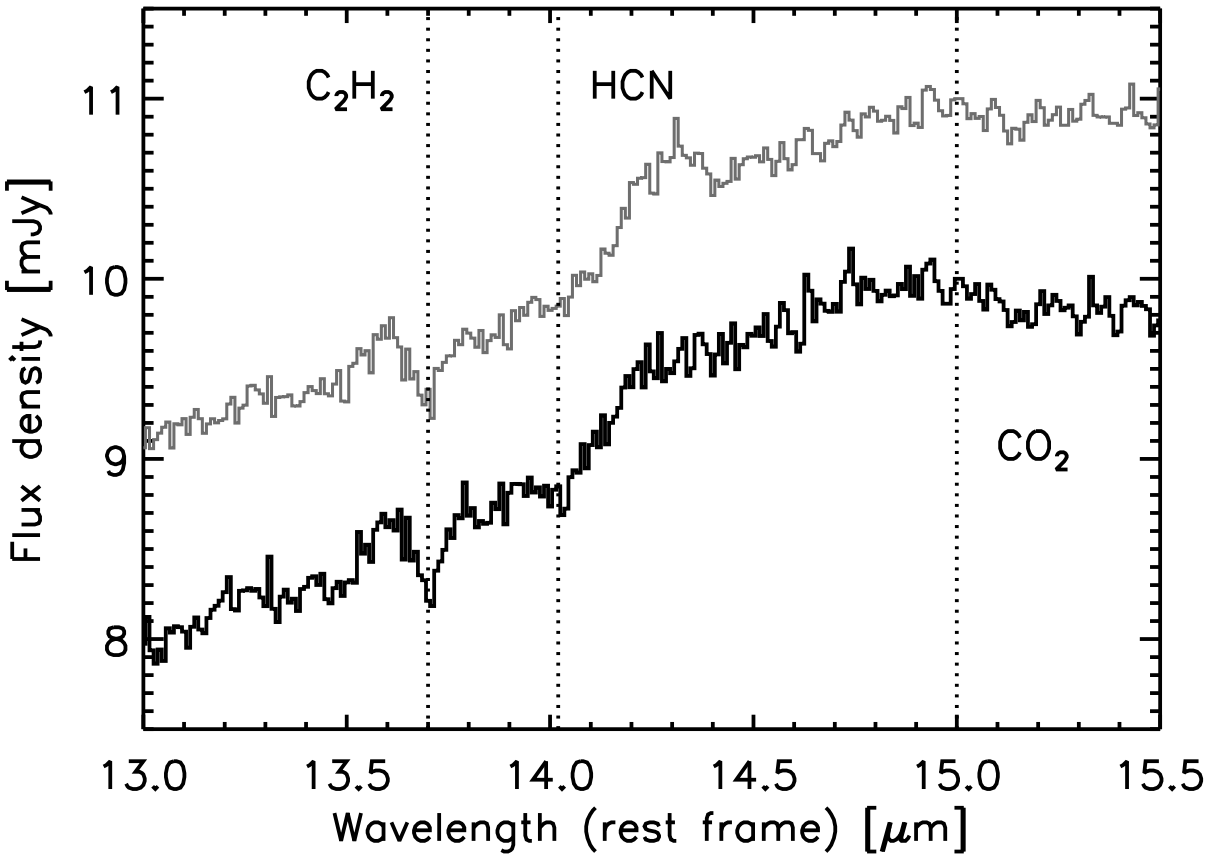

Figure 2.9 Medianed HR spectra for both OHMs (*black*) and non-masing (*grey*) galaxies, sampled at intervals of 0.01 μm and normalized in flux at 15 μm. PAH emission is visible in bands centered at 13.6 and 14.2 μm. The dotted lines mark locations of gas-phase absorption in C_2H_2 (13.7 μm), HCN (14.02 μm), and CO_2 (15.0 μm). The spectra are vertically offset to highlight the differences between the samples.

Table 2.9. Properties of OH gas-phase absorption

OHM	f_{OH} [10^{-21} W cm^{-2}]	τ_{peak}	EW [10^{-3} μm]	N_{OH} [cm^{-2}]	γ_{abs} [ph/s]	γ_{OHM} [ph/s]	ϕ_{pump} %
IRAS 01418+1651 (III Zw 35)	-6.1	0.15	5.5	1.1×10^{17}	1.7×10^{54}	1.8×10^{53}	10
IRAS 13428+5608 (Mrk 273)	-28.5	0.14	10.2	2.1×10^{17}	1.7×10^{55}	1.4×10^{53}	0.8
IRAS 15327+2340 (Arp 220)	-172	0.21	15.0	3.0×10^{17}	2.3×10^{55}	1.6×10^{53}	0.7

Note. — The pumping efficiency ($\phi_{pump} = \gamma_{OHM}/\gamma_{abs} \times 100$) assumes all pumping comes from the 34.6 μm transition.

2.4.5.5 Gas-phase OH

For three OHMs, we report detection of the $^2\Pi_{1/2}$ (J=5/2) $\rightarrow$ $^2\Pi_{3/2}$ (J=3/2) OH absorption doublet near 34.616 μm: III Zw 35 (IRAS 01418+1651), Mrk 273 (IRAS 13428+5608), and Arp 220 (IRAS 15327+2340). This feature is generally difficult to detect since it lies near the noisy, far-red edge of the LH module; for all objects with $z > 0.08$, it is redshifted out of the IRS range. OH absorption at 34.6 μm in Arp 220 was first reported by Skinner et al. (1997) using ISO data and confirmed with the IRS by Farrah et al. (2007), who incorrectly identified it as the OH^- ion. All OH absorption features are well fit with a single Gaussian, since the separation between the doublet features ($\Delta\lambda \simeq 0.02$ μm) is comparable to the resolution element in the LH module. No detection of OH absorption was made for any of the non-masing galaxies.

Assuming the OH transitions are optically thin, we can use the EW to derive a column density for the OH ground state, which is likely to be a good proxy for the total column at typical molecular cloud densities (Bradford et al., 1999):

$$N_l = \frac{EW}{A_{ul}} \frac{8\pi c}{\lambda^4} \frac{g_l}{g_u}. \tag{2.6}$$

OH column densities for all galaxies are quite similar, lying between $(1-3) \times 10^{17}$ cm^{-2} (Table 2.9). The measured N_{OH} from the IRS data for Arp 220 also agrees within a factor of 2 of the column measured with ISO data (Skinner et al., 1997). Limits for galaxies in which the 34.6 μm OH feature is not detected are of order $N_{OH} \lesssim 1 \times 10^{17}$ cm^{-2}.

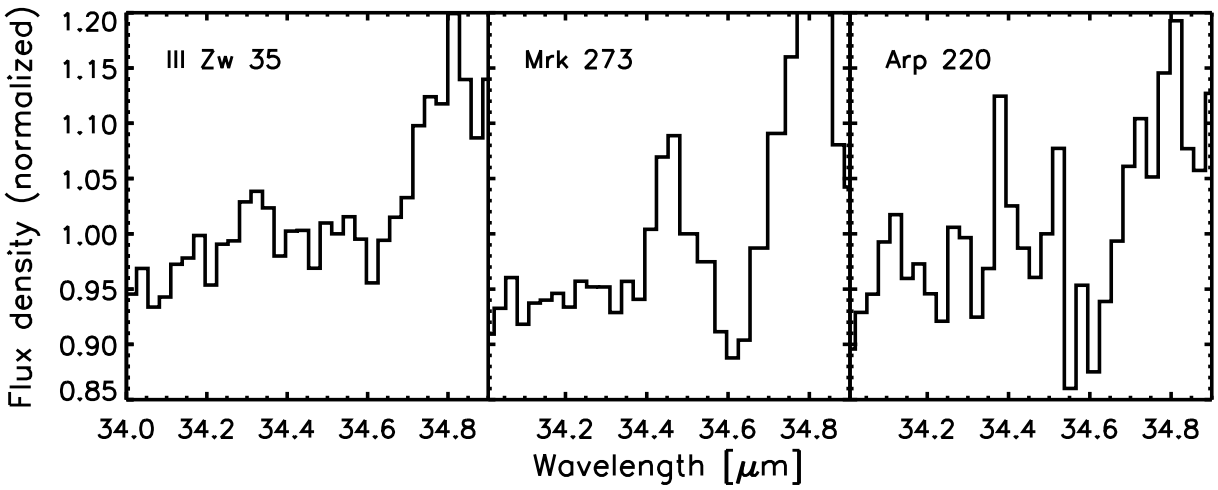

Figure 2.10 The 34.6 μm OH absorption feature in III Zw 35, Mrk 273, and Arp 220. All spectra are normalized in flux near 34.5 μm.

We compare the N_{OH} derived from the rotational 34.6 μm transitions to the OH column density measured in galaxies who show the hyperfine 1667 MHz feature in absorption. The majority of such galaxies are ULIRGs of comparable luminosity to the galaxies in our non-masing sample. Measurements from ten OH absorbers (Baan et al., 1992a; Darling, 2007) give $N_{OH} = T_{ex}(1.8 \pm 1.9) \times 10^{15}$ cm^{-2}, where T_{ex} is the OH excitation temperature in K. If the dust and gas are well-mixed, then the temperature of the dust ($\sim 50 - 100$ K) can be used as a proxy for T_{ex}. This gives OH column densities for both OHMs (34.6 μm) and non-masing galaxies (1667 MHz) with comparable values of $N_{OH} \simeq 10^{17}$ cm^{-2}. If so, then this addresses one of the crucial differences between OHMs and non-masing ULIRGs - namely, that differences in the abundance of masing molecules are *not* a key factor for triggering an OHM.

The amount of OH available in the galaxy can also test models of the OHM pumping mechanism. Skinner et al. (1997) computed the photon flux ($\gamma_{abs} = L_{abs}^{OH}/h\nu_{OH}$) absorbed in the 34.6 μm transition from the OHM Arp 220. They found that γ_{abs} is roughly 1% of the photon flux in the OHM ($\gamma_{OHM} = L_{OHM}/h\nu_{OHM}$). If the 18-cm and mid-infrared pumping photons lie along the same line of sight, this means that pumping photons from the 34.6 μm transition alone can power the OHM (given an efficiency of $\sim 1\%$ or higher). While radiative transfer models from

Lockett & Elitzur (2008) suggest that the 53 μm OH transition likely contributes more pumping photons than the 34.6 μm line, the energetics are consistent with the basic accepted mid-infrared pumping model.

For the galaxies in our sample with OH absorption, Arp 220 and Mrk 273 would require pumping efficiencies on the order of 1% to power the OHMs from the 34.6 μm transition alone. III Zw 35 shows the weakest OH absorption among our detections and would require an efficiency of $\phi_{pump} \simeq 10\%$.

2.5 Conclusions

We present mid-infrared spectra and photometry for 51 OH megamasers taken with the IRS on *Spitzer*, along with 15 galaxies confirmed to have **no** megamaser emission above $L_{OH} = 10^{2.3} L_{\odot}$. All objects in both samples have full coverage in both the low- and high-resolution IRS modules. We measure both emission (PAH, H_2, and fine-structure atomic transitions) and absorption (silicates, hydrogenated amorphous carbon grains, and molecular bands) features, with full spectra, line fluxes, equivalent widths, and absorption depths presented for each object.

The majority of the galaxies closely resemble standard mid-infrared ULIRG templates, with the low-resolution emission dominated by moderate-to-deep amorphous silicate absorption at 9.7 and 18 μm and PAH features at 6.2, 7.7, 8.6, 11.3 and 12.7 μm. The OHMs (on average) show deeper silicate absorption and steeper continuum slopes than the non-masing galaxies. Crystalline silicate absorption is detected in roughly a third of OHMs, but in only 1 out of 15 non-masing galaxies. OHMs are also the only galaxies in our sample to show absorption from hydrogenated amorphous carbon (HAC), gas-phase HCN, C_2H_2, and CO_2; however, higher average noise in the non-masing spectra mean that features at similar absorption depths could be obscured due to lack of sensitivity. High-resolution spectra show emission from [Ne II] and [Ne III] in almost all galaxies, with emission from [S III], [S IV], and [O IV] commonly detected. The high-ionization [Ne V] line (a clear tracer of AGN) is detected in $< 10\%$ of OHMs and in 53% of the non-masing galaxies. Almost all galaxies in both samples also show emission in multiple H_2 rotational transitions.

We also measure the 34.6 μm OH transition in three OHMs. OH column densities derived from the mid-infrared OH transition are of the same order of magnitude as the column densities derived from the 1667 MHz OH transition for ULIRGs in the literature. We interpret this as evidence that the OH abundances in both OHMs and non-masing galaxies are similar, and are not a limiting factor for megamaser emission.

Chapter 3

Mid-infrared triggers for OH megamaser emission

OH megamasers (OHMs) are 18-cm masers located in the nuclear regions of merging, (ultra)luminous infrared galaxies ([U]LIRGs). Possessing isotropic line luminosities from $10^1 - 10^4\ L_\odot$, their hyperfine ratios, extremely broad linewidths, and large physical sizes point to a fundamentally different origin than the Galactic OH masers of the Milky Way (Lo, 2005). A rare phenomenon in the local universe (roughly 100 have been identified out to a redshift of $z = 0.265$), OHMs are exceptional probes of their environment due to their ability to be detected at cosmic distances (Darling & Giovanelli, 2002a). The association of the megamaser emission with merging galaxies means that OHMs trace numerous extreme astrophysical processes, including high-intensity star formation, accretion in the central parts of galaxies, and the eventual formation of massive black holes via binary black hole mergers.

In order to use OHMs as tracers, however, the relationship between the maser emission and the environment of the host galaxies must be well quantified. Previous studies found no systematic difference between OHM hosts and ULIRGs of similar masses in the radio (Lonsdale et al., 1998; Pihlström et al., 2005), optical (Baan et al., 1998; Darling & Giovanelli, 2006), or X-ray (Vignali et al., 2005) regimes. OHM galaxies do, however, show exceptionally high dense gas fractions and have a distinctly non-linear IR-CO relation (Darling, 2007). Since OHMs are generated deep within the nuclear regions of ULIRGs, however, the maser emission regions are almost always highly obscured, even at near-infrared wavelengths. This means that observations capable of probing through the dust are critical both for determining the parameters necessary for

production of an OHM and determining its relation with the properties of the host galaxy.

Mid-infrared studies of OHM hosts to date are based primarily on photometry from the IRAS satellite; OHMs tend to occur in galaxies with color excesses at 25 and 60 μm (Henkel et al., 1986), high infrared luminosities (Baan, 1989; Darling & Giovanelli, 2002b), and steep far-infrared spectral indices (Chen et al., 2007). Spectroscopic studies of the mid-infrared emission, however, offer much more powerful diagnostics that can explore the nature of the maser pumping mechanism and the associated OH emission. We used the Infrared Spectrograph (IRS) aboard the *Spitzer Space Telescope* (Werner et al., 2004) to examine the nuclear regions of the merging OHM hosts. Mid-infrared observations offer a particularly rich set of diagnostics for ULIRGs, with measurements of AGN activity (high-ionization lines), obscuring dust (absorption features and infrared photometry), gas reservoirs (molecular absorption and H_2 emission), and possible OH reservoirs (hydrocarbons and ices) all visible in the 5–35 μm region. For some galaxies, the masing gas can also be directly traced via the 34.6 μm OH transition.

Chapter 2 presented details of the observations and data reduction process, and contains all data referred to in this chapter. In §3.1, I present analysis of the mid-infrared properties of the OHMs and non-masing ULIRGs. §3.2 derives physical conditions in the galaxies based on the IRS data, including kinematics, star formation rates, and tracers of AGN activity. A thorough statistical comparison between the masing and non-masing samples is given in §3.4. Finally, §3.5 uses the IRS data to test current models of OHM pumping mechanisms, and suggests how the results can serve as useful selection techniques for future OHM surveys. Results are summarized in §3.6.

The majority of this chapter has been published in the *Astrophysical Journal* as Willett et al. (2011b).

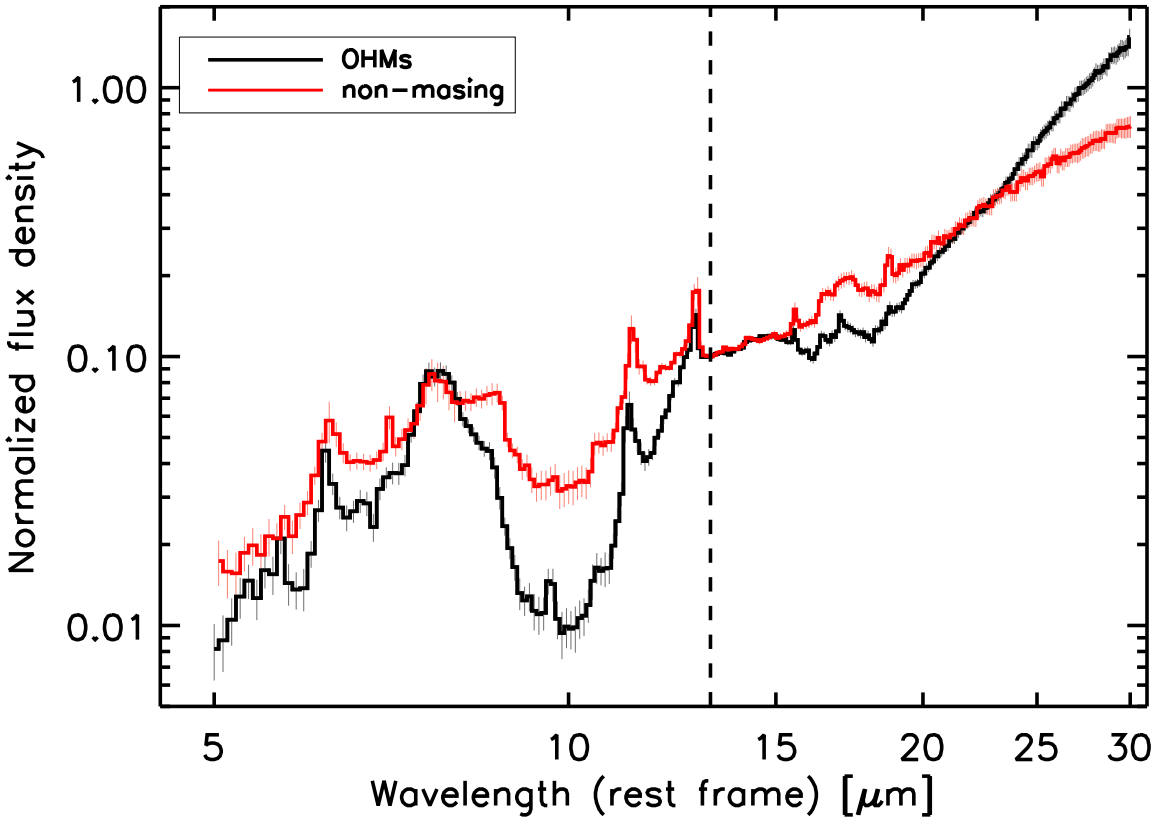

Figure 3.1 Medianed low-resolution spectra for all OHMs (*black*) and non-masing galaxies (*red*). The 1σ error bars for each pixel are also shown. The dashed line shows where the fluxes are normalized at 15 μm.

3.1 Analysis of the *Spitzer* IRS data

3.1.1 Spectral energy distributions

The low-resolution (LR) IRS spectra are powerful indicators of the overall spectral shape of the galaxies, typically dominated by reprocessed emission from dust heated by star formation and/or an active nucleus (e.g., Armus et al., 2007; Hao et al., 2007). Figure 3.1 shows the median LR spectra for all galaxies in both the OHM and non-masing samples. A clear difference in the spectral shape between the two samples is apparent; the OHMs show deeper absorption at both 9.7 μm and 18 μm and steeper continuum from 15–35 μm. Discrepancies in individual emission and absorption features are also apparent; the PAH emission at 7.7 μm is broader in the OHM template, with the 8.6 μm feature largely suppressed (possibly due to extinction from silicate dust). Similarly, the H_2 S(3) λ9.67 line is clearly seen in the median OHM template and suppressed in the non-masing sample.

The medianed OHM spectra also reveals a clear absorption feature near 6 μm associated with water ice (Spoon et al., 2002, 2004); the same feature is not seen in the medianed template of the non-masing galaxies. This is consistent with individual detection rates in the two samples (24/51 OHMs, 3/15 non-masing galaxies). Since water ice is a possible reservoir for the masing OH molecules in their ISM gas-phase, distinct difference between the two populations have implications for OHM emission. If large fractions of the available OH are locked up in solid forms (ice mantles on dust grains, for example), then the reservoir of gas-phase OH could be depleted to a degree that would quench maser emission. This could be due to a harder radiation environment in the non-masing ULIRGs, as sufficiently strong UV radiation can dissociate OH even in the ice phase (Andersson & van Dishoeck, 2008).

3.1.2 Ionization state of the atomic gas

We traced the hardness of the radiation field by comparing the excitation states of the fine-structure neon and sulfur lines, plotting the ratio [Ne III]/[Ne II] against the [S IV]λ10.5/[S III] λ18.71

(Figure 3.2). Detection of all four lines occurred in less than 50% of the sample (14/51 OHMs, 8/15 non-masing galaxies); non-detection of [S IV] is the limiting factor for almost all galaxies. Since [S IV] lies near the silicate absorption at 9.7 μm, extinction caused by mixing of the dust and ionized gas may suppress observation of this line for dust-rich galaxies.

The line ratios from our samples are compared to larger populations of ULIRGs (Farrah et al., 2007), active galaxies (Sturm et al., 2002; Tommasin et al., 2008), and starbursts (Verma et al., 2003). All galaxies show a correlation between higher ionization states for both species, with galaxy types relatively evenly distributed through the total range of line ratios. Fits for each set are consistent with a slope between 0.5 and 1.0; although OHMs have a shallower slope (0.5 ± 0.7) than the non-masing galaxies (0.8 ± 0.7), the uncertainties in both fits are too large to distinguish them from each other or the larger population of ULIRGs. These slopes are also consistent with the results of Dale et al. (2006), who found that nuclear regions of galaxies in the SINGS sample exhibited a similar trend (although they used [S III] λ33.48 instead of [S III] λ18.71). Mixing of the line ratios for OHM hosts and non-masing galaxies, along with the lack of a clear locus for either population, suggests that the ionization state of the gas is not a factor in triggering an OHM.

3.2 Derived properties

3.2.1 Radial velocities

The IRS high-resolution spectra contain multiple narrow lines that can be used for accurate redshift measurements. We computed a systemic infrared velocity from the weighted mean of all detected HR line centroids, typically fixed by the strongest transitions (including H_2, [Ne II], and [Ne III]). The scatter of the individual species around the mean velocity is $\sim$ 200 km s^{-1}for the strongest lines, while the velocity resolution of the IRS is $\sim$ 500 km s^{-1}. There is also a possible unknown velocity component from the *Spitzer* spacecraft, which may be as high as 30 km s^{-1}. We found no statistically significant trend for individual species versus redshift, similar to the trend found in OHM host optical line redshifts by Darling & Giovanelli (2006).

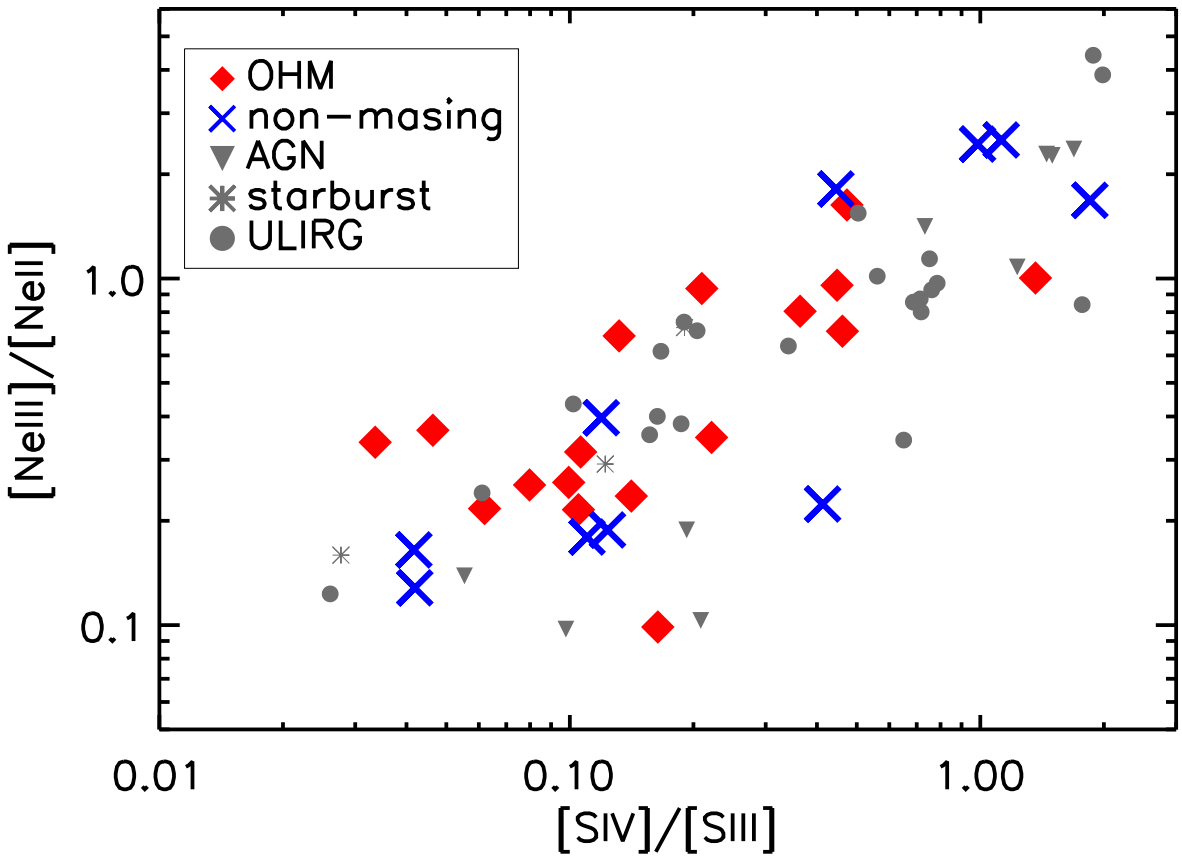

Figure 3.2 Diagnostic of the excitation state in the narrow-line region for OHMs (*red*) and non-masing galaxies (*blue*) in which all four of the [Ne II], [Ne III], [S III], and [S IV] transitions are detected. Also shown are line ratios for ULIRGs (Farrah et al., 2007), active galaxies (Sturm et al., 2002; Tommasin et al., 2008), and starburst galaxies (Verma et al., 2003).

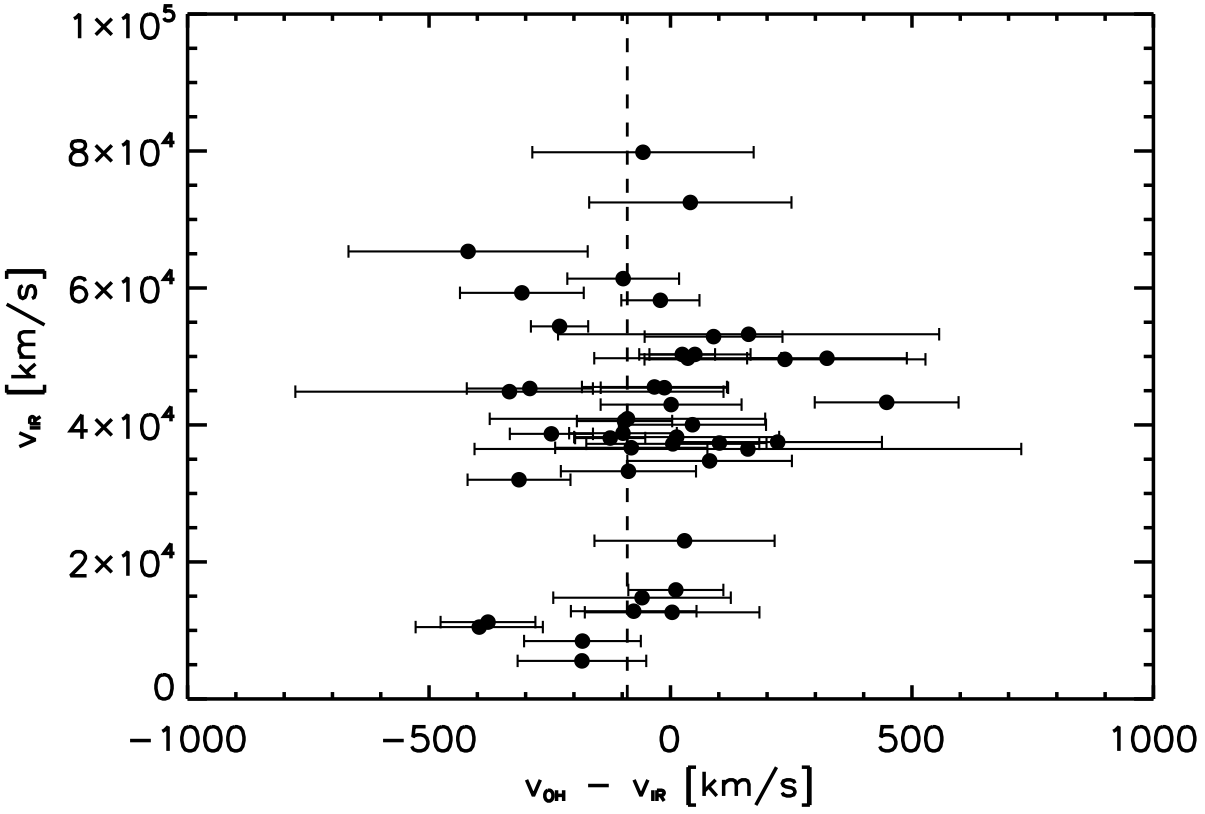

Figure 3.3 OH-IR velocity offset vs. the systemic infrared velocity for the OHMs. The mean velocity offset (*dashed*) for the sample is -90 ± 19 km s^{-1}, showing a blueshift of the OHM relative to the mid-infrared emission lines. Plotted uncertainties are statistical only, and do not account for the unknown velocity ($\lesssim 30$ km s^{-1}) of the spacecraft at the time of observation.

We compared both the individual and systemic infrared velocities to those measured from optical spectroscopy and to the velocity of the OHM itself. Darling & Giovanelli (2006) found a significant asymmetry in the OHM-optical redshift distribution, with the OHM emission somewhat blueshifted with respect to the optical emission. The results for the mean OH-IR velocity offset show a similar blueshift of $\Delta v_{avg} = -90 \pm 19$ km s^{-1}(Figure 3.3). This is consistent with our measurement of no systematic offset between the infrared and optical velocities ($\Delta v_{opt-IR} = -13 \pm 20$ km s^{-1}). While this agrees with the results of Darling (2007), the optical/IR agreement is somewhat puzzling given the large amounts of dust in the actively merging galaxies. If the infrared lines truly come from the nuclear regions and the optical lines from superficial gas, an offset between the two sets of transitions might be expected - non-detection of this effect (and relatively small scatter) may imply that many of the infrared lines are superficial. This is supported by the detection of H_2 S(3) and [S IV] emission on top of the 9.7 μm dust absorption feature. We note that for high-ionization lines that must originate near the nucleus ([Ne V] 14 and 24 μm), we do not have enough detections to measure a significant statistical offset.

The alignment of the mean infrared and optical velocities could be partly due to a selection effect, since the lines are primarily identified on the basis of pre-existing optical redshifts (although mis-identification of lines would require offsets of thousands of km s^{-1} or greater). Spoon & Holt (2009) showed that [Ne III] and [Ne V] emission in ULIRGs can be offset by more than 200 km s^{-1}, likely explained by decelerating outflows that are photoionized by AGN. The lack of a systematic blueshift of the OHM in our sample may be an indicator that outflows are not common in the host galaxies, a further indication of a tendency for OHMs not to be associated with AGN. A two-sided Kolmogorov-Smirnov test showed no significant difference in Δv_{opt-IR} for the OHM and non-masing populations.

Darling & Giovanelli (2006) also found a weak correlation between the magnitude of the OHM blueshift and the strength of the OHM (as measured by log L_{OH} and the linewidth W_{1667}). The blueshift of the OHM with respect to the mid-infrared emission showed no significant correlation for either parameter for the galaxies in our sample.

3.2.2 Star formation tracers

We also examined the relationship between the OHM and the star formation rate (SFR) in the host galaxies. Ho & Keto (2007) use the fine-structure [Ne II] and [Ne III] lines as diagnostics in galaxies spanning more than five decades of infrared luminosity. Neon emission is a useful tracer for the SFR due to its abundance in HII regions, ionization energies that make the singly- and doubly-ionized species among the primary coolants for gas heated by massive stars, and relative insensitivity to dust extinction (particularly when compared to common tracers in the optical/UV such as [O III] $\lambda 5007\mathring{A}$ and Hα).

Figure 3.4 shows the relationship between the far-infrared luminosity (L_{IR}; measured using the method of Sanders & Mirabel, 1996) and the integrated luminosity of the neon lines. We plot the results for both samples in Figure 3.4 along with a least-squares linear fit. We also overplot the relations found from the broader sample in Ho & Keto (2007). Although there is a moderate correlation between L_{Ne} and L_{IR} (as is expected for any comparison involving two luminosities), the scatter is considerable. The combined neon luminosities for the OHMs yield a fit of

$$\log\,[L_{NeII+NeIII}] = (1.0 \pm 0.5)\,\log\,[L_{IR}] - (4 \pm 6), \tag{3.1}$$

with both luminosities measured in $L_{\odot}$. The fit to the non-masing galaxies is:

$$\log\,[L_{NeII+NeIII}] = (1.5 \pm 0.4)\,\log\,[L_{IR}] - (10 \pm 5). \tag{3.2}$$

Both the slope and offset for the OHMs are consistent with the relationship found by Ho & Keto (2007): $\log\,[L_{NeII+NeIII}] = (0.98 \pm 0.069)\,\log\,[L_{IR}] - (2.78 \pm 0.70)$. The fits for the OHMs and non-masing galaxies are also consistent within the large scatter. The fits to the Ho & Keto (2007) and non-masing galaxies, however, do not overlap (within their respective 1σ scatter), indicating a possible marginal difference in SFR.

The larger uncertainties in the OHM and non-masing galaxies' slopes are attributed to their narrow range in L_{IR}. Both samples have a lower limit on L_{IR} that lies at the high end of the Ho &

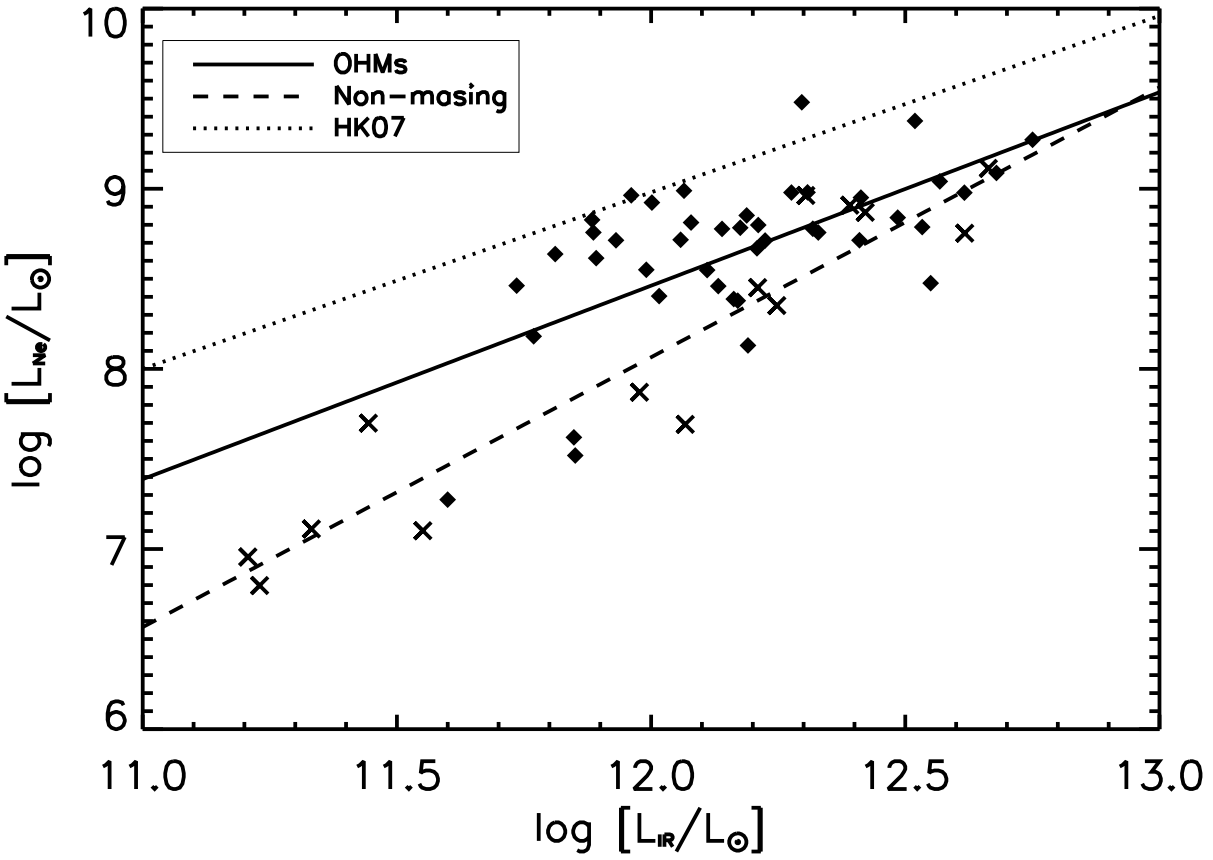

Figure 3.4 Luminosity of [Ne II] + [Ne III] lines as a function of L_{IR} for the OHM (*diamond*) and non-masing (*cross*) samples. Linear fits to both samples are shown by the solid (OHMs) and dashed (non-masing) lines; the dotted line shows the fit for the much larger sample of Ho & Keto (2007). The fit to the OHMs is within the scatter of both the other two samples; fits to the HK07 and non-masing galaxies, however, do not agree.

Keto (2007) data. The upper end of the L_{IR} range reflects the low space density of HyLIRGs with $L_{IR} > 10^{12.5}\ L_{\odot}$. The net effect yields only ~ 1.5 dex of L_{IR} over which a relation can be fit; since the galaxies in Ho & Keto (2007) is over more than five decades of L_{IR}, their correlation is much tighter. Farrah et al. (2007) suggest the offset between the slopes is a result of higher extinction in the nuclear regions of ULIRGs relative to lower-luminosity starbursts that fix the height of the Ho & Keto (2007) relation. The fact that both samples are neon-underluminous compared to the larger data set agrees with the high extinction ($\tau_V \sim 300$) found by fitting dust models (§3.3). Since the non-masing galaxies have even lower neon fluxes, their total L_{IR} likely has a lower overall contribution from star formation.

We computed star formation rates for our samples using two diagnostics: L_{Ne} from Ho & Keto (2007) and the starburst far-infrared luminosity calibration from Kennicutt (1998) (Table 3.1). For the neon relation, we assume an ionization fraction of $f_{ion} = 0.6$ and neon ionization fractions of $f_{Ne^+} = 0.75$ and $f_{Ne^{++}} = 0.1$. The OHM mean star formation rate is $\langle SFR_{Ne} \rangle = 120 \pm 16\ M_{\odot}\ \mathrm{yr}^{-1}$, compared to $\langle SFR_{Ne} \rangle = 65 \pm 21\ M_{\odot}\ \mathrm{yr}^{-1}$ for non-masing galaxies. Using the L_{FIR} calibration with IRAS photometry yields a higher average SFR and larger scatter for both samples, with $\langle SFR_{FIR} \rangle = 300 \pm 30\ M_{\odot}\ \mathrm{yr}^{-1}$ for OHMs and $\langle SFR_{Ne} \rangle = 210 \pm 50\ M_{\odot}\ \mathrm{yr}^{-1}$ for non-masing galaxies. The closer agreement between the two populations for this calibrator reflects the L_{IR} criterion used in selecting the non-masing sample.

Table 3.1. Derived mid-infrared properties for OHMs and non-masing galaxies

	Object	Star formation rates			DUSTY best-fit parameters					LE08 predictions	
		SFR_{Ne} [$M_\odot$ yr^{-1}]	SFR_{FIR} [$M_\odot$ yr^{-1}]	T^{gb}_{dust} [K]	Y	q	τ_V	T_{dust} [K]	τ^{app}_{1667}	τ^{IRS}_{1667}	τ^{DUSTY}_{1667}
OHMs	IRAS 01355−1814	163	502	60	250	0.0	410	64	–	−1.0	**
	IRAS 01418+1651	3	69	54	250	0.0	410	64	−1.9	−1.0	**
	IRAS 01562+2528	64	250	57	950	0.0	55	43	−0.7	0.0	0.0
	IRAS 02524+2046	–	204	62	350	0.0	410	55	−2.7	−1.0	**
	IRAS 03521+0028	111	595	62	250	0.0	410	64	−0.3	−1.5	**
	IRAS 04121+0223	–	80	63	300	0.0	300	61	−0.6	−1.0	−1.0
	IRAS 04454−4838	7	122	64	300	0.0	410	59	–	−1.5	**
	IRAS 06487+2208	551	384	76	200	0.0	190	74	−0.5	−2.0	−1.5
	IRAS 07163+0817	52	105	61	250	0.0	310	65	−0.8	−1.0	**
	IRAS 07572+0533	–	350	81	1000	0.0	46	43	−0.4	−2.0	0.0
	IRAS 08201+2801	114	315	71	200	0.0	410	70	−0.6	−2.0	**
	IRAS 08449+2332	153	194	70	200	0.0	340	71	−0.3	−1.5	**
	IRAS 08474+1813	34	251	61	250	0.0	410	64	−0.4	−1.5	**
	IRAS 09039+0503	95	221	58	300	0.0	290	61	−0.6	0.0	−1.0
	IRAS 09539+0857	–	190	49	250	0.0	380	64	−0.9	−2.5	**
	IRAS 10035+2740	85	313	58	300	0.0	410	59	−0.3	−1.0	**
	IRAS 10039−3338	27	88	71	1000	1.0	120	37	−2.6	−2.5	0.0
	IRAS 10173+0828	6	108	51	300	0.0	410	59	−2.4	−1.0	**
	IRAS 10339+1548	174	394	63	250	0.0	380	64	−0.8	−1.0	**
	IRAS 10378+1109	109	348	69	200	0.0	410	70	−0.9	−2.0	**

Table 3.1 (cont'd)

Object	Star formation rates			DUSTY best-fit parameters					LE08 predictions	
	SFR_{Ne} [$M_\odot$ yr^{-1}]	SFR_{FIR} [$M_\odot$ yr^{-1}]	T_{dust}^{gb} [K]	Y	q	τ_V	T_{dust} [K]	τ_{1667}^{app}	τ_{1667}^{IRS}	τ_{1667}^{DUSTY}
IRAS 10485−1447	52	263	64	250	0.0	410	64	–	−1.5	**
IRAS 11028+3130	0	420	55	250	0.0	410	64	−0.6	−1.0	**
IRAS 11180+1623	94	325	62	250	0.0	410	64	−0.4	−1.5	**
IRAS 11524+1058	–	268	58	350	0.0	250	58	−0.5	−1.0	−1.0
IRAS 12018+1941	126	454	74	150	0.0	200	83	−0.4	−3.0	−1.5
IRAS 12032+1707	434	641	94	200	0.0	410	70	−0.4	−2.0	**
IRAS 12112+0305	104	372	55	300	0.0	410	59	−1.1	−0.5	**
IRAS 12540+5708	54	419	77	950	0.5	50	43	−0.1	−2.5	0.0
IRAS 13218+0552	–	415	95	950	1.5	56	41	−0.6	−3.0	0.0
IRAS 13428+5608	110	244	65	250	0.0	200	67	−0.4	−1.5	−1.5
IRAS 13451+1232	174	253	68	1000	0.0	34	44	−0.0003	−2.0	0.0
IRAS 14059+2000	104	149	63	950	0.0	61	43	−1.1	−0.5	0.0
IRAS 14070+0525	341	1092	95	250	0.0	410	64	−1.1	−1.5	**
IRAS 14553+1245	122	128	73	250	0.0	190	68	−0.6	−2.0	−1.5
IRAS 15327+2340	24	266	60	250	0.0	410	64	−0.6	−1.5	**
IRAS 16090−0139	200	607	62	300	0.0	190	63	−0.4	−1.5	−1.5
IRAS 16255+2801	64	151	70	250	0.0	210	67	−0.9	−2.0	−1.5
IRAS 16300+1558	223	927	54	300	0.0	410	59	−0.3	−1.5	**
IRAS 17207−0014	94	456	59	300	0.0	410	59	−1.0	−1.5	**
IRAS 18368+3549	129	299	56	300	0.0	260	61	−0.2	0.0	−1.0

Table 3.1 (cont'd)

	Object	Star formation rates			DUSTY best-fit parameters					LE08 predictions	
		SFR_{Ne} [$M_\odot$ yr^{-1}]	SFR_{FIR} [$M_\odot$ yr^{-1}]	T_{dust}^{gb} [K]	Y	q	τ_V	T_{dust} [K]	τ_{1667}^{app}	τ_{1667}^{IRS}	τ_{1667}^{DUSTY}
	IRAS 18588+3517	94	144	71	250	0.0	280	66	−0.8	−2.0	−1.0
	IRAS 20100−4156	173	732	62	250	0.0	410	64	–	−1.0	**
	IRAS 20286+1846	46	201	37	250	0.0	230	67	−1.4	0.0	−1.5
	IRAS 21077+3358	167	177	76	200	0.0	410	70	−0.4	−2.5	**
	IRAS 21272+2514	75	151	77	200	0.0	410	70	−1.5	−2.0	**
	IRAS 22055+3024	109	267	71	200	0.0	240	73	−0.7	−2.0	−1.5
	IRAS 22116+0437	178	225	76	200	0.0	380	71	−0.2	−2.5	**
	IRAS 22491−1808	44	246	58	250	0.0	410	64	−1.1	−1.5	**
	IRAS 23028+0725	79	125	91	–	–	–	–	–	–	–
	IRAS 23233+0946	118	232	67	200	0.0	380	71	−0.3	0.0	**
	IRAS 23365+3604	43	245	70	200	0.0	410	70	–	−2.0	**
Non-masing	IRAS 00163−1039	69	40	52	1000	0.0	50	43	–	0.0	0.0
	IRAS 01572+0009	559	513	81	850	0.0	23	48	–	−0.5	0.0
	IRAS 05083+7936	181	148	43	1000	0.0	34	44	–	0.0	0.0
	IRAS 06538+4628	26	30	51	75	0.0	380	109	–	0.0	**
	IRAS 08559+1053	288	261	74	1000	0.5	46	42	–	−1.5	0.0
	IRAS 09437+0317	4	24	38	1000	0.0	46	43	–	0.0	0.0
	IRAS 10565+2448	139	188	55	950	0.0	67	43	–	−0.5	0.0
	IRAS 11119+3257	196	519	78	150	1.0	51	82	–	−2.0	−2.5
	IRAS 13349+2438	69	42	244	950	2.0	90	40	–	–	0.0

Table 3.1 (cont'd)

Object	Star formation rates			DUSTY best-fit parameters					LE08 predictions	
	SFR_{Ne} [$M_\odot$ yr^{-1}]	SFR_{FIR} [$M_\odot$ yr^{-1}]	T^{gb}_{dust} [K]	Y	q	τ_V	T_{dust} [K]	τ^{app}_{1667}	τ^{IRS}_{1667}	τ^{DUSTY}_{1667}
IRAS 15001+1433	318	454	67	1000	0.0	55	43	–	−1.5	0.0
IRAS 15206+3342	591	237	78	1000	0.0	34	44	–	−1.5	0.0
IRAS 20460+1925	–	186	112	–	–	–	–	–	–	–
IRAS 23007+0836	50	45	79	650	0.0	28	53	–	−1.5	0.0
IRAS 23394−0353	28	22	44	700	0.0	56	49	–	0.0	0.0
IRAS 23498+2423	662	477	93	500	1.0	45	53	–	−3.0	0.0

Note. — T^{gb}_{dust} is the dust temperature fit to the photometric greybody; the second T_{dust} is the temperature at the outer envelope fit by the DUSTY models. τ^{app}_{1667} is the apparent maser optical depth calculated from radio fluxes in the literature (Equation 3.4), while τ^{IRS}_{1667} and τ^{DUSTY}_{1667} are predicted values from the LE08 model based on the data in §3.5.1 and §3.5.2, respectively. ** indicates that the predicted τ_{1667} fell outside the available contours for the LE08 model.

Both the large scatter and the difference in SFR between the diagnostics illustrate the difficulties in characterizing a local phenomenon over a large volume. This emphasizes the fact that all OHMs are mergers with multiple components, with sites of star formation likely separated by tens of kpc. The linear correlation between the two SFRs is also relatively low, with a Spearman's estimator of $\rho = 0.54$. This could indicate a component for heating the dust that does not come from star formation, such as an AGN.

3.2.3 AGN vs. starburst

A key issue surrounding ULIRGs is their central source of power - does it come from AGN or starbursts? Baan et al. (1998) use optical classifications of OHM hosts to claim that 45% of the host galaxies show signs of a pure AGN (Seyfert and LINER spectra), with an additional 22.5% displaying composite spectra with characteristics from both AGN and starburst activity. Darling & Giovanelli (2006) compare a sample of OHM host galaxies vs. non-masing ULIRGs and find that 42% are LINERs, 25% Seyfert 2 galaxies, and 33% starbursts; classifications are similar for both samples. They also find few significant correlations between the OHM emission and the optical properties of their host galaxies. Classification using the radio and far-infrared properties of the nuclei, however, show only 34% of the sample with AGN characteristics (Baan & Klöckner, 2006); these include multiple objects optically classified as LINERs or composite objects that show no AGN activity in the radio. It is suggested that the differences in classification lie in the large amounts of extinction at optical wavelengths due to dust obscuring the nucleus.

In the mid-infrared, high-ionization fine structure emission lines are the simplest and most unambiguous tracers of AGN activity. [Ne V] has an ionization energy of 97.02 eV, a level typically too high to be reached by young O and B stars. [O IV] has a smaller ionization energy of 55.89 eV, which is often seen in AGN and in several optically-identified starburst galaxies. In contrast, the [Ne V] line is **only** seen in integrated galactic spectra that harbor AGN, although it is not ubiquitous - Dudik et al. (2007) detect [Ne V] in 19/41 Seyfert and LINER galaxies, for example. It is possible in these cases that lines are present, but that differential extinction in the mid-infrared obscures

their emission. Since AGN occupy a much smaller volume ($<$ 1 pc) than a typical starburst and have harder radiation fields, the high-ionization regions where the neon and oxygen are emitted are likely to be more deeply obscured than their low-ionization counterparts.

[Ne V] λ14.3 is detected in 4/51 OHMs and 8/15 non-masing galaxies (Willett et al., 2011a). ULIRGs in the larger sample of Farrah et al. (2007) show [Ne V] λ14.3 in 22/53 galaxies, three of which are OHMs that overlap with our sample. [O IV] is seen in 21/22 galaxies in their sample that display [Ne V] and only in two that do not, demonstrating a close but not perfect association. The difference in detection rates suggests that the presence of an OHM selects against AGN with high-ionization emission; this may relate to the timescale of the galactic merger. If OHMs are associated with a particular phase since the onset of the host galaxies' merger (and possibly a delay before the activation of the AGN), then this would explain why the OHM sample has so few [Ne V] detections compared to non-masing galaxies and ULIRGs in general.

Given the strong differences in the [Ne V] detection rate between the samples, we examined whether galaxies emitting [Ne V] might reveal other parameters relevant to OHM formation. In the average IRS LR spectra for OHMs (Figure 3.5), galaxies with [Ne V] emission show a shallower 30–20 μm slope than galaxies without high-ionization lines (α_{30-20} = 3.7 vs. 5.4). The silicate depths and PAH luminosities, however, are broadly consistent for both samples. For non-masing galaxies, Figure 3.5 shows that the average 9.7 μm silicate depth is shallower for galaxies that show [Ne V] ($S_{9.7}$ = 0.5 vs 0.7), but that the α_{30-20} slopes are similar. The EW of the 6.2 μm PAH feature is also smaller in galaxies with [Ne V]; the high-ionization lines are consistent with the presence of an AGN that dissociates large molecules. For the OHMs, the presence of [Ne V] shows no effect on either L_{OH} or the peak flux at 1667 MHz.

Other mid-infrared diagnostics can also be used to characterize the contribution of AGN and/or starburst features. Spoon et al. (2007) plot the PAH 6.2 μm EW against the silicate 9.7 μm strength in a "fork" diagram. IRS data show two distinct branches of galaxies for this diagnostic, with one representing a largely AGN-dominated population (weak PAH emission and little to no silicate absorption) and another containing ULIRGs/HyLIRGs, obscured AGN, and

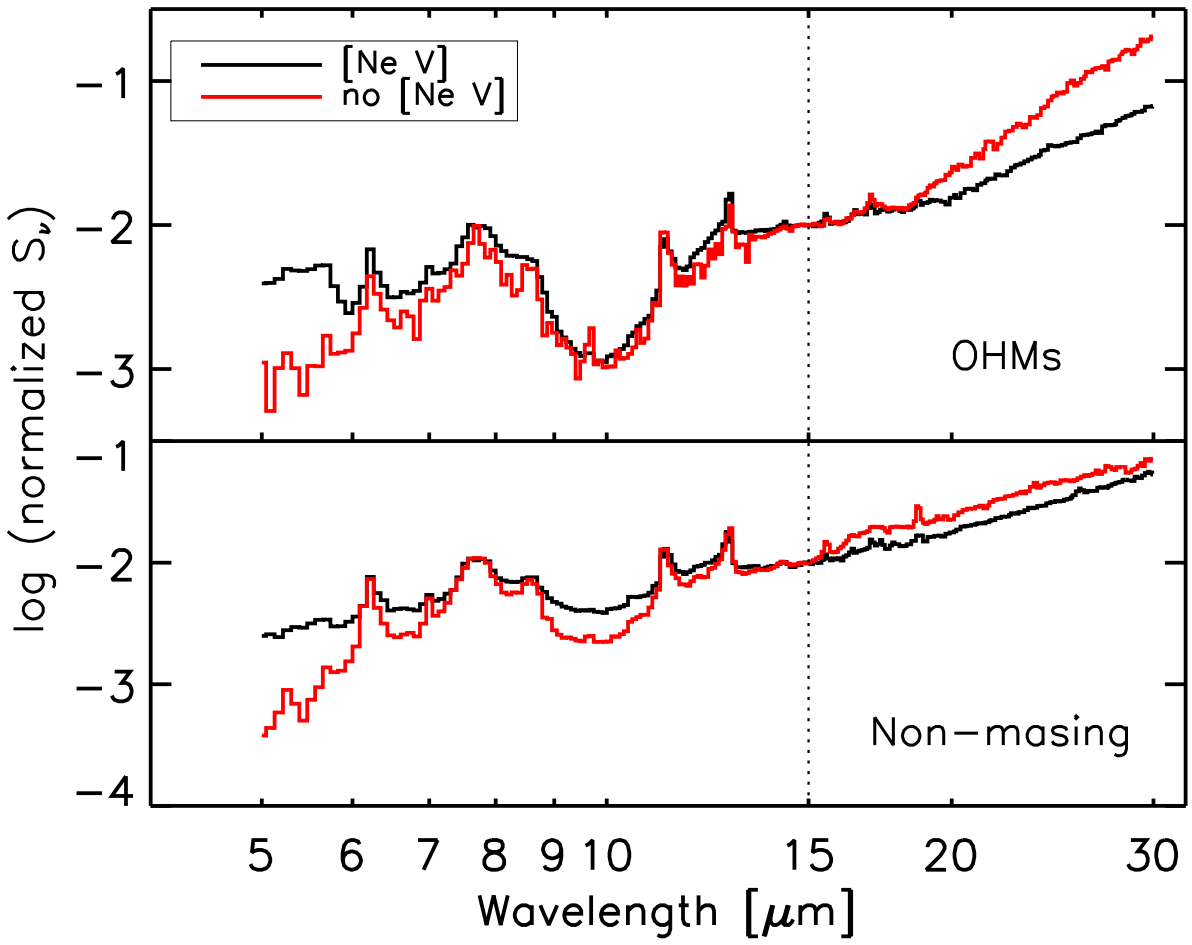

Figure 3.5 IRS low-resolution spectra showing the difference in the median-stacked spectra for galaxies with [Ne V] emission (*black*) and with [Ne V] upper limits (*red*). [Ne V] was detected in 4/51 OHMs (*top*) and 8/15 non-masing galaxies (*bottom*). Spectra are normalized in flux at $\lambda = 15$ μm (*dotted line*).

starburst galaxies (stronger PAH emission coupled with deeper silicate strengths).

We reproduce the fork diagram from Spoon et al. (2007) with our IRS data overlaid on the broader sample of ULIRGs, starburst galaxies, and AGN in Figure 3.6. OHMs lie almost exclusively along the top branch and share significant overlap with optically identified starburst galaxies, which typically have strong PAH emission but weak to moderate silicate absorption. The locus of the OHMs on the fork diagram agrees with the [Ne V] and [O IV] data; only four OHMs lie on the horizontal, AGN-dominated branch. The non-masing galaxies are principally found along the horizontal branch, with a wide range of PAH EW but lower $S_{9.7}$ than the OHMs. A small region of overlap does exist between the two samples near the "knee" (high PAH EW and weaker silicate absorption). The absence of non-masing ULIRGs on the upper branch is one of the first clear spectral diagnostics of OHMs, based only on the properties of the host galaxy.

Using the mid-infrared diagnostics, we estimate the AGN contribution by assuming that [Ne V] clearly indicates an AGN and that [O IV] detection or placement on the horizontal branch in the fork diagram indicates a possible AGN. Based on the IRS data, the AGN fraction of OHMs is between 10 and 25%, compared to a much higher fraction of 50–95% for non-masing ULIRGs. The AGN contributions for the combined samples are consistent with that estimated from radio/far-infrared diagnostics (Baan & Klöckner, 2006). The co-existence of AGN and starbursts in some nuclei is also supported by the presence of galaxies showing both high-ionization emission and large PAH equivalent widths. The mid-infrared AGN fraction for OHMs, however, is significantly lower than that estimated from optical diagnostics (45–70%; Baan et al., 1998), which can be significantly affected by dust obscuration around the nuclear regions.

3.2.4 Dust temperatures

We computed dust temperatures for both samples using two methods. The first is a single fit to the integrated infrared emission by assuming a single-temperature modified blackbody as a template (the second is taken from the model fits in §3.3). We adapt the broad SED of Yun & Carilli (2002), where the emission follows a thermal blackbody above a critical frequency ν_c where

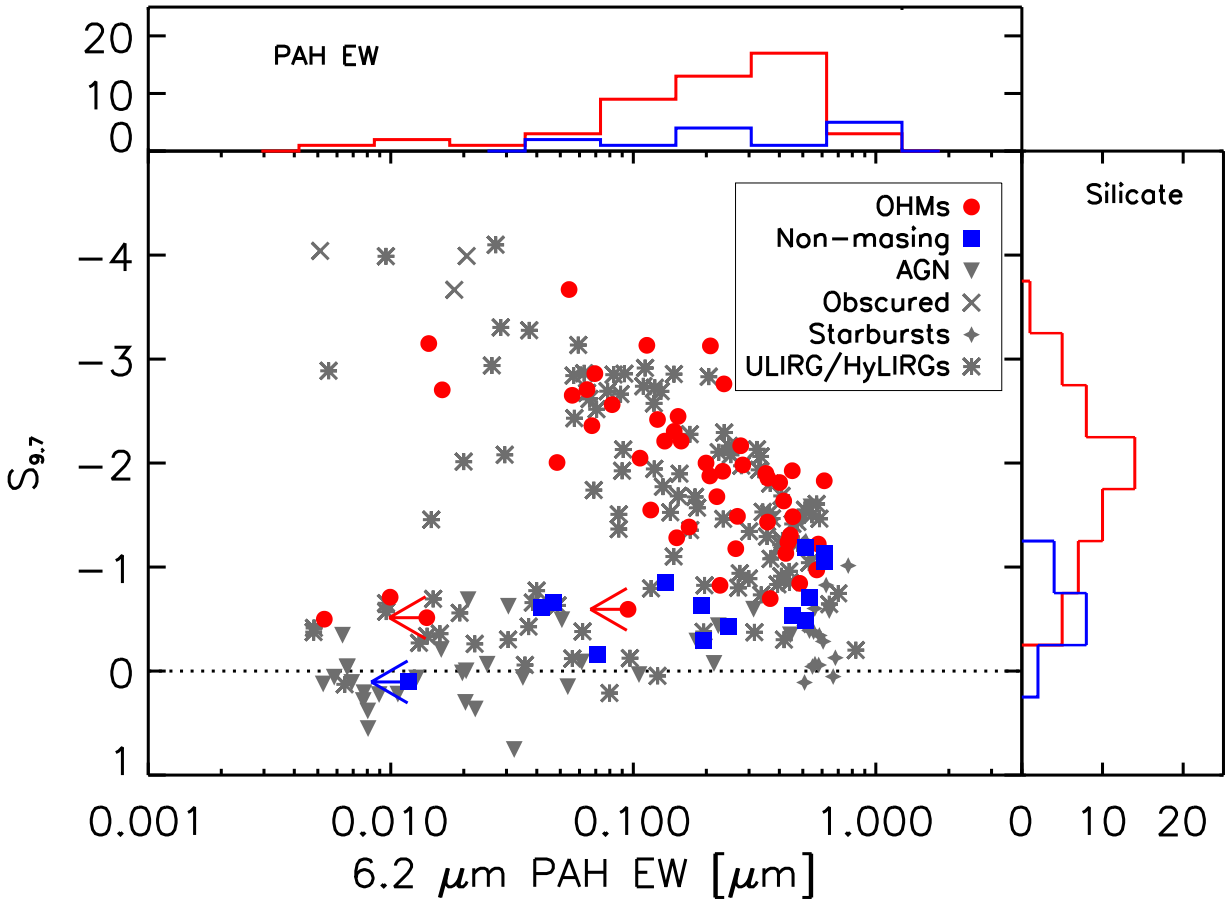

Figure 3.6 "Fork" diagram displaying the 6.2 μm PAH equivalent width vs. the silicate strength at 9.7 μm. OHM galaxies from both our program and the archive are shown in red; non-masing galaxies are shown in blue. *Top*: binned distribution of PAH EW for both samples; *Right*: binned distribution of $S_{9.7}$. Additional *Spitzer* data are from Spoon et al. (2007).

the dust clouds become optically thick and a greybody spectrum below ν_c. For an object subtending an angular diameter θ [arcsec], the expected flux density at frequency ν [GHz] is

$$S_d[\nu] = 2.8 \times 10^{-8} \frac{\nu^3 \theta^2}{e^{0.048\nu/T_d} - 1} \left(1 - e^{(\nu/\nu_c)^\beta}\right) \text{ Jy.} \tag{3.3}$$

In our analysis, θ is a free parameter (accounting for the dependence of flux density on distance) and assumed $\nu_c = 2000$ GHz (150 μm) and an emissivity index $\beta = 1.35$. The fits are relatively insensitive to the choice of β since for most galaxies we lack photometric data points below the critical frequency. We used fluxes from IRAS and IRS peakups to fit the curve with photometry from 12–100 μm, allowing both the physical temperature and the peak intensity (a function of both distance and extinction) to vary. The majority of the galaxies only have IRAS detections at 60 and/or 100 μm, in addition to the IRS peakups.

The mean temperature for the OHMs is $T_{dust} = 66 \pm 12$ K, while the non-masing galaxies have $T_{dust} = 80 \pm 50$ K. These uncertainties are the statistical 1σ envelopes for the sample and do not address the physical relevance of fitting the galaxies with a single temperature fit. The hottest temperature measured is in the non-masing galaxy IRAS 13349+2438 ($T_{dust} = 243$ K), which is more than twice as hot as the next-highest galaxy. The greybody temperatures for all galaxies are listed as T^{gb}_{dust} in Table 3.1.

3.3 Modeling the dust environment

The infrared emission of ULIRGs is dominated by radiation from heated dust; thus, differences in the distribution of dust have significant influences on the mid-infrared spectra. Since the mid-infrared photons are responsible for maser pumping, this may also have an important effect on the presence of OHMs in ULIRGs. Using the radiative transfer code DUSTY, we modeled the dust environment of the galaxies in our sample for two geometries: a smooth, thick dust shell and a clumpy torus.

The DUSTY code models the dust environment as a smooth, spherical distribution of cen-

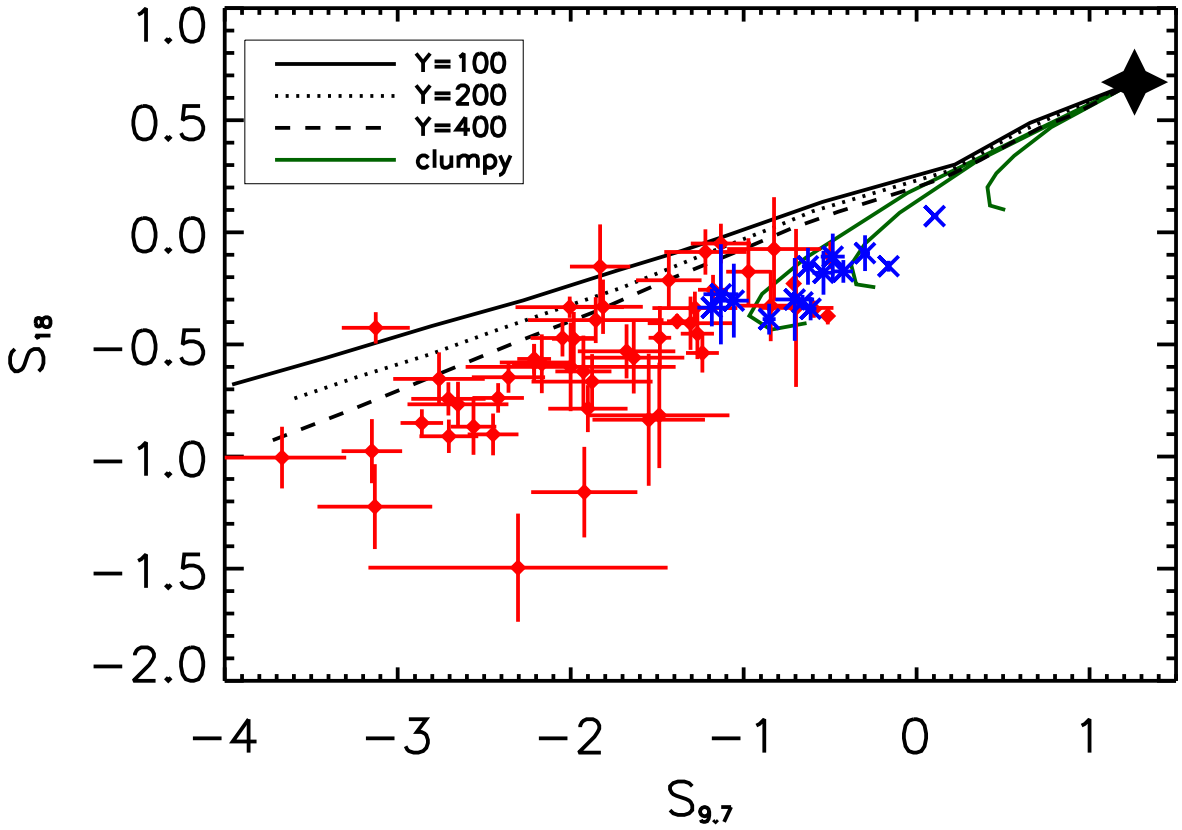

Figure 3.7 Feature-feature diagram plotting the relative strengths of the 9.7 and 18 μm silicate features. The lines represent models of different dust geometries for cool, oxygen-rich silicates (Sirocky et al., 2008). Dotted, dashed, and solid lines represent the thickness of the dust shell in the smooth models ($Y = R_{outer}/R_{inner}$) with a flat radial density distribution ($q = 0$, where $\rho[r] \propto r^{-q}$). The green tracks model clumpy geometries with varying numbers of dust clouds located along the line of sight ($N_0 = 1, 3, 5$ from upper right to lower left). The black star in the upper right corner is the starting point for all optically thin dust in the models ($S_{9.7} = 1.26, S_{18} = 0.67$). Silicate strengths from the IRS data are shown for the OHMS (*red*) and non-masing galaxies (*blue*).

trally illuminated dust (Ivezic & Elitzur, 1997). Our models assumed the dust was composed of cool, oxygen-rich silicates (Ossenkopf et al., 1992) and that the heating source follows a broken-power law luminosity function. The code fits for the thickness of the dust shell ($Y = R_{outer}/R_{inner}$), the power-law index q of the radial density profile ($\rho[r] \propto r^{-q}$), and the total optical depth τ_V at 0.55 μm. The inner dust radius, which is defined by the source luminosity and dust sublimation temperature, is the only free physical parameter in the code. DUSTY then generates a grid of artificial spectra at a variety of radii, from which parameters such as the dust temperature can be extracted.

Motivated by the evidence that some fraction of our galaxies host AGN, we generated a second set of models for a clumpy distribution of dust, which may better represent the environment around active galaxies (Landt et al., 2010). We calculate the source function for individual clumps using DUSTY and used the code CLUMPY (Nenkova et al., 2002, 2008a,b) to account for the new geometry. CLUMPY assumes a distribution of individual dusty clouds in a torus around the central illuminating source. The code fits for Y, q, and τ_V as well as the number of clouds along the line of sight (N_0), the angular dependence of cloud distribution away from the equatorial plane (σ), and the inclination angle of the galaxy (i). Neither σ nor i were well-constrained parameters in our models.

We first used both the DUSTY and CLUMPY models to examine the overall dust distributions of the galaxies in our sample. The "feature-feature" diagram, developed by Sirocky et al. (2008), plots the depths of the 9.7 and 18 μm silicate features against each other. These are compared to tracks from the radiative transfer models; we used a small set of dust geometries and plotted the expected silicate ratios for a large range of optical depths. Following Sirocky et al. (2008), we generated tracks for three smooth geometries that vary in shell thickness ($Y = 100, 200, 400$ for $q = 0.0$) and three clumpy geometries that vary in the number of clouds ($N_0 = 1, 3, 5$ for $q = 0$, $Y = 30$); the optical depth is then allowed to vary for each model from 0 to 80.

Figure 3.7 shows the tracks for the different dust geometries, as well as the measured silicate ratios for the OHMs and non-masing galaxies from the IRS spectra. The non-masing galaxies occupy

a much smaller locus of possible dust geometries than the OHMs, showing no deep absorption ($S < -1.2$) in either silicate feature. As a result, most non-masing galaxies are best fit by one of the clumpy dust geometries. The OHMs occupy a much larger region; while a few galaxies fall close to the clumpy tracks, the majority of OHMs have deep 9.7 μm absorption that only be achieved with a smooth, embedding medium. Levenson et al. (2007) show that such deep absorption requires a large temperature gradient across the absorbing medium, which can only be achieved if the dust screen is both geometrically and optically thick. While the silicate ratios are not sensitive enough to strongly constrain either Y or N_0, it does demonstrate a clear difference in the dust environments of the two ULIRG populations.

Puzzlingly, most of the OHMs fall below the tracks predicted for the smooth dust geometries at $S_{9.7} < -1.5$. If this is a systematic effect, then this implies that either the 18 μm feature is being overestimated or the 9.7 μm feature underestimated with respect to the models. We consider the former more physically probable; if the OHMs were shifted to the left in Figure 3.7 to lie on the smooth tracks, this would imply absorption depths of up to $S_{9.7} \simeq 6 - 7$, much deeper than any seen in a ULIRG to date. As a check, we directly compared our measured silicate depths to those published in Sirocky et al. (2008) for ten galaxies that appear in both samples; however, no systematic difference in absorption strengths was found. Assuming the methods are consistent, this may indicate that a different geometry must be implemented in the code for the most heavily embedded ULIRGs.

Figure 3.7 suggests that OHMs are best modeled by a smooth geometry; based on these results, we attempted to further constrain the dust geometry for our galaxies by fitting each IRS spectra with the smooth-shell model. We used DUSTY to generate a grid of 13860 artificial spectra; the parameter ranges are in Table 3.2. We chose these values to span the expected physical range for ULIRGs: these include shell thicknesses out to $Y = 1000$ (400 pc for typical values of dust sublimation temperature and the heating source luminosity), power-law indices from $0 - 3$, and τ_V extending up to 500.

After generating the grid of artificial spectra, we needed to identify the best fit for each IRS

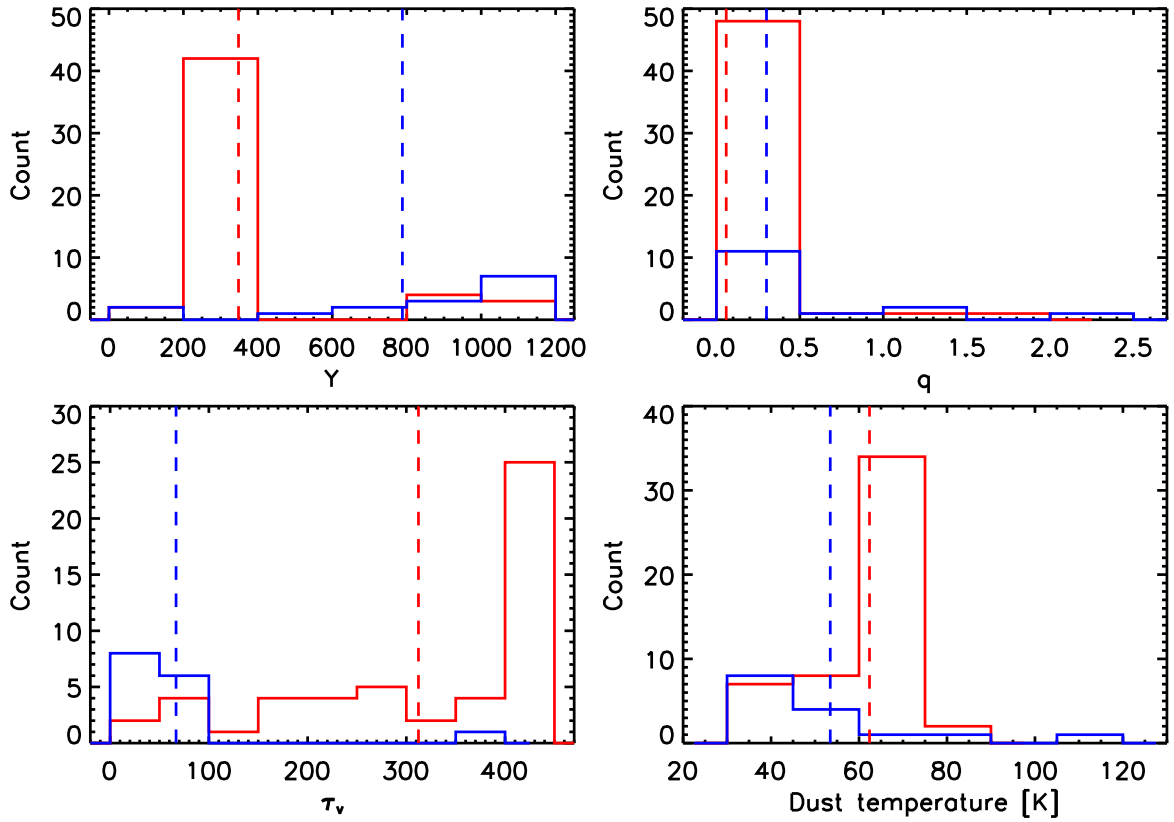

Figure 3.8 Distribution of the dust geometry parameters from DUSTY for the best fits to the IRS spectra. We modeled: (*top left*) the thickness of the dust shell ($Y = R_{outer}/R_{inner}$), the radial power-law index of the dust density q (*top right*), the total optical depth τ_V (*bottom left*), and the dust temperature at the outer edge (*bottom right*). OHMs are in red and non-masing galaxies in blue, with the mean values for each samples indicated with dashed lines.

Table 3.2. Grid parameters for DUSTY model fits

	DUSTY grid
Y	2, 5, 10, 15, 20, 30, 50, 75, 100, 150, 200, 300, 400, 500, 750, 1000
q	0, 0.5, 1.0, 1.5, 2.0, 2.5, 3.0
τ_V	$0.1 - 500$

Note. — τ_V is binned on a logarithmic scale with 180 steps between 0.1 and 500.

spectrum. Since DUSTY only models continuum and dust features, we removed the PAH, atomic, and molecular lines from the IRS data to improve the quality of the fit. For this we employed PAHFIT, a set of IDL routines that performs spectral decomposition of low-resolution IRS data (Smith et al., 2007). While removing narrow line emission was typically clean, subtraction of the PAH emission often increased the area of the 9.7 μm silicate feature, since the wings of the 8.6 and 11.3 PAH profiles fill in the dust absorption. Once the IRS spectra were reduced to continuum + dust features, we re-binned the data to the resolution of the DUSTY grid and found the best fit following the error minimization technique of Nikutta et al. (2009). Results of the best fit Y, q, τ_V, and T_{dust} at the outer edge for each galaxy are given in Table 3.1.

Figure 3.8 shows the distributions of the model parameters for the best DUSTY fits to the OHMs and non-masing galaxies. The best fits have a uniformly flat density profile for almost all galaxies in our sample; only 3/51 OHMs and 4/15 non-masing galaxies had best fits with $q > 0$. The two samples also have similar dust temperatures, with OHMs slightly warmer on average than the non-masing galaxies ($\langle T_{dust} \rangle = 62$ vs. 53 K), confirming the results of Darling & Giovanelli (2002a). These values are consistent with the greybody dust temperature measured with infrared photometry (Equation 3.3), where $T_{dust} \sim 45 - 75$ K for OHMs and $\sim 40 - 120$ K for non-masing galaxies.

In contrast, the best fits for both the dust shell thickness (Y) and optical depth (τ_V) are markedly different for OHMs and non-masing galaxies. The mean Y for non-masing galaxies (770 ± 320) is nearly twice as thick as the mean value for OHMs (350 ± 260), although within the large scatter on both parameters. Rather than a physical difference in the shell thicknesses, however, we reiterate that this is a likely consequence of the non-masing galaxies being better fit by clumpy models (Figure 3.7) and thus a fundamentally different geometry. The dust optical depths for the OHMs have a broad distribution of τ_V between 0 and 450, with more than 50% having $\tau_V > 350$ and a mean of 300. With the exception of a single galaxy with $\tau_V = 380$ (IRAS 06538+4628), all non-masing galaxies have $\tau_V < 100$ and a median of less than 50.

Overall, fits to the IRS from radiative transfer models show a marked difference between the

dust geometries of masing and non-masing galaxies. Non-masing galaxies are better fit by models with lower optical depth and slightly cooler dust temperatures - based on Figure 3.7, this may be due to dust in the form of a clumpy, obscuring torus (and possibly a partially visible AGN). OHMs are almost all well fit by a smooth screen of dust with a thinner shell, but with much higher optical depths. We emphasize that this "smoothness" is in the context of the entire nuclear region (and possibly beyond) of the merging galaxies. Smaller overdensities within that smooth framework are likely sites of star formation and are necessary to provide the cloud-cloud overlap that produces an OHM.

3.4 Statistical comparisons

The primary goal in observing non-masing ULIRGs was to directly compare the samples and identify differences that could be triggers of the OHM. Here, we present statistical tests comparing the mid-infrared and radio properties of both samples.

3.4.1 Rank correlations of infrared and radio properties

A first-order method of comparing the samples is correlation between physical parameters. We computed the Spearman's rank correlation coefficient (ρ) for a range of properties from Chapter 2 both in the mid-infrared and radio regimes. For the mid-infrared, we tested relationships between PAH 6.2 and 11.3 μm EW and luminosities, continuum spectral indices, silicate absorption depths, greybody T_{dust}^{gb}, and constraints on the geometry from the DUSTY best-fit models (Table 3.1). The radio properties we explored included the continuum power at 1420 MHz (P_{1420}), integrated L_{OH} and the peak OHM flux density at 1667 MHz (P_{1667}; Darling & Giovanelli, 2000, 2001, 2002a). Results for the Spearman's ρ tests are shown in Table 3.3. We omit several parameters from this table that were measured, but showed no significant correlations; these included the mid-infrared fine-structure line ratios ([Ne III]/[Ne II], [O IV]/[Ne II], and [Ne V]/[Ne II]), H_2 temperature and gas mass, depth of the 6 μm water ice feature, and the OH hyperfine ratio $R_H = F_{1667}/F_{1665}$.

Table 3.3. Spearman rank correlation z-scores for OHMs

								DUSTY model fits			OHM radio properties		
	α_{15-6}	α_{30-20}	$EW_{6.2}$	log $L_{6.2}$	$S_{9.7}$	S_{18}	T^{gb}_{dust}	Y	τ_V	T_{dust}	log P_{1420}	log P_{1667}	log L_{OH}
log L_{FIR}	0.1	−0.6	−1.4	1.8	−0.4	−0.2	−0.5	0.0	0.9	−0.5	**4.4**	1.5	2.0
α_{15-6}	–	−0.4	1.4	−1.4	0.4	−0.4	1.0	−2.9	2.5	2.5	0.1	−0.8	−1.9
α_{30-20}	...	–	2.3	−1.0	−2.3	−2.8	**−5.1**	2.2	3.3	−2.7	−2.9	1.0	−0.0
$EW_{6.2}$	...	...	–	2.5	−2.5	−1.9	−2.0	−1.5	3.7	0.9	−0.5	0.1	−0.1
log $L_{6.2}$	...	...	...	–	−3.6	−2.6	2.1	−1.0	0.5	0.8	2.5	1.7	2.4
$S_{9.7}$	...	...	...	...	–	**5.3**	0.9	2.0	−3.5	−1.5	0.1	−2.9	−2.0
S_{18}	...	...	...	...	...	–	0.7	0.9	−2.9	−0.4	−0.0	−2.3	−2.1
T^{gb}_{dust}	...	...	...	...	...	...	–	−1.7	−2.2	1.9	1.6	−0.3	−0.1
Y	...	...	...	...	...	...	...	–	−2.7	**−6.9**	−0.5	−0.1	0.1
τ_V	...	...	...	...	...	...	...	...	–	1.5	−0.7	2.1	0.7
T_{dust}	...	...	...	...	...	...	...	...	...	–	0.4	−0.6	−0.6
log P_{1420}	...	...	...	...	...	...	...	...	...	...	–	1.0	2.7
log P_{1667}	...	...	...	...	...	...	...	...	...	...	...	–	**5.3**

Note. — The Spearman's rank correlation tests statistical dependence of two variables on being monotonic functions, without assuming linearity. The z-scores in this table represent the number of standard deviations by which the correlation differs from the null hypothesis of no statistical dependence. Correlations higher than 4σ are in boldface.

Several of the correlations in Table 3.3 with high significance reflect well-known physical relationships; for example, the correlation between P_{1420} and L_{FIR}. The relation of the spectral index α_{30-20} to T_{dust}^{gb} is expected since α_{30-20} samples the Wien side of a blackbody peaking near 60 μm. The silicate depths at 9.7 and 18 μm are also correlated, as expected from the results of the DUSTY models.

The dust temperature and shell thickness Y from the DUSTY best-fit models showed a strong anti-correlation in OHMs. This picture fits with a smooth dust screen enveloping a central source of illumination - thicker shells absorb more energy near the inner boundary, resulting in a cooler T_{dust} near the outer boundary. Y-T_{dust} also was the only correlation coefficient that showed significant differences between the masing and non-masing samples ($\rho_{OHM} = -0.97$, $\rho_{non} = -0.64$). We attribute this to the evidence that non-masing galaxies are poorly fit by DUSTY and likely favor a clumpy geometry (Figure 3.7).

For the OH maser emission itself, the only strong correlation observed was between the peak OHM power and the integrated OHM luminosity. No Spearman correlations between an OHM parameter (L_{OH}, P_{1667}) and the IRS data were found with $> 4\sigma$ significance, despite the fact that several infrared features related to dust geometry revealed a clear separation of loci between OHMs and non-masing galaxies (see Figures 3.6 and 3.12). While these parameters have a clear effect on the **existence** of the OHM, the lack of correlation suggests either that specific line properties are not well tracked by these parameters, or that no single trigger among these is responsible for megamaser production. Alternatively, the OHM might be the results of stochastic amplification of small-scale conditions, with masing simply becoming more common when conditions are favorable.

3.4.2 Statistical differences between the samples

A second method of analyzing statistical differences between OHMs and non-masing galaxies is the two-sided Kolmogorov-Smirnov (K-S) test, which tests the null hypothesis that the two samples come from the same parent distribution. Selected results from the K-S tests are given in Table 3.4, where D_{KS} is the maximum separation between the scaled cumulative distribution

Table 3.4. Kolmogorov-Smirnov tests for OHMs and non-masing galaxies

	D_{KS}	N_σ	μ_{OHM}	σ_{OHM}	μ_{non}	σ_{non}
$EW_{6.2}$ [μm]	0.440	2.4	9.4	47.5	1.13	1.32
log $L_{6.2}$ [$L_\odot$]	0.193	0.3	9.70	0.38	9.63	0.48
log L_{FIR} [$L_\odot$]	0.400	2.1	12.18	0.27	11.85	0.52
f_{60}/f_{100}	0.318	1.2	−0.08	0.12	−0.15	0.12
α_{15-6}	0.326	1.4	2.08	0.61	1.80	0.58
α_{30-20}	0.816	**5.3**	4.89	1.08	2.50	0.89
$S_{9.7}$	0.800	**5.1**	−1.83	0.76	−0.62	0.37
S_{18}	0.686	**4.4**	−0.56	0.31	−0.23	0.13
T_{gb} [K]	0.369	1.9	65	11	79	49
T_{30-20} [K]	0.882	**5.8**	75	14	113	29
T_{DUSTY} [K]	0.663	**4.2**	62	10	53	19
τ_V	0.816	**5.3**	310	130	67	88
Y	0.729	**4.7**	350	250	790	320
q	0.518	3.0	0.06	0.26	0.30	0.59

Note. — The parameters τ_V, T_{DUSTY}, Y, and q are the best fit of IRS spectra to DUSTY models. Results greater than 4σ significance are in boldface.

functions and N_σ is the number of standard deviations by which D_{KS} differs from the null hypothesis (ie, the significance of the result). We also give the mean values and 1σ standard deviations of the properties for both samples. As with Table 3.3, this omits numerous mid-infrared and radio properties on which we performed K-S tests, but which showed no significant difference.

The majority of the data show K-S results consistent with origins from the same distribution; the exceptions all relate to dust properties of the galaxies. Two of these are quantities directly measured from IRS data: the 30-20 μm spectral index and the 9.7 μm silicate depth. The remaining significant parameters describe the dust environment modeled by DUSTY: Y, τ_V, and T_{dust} all support a fundamentally different distribution of the silicate dust for the two samples at the 4σ level.

This analysis was extended by refining the greybody T_{dust} measured with Equation 3.3, which shows only a mild significance in the original K-S test (2σ). The continuum slopes are largely determined by the amount of dust in various temperature regimes; however, α_{30-20} shows a strong difference while α_{15-6} (which samples hotter dust) does not. This may indicate that only dust **in certain temperature regimes** (ie, the $\sim 50-100$ K region sampled by 20–30 μm continuum)

is important in triggering OHM emission. We tested this by restricting the fit of our dust temperature only to data from 20–30 μm, where the Wien approximation applies for typical ULIRG dust temperatures. In this case, the K-S test yields a much higher and statistically significant (6σ) difference for the modified dust temperature (T_{30-20}) between the OHMs and non-masing galaxies.

K-S tests were also used to quantify the differences seen between the samples on the fits with the DUSTY code. In particular, the optical depth τ_V showed a 5σ difference between the two samples, with the typical OHM having τ_V a factor of several above a non-masing galaxy (and consistent with D_{KS} for the 9.7 μm feature). The other DUSTY parameters show moderate significance (3–5σ); however, the results for different distributions of Y likely come from a clumpy geometry, rather than a true increase in the shell thickness (§3.3). Given that the optical depth and dust temperature are **not** independent parameters in DUSTY, all results from the K-S tests strongly indicate that the temperature/optical depth of the dust (which depends on its geometry) is a key factor in triggering an OHM.

3.4.3 Survival analysis

We extended the K-S tests by performing a series of survival analyses on the same data. Survival analysis is particularly suited for flux-limited samples because it properly treats upper limits for features not detected in all galaxies (Feigelson & Nelson, 1985; Isobe et al., 1986). We used the ASURV package in IRAF (Lavalley et al., 1992), which includes the Gehan's generalized Wilcoxon, logrank, Peto & Peto, and Peto & Prentice tests. Running survival analysis on all measured mid-infrared features (including atomic and molecular line emission, hydrocarbon and gas-phase absorption, PAH, dust and continuum features) gave similar results to the K-S tests; no parameter showed significant differences between the two samples with the exceptions of α_{30-20} and $S_{9.7}$. All tests yielded statistically significant differences for these features, with an mean significance of 6σ for $S_{9.7}$ and 5σ for α_{30-20}.

Importantly, the results of our survival analysis also discount the possibility that other mid-infrared features are directly related to the presence of an OHM. In particular, we detected ab-

sorption from hydrocarbons (HACs), gas-phase molecules (C_2H_2, HCN, and CO_2) and crystalline silicates almost exclusively in the OHM sample (Willett et al., 2011a). Using the upper limits on the absorption features in our survival analyses, however, we cannot confirm that the lack of detections in the non-masing sample is significant above the 3σ level for any of these parameters. This is largely due to lack of sensitivity in the non-masing galaxies, since the limits on non-detections are of similar magnitudes to the detected absorption in many galaxies.

3.5 Comparing observations and theory

Importantly, the IRS data can explore the physics of OHMs by testing the predictions of maser pumping models. The most recent and complete pumping calculations come from Lockett & Elitzur (2008, hereafter LE08). The model assumes a slab geometry and uses the escape probability method to solve for the level populations of the OH molecule. Given assumptions on the physical conditions in the masing regions, the overall strength of the OHM (if any) can be predicted. For a range of parameters influenced by the clumpy OHM model of Parra et al. (2005), they find that the maser optical depth depends most strongly on the dust temperature and optical depth. Since both these parameters can be estimated from IRS data, our sample offers the first opportunity for testing such a model on a large number of galaxies.

The strength of the OHM in the LE08 model is parameterized as the optical depth in the OH line (τ_{1667}, which becomes more negative for higher maser gain). To compare this to observations, we use the line-to-continuum ratio to estimate the apparent observed OH optical depth (Table 3.1):

$$\tau_{1667}^{app} = -\ln\left(\frac{S_{1420} + S_{1667}}{S_{1420}}\right). \tag{3.4}$$

Here S_{1667} is the peak flux density of the OHM at 1667 MHz (taken from Darling & Giovanelli, 2000, 2001, 2002a) and S_{1420} is the flux density of the radio continuum at 1420 MHz from the NRAO VLA Sky Survey (Condon et al., 1998).

The largest uncertainty in Equation 3.4 is that it assumes an OH filling factor of 1; however,

VLBI maps of OHM galaxies show the OH emission to have both diffuse and compact components. In addition, the 1420 MHz radio continuum comes from a much larger physical area than the OH emission. Therefore, τ_{1667}^{app} will be a weaker limit to the true 1667 MHz optical depth. VLBI observations have mapped the OHM emission for a handful of nearby galaxies (Yates et al., 2000; Pihlström et al., 2001, 2005; Klöckner et al., 2003; Lonsdale et al., 2003; Rovilos et al., 2003; Klöckner & Baan, 2004; Richards et al., 2005; Momjian et al., 2006), showing that the difference in apparent optical depth between the entire galaxy and the brightest individual maser spots varies by as much as $\Delta\tau \simeq 1-4$. Furthermore, the gain for individual maser spots with cloud-cloud overlap can be as high as several hundred (eg, III Zw 35; Diamond et al., 1999; Parra et al., 2005), compared to the diffuse background. Since high-resolution OH maps do not exist for the vast majority of the IRS galaxies, however, we use τ_{1667}^{app} while remaining mindful of the above caveats.

We present tests of the LE08 model parameters using two different techniques: one method estimating T_{dust} and τ_V directly from the IRS spectra, and the second using parameters extracted from the models fit to the IRS data using the DUSTY code.

3.5.1 Testing OHM pumping models with T_{dust} and τ_V from IRS data

The pumping flux of the OHM in the LE08 model depends most strongly on the pumping flux, which is controlled by two factors: the Planck function (depending on T_{dust}) and the self-absorption of the dust (depending on τ_V). The 9.7 μm silicate feature in the IRS data can be used to estimate the total τ_V using the Galactic calibration of (Roche & Aitken, 1984):

$$\tau_V = (17.0 \pm 1.4) \times \tau_{9.7}. \tag{3.5}$$

Secondly, the dust temperature in the masing region is estimated from the greybody fit to the IRS and IRAS data (§3.2.4; Table 3.1). Once both parameters for a galaxy are estimated, we plot the data on the contours of LE08-predicted τ_{1667} emission (Figure 3.9). The color of the OHM symbols shows their τ_{1667}^{app} on the same scale as the LE08 contours.

According to the standard LE08 model, the most luminous OHMs are expected to have

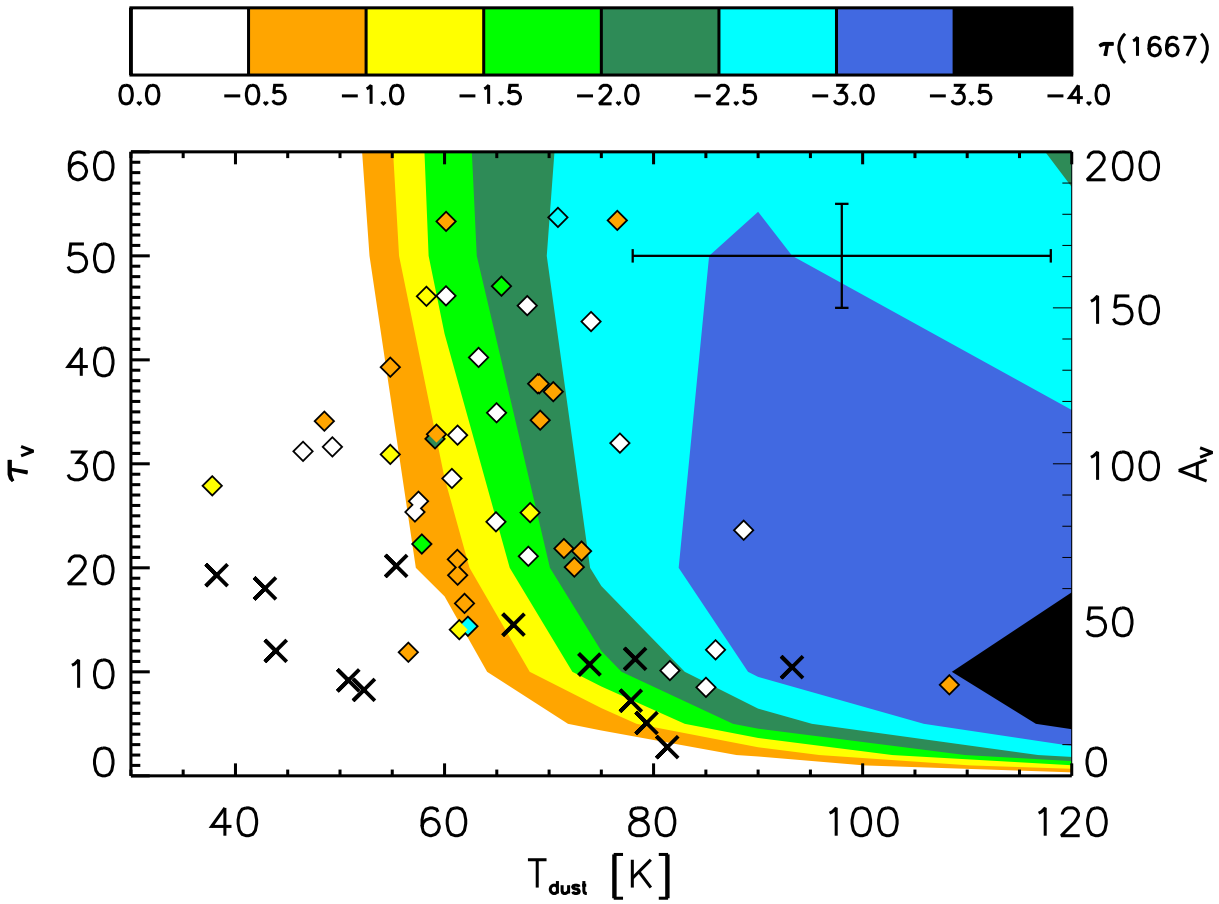

Figure 3.9 Apparent optical depth of the OHM emission (*filled diamonds*) as a function of τ_V (Equation 3.5) and dust temperature (Table 3.1), based on greybody photometry and the 9.7 μm silicate depth. Crosses show temperatures and depths of the non-masing sample. The error bars in the top left are the average systematic uncertainties ($\sigma_T = 20$ K, $\sigma_\tau = 5$). Contours are a zoomed-in region of the OHM model of Lockett & Elitzur (2008).

$T_{dust} \sim 90 - 150$ K and τ_V of a few tens. None of the OHMs with $\tau_{1667}^{app} < -3.0$ were located near this region; in addition, the parameters for virtually all observed OHMs lie well away from the highest predicted τ_{1667} in Figure 3.9, with $T_{dust} = 40 - 100$ K and $\tau_V = 10 - 50$. Roughly 15% of the confirmed OHMs have predicted $\tau_{1667} > -0.5$, which would predict almost no masing activity and would fall well below the limit for inclusion in our sample.

To assess the overall fit of the LE08 model, the errors on our estimates of τ_V and T_{dust} must be quantified. Yun & Carilli (2002) found that accurate temperature fits using Equation 3.3 required much higher photometric sampling than we possess, in addition to radio and sub-mm data. Other SED models (Frayer et al., 1999; Dunne & Eales, 2001) typically fit two- and three-component models with differences in dust temperatures ranging up to 100 K. As a result, we estimate the average $\sigma_{T_{dust}}$ for each galaxy to be ~ 20 K. This is quite high, but is mitigated somewhat by the number of galaxies in our sample. The mean error on the extinction is estimated as $\sigma_{\tau_V} = 5$, based on the silicate measurement technique, the possibility of saturation, and calibration (Equation 3.5). Average error bars are shown in the upper right corner of Figure 3.9.

The large uncertainties result in considerable scatter in the predicted OHM strength, with $\Delta\tau_{1667}$ as high as 1–2 depending on the local gradient of the LE08 model. Many of the OHMs lie near contours where τ_{1667} is a sensitive function of T_{dust}; a shift of ~ 5 K could result in a change of up to $\Delta\tau_{1667} = 0.5$, while at the same time being relatively insensitive to τ_V. We show the distribution of the difference between τ_{1667}^{app} and the predicted τ_{1667} from the LE08 model in Figure 3.10. The measured OH strengths are on average weaker than those predicted by the model ($\langle\Delta\tau_{1667}\rangle = -0.8$); this is consistent, however, with the lower bound on τ_{1667}^{app} from the OH filling factor. The $\chi^2_{reduced}$ for the model using this data is 29.1, which rejects a correlation hypothesis at the 5σ level.

While the agreement for individual OHMs is not strong, our data is consistent with other predictions of the LE08 model. Based on pumping calculations, they show that ULIRGs must have a dust temperature greater than 45 K in order to achieve population inversion; cooler temperatures move the peak of the blackbody too far from the main pumping lines to support the necessary

pumping flux. 90% of the OHMs have $T_{dust} > 45$ K, with the coolest OHM at 37 K; uncertainties of ~ 20 K mean that the dust temperatures for all OHMs are fully consistent with this predicted lower limit.

Figure 3.9 also displays the dust parameters for the non-masing galaxies. Half of the non-masing galaxies have predicted OH luminosities consistent with little masing to none at all (such that $|\tau_{1667}|$ is small), and the τ_{1667} predicted by the LE08 model would lie below our detection threshold of $L_{OH} \leq 10^{2.3}$ $L_{\odot}$ for almost the entire sample. Based on the LE08 model and IRS data, only a single non-masing galaxy (IRAS 23498+2423, in the far lower right of Figure 3.9) would have been expected to show strong megamaser emission. Interestingly, IRAS 23498+2423 was the object with the **highest** upper limit on maser emission in the non-masing sample, with $L_{OH} < 2.25$. We re-observed this galaxy at the Arecibo Observatory[1] in October 2009 to test the LE08 prediction; no detection of OH was made, confirming an upper limit of $L_{OH} \leq 10^{2.27}$ $L_{\odot}$.

3.5.2 Testing OHM pumping models with fits to IRS data from DUSTY

Our second approach for testing the LE08 model calculates T_{dust} and τ_V from the best fits to the IRS data with DUSTY (§3.3; Table 3.1). As discussed in §3.4.2, these fits give dust temperatures similar to those from the greybody fit, but with optical depths much higher than those calculated using only the 9.7 μm feature, which can be saturated in ULIRGs. The T_{dust} used here is the value at the shell's outer edge; since the radial temperature profile of the dust is very steep close to the center and shallow at the edges (changing by only a few tens of K over the outer half of the shell), this represents the bulk of the dust mass and is likely a reasonable approximation for conditions in the masing regions.

Figure 3.11 shows the LE08 predictions with data from the DUSTY best fits to the OHMs and non-masing galaxies. We note that LE08 contours are not complete at $\tau_V > 300$, and that the apparent horizontal feature at $\tau_V = 410$ is likely an artifact of gridding in the code. The

[1] The Arecibo Observatory is part of the National Astronomy and Ionosphere Center, which is operated by Cornell University under a cooperative agreement with the National Science Foundation. We are indebted to them for partially funding the publication costs of this research.

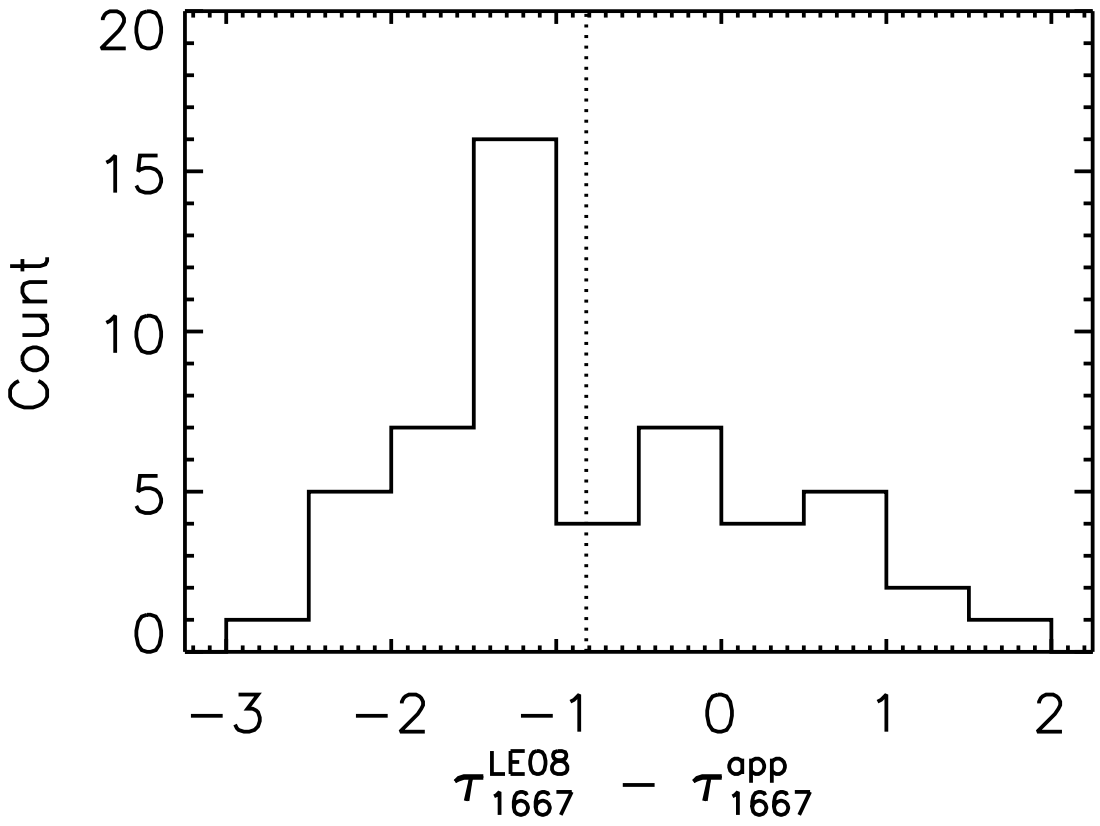

Figure 3.10 Distribution of the difference in Figure 3.9 between the predicted τ_{1667} from the Lockett & Elitzur (2008) model and the apparent τ_{1667}^{app} measured from radio data. The dotted line shows the mean of the distribution at $\Delta\tau_{1667} = -0.8$, showing that the LE08 model tends to overpredict the strength of the maser.

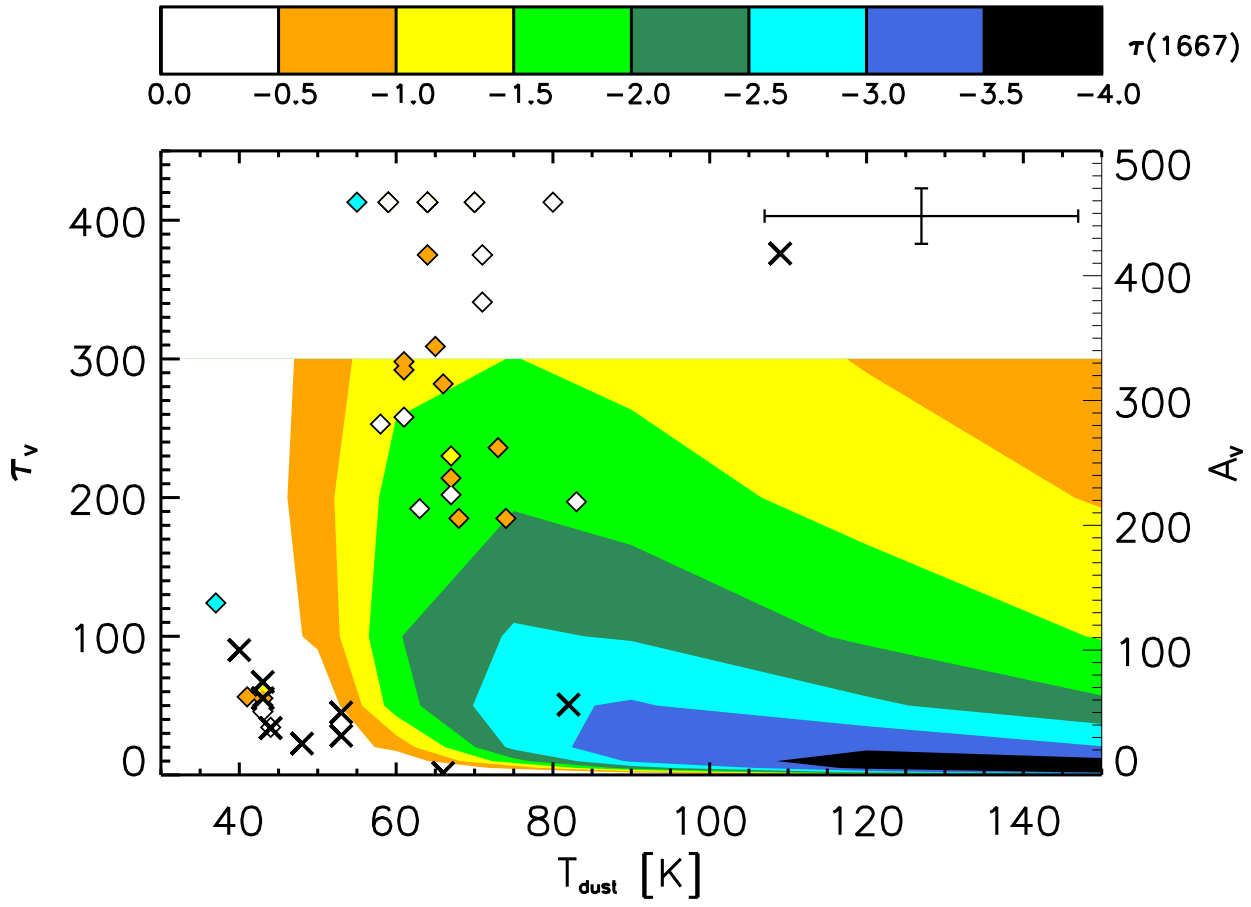

Figure 3.11 Apparent optical depth of the OHM emission (*filled diamonds*) as a function of τ_V and dust temperature based on fits from DUSTY. Black crosses are the non-masing galaxies; the error bar in the upper right corner shows the average uncertainty ($\sigma_\tau \sim 20, \sigma_T \sim 20$ K). Contours show the predicted maser strength for the LE08 model, which are not complete at $\tau_V > 300$. Due to the coarse gridding of DUSTY models, several galaxies have overlapping points on this plot (e.g., five galaxies have best fits of $T_{dust} = 70$ K and $\tau_V = 410$).

distribution of the galaxies is very different from that in Figure 3.9; the OHMs occupy a much larger range in optical depth, increasing τ_V by an order of magnitude. Two distinct loci are visible; the lower left corner contains the majority of the non-masing galaxies and several OHM with $T_{dust} \simeq 40 - 60$ K and $\tau_V < 100$. The LE08 model predicts that these galaxies would show little to no maser emission. The second group is almost exclusively composed of OHMs, with warmer temperatures ($T_{dust} \simeq 60 - 80$ K) and τ_V of several hundred. Two non-masing galaxies with warm temperatures do not seem associated with either group.

The overlapping region of OHMs and non-masing galaxies with cooler dust temperatures and $\tau_V < 150$ is very interesting. The dust parameters for these galaxies lie well away from the predicted τ_{1667} peak and are close to the minimum predicted inversion temperature of 45 K. The overlapping populations at this locus (which includes at least one powerful gigamaser) requires that there must be some triggering factor for an OHM beyond T_{dust} and τ_V. This is supported by the fact that **all** OHMs in this region also lie on the horizontal branch of the fork diagram (Figure 3.6), classifying them as likely AGN hosts. The T_{dust} from DUSTY for all of these OHMs is also significantly cooler than that measured with the greybody method; a buried AGN might thus be better fit with a multi-temperature model. The connection of an AGN to OHM suppression, however, is not clear; it could represent a different dust geometry not conducive to cloud-cloud overlap, or signal a more advanced stage in the galaxy merger, thus putting a limit on the effective lifetime (and thus observability) of the OHM.

Since the contours in Figure 3.11 are incomplete, we cannot fully measure the goodness-of-fit in a method similar to Figure 3.10. Qualitatively, the model makes good predictions for the dust parameters for almost all of the non-masing galaxies. The exceptions are IRAS 11119+3257 ($\log \tau_{1667}^{pred} \simeq -3.0$) and IRAS 06538+4628 ($\log \tau_{1667}^{pred} \simeq -1$). The former is the only object whose predicted emission lies well above its observational limits on L_{OH}. This galaxy is known to show an exceptional radio excess as measured by its q-parameter (Condon et al., 1991), with its value of $q = 1.23$ falling well below the mean value for OHMs found by Darling & Giovanelli (2002a). Such an excess commonly indicates that the galaxy hosts an AGN; this is supported by the low 6.2 PAH

EW of IRAS 11119+3257 and its position on the fork diagram (Figure 3.6). IRAS 06538+4628 is the only non-masing galaxy in our sample for which dust temperatures might be too warm to support a strong population inversion.

There are several reasons why the T_{dust} and τ_V fit from DUSTY might differ from methods used in §3.5.1. τ_V for deeply embedded galaxies can suffer from saturation in the 9.7 μm feature. Using data from the full dust profile, as we do in DUSTY, samples the broader wings of the feature it advances up the curve of growth. DUSTY also samples the SED at a much higher resolution than the greybody fit, albeit in a more limited wavelength regime. Finally, the conversion from $S_{9.7}$ to τ_V is based on a Galactic calibration; it is not known how dust composition might be different in the Milky Way and ULIRGs, for example. On the other hand, the DUSTY models require the assumption of a specific geometry which may not be appropriate (see Figure 3.7) for non-masing galaxies and the dustiest OHMs. While neither method is without drawbacks, we believe both to have at least some physical merit (and are encouraged by the fact that T_{dust} is mostly consistent).

3.5.3 Predictions and future observations

Overall, comparing the IRS data to predictions from the LE08 model yielded mixed results. Using parameters from the DUSTY code, the LE08 model correctly predicted that most non-masing galaxies should have cool dust temperatures and low optical depths; however, several megamasers also have T_{dust} that would be too cool for inversion under this model. The observed τ_{1667}^{app} for individual sources shows a great deal of scatter; however, this is dominated by observational uncertainties in the OH filling factor. Both estimates are consistent with the LE08 claim that a minimum dust temperature of 45 K is required for maser action; within uncertainties, all OHMs have T_{dust} above this value. Based on results from the feature-feature diagram, we suggest that future pumping models include both clumpy and smooth shell dust geometries; treatment of OH kinematics might also be necessary to model individual sources in more detail.

Interestingly, the OHM luminosity (which typically depends strongly on the total linewidth) does not appear to be a strong function of the currently observable global host properties. An

improved test of the L_{OH}-host galaxy relationship could use VLBI maps of OHM galaxies to constrain the true gain in individual clouds to determine the filling factor, and then compare these results to spatially resolved infrared data in the same regions to measure T_{dust} and τ_V. If the parameters for OHM production can be fine-tuned based on size scales of $\sim$ 100 pc for nearby galaxies, this will greatly assist in comparisons of galaxy-wide SEDs for OHMs to non-masing ULIRGs at much greater distances.

The LE08 model depends on a number of other ISM properties, some of which can be further constrained by the IRS data. These include the ortho-para ratio of H_2, which affects collision rates and thermalization of the gas. LE08 assumes a constant ortho-para ratio of 3; the IRS data show that this is only valid for 4/9 ULIRGs for which the ratio can be constrained (and can be as low as 0.5). The OH column densities measured using the 34.6 μm transition lie in the range $N_{OH} = (1-3) \times 10^{17}$ cm^{-2}; this is roughly a factor of two higher than the standard value assumed in the LE08 model.

Results from our IRS data can also narrow potential searches for new OHMs, especially at higher redshifts. The most distant OHM known lies at $z = 0.265$ (Baan et al., 1992b). Since OHMs are associated with merging galaxies, which are most plentiful between $z \sim 1-3$, we expect a higher spatial density of OHMs in the early universe (Darling & Giovanelli, 2002b). While surveys for more distant OHMs are restricted both by sensitivity constraints and low-frequency RFI, a significant obstacle has been identification of a suitable target sample of host galaxies. Based on the IRS data, we suggest that future OHM surveys target galaxies with dust peaks near $\lambda_{rest} = 53$ μm, steep $30-20$ μm slopes, deep dust absorption, and that do not show evidence of hosting an AGN. Figure 3.12 shows how the combination of α_{30-20} and $S_{9.7}$ can clearly separate almost all OHMs from non-masing galaxies in the mid-infrared. This may be a valuable tool in future searches for OHMs; for galaxies in which low-resolution IR spectroscopy is available, pre-selecting OHM candidates based on these diagnostics should have a success rate far in excess of blindly selecting ULIRGs from the field. The growing number of sub-millimeter galaxy catalogs and multiwavelength deep fields offer excellent opportunities in the near future for such surveys.

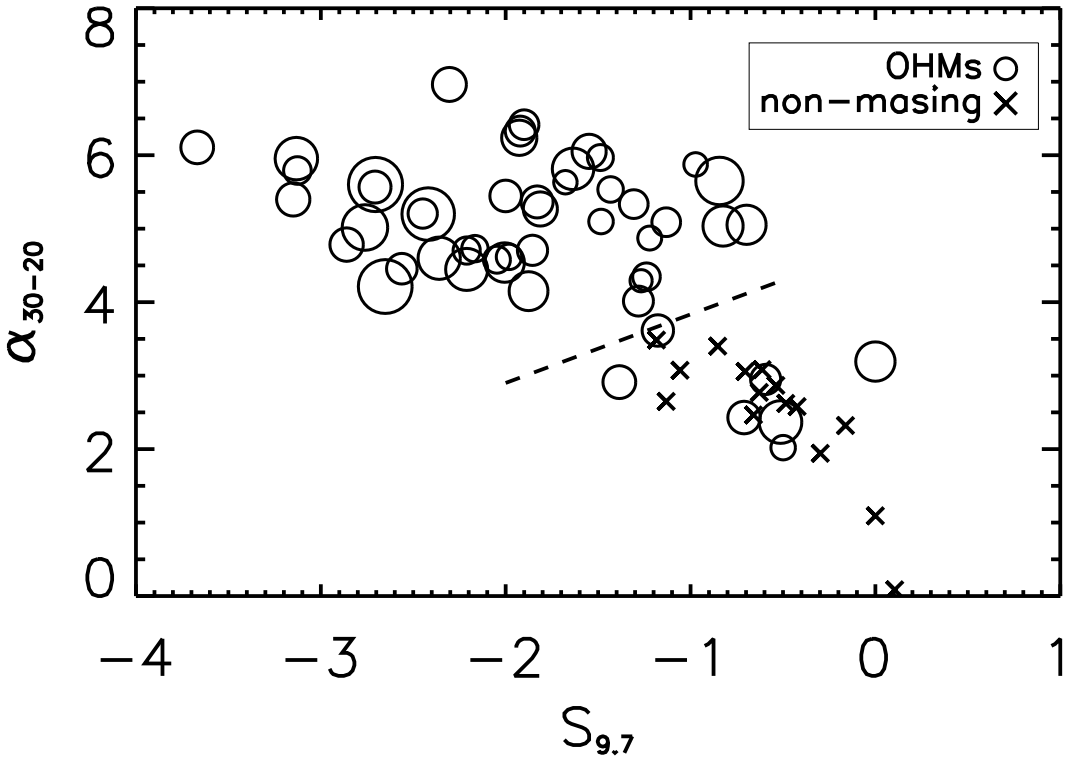

Figure 3.12 Peak silicate depth at 9.7 μm vs. the spectral slope between 20 and 30 μm for OHMs (*circles*) and non-masing galaxies (*crosses*). For OHMs, the symbol size is proportional to log L_{OH}. The dashed line shows the rough separation between the loci of OHMs and non-masing galaxies. Preselecting OHM hosts based on a $\alpha_{30-20} - S_{9.7}$ cut may be a powerful technique for future megamaser surveys.

Finally, new observatories are offering opportunities for completing the OHM picture. There are only a few OHMs in which the important 53 μm transition has been measured (e.g., He & Chen, 2004); this could be potentially obserbed in larger numbers of galaxies with SOFIA. The Herschel observatory can also supplement the IRS by measuring the 79 and 119 μm OH transitions in large samples of ULIRGs (e.g., Fischer et al., 2010). If models such as LE08 can be refined based on direct OH measurements, then the pumping efficiencies for the megamaser could be evaluated for a statistically significant sample. Photometric measurements from these instruments and from JWST will also generate SEDs with much broader spectral coverage, increasing our knowledge of the physics needed for radiative transfer models and modeling the OHM environment.

3.6 Conclusions

We present results from the *Spitzer* Infrared Spectrograph comparing the mid-infrared properties of OH megamaser hosts to galaxies with confirmed upper limits on the megamaser emission. No significant differences between the samples were found for the average excitation states, line velocities, or star formation rates. 10–25% of the OHMs show clear evidence in the mid-infrared for an AGN, significantly lower than previous optical and radio studies which placed the AGN fraction of OHMs between 30–70%. In non-masing ULIRGs, between 50–60% of the galaxies have mid-infrared evidence for an AGN.

Fits of radiative transfer models to the IRS spectra with the DUSTY code show that OHMs have warmer T_{dust} and deeper silicate absorption associated with a smooth, thick dust shell surrounding the nucleus. This implies the presence of a large dust reservoir in OHMs with a smooth geometry and temperatures from $\sim 50 - 100$ K. Non-masing galaxies show weaker dust absorption, shallower mid-infrared continuum, and cooler dust (by ~ 10 K) than the typical OHM host. The relative strength of silicate features in non-masing galaxies suggests that they are best fit with a clumpy dust geometry.

We used IRS data to evaluate predictions from the OH pumping model of Lockett & Elitzur (2008), the first direct test of OHM production using observed properties of the host galaxies.

The dust opacities for OHMs derived from the best-fit DUSTY models suggest that much higher opacities ($\tau_V \sim 100 - 400$) are necessary for OHM production. All the IRS data are consistent with the LE08 claim that a minimum $T_{dust} = 45$ K is required for maser action. Limits on the OH emission for most non-masing galaxies are predicted by the LE08 model, based on their comparatively cool dust temperatures ($T_{dust} < 60$ K) and low dust opacity ($\tau_V < 100$). Finally, the IRS data constrain several parameters necessary to develop future OHM pumping models, including the dust optical depth, temperature, and overall geometry.

For the first time, we present spectral diagnostics that can distinguish OHMs from non-masing galaxies based on their host galaxy properties, the clearest of which is the $S_{9.7} - \alpha_{30-20}$ relation. These parameters can be relatively easily measured in low-resolution spectra, and may signify a powerful method for preselecting OHM candidates for follow-up radio surveys at higher redshift.

Chapter 4

A radio-wavelength survey for new OH megamasers at $z \sim 1$

OH megamasers (OHMs) trace of some of the most extreme physical conditions in the universe - in particular, the presence of an OHM signals specific stages in the merger process of gas-rich galaxies. OHMs can thus be used as probes of their environments, both directly and indirectly. Characteristics of the maser emission itself can be used to measure extragalactic magnetic fields (via Zeeman splitting) and gas kinematics, while the *presence* of an OHM is a signpost for phenomena associated with galaxy mergers, including extreme star formation and merging black holes. OHMs are a unique tool in this respect due to their extreme luminosities and ability to be seen at cosmic distances.

The total number of OHMs detected, however, is still low. As of 2011, there are $\sim$ 113 OHMs published in the literature, with roughly 50% discovered in the Arecibo survey of Darling & Giovanelli (2000, 2001, 2002a). The association of OHMs with IR-bright merging galaxies, however, means that the density of OHMs is expected to be much higher at $z \simeq 1 - 2$, coinciding with an increase in both merging rate and cosmic star formation.

No OHMs at a luminosity distance of greater than 1336 Mpc ($z = 0.265$) have been detected, and no large, systematic searches for high-z OHMs have been carried out. This has been historically due to a combination of available observing facilities and target catalogs. High-redshift radio observations require telescopes with excellent sensitivity and continuous frequency coverage at $\nu < 1$ GHz, and must also have techniques to mitigate terrestrial radio interference. Efficient surveys also require large samples of candidate galaxies which are expected to host an OHM; for

high-redshift galaxies, this requires accurate redshifts and a well-sampled SED to determine the galaxy type and luminosity.

Fortunately for the field of OHMs, both survey requirements can now be met. The 100m Green Bank Telescope (GBT), completed in 2000, is the first telescope with the sensitivity, continuous frequency coverage, and low-interference environment to accomplish a large OH survey. In addition, there now exist several catalogs with multi-wavelength data (mostly deep field galaxies) for which redshifts and galaxy types can be determined for millions of objects. By combining these catalogs with low-redshift information on the typical properties of an OHM host, target candidates can now be identified out to redshifts as high as $z \sim 2$.

This chapter describes a targeted survey for OHMs from $z = (0.1 - 1.55)$ using data from the GBT. §4.1 outlines results of previous OHM searches and the motivation for a new high-redshift survey. §4.2 describes the selection criteria for the galaxies in our samples. §4.3 gives details of the observations and data reduction from the GBT. §4.4 presents measurements of two new OHMs and statistics of the 77 galaxies for which we placed upper limits on the OH emission. §4.5 discusses our results in the context of the OHM luminosity function and its usefulness in constraining galaxy merger scenarios. Reduced spectra for the OHM non-detections in this survey are presented in Appendix C.

This chapter assumes a cosmology of $H_0 = 75$ km s^{-1} Mpc^{-1}, $\Omega_M = 0.3$, and $\Omega_\Lambda = 0.7$.

4.1 Background

OHMs have so far only been observed at relatively "moderate" redshifts, compared to detections of H_2O megamasers out to $z = 2.64$ (Impellizzeri et al., 2008) and CO emission out to $z \sim 6$ (Walter et al., 2011). The first OHM was discovered in Arp 220 by Baan et al. (1982), who were originally using the Arecibo telescope to search for hydroxyl absorption. Further detections of OHMs came from a mixture of serendipitous discoveries (individual targeting of infrared- or radio-bright galaxies) and systematic surveys, primarily with the GBT 300-ft. telescope in the northern hemisphere (Baan et al., 1992a) and the 64-m Parkes telescope in the southern hemi-

sphere (Staveley-Smith et al., 1992). The most recent large survey was carried out by Darling & Giovanelli (2000, 2001, 2002a) using the Arecibo telescope and observing ULIRGs detected in the all-sky survey of the IRAS satellite. The combination of flux-limited surveys and the limit on observable frequency ranges yielded an effective upper redshift limit for these surveys of $z \simeq 0.25$.

The most distant OHM (IRAS 14070+0525; $z = 0.265$), however, was discovered relatively early in the history of extragalactic masers, due in part to its extreme luminosity (Baan et al., 1992b). In fact, roughly half of known OHMs are bright enough to have been detected in comparable detection times at significantly higher redshifts (similar to quasars). For example, IRAS 02524+2046 ($z = 0.18$) could have been detected at $z = 1$ in the 12-minute scan duration of the Arecibo survey of Darling & Giovanelli (2000, 2001, 2002b). These results suggest that many more OHMs might be detectable with current instrumentation beyond $z = 0.25$. This is supported by the fact that the sky density of OHMs is predicted to increase with redshift up to at least $z = 2$ (Darling & Giovanelli, 2002b), since both the star formation rate and galaxy merger rate are higher in the early universe (Madau et al., 1998; Le Floc'h et al., 2005). This argues for the need for a systematic survey of OH emission at high redshifts.

Searches for OHMs at distances greater than ~ 1 Gpc ($z > 0.2$) have met with a number of challenges. The first is a lack of suitable targets for high-redshift OH searches. OHMs occur in (ultra)luminous infrared galaxies ([U]LIRGs), in which the dusty environment provides sufficient numbers of mid-infrared photons to pump the upper rotational ladders of the OH molecule and trigger masing. The rest-frame spectral energy distributions (SEDs) of these galaxies peak between 50 and 100 μm; at $z \sim 1$, the peak emission is redshifted into the far-infrared and sub-millimeter (sub-mm) ranges. Large-scale catalogs of sub-mm galaxies (which are ULIRGs in their rest frames) have only recently become available, thanks to developments in both ground- and space-based observatories.

Additional problems for observing high-redshift OHMs are technical in nature. For galaxies at $z \sim 1$, the frequency of redshifted 18-cm OH lines lies at $\nu_{obs} \simeq 830$ MHz. For terrestrial radio observatories, the spectrum allocation below 1 GHz is filled with artificial radio emission, including

signals from mobile phones, television, air-to-ground radar, and satellite communications; all are typically many orders of magnitude more powerful than astronomical signals. This radio frequency interference (RFI) makes sensitive surveys much more difficult, and renders certain parts of the radio spectrum (or redshift bins, in astronomical terms) effectively off-limits from ground-based observations. Figure 4.1 shows an example of the RFI that is near-ubiquitous at the wavelengths in question.

The copious RFI near the frequencies of redshifted OH means that potential megamaser hosts must have a precise, typically spectroscopic redshift to avoid the noise. Given the spectral density of RFI in the $600 - 1000$ MHz range, the expected observed frequency of an OH line must be known to within at least 10 MHz ($\Delta z \sim 0.02$ at $z = 1$). This is necessary both so that lines can be distinguished from possible nearby RFI, and so that robust upper limits can be placed on non-detections. The lack of sub-mm galaxies with precise redshifts has historically resulted in few targets suitable for high-redshift OHM observations. Catalogs of potential targets now number in the thousands, however, thanks to a combination of deep field surveys and sensitive sub-mm detectors.

4.2 Sample selection

We constructed two separate samples for our surveys of high-redshift OHMs with the GBT. Galaxies were drawn from flux-limited surveys when possible, and were designed to be sufficiently large to construct an OH luminosity function at $z \sim 1$; we estimated this would require 10–15 new detections. The inclusion of potential targets was also limited by visibility from the GBT; all objects in our sample have declinations $\delta > -5^\circ$, which ensures at least a ∼10-hour observing window and minimum zenith elevation of 45° from the latitude of Green Bank. The combined samples yielded a total of 85 galaxies, 79 of which were observed with the GBT for OH. The selection criteria are described below in more detail.

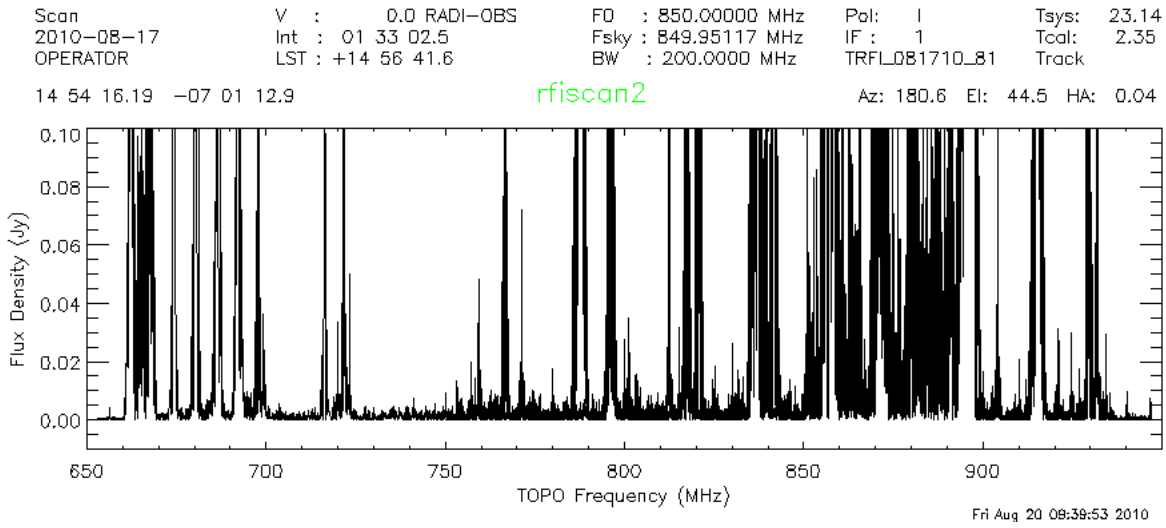

Figure 4.1 A sample RFI scan from the Green Bank Telescope Prime Focus 1-4 receiver (PF1-800), covering a frequency range from $\nu = 680 - 920$ MHz. This data was taken on August 17, 2010. Identified sources of RFI include allocations for mobile telephones ($824 - 829$ MHz), broadband digital transmission from television stations (741 and 745 MHz), and air-to-ground communication from commercial airliners ($894 - 896$ MHz).

4.2.1 Sample 1: Sub-mm and ULIRG galaxies from the field

The first sample of potential OHM hosts was assembled from flux-limited catalogs of ULIRGs at $z \leq 1$ and sub-mm galaxies (which are redshifted ULIRGs) at $z < 1.55$. The most comprehensive, least-biased sample of ULIRGs available at the time of observations was the FSC-FIRST (FF) catalog (Stanford et al., 2000), which consists of galaxies detected in both the infrared (IRAS Faint Source Catalog) and the 20-cm VLA FIRST survey. A subset of 36 FF galaxies observed by Yang et al. (2007) at 350 μm confirmed the far-infrared luminosities of the sample, with median $\log\,(L_{FIR}/L_{\odot}) = (12.2 \pm 0.5)$. We selected 35 FF galaxies for OH observations, eliminating only FF 0123+0114 (its redshift of $z = 0.08$ fell below our distance cutoff). These galaxies are listed in Table 4.1 with the prefix "FF".

Additional ULIRGs at $z < 1$ were selected from targets in the Extended Groth Strip (Lin et al., 2007). The galaxies in this sample have redshifts from DEEP2 optical spectroscopy and mid-infrared imaging at 24 μm from the MIPS instrument on *Spitzer*. Mid-infrared images were used to identify close galaxy pairs that are potential mergers, which are good candidates for OHMs. Five interacting systems from this catalog had infrared luminosities exceeding the ULIRG threshold ($L_{IR} > 10^{12}\ L_{\odot}$) and were selected for OH observations; they are listed in Table 4.1 with the prefix "DEEP2".

Galaxies at $z > 1$ are typically dependent on sub-mm observations to confirm their infrared luminosities and potential status as redshifted ULIRGs. For sub-mm galaxies that are also detected in the 20-cm radio continuum, a precise position can be used to locate optical counterparts and thus yield a spectroscopic redshift. OHM candidates were selected from the optically-identified sub-mm galaxy catalogs of Smail et al. (2004); Chapman et al. (2005); Ivison et al. (2005); Takata et al. (2006). The primary requirement for inclusion in our sample was a redshift cutoff; although most known sub-mm galaxies have $z \sim (1 - 3)$, we set an upper limit of $z < 1.55$ based on the expected sensitivity of the GBT to OH emission. The four sub-mm catalogs yielded 26 galaxies that met this criteria, of which 13 exceeded the ULIRG threshold of $L_{IR} > 10^{12}\ L_{\odot}$. These galaxies are listed in

Table 4.1 with the prefixes "LH", "RG", and "SMM".

In summary, the first sample of high-redshift OHM candidates included 66 galaxies, all with $L_{IR} > 10^{11} L_{\odot}$ and more than half with $L_{IR} > 10^{12} L_{\odot}$. All galaxies have verified redshifts from optical spectroscopy, and are distributed between $0.1 < z < 1.55$. Only five of the targets (from the DEEP2 survey) were selected based on morphological characteristics; the remainder of the targets were drawn from flux-limited samples based only on their redshifts and rest-frame infrared luminosities.

4.2.2 Sample 2: Galaxies from the COSMOS survey

The second group of OHM candidates was selected more than a year after observations on the first sample began, having yielded an OHM detection rate of $< 10\%$. The goal in assembling the second sample was to identify galaxies with higher probabilities of hosting an OHM. We also intended to apply lessons learned from the non-detections in the first half of the survey, where possible.

Galaxies for the second OHM sample were selected exclusively from the COSMOS field, a 2-deg^2 survey with deep spectral coverage from X-ray through radio wavelengths (Scoville et al., 2007). The choice to search COSMOS for OHMs was motivated by multiple reasons: the first was the large number of targets, comprising over 1 million galaxies between redshifts of $0.01 < z < 3.5$. While most galaxies in COSMOS are not ULIRGs, the sheer number of targets gave a large enough sample that good candidates for OHMs could be obtained.

The broad spectral coverage of the COSMOS data served several important purposes. Since the SEDs for these galaxies are much more well-sampled than that of an average sub-mm galaxy, the estimate of the total luminosity is typically much more accurate - the L_{IR} for galaxies in the first group were sometimes estimated using only a single photometric measurement, usually the 60 or 100 μm flux from IRAS. The SEDs also allow accurate classification of galaxies by spectral type. Both infrared (Willett et al., 2011b) and radio (Baan & Klöckner, 2006) studies show that while OHMs are found in infrared-bright galaxies, the OHM fraction is much higher for starburst-

dominated galaxies vs. AGN. As a result, selecting against AGN-dominated galaxies was expected to substantially increase the OHM detection fraction. Finally, although most COSMOS galaxies do not have spectroscopic redshifts, the SED is sufficiently well-sampled to yield photometric redshifts to within the required precision (Ilbert et al., 2009).

Selection of OHM candidates began with COSMOS galaxies detected by *Spitzer* at 70 μm, and then eliminating all targets except the LIRGs, ULIRGs, and HyLIRGs identified by Kartaltepe et al. (2010). We removed all galaxies identified as AGN, including those with high X-ray fluxes, power-law SEDs, and obscured AGN identified by near-infrared color selection. We next eliminated galaxies with $L_{IR} < 10^{12} L_{\odot}$, since the predicted OH luminosity is a function of L_{IR} (Darling & Giovanelli, 2002a). Finally, we culled the target list based on the expected RFI conditions near the observed frequency bands. The initial sample of OHM candidates (§4.2.1), provided an almost-continuous spectral coverage of the real-time RFI situation near Green Bank from $620 - 1500$ MHz. This allowed us to identify regions of persistent and/or powerful RFI that render spectral line measurements highly difficult or impossible. By limiting the observed frequencies to cleaner regions, we have a broader margin for error on the redshift and also improve the sensitivity of the observations, since RFI will affect the balance of the spectrometer even when located away from the bandpass center. We identified two clean windows from $\nu_{obs} = 825 - 830$ MHz and $960 - 1005$ MHz, equivalent to redshifted OH at $0.97 < z < 1.01$ and $0.67 < z < 0.73$, respectively (Figure 4.2).

The final selection of galaxies, based on $L_{IR} > 10^{12}\ L_{\odot}$, high star formation rates, and location in clean frequency windows, yielded 19 targets in the COSMOS field. Three of the galaxies have redshifts near $z \sim 0.7$ and 16 galaxies near $z \sim 1.0$; the galaxies are roughly evenly distributed spatially throughout the COSMOS field (Figure 4.3).

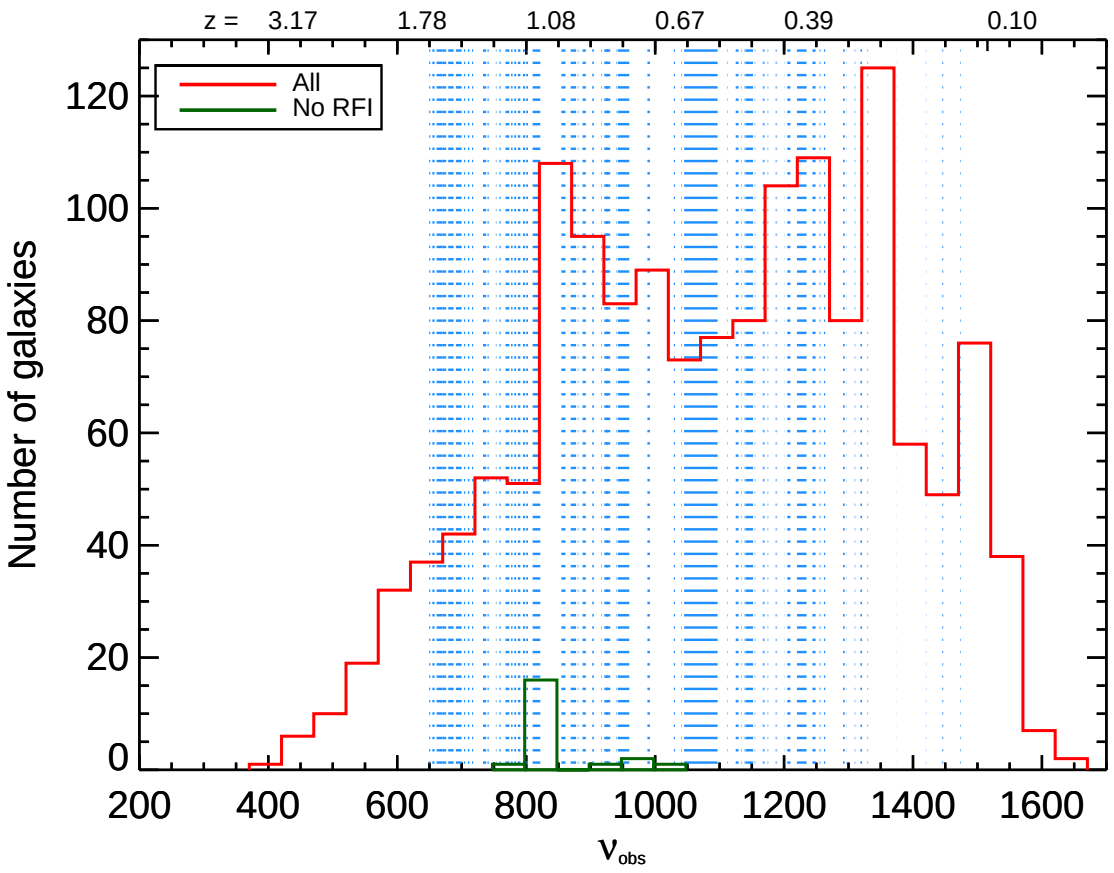

Figure 4.2 Distribution of the 70 μm-selected COSMOS galaxies (Kartaltepe et al., 2010) as a function of the frequency at which redshifted OH would be observed. The red histogram is for all 1503 galaxies in the COSMOS 70 μm sample; the blue regions show frequencies that are effectively unobservable at GBT due to severe RFI. The green histogram shows the 19 galaxies that are located in clean frequency windows and which match our other criteria for L_{IR} and starbursts.

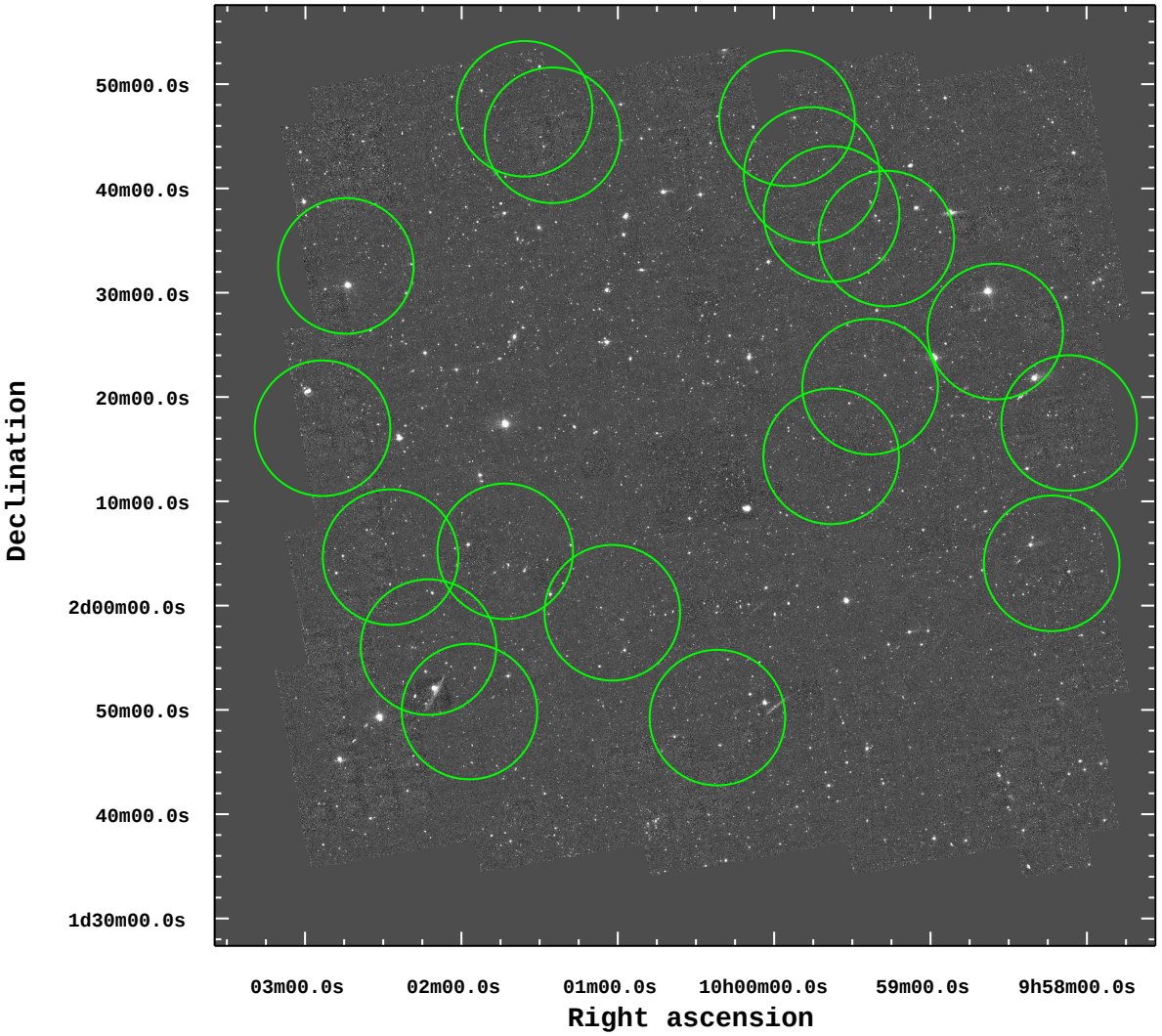

Figure 4.3 Hubble Space Telescope ACS image of the COSMOS field, a $1.4^\circ \times 1.4^\circ$ square centered at $[\alpha, \delta] = [10^h00^m28.6^s, +02^\circ12'21.0'']$. Green circles show the locations of the candidate OHM galaxies described in §4.2.2; the size of the circle shows the FWHM of the GBT beam, which is $13'$ at 800 MHz.

Table 4.1. OHM candidate galaxies: general properties

Target	RA J2000	Dec J2000	$z_\odot$	Ref.[a]	D_L [h_{71}^{-1} Mpc]	$S_{1.4}$ [mJy]	log L [$L_\odot$]	Lum.[b] type
COSMOS J095806.766+021730.81	09 58 06.766	+02 17 30.81	0.97	K10	6273 (79)	0.24	12.57	L_{IR}
COSMOS J095813.471+020403.42	09 58 13.471	+02 04 03.42	0.98	K10	6353 (80)	0.08	12.05	L_{IR}
COSMOS J095835.102+022616.99	09 58 35.102	+02 26 16.99	1.01	K10	6595 (80)	–	12.14	L_{IR}
COSMOS J095916.889+023512.27	09 59 16.889	+02 35 12.27	0.98	K10	6353 (80)	0.07	12.24	L_{IR}
COSMOS J095923.134+022100.18	09 59 23.134	+02 21 00.18	1.01	K10	6595 (80)	–	12.37	L_{IR}
COSMOS J095937.925+023733.69	09 59 37.925	+02 37 33.69	1.00	K10	6514 (80)	–	12.17	L_{IR}
COSMOS J095938.095+021419.40	09 59 38.095	+02 14 19.40	0.99	K10	6434 (80)	0.16	12.23	L_{IR}
COSMOS J095945.562+024118.05	09 59 45.562	+02 41 18.05	0.99	K10	6434 (80)	0.20	12.49	L_{IR}
COSMOS J095955.022+024644.73	09 59 55.022	+02 46 44.73	1.01	K10	6595 (80)	–	12.25	L_{IR}
COSMOS J100021.782+014916.18	10 00 21.782	+01 49 16.18	1.00	K10	6514 (80)	–	12.30	L_{IR}
COSMOS J100102.112+015919.58	10 01 02.112	+01 59 19.58	0.73	K10	4421 (74)	–	12.24	L_{IR}
COSMOS J100125.118+024506.54	10 01 25.118	+02 45 06.54	0.98	K10	6353 (80)	0.09	12.62	L_{IR}
COSMOS J100135.844+024739.12	10 01 35.844	+02 47 39.12	0.71	K10	4273 (73)	0.37	12.28	L_{IR}
COSMOS J100143.238+020512.82	10 01 43.238	+02 05 12.82	0.67	K10	3980 (72)	0.29	12.30	L_{IR}
COSMOS J100156.942+014951.03	10 01 56.942	+01 49 51.03	1.01	K10	6595 (80)	0.21	12.40	L_{IR}
COSMOS J100212.662+015601.51	10 02 12.662	+01 56 01.51	1.00	K10	6514 (80)	0.13	12.31	L_{IR}
COSMOS J100227.235+020439.01	10 02 27.235	+02 04 39.01	0.99	K10	6434 (80)	–	12.17	L_{IR}
COSMOS J100244.438+023234.52	10 02 44.438	+02 32 34.52	1.00	K10	6514 (80)	0.10	12.45	L_{IR}
COSMOS J100253.374+021700.63	10 02 53.374	+02 17 00.63	1.00	K10	6514 (80)	0.10	12.01	L_{IR}
DEEP2 11020790	14 14 59.71	+52 05 09.3	0.92852	L07	5944 (1)	–	12.43	L_{IR}
DEEP2 12027947	14 19 19.6	+52 47 15	1.018	L07	6659 (8)	–	12.11	L_{IR}
DEEP2 13019982	14 19 16.56	+52 53 52.2	0.77889	L07	4787 (1)	–	12.22	L_{IR}
DEEP2 13034619	14 20 20.34	+53 01 56.6	0.95513	L07	6155 (1)	–	12.24	L_{IR}
FF 0030−0027	00 30 09.099	−00 27 44.40	0.242	S00	1197 (5)	2.52	12.25	L_{FIR}
FF 0050−0039	00 50 09.806	−00 39 00.96	0.727	S00	4398 (7)	4.32	12.84	L_{FIR}
FF 0240−0042	04 40 08.576	−00 42 03.56	0.41	S00	2204 (63)	0.84	12.40	L_{FIR}
FF 0245+0123	02 45 55.355	+01 23 28.40	0.798	S00	4931 (7)	2.03	12.95	L_{FIR}
FF 0312+0058	03 12 38.445	+00 58 33.86	0.130	S00	601 (5)	3.84	11.43	L_{FIR}
FF 0317−0129	03 17 43.635	−01 29 07.33	0.265	S00	1327 (5)	1.67	11.91	L_{FIR}
FF 0748+3343	07 48 10.591	+33 43 27.13	0.356	S00	1867 (6)	2.03	12.64	L_{FIR}
FF 0758+2851	07 58 45.956	+28 51 32.76	0.126	S00	581 (4)	3.72	11.58	L_{FIR}

Table 4.1 (cont'd)

Target	RA J2000	Dec J2000	$z_\odot$	Ref.[a]	D_L [h_{71}^{-1} Mpc]	$S_{1.4}$ [mJy]	log L [$L_\odot$]	Lum.[b] type
FF 0804+3919	08 04 07.399	+39 19 27.63	0.164	S00	775 (5)	5.90	11.40	L_{FIR}
FF 0823+3202	08 23 54.616	+32 02 12.03	0.396	S00	2116 (6)	0.97	12.38	L_{FIR}
FF 0826+3042	08 26 11.644	+30 42 44.17	0.248	S00	1231 (5)	3.19	12.15	L_{FIR}
FF 0835+3559	08 35 27.440	+35 59 33.07	0.201	S00	971 (5)	0.85	11.85	L_{FIR}
FF 0856+3450	08 56 24.852	+34 50 24.82	0.220	S00	1075 (5)	8.51	11.93	L_{FIR}
FF 0907+3931	09 07 42.264	+39 31 49.47	0.224	S00	1097 (5)	1.24	11.79	L_{FIR}
FF 1016+3951	10 16 08.616	+39 51 20.46	0.307	S00	1572 (5)	2.10	12.01	L_{FIR}
FF 1018+3649	10 18 34.539	+36 49 51.75	0.490	S00	2726 (6)	9.18	12.58	L_{FIR}
FF 1042+3231	10 42 40.815	+32 31 30.99	0.633	S00	3714 (7)	6.34	12.76	L_{FIR}
FF 1106+3201	11 06 35.716	+32 01 46.39	0.900	S00	5719 (7)	13.7	13.09	L_{FIR}
FF 1242+2905	12 42 32.497	+29 05 14.75	0.260	S00	1299 (5)	1.34	11.95	L_{FIR}
FF 1412+3014	14 12 24.952	+30 14 09.78	0.257	S00	1282 (5)	2.06	11.86	L_{FIR}
FF 1456+3337	14 56 58.427	+33 37 09.98	0.443	S00	2417 (6)	1.43	12.55	L_{FIR}
FF 1532+3242	15 32 44.052	+32 42 46.73	0.926	S00	5924 (7)	5.89	13.12	L_{FIR}
FF 1614+3234	16 14 22.105	+32 34 03.66	0.710	S00	4273 (7)	1.19	12.66	L_{FIR}
FF 1659+3549	16 59 24.669	+35 49 01.74	0.371	S00	1960 (6)	0.79	12.22	L_{FIR}
FF 1707+3725	17 07 11.795	+37 25 55.32	0.311	S00	1595 (5)	2.11	12.08	L_{FIR}
FF 1713+3843	17 13 46.085	+38 43 04.77	0.171	S00	812 (5)	1.66	11.72	L_{FIR}
FF 2131−0141	21 31 53.490	−01 41 43.35	0.730	S00	4421 (7)	2.79	12.82	L_{FIR}
FF 2136−0112	21 36 34.229	−01 12 08.38	0.21	S00	1020 (54)	3.20	11.86	L_{FIR}
FF 2200+0108	22 00 51.859	+01 08 27.08	0.164	S00	775 (5)	2.82	11.53	L_{FIR}
FF 2216+0058	22 16 02.721	+00 58 10.65	0.212	S00	1031 (5)	1.31	11.96	L_{FIR}
FF 2221−0042	22 21 26.066	−00 42 39.08	0.189	S00	907 (5)	0.66	11.54	L_{FIR}
FF 2330−0025	23 30 34.920	−00 25 03.98	0.252	S00	1253 (5)	1.65	12.08	L_{FIR}
FF 2352−0015	23 52 53.171	−00 15 24.69	0.227	S00	1113 (5)	0.59	11.74	L_{FIR}
LH 1200.008	10 51 41.9	+57 19 51	1.21	I05	8247 (84)	0.32	–	–
LH 1200.014	10 52 00.0	+57 24 24	0.69	I05	4126 (73)	0.08	11.52	L_{bol}
LH 1200.096	10 51 51.4	+57 26 40	1.15	I05	7744 (83)	0.14	12.20	L_{bol}
RG 105204.22+572715.7	10 52 04.22	+57 27 15.7	0.934	S04	5987 (7)	–	–	–
SMM J02399-0134	02 39 56.4	−01 34 27.0	1.061	T06	7009 (8)	0.53	12.81	L_{FIR}
SMM J030227.73+000653.5	03 02 27.73	+00 06 53.5	1.408	S04	9947 (8)	0.22	13.44	L_{bol}

4.3 Green Bank Telescope observations

Observations of the two samples were carried out at the Green Bank Telescope (GBT) in West Virginia between Jan 2008 and Oct 2010. The choice of the GBT was driven by three considerations: sensitivity, frequency coverage, and RFI mitigation. Detection of spectral lines at the level of a few mJy requires a telescope with a large collecting area and low system temperature. These observations required continuous frequency coverage from 650 MHz $< \nu_{obs} <$ 1667 MHz to cover an uninterrupted redshift distribution. Finally, given problems with terrestrial RFI at $\nu < 1$ GHz, a telescope in a remote site with RFI mitigation techniques was necessary.

To fulfill all three requirements, the GBT is the best choice for a high-redshift OHM survey. The GBT has an off-axis design with a collecting area of 100m $\times$ 110m, making it the largest fully-steerable single dish telescope in the world. The telescope has continuous coverage near the frequencies of redshifted OH. Finally, the GBT is located in the middle of an RFI-mitigated region designated as the National Radio Quiet Zone (NRQZ). Its location near 38° N latitude allows for observations of 85% of the celestial sphere, including access to the deep fields from which many of the targets were selected.

Observations of the OHM candidate galaxies were taken in position-switched mode, in which the telescope nods back and forth between the target and a nearby patch of "blank" sky thought to be devoid of radio emission. The "on" and "off" observations are of equal duration; the default configuration cycle was 5 minutes on-source followed by 5 minutes off-source. We repeated these cycles until the desired noise level of the observation was achieved:

$$\sigma_{noise} = \frac{K_1\ T_{sys}}{\sqrt{K_2\ t_{eff}\ N_{pol}\ BW/N_{chan}}}. \tag{4.1}$$

Here, σ is the rms noise, K_1 is a constant defined by the backend sampling efficiency, T_{sys} is the system temperature of the telescope, K_2 is the weighting function from the autocorrelator channels, t_{eff} is the effective integration time, N_{pol} the number of polarizations, BW the spectral bandwidth, and N_{chan} the number of spectral channels.

Table 4.1 (cont'd)

Target	RA J2000	Dec J2000	$z_\odot$	Ref.[a]	D_L [h_{71}^{-1} Mpc]	$S_{1.4}$ [mJy]	log L [$L_\odot$]	Lum.[b] type
SMM J030231.81+001031.3	03 02 31.81	+00 10 31.3	1.316	S04	9150 (8)	0.05	12.11	L_{bol}
SMM J030238.62+001106.3	03 02 38.62	+00 11 06.3	0.276	S04	1390 (5)	0.35	11.32	L_{bol}
SMM J030244.82+000632.3	03 02 44.82	+00 06 32.3	0.176	C05	838 (5)	0.15	11.08	L_{bol}
SMM J105151.69+575636.0	10 51 51.69	+57 56 36.0	1.147	C05	7719 (8)	0.13	12.20	L_{bol}
SMM J105200.22+572420.2	10 52 00.22	+57 24 20.2	0.689	S04	4119 (7)	0.06	11.52	L_{bol}
SMM J105217.88+571930.2	10 52 17.88	+57 19 30.2	1.026	S04	6724 (8)	–	–	–
SMM J123629.13+621045.8	12 36 29.13	+62 10 45.8	1.013	S04	6619 (8)	0.08	12.08	L_{bol}
SMM J123634.51+621241.0	12 36 34.51	+62 12 41.0	1.219	S04	8323 (8)	0.23	12.74	L_{bol}
SMM J123721.87+621035.3	12 37 21.87	+62 10 35.3	0.979	S04	6345 (8)	0.04	11.72	L_{bol}
SMM J131208.82+424129.1	13 12 08.82	+42 41 29.1	1.544	S04	11146 (8)	0.08	12.57	L_{bol}
SMM J131225.20+424344.5	13 12 25.20	+42 43 44.5	1.038	S04	6822 (8)	0.08	12.08	L_{bol}
SMM J131225.73+423941.4	13 12 25.73	+42 39 41.4	1.554	S04	11235 (8)	0.75	13.53	L_{bol}
SMM J141741.81+522823.0	14 17 41.81	+52 28 23.0	1.150	S04	7744 (8)	0.08	12.23	L_{bol}
SMM J141742.04+523025.7	14 17 42.04	+52 30 25.7	0.661	C05	3915 (7)	0.23	12.08	L_{bol}
SMM J163658.78+405728.1	16 36 58.78	+40 57 28.1	1.190	S04	8078 (8)	0.07	12.23	L_{bol}
SMM J163704.34+410530.3	16 37 04.34	+41 05 30.3	0.840	S04	5253 (7)	0.05	11.60	L_{bol}
SMM J221733.02+000906.0	22 17 33.02	+00 09 06.0	0.926	S04	5924 (7)	0.16	12.28	L_{bol}

[a]References for redshifts are from: L07=L. Lin (priv.comm.); S00=Stanford et al. (2000); I05=Ivison et al. (2005); T06=Takata et al. (2006); S04=Smail et al. (2004); C05=Chapman et al. (2005); K10=Kartaltepe et al. (2010).

[b]Wavelengths over which the integrated luminosity is quoted in the literature. L_{IR} and L_{FIR} give the integrated luminosities from $8-1000$ μm and $40-500$ μm, respectively (Sanders & Mirabel, 1996). L_{bol} is the integrated luminosity of the galaxy over **all** wavelengths, calculated using a model SED.

To minimize the noise levels, we used nine-level sampling on the GBT autocorrelation spectrometer, which yields $K_1 = 1.032$ and $K_2 = 1.21$. The receivers used (prime focus receivers PF1-600, PF1-800, and PF2 plus the Gregorian L-band receiver) all have native linear polarizations in XX and YY, giving $N_{pol} = 2$. We used the maximum bandwidth of 50 MHz for most galaxies to accommodate uncertainties in the target's redshift. For a few targets in which strong RFI near the edge of the 50 MHz bandpass unbalanced the voltage levels in the spectrometer, we reduced the observing bandwidth to 12.5 MHz. We used the highest number of channels available in each spectrometer configuration to maximize spectral resolution, with $N_{chan} = 8192$. In post-processing, the spectra were smoothed to various levels of rest-frame velocity resolution such that $\Delta v_{obs}/c = (1+z) \times \Delta\nu_{obs}/\nu_{rest}$.

The effective integration time (t_{eff}) is defined as:

$$t_{eff} = \frac{t_{on} t_{off}}{t_{on} + t_{off}}. \tag{4.2}$$

In standard position-switched mode where $t_{on} = t_{off}$ and $t_{total} = t_{on} + t_{off}$, this reduces to $t_{eff} = t_{total}/4$. We assume a standard system temperature of ~ 30 K, a gain of 2.02 K/Jy and smoothing of the spectra to a resolution of $\Delta v = 10$ km s^{-1}. We used these noise levels to plan the total integration time necessary for each target; for a galaxy at redshift z, the total integration time is:

$$t_{total} = (1.93 \text{ hours}) \times \frac{1+z}{(\sigma \text{ [mJy]})^2} \tag{4.3}$$

This equation calculates only the thermal noise expected per beam, and does not account for the noise introduced by RFI (which was ubiquitous in the OHM observations).

Expected noise levels ($0.8 - 1.2$ mJy) were selected so that OHMs with line strengths of $L_{OH} = 10^{3-4}\ L_{\odot}$ would be detectable. For galaxies observed with the L-band and PF2 receivers ($z = 0.1 - 0.8$), we allotted $\sim$2 hrs per object; for the higher redshift galaxies observed with the PF1-800 and PF1-600 receivers ($z = 0.8 - 1.55$), this increased to $\sim$4 hrs per object. The total

integration time spent on each galaxy is given in Tables 4.2 and 4.3.

4.3.1 GBT data reduction

We reduced the GBT data using standard routines in the software package GBTIDL.[1] Each pair of 5-minute off-on position-switched scans was individually examined for RFI or irregular spectral baseline structure. The scans contain integrations over timescales of $2-6$ seconds; these were flagged for time-variable RFI that could be removed to the improvement of the entire scan. In many cases, we used an automated sigma-clipping routine to remove obvious RFI features. RFI in the integrated spectra was identified manually, looking for sharp features in the spectral domain and/or large amounts of power in the off scans. These features were automatically removed by identifying a region of continuum and removing affected channels with flux densities several standard deviations above or below this continuum level. Identified sources of RFI included orbiting GPS and communications satellites, terrestrial radio and television transmissions, and air-to-ground radar from nearby aircraft.

After the majority of RFI features were removed from the spectra, we fit the radio continuum around the expected line center with a polynomial function of order $n = 5$. This removed both intrinsic continuum structure from the target itself (typically power-law emission from synchrotron radiation) and any baseline structure not removed by the position-switching technique of the telescope. The spectra are then initially smoothed with a Hanning filter.

After flagging and the first round of smoothing, we experimented with several different forms of stacking scans for a given target. The first method uses the weighted mean of the scans via the `ACCUM` function in GBTIDL, for which the relative weights of each scan are $(t_{eff} \times \Delta\nu / T_{sys}^2)$. Since t_{eff} and $\Delta\nu$ are constant and T_{sys} is usually stable over the course of a few hours, weights are typically uniform for a single observation session. The second method uses a simple median stack of each scan, which is useful as a secondary method of removing time-dependent RFI features in the data. Finally, we also look at results from taking the median value of each *integration* within

[1] http://gbtidl.nrao.edu

each scan, then taking the weighted mean via the first method. We used each stacking method (and combinations thereof) on candidate OHM spectra, choosing the method which yielded the lowest continuum rms for each target.

After stacking, the data were smoothed to three different velocity resolutions: $\Delta v = 10, 50,$ and 150 km s^{-1}. 10 km s^{-1} is the approximate width of the narrowest OH features observed in other known megamasers, while the broadest velocity width can extend to at least several hundred km s^{-1}. We report the rms noise for each velocity smoothing in Table 4.3.

4.3.2 Measured sensitivity of GBT receivers

The sensitivity of the OHM survey was somewhat lower than that expected from the predicted noise levels for the GBT receivers (Equation 4.3). Figure 4.4 shows the predicted sensitivities as a function of time for each of the four receivers employed in the OHM survey. The actual rms measured from the data over a region of continuum centered at the expected line location is also shown for all objects in the sample. The highest-frequency receiver (L-band) had the best performance, with almost all observations within a factor of two of the expected theoretical rms. Performance noticeably decreased for observations at $\nu < 1$ GHz, with observed noise levels typically at 2–5 times the predicted rms and more than 10 times as high in some cases. The main cause for the drop in sensitivity is RFI, from both within the measured bandpass and from excess power leaking in from adjacent frequencies.

4.4 Results

The OHM candidate galaxies from our sample were observed for a total of 166 hours at the GBT. Data from six galaxies had RFI or telescope feed resonances too strong to yield any useful 18-cm results, and were not observed for more than a single integration. No data for these targets (DEEP2 11045892, FF 0738+2856, FF 1514+3629, LH 1200.003, SMM J123636.75+621156.0, and SMM J221724.69+001242.1) are included in the results or analysis.

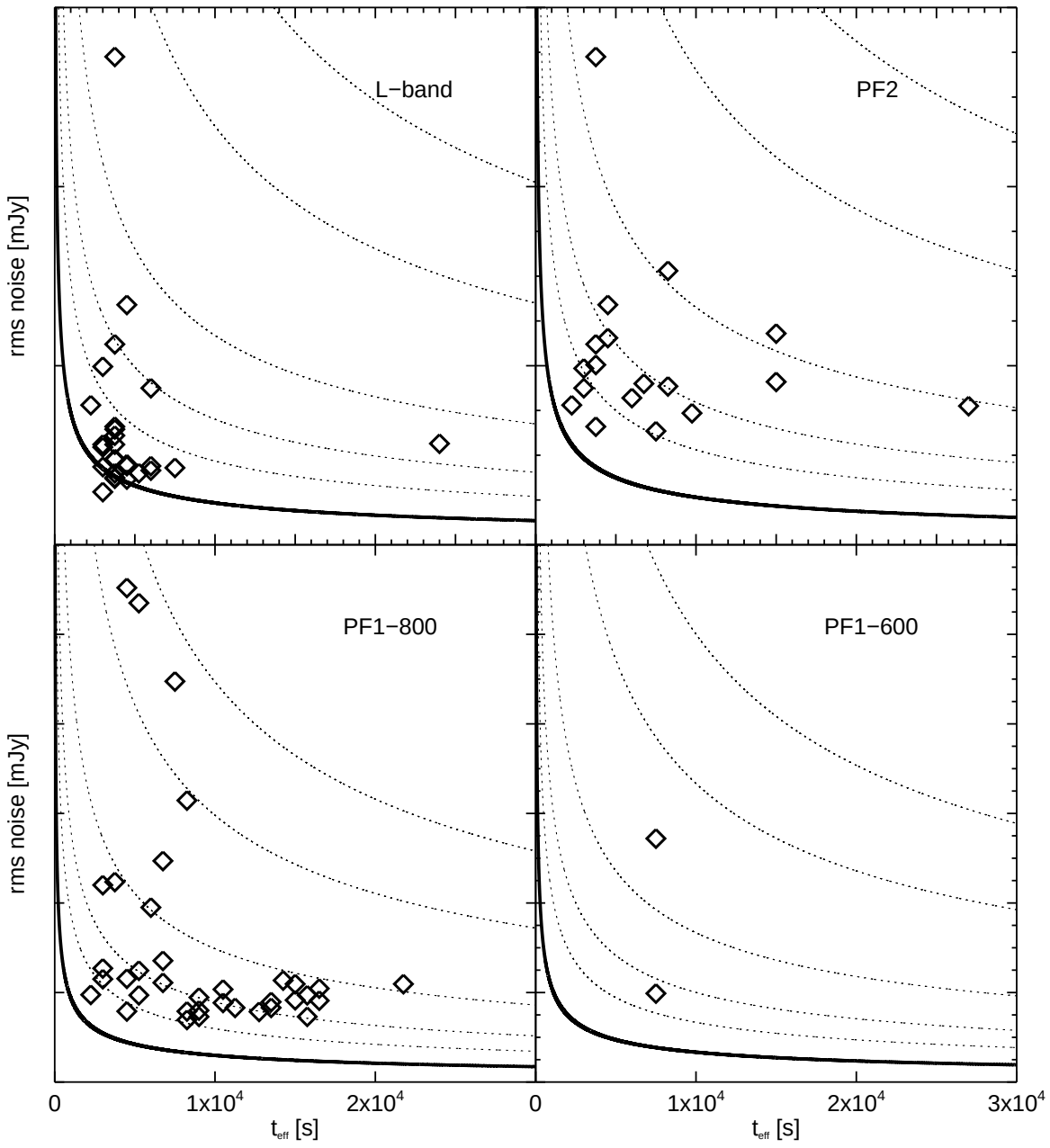

Figure 4.4 Measured rms sensitivity of the GBT receivers as a function of integration time for high-redshift OHM candidates. Panels show the data (diamond points) and theoretical noise curves (solid line; Equation 4.3) for each receiver, smoothed to a resolution of $\Delta v = 10$ km s^{-1}. The dashed lines show predictions for 2, 3, 5, 10, and 15 times the theoretical rms.

4.4.1 Detection of two new OH megamasers

Out of the 79 objects in the final sample, two had confirmed OH megamaser emission: FF 0758+2851 and FF 2216+0058 (Figure 4.5). Both galaxies are from the FSC-FIRST catalog and have redshifts near the lower end of the sample distribution ($z = 0.126$ and 0.212, respectively). The observed frequencies of both detections are in the range of $1300-1500$ MHz, which is covered by the L-band receiver and has relatively little RFI compared to the prime focus bands. Both OHMs were detected in shorter scans of 20 minutes, and later confirmed with follow-up observations.

Table 4.2 lists the 18-cm radio properties of the two new OHM detections. For the GBT observations, we give the expected observed frequency of the 1667 MHz line (ν_{1667}), the total time spent observing on-source (t_{int}), and the rms noise at 10 km s^{-1} smoothing (σ_{10}). For the OH emission itself, we give the peak flux density of the OHM (S_{1667}^{peak}), the equivalent width of the feature (W_{1667}), and the heliocentric velocity of the peak emission (v_{1667}). We also report the hyperfine ratio $R_H = F_{1667}/F_{1665}$; for gas in thermodynamic equilibrium, $R_H = 1.8$. In both cases the presumably weaker 1665 MHz emission is not detected, and so we place an upper limit on F_{1665} using a boxcar with height 1σ and a width equivalent to that of the 1667 MHz feature. Finally, we give both the measured OH luminosity ($\log L_{OH}$) in addition to the predicted OH luminosity (L_{OH}^{pred}) from the $L_{OH}-L_{FIR}$ relationship in Darling & Giovanelli (2002a). Details on the individual detections are given below.

FF 0758+2851: The OH emission for this galaxy is reasonably fit with a single Gaussian centered at $cz_{hel} = 37939 \pm 7$ km s^{-1}, which is 160 km s^{-1} redshifted from the optical velocity. There is no indication of emission from the 1665 MHz line; the limit on the hyperfine ratio gives $R_H > 2.9$. The OHM has a peak flux density of 3.98 mJy and a FWHM of 223 km s^{-1}, which gives a total luminosity of $\log (L_{OH}/L_\odot) = 2.67$.

The host galaxy of FF 0758+2851 is classified in the FIRST catalog as a point source at 20-cm. K-band imaging reveals a 15th-magnitude object classified as an interacting system, with a bright elliptical source bordered by a much fainter nucleus to the south and a possible tidal tail

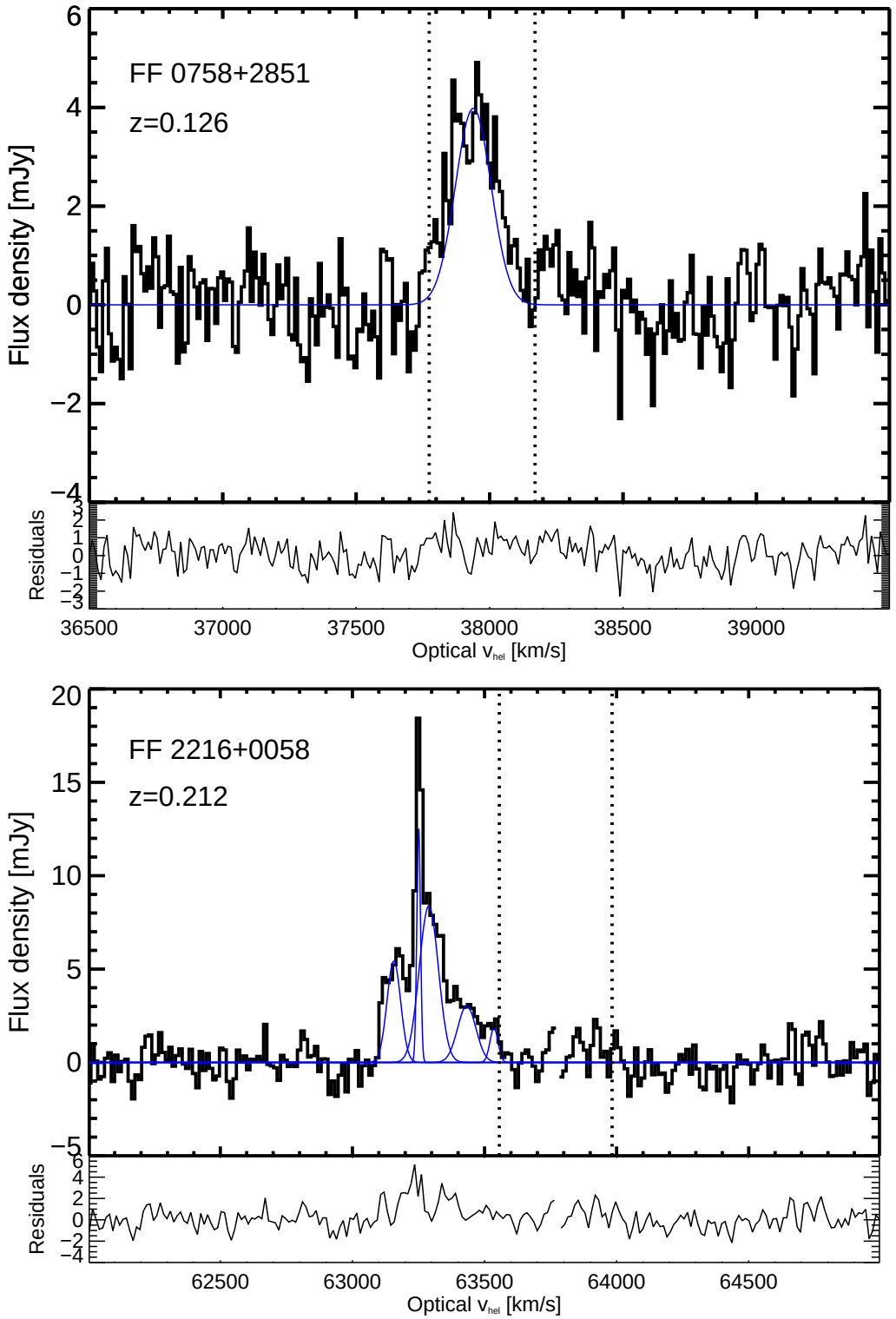

Figure 4.5 GBT spectra of the two new OHM detections. The main panels show the data overlaid with Gaussian fits to the peak(s) in blue; the residuals from the fit are shown below the data. The two dotted lines show the expected velocities of the main OH lines at 1667.3590 and 1665.4018 MHz based on the optical redshift; the 1667 MHz line is on the left.

Table 4.2. OHM detections from the GBT survey

Target	ν_{1667} [MHz]	t_{int} [min]	σ_{10} [mJy]	S_{1667}^{peak} [mJy]	W_{1667} [km s^{-1}]	v_{1667} [km s^{-1}]	R_H	log L_{OH} [L$_\odot$]	log L_{OH}^{pred} [L$_\odot$]
FF 0758+2851	1480	40	0.75	3.98	206	37953 (10)	> 2.9	2.67	2.39
FF 2216+0058	1376	30	0.80	18.4	126	63248 (10)	$\gtrsim 7.5$	3.53	2.58

extending to the northwest (Stanford et al., 2000).

FF 2216+0058: The OH emission in this galaxy is complex, with several distinct components separated by a total velocity of ~ 400 km s^{-1}. We fit the OH emission with five Gaussian components - this is not an unusual number for an OHM, and re-observations of FF 2216+0058 with Arecibo at higher resolution indicates that it may have at least ~ 10 components (J. McBride, pers. comm). The brightest OH peak is blueshifted from the optical velocity by -300 km s^{-1}. The peak flux density of the OHM is 18.4 mJy; the total integrated flux of the Gaussian components gives a luminosity of $L_{OH} = 10^{3.53}\ L_\odot$. There is no indication of 1665 MHz emission in this spectrum, for which we calculate a lower limit of $R_H \gtrsim 7.5$ using the width at 10% of the peak 1667 MHz flux density. RFI near $v_{hel} = 63750$ km s^{-1} has been masked in its spectrum (Figure 4.5).

The host galaxy of FF 2216+0058 is also a point source at 20-cm, but with an asymmetric K-band morphology (Stanford et al., 2000). Images in K and the SDSS z-band show that the nucleus has a mild ellipticity along the east-west axis, and a possible diffuse extension to the southeast that could be a tidal tail. There is no clear evidence from near-infrared imaging to indicate if this galaxy is in a merging system.

FF 2216+0058 is the sixth-most distant ($z = 0.212$) and tenth-most luminous OHM yet discovered. It is also the second-most distant OHM not to have been detected with the Arecibo telescope.

4.4.2 OHM non-detections

77 galaxies in the sample showed no confirmed detections of OH; their 18-cm properties are listed in Table 4.3. We list the observed frequency at which 1667 MHz emission was expected

(ν_{1667}), the total integration time spent on-source (t_{int}), the rms noise in the spectrum at velocity smoothings of 10, 50, and 150 km s^{-1} ($\sigma_{10}, \sigma_{50}, \sigma_{150}$), and the maximum OH luminosity (L_{OH}^{max}) based on the rms. The smoothing levels are chosen based on the range of velocity widths in known OHMs, which can be high as $\sim$ 1000 km s^{-1}; the minimum smoothing level is driven by the resolution of the GBT spectrometer at the lowest observed frequencies. The reduced spectra for all the OH non-detections are given in Appendix C as Figures C.1-C.77.

Upper limits on OH emission are conservatively derived assuming a boxcar line profile with a linewidth $\Delta v = 150$ km s^{-1} and a 1.5σ detection:

$$L_{OH}^{max} = 4\pi D_L^2 (1.5\sigma) \left(\frac{\Delta v}{c}\right) \left(\frac{\nu_0}{1+z}\right). \tag{4.4}$$

The rms noise was measured from baseline-subtracted continuum centered on the optical redshift of the galaxy and in a frequency range sufficient to cover the uncertainty in the optical redshift ($\Delta\nu_{obs} = \Delta z \times \nu_{rest}/[1+z]$). This often included one or more powerful RFI features that significantly increased the rms. While we occasionally shortened the frequency range slightly to avoid interference near the edge, the estimate of the noise is always made over a continuous portion of the spectrum. Estimates of the rms from a "piecewise" method (in which areas of cleaner continuum are selected from between narrow RFI spikes) resulted in a decrease in the rms up to a factor of $2-3$. We used the noise from the continuous method in all calculations for L_{OH}^{max} (Figure 4.6).

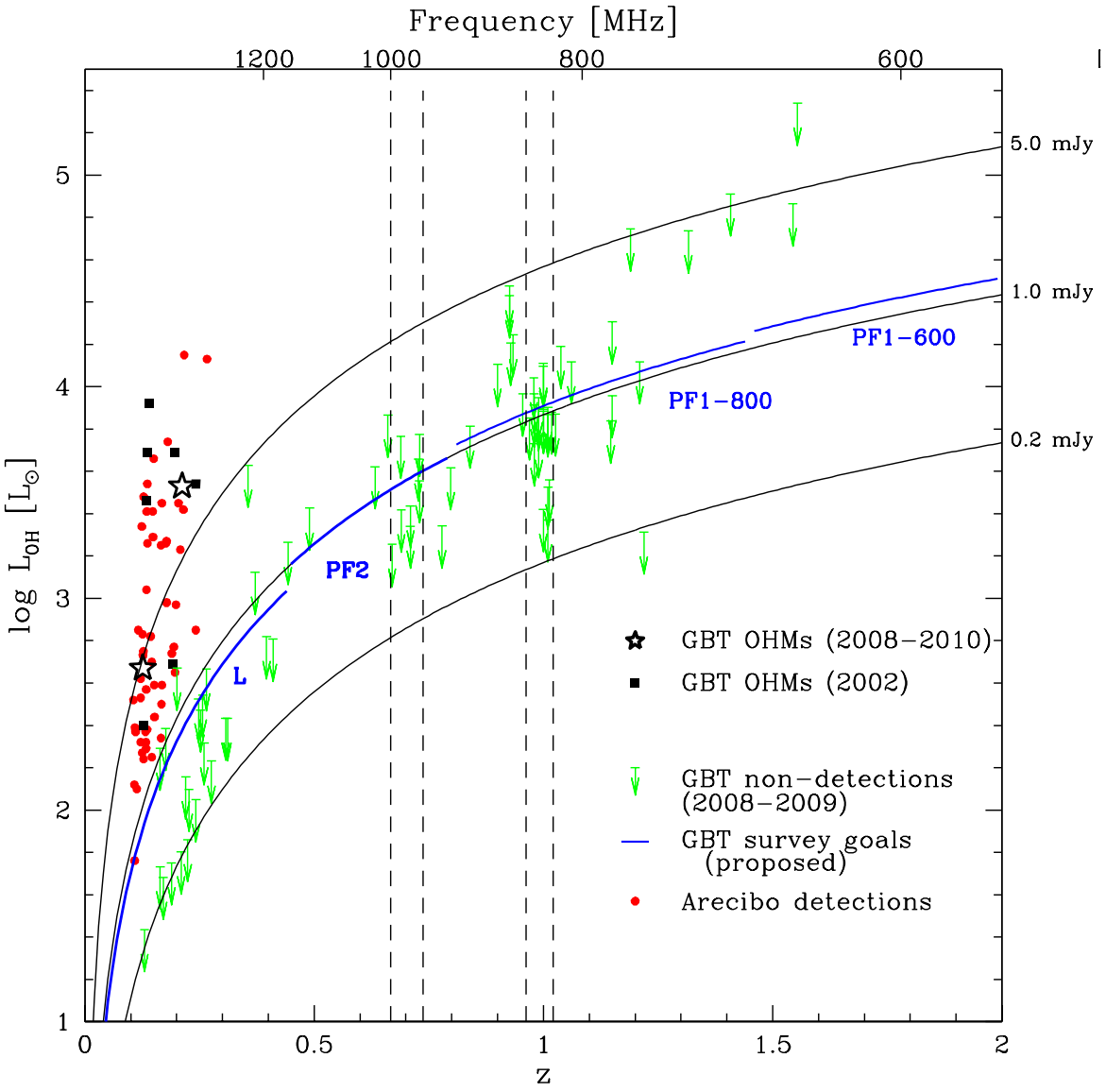

Figure 4.6 GBT sensitivity to OH megamasers as a function of redshift, based on a 1.5σ-detection and 1–2 hours of position-switched observing. Successful OHM detections with the GBT are marked with black stars (this survey) and black squares (Kent et al., 2002). Limits for the non-detections in our survey are labeled in green. The main cause of the lack of sensitivity to a typical $10^3 - 10^4$ $L_\odot$ OHM is RFI contamination at $\nu_{obs} < 1$ GHz. The dashed lines indicate the two RFI-clean windows in which the COSMOS candidates are located.

Table 4.3. OHM non-detections from the GBT survey

Target	ν_{1667} [MHz]	t_{int} [min]	rms for velocity smoothings σ_{10} [mJy]	σ_{50} [mJy]	σ_{150} [mJy]	L_{OH}^{max} for velocity smoothings 10 km s^{-1} [log $L_\odot$]	50 km s^{-1} [log $L_\odot$]	150 km s^{-1} [log $L_\odot$]	L_{OH}^{pred} [log $L_\odot$]
COSMOS J095806.766+021730.81	998	70	1.66	1.15	0.92	4.14	3.98	3.88	3.97
COSMOS J095813.471+020403.42	975	90	2.07	1.26	1.04	4.18	3.96	3.88	3.16
COSMOS J095835.102+022616.99	963	110	1.66	1.07	0.95	4.11	3.92	3.87	3.30
COSMOS J095916.889+023512.27	846	70	1.82	0.90	0.68	4.13	3.82	3.70	3.46
COSMOS J095923.134+022100.18	842	100	1.77	1.10	0.88	4.20	4.00	3.90	3.66
COSMOS J095937.925+023733.69	842	90	1.83	1.13	0.95	4.15	3.94	3.86	3.35
COSMOS J095938.095+021419.40	842	105	1.79	1.25	1.10	4.19	4.03	3.98	3.44
COSMOS J095945.562+024118.05	837	85	1.46	0.87	0.73	4.10	3.88	3.80	3.85
COSMOS J095955.022+024644.73	837	110	1.57	0.62	0.28	4.15	3.75	3.40	3.47
COSMOS J100021.782+014916.18	837	100	2.09	1.61	1.57	4.26	4.15	4.14	3.55
COSMOS J100102.112+015919.58	833	55	1.82	1.14	0.82	3.85	3.65	3.50	3.46
COSMOS J100125.118+024506.54	833	180	1.58	1.27	1.17	4.12	4.03	4.00	4.05
COSMOS J100135.844+024739.12	833	50	1.55	1.02	0.66	3.75	3.57	3.38	3.52
COSMOS J100143.238+020512.82	833	60	1.27	0.67	0.49	3.61	3.34	3.20	3.55
COSMOS J100156.942+014951.03	833	100	1.46	0.79	0.40	4.12	3.85	3.55	3.71
COSMOS J100212.662+015601.51	829	95	2.19	1.25	0.93	4.29	4.04	3.91	3.57
COSMOS J100227.235+020439.01	829	60	2.27	1.25	0.98	3.98	3.72	3.61	3.35
COSMOS J100244.438+023234.52	829	105	1.60	0.67	0.32	4.15	3.77	3.45	3.79
COSMOS J100253.374+021700.63	829	85	1.94	1.23	1.52	4.17	3.98	4.07	3.10
DEEP2 11020790	865	25	4.47	2.79	2.26	4.53	4.33	4.23	3.76

Table 4.3 (cont'd)

Target	ν_{1667} [MHz]	t_{int} [min]	rms for velocity smoothings σ_{10} [mJy]	σ_{50} [mJy]	σ_{150} [mJy]	L_{OH}^{max} for velocity smoothings 10 km s^{-1} [log $L_\odot$]	50 km s^{-1} [log $L_\odot$]	150 km s^{-1} [log $L_\odot$]	L_{OH}^{pred} [log $L_\odot$]
DEEP2 12027947	826	65	1.89	1.08	0.89	4.24	3.99	3.91	3.25
DEEP2 13019982	937	40	1.47	0.67	0.44	3.89	3.55	3.37	3.43
DEEP2 13034619	853	30	3.90	1.91	1.23	4.50	4.18	3.99	3.46
FF 0030−0027	1343	30	0.73	0.37	0.25	2.52	2.23	2.06	3.47
FF 0050−0039	965	25	2.31	1.39	1.05	4.03	3.80	3.68	4.40
FF 0240−0042	1182	45	1.32	0.69	0.48	3.26	2.98	2.82	3.71
FF 0245+0123	927	40	1.80	1.02	0.79	4.00	3.75	3.64	4.57
FF 0312+0058	1475	25	0.83	0.35	0.22	2.02	1.65	1.43	2.19
FF 0317−0129	1318	25	1.22	0.95	0.86	2.83	2.72	2.68	2.94
FF 0748+3343	1230	25	5.45	4.93	4.27	3.75	3.70	3.64	4.08
FF 0804+3919	1432	15	1.75	1.14	0.98	2.55	2.37	2.30	2.14
FF 0823+3202	1194	20	1.56	0.87	0.53	3.30	3.05	2.84	3.68
FF 0826+3042	1336	20	1.09	0.80	0.71	2.72	2.58	2.53	3.32
FF 0835+3559	1388	20	1.99	1.66	1.54	2.79	2.71	2.68	2.84
FF 0856+3450	1366	25	0.87	0.48	0.39	2.51	2.26	2.16	2.97
FF 0907+3931	1362	20	0.74	0.31	0.19	2.46	2.08	1.88	2.75
FF 1016+3951	1275	25	1.12	0.57	0.37	2.93	2.63	2.45	3.10
FF 1018+3649	1119	20	2.01	1.12	1.38	3.61	3.35	3.44	3.99
FF 1042+3231	1021	20	1.97	1.44	1.28	3.83	3.69	3.64	4.27
FF 1106+3201	878	160	2.30	1.96	1.91	4.21	4.15	4.13	4.79

Table 4.3 (cont'd)

Target	ν_{1667} [MHz]	t_{int} [min]	rms for velocity smoothings σ_{10} [mJy]	σ_{50} [mJy]	σ_{150} [mJy]	L_{OH}^{max} for velocity smoothings 10 km s^{-1} [log $L_\odot$]	50 km s^{-1} [log $L_\odot$]	150 km s^{-1} [log $L_\odot$]	L_{OH}^{pred} [log $L_\odot$]
FF 1242+2905	1323	25	1.13	0.65	0.40	2.78	2.54	2.32	3.00
FF 1412+3014	1326	30	0.95	0.70	0.69	2.69	2.56	2.55	2.86
FF 1456+3337	1155	35	2.68	1.80	1.17	3.64	3.47	3.28	3.94
FF 1532+3242	866	20	10.70	5.10	4.23	4.91	4.58	4.50	4.84
FF 1614+3234	975	25	1.75	0.77	0.53	3.88	3.53	3.36	4.12
FF 1659+3549	1216	25	2.24	1.62	1.22	3.40	3.26	3.14	3.43
FF 1707+3725	1272	20	1.29	0.59	0.36	3.00	2.66	2.44	3.21
FF 1713+3843	1424	55	0.59	0.29	0.22	2.12	1.81	1.69	2.64
FF 2131−0141	964	40	1.77	1.19	1.36	3.91	3.74	3.80	4.37
FF 2136−0112	1378	25	0.88	0.39	0.19	2.47	2.12	1.80	2.86
FF 2200+0108	1433	25	1.12	0.48	0.27	2.36	1.99	1.74	2.34
FF 2221−0042	1402	25	0.88	0.47	0.21	2.38	2.11	1.76	2.36
FF 2330−0025	1331	30	0.96	0.70	0.61	2.68	2.54	2.48	3.21
FF 2352−0015	1359	20	0.90	0.42	0.32	2.55	2.23	2.10	2.67
LH 1200.008	754	40	2.54	1.35	1.10	4.51	4.24	4.15	–
LH 1200.014	987	35	1.64	0.92	0.67	3.83	3.58	3.44	2.33
LH 1200.096	775	45	2.49	1.22	0.84	4.46	4.15	3.99	3.39
RG 105204.22+572715.7	862	30	4.94	2.76	2.45	4.58	4.33	4.27	–
SMM J02399-0134	809	50	2.31	1.60	1.42	4.36	4.20	4.15	4.35
SMM J030227.73+000653.5	692	30	8.95	7.52	5.11	5.19	5.11	4.95	5.34

Table 4.3 (cont'd)

Target	ν_{1667} [MHz]	t_{int} [min]	rms for velocity smoothings σ_{10} [mJy]	σ_{50} [mJy]	σ_{150} [mJy]	L_{OH}^{max} for velocity smoothings 10 km s^{-1} [log $L_\odot$]	50 km s^{-1} [log $L_\odot$]	150 km s^{-1} [log $L_\odot$]	L_{OH}^{pred} [log $L_\odot$]
SMM J030231.81+001031.3	720	50	11.04	5.67	3.89	5.22	4.94	4.77	3.25
SMM J030238.62+001106.3	1307	35	0.86	0.41	0.29	2.71	2.39	2.24	2.01
SMM J030244.82+000632.3	1418	30	0.80	0.35	1.05	2.28	1.91	2.39	1.64
SMM J105151.69+575636.0	777	100	1.58	0.85	0.64	4.26	3.99	3.87	3.39
SMM J105200.22+572420.2	987	15	2.36	1.68	1.50	3.99	3.84	3.79	2.33
SMM J105217.88+571930.2	823	35	1.95	0.90	0.86	4.26	3.92	3.90	–
SMM J123629.13+621045.8	828	55	1.94	0.77	0.43	4.24	3.84	3.59	3.21
SMM J123634.51+621241.0	751	145	1.39	0.52	0.17	4.26	3.83	3.34	4.24
SMM J123721.87+621035.3	843	50	2.19	1.53	1.40	4.27	4.11	4.07	2.64
SMM J131208.82+424129.1	655	60	5.44	3.86	–	5.05	4.90	–	3.97
SMM J131225.20+424344.5	818	45	1.98	1.17	1.75	4.27	4.04	4.22	3.21
SMM J131225.73+423941.4	653	50	12.97	11.40	–	5.43	5.38	–	5.48
SMM J141741.81+522823.0	775	55	2.71	2.37	1.87	4.50	4.44	4.34	3.44
SMM J141742.04+523025.7	1004	20	3.06	2.31	2.05	4.06	3.94	3.89	3.21
SMM J163658.78+405728.1	761	45	4.40	3.19	4.82	4.74	4.60	4.78	3.44
SMM J163704.34+410530.3	906	55	2.22	1.28	1.12	4.14	3.90	3.84	2.45
SMM J221733.02+000906.0	866	75	6.29	3.75	3.81	4.68	4.45	4.46	3.52

Note. — L_{OH}^{max} assumes a 1.5σ detection at $\Delta v = 150$ km s^{-1} (Equation 4.4). Galaxies at $z > 1.5$ had insufficient spectral resolution to smooth to $\Delta v = 150$ km s^{-1}.

Table 4.3 also lists the predicted OH luminosity (L_{OH}^{pred}) from the $L_{FIR} - L_{OH}$ relation in Darling & Giovanelli (2002a). The majority of the OHM candidates do not have 60 or 100 μm photometry, which are typically used to compute L_{FIR} (Sanders & Mirabel, 1996); as a result, we use the proxies of L_{IR} and L_{bol} (Table 4.1) in place of L_{FIR}. The three luminosities differ slightly in the wavelength ranges over which the energy output is measured; L_{IR} uses the flux from the rest-frame $8 - 1000$ μm, L_{FIR} from $40 - 500$ μm, and L_{bol} integrates the entire flux over the spectral output of the galaxy using fits to a model SED. All three values are similar for ULIRGs, in which the energy density peaks near ~ 100 μm; a galaxy with a 60 μm flux of 1 Jy, for example, will have a difference between L_{IR} and L_{FIR} of less than 0.05 dex.

Figure 4.7 shows the distribution of L_{OH}^{max} as a function of L_{IR}. We overplot the $L_{FIR} - L_{OH}$ fit to all previously known OHMs, which has a slope of 1.57 when not corrected for Malmquist bias. 51% of the targets in the sample have $L_{OH}^{max} > L_{OH}^{pred}$ and have sensitivity limits that do not conflict with the expected OHM brightness. Galaxies below the predicted relation have significant scatter, with a mean of $(L_{OH}^{max} - L_{OH}^{pred}) = -1.0$ $L_{\odot}$ and a maximum underprediction of $\Delta \log L_{OH} = -3.6$ $L_{\odot}$. This significantly exceeds the maximum underprediction of -1.0 $L_{\odot}$ for the fit to the larger Arecibo sample of Darling & Giovanelli (2002a).

4.5 Discussion

4.5.1 Why is the OHM fraction lower than expected?

The Arecibo survey of Darling & Giovanelli (2002a) detected a total of 50 new OHMs out of 297 galaxies observed; the OHM detection fraction was shown to be an increasing function of both L_{FIR} and the far-infrared colors of the host galaxies. The Arecibo survey targeted IRAS 60 μm detections from $z = 0.1$ to $z = 0.45$, with detection rates ranging from $20 - 100\%$ for galaxies with $L_{FIR} > 10^{11.6}$ $L_{\odot}$. Since $> 90\%$ of the galaxies in our sample have L_{FIR} above this threshold, we had conservatively estimated that the GBT survey would yield $12 - 20$ new OHMs if local relationships held at $z \sim 1$. This estimate included potential losses from RFI and sensitivity

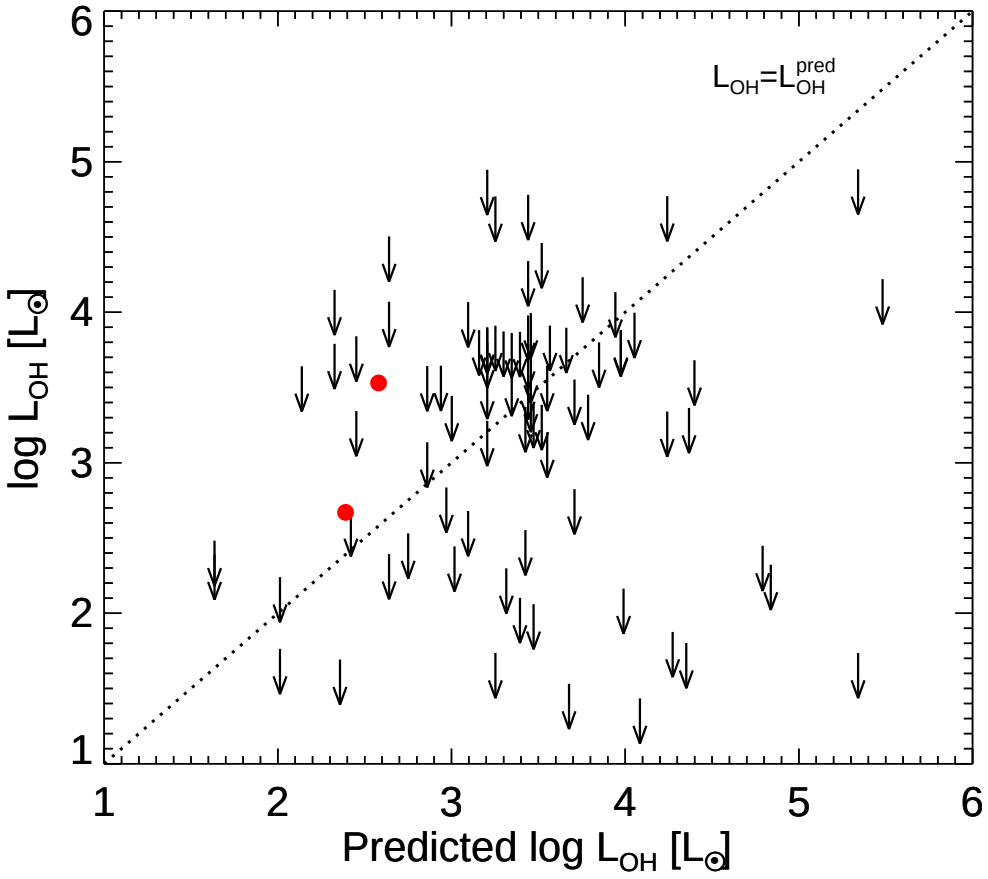

Figure 4.7 Survey completeness: L_{OH} for the OHM candidates as a function of L_{OH}^{pred} calculated from the galaxies' L_{IR}, L_{FIR}, or L_{bol}. The red circles are the two new OHM detections; all other arrows indicate the L_{OH} upper limit. The $L_{OH} - L_{FIR}$ fit to the larger OHM sample of Darling & Giovanelli (2002a) is overplotted as the dotted line.

limits.

The actual OHM detection rate for the GBT survey was roughly an order of magnitude lower than our prediction, with two confirmed detections out of 79 targets observed. Figure 4.8 shows the limits on the OH emission for the candidate galaxies as a function of the host galaxy's infrared luminosity. The OHM fraction for the GBT survey is compared to that of the Arecibo survey as a function of L_{FIR} – as before, we use L_{bol} and L_{IR} as a proxy for L_{FIR} for certain sub-mm galaxies. The Arecibo survey found that the OHM fraction steadily increased above $L_{FIR} = 10^{11}\ L_{\odot}$. The GBT survey has many more galaxies above $L_{FIR} = 10^{12}\ L_{\odot}$ than the Arecibo survey, thanks to its larger volume of space. The lower-luminosity GBT detection (FF 0758+2851) is not inconsistent with the Arecibo OHM fraction at $L_{FIR} = 10^{11.6}\ L_{\odot}$ (22/101 = 22%) if Poisson statistics are assumed. The bin containing the higher-luminosity GBT OHM (FF 2216+0058), however, had an OHM fraction of 1/7 (15%), falling short of the OHM fraction at the same luminosity for the Arecibo survey (20/55 = 36%). The infrared luminosity bins from ($11.8 < \log\ L_{FIR}\ [L_{\odot}] < 12.4$) for the GBT survey are all inconsistent with the Arecibo OHM fraction, assuming small-number statistics.

We also examined the OHM fraction as a function of L_{OH}; that is, what percentage of OHMs above a given luminosity were measured in the survey. For an ideal survey, the detection fraction at the highest luminosities would be 100%, meaning that all objects had been observed to a sensitivity such that the brightest object in the sample would have been detected. For the Arecibo survey, $L_{OH}^{max} < 10^{2.5}\ L_{\odot}$ for all targets, with several dozen detections above this limit. The detection rate in the GBT survey is much lower; 48% of all galaxies in the sample have upper limits on L_{OH} higher than the brightest detection, extending to more than 1 dex in difference. Assuming small-number statistics apply, the L_{OH} OHM fraction is also inconsistent for the samples in the range $2.0 < \log\ L_{OH}\ [L_{\odot}] < 4.0$.

We ran a survival analysis (Lavalley et al., 1992) on the distribution of $\log L_{OH}$ for data in the GBT and Arecibo samples. Survival analysis is useful for flux-limited surveys since it can properly account for upper limits on non-detections in the data. None of the tests used (which include the

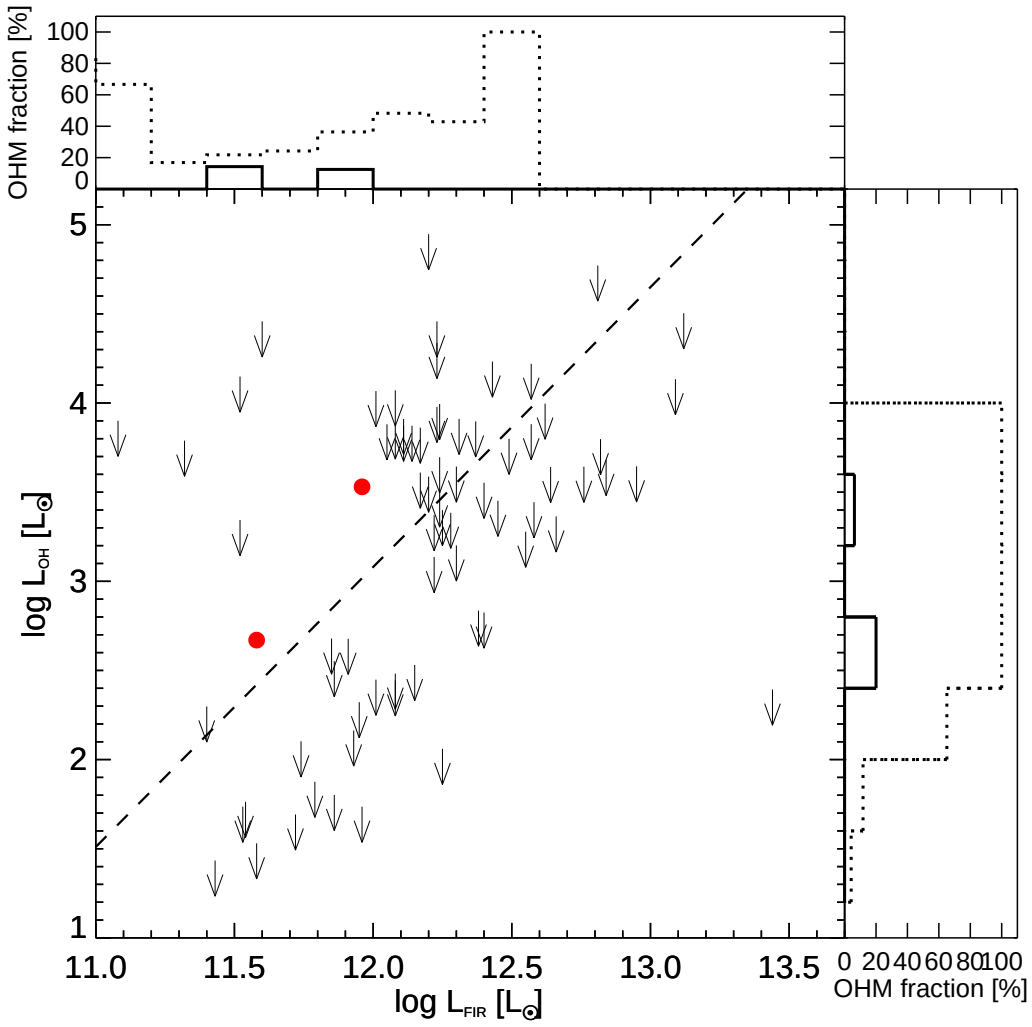

Figure 4.8 $L_{FIR} - L_{OH}$ plot for the GBT OHM survey, with detected OHMs shown as red circles and upper limits shown with arrows. The dashed line is the $L_{FIR} - L_{OH}$ relation from Darling & Giovanelli (2002a). The histogram on the top shows the OHM fraction as a function of L_{FIR}, while the histogram on the right shows the OHM fraction as a function of the combined L_{OH}+L_{OH}^{max} for each luminosity bin. In both histograms, the solid line shows the OHM fraction for the GBT survey, while the dotted line is the OHM fraction for the Arecibo sample of OHMs (Darling & Giovanelli, 2000, 2001, 2002a).

Gehan's, Peto & Peto, and Peto & Prentice generalized Wilcoxon tests as well as a logrank test) show a statistically significant difference in the distribution of log L_{OH} and log L_{OH}^{max} for the two surveys. The Kaplan-Meier estimate of the mean is log $(L_{OH}/L_{\odot}) = 1.608 \pm 0.036$ for the Arecibo survey and log $(L_{OH}^{max}/L_{\odot}) = 1.547 \pm 0.080$ for the GBT survey. We do not interpret this as evidence that the samples are consistent; rather, that the ability of survival analysis to distinguish between distributions is limited due to the fact that nearly all of the GBT measurements are not-particularly-stringent upper limits.

An obvious culprit for the lower OHM fraction in the GBT survey is the effect of RFI and increased noise on the survey results. As discussed in §4.3.2, the sensitivity of the low-frequency GBT receivers was a factor of $\sim 2-10$ worse than expected, especially at lower frequencies. The original goal of the survey was to achieve an rms of 0.8 mJy in 20 km s^{-1} channels at 800 MHz, which would have corresponded to an upper limit of $L_{OH}^{max} = 10^{3.8}$ $L_{\odot}$ at $z = 1$. Our actual sensitivity in this redshift range was from $1-5$ mJy, which translate to upper limits of $L_{OH} = 10^{4-5}$ $L_{\odot}$. Since this rules out detection of only the very brightest OH gigamasers, the observed OHM fraction is much lower than in the Arecibo survey.

It must also be mentioned that the presence of RFI may be suppressing the observed OHM fraction as a result of individual features in the spectrum. While each spectrum undergoes intense flagging to remove RFI wherever possible, strong features are still visible in much of the data. Depending on the spectral width of the feature, the presence of RFI may be masking the weaker emission from OHMs in some percentage of our galaxies; in a galaxy such as SMM J131225.73+423941.4, for example (Figure C.72), RFI effectively wipes out roughly half of the possible redshift range for an OHM detection. Finally, there are several spectra with features resembling broad emission, but which for a variety of reasons we have classified as contamination by RFI (e.g., FF 1412+3014; Figure C.42). It is possible that a handful of OHMs could have been misidentified in the survey as RFI and classified as non-detections.

Even considering the increased noise and RFI contamination, however, it is surprising that half of the galaxies in our sample have upper limits that fall below the expected $L_{IR} - L_{OH}^{pred}$ relation

(Figure 4.8). We suggest two possible causes: either the properties of the galaxies in our sample are fundamentally different from those in the Arecibo sample (in a way that affects maser production), or OHM galaxies are genuinely rarer at $z \sim 1$ than in the present day.

In selecting galaxies for the GBT survey, we attempted to choose galaxies that were more likely to be OHM hosts, based on their high L_{IR} and starburst nature. This is in contrast to the Arecibo survey, for which the sample was flux-limited at $\lambda = 60$ μm. If the most infrared-luminous galaxies with stringent OH limits are not starburst-dominated mergers and are instead AGN dominated, this would strongly select against OHM hosts. This explanation was proposed for the non-detection of OHMs in high-redshift observations of HyLIRGs using the GMRT (J. Darling, priv. comm). Kartaltepe et al. (2010) find that the AGN fraction increases strongly with L_{IR} out to $z \sim 3.5$, and that the AGN fraction could be as high as 70% for galaxies with $L_{IR} > 10^{13}$ $L_{\odot}$. For the sub-mm galaxies for no which information on the power source is available, a large number will also be expected to host an AGN.

The physics of emission in potential OHM hosts may also play an important role. Willett et al. (2011b) find that OHM galaxies have a typical dust temperature of between $(40 - 80)$ K, which supports the models of Lockett & Elitzur (2008) that a minimum $T_{dust} = 35$ K is required for population inversion. This is analogous to the warm far-IR color correlation observed by Henkel et al. (e.g., 1986); Baan et al. (e.g., 1992a); Darling & Giovanelli (e.g., 2002a). For ULIRGs at a variety of redshifts, Yang et al. (2007) find an approximate relationship such that:

$$L_{FIR} \propto \kappa_0 M_{dust} T_{dust}^{4+\beta}, \tag{4.5}$$

where κ_0 is the dust mass absorption coefficient, M_{dust} the dust mass, and $\beta = 1.5$ the dust emissivity index for the galaxy (Figure 4.9). Importantly for OHMs, the mean T_{dust} found for ULIRGs near $z \sim 1$ is roughly 40 K, close to the theoretical masing limit. If so, this implies that color selection (a function of T_{dust}) is more important at high redshifts than in the local Universe, and that a large fraction of the galaxies in our sample may simply be too cool to support masing

action.

We note that the two OHM detections in our sample (FF 0758+2851 and FF 2216+0058) have dust temperatures derived from their 60, 100, and 350 μm fluxes of 40.0 and 46.8 K, respectively (Yang et al., 2007). Both values are within 1σ of the mean T_{dust} (42.8 ± 7.1 K) for the FF sample. Among the remaining GBT galaxies, the three LH candidates have millimeter flux ratios that suggest either low redshifts or hotter dust (Ivison et al., 2005), while the COSMOS galaxies do not have sufficient photometric accuracy to fit robust T_{dust} (Kartaltepe et al., 2010). The sub-mm galaxies from Chapman et al. (2005) have a cooler average dust temperature of $T_{dust} = 36 \pm 7$ K; there is no published information on the dust temperature for the DEEP2 galaxies.

4.5.2 OHM luminosity function

One of the goals of performing a search for OHMs at higher redshifts was to improve the measurements on the OH megamaser luminosity function (LF). Darling & Giovanelli (2002b) used the results of the flux-limited Arecibo survey to construct a well-sampled LF between $10^{2.2}\ L_{\odot} < L_{OH} < 10^{3.8} L_{\odot}$, which followed a power law in integrated line luminosity of $\Phi \propto L_{OH}^{-0.64}$ Mpc^{-3} dex^{-1}. This measurement is limited to a relatively narrow redshift range, however, spanning $0.1 < z < 0.23$. In order to use OHMs as tracers for merging galaxies, however, it must be determined whether the LF evolves as a function of redshift. Mid- and far-infrared photometry suggests that the redshift evolution of LIRGs and ULIRGs is consistent with pure luminosity evolution out to $z < 1.3$ (Magnelli et al., 2009). If the OHM fraction in merging galaxies is the same at $z \sim 1$, this implies that the co-moving number density of OHMs should be higher, but that the shape of the LF will be constant. A flux-limited survey of OHMs at high redshift would provide an independent method for verifying this evolution.

An OH luminosity function for the GBT detections was constructed following the technique of Darling & Giovanelli (2002b), which uses the $1/V_a$ method and combines limits on both the spectral line and continuum emission from the galaxy. The total number of targets included the two galaxies discovered in our survey plus seven detections of OHMs made in the early commissioning phase of

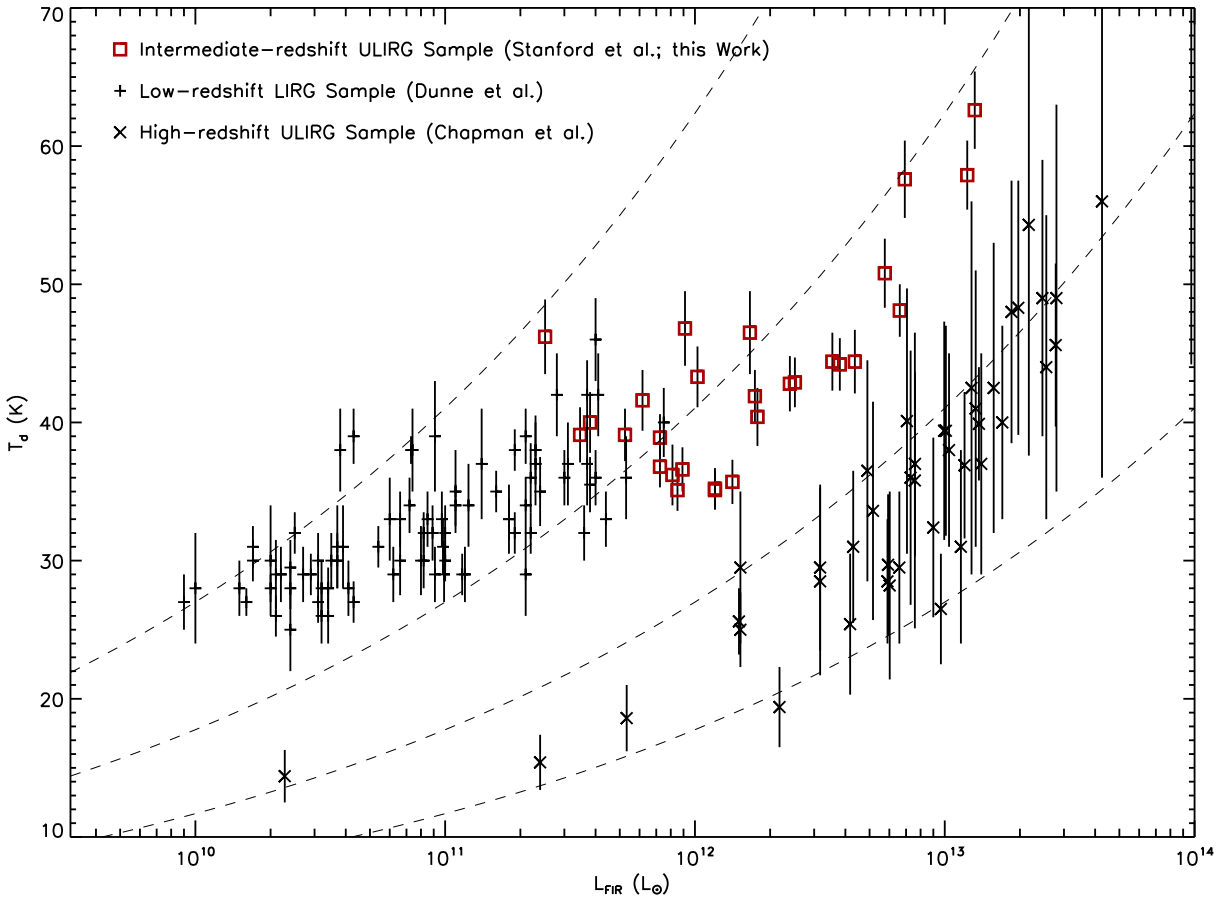

Figure 4.9 $L_{FIR} - T_{dust}$ plot for samples of ULIRGs at distinct redshifts, from Yang et al. (2007). "Low-redshift" ULIRGs have $z < 0.07$, while "intermediate-redshift" ULIRGs are from $0.089 < z < 0.926$ and "high-redshift" ULIRGs for $0.93 < z < 3.5$. Dashed lines are from Equation 4.5 for dust masses ranging from $10^7 - 10^{10}$ $M_\odot$ (*top to bottom*).

the GBT (Kent et al., 2002). Candidate galaxies for these observations were drawn from the PSCz sample for ULIRGs lying outside the declination range of Arecibo, and cover a redshift range from $0.1 < z < 0.45$; their effective area covered is $\Omega = 0.42$ sr. Their OHM detection rate was $\sim 15\%$ (7/47); we note that the average rms of their non-detections are at least a factor of several higher than those in our survey.

Figure 4.10 displays the OH luminosity function for both the Arecibo and GBT samples; the bin size for both is set at $\Delta \log (L_{OH}/L_{\odot}) = 0.5$, following Scott's choice for optimal histogram binning. We fit a power-law to all bins with more than one detection for each survey. The fit for the Arecibo OHMs yields:

$$\log \Phi = (-0.71 \pm 0.16) \log L_{OH} - (4.87 \pm 0.47). \tag{4.6}$$

and for the GBT OHMs:

$$\log \Phi = (-0.22 \pm 0.27) \log L_{OH} - (6.88 \pm 0.90), \tag{4.7}$$

where Φ is measured in Mpc^{-3} dex^{-1} and L_{OH} in $L_{\odot}$.

Equation 4.6 is consistent with the analysis of Darling & Giovanelli (2002b), who found $\log \Phi = (-0.64 \pm 0.21) \log L_{OH} - (5.0 \pm 0.6)$ using a slightly different bin size, sampling criterion, and fitting routine. The fits for the Arecibo and GBT samples are not consistent with each other; a probable cause for this is the significant undersampling of the GBT LF. This is emphasized by the results of the $\langle V/V_a \rangle$ test; for a uniformly distributed sample, this value will be 0.5. The luminosity bins for the GBT OHMs have a mean value of $\langle V/V_a \rangle = 0.2$, indicating that the distribution of detected OHMs is clustered toward lower-redshift objects. Undersampling is also supported by the noise limits on non-detections in the Kent et al. (2002) sample, many of which are significantly higher than the peak flux densities of OHM detections; this implies that several OHMs are likely to be hidden in the noise. We note that an additional detection of a single OHM at the median L_{OH} and z of the sample would produce an LF consistent with Equation 4.6.

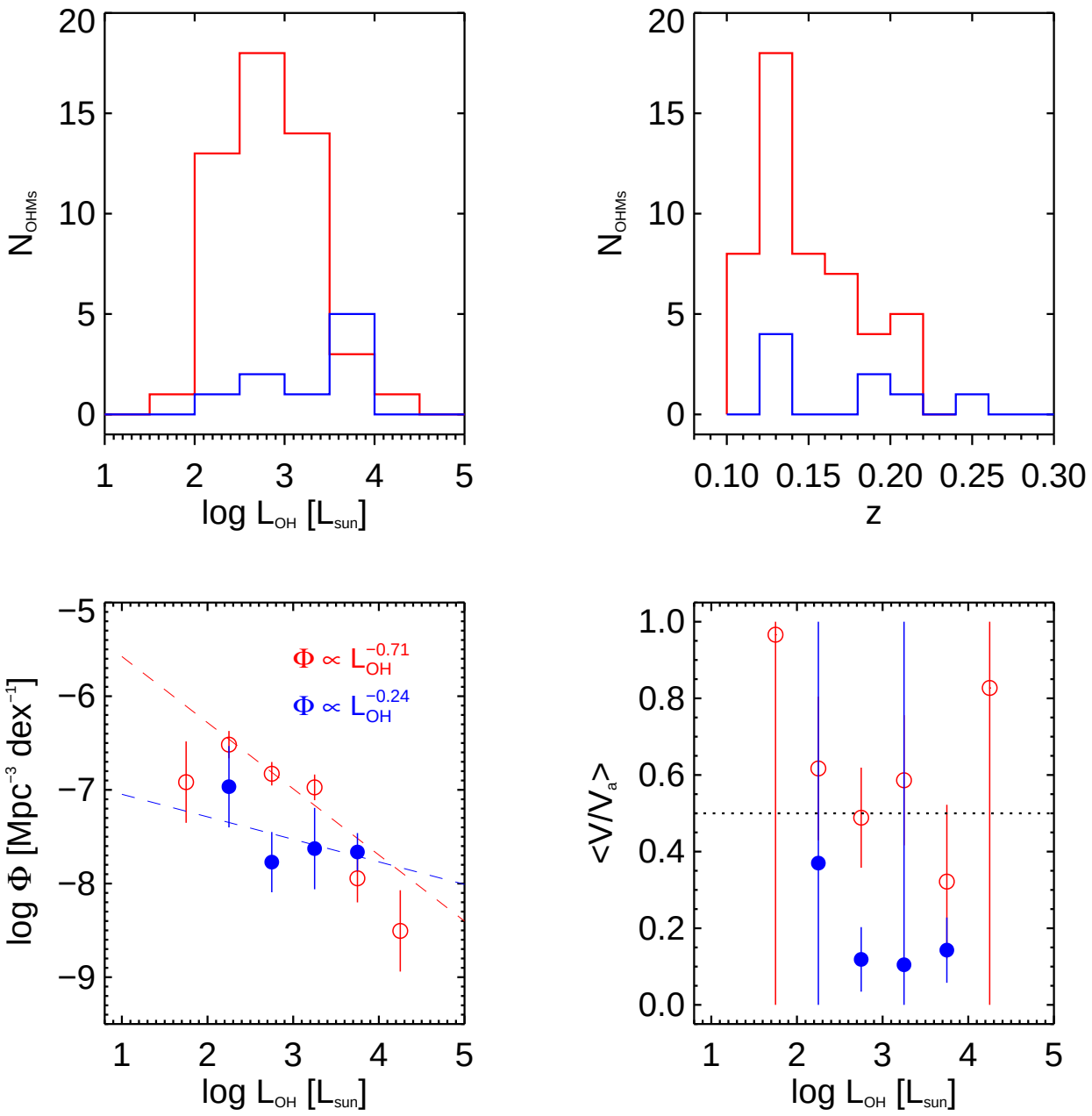

Figure 4.10 OH megamaser luminosity function for the Arecibo survey (*red*; Darling & Giovanelli, 2002b) and the combined GBT detections from Kent et al. (2002) and this chapter (*blue*). Top left: distribution of OHM detections as a function of L_{OH}. Top right: Distribution of OHM detections as a function of redshift. Bottom left: the OH megamaser LF with power-law fits to the well-sampled luminosity bins. Bottom right: Average ratio of V/V_a for the well-sampled luminosity bins. The dashed line shows the expected value for a uniformly distributed sample ($\langle V/V_a \rangle = 0.5$).

Table 4.4. OHM luminosity function

$\log L_{OH}$ $[L_\odot]$	N_{OHM}	Φ [Mpc^{-3} dex^{-1}]	$\langle V/V_a \rangle$	OHM frac.
$1.5 - 2.0$	1	$(1.2 \pm 0.9) \times 10^{-7}$	$0.97 \pm \ldots$	0.03
$2.0 - 2.5$	14	$(4.0 \pm 1.0) \times 10^{-7}$	0.60 ± 0.18	0.16
$2.5 - 3.0$	21	$(2.5 \pm 0.7) \times 10^{-7}$	0.45 ± 0.12	0.80
$3.0 - 3.5$	15	$(1.3 \pm 0.3) \times 10^{-7}$	0.56 ± 0.16	0.75
$3.5 - 4.0$	8	$(3.4 \pm 0.9) \times 10^{-8}$	0.21 ± 0.09	0.41
$4.0 - 4.5$	1	$(3.1 \pm 2.2) \times 10^{-9}$	$0.83 \pm \ldots$	0.43

Note. — Results are for the LF from the combined Arecibo and GBT samples in Figure 4.11.

There are several caveats that should be emphasized when considering the GBT LF as a predictor of OH luminosity on its own. First, the candidate galaxies were not drawn from a purely flux-limited survey, as were the Arecibo OHMs; this is primarily a result of the low fraction of galaxies with spectroscopic redshifts at $z > 0.1$. The low number of detections also limits the robustness of any fit to Φ. No K-corrections have been applied to the f_{60} data for the GBT OHMs, which adds uncertainty to the continuum V_a. Finally, the RFI conditions at Green Bank will effectively rule out thin shells of volume in which OHMs cannot be detected; these effects have not been taken into account here.

A more useful result looks at whether the OHM LF from Darling & Giovanelli (2002b) changes with the addition of the newly discovered GBT megamasers. We find that this has very little effect on the overall fit; adding the nine GBT OHMs yields:

$$\log \Phi = (-0.66 \pm 0.14) \log L_{OH} - (4.91 \pm 0.41). \tag{4.8}$$

which only changes the offset by -0.04 and the slope by $+0.05$. Both values are well within the uncertainties of the combined LF, as well as that of the original Arecibo LF. Figure 4.11 shows the results of the new OHM LF for the combined samples; values for Φ, V/V_a, and the OHM fraction are tabulated in Table 4.4.

We compare the OHM LF in Table 4.4 to that of ULIRGs in the local Universe. Assuming

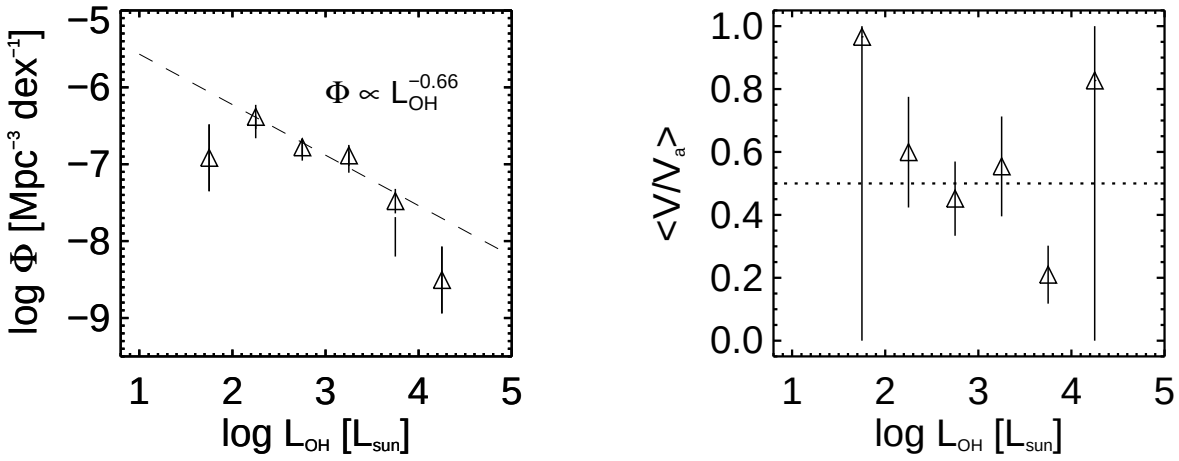

Figure 4.11 OH megamaser luminosity function for the combined Arecibo and GBT detections. Left: the OH megamaser LF with power-law fits to the well-sampled luminosity bins. Right: Average ratio of V/V_a for the well-sampled luminosity bins. The dashed line shows the expected value for a uniformly distributed sample.

the Malmquist-corrected relationship of $L_{OH} \propto L_{IR}^{1.2}$ from Darling & Giovanelli (2002a), this gives $\Phi[L_{IR}] \propto L_{IR}^{-0.83\pm0.18}$. The total luminosity function of galaxies in the local Universe was measured by Goto et al. (2011) using data from the AKARI satellite. They found that galaxies with $L_{IR} > 10^{11}\ L_{\odot}$ have a slope of (-2.6 ± 0.1), significantly steeper than the relationship found for OHMs. However, this assumes that the OHM fraction is constant; the results of the Arecibo survey show that the OHM fraction increases above $10^{11}\ L_{\odot}$ up to at least $10^{12.5}\ L_{\odot}$ (Figure 4.8). By folding in the measured OHM fractions from extant surveys, a better comparison of the true luminosity function of OHMs can be made.

Figure 4.12 shows the OHM LF from Equation 4.8 translated into an IR luminosity function and compared to the results for the larger sample of AKARI galaxies. Folding in the observed OHM fraction as a function of luminosity steepens the slope of the OHM LF, since OHMs are rarer in LIRGs compared to ULIRGs. We use two empirically-derived OHM fractions: one from the Arecibo survey and one from the combined Arecibo and GBT samples. For the GBT data, we use only the non-detections for which $L_{OH}^{max} < L_{OH}^{pred}$ in computing the OHM fraction. The revised slope between $10^{11}\ L_{\odot} < L_{IR} < 10^{12.5}\ L_{\odot}$ is (-1.3 ± 0.3) for the Arecibo OHM fraction and (-0.6 ± 0.2) for the total OHM fraction, neither of which are consistent with the slope from Goto et al. (2011). The OHM and AKARI luminosity functions overlap near $L_{IR} = 10^{12}\ L_{\odot}$, which coincides with the best-sampled portion of the OHM LF.

There are several possible causes for the observed difference in the OHM and overall luminosity functions. The conversion from an LF measured in L_{IR} from L_{OH} is an empirical fit to available data, and implies either that OHMs are highly saturated or that the OHM strength is only weakly correlated with global properties such as L_{IR} (Darling & Giovanelli, 2002a). Previous OHM LFs (Baan, 1991; Briggs, 1998) assumed a quadratic OH-IR relation (unsaturated masing); a decrease in saturation could potentially steepen the OHM LF up to a slope of -1.5. Finally, we note that the infrared LF does show signs of flattening at $L_{IR} > 10^{12}\ L_{\odot}$ (Kim & Sanders, 1998); we note that both the slope and OHM density are consistent for the OH and total LFs if only the two highest luminosity bins of Goto et al. (2011) are considered. For the LIRGs near $10^{11}\ L_{\odot}$, Figure 4.12

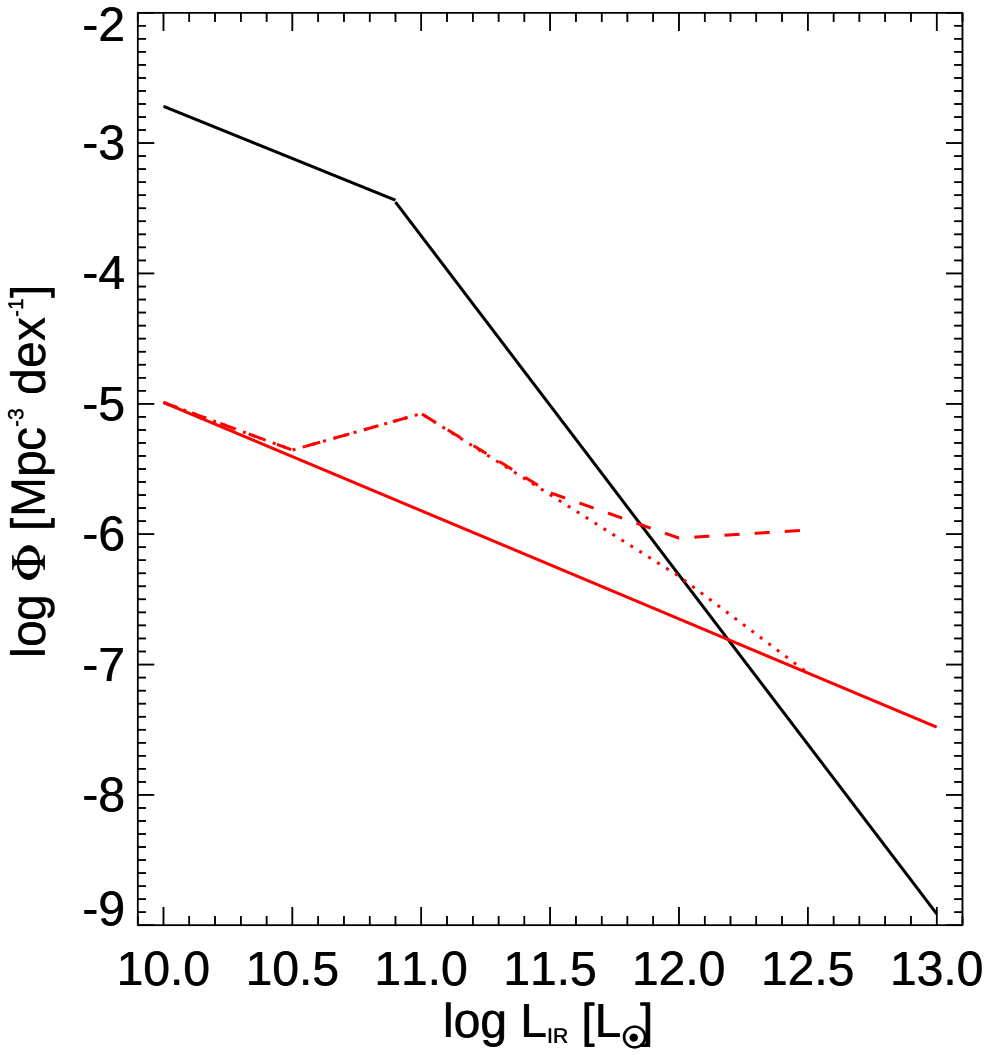

Figure 4.12 Comparison of luminosity functions (LF) in the local Universe. The black line shows the LF for a complete, 60 μm flux-limited sample of local galaxies from the AKARI satellite (Goto et al., 2011). The solid red line shows the OHM LF derived from our data, assuming $L_{OH} \propto L_{IR}^{1.2}$ (Darling & Giovanelli, 2002a). Other red lines show the effect on the OHM LF of the increasing OHM fraction as a function of L_{IR}; the dotted and dashed lines use binned OHM fractions from the Arecibo and the combined (Arecibo + GBT) samples, respectively.

suggests that the OHM fraction is still underestimated for galaxies in this redshift range.

Finally, we consider the OH LF as a function of redshift. Contrary to expectations when we began the GBT OHM survey, we found no new OHMs above the previous redshift recordholder of $z = 0.265$. This can be compared to the number of non-detections in the survey; we discuss results from the COSMOS field, since it is both flux-limited and provides well-defined volume and redshift constraints. For an OHM of 10^3 $L_\odot$, Equation 4.8 predicts $\sim 10^{-7}$ OHMs per Mpc^3 per dex. In the COSMOS field, the total co-moving volume searched for ULIRGs at $L_{IR} \simeq 10^{12}$ $L_\odot$ was 1.3×10^7 Mpc^3, which would predict only ~ 1 OHM per luminosity dex. No evolution of the LF is thus required to explain the non-detection of OHMs at the current sensitivity.

4.5.3 Comparison of OHM luminosity function to merger rate scenarios

One of the ultimate goals of high-redshift OHM surveys is to use them as tracers of the populations of merging galaxies as a function of redshift. As a result, the sky density of OHMs can serve as an independent constraint for the number density of galaxies in a specific epoch. Models of the merger rate as a function of redshift are typically parameterized with an evolutionary factor of $(1 + z)^m$. The value of m, however, is not well-constrained - observations have estimated an exponent as high as $m = 7.6 \pm 3.2$ (Kim & Sanders, 1998), while lower values of m are favored by more recent studies from both observations of interacting galaxies ($m = 2.25 \pm 0.24$; Bridge et al., 2010) and cosmological simulations ($m \simeq 2.5$; Fakhouri et al., 2010).

Sufficiently deep surveys of OHMs can provide an independent constraint on the parametrization of the merging rate. We calculate the predicted sky density of OHMs as a function of redshift, following Darling & Giovanelli (2002b):

$$\frac{dN}{d\Omega d\nu}[z] = \frac{cD_L^2}{H_0\nu_0\sqrt{(1+z)^3\Omega_M + \Omega_\Lambda}} \left(\frac{b}{a\ \ln 10}\right) \left((L_{OH,max})^a - (L_{OH,min})^a\right), \tag{4.9}$$

where a and b are parameters of the OHM LF from Equation 4.8 ($\Phi[L_{OH}] = bL_{OH}^a$), $L_{OH,min}$ is the minimum OH luminosity that could be observed at a given sensitivity level, and $L_{OH,max}$ is the upper physical limit on OHM luminosity (assumed to be $10^{4.4}$ $L_\odot$, twice that of the brightest-known

OHM).

Figure 4.13 shows the sky density of OHMs scaled to the areal size and frequency coverage of our observations in the COSMOS field, for which we observed all suitable ULIRGs within 2 square degrees over the redshift range $0.97 < z < 1.01$. From our result of no detections for ULIRGs at $z \sim 1$, an upper limit on the sky density of OHMs can still constrain the evolution of the merger rate. Assuming that no more than 1–2 OHMs were missed due to RFI or other losses, our single data point suggests that $m \lesssim 6$. While this is still within uncertainties for even high values of m, the COSMOS limit is an important first step in using OHMs as an independent tracer, and we are encouraged by its agreement with recent results. Further measurements of deep fields at a variety of redshifts (ideally at $z > 0.5$, where different exponents can be more clearly distinguished), will be crucial for more precise development of this technique.

4.6 Conclusions and future work

The results of the GBT survey suggest several avenues for future work. First, the increased integration times and significant losses from RFI in the survey highlight the difficulties of low-frequency, single-dish, ground-based radio observations. Even at a telescope with the sensitivity and relative isolation of the GBT, the time required to observe galaxies at $z \sim 1$ is at least 2–4 hours, and often higher. A relatively simple solution in the future will be to carry out high-redshift OH surveys using interferometers. Interferometers enjoy a distinct advantage over single-dish observations since terrestrial RFI will be uncorrelated for data in each dish, and thus will cancel out when the signal is processed in the correlator. The updated EVLA in New Mexico will be a good candidate for OHMs at low- and intermediate redshifts; limits will arise from the EVLA's frequency coverage, which currently only extends down to 1 GHz ($z_{OH} \sim 0.7$). Other possibilities include the GMRT in India and the under-construction ASKAP telescope in Western Australia. The latter will particularly benefit from being in one of the most radio-quiet locations remaining on Earth as well as its frequency coverage down to $\nu = 700$ MHz.

OHMs at higher redshifts are also likely to be discovered as better candidate galaxies are

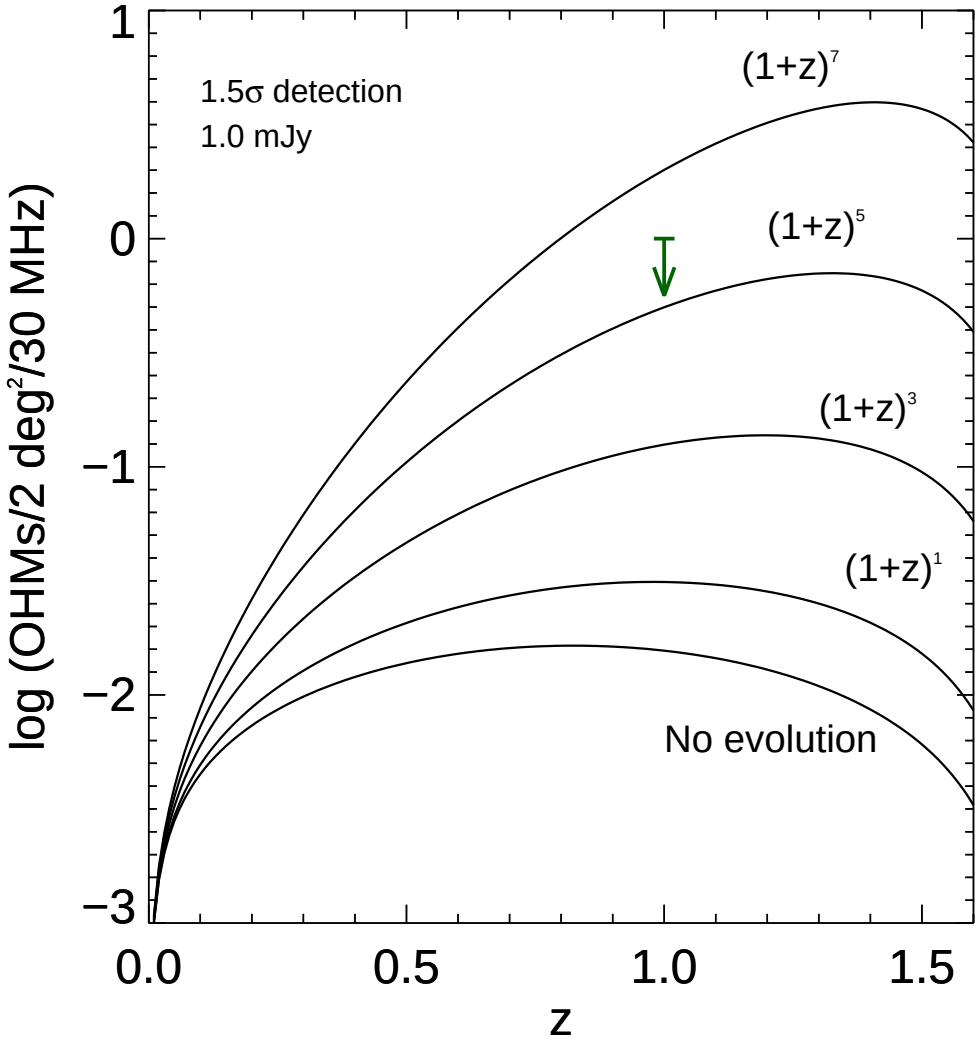

Figure 4.13 Predicted sky density of OHMs as a function of redshift. The angle and frequency coverage of $dN/(d\Omega d\nu)$ match the GBT observations of the COSMOS field at $z \sim 1$. Solid lines show the expected sky density for different merger scenarios, parametrized by various values of m for $dN/(d\Omega d\nu) \propto (1+z)^m$. The green arrow shows the upper limit for a single OHM detection in COSMOS at $z \sim 1$.

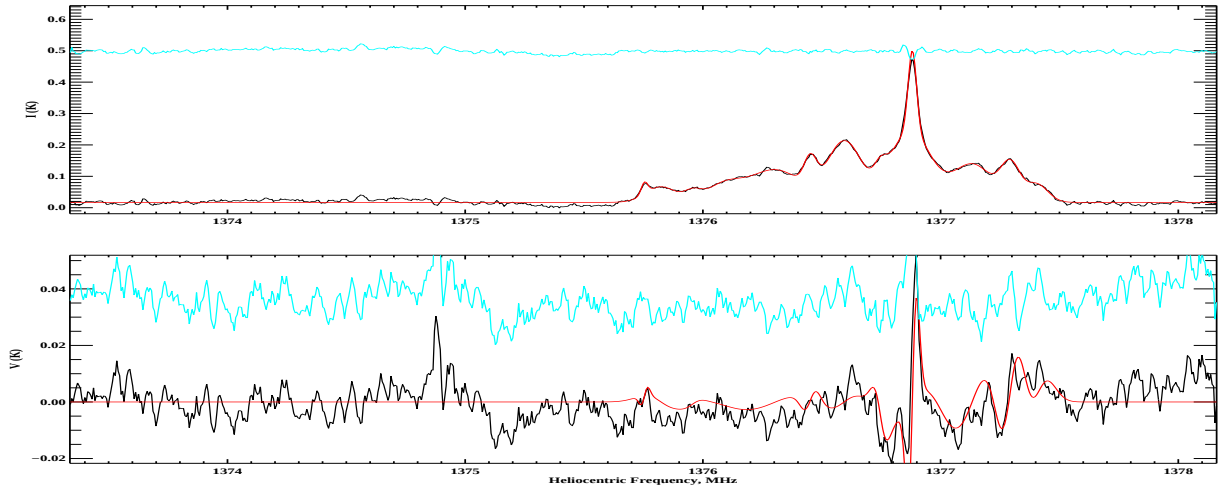

Figure 4.14 Arecibo 18-cm observations of the OHM FF 2216+0058. The top panel shows the total intensity of the unpolarized emission (Stokes I), while the bottom shows the circular polarization of the OH emission (Stokes V). The $\mathcal{S}$-curve in the polarization data is the signature of Zeeman splitting, measured at $B_{||} \sim -10$ mG for the brightest component. Data courtesy J. McBride.

identified. Almost every OHM found in the last 20 years has a host galaxy detected in the IRAS survey. Two new surveys will offer much larger and deeper samples of LIRGs and ULIRGs that will be potential OHM candidates: AKARI, with coverage in six bands from 9–160 μm, and WISE, which has coverage from 3.4 to 22 μm. The two surveys also have $3-10$ and $\sim$ 500 times the sensitivity of IRAS, respectively. Both catalogs will require additional observations to secure spectroscopic redshifts for new targets; however, photometry will identify candidate (U)LIRGs based on their L_{IR}, and optical redshifts can be relatively quickly obtained with only a medium-aperture telescope (such as the 3.5m ARC at Apache Point Observatory). For OHMs at $z = 1$ and beyond, deep field surveys with sub-mm observations are of particular use. The advantage of deep field observations are the completeness of flux-limited surveys to high volumes, as well as ancillary multi-wavelength data which can be used to eliminate unlikely candidates such as IR-bright AGN. Data sets such as the Hubble and Chandra Deep Fields, GOODS, and COSMOS all have large sub-mm catalogs that can be further mined. We will also benefit from improvements in SED models that will better constrain parameters such as L_{IR}, T_{dust}, and photometric redshifts, all of which are crucial for pre-selecting OHM candidates.

Discoveries of new OHMs are also enabling new science through studies of individual objects. A particularly useful property of OH lines are their susceptibility to Zeeman splitting, which measures the *in situ* magnetic field at the source of emission. This provides one of a very few (if not only) methods for directly studying magnetic fields at cosmic distances, which has immense importance for the structure and dynamics of the ISM (Robishaw, 2008). Studies of Zeeman splitting in OHMs have measured magnetic fields with strengths up to 18 mG in their host galaxies (Robishaw et al., 2008). The OHM FF 2216+0058, which was discovered in our GBT survey, was recently observed at the Arecibo Observatory in Stokes I and V. Measurements of Zeeman splitting indicate the presence of a magnetic field of $B_{||} \sim -10$ mG in the OHM host galaxy (Figure 4.14; J. McBride, priv. comm). Surveys for OHMs at high redshift should be able to provide many more measurements of the B-field strength in galaxies than are currently known, and may be able to constrain the evolution of magnetic fields in galaxies as a function of cosmic time.

Finally, the discovery of even a single OHM at $z > 1$ could be used to test possible variations in fundamental constants of physics. Several current models of particle physics predict that "constants" such as α, the fine-structure constant, or $\mu = m_p/m_e$, the proton-to-electron mass ratio, vary with both space and time (e.g., Marciano, 1984). Since different spectral transitions have different dependences on various fundamental constants, measurements of one or more transitions at high-redshift provide constraints on the variation of α, μ, etc. over periods of several Gyr (Uzan, 2003; Kanekar, 2009). OH lines are useful laboratories for measuring changes in α, especially since conjugate absorption/emission in the OH satellite transitions can test whether spectral transitions are generated in the same physical location, thus removing a serious systematic uncertainty from the data (Darling, 2003). Detection of OH in a single galaxy at $z = 0.247$ has resulted in a tentative determination of $\Delta\alpha/\alpha = (3.1 \pm 1.2) \times 10^{-6}$ (Darling, 2004; Kanekar et al., 2010), but a lack of known OH sources at $z > 1$ limits the timescale over which changes can be determined. Thus, detection of even a single OHM at high redshift would be a noteworthy discovery, meriting deep follow-up in all of the 18- and 6-cm OH transitions to measure the precise evolution of fundamental constants.

Chapter 5

An OH survey of the Andromeda galaxy (M31)

The Local Group (LG) of galaxies are a gravitationally bound collection of galaxies containing our own Milky Way. Spanning a distance of a few megaparsecs, its two most massive galaxies by far are the Milky Way and Andromeda (M31) galaxies; their gravitational fields and relative motions dominate the movements of smaller satellite galaxies.

As the nearest group of galaxies, the Local Group offers a laboratory to test many critical facts about galactic dynamics and evolution. By measuring the motions of the constituent galaxies with respect to each other, the dynamical history of the Local Group can be traced, exploring conditions under which structure formation and virialization took place in the early Universe. These motions can also be used to examine galaxies that would have interacted and possibly merged in the past. Since galaxy masses are dominated by their non-luminous dark matter haloes, their relative motions also constrain the total dark matter content of the group; these can test the fundamental assumption that the galaxy luminosities trace the mass distribution of these haloes. Finally, the ultimate fate of our local environment can be predicted by extrapolating the relative positions of Local Group galaxies into the future. All these questions, however, rest on accurate measurements of the current three-dimensional velocities of the Local Group galaxies with respect to each other, especially of the Milky Way and M31.

It has been known for many years from radial velocity measurements that M31 and the Milky Way are approaching each other at a velocity of 119 km s^{-1}. As a result, the galaxies are expected to collide sometime within the next 5 Gyr. This will likely trigger a large new burst of star

formation and severely disrupt the current spiral structure of both galaxies, eventually forming a massive elliptical galaxy. However, this timescale has a fundamental uncertainty due to the fact that the proper (transverse, or tangential) motion of M31 with respect to the Milky Way is unknown. Measurements of the transverse velocity of M31 have been attempted for many decades; however, no firm detection has yet been accomplished due to the high precision of astrometry required. As a result, the lack of a proper motion measurement severely limits our current ability to explore the Local Group's dynamical history.

In this chapter, I report on the results of a radio-frequency survey to discover OH masers in M31. Masers are an ideal tool for measuring proper motions on the sky, due to their intrinsic beaming, high luminosities, frequency stabilities, and small spatial scales. Many OH masers exist in the Milky Way, and measurements of water masers in other Local Group satellite galaxies have successfully been used to measure their transverse motions. The discovery of a maser in M31 would permit the first accurate measurement of its transverse motion with respect to the Milky Way. I present results of the first complete OH survey of M31, which established an upper limit on OH maser emission of 10 mJy. I also describe recent discoveries of new sources in M31 which may constrain its transverse motion, and discuss plans for future OH observations in M31 and the Local Group.

5.1 Background

5.1.1 M31 and the Local Group

The Local Group contains at least 80 identified galaxies (Bullock et al., 2009; Johnston et al., 2009; Willman, 2010), although cosmological simulations predict that the total number of satellite galaxies may be as high as several hundred. M31 and the Milky Way account for more than 90% of the total luminosity and mass of the Local Group, and the majority of other galaxies in the group belong to either the M31 or Milky Way subgroup. M31 is orbited by at least several dozen satellite galaxies; its most massive companion is the spiral galaxy M33, located at a distance of

203 kpc from M31 (Figure 5.1); other galaxies orbiting M31 include IC 10, M32, and NGC 205. The existence of an HI stream between M31 and M33 is an indicator of a possible past interaction between the galaxies (Braun & Thilker, 2004; Bekki, 2008). The majority of the satellite galaxies of M31 are dwarf spheroidals, with virtually no gas or recent star formation (Richardson et al., 2011).

M31 and the Milky Way are in many ways comparable galaxies. Their masses are similar to within a factor of ~ 2, although evidence has been presented favoring both M31 and the Milky Way as the more massive galaxy (see Reid et al., 2009b; Watkins et al., 2010). Both galaxies have spiral structure and comparable luminosities of stellar haloes (Ibata et al., 2007). The majority of the ongoing star formation in M31 is concentrated in the galactic plane in the nuclear region ($R < 0.7$ kpc) and between radii of 9 and 17 kpc, as traced by Hα, molecular gas, warm dust, and ultraviolet emission (Kang et al., 2009; Tabatabaei & Berkhuijsen, 2010). The area of brightest emission is referred to as the "10-kpc ring". The HI, CO, and 20-cm emission in M31 also all have peaks at a radius of 10 kpc, thus identifying the ring as a likely site for maser detection. The total star formation rate in the 10-kpc ring of M31 is $\simeq 0.3\ M_{\odot}\ \mathrm{yr}^{-1}$, a factor of 2–12 lower than that of the Milky Way ($0.6 - 4.0\ M_{\odot}\ \mathrm{yr}^{-1}$; Diehl et al., 2006; Robitaille & Whitney, 2010). Given the association of OH masers with molecular clouds and star forming regions, the OH maser rate in M31 should scale with the star formation rate if the physical conditions in star forming regions are similar in the two galaxies.

5.1.2 Direct measurements of the proper motion of M31

Loeb et al. (2005) have used numerical simulations to show that M33 would have passed near the current location of M31 at some point in the last 10 Gyr. Since M33's stellar disk shows no morphological signatures that would result from such an interaction (although it does show some signs of triggered star formation and extended HI), this indicates that a non-zero component is likely for M31's transverse velocity (v_t).

Previous efforts to measure M31's proper motion began with optical studies. Early publica-

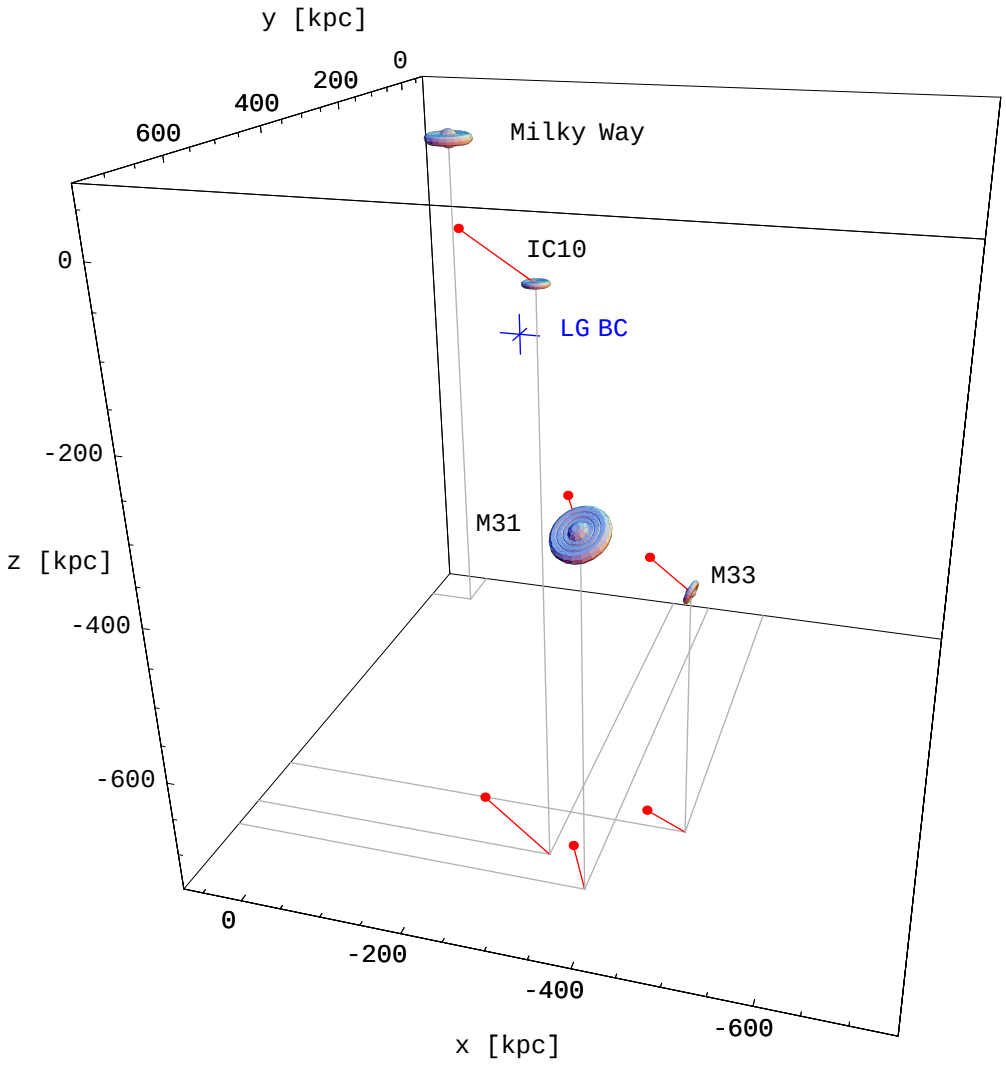

Figure 5.1 Schematic of the relative positions and velocities of the major galaxies in the Local Group (Brunthaler et al., 2007). Red lines indicate the 3-D velocities of M33 and IC 10 relative to the Milky Way; for M31, only the radial component is shown. The blue cross indicates the location of the Local Group barycenter (van den Bergh, 1999).

tions by Barnard (1917) and van Maanen (1918) measured the position of M31's galactic nucleus with respect to foreground stars in the Milky Way. Neither observation resulted in detection of a measurable parallax, with upper proper motion limits of $\mu \lesssim 0.005''$ yr^{-1}. Predictions of the proper motion of M31 have also been made based on orbital models for the Local Group. Raychaudhury & Lynden-Bell (1989) predicted a proper motion for M31 (in Galactic coordinates) of $\mu_l = 50$ μas yr^{-1}, $\mu_b = -19$ μas yr^{-1}, while Sawa & Fujimoto (2005) predicted $\mu_l = 38$ μas yr^{-1}, $\mu_b = -49$ μas yr^{-1}. The total magnitude of both predictions is significantly less than could be directly measured at the time. Several proposals for the measurement of M31's proper motion depended on capabilities in future missions, such as the (now-canceled) Space Interferometry Mission or an upgraded VLBA (Reid et al., 2009a).

The primary limiting factor in measuring the proper motion of M31 is the identification of individual sources in the galaxy that are bright, but sufficiently compact to measure angular shifts on the order of tens of microarcseconds (equivalent to $\sim$ 100 km s^{-1} at 785 kpc). Observing these shifts in optical wavelengths is difficult due to both the diffraction limit of telescopes and the pixel sizes of available instrumentation. The pixels in Wide Field Camera 3 (WFC3) camera on the Hubble Space Telescope are $0.04''$ on a side in the UVIS channel; this means that angles of ~ 50 μas require centroiding a position to within accuracies of hundredths or thousandths of a pixel. This is challenging without signal-to-noise ratios (S/N) of at least several hundreds for an optically unresolved source. Alternatively, optical measurements have also been attempted using ground-based radial velocity spectra of the halo stars of M31, in which the effect of a net tangential motion would be detectable as a function of the stars' distance from M31 (Guhathakurta et al., 2007).

Although radio wavelengths have poorer angular resolution than optical for a given telescope diameter ($\sim \lambda/D$), interferometers with very long baselines can achieve microarcsecond-level astrometry in the radio. The limiting factor in M31 is a lack of known radio-bright sources in the galaxy. The nucleus of M31 has a radio continuum source with a peak flux density of 30 μJy, for which astrometry at ~ 10 μas yr^{-1} might be possible with the VLBA if the data recording rate were

upgraded to 32 Gbps (Reid et al., 2009a). A similar increase in sensitivity could also be achieved with an upgrade in collecting area, such as the Square Kilometer Array; such telescopes are likely at least a decade away from completion, however.

5.1.3 Statistical estimates of the proper motion of M31

Other attempts to measure M31's transverse motion have relied on statistical techniques. These methods rely on the assumption that the orbits of satellite galaxies tend to follow motion of their local barycenter through space. This can be used both for the satellites of M31 and for the ensemble of all galaxies in the Local Group, since the location of the LG barycenter changes based on the relative positions of M31 and the Milky Way (and thus their relative velocity vectors; Lynden-Bell & Lin, 1977; Yahil et al., 1977). Einasto & Lynden-Bell (1982) measured a transverse velocity of 60 ± 30 km s^{-1} using this method. Using an expanded sample of 22 Local Group galaxies, van der Marel & Guhathakurta (2008) estimated the transverse velocity using four independent and mutually consistent methods: the average line-of-sight velocity of M31 satellite galaxies, the 3-D velocities of M33 and IC 10, and the line-of-sight velocities of galaxies near the turnaround radius of the Local Group. The weighted average of these four methods estimated the west and north components of the transverse velocity at $v_W = -78 \pm 41$ km s^{-1} and $v_N = -38 \pm 34$ km s^{-1}.

Constraints on the proper motion of M31 can also be made based on the morphology of its satellite galaxy. M33, which orbits M31 at a distance of ~ 200 kpc, is a spiral galaxy with no large-scale tidal distortion or stripping of its halo stars. Based on current relative positions and motions of galaxies in the Local Group, Loeb et al. (2005) calculated the possible past orbits for M31 based on the constraint that M33's stellar disk has not been tidally stripped by either M31 or the Milky Way. Their simulations favored a proper motion amplitude of $v_t = 100 \pm 20$ km s^{-1} for M31, primarily ruling out a significant transverse component in the western direction. This result largely conflicts with the vector calculated by van der Marel & Guhathakurta (2008), but the two estimates are not completely mutually exclusive. Discrepancies between the two models are partially a result of the larger value for the Local Group mass used by van der Marel & Guhathakurta (2008), and

the possible existence of faint tidal tails that would narrow the region of exclusion proposed by Loeb et al. (2005).

The age and mass of the Local Group galaxies can also be used to constrain the transverse motion of M31 in what is known as the "timing argument." In its simplest form, the argument rests on the assumption that M31 and the Milky Way were originally formed much closer together in space - the limiting case of the Big Bang would imply a galactic separation of zero. The fact that the galaxies are currently on an approach vector means that their relative motions decoupled from the Hubble flow at some point (likely at a high redshift) and are thus completing their first orbit. A binary orbit with semimajor axis a and eccentricity e can have its radial separation r and orbital time t parametrized as a cycloid:

$$r = a(1 - e\cos[\eta]), \tag{5.1}$$

$$t = \sqrt{\frac{a^3}{GM}}(\eta - e\sin[\eta]), \tag{5.2}$$

where M is the total mass of the system and η, the eccentric anomaly, is essentially a phase describing the number of passages made since the first perigalacticon. If M31 and the Milky Way are completing their first orbit, then η will be between π and 2π. The conservation of energy and angular momentum then define the radial and tangential velocities in the center-of-mass frame as (van der Marel & Guhathakurta, 2008):

$$v_r = \sqrt{\frac{GM}{a}}\ (e\sin[\eta])\ (1 - e\cos[\eta]), \tag{5.3}$$

$$v_t = \sqrt{\frac{GM}{a}}\left(\frac{\sqrt{1-e^2}}{1 - e\cos[\eta]}\right). \tag{5.4}$$

In this orbital scenario, v_r, v_t, and the present-day separation r are all measurable quantities for the M31-Milky Way system; the current orbital time t is assumed to be the age of the Universe since the Big Bang. If these values are known, then Equations 5.1-5.4 can be solved for M, a, η, and e. The ability to constrain these orbital parameters thus depends on v_t, the largest unknown

among observational quantities.

Early versions of the timing argument treated the orbits of M31 and the Milky Way as purely radial, with no transverse component (Kahn & Woltjer, 1959; Lynden-Bell, 1981). Raychaudhury & Lynden-Bell (1989) modeled a quadrupolar gravitational field and showed that angular momentum in the M31-Milky Way system was a result of the influences of galaxies lying outside the Local Group. Simulations of galaxy orbits (Kroeker & Carlberg, 1991) showed that the mass derived from timing measurements does not correlate well with the enclosed total masses of the simulated galaxies, and required the existence of extensive dark matter haloes. van der Marel & Guhathakurta (2008) used improved constraints on the age of the Universe and statistical estimates for v_t to make the most precise estimates of the M31-Milky Way orbit to date. Values of v_t larger than their assumed value ($v_W = -78 \pm 41$ km s^{-1}, $v_N = -38 \pm 34$ km s^{-1}) would increase estimates of M, a, and η while decreasing e. The time required for a full orbit (which predicts when M31 and the Milky Way will collide) and the perigalacticon r_{peri} will also both increase if the magnitude of v_t increases.

5.1.4 Extragalactic masers as proper motion tracers

The most accurate method developed for measuring extragalactic proper motion is through observations of masers. Brunthaler et al. (2005, 2007) tracked the positions of H_2O masers in the Local Group galaxies M33 and IC 10 relative to background quasars using the VLBA. Their observations achieved accuracies of $\Delta\mu/\mu = 20-30\%$ over epochs spanning 3–4 years. Measurement of the galaxies' proper motions also yielded a geometric determination of the distance to M33 and the 3-dimensional velocities of both galaxies with respect to the Milky Way. Only a single maser in IC 10 and two masers in M33 were used, with peak brightnesses of 1–2 Jy.

The advantages of using masers for proper motion measurements are their spatial compactness (the astrometric accuracy increases if phase referencing can be done on the source itself), narrow beaming angle, and the high angular resolution offered by Very Long Baseline Interferometry (VLBI). Since the angular resolution is a linear function of wavelength for a given telescope

Table 5.1. Basic parameters of M31

Parameter	Value	Reference
Right ascension [J2000.0] of nucleus	$00^h42^m46.0^s$	Beck et al. (1998)
Declination [J2000.0] of nucleus	$+41°16^m11.8^s$	Beck et al. (1998)
Distance	785 ± 25 kpc	McConnachie et al. (2005)
$(m - M)$	24.47 ± 0.07	McConnachie et al. (2005)
Inclination	77°	Walterbos & Kennicutt (1987)
Position angle	35°	Walterbos & Kennicutt (1987)
Systemic velocity	-300 km s^{-1}	de Vaucouleurs et al. (1991)

diameter, water masers ($\nu = 22.2$ GHz) will be roughly 3.3× more precise than methanol masers ($\nu = 6.7$ GHz) and 13× more precise than OH masers ($\nu = 1.6$ GHz). The use of a single source, rather than measuring the average proper motions of multiple sources such as stars, also means that individual sources can be more precisely modeled with respect to the internal dynamics of the galaxy. Disadvantages of radio observations include the intrinsic variability of masers, the need for a nearby background quasar as a reference source, and the lack of identified radio-bright (> 10 mJy) sources in Local Group galaxies.

While H_2O masers are the best option for astrometric accuracy, their higher frequencies also make large areal surveys for masers inefficient, since the size of the primary beam for an interferometer scales as the inverse of the observing frequency. For a galaxy the size of M31 ($2° \times 0.5°$ on the sky), a full survey would require ~ 1000 pointings with the Very Large Array (VLA). The large amount of time necessary to complete such a survey makes this an unfeasible project. Observations of OH masers at 1.6 GHz, by contrast, can cover the entire galaxy in only 10–20 pointings. Since more than 80% of Galactic OH masers show a methanol (Caswell, 2009) or water maser (Breen et al., 2010) at the same site, an OH maser map would provide a logical first step toward identifying masers for future proper motion studies. The probability of a maser detection at higher frequencies is further increased by the fact that OH emission is often the weakest among the three species. We carried out an 18-cm survey of M31 in 2008 with the VLA with the goal of finding the first OH masers in the galaxy.

5.2 Very Large Array observations

5.2.1 Previous searches for masers in M31

No masers of any type had been detected in M31 at the beginning of our OH survey - the goal of our observations was to find the first maser of any type. Recent discoveries of other maser species in M31 are discussed in Sections 5.5.2 and 5.5.3. Greenhill et al. (1995) and Imai et al. (2001) conducted pointed H_2O maser surveys toward HII regions in M31 with small beams ($40''$ and $74''$) and low sensitivity, reaching respective 1-σ rms noise levels of 29 and 70 mJy. Their non-detections were consistent with the aggregate star formation rate of M31; however, the surveys covered less than 50% of regions containing M31's molecular gas and were not sufficiently sensitive to have detected a typical Galactic maser at the distance of M31 (Brunthaler et al., 2006). There is no record of any previous search for OH in M31, either in emission or absorption.

The ultimate goals of the OH line survey in M31 were: (1) to provide an OH maser map for H_2O and CH_3OH follow-up as VLBI proper motion targets, (2) to take a census of OH maser emission in M31 for studies of star formation and molecular gas excitation via detailed comparison with CO, HI, IR, radio continuum, and dust maps, (3) to provide a target list for full Stokes studies of magnetic fields in M31 via Zeeman splitting of OH masers, (4) to make a deep radio continuum map at 18 cm in two polarizations, (5) to search for OH absorption lines toward strong radio continuum sources.

5.2.2 OH survey strategy

Figure 5.2 shows the distribution of gas in M31, which traces likely sites of maser action. The CO emission (Nieten et al., 2006) traces the molecular gas in the galaxy; the distribution of OH likely follows CO, although maps of OH in other galaxies have been shown to be more spatially extended than CO. A radio continuum map of M31 made at 20 cm (Beck et al., 1998) represents regions where stimulated emission may occur through amplification of the radio background. Both maps show that the strongest peaks located in the 10-kpc ring and near M31's nucleus at $R < 0.7$ kpc.

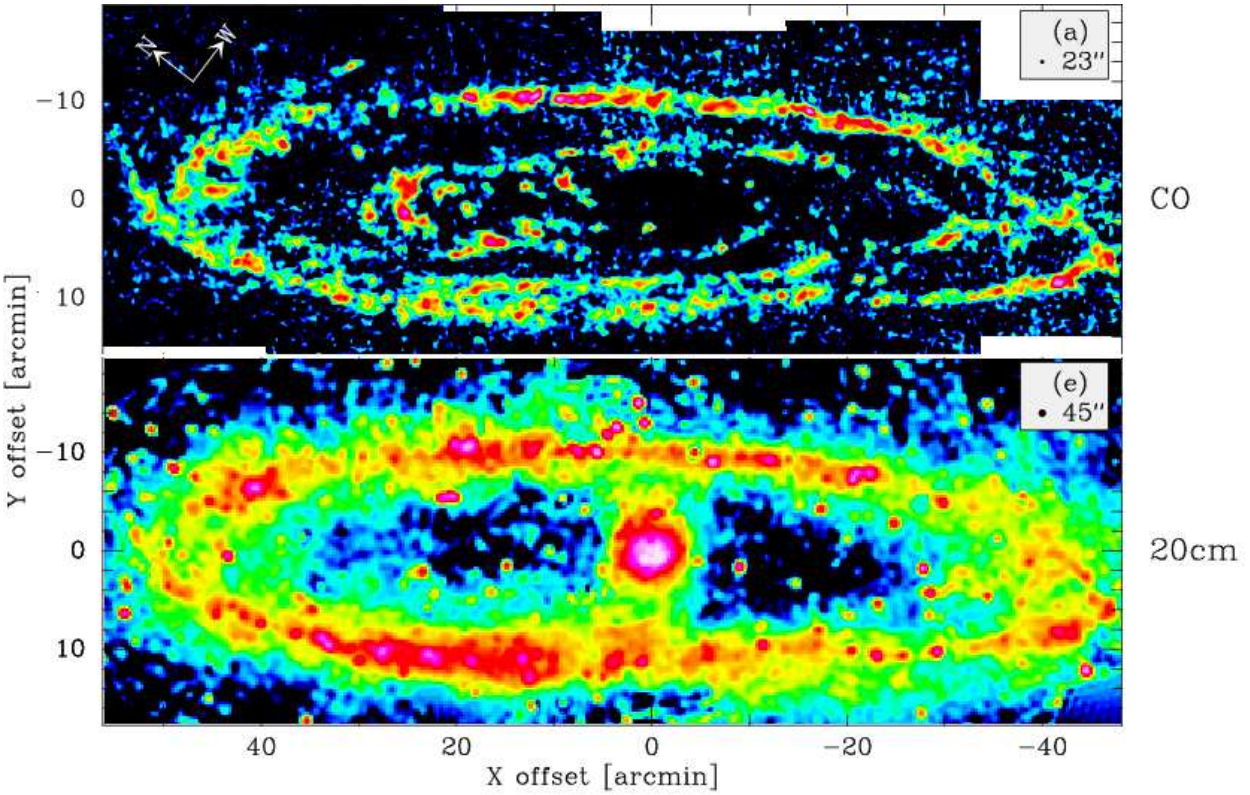

Figure 5.2 CO line and 20 cm radio continuum maps of M31, after Nieten et al. (2006). The upper panel shows the 2° × 0.5° CO (1–0) map by Nieten et al. (2006) with angular resolution 23" or ∼85 pc. The lower panel shows the VLA D-array 20 cm radio continuum map by Beck et al. (1998) with a 45" beam. The 20 cm radio continuum map is a mosaic of 7 pointing centers, and provides a guide for an OH survey of M31 with the VLA. The CO map represents regions where OH is present (it is distributed roughly following CO, but may be more extended), and the radio continuum map represents regions where stimulated emission may occur.

The brightness of observable masers will be determined by the product of the background radio continuum and the maser gain. The close spatial association of the molecular gas and the radio continuum yield a large range of environments that an OH maser survey will sample.

We used the VLA[1] in New Mexico to carry out the 18-cm observations. The VLA was chosen based on its sensitivity, angular resolution, spectral coverage, and field-of-view capabilities. We designed the observations to use the telescope in its most compact configuration (D-array; $b_{max} \sim$ 1 km), which minimized the synthesized beam size and thus maximized the angular resolution of the survey (Figure 5.3).

Beck et al. (1998) made a 7-pointing, 20-cm continuum mosaic of M31 with the VLA in D-array. The configuration for a 20 cm survey is similar to that required for 18 cm OH line observations, but their map is undersampled at the edges of the pointings. For the OH survey we designed a 15-pointing pattern (Figure 5.4) to obtain Nyquist sampling of regions with molecular gas and radio continuum, making sure to include the entire 10-kpc ring. Our mapping strategy also includes a single pointing at the center of M31, since roughly 50% of the strongest OH masers detected in the Milky Way are found in complexes near the Galactic center. The primary beam[2] of the VLA is $27'$ at 1.6 GHz, and the total region mapped is $2^\circ \times 0.5^\circ$. Since any maser emission will be compact and unresolved at the distance of M31, single-dish spacings were not necessary for an initial discovery phase.

In Galactic OH masers, the 1665 MHz line is the brighter of the two main line transitions, and so we chose $\nu_{rest} = 1665.4018$ MHz as the spectral tuning center. Since OH maser lines can exhibit strong circular polarization, both LL and RR polarizations were observed in adjoining sidebands. With Hanning smoothing and two intermediate frequency bands (IFs), the L-band receiver setup had 128 channels with $\Delta v = 4.4$ km s^{-1}, with a total bandpass of 563 km s^{-1}. The total velocity span of the molecular gas in M31 is about 600 km s^{-1}, based on its CO emission (Nieten et al., 2006). As a result, full coverage of M31 required two overlapping spectral windows centered at

[1] The VLA is operated by the National Radio Astronomy Observatory and is a facility of the National Science Foundation operated under cooperative agreement by Associated Universities, Inc.

[2] The full-width half-power of the VLA primary beam is $\theta_{PB} = 45'/\nu\ [GHz]$.

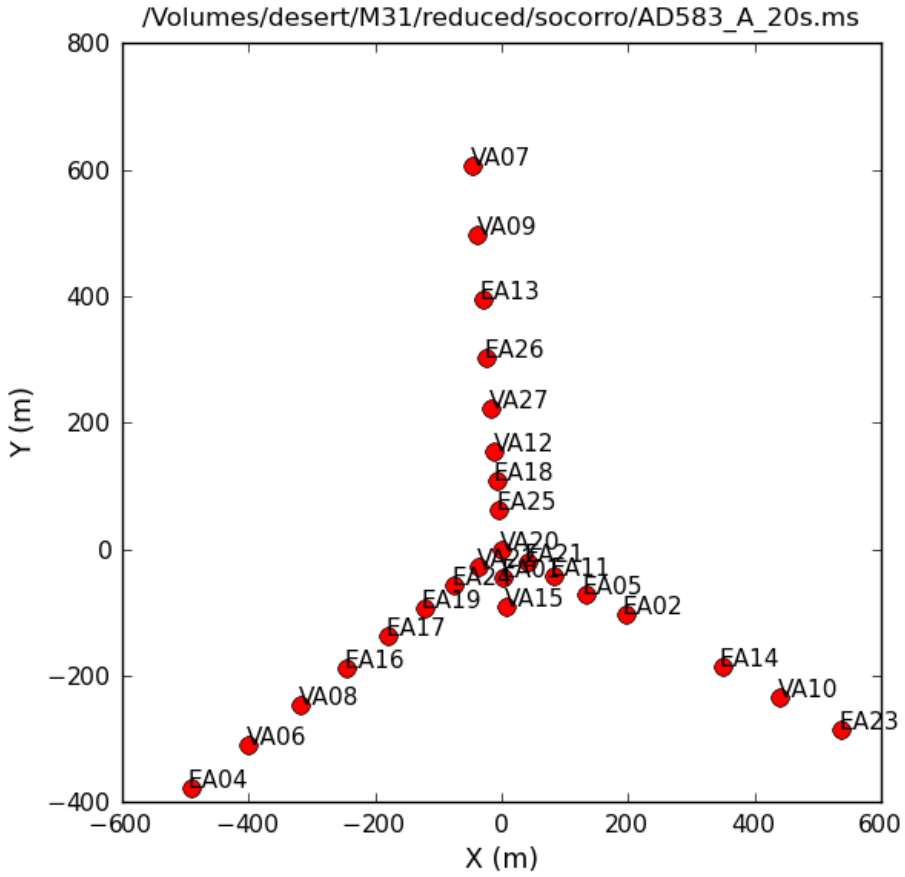

Figure 5.3 Position of the 26 deployed VLA/EVLA antennas in D-array on July 14, 2008, the first of the ten observing sessions of M31. VLA antennas are marked with the prefix "VA", while EVLA antennas are marked with "EA". The maximum baseline in this configuration is 1.03 km, with a synthesized beam width of $\theta \simeq 36''$.

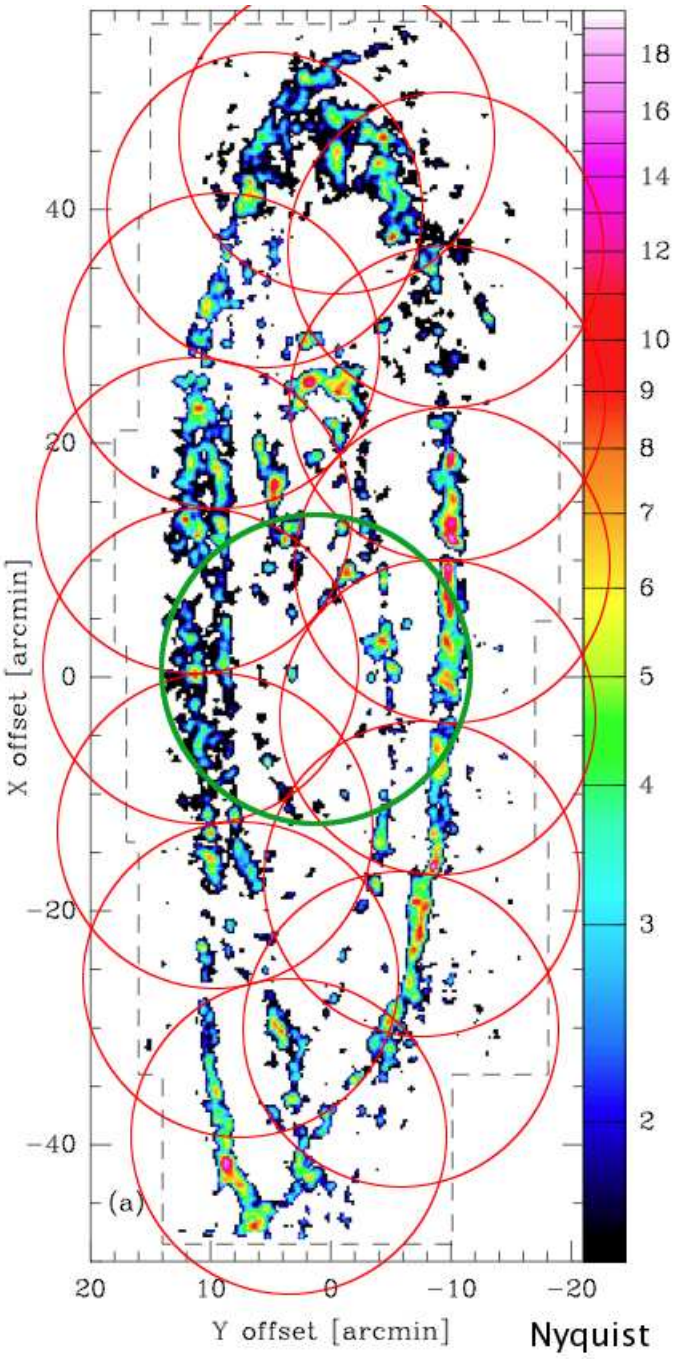

Figure 5.4 Pointings for the 15 fields of the VLA OH survey of M31, overlaid on the CO intensity map of Nieten et al. (2006). The size of the circles (27′) indicates the diameter of the VLA primary beam at 1.6 GHz. The centers of each pointing were chosen so that each position in M31 is observed in at least two fields. The bottom seven fields were observed in the first velocity tuning, while the top eight fields, including M31's nucleus (green circle), were observed in the second velocity tuning.

$v_{hel} = -375$ and -250 km s^{-1}, giving a total velocity coverage of -650 to -30 km s^{-1}. Seven of the fifteen M31 fields were observed in the first spectral window (centered at $v = -375$ km s^{-1}), with the remaining eight fields (including the nucleus) in the second spectral window (Table 5.2).

The initial VLA proposal for the 18-cm survey was not accepted for normal block scheduling, and was instead allocated to a dynamic scheduling mode in which observation sessions are assigned on-the-fly based on the day-to-day availability of the telescope. The inability to specify the date and time of the observations resulted in two changes to our observing strategy. First, the central observing frequency needed to be updated regularly, since the motion of the Earth around the Sun continually changes the topocentric velocity. Since we required a large fraction of the available bandpass to cover the M31 velocity range, we needed to update the Doppler tracking of the telescope every 4–5 days using the online DOPSET tool.[3] Secondly, the uncertainty in the time of observation meant that we had to build in much larger slew times and overhead in the scheduling files. We estimate that we lost $\sim 5 - 10\%$ of the total time to slewing and unnecessarily long integrations on calibration sources.

Mapping of M31 was conducted in a many-visit mode, split into shorter sessions to increase the probability of each block being dynamically scheduled. Each 2.5-hour session observed the bright flux calibrator 3C48 in both spectral windows for 2–10 minutes each (depending the slew time from the last telescope position), and then integrated on the phase calibrator $0029 + 349$ in both spectral windows for 2–10 minutes. We observed the seven M31 fields in the first spectral window for 200 seconds apiece, reset the receiver to its new spectral tuning, and observed the remaining eight fields in the second spectral window. We then re-observed the phase calibrator in both spectral windows, repeated the cadence through the M31 fields, and ended the session by observing both the phase and flux calibrators one final time. The order of the spectral windows was flipped for each observation of the phase calibrator to reduce the overhead accrued by retuning the receiver. Observing time was allocated in ten blocks of 2.5 hours each, scheduled between July and September 2008 as project AD583 (Table 5.3).

[3] Thankfully, this is now done automatically with the upgraded EVLA system.

Table 5.2. Fields observed with the VLA

Field	RA J2000.0	Dec. J2000.0	Total t_{int} [hr]	Velocity tuning	σ_{rms} [mJy]	Notes
3C48	01:37:41.299	+33:09:35.13	3.8	[0,1]	1.7	Flux calibrator
0029+349	00:29:14.242	+34:56:32.25	2.3	[0,1]	0.8	Phase calibrator
M31_0	00:41:54.972	+41:20:08.28	1.0	[0]	1.3	
M31_1	00:41:18.250	+41:07:26.95	1.0	[0]	0.8	
M31_2	00:40:41.139	+40:56:20.98	1.0	[0]	0.8	
M31_3	00:40:49.199	+40:43:25.63	1.0	[0]	0.6	
M31_4	00:41:49.177	+40:51:51.40	1.0	[0]	0.7	
M31_5	00:42:39.586	+41:00:58.49	1.0	[0]	0.7	
M31_6	00:43:31.578	+41:11:08.04	1.0	[0]	0.7	
M31_7	00:44:17.829	+41:20:45.43	1.0	[1]	0.8	
M31_8	00:44:51.016	+41:33:40.19	1.0	[1]	0.6	
M31_9	00:45:16.588	+41:44:29.95	1.0	[1]	0.4	
M31_10	00:45:17.022	+41:54:57.21	1.0	[1]	0.7	
M31_11	00:44:02.438	+41:51:56.40	1.0	[1]	0.8	
M31_12	00:43:18.422	+41:40:45.31	1.0	[1]	1.3	
M31_13	00:42:36.205	+41:31:00.93	1.0	[1]	3.1	
M31_14	00:42:44.451	+41:16:28.77	1.0	[1]	1.5	M31 nucleus

Note. — The velocity tuning corresponds to the two spectral windows needed to fully cover the velocity range of the M31 gas as inferred from ^{12}CO. The LSRK velocity range of window [0] is -650 to -95 km s^{-1}, and window [1] is from -530 to $+30$ km s^{-1}. σ_{rms} is the measured continuum rms noise for each field with combined polarizations.

Table 5.3. Summary of VLA observing blocks for OH line survey

Session	Date	Blanked channels		Flagged antennas
		spw 0	spw 1	
AD583_A	14 Jul 2008	58,59,84	56,84∼87	VA10,EA23,EA25
AD583_B	16 Jul 2008	58,84	56	
AD583_C	22 Jul 2008	58,84	56	VA20
AD583_D	29 Jul 2008	84	56	VA20
AD583_E	03 Aug 2008	84	56	VA20, VA22, EA04
AD583_F	09 Aug 2008	58,84	56	EA11
AD583_G	13 Aug 2008	84	56	EA11
AD583_H	25 Aug 2008	83	55	VA20, EA11
AD583_I	05 Sep 2008	83	54	VA20, EA11
AD583_J	06 Sep 2008	83	54	VA20, EA11

5.2.3 Sensitivity

The planned sensitivity limits for the OH line survey were driven by the goal of mapping M31 down to the flux density limit at which VLBI astrometry is possible. This limit is about 10 mJy with the Very Long Baseline Array (VLBA) at its current recording rate of 512 Mbps. We originally requested a total of two hours per pointing for a total of 46 hours of observing. When the proposal was assigned to dynamic scheduling, however, we were allotted a total of only 25 hours due to the high perceived risk of the project. The increased overhead factor from slewing and dynamic scheduling resulted in a total of only 1.0 hour of integration per pointing on M31.

The theoretical rms noise for an observation of a point source over integrations of duration t_{int} is:

$$\Delta S = \frac{K}{\sqrt{N(N-1)N_{IF}t_{int}\Delta\nu}}, \tag{5.5}$$

where K is a system constant based on the antenna temperature and collecting area, N is the total number of antennas, N_{IF} is the number of combined polarizations + intermediate frequencies (IFs), and $\Delta\nu$ is the observing bandwidth (Rohlfs & Wilson, 2004). For K=50 mJy,[4] $N = 26$, $N_{IF} = 2$, and a channel width of $\Delta\nu = 24.4$ kHz, we expected a 1 σ rms of 2.02 mJy beam^{-1} channel^{-1} for $t_{int} = 1.0$ hr, and 1.43 mJy beam^{-1} channel^{-1} for $t_{int} = 2.0$ hr. This meant that even for the reduced integration time, a 5 σ detection would still be very close to the flux density limit for VLBI observations. Overlapping fields in the mosaic of M31 will increase the effective integration time and bring down the rms; however, flagging data, radio frequency interference (RFI), missing antennas, and variations in antenna gain will all increase the rms noise. As a result, the actual sensitivity will vary from field to field and from channel to channel.

The sensitivity limit can also be evaluated with the expectation of detecting an OH maser in M31. The most complete survey of OH masers in the Milky Way comes from the VLA survey of Argon et al. (2000). The brightest Milky Way OH maser is in the HII region W3 (OH), with a peak

[4] L-band performance in mid-2009 from VLA Observing Status Memo.

flux density of 200 Jy at a distance of 2.04 ± 0.06 kpc (Hachisuka et al., 2006). Assuming a constant luminosity, the observed brightness will scale with the distance squared; masers at the distance of M31 (785 ± 25 kpc) will be a factor of $(D_{M31}/D_{MW})^2 = (\sim 785 \text{ kpc}/10 \text{ kpc})^2 \simeq 6000$ dimmer than in the Milky Way. A 10 mJy lower limit will therefore be sensitive to masers of $\gtrsim 60$ Jy, several dozen of which are known to exist in the Milky Way. Assuming the number of masers scales with the galactic star formation rate (which is a factor of 2–12 lower in M31 than the Milky Way), 1–2 OH masers would be expected to be detectable in M31 at a brightness of > 10 mJy.

5.2.4 The VLA-EVLA transition

It should be noted that during the period of the 18-cm observations, the VLA was in the midst of a massive hardware and software upgrade that would eventually result in the Expanded Very Large Array (EVLA). During this transition period, the 28 antennas of the telescope were retrofitted one-by-one with upgraded receivers and electronics. This meant that our observations used a combination of 10 VLA antennas and 16–17 upgraded EVLA antennas (antenna EA03 was placed in the array for observing sessions AD583_H, AD583_I, and AD583_J). All data were processed with the old VLA correlator before it was replaced with the WIDAR correlator in early 2010. While the VLA was designed to be fully functional during the upgrade, several transition issues have been known to arise with hybrid EVLA-VLA data; we note problems in our 18-cm data in Section 5.3.3.

5.3 Data reduction

5.3.1 Flagging and calibration

Reduction of the VLA data was carried out using the Common Astronomy Software Applications (CASA) package.[5] After importing the raw data into a measurement set (MS), we averaged the time bins over a 20s period (two integrations) to decrease the total data size. We updated the antenna positions using the archived baseline corrections and flagged all data identified by the

[5] `http://casa.nrao.edu`

operator as unreliable. The MS was then extensively examined and flagged for obvious outliers, including automated sigma clipping, aliasing into specific channels, and fluctuating gains on the telescope.

We used 3C48 to set the absolute flux scale and as a bandpass calibrator. The calibration for antenna-based phase and amplitude gains was made with 0029+349, observations of which bracketed each science target in the scheduling blocks. After eliminating ~ 10 noisy channels from both edges of each spectral window (the final data cubes have 101 channels per spectral window), we split the data into separate measurement sets for cleaning and imaging. These included the flux and phase calibrators as well as the M31 science fields in three polarization sets (LL, RR, and combined), as well as separating the two spectral windows. Subtraction of the continuum for spectral line analysis was done with the task `uvcontsub2()`, which fit a linear function to the data in (u, v)-space to produce continuum and continuum-subtracted measurement sets.

After separately flagging and reducing each of the scheduling blocks, we concatenated all (u, v) data to produce the final images. Shifting of the observed center frequency due to Doppler tracking required setting a tolerance of 5×10^5 Hz for each spectral window.

5.3.2 Imaging and mosaicking

We imaged two mosaicked fields of M31 (one for each spectral window) using an interactive CLEAN algorithm. Continuum point sources (mostly HII regions) were identified using the catalog of Walterbos et al. (1985) as a guide, with cleanboxes placed around each. After the first few rounds of cleaning removed point sources with $S \gtrsim 10$ mJy, we also added cleanboxes around the diffuse emission in the nucleus and 10-kpc ring. The threshold for the CLEAN algorithm was chosen by taking the rms from a sky-dominated region of a dirty image as the lower limit. This noise threshold was 0.8 mJy for the continuum image and 2.4 mJy/channel for the continuum-subtracted line emission.

The overlapping fields of M31 in each spectral window were combined in (u, v)-space by mosaicking, individually weighting each field and using the primary beam for joint deconvolution.

We explored alternative mosaicking techniques such as the Cotton-Schwab algorithm, but found no significant differences in the noise levels or dynamic range for the data. The galaxy was well-sampled in the final mosaics, with the 10-kpc ring imaged at $> 80\%$ of the peak weighted response pattern near the center of the beam (Figure 5.5).

The J2000.0 phase centers of the mosaicked M31 images are $[\alpha, \delta]$=[00:41:46.8,+41:03:19.7] for spectral window 0 and $[\alpha, \delta]$=[00:43:53.9,+41:34:57.1] for spectral window 1. We made 300×300-pixel images for the separate spectral windows and 450×450-pixel images for the combined spectral window, with $15''$ square pixels. This oversamples the synthesized beam by a factor of 2–3. The restoring beam for the mosaic was $36.2'' \times 31.7''$, with a position angle of 89.9°.

5.3.3 Aliasing and bad channels

All ten of the observation sessions were found to suffer from excess power in various channels, possibly as a result of aliasing. Aliasing occurs when the sky brightness is not uniformly zero outside the primary beam, and the image (a Fourier transform of the resampled function) contains power 'folded back' into the beam. The root causes of aliasing are undersampling of the visibility data as well as truncation of the sampling function at the boundaries of (u, v) coverage (Briggs et al., 1999).

In the 18-cm data, significant amounts of excess power were found over all channels for EVLA-EVLA antenna baselines. The ~ 120 EVLA-EVLA baselines showed power more than an order of magnitude greater than that in VLA-VLA or VLA-EVLA baselines, with a wide, single peak centered on channel 58 in spectral window 0 and channel 84 in spectral window 1 (Figure 5.6). Similar peaks appeared in the 45 VLA-VLA and 160 VLA-EVLA baselines, but was limited to only one or two channels. We flagged data from all EVLA-EVLA baselines in each session as a result (Figure 5.7), and flagged data from the remaining peaks (< 4 channels) in both spectral windows. This resulted in the exclusion of two small velocity ranges ($v_{LSRK} = -475$ to -457 and -227 to -218 km s^{-1}) from the final data cubes due to the blanked channels (Table 5.3).

Removing the EVLA-EVLA baselines increased the noise by a factor of:

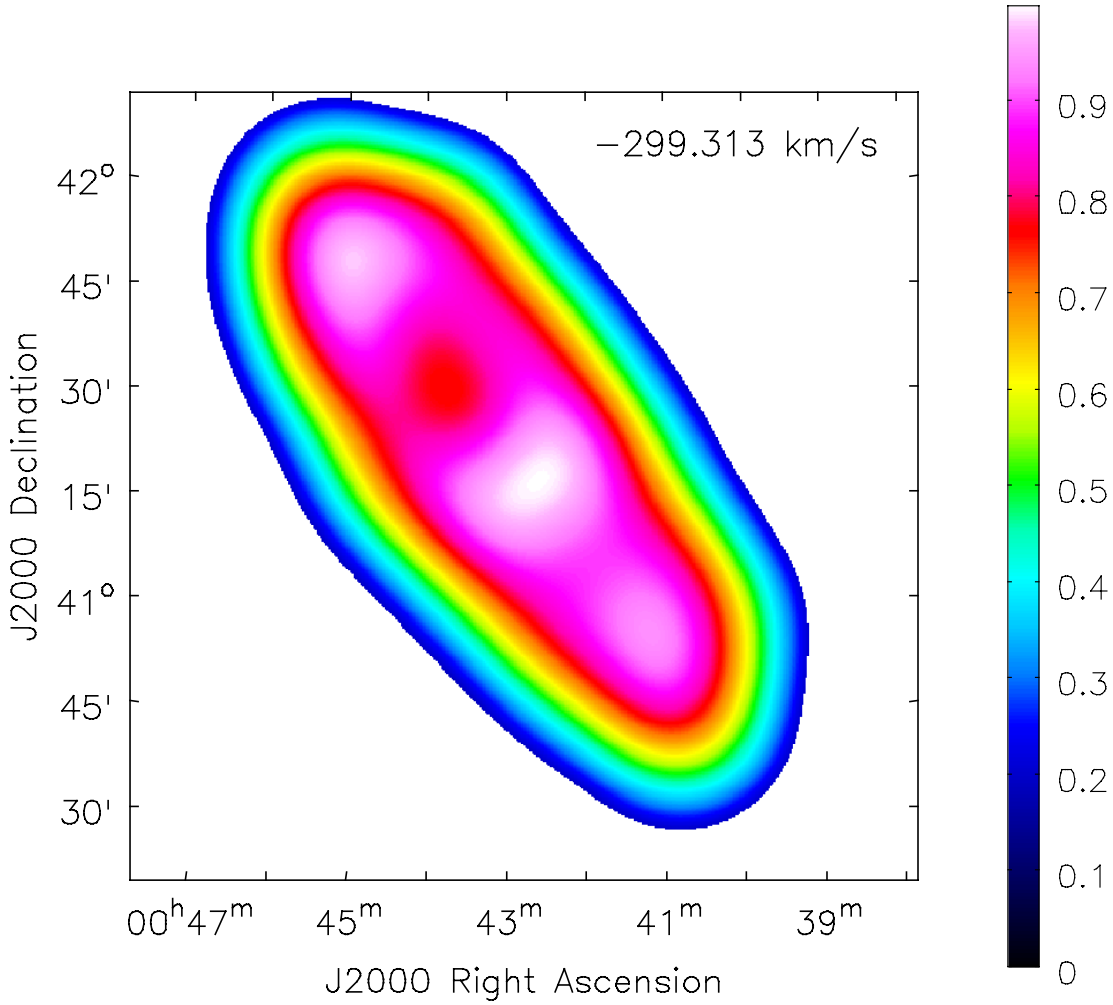

Figure 5.5 Primary beam coverage of the mosaicked VLA data for M31; the channel displayed here ($v_{obs} = -299$ km s^{-1}) is included in both spectral tunings. The colorbar shows the effective weighted response pattern of the beam normalized to its peak value.

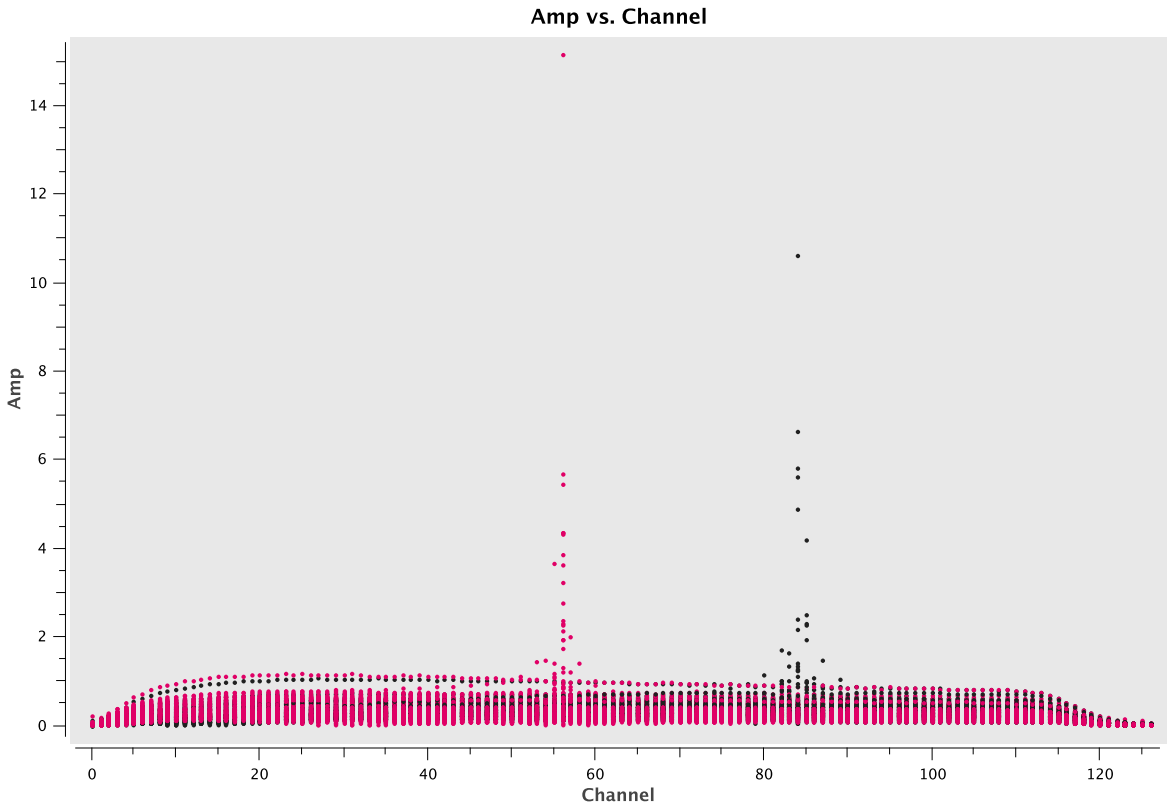

Figure 5.6 Spectrum of uncalibrated (u, v) data for the flux calibrator 3C48 in session AD583_E. Data are averaged over all integrations and antennas; colors mark data from the two spectral windows. The peaks near channels 57 (spw 0) and 84 (spw 1) are dominated by power in the EVLA-EVLA baselines, possibly as a result of aliasing.

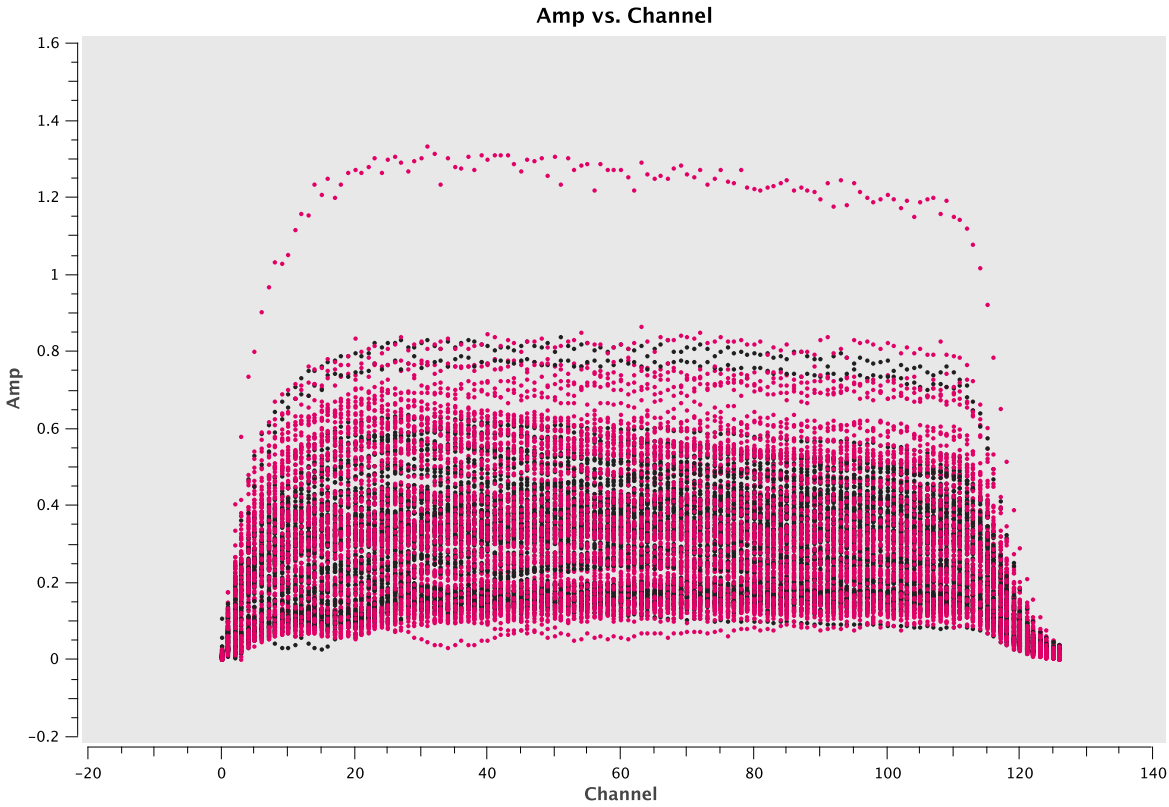

Figure 5.7 Spectrum of uncalibrated (u, v) data for the flux calibrator 3C48 in session AD583_E, with all EVLA-EVLA baselines flagged. Data are averaged over all integrations and antennas; colors mark data from the two spectral windows. The excess power in channels 57 (spw 0) and 84 (spw 1) is greatly decreased when data from the offending baselines are removed.

$$\frac{\sqrt{N_{all} \times (N_{all} - 1)}}{\sqrt{N_{VLA} \times (N_{VLA} - 1) + (N_{VLA} \times N_{EVLA})}}, \tag{5.6}$$

roughly a factor of 1.6 for the VLA data. This does not take into account the additional flagging of individual suspect antennas, baselines, and integrations carried out for each observation session.

5.3.4 Image defects

In the continuum images, the strongest point source in the image is 37W115 (Walterbos et al., 1985), which has a peak flux density of 373.4 mJy at 20 cm. We recover a maximum flux density of 272.3 mJy for this source, which is surrounded by artifacts that indicate a likely error in the imaging. 37W115 is also the only continuum source that appears in all channels of the OH line data cube, having not been fully removed by the (u, v) continuum subtraction. We speculate that this is due to non-linear terms in the (u, v) continuum not subtracted by the model; since higher-order baseline subtraction is not yet available in CASA, however, we simply masked out the 5×5-pixel region centered on 37W115 in all OH line searches.

5.4 Results of the OH line survey

5.4.1 Continuum

Figure 5.8 shows the 18-cm continuum image of M31. The image is dominated in the NW quadrant by the image artifacts centered on 37W115, the brightest point source within the primary beam of the VLA. Several dozen additional point sources are visible, all of which were catalogued by Walterbos et al. (1985) and re-observed by Beck et al. (1998) at 20 cm; these are likely HII regions or supernova remnants. Integrated flux densities for the 24 point sources within the VLA beam and with $S > 10$ mJy agree with the values reported by Walterbos et al. (1985), although with significant scatter ($\sim 30\%$). The exception is 37W115, for which strong negative artifacts near the source results in recovery of only $\sim 50\%$ of the reported 20 cm flux.

In addition to the point sources, the diffuse radio continuum of M31 is also detected; the

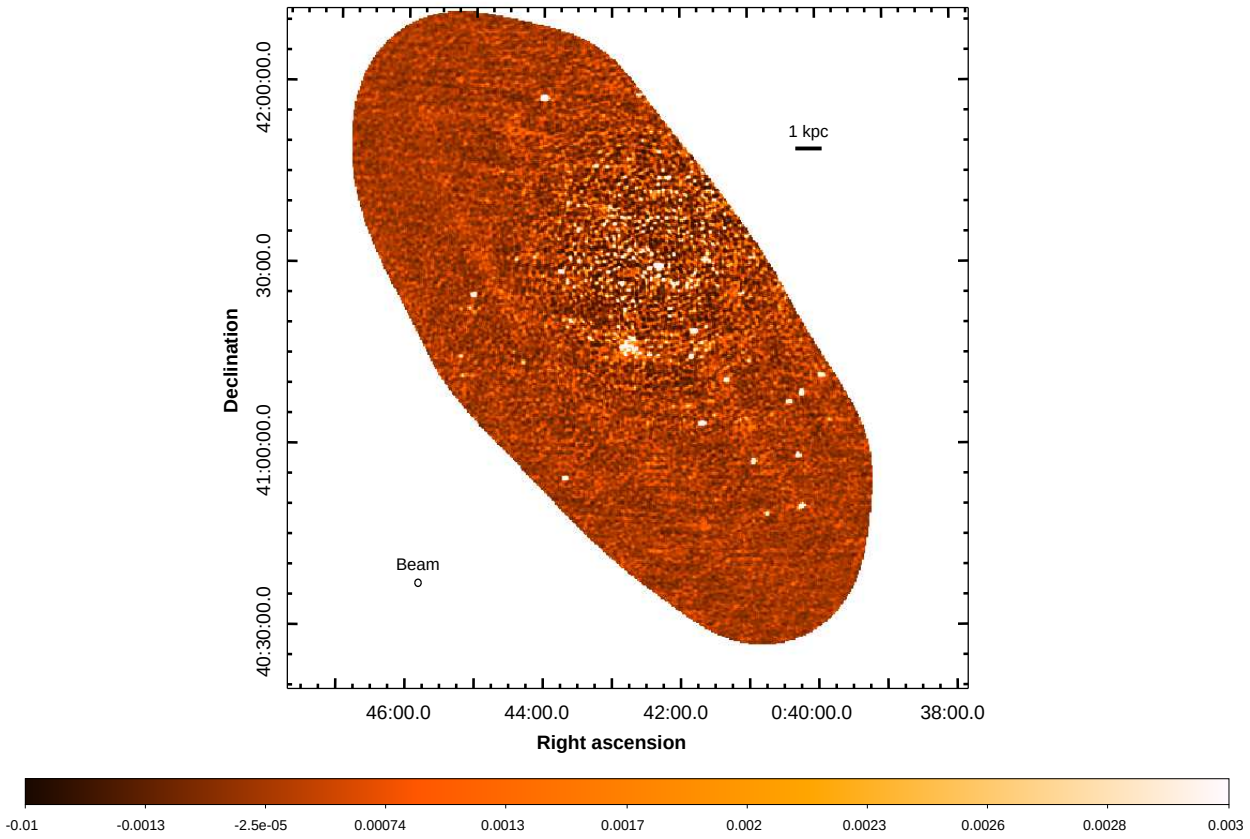

Figure 5.8 The 18-cm continuum image of M31 taken with the VLA. This image is a mosaic of 15 overlapping fields. While the NW corner of the image is dominated by image defects caused by a bright point source, the 10-kpc ring, galactic nucleus, and other point sources (HII regions or supernovae remnants) are all clearly detected. The restoring beam is $36.2'' \times 31.7''$, with a position angle of 89.9°. Units on the colorbar are Jy beam^{-1}.

emission is concentrated in the 10-kpc ring and the galactic nucleus. The peak flux density in the nucleus is 8.0 mJy, while the emission in the 10-kpc ring is typically less than ~ 3 mJy. The measured sky rms in the continuum image is 0.4 mJy; the decrease in noise compared to the thermal prediction (Equation 5.5) is due to the fact that most of the primary beam was observed in multiple sessions, with a large fraction of the galaxy covered by three or more pointings.

5.4.2 Spectral line

Searching the OH line cubes for emission from a possible OH maser revealed no strong peaks that would be unambiguous signs of a maser. Galactic OH masers can be very narrow, with velocity widths less than the VLA channel spacing of 4.4 km s^{-1}, and will be unresolved at the distance of M31. Therefore, compact, single-channel peaks are still viable maser candidates. Techniques for identifying possible masers included:

- Simple peak finding in both spatial and spectral domain
- Cross-correlation and Gaussian fitting in the spectral domain
- Smoothing with variable kernels and peak-finding in the spatial domain

The initial search of the VLA data for OH line emission began with identifying peaks above the local noise threshold in both the spatial and spectral domain. In the spectral domain, we analyzed each pixel and searched for peaks above the measured rms in each spectrum (S/N=peak/rms). Since each pixel is not a separate resolution element, a true signal would be expected to show increased emission over the entire beam area (~ 6.3 pixels). We performed a similar search in the spatial domain, searching for peaks in each plane.

Results of the peak-finding algorithm are shown in Figure 5.9, which includes data from both spectral windows and for the velocity space in which the spectral windows overlap. We also plot the expected distribution of peaks as a function of S/N if the maps were dominated by Gaussian random noise. If Gaussian statistics dominate, one would expect no peaks greater than 5 σ significance in

either spectral window. The 18-cm data has 68 spectral and 27 spatial peaks with S/N$>$ 4.5; only $\sim 15\%$ of peaks had $> 4.5\sigma$ significance in both the spectral and spatial domains.

We refined the peak-finding algorithms by cross-correlating the data with templates for the maser emission, which is more sensitive to both the full beam size and broader velocity widths. In the spectral domain, we based our technique on the signal extraction utilities developed for the ALFALFA survey by Saintonge (2007). For each pixel, a set of Gaussian templates with varying widths are generated and then cross-correlated them with the 18-cm spectra. The largest value of the cross-correlation function gives the center channel, width, and amplitude of the best-fit Gaussian for that spectrum. We verify the result of the cross-correlation with a least-squares Gaussian fit at the center channel. Possible candidates for maser emission are considered by the figure of merit S_W:

$$S_W = \left(\frac{F/W}{\sqrt{3\pi}\sigma}\right)\left(\frac{W/2}{\Delta v}\right)^{1/2}, \tag{5.7}$$

where F is the integrated flux of the feature, W its velocity width, σ the rms noise, and Δv the channel width. The second factor in Equation 5.7 re-smooths the spectrum to half its velocity width. The normalizing factor of $(3\pi)^{-1/2}$ makes $S_W = N$ if (as we assume for non-detections) the feature is a Gaussian with $W = 3$ channels and a peak flux density $N \times \sigma$. This normalization allows the distributions in Figures 5.9 and 5.10 to be more easily compared. Using the spectral cross-correlation technique, we identified 61 features with $S_W > 4.5$ in spectral windows 0 and 1.

Similar correlation techniques were used to search for peaks in the spatial domain. We smoothed each velocity plane with a Gaussian template equivalent to the restoring beam size for the spectral window, and then searched each smoothed plane for peaks above the sample noise. Candidate peaks were fit with a 2-D Gaussian, for which we used the ratio of the peak flux to the image plane rms as the criterion for a possible detection (since all sources are assumed to be unresolved Gaussians, the S/N is determined exclusively by the peak flux). No detections with significance $> 4.5\sigma$ were made in the 18-cm data using this method.

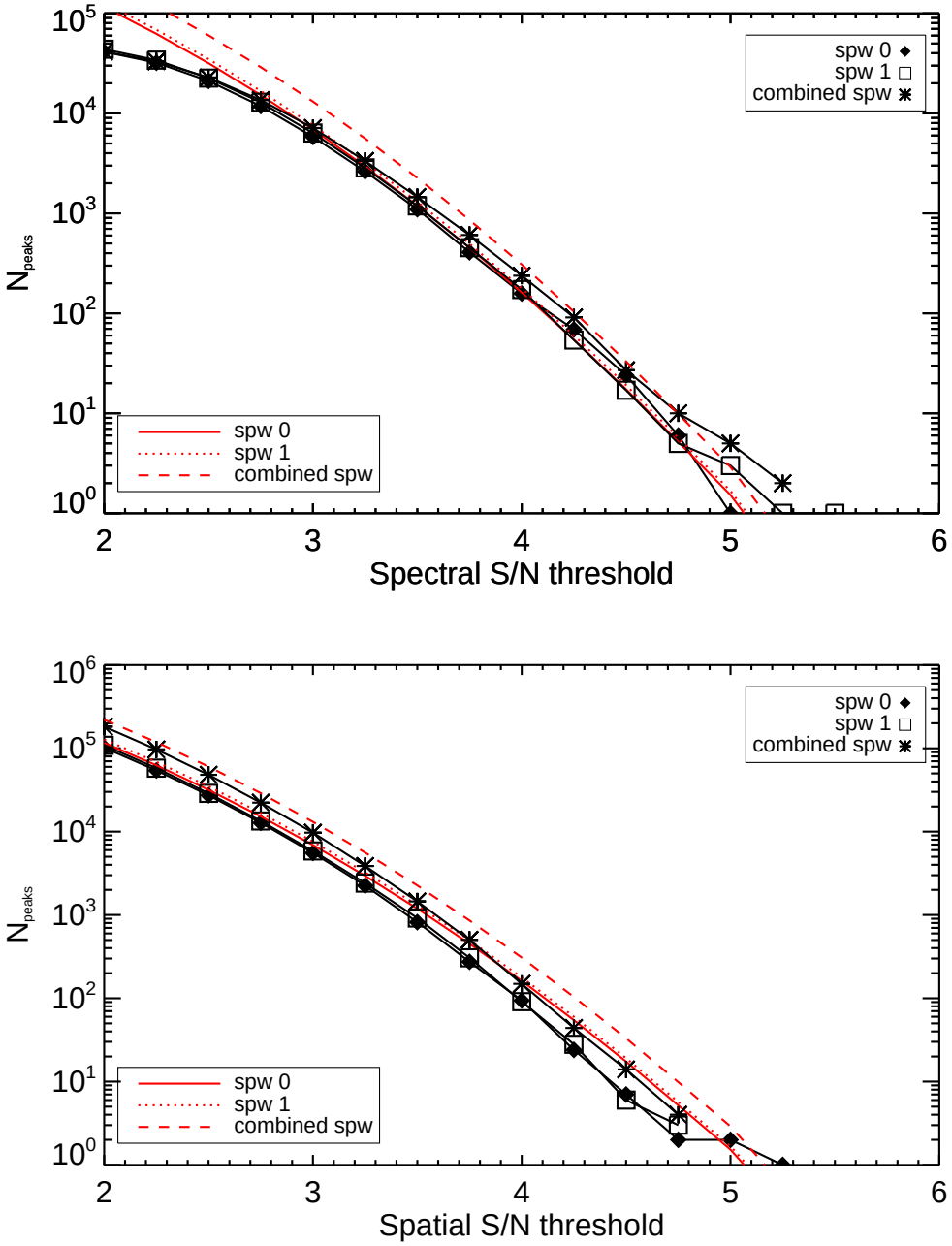

Figure 5.9 Number of peaks found as a function of the measured signal-to-noise ratio in the continuum-subtracted, mosaicked VLA 18-cm images of M31. The top panel shows peaks found in the spectral domain, pixel-by-pixel. The bottom panel shows peaks found in the spatial domain of each spectral/velocity slice. Red lines show the expected number of peaks for a Gaussian distribution of random noise.

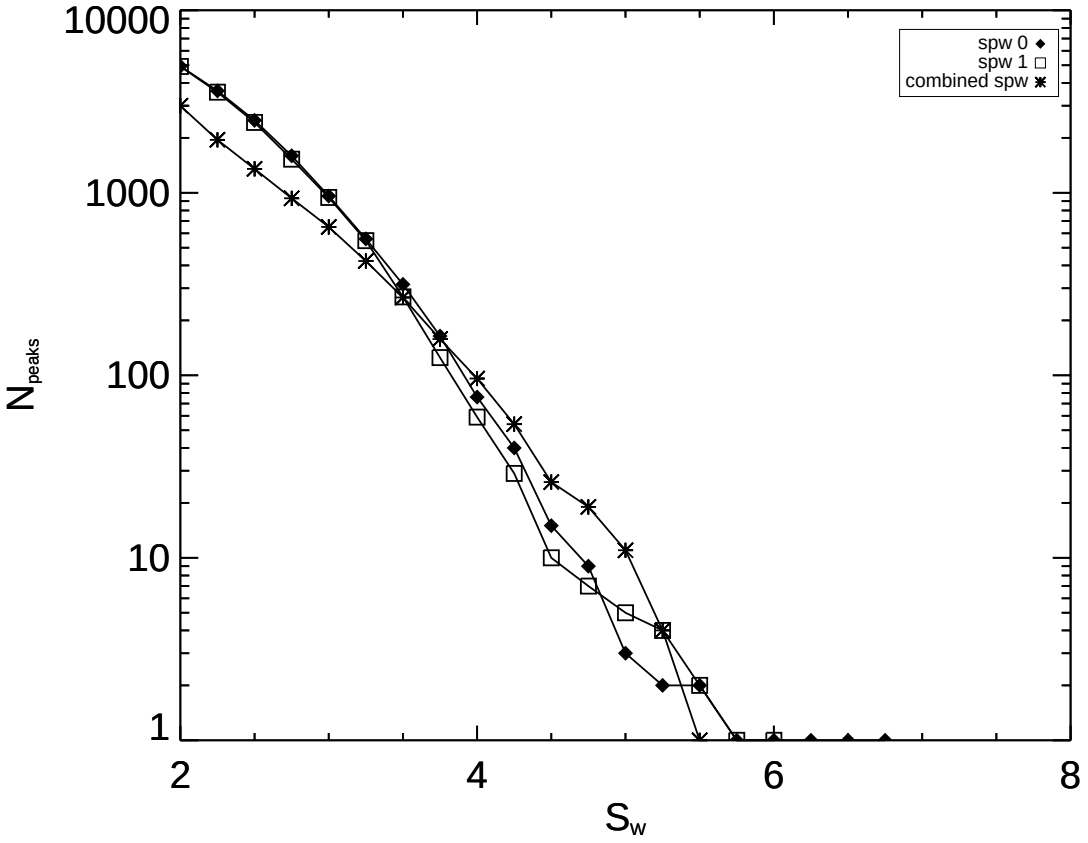

Figure 5.10 Number of 18-cm peaks found in M31 via spectral cross-correlation as a function of S_W (Equation 5.7); higher values of S_W correspond to a more significant detection.

Table 5.4. Candidate OH maser detections in M31, $> 4.5\sigma$

Candidate	18 cm peak flux density[a]			v_{LSRK}	v_{HI}	v_{CO}	Detection
	Both pols. [mJy]	LL [mJy]	RR [mJy]	[km s^{-1}]	[km s^{-1}]	[km s^{-1}]	method
003928.9+410244.6	6.9	10.3	2.4	−356	−374	−−	Spectral peak
003938.9+410517.3	7.1	4.7	9.1	−352	−368	−−	Spectral peak
003942.0+410645.5	8.0	6.4	10.0	−356	−364	−−	Spectral peak
003942.0+410745.5	8.1	5.3	10.6	−351	−360	−−	Spectral peak
003942.3+405900.5	8.1	6.3	9.5	−356	−392	−−	Spectral peak
003952.7+410416.2	6.4	3.6	8.6	−356	−374	−−	Spectral X-corr.
004003.1+411231.8	7.1	8.5	5.7	−343	−347	−−	Spatial peak
004015.5+411920.7	8.4	9.0	7.9	−303	−331	−−	Spectral/spatial peak
004021.8+410902.8	7.6	3.8	10.2	−356	−365	−−	Spectral peak
004045.6+411318.7	10.0	8.5	10.6	−351	−348	−−	Spectral peak
004049.7+410918.8	7.0	10.6	4.0	−356	−368	−−	Spectral peak
004055.2+405719.0	8.0	7.3	8.6	−492	−478	−−	Spatial peak
004059.7+410923.7	2.9	3.2	2.7	−400	−373	−−	Spectral X-corr.
004111.5+411724.4	7.6	7.8	7.0	−356	−330	−−	Spectral peak
004119.3+412739.8	5.7	6.5	5.1	−325	−299	−−	Spatial peak
004132.2+413351.7	8.1	5.2	11.2	−244	−282	−−	Spectral peak
004134.6+414136.9	6.3	4.3	7.9	−297	−270	−−	Spectral peak
004139.2+412552.2	6.5	5.0	8.1	−275	−297	−−	Spectral peak
004148.5+413410.9	5.6	5.5	5.5	−250	−275	−−	Spectral peak
004152.2+413523.1	8.3	9.1	7.6	−297	−271	−−	Spectral peak
004152.5+413441.0	5.3	6.2	4.3	−312	−272	−−	Spectral peak
004202.6+403356.2	5.8	7.0	4.6	−378	−411	−−	Spatial peak
004224.6+413811.7	4.7	7.0	2.5	−268	−247	−−	Spectral peak
004233.2+410304.1	6.5	7.8	5.5	−457	−412	−−	Spatial peak
004235.7+410010.4	8.2	7.1	9.5	−407	−393	−−	Spectral peak
004256.7+413211.8	3.9	3.6	4.1	−163	−200	−−	Spectral X-corr.
004341.8+405131.1	7.6	4.7	10.3	−351	−334	−−	Spectral peak
004343.9+411546.0	6.5	7.8	4.8	−286	−267	−291	Spectral X-corr.
004348.5+415257.1	7.8	10.8	4.9	−196	−159	−−	Spatial peak
004412.7+410259.0	4.7	5.5	4.1	−338	−303	−−	Spectral X-corr.

Table 5.4 (cont'd)

Candidate	18 cm peak flux density[a]			v_{LSRK}	v_{HI}	v_{CO}	Detection
	Both pols. [mJy]	LL [mJy]	RR [mJy]	[km s^{-1}]	[km s^{-1}]	[km s^{-1}]	method
004523.2+412239.9	7.3	7.6	6.9	−249	−242	−−	Spectral peak
004609.3+414522.2	5.9	6.3	5.5	−117	−153	−−	Spectral X-corr.

[a]Measured flux density after continuum subtraction.

5.4.3 Verification of potential OH masers

Since all the OH maser candidates listed in Table 5.4 are of only moderate significance ($\sim 4.5\sigma$), we used ancillary data to help assess the likelihood that the 18-cm peaks are actual detections. This includes tests from the 18-cm data itself (polarization, observed linewidth) as well as information from other wavelengths (velocities from HI and CO, 24 μm emission).

5.4.3.1 Matching the gas velocity

One of the main verification techniques focused on the measured velocity of candidate peaks. M31 is a rotating spiral galaxy in which the interstellar gas has been mapped in multiple species. If the masers follow the bulk motion of the gas and have low peculiar motions compared to the disk, the observed velocity of the maser should match that of the gas. This is considered to be the strongest criterion for rejection of spurious weak candidates.

The rotational velocity in the rest frame of M31 must first be transformed to the observed LSRK velocity. For an inclined flat disk with orbits assumed to be concentric and circular, the line-of-sight velocity for a point on the disk is $v_{los} = \Omega[r]\ \sin(i)\ \mathbf{r} \cdot \hat{\mathbf{k}}$, where $\Omega[r]$ is the angular rotational velocity, i is the inclination angle, $\mathbf{r}$ is the vector between the center and a point on the disk, and $\hat{\mathbf{k}}$ is the unit vector parallel to the galaxy's observed major axis (Binney & Merrifield, 1998). The observed velocity for a rotating point in an inclined disk will be:

$$v_{obs} = v_{sys} + v_{rot}\ \sin[\phi]\ \sin[i], \tag{5.8}$$

where v_{sys} is the systemic velocity of the galaxy with respect to the observing frame, v_{rot} the rotational velocity, ϕ the azimuthal angle from the galaxy's major axis, and i the inclination of the disk. Both v_{sys} and v_{obs} are the radial component of velocities and can be calculated from Doppler shifts. From an observing standpoint, a single point on the disk in RA and declination must be deprojected (to find the true values of ϕ and R, both of which are foreshortened by inclination) and then transformed in velocity frames, which we have done for M31.

The velocities of possible OH maser detections are compared to two probes of the M31 gas content: the molecular gas from CO emission (Nieten et al., 2006) and the atomic gas from HI (Chemin et al., 2009; Corbelli et al., 2010). The HI gas was mapped in two independent 21-cm surveys, with a rotation curve fit to M31 as a function of radius. The rotation curves of Chemin et al. (2009) and Corbelli et al. (2010) have a systematic offset of $\simeq 20$ km s^{-1} near the 10-kpc ring. For the 18-cm data, we calculated the galactocentric radius R of each candidate and took the weighted mean of $v_{rot}[R]$ from the two rotation curves. Only data from Chemin et al. (2009) is used for $R < 8$ kpc. An OH line was considered a potential velocity match if v_{OH} was within 25 km s^{-1} of v_{HI}. This conservative bound was chosen to encompass the width of the VLA channels (4.4 km s^{-1}), the statistical and systematic uncertainties (each ~ 20 km s^{-1}) in the HI rotation curves, and possible peculiar motions of the maser with respect to the atomic gas.

For the candidates discovered by the peak-finding algorithm, 21/68 spectral peaks and 8/27 spatial peaks had 18-cm velocities within 25 km s^{-1} of the velocity implied by the HI rotation curve. For the peaks identified through spectral cross-correlation, 6/61 peaks had matching OH and HI velocities (Table 5.4).

The second set of velocities to which we compare the 18-cm data is from the ^{12}CO (1-0) map of Nieten et al. (2006). The CO gas closely traces the HI within $R < 18$ kpc, with an average deviation of the mean HI and CO velocities of only $\simeq 10$ km s^{-1}. While the overall velocity field is well-ordered in the 10-kpc ring, there do exist small cloud complexes that can differ from the bulk velocity by more than 100 km s^{-1}. Possible OH detections were thus mapped to a CO velocity only if it directly overlaid a measured location in the Nieten et al. (2006) velocity field. Due to the low

filling factor of the CO emission, only one 18-cm peak had a confirmed CO velocity; this is within 5 km s^{-1} of the HI velocity at that location.

5.4.3.2 Polarization

Since Galactic OH masers can be strongly polarized, we separately examined the emission from the two linear polarizations (LL and RR) in the VLA data. This serves as a likely confirmation criterion (but not rejection) for weak spectral line emission; a polarized maser may have strong emission in one polarization and be much weaker in the other, resulting in a marginal detection when the data are combined and averaged. The detection of a signal in both polarizations at the same location and frequency, however, would provide stronger evidence that a feature is real. We note that these are not true polarization maps, as we did not observe a polarization calibrator in conjunction with the data.

Candidate OH maser flux densities in both the LL and RR polarizations are given in Table 5.4. The flux density from the combined polarizations is close to the geometric mean from the individual polarizations, as expected, with the largest variation in polarized fluxes on the order of 50%. The difference in flux between combined and statistical polarizations for the sample shows no significant difference from a mean of zero, with a Student's t-test value of $t = 0.302$. Five peaks (003928.9+410244.6, 004049.7+410918.8, 004132.2+413351.7, 004224.6+413811.7, and 004348.5+415257.1) passed the significance test in one of the individual polarizations; no peaks had $> 4.5\sigma$ in both LL and RR.

A difference image of the continuum emission was made by subtracting the RR polarization data from LL (Figure 5.12). The resulting map is consistent with a Gaussian noise distribution with a mean level of zero and an rms of 0.52 mJy. We detected no structure in the differenced image (from either a point source or extended emission) that would be a result of significant polarization. These results are consistent with the 20 cm data of Beck et al. (1998), who found that polarization in M31 out to a 12 kpc radius was only $\sim 6\%$, with brighter emission having smaller degrees of polarization.

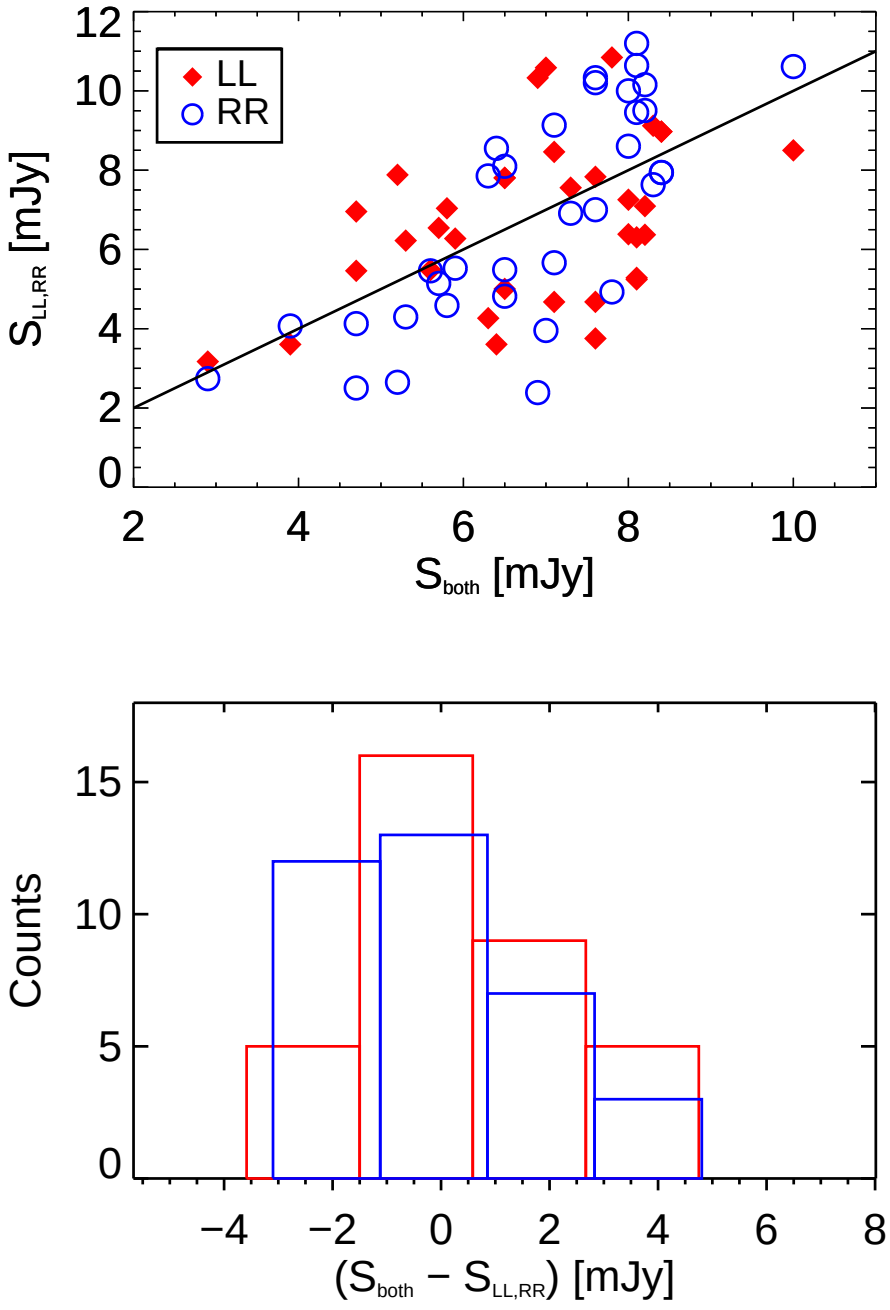

Figure 5.11 Comparison of the peak flux densities for 18-cm maser candidates for polarization data. Top: Peak flux density for combined polarization vs. data in LL and RR; the solid line is a 1:1 match. Bottom: histogram of the difference between combined and polarized data for the sample.

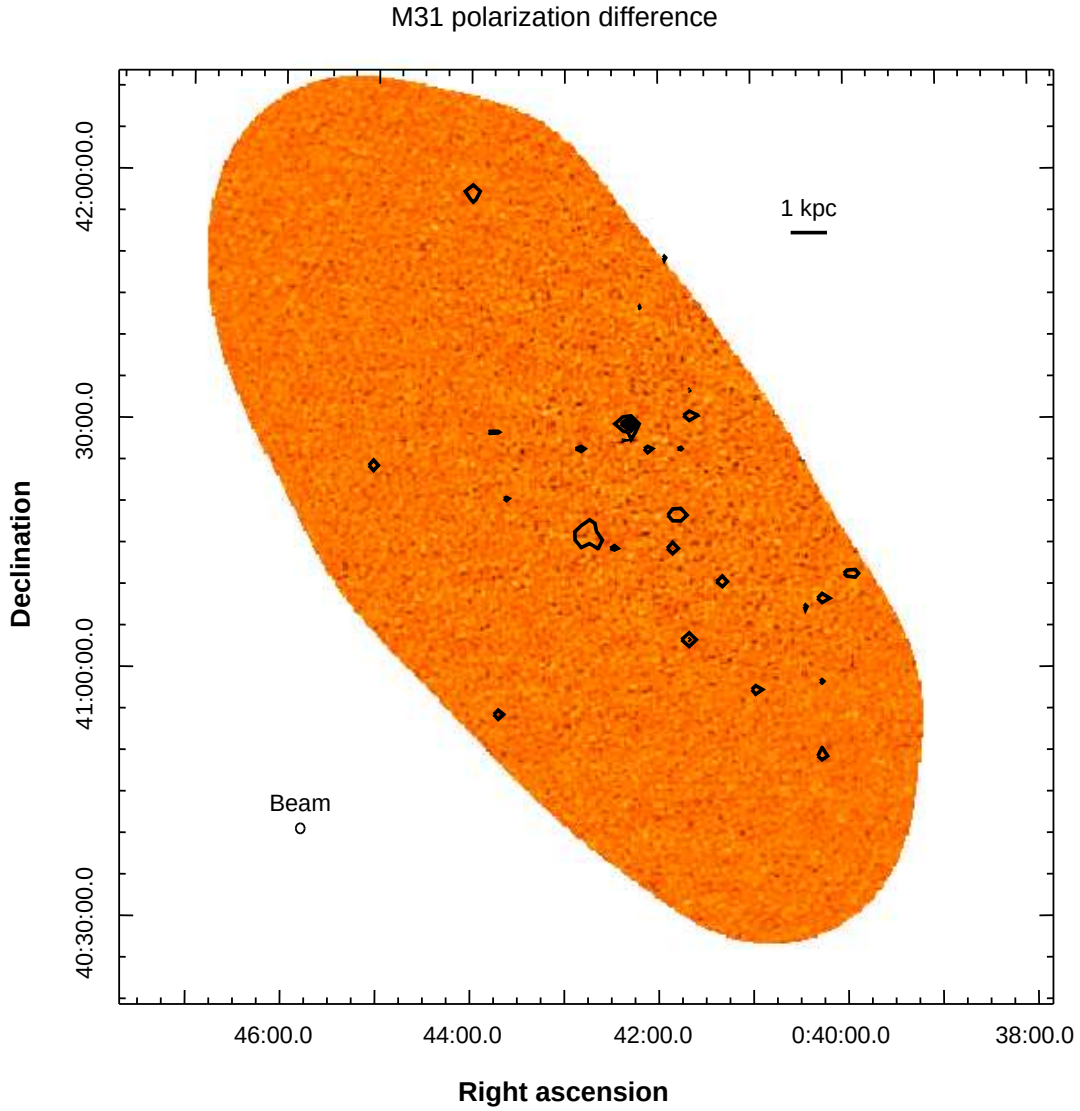

Figure 5.12 Difference image of LL and RR polarization maps of M31 at 18 cm. Contours show the strongest emission from the 18-cm continuum images with combined polarizations; displayed contour levels are 10–50 mJy. No structure or point sources are apparent in the differenced image.

5.4.3.3 Observed linewidths

The most luminous complex of OH masers in the Galaxy (W3 OH) has a linewidth of $\Delta v_{1665} \simeq 3$ km s^{-1} (Argon et al., 2000), which is less than the velocity resolution of the 18-cm VLA observations. As a result, single-channel peaks resembling spectral delta functions cannot be ruled out as possible candidates; however, strong emission in neighboring velocity channels may be of additional help in verifying possible candidates. Like the 18-cm polarization, velocity widths cannot serve as a rejection criterion, but could support the case for a marginal candidate.

From the candidate peaks with $> 4.5\sigma$ significance that matched the expected HI velocity, only 9/32 had full-width half-maxima greater than one channel. These include all of the candidates identified through spectral cross-correlation, which weights the feature width more heavily than simple peak-finding when evaluating a detection.

5.4.3.4 24 μm emission

The final steps in evaluating the likelihood of an OH detection examined the candidate environments to see if they might be expected to show maser emission. The most basic requirements for the production of a maser are the existence of a maser pump and a background source that can be amplified. We compared the locations of the OH maser candidates to two maps of M31: a 24 μm map that traces the distribution of dusty star-forming regions (presumably the source of OH pumping photons), and a 20-cm radio map that identifies sources of background continuum.

A 24 μm image from the MIPS instrument on *Spitzer* (Gordon et al., 2006) shows the distribution of HII regions in M31. The brightest compact sources are likely (ultra)compact HII regions, which are known to be a likely indicator of H_2O maser emission (Castangia et al., 2008). Figure 5.13 shows the locations of the candidate 18-cm detections overlaid on the 24 μm emission. The majority of the 18-cm peaks lie outside the 10-kpc ring, which hosts the bulk of the brightest and most compact 24 μm sources. None of the 18-cm peaks have a strong 24 μm source (down to a level of 1 MJy/sr) within the VLA beam. For comparison, we also show the locations of five 22.0 GHz

H_2O masers (Darling, 2011) and one 6.7 GHz CH_3OH maser (Sjouwerman et al., 2010) on the same map; all six of these masers are associated with a compact 24 μm source brighter than 4 MJy/sr. Although Darling (2011) shows that the 24 μm emission is not predictive of the maser luminosity (likely due to non-linearities in the pumping mechanism), the lack of any association of the 18-cm peaks with star-forming regions argues against the 18-cm candidates being true detections. This is supported by the dearth of peaks within the 10-kpc star-forming ring or the M31 nucleus.

We also compared the location of the 18-cm candidates to published maps of the radio continuum background. Figure 5.14 shows a 20-cm map of M31 from Beck et al. (1998). The dynamic range in this map is dominated by the strong emission from point sources (several hundreds of mJy beam^{-1}), while the diffuse emission from the 10-kpc ring has a brightness of only 1–2 mJy beam^{-1}. Among the 18-cm peaks, two candidates show possible associations with a strong radio continuum source: 004055.2+405719.0 (with the 20-cm source 37W067) and 003952.7+410416.2 (with 37W043; Walterbos et al., 1985). We also analyzed the radio continuum in a second map of M31 with lower dynamic range, in which point sources with $S_{20} > 2$ mJy were removed; none of the OH peaks are associated with weaker sources of compact radio continuum.

The final analysis of the OH maser candidates, based on the quality of the 18-cm data and ancillary evidence, suggests that we have detected no masers in M31 above a limit of $S_{peak} = 10$ mJy. None of the candidates listed in Table 5.4 have peak flux densities that are more than 6 σ above the noise in the 18-cm data, and none are located in the primary star-forming regions of M31 (the 10-kpc ring and the galactic nucleus) where one would expect masers to be found. Several OH peaks are likely good candidates for follow-up searches, including 004045.6+411318.7 (highest peak flux density in the sample), 003952.7+410416.2 and 004055.2+405719.0 (possible association with radio continuum emission), and the five peaks detected above the significance threshold in one of the two polarizations. The remainder of the discussion in this chapter, however, assumes that no clear detections of OH emission have been made based on the VLA observations.

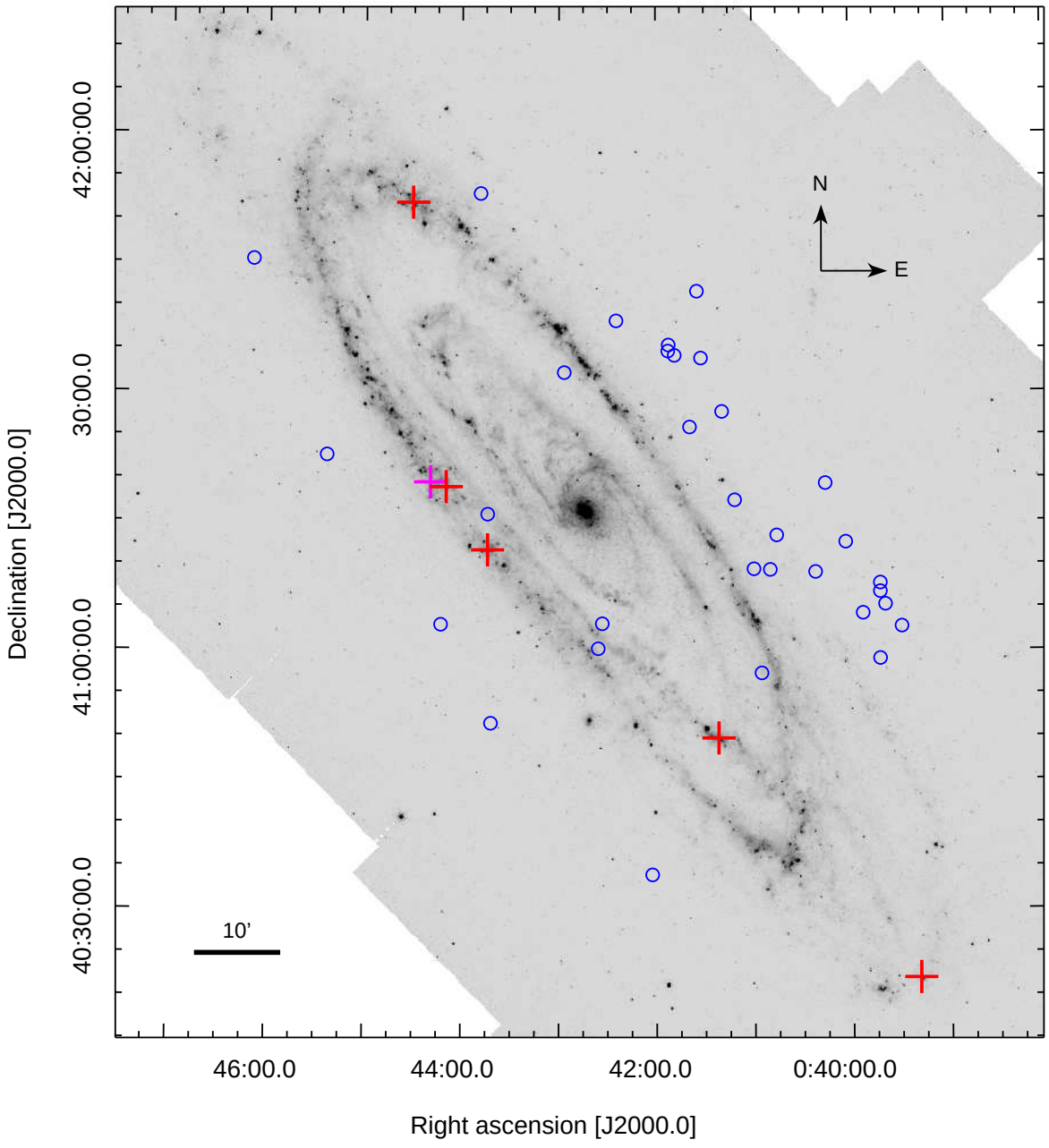

Figure 5.13 *Spitzer* 24 μm image of M31 from Gordon et al. (2006). The blue circles mark the locations of possible 18-cm OH maser detections (Table 5.4; the size of the circle shows the 45″ diameter of the VLA beam. Crosses show the locations of the recently-discovered CH_3OH (magenta; Sjouwerman et al., 2010) and H_2O (red; Darling, 2011) masers in M31.

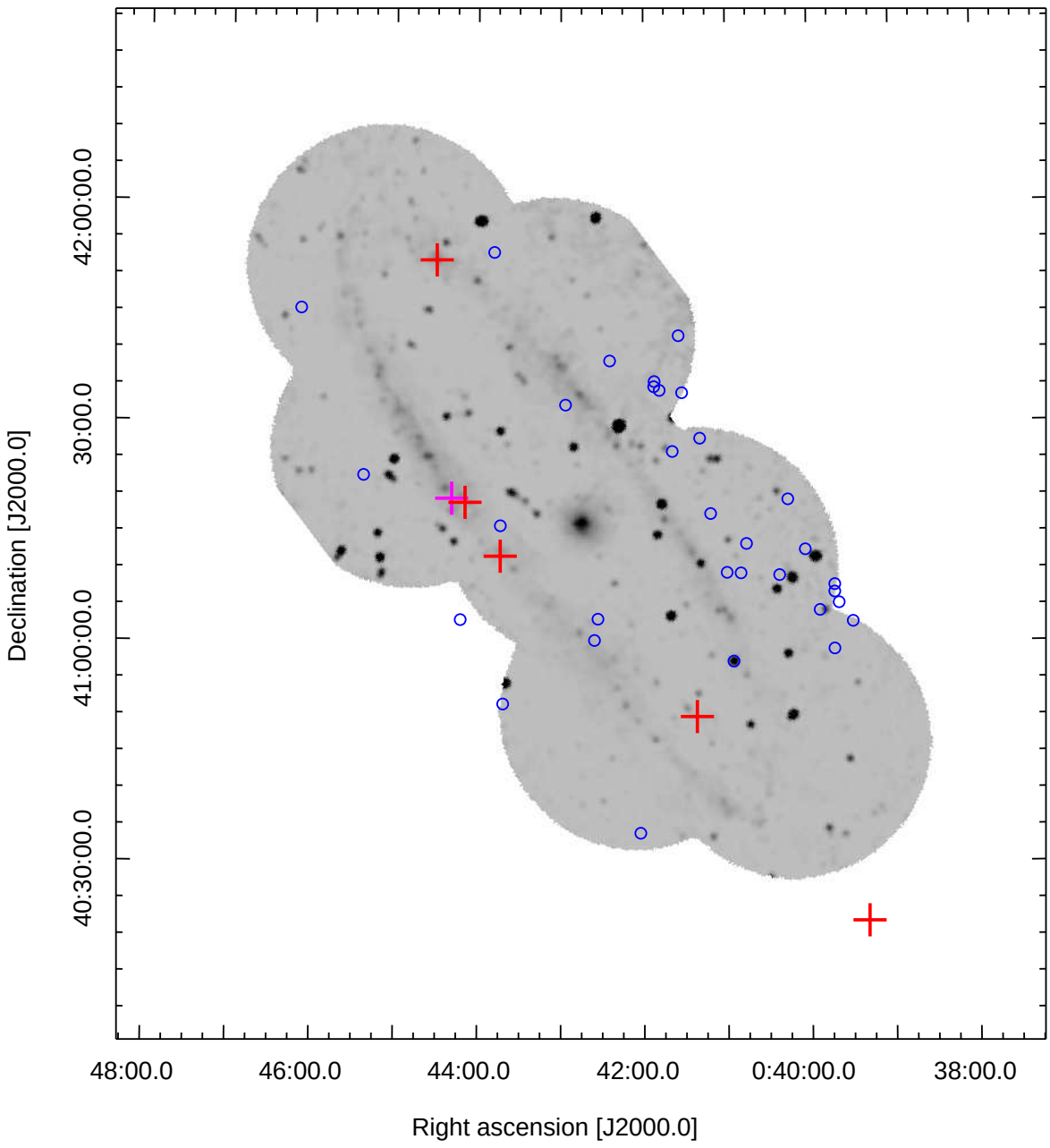

Figure 5.14 VLA 20 cm image of M31 (Beck et al., 1998). Symbols are the same as in Figure 5.13. The peak flux density of the image is 260.4 mJy beam^{-1} for the point source 37W115, with an rms noise of $45 - 85$ μJy beam^{-1} for the map.

5.4.4 Absorption of OH lines toward continuum sources

In addition to possible maser lines, an 18-cm spectral line map can also be used to search for OH absorption toward radio-bright continuum. We examined point sources from the 20-cm survey of Walterbos et al. (1985), which are likely HII regions or supernova remnants. Excluding 37W115 (which displays obvious image defects), there are 25 objects in the 18-cm primary beam that we measure with peak flux densities above the survey of 10 mJy (Table 5.5). We computed optical depths and analyzed spectra near the velocity implied by the HI gas (covering a velocity width of $\Delta v = 25$ km s^{-1}).

None of the bright 18-cm continuum point sources showed evidence for OH absorption. The average 1-σ upper limit on the peak optical depth was $\tau = 0.26 \pm 0.23$ (Table 5.5). If the OH gas in the galaxy is optically thin and in LTE, the total column density of an absorption feature is (e.g. Liszt & Lucas, 1996):

$$N_{OH} = 4.03 \times 10^{14} \left(\frac{T_{ex}}{f_c} \right) \int \tau_{1665} \, dv \text{ cm}^{-2}, \tag{5.9}$$

where T_{ex} is the excitation temperature in K, f_c is the covering factor of the OH gas, and dv is in km s^{-1}. The prefactor from Liszt & Lucas (1996) has been multiplied by a factor of 1.8 to account for the 9:5 ratio of the thermal 1667 and 1665 MHz line intensities (Equation 1.20). For a Gaussian with FWHM=15 km s^{-1}, the limits on τ_{peak} imply an average upper limit on the OH column density of $N_{OH} < 1.7 \times 10^{15} \left(\frac{T_{ex}}{f_c} \right)$ cm^{-2}. This is three orders of magnitude higher than the average OH column in the Milky Way measured away from the Galactic plane (Colgan et al., 1989), and thus does not place a strong limit on the molecular gas content of M31. We note that this limit is consistent with measurements of HI absorption in M31 (Dickey & Brinks, 1993) if the OH abundance is $N_{OH}/N_{HI} \lesssim 10^{-6}$.

Table 5.5. Continuum sources and OH absorption limits in M31

Name	RA J2000	Dec. J2000	S_{1420} [mJy]	S_{1665} [mJy]	v_{HI} [km s^{-1}]	N_{OH} 10^{14} cm^{-2}
37W043	00:39:49.4	+41:04:21.8	11.5	14.1	−373	< 54.
37W045	00:39:56.3	+41:11:39.0	54.7	28.5	−351	< 22.
37W050	00:40:13.4	+41:08:44.2	34.9	34.1	−361	< 17.
37W051	00:40:13.7	+40:50:04.9	34.7	31.2	−468	< 16.
37W052	00:40:16.8	+40:58:25.9	24.8	17.8	−413	< 45.
37W057	00:40:24.5	+41:07:13.0	31.3	21.6	−370	< 29.
37W063	00:40:44.4	+40:48:45.6	12.8	13.7	−524	< 45.
37W067	00:40:55.9	+40:57:24.1	29.9	27.5	−468	< 13.
37W081	00:41:19.7	+41:10:43.1	19.6	32.3	−370	< 33.
37W089	00:41:39.3	+41:30:29.7	35.8	46.9	−286	< 50.
37W091	00:41:41.2	+41:03:34.5	56.8	45.2	−507	< 7.1
37W094	00:41:47.8	+41:18:48.9	46.8	56.2	−322	< 16.
37W095	00:41:51.0	+41:14:38.0	26.9	36.0	−353	< 33.
37W115	00:42:18.7	+41:29:27.1	373.4	272.3	−262	−−
37W131	00:42:35.7	+41:57:46.5	76.4	20.9	−229	< 16.
37W144	00:42:51.6	+41:26:29.3	23.7	43.6	−205	< 43.
37W168	00:43:41.2	+40:54:29.1	64.9	22.7	−331	< 37.
37W169	00:43:44.7	+41:28:43.0	25.3	34.5	−71	< 71.
37W175	00:43:58.9	+41:57:17.2	58.1	48.1	−154	< 9.6
37W185	00:44:18.4	+41:13:38.5	12.6	12.1	−272	< 170.
37W188	00:44:24.0	+41:30:43.2	11.7	11.5	−153	< 62.
37W205	00:45:02.0	+41:24:52.7	43.3	24.9	−228	< 50.
37W207	00:45:05.9	+41:22:43.6	13.6	18.2	−238	< 65.
37W210	00:45:10.9	+41:09:15.8	10.9	8.8	−278	< 140.
37W211	00:45:11.7	+41:11:27.8	32.1	16.7	−273	< 67.
37W213	00:45:13.5	+41:14:47.5	22.6	13.7	−265	< 100.

Note. — Nomenclature of the sources is from Walterbos et al. (1985); S_{1420} is the peak flux they measure at 1420 MHz. S_{1665} is the peak flux measured at 1665 MHz; v_{HI} is the expected LSRK velocity of OH absorption based on the HI rotation curve. Limits on N_{OH} assume a 3σ detection at FWHM=15 km s^{-1}, $T_{ex} = 10$ K, and $f_c = 1$.

5.5 Discussion

5.5.1 Expected number of OH masers in M31

The non-detection of any OH masers in M31 can be compared to the expected number of detections by extrapolating from the luminosity distribution of masers in the Milky Way. The Argon et al. (2000) survey of Galactic OH masers contains 91 complexes and is essentially complete for masers with peak flux densities above 1 Jy in the Galactic plane ($|l| < 0.3°$). The number of masers N with features more luminous than L_{OH} can then be parametrized as:

$$\log\ N = -\alpha(N_0 + \log\ [L_{OH}/L_{\odot}]), \tag{5.10}$$

where α is the slope of the power law distribution and N_0 the upper luminosity limit where one would expect only a single maser detection (Greenhill et al., 1990). Figure 5.10 shows the Galactic OH maser luminosity function along with a fit to the power-law portion ($-7.5 < \log\ [L_{OH}/L_{\odot}] < -5.0$) before the distribution begins to turn over. We fit a slope of $\alpha = -1.0$ and $N_0 = 4.8$ to the Milky Way data, implying that a galaxy with similar maser environments will host $\sim 1 - 2$ OH masers as luminous as $L_{OH} \sim 10^{-5}\ L_{\odot}$.

The isotropic line luminosity limit for an OH maser in the 18-cm data is calculated from Darling & Giovanelli (2000):

$$L_{OH}^{max} = 4\pi D_{M31}^2 (N\sigma) \left(\frac{\Delta v}{c}\right) \nu_{1665} \tag{5.11}$$

which assumes a boxcar line profile with velocity width Δv and height ($N\sigma$) above the rms noise of a non-detection spectrum. For the channel width of the VLA 18-cm data ($\Delta v = 4.4$ km s^{-1}) and a ($5\sigma = 10$ mJy) detection, $\log\ L_{OH}^{max} = -4.3\ L_{\odot}$. Figure 5.15 shows that this is larger than the limit for the brightest known masers in the Milky Way.

Finally, the OH luminosity function for the Milky Way must be scaled to the conditions in M31. Previous comparisons of maser luminosities (e.g., Brunthaler et al., 2006) scale N to the global star formation rate, which is assumed to be proportional to the maser population. Adopting

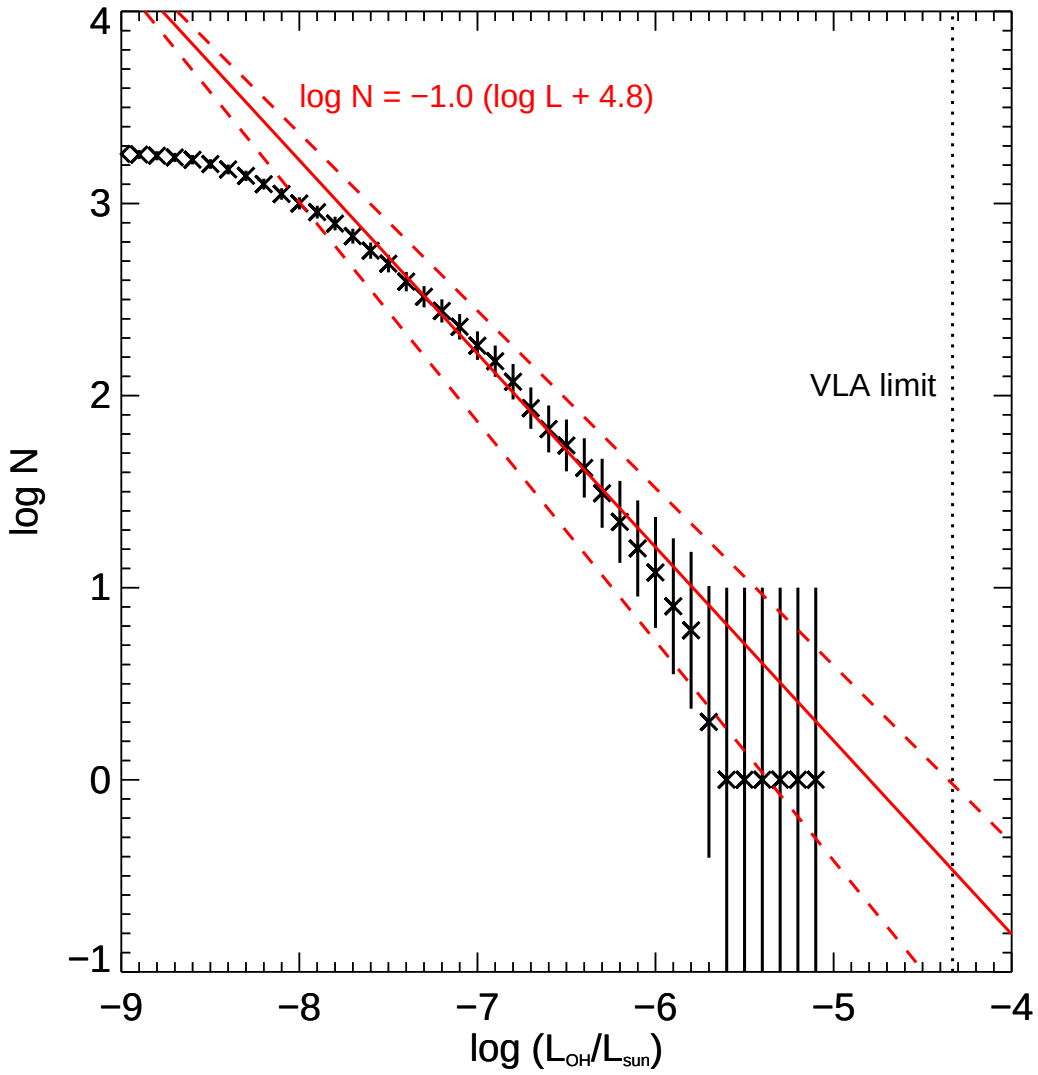

Figure 5.15 Galactic OH luminosity function showing the number of masers N brighter than a given luminosity L_{OH}; uncertainties are assumed to be Poisson-distributed. The Galactic OH maser data is taken from Argon et al. (2000). The red line shows the power-law fit to the luminosity function over the 3 most luminous dex and assuming a characteristic distance of $D = 3$ kpc for the OH masers; the dotted red lines show the fit if $D = 2$ and 4 kpc. The dotted line shows the luminosity limit for the 18-cm VLA survey of M31.

star formation rates of 4 $M_\odot$ yr^{-1} for the Milky Way (Diehl et al., 2006) and 0.35 $M_\odot$ yr^{-1} for M31 (Tabatabaei & Berkhuijsen, 2010), the OH luminosity function implies that we would have expected to detect $N \sim 10^{-1.0(-4.3+4.8)} \times (0.35/4) \simeq 0.03$ masers in M31, which is consistent with the result of no detections in our 18-cm VLA survey.

The expected number of masers calculated from Equation 5.10 does rest on a number of different assumptions which could change our estimate of N. The majority of OH maser complexes in the Galaxy do not have well-determined distances, and so the luminosity function is estimated using the OH peak brightness and a characteristic distance of $D = 3$ kpc. Increasing (or decreasing) D by 1 kpc changes the estimate of N at the VLA sensitivity limit by ~ 0.5 dex; N increases if the Galactic masers are more distant. The relative scaling of the luminosity functions is also uncertain; Robitaille & Whitney (2010) measure a total SFR for the Milky Way of $(0.68 - 1.45)$ $M_\odot$ yr^{-1}, which would increase the estimate of N by a factor of $2.5 - 6$. Finally, the quoted sensitivity for the 18-cm data is based on a conservative 5σ limit; lowering this would also increase the expectation of N. In the most permissive case, a 3σ limit with $SFR_{MW} = 0.68$ $M_\odot$ yr^{-1} and $D = 4$ kpc would predict $N \simeq 0.8$ masers, still well within the expectations of no detections. By the same line of reasoning, however, the lowest estimate of N would predict ~ 0.006 OH masers in M31 detectable at the VLA sensitivity limit.

We conclude that the non-detection of any OH masers in M31 is consistent with the known environmental properties of M31. Without an increase in survey sensitivity by at least 1–2 orders of magnitude, there is no evidence from OH that conditions in star formation regions within M31 are significantly different from those in the Milky Way.

5.5.2 Water masers in M31

The primary goal of the original OH survey was to use OH masers as tracers for follow-up observations of higher-frequency masers, particularly H_2O. In the Milky Way, the presence of an OH maser in a star-forming region is associated with a H_2O maser $\sim 80\%$ of the time (Breen et al., 2010), a similar rate to that of OH and methanol masers. This likely association between

maser species, combined with the possibility of a complete survey of M31 in OH due to its larger beam size, motivated the initial search at 18-cm. Following our 18-cm observations (but prior to publication of this thesis), Darling (2011) reported the detection of five H_2O maser complexes in Andromeda by targeting sources of bright 24 μm emission with the Green Bank Telescope (GBT).

Given the known association between OH and water masers in the Galaxy and the brightness of the M31 H_2O masers (up to 122 mJy), we examined the 18-cm data closely for OH at the five positions reported by Darling (2011). The physical locations of the H_2O masers are shown in Figure 5.13; 4/5 lie in the 10-kpc ring and within the primary beam of the 18-cm observations. None of the beams for H_2O maser detections overlap with those of possible 18-cm detections (Table 5.4). The 18-cm spectra at each location are shown in Figure 5.16; all are also consistent with non-detections of OH in these channels. The peak flux densities for the four masers within the 18-cm beam are all less than 2 mJy, with 2σ limits of $2-4$ mJy for the 4.4 km s^{-1} channels.

5.5.3 Methanol masers in M31

Shortly before the publication of this thesis, Sjouwerman et al. (2010) also reported the detection of a single 6.7 GHz Class II CH_3OH maser using the VLA. This was the second methanol maser discovered outside the Milky Way (after the LMC) and the first maser detection of any kind in M31. Detection was confirmed with follow-up observations with the EVLA in 2010.

The methanol maser has a peak flux of 8 mJy beam^{-1} and a linewidth of 5 km s^{-1}. It is located near the edge of the 10-kpc ring, at a galactocentric radius of 12.7 kpc. Nearby peaks in CO and mid-infrared emission indicate the presence of molecular gas and warm dust, indicating a possible relation between the maser and a star-forming region. The resolution of the CO is insufficient to determine if the peaks are truly associated with each other; however, *Spitzer* 24 μm data show that the compact infrared source IRAS 00416+4104 is coincident with the methanol maser. Sjouwerman et al. (2010) also reported non-detection of H_2O maser emission at the same location with a 2σ limit of 10 mJy beam^{-1} in 0.42 km s^{-1} channels. No observations were reported in their paper for searches of OH masers near the methanol detection.

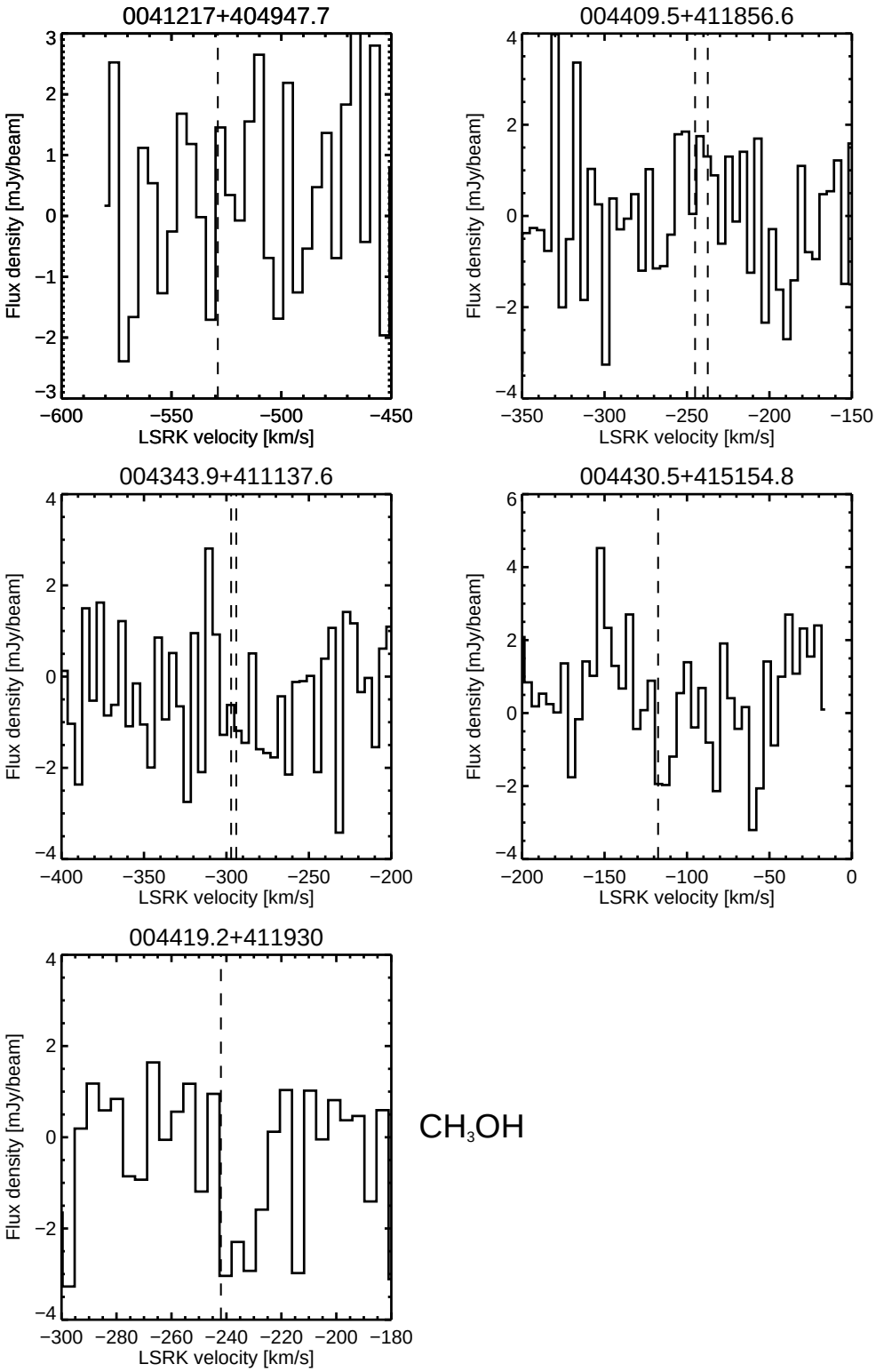

Figure 5.16 VLA 18-cm spectra of M31 at the locations of four H_2O masers (*top four*) from Darling (2011) and one CH_3OH maser (*bottom*) from Sjouwerman et al. (2010). The central velocities of the masers are indicated with dashed lines; the H_2O masers 004409.5+411856.6 and 004343+411137.6 both have two identified components. There is no 18-cm data for the fifth H_2O maser, which lies outside the primary beam of our survey.

Following the discovery of the methanol maser, we made a close inspection of the 18-cm data in the same region. The methanol maser is located at $\alpha = 00^h44^m19.2^s, \delta = 41°19'30''$ [J2000]. The peak flux at this location in the 18-cm radio continuum image is 0.50 mJy beam^{-1}, consistent with the average flux density along the 10-kpc ring. The OH spectrum for this location is also displayed in Figure 5.16. There is no indication of OH emission at the matching velocity, with a 2σ limit of 3.3 mJy beam^{-1} in 4.4 km s^{-1} channels. Similarly, the channel map at $v_{LSRK} = -240$ km s^{-1} shows no spatial peak at the location of the methanol maser (Figure 5.17).

We note that the brightest confirmed Galactic methanol maser, W3(OH), would be only three times brighter than the M31 methanol maser if placed at the same distance. While Galactic OH and methanol masers show a weak correlation in their peak flux densities, the methanol is typically an order of magnitude brighter than OH (Caswell et al., 1995). As a result, it has not been firmly established if methanol and OH masers are generated in the same physical locations within HII regions. Our non-detection of OH at the location of the M31 methanol maser is thus consistent with known statistics on Galactic-analog masers.

No information was given in the publication on the spatial coverage or flux limits of the methanol survey. The peak flux density of the methanol maser (8 mJy beam^{-1}), however, would place it on the high-end tail of the distribution of peak flux densities for known CH_3OH masers in the Milky Way (Goldsmith et al., 2008). It is thus possible that this is the brightest CH_3OH source in M31, especially considering the association of methanol masers with massive star forming regions and the lower SFR of M31 compared to the Milky Way. This is supported by non-detections of methanol masers in M33 (Goldsmith et al., 2008) and a low detection rate of methanol in the Magellanic Clouds (Beasley et al., 1996). Observations of M31 in methanol are continuing, both to search for additional masers and to begin VLBI measurements of the CH_3OH detection.

5.5.4 Hubble Space Telescope observations of the proper motion of M31

While the discovery of both the CH_3OH and H_2O masers have identified sources that could be used to measure v_t within epochs of 2–3 years, an independent method has announced the first

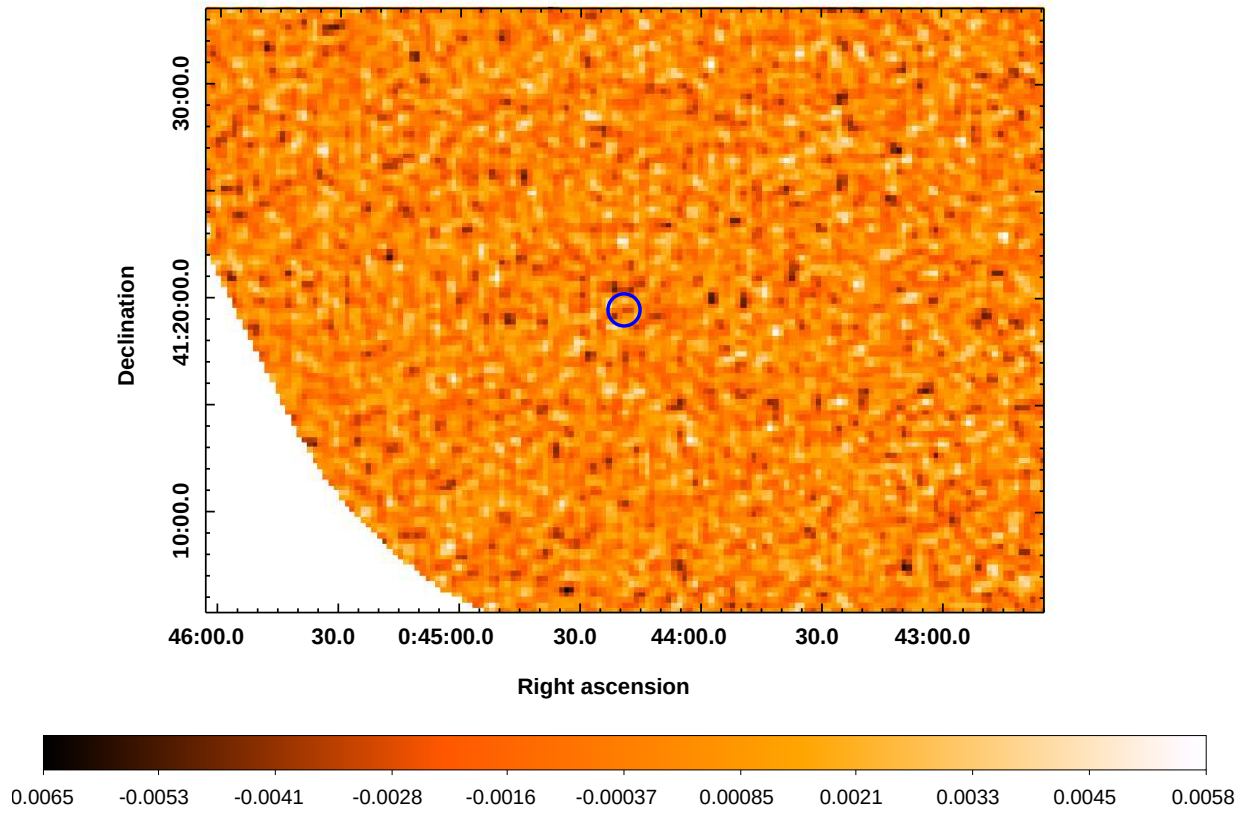

Figure 5.17 VLA image of the OH spectral line map of M31 at $v_{LSRK} = -240$ km s^{-1}. The blue circle at ($\alpha = 00^h44^m19.2^s, \delta = 41°19'30''$) indicates the location of the CH_3OH maser reported by Sjouwerman et al. (2010); the diameter of the circle is twice the beamwidth of the VLA synthesized beam at 1.6 GHz.

measurement of M31's transverse motion. van der Marel (2008) utilized optical images from the Hubble Space Telescope to measure the proper motion of M31, using high-precision astrometry of three star fields. Observations were made using both the ACS and WFC3 instruments in epochs separated by 6–8 years. In results announced (but not yet published) just before the defense of this thesis, they measured heliocentric proper motions corresponding to $v_N = -134 \pm 47$ km s^{-1} and $v_W = -103 \pm 47$ km s^{-1}, with an accuracy of 13 μas yr^{-1} (49 km s^{-1}). The total galactocentric magnitude of their measurement for v_t is less than 35 km s^{-1}, consistent with a pure radial orbit for M31. It also implies that the M31-M33 system is tightly bound, placing constraints on the tidal disruption of M33 by M31 (Bekki, 2008).

5.6 Future work

The independent discovery of other maser species in M31, especially that of H_2O, removes several of the unique capabilities of an OH maser survey in the galaxy. However, the future of OH studies in M31 (and of its proper motion) is far from over. Measurements of proper motion by their very nature benefit from having multiple sources to which an astrometric solution can be fit; relative displacements on the sky will have components from the galaxy's transverse motion, its own rotation, and relative motions of masers within the galaxy (omitting rotation). While all these components can be fit, given sufficient accuracy and models of the galaxy rotation (Brunthaler et al., 2005, 2007), detection of multiple sources will decrease the uncertainty and permit measurements to be made over a shorter epoch. Therefore, the detection of *any* maser species will be of use in constraining further measurements of v_t.

Continued upgrades in instrumentation may also facilitate independent methods of measuring M31's proper motion. Our 18-cm survey re-confirmed the existence of several dozen radio-bright point sources within M31, likely HII regions or supernova remnants. Continuum sources can also be used to track proper motions; since even ultracompact HII regions would be resolved by the VLBA at a distance of 785 kpc, the brightness temperature (T_b) exclusively determines the flux density at which emission can be detected. For a typical HII region with $T_b = 10^4$ K, a beam of

1 milliarcsecond would have an rms of ~ 1 μJy. This level approaches the current sensitivity[6] of the High Sensitivity Array (HSA), with a current sensitivity level of $\sim 3-4$ μJy in an eight-hour integration for a 1 Gbps data recording rate. The data rate is in the midst of being upgraded to 4 Gbps for the VLBA, which should place such experiments on the threshold of possibility. Observations would also benefit for unusual HII regions where $T_b > 10^4$ K. If successful, this would provide a third method for measuring the transverse motion of M31, in addition to the maser and optical experiments.

The 18-cm observations have also demonstrated the limits on our knowledge of the OH component in M31. The limits placed on both emission and absorption from our survey are the first ever published for M31, but fall short of the levels necessary to use them as relevant physical diagnostics. Future OH observations will be significantly helped by two recent developments. The first is the new list of candidate OH targets consisting of the strongest peaks from our sample plus the six maser detections of Sjouwerman et al. (2010) and Darling (2011). Since the entirety of the disk has already been surveyed, a useful strategy will be to integrate deeply on these targets with a much smaller field of view and higher sensitivity. This will be a much more stringent test of whether multiple species of masers are located in the same star-forming regions (as they are in the Milky Way). Secondly, these observations will be able to make use of the increases in both sensitivity and bandwidth made capable by the completion of the EVLA. The expected 1σ rms for 1 km s^{-1} lines will be 0.5 mJy for a single 9-hr observation. This will improve on our VLA observations by at least an order of magnitude due to gains in both sensitivity and spectral resolution (Equation 5.11). Time allocation committees willing, these sources will be re-observed soon to finally measure (or at least strongly constrain) the OH content of our nearest major neighbor.

[6] `http://www.evlbi.org/cgi-bin/EVNcalc`

Bibliography

Alakoz, A. V., Slysh, V. I., Popov, M. V., & Val'tts, I. E. 2005, Astronomy Letters, 31, 375

Andersson, S., & van Dishoeck, E. F. 2008, A&A, 491, 907

Argon, A. L., Reid, M. J., & Menten, K. M. 2000, ApJS, 129, 159

Armus, L., Charmandaris, V., Bernard-Salas, J., Spoon, H. W. W., Marshall, J. A., Higdon, S. J. U., Desai, V., Teplitz, H. I., Hao, L., Devost, D., Brandl, B. R., Wu, Y., Sloan, G. C., Soifer, B. T., Houck, J. R., & Herter, T. L. 2007, ApJ, 656, 148

Armus, L., Charmandaris, V., Spoon, H. W. W., Houck, J. R., Soifer, B. T., Brandl, B. R., Appleton, P. N., Teplitz, H. I., Higdon, S. J. U., Weedman, D. W., Devost, D., Morris, P. W., Uchida, K. I., van Cleve, J., Barry, D. J., Sloan, G. C., Grillmair, C. J., Burgdorf, M. J., Fajardo-Acosta, S. B., Ingalls, J. G., Higdon, J., Hao, L., Bernard-Salas, J., Herter, T., Troeltzsch, J., Unruh, B., & Winghart, M. 2004, ApJS, 154, 178

Baan, W. A. 1989, ApJ, 338, 804

Baan, W. A. 1991, in Astronomical Society of the Pacific Conference Series, Vol. 16, Atoms, Ions and Molecules: New Results in Spectral Line Astrophysics, ed. A. D. Haschick & P. T. P. Ho, 45–+

Baan, W. A., Haschick, A., & Henkel, C. 1992a, AJ, 103, 728

Baan, W. A., Haschick, A. D., Buckley, D., & Schmelz, J. T. 1985, ApJ, 293, 394

Baan, W. A., Henkel, C., Loenen, A. F., Baudry, A., & Wiklind, T. 2008, A&A, 477, 747

Baan, W. A., & Klöckner, H.-R. 2006, A&A, 449, 559

Baan, W. A., Rhoads, J., Fisher, K., Altschuler, D. R., & Haschick, A. 1992b, ApJL, 396, L99

Baan, W. A., Salzer, J. J., & Lewinter, R. D. 1998, ApJ, 509, 633

Baan, W. A., Wood, P. A. D., & Haschick, A. D. 1982, ApJL, 260, L49

Barnard, E. E. 1917, AJ, 30, 175

Baudry, A., Walmsley, C. M., Winnberg, A., & Wilson, T. L. 1981, A&A, 102, 287

Beasley, A. J., Ellingsen, S. P., Claussen, M. J., & Wilcots, E. 1996, ApJ, 459, 600

Beck, R., Berkhuijsen, E. M., & Hoernes, P. 1998, A&AS, 129, 329

Bekki, K. 2008, MNRAS, 390, L24

Binney, J., & Merrifield, M. 1998, Galactic Astronomy (Princeton University Press)

Biraud, F., Bourgois, G., Crovisier, J., Fillit, R., Gerard, E., & Kazes, I. 1974, A&A, 34, 163

Bradford, C. M., Stacey, G. J., Fischer, J., Smith, H. A., Cohen, R. J., Greenhouse, M. A., Lord, S. D., Lutz, D., Maiolino, R., Malkan, M. A., & Rieu, N. Q. 1999, in ESA Special Publication, Vol. 427, The Universe as Seen by ISO, ed. P. Cox & M. Kessler, 861–+

Brandl, B. R., Bernard-Salas, J., Spoon, H. W. W., Devost, D., Sloan, G. C., Guilles, S., Wu, Y., Houck, J. R., Weedman, D. W., Armus, L., Appleton, P. N., Soifer, B. T., Charmandaris, V., Hao, L., Higdon, J. A. M. S. J., & Herter, T. L. 2006, ApJ, 653, 1129

Braun, R., & Thilker, D. A. 2004, A&A, 417, 421

Breen, S. L., Caswell, J. L., Ellingsen, S. P., & Phillips, C. J. 2010, MNRAS, 406, 1487

Bridge, C. R., Carlberg, R. G., & Sullivan, M. 2010, ApJ, 709, 1067

Briggs, D. S., Schwab, F. R., & Sramek, R. A. 1999, in Astronomical Society of the Pacific Conference Series, Vol. 180, Synthesis Imaging in Radio Astronomy II, ed. G. B. Taylor, C. L. Carilli, & R. A. Perley, 127–+

Briggs, F. H. 1998, A&A, 336, 815

Brown, J. M., Kaise, M., Kerr, C. M. L., & Milton, D. J. 1978, Molecular Physics, 36, 553

Brunthaler, A., Henkel, C., de Blok, W. J. G., Reid, M. J., Greenhill, L. J., & Falcke, H. 2006, A&A, 457, 109

Brunthaler, A., Reid, M. J., Falcke, H., Greenhill, L. J., & Henkel, C. 2005, Science, 307, 1440

Brunthaler, A., Reid, M. J., Falcke, H., Henkel, C., & Menten, K. M. 2007, A&A, 462, 101

Bullock, J. S., Kaplinghat, M., Fruchter, A., Geha, M., Simon, J., Strigari, L. E., & Willman, B. 2009, in Astronomy, Vol. 2010, astro2010: The Astronomy and Astrophysics Decadal Survey, 32–+

Castangia, P., Tarchi, A., Henkel, C., & Menten, K. M. 2008, A&A, 479, 111

Caswell, J. L. 2009, PASA, 26, 454

Caswell, J. L., & Haynes, R. F. 1981, MNRAS, 194, 33P

Caswell, J. L., Vaile, R. A., & Forster, J. R. 1995, MNRAS, 277, 210

Cesaroni, R., & Walmsley, C. M. 1991, A&A, 241, 537

Chapman, S. C., Blain, A. W., Smail, I., & Ivison, R. J. 2005, ApJ, 622, 772

Chemin, L., Carignan, C., & Foster, T. 2009, ApJ, 705, 1395

Chen, P. S., Shan, H. G., & Gao, Y. F. 2007, AJ, 133, 496

Chiar, J. E., Tielens, A. G. G. M., Whittet, D. C. B., Schutte, W. A., Boogert, A. C. A., Lutz, D., van Dishoeck, E. F., & Bernstein, M. P. 2000, ApJ, 537, 749

Colgan, S. W. J., Salpeter, E. E., & Terzian, Y. 1989, ApJ, 336, 231

Condon, J. J., Anderson, M. L., & Helou, G. 1991, ApJ, 376, 95

Condon, J. J., Cotton, W. D., Greisen, E. W., Yin, Q. F., Perley, R. A., Taylor, G. B., & Broderick, J. J. 1998, AJ, 115, 1693

Corbelli, E., Lorenzoni, S., Walterbos, R., Braun, R., & Thilker, D. 2010, A&A, 511, A89+

Dale, D. A., Smith, J. D. T., Armus, L., Buckalew, B. A., Helou, G., Kennicutt, Jr., R. C., Moustakas, J., Roussel, H., Sheth, K., Bendo, G. J., Calzetti, D., Draine, B. T., Engelbracht, C. W., Gordon, K. D., Hollenbach, D. J., Jarrett, T. H., Kewley, L. J., Leitherer, C., Li, A., Malhotra, S., Murphy, E. J., & Walter, F. 2006, ApJ, 646, 161

Darling, J. 2003, Physical Review Letters, 91, 011301

—. 2004, ApJ, 612, 58

—. 2007, ApJL, 669, L9

—. 2011, ApJL, 732, L2+

Darling, J., & Giovanelli, R. 2000, AJ, 119, 3003

—. 2001, AJ, 121, 1278

—. 2002a, AJ, 124, 100

—. 2002b, ApJ, 572, 810

—. 2006, AJ, 132, 2596

Dartois, E., Geballe, T. R., Pino, T., Cao, A.-T., Jones, A., Deboffle, D., Guerrini, V., Bréchignac, P., & D'Hendecourt, L. 2007, A&A, 463, 635

Dartois, E., & Muñoz-Caro, G. M. 2007, A&A, 476, 1235

de Vaucouleurs, G., de Vaucouleurs, A., Corwin, Jr., H. G., Buta, R. J., Paturel, G., & Fouque, P. 1991, Third Reference Catalogue of Bright Galaxies (Springer-Verlag)

Desai, V., Armus, L., Spoon, H. W. W., Charmandaris, V., Bernard-Salas, J., Brandl, B. R., Farrah, D., Soifer, B. T., Teplitz, H. I., Ogle, P. M., Devost, D., Higdon, S. J. U., Marshall, J. A., & Houck, J. R. 2007, ApJ, 669, 810

Diamond, P. J., Lonsdale, C. J., Lonsdale, C. J., & Smith, H. E. 1999, ApJ, 511, 178

Díaz-Santos, T., Charmandaris, V., Armus, L., Petric, A. O., Howell, J. H., Murphy, E. J., Mazzarella, J. M., Veilleux, S., Bothun, G., Inami, H., Appleton, P. N., Evans, A. S., Haan, S., Marshall, J. A., Sanders, D. B., Stierwalt, S., & Surace, J. A. 2010, ApJ, 723, 993

Dickey, J. M., & Brinks, E. 1993, ApJ, 405, 153

Diehl, R., Halloin, H., Kretschmer, K., Lichti, G. G., Schönfelder, V., Strong, A. W., von Kienlin, A., Wang, W., Jean, P., Knödlseder, J., Roques, J., Weidenspointner, G., Schanne, S., Hartmann, D. H., Winkler, C., & Wunderer, C. 2006, Nature, 439, 45

Downes, D., & Solomon, P. M. 1998, ApJ, 507, 615

Draine, B. T. 2003, ARA&A, 41, 241

Dudik, R. P., Weingartner, J. C., Satyapal, S., Fischer, J., Dudley, C. C., & O'Halloran, B. 2007, ApJ, 664, 71

Dunne, L., & Eales, S. A. 2001, MNRAS, 327, 697

Einasto, J., & Lynden-Bell, D. 1982, MNRAS, 199, 67

Elitzur, M. 1992a, Astronomical Masers (Kluwer Academic Publishers)

—. 1992b, ARA&A, 30, 75

Fakhouri, O., Ma, C., & Boylan-Kolchin, M. 2010, MNRAS, 406, 2267

Farrah, D., Bernard-Salas, J., Spoon, H. W. W., Soifer, B. T., Armus, L., Brandl, B., Charmandaris, V., Desai, V., Higdon, S., Devost, D., & Houck, J. 2007, ApJ, 667, 149

Feigelson, E. D., & Nelson, P. I. 1985, ApJ, 293, 192

Fischer, J., Sturm, E., González-Alfonso, E., Graciá-Carpio, J., Hailey-Dunsheath, S., Poglitsch, A., Contursi, A., Lutz, D., Genzel, R., Sternberg, A., Verma, A., & Tacconi, L. 2010, A&A, 518, L41+

Fish, V. L. 2007, in IAU Symposium, Vol. 242, IAU Symposium, ed. J. M. Chapman & W. A. Baan, 71–80

Frail, D. A., Goss, W. M., & Slysh, V. I. 1994, ApJL, 424, L111

Frayer, D. T., Ivison, R. J., Smail, I., Yun, M. S., & Armus, L. 1999, AJ, 118, 139

Galliano, F., Madden, S. C., Tielens, A. G. G. M., Peeters, E., & Jones, A. P. 2008, ApJ, 679, 310

Gao, Y., & Solomon, P. M. 2004a, ApJS, 152, 63

—. 2004b, ApJ, 606, 271

Genzel, R., Lutz, D., Sturm, E., Egami, E., Kunze, D., Moorwood, A. F. M., Rigopoulou, D., Spoon, H. W. W., Sternberg, A., Tacconi-Garman, L. E., Tacconi, L., & Thatte, N. 1998, ApJ, 498, 579

Goldreich, P., & Keeley, D. A. 1972, ApJ, 174, 517

Goldsmith, P. F., Pandian, J. D., & Deshpande, A. A. 2008, ApJ, 680, 1132

Gordon, K. D., Bailin, J., Engelbracht, C. W., Rieke, G. H., Misselt, K. A., Latter, W. B., Young, E. T., Ashby, M. L. N., Barmby, P., Gibson, B. K., Hines, D. C., Hinz, J., Krause, O., Levine, D. A., Marleau, F. R., Noriega-Crespo, A., Stolovy, S., Thilker, D. A., & Werner, M. W. 2006, ApJL, 638, L87

Goto, T., Arnouts, S., Inami, H., Matsuhara, H., Pearson, C., Takeuchi, T. T., Le Floc'h, E., Takagi, T., Wada, T., Nakagawa, T., Oyabu, S., Ishihara, D., Mok Lee, H., Jeong, W., Yamauchi, C., Serjeant, S., Sedgwick, C., & Treister, E. 2011, MNRAS, 410, 573

Greenhill, L. J., Henkel, C., Becker, R., Wilson, T. L., & Wouterloot, J. G. A. 1995, A&A, 304, 21

Greenhill, L. J., Moran, J. M., Reid, M. J., Gwinn, C. R., Menten, K. M., Eckart, A., & Hirabayashi, H. 1990, ApJ, 364, 513

Guhathakurta, P., van der Marel, R., Gilbert, K. M., Kalirai, J. S., Kollipara, P., Yniguez, B., Geha, M. C., Majewski, S. R., Beaton, R. L., Patterson, R. J., & SPLASH collaboration. 2007, in Bulletin of the American Astronomical Society, Vol. 38, American Astronomical Society Meeting Abstracts, 777–+

Gundermann, E. J. 1965, PhD thesis, Harvard University

Hachisuka, K., Brunthaler, A., Menten, K. M., Reid, M. J., Imai, H., Hagiwara, Y., Miyoshi, M., Horiuchi, S., & Sasao, T. 2006, ApJ, 645, 337

Hao, L., Spoon, H. W. W., Sloan, G. C., Marshall, J. A., Armus, L., Tielens, A. G. G. M., Sargent, B., van Bemmel, I. M., Charmandaris, V., Weedman, D. W., & Houck, J. R. 2005, ApJL, 625, L75

Hao, L., Weedman, D. W., Spoon, H. W. W., Marshall, J. A., Levenson, N. A., Elitzur, M., & Houck, J. R. 2007, ApJL, 655, L77

He, J. H., & Chen, P. S. 2004, New Astronomy, 9, 545

Henkel, C., Guesten, R., & Baan, W. A. 1987, A&A, 185, 14

Henkel, C., & Wilson, T. L. 1990, A&A, 229, 431

Henkel, C., Wouterloot, J. G. A., & Bally, J. 1986, A&A, 155, 193

Higdon, S. J. U., Armus, L., Higdon, J. L., Soifer, B. T., & Spoon, H. W. W. 2006, ApJ, 648, 323

Higdon, S. J. U., Devost, D., Higdon, J. L., Brandl, B. R., Houck, J. R., Hall, P., Barry, D., Charmandaris, V., Smith, J. D. T., Sloan, G. C., & Green, J. 2004, PASP, 116, 975

Hinshaw, G., Weiland, J. L., Hill, R. S., Odegard, N., Larson, D., Bennett, C. L., Dunkley, J., Gold, B., Greason, M. R., Jarosik, N., Komatsu, E., Nolta, M. R., Page, L., Spergel, D. N., Wollack, E., Halpern, M., Kogut, A., Limon, M., Meyer, S. S., Tucker, G. S., & Wright, E. L. 2009, ApJS, 180, 225

Ho, L. C., & Keto, E. 2007, ApJ, 658, 314

Houck, J. R., Roellig, T. L., van Cleve, J., Forrest, W. J., Herter, T., Lawrence, C. R., Matthews, K., Reitsema, H. J., Soifer, B. T., Watson, D. M., Weedman, D., Huisjen, M., Troeltzsch, J., Barry, D. J., Bernard-Salas, J., Blacken, C. E., Brandl, B. R., Charmandaris, V., Devost, D., Gull, G. E., Hall, P., Henderson, C. P., Higdon, S. J. U., Pirger, B. E., Schoenwald, J., Sloan, G. C., Uchida, K. I., Appleton, P. N., Armus, L., Burgdorf, M. J., Fajardo-Acosta, S. B., Grillmair, C. J., Ingalls, J. G., Morris, P. W., & Teplitz, H. I. 2004, ApJS, 154, 18

Hougens, J. 1970, The Calculation of Rotational Energy Levels and Rotational Line Intensities in Diatomic Molecules, Tech. rep., NIST

Hudson, E. R., Lewandowski, H. J., Sawyer, B. C., & Ye, J. 2006, Physical Review Letters, 96, 143004

Ibata, R., Martin, N. F., Irwin, M., Chapman, S., Ferguson, A. M. N., Lewis, G. F., & McConnachie, A. W. 2007, ApJ, 671, 1591

Ilbert, O., Capak, P., Salvato, M., Aussel, H., McCracken, H. J., Sanders, D. B., Scoville, N., Kartaltepe, J., Arnouts, S., Le Floc'h, E., Mobasher, B., Taniguchi, Y., Lamareille, F., Leauthaud, A., Sasaki, S., Thompson, D., Zamojski, M., Zamorani, G., Bardelli, S., Bolzonella, M., Bongiorno, A., Brusa, M., Caputi, K. I., Carollo, C. M., Contini, T., Cook, R., Coppa, G., Cucciati, O., de la Torre, S., de Ravel, L., Franzetti, P., Garilli, B., Hasinger, G., Iovino, A., Kampczyk, P., Kneib, J., Knobel, C., Kovac, K., Le Borgne, J. F., Le Brun, V., Fèvre, O. L., Lilly, S., Looper, D., Maier, C., Mainieri, V., Mellier, Y., Mignoli, M., Murayama, T., Pellò, R., Peng, Y., Pérez-Montero, E., Renzini, A., Ricciardelli, E., Schiminovich, D., Scodeggio, M., Shioya, Y., Silverman, J., Surace, J., Tanaka, M., Tasca, L., Tresse, L., Vergani, D., & Zucca, E. 2009, ApJ, 690, 1236

Imai, H., Ishihara, Y., Kameya, O., & Nakai, N. 2001, PASJ, 53, 489

Imanishi, M., Dudley, C. C., Maiolino, R., Maloney, P. R., Nakagawa, T., & Risaliti, G. 2007, ApJS, 171, 72

Impellizzeri, C. M. V., McKean, J. P., Castangia, P., Roy, A. L., Henkel, C., Brunthaler, A., & Wucknitz, O. 2008, Nature, 456, 927

Isobe, T., Feigelson, E. D., & Nelson, P. I. 1986, ApJ, 306, 490

Ivezic, Z., & Elitzur, M. 1997, MNRAS, 287, 799

Ivison, R. J., Smail, I., Dunlop, J. S., Greve, T. R., Swinbank, A. M., Stevens, J. A., Mortier, A. M. J., Serjeant, S., Targett, T. A., Bertoldi, F., Blain, A. W., & Chapman, S. C. 2005, MNRAS, 364, 1025

Johnston, K., Bullock, J. S., & Strauss, M. 2009, in Astronomy, Vol. 2010, astro2010: The Astronomy and Astrophysics Decadal Survey, 142–+

Kahn, F. D., & Woltjer, L. 1959, ApJ, 130, 705

Kandalian, R. A. 1996, Astrophysics, 39, 237

Kanekar, N. 2009, in Astronomy, Vol. 2010, astro2010: The Astronomy and Astrophysics Decadal Survey, 148–+

Kanekar, N., Chengalur, J. N., & Ghosh, T. 2010, ApJL, 716, L23

Kang, Y., Bianchi, L., & Rey, S. 2009, ApJ, 703, 614

Kartaltepe, J. S., Sanders, D. B., Le Floc'h, E., Frayer, D. T., Aussel, H., Arnouts, S., Ilbert, O., Salvato, M., Scoville, N. Z., Surace, J., Yan, L., Brusa, M., Capak, P., Caputi, K., Carollo, C. M., Civano, F., Elvis, M., Faure, C., Hasinger, G., Koekemoer, A. M., Lee, N., Lilly, S., Liu, C. T., McCracken, H. J., Schinnerer, E., Smolčić, V., Taniguchi, Y., Thompson, D. J., & Trump, J. 2010, ApJ, 709, 572

Kennicutt, Jr., R. C. 1998, ApJ, 498, 541

Kent, B., Braatz, J., & Darling, J. 2002, in Bulletin of the American Astronomical Society, Vol. 34, 1194–+

Kim, D., & Sanders, D. B. 1998, ApJS, 119, 41

Klöckner, H., & Baan, W. A. 2004, A&A, 419, 887

Klöckner, H., Baan, W. A., & Garrett, M. A. 2003, Nature, 421, 821

Knacke, R. F., & Thomson, R. K. 1973, PASP, 85, 341

Knowles, S. H., Johnson, K. J., Moran, J. M., & Ball, J. A. 1973, ApJL, 180, L117+

Kroeker, T. L., & Carlberg, R. G. 1991, ApJ, 376, 1

Lahuis, F., Spoon, H. W. W., Tielens, A. G. G. M., Doty, S. D., Armus, L., Charmandaris, V., Houck, J. R., Stäuber, P., & van Dishoeck, E. F. 2007, ApJ, 659, 296

Landt, H., Buchanan, C. L., & Barmby, P. 2010, MNRAS, 408, 1982

Lavalley, M., Isobe, T., & Feigelson, E. 1992, in Astronomical Society of the Pacific Conference Series, Vol. 25, Astronomical Data Analysis Software and Systems I, ed. D. M. Worrall, C. Biemesderfer, & J. Barnes, 245–+

Le Floc'h, E., Mirabel, I. F., Laurent, O., Charmandaris, V., Gallais, P., Sauvage, M., Vigroux, L., & Cesarsky, C. 2001, A&A, 367, 487

Le Floc'h, E., Papovich, C., Dole, H., Bell, E. F., Lagache, G., Rieke, G. H., Egami, E., Pérez-González, P. G., Alonso-Herrero, A., Rieke, M. J., Blaylock, M., Engelbracht, C. W., Gordon, K. D., Hines, D. C., Misselt, K. A., Morrison, J. E., & Mould, J. 2005, ApJ, 632, 169

Lequeux, J. 2005, The interstellar medium (Springer-Verlag)

Lev, B. L., Meyer, E. R., Hudson, E. R., Sawyer, B. C., Bohn, J. L., & Ye, J. 2006, Phys. Rev. A, 74, 061402

Levenson, N. A., Sirocky, M. M., Hao, L., Spoon, H. W. W., Marshall, J. A., Elitzur, M., & Houck, J. R. 2007, ApJL, 654, L45

Lin, L., Koo, D. C., Weiner, B. J., Chiueh, T., Coil, A. L., Lotz, J., Conselice, C. J., Willner, S. P., Smith, H. A., Guhathakurta, P., Huang, J.-S., Le Floc'h, E., Noeske, K. G., Willmer, C. N. A., Cooper, M. C., & Phillips, A. C. 2007, ApJL, 660, L51

Liszt, H., & Lucas, R. 1996, A&A, 314, 917

Litvak, M. M. 1969, ApJ, 156, 471

Litvak, M. M., McWhorter, A. L., Meeks, M. L., & Zeiger, H. J. 1966, Phys. Rev. Lett., 17, 821

Lo, K. Y. 2005, ARA&A, 43, 625

Lockett, P., & Elitzur, M. 2008, ApJ, 677, 985

Loeb, A., Reid, M. J., Brunthaler, A., & Falcke, H. 2005, ApJ, 633, 894

Lonsdale, C. J. 2002, in IAU Symposium, Vol. 206, Cosmic Masers: From Proto-Stars to Black Holes, ed. V. Migenes & M. J. Reid, 413–+

Lonsdale, C. J., Lonsdale, C. J., Diamond, P. J., & Smith, H. E. 1998, ApJL, 493, L13

Lonsdale, C. J., Lonsdale, C. J., Smith, H. E., & Diamond, P. J. 2003, ApJ, 592, 804

Lutz, D., Spoon, H. W. W., Rigopoulou, D., Moorwood, A. F. M., & Genzel, R. 1998, ApJL, 505, L103

Lynden-Bell, D. 1981, The Observatory, 101, 111

Lynden-Bell, D., & Lin, D. N. C. 1977, MNRAS, 181, 37

Madau, P., Pozzetti, L., & Dickinson, M. 1998, ApJ, 498, 106

Magnelli, B., Elbaz, D., Chary, R. R., Dickinson, M., Le Borgne, D., Frayer, D. T., & Willmer, C. N. A. 2009, A&A, 496, 57

Marciano, W. J. 1984, Physical Review Letters, 52, 489

Marshall, J. A., Herter, T. L., Armus, L., Charmandaris, V., Spoon, H. W. W., Bernard-Salas, J., & Houck, J. R. 2007, ApJ, 670, 129

McConnachie, A. W., Irwin, M. J., Ferguson, A. M. N., Ibata, R. A., Lewis, G. F., & Tanvir, N. 2005, MNRAS, 356, 979

McGee, R. X., Robinson, B. J., Gardner, F. F., & Bolton, J. G. 1965, Nature, 208, 1193

Momjian, E., Romney, J. D., Carilli, C. L., & Troland, T. H. 2006, ApJ, 653, 1172

Murphy, E. J., Chary, R., Alexander, D. M., Dickinson, M., Magnelli, B., Morrison, G., Pope, A., & Teplitz, H. I. 2009, ApJ, 698, 1380

Nenkova, M., Ivezić, Ž., & Elitzur, M. 2002, ApJL, 570, L9

Nenkova, M., Sirocky, M. M., Ivezić, Ž., & Elitzur, M. 2008a, ApJ, 685, 147

Nenkova, M., Sirocky, M. M., Nikutta, R., Ivezić, Ž., & Elitzur, M. 2008b, ApJ, 685, 160

Nieten, C., Neininger, N., Guélin, M., Ungerechts, H., Lucas, R., Berkhuijsen, E. M., Beck, R., & Wielebinski, R. 2006, A&A, 453, 459

Nikutta, R., Elitzur, M., & Lacy, M. 2009, ApJ, 707, 1550

Norris, R. P., Gardner, F. F., Whiteoak, J. B., Allen, D. A., & Roche, P. F. 1989, MNRAS, 237, 673

Ossenkopf, V., Henning, T., & Mathis, J. S. 1992, A&A, 261, 567

Parra, R., Conway, J. E., Elitzur, M., & Pihlström, Y. M. 2005, A&A, 443, 383

Peeters, E., Spoon, H. W. W., & Tielens, A. G. G. M. 2004, ApJ, 613, 986

Perkins, F., Gold, T., & Salpeter, E. E. 1966, ApJ, 145, 361

Pihlström, Y. M., Baan, W. A., Darling, J., & Klöckner, H.-R. 2005, ApJ, 618, 705

Pihlström, Y. M., Conway, J. E., Booth, R. S., Diamond, P. J., & Polatidis, A. G. 2001, A&A, 377, 413

Pihlström, Y. M., Fish, V. L., Sjouwerman, L. O., Zschaechner, L. K., Lockett, P. B., & Elitzur, M. 2008, ApJ, 676, 371

Raychaudhury, S., & Lynden-Bell, D. 1989, MNRAS, 240, 195

Reid, M. J. 2007, in IAU Symposium, Vol. 242, IAU Symposium, ed. J. M. Chapman & W. A. Baan, 522–529

Reid, M. J., Brunthaler, A., Menten, K. M., Loinard, L., & Wrobel, J. 2009a, ArXiv e-prints

Reid, M. J., Menten, K. M., Zheng, X. W., Brunthaler, A., Moscadelli, L., Xu, Y., Zhang, B., Sato, M., Honma, M., Hirota, T., Hachisuka, K., Choi, Y. K., Moellenbrock, G. A., & Bartkiewicz, A. 2009b, ApJ, 700, 137

Reid, M. J., & Moran, J. M. 1981, ARA&A, 19, 231

Richards, A. M. S., Knapen, J. H., Yates, J. A., Cohen, R. J., Collett, J. L., Wright, M. M., Gray, M. D., & Field, D. 2005, MNRAS, 364, 353

Richardson, J. C., Irwin, M., McConnachie, A. W., Martin, N. F., Dotter, A., Ferguson, A. M. N., Ibata, R. A., Chapman, S., Lewis, G. F., Tanvir, N. R., & Rich, R. M. 2011, ArXiv e-prints

Rigopoulou, D., Kunze, D., Lutz, D., Genzel, R., & Moorwood, A. F. M. 2002, A&A, 389, 374

Robishaw, T. 2008, PhD thesis, University of California, Berkeley

Robishaw, T., Quataert, E., & Heiles, C. 2008, ApJ, 680, 981

Robitaille, T. P., & Whitney, B. A. 2010, ApJL, 710, L11

Roche, P. F., & Aitken, D. K. 1984, MNRAS, 208, 481

Rohlfs, K., & Wilson, T. L. 2004, Tools of radio astronomy (Springer)

Roussel, H., Helou, G., Hollenbach, D. J., Draine, B. T., Smith, J. D., Armus, L., Schinnerer, E., Walter, F., Engelbracht, C. W., Thornley, M. D., Kennicutt, R. C., Calzetti, D., Dale, D. A., Murphy, E. J., & Bot, C. 2007, ApJ, 669, 959

Rovilos, E., Diamond, P. J., Lonsdale, C. J., Lonsdale, C. J., & Smith, H. E. 2003, MNRAS, 342, 373

Rybicki, G. B., & Lightman, A. P. 1979, Radiative processes in astrophysics (Wiley-VCH)

Saintonge, A. 2007, AJ, 133, 2087

Sanders, D. B., Mazzarella, J. M., Kim, D.-C., Surace, J. A., & Soifer, B. T. 2003, AJ, 126, 1607

Sanders, D. B., & Mirabel, I. F. 1996, ARA&A, 34, 749

Sawa, T., & Fujimoto, M. 2005, PASJ, 57, 429

Schmelz, J. T., Baan, W. A., Haschick, A. D., & Eder, J. 1986, AJ, 92, 1291

Schweitzer, M., Groves, B., Netzer, H., Lutz, D., Sturm, E., Contursi, A., Genzel, R., Tacconi, L. J., Veilleux, S., Kim, D., Rupke, D., & Baker, A. J. 2008, ApJ, 679, 101

Schweitzer, M., Lutz, D., Sturm, E., Contursi, A., Tacconi, L. J., Lehnert, M. D., Dasyra, K. M., Genzel, R., Veilleux, S., Rupke, D., Kim, D.-C., Baker, A. J., Netzer, H., Sternberg, A., Mazzarella, J., & Lord, S. 2006, ApJ, 649, 79

Scoville, N., Aussel, H., Brusa, M., Capak, P., Carollo, C. M., Elvis, M., Giavalisco, M., Guzzo, L., Hasinger, G., Impey, C., Kneib, J., LeFevre, O., Lilly, S. J., Mobasher, B., Renzini, A., Rich, R. M., Sanders, D. B., Schinnerer, E., Schminovich, D., Shopbell, P., Taniguchi, Y., & Tyson, N. D. 2007, ApJS, 172, 1

Siebenmorgen, R., Haas, M., Krügel, E., & Schulz, B. 2005, A&A, 436, L5

Sirocky, M. M., Levenson, N. A., Elitzur, M., Spoon, H. W. W., & Armus, L. 2008, ApJ, 678, 729

Sjouwerman, L. O., Murray, C. E., Pihlström, Y. M., Fish, V. L., & Araya, E. D. 2010, ApJL, 724, L158

Skinner, C. J., Smith, H. A., Sturm, E., Barlow, M. J., Cohen, R. J., & Stacey, G. J. 1997, Nature, 386, 472

Smail, I., Chapman, S. C., Blain, A. W., & Ivison, R. J. 2004, ApJ, 616, 71

Smith, J. D. T., Draine, B. T., Dale, D. A., Moustakas, J., Kennicutt, Jr., R. C., Helou, G., Armus, L., Roussel, H., Sheth, K., Bendo, G. J., Buckalew, B. A., Calzetti, D., Engelbracht, C. W., Gordon, K. D., Hollenbach, D. J., Li, A., Malhotra, S., Murphy, E. J., & Walter, F. 2007, ApJ, 656, 770

Soifer, B. T., Helou, G., & Werner, M. 2008, ARA&A, 46, 201

Solomon, P. M., Downes, D., Radford, S. J. E., & Barrett, J. W. 1997, ApJ, 478, 144

Spoon, H. W. W., Armus, L., Cami, J., Tielens, A. G. G. M., Chiar, J. E., Peeters, E., Keane, J. V., Charmandaris, V., Appleton, P. N., Teplitz, H. I., & Burgdorf, M. J. 2004, ApJS, 154, 184

Spoon, H. W. W., & Holt, J. 2009, ApJL, 702, L42

Spoon, H. W. W., Keane, J. V., Cami, J., Lahuis, F., Tielens, A. G. G. M., Armus, L., & Charmandaris, V. 2005, in IAU Symposium, Vol. 231, Astrochemistry: Recent Successes and Current Challenges, ed. D. C. Lis, G. A. Blake, & E. Herbst, 281–290

Spoon, H. W. W., Keane, J. V., Tielens, A. G. G. M., Lutz, D., & Moorwood, A. F. M. 2001, A&A, 365, L353

Spoon, H. W. W., Keane, J. V., Tielens, A. G. G. M., Lutz, D., Moorwood, A. F. M., & Laurent, O. 2002, A&A, 385, 1022

Spoon, H. W. W., Koornneef, J., Moorwood, A. F. M., Lutz, D., & Tielens, A. G. G. M. 2000, A&A, 357, 898

Spoon, H. W. W., Marshall, J. A., Houck, J. R., Elitzur, M., Hao, L., Armus, L., Brandl, B. R., & Charmandaris, V. 2007, ApJL, 654, L49

Spoon, H. W. W., Tielens, A. G. G. M., Armus, L., Sloan, G. C., Sargent, B., Cami, J., Charmandaris, V., Houck, J. R., & Soifer, B. T. 2006, ApJ, 638, 759

Stanford, S. A., Stern, D., van Breugel, W., & De Breuck, C. 2000, ApJS, 131, 185

Staveley-Smith, L., Cohen, R. J., Chapman, J. M., Pointon, L., & Unger, S. W. 1987, MNRAS, 226, 689

Staveley-Smith, L., Norris, R. P., Chapman, J. M., Allen, D. A., Whiteoak, J. B., & Roy, A. L. 1992, MNRAS, 258, 725

Sturm, E., Lutz, D., Tran, D., Feuchtgruber, H., Genzel, R., Kunze, D., Moorwood, A. F. M., & Thornley, M. D. 2000, A&A, 358, 481

Sturm, E., Lutz, D., Verma, A., Netzer, H., Sternberg, A., Moorwood, A. F. M., Oliva, E., & Genzel, R. 2002, A&A, 393, 821

Sturm, E., Schweitzer, M., Lutz, D., Contursi, A., Genzel, R., Lehnert, M. D., Tacconi, L. J., Veilleux, S., Rupke, D. S., Kim, D.-C., Sternberg, A., Maoz, D., Lord, S., Mazzarella, J., & Sanders, D. B. 2005, ApJL, 629, L21

Tabatabaei, F. S., & Berkhuijsen, E. M. 2010, A&A, 517, A77+

Takata, T., Sekiguchi, K., Smail, I., Chapman, S. C., Geach, J. E., Swinbank, A. M., Blain, A., & Ivison, R. J. 2006, ApJ, 651, 713

Tommasin, S., Spinoglio, L., Malkan, M. A., Smith, H., González-Alfonso, E., & Charmandaris, V. 2008, ApJ, 676, 836

Townes, C. H., & Schawlow, A. L. 1955, Microwave Spectroscopy (McGraw-Hill)

Uzan, J.-P. 2003, Reviews of Modern Physics, 75, 403

van den Bergh, S. 1999, A&A Rev., 9, 273

van der Marel, R. 2008, in HST Proposal, 11684–+

van der Marel, R. P., & Guhathakurta, P. 2008, ApJ, 678, 187

van Maanen, A. 1918, PASP, 30, 307

Verma, A., Lutz, D., Sturm, E., Sternberg, A., Genzel, R., & Vacca, W. 2003, A&A, 403, 829

Vignali, C., Brandt, W. N., Comastri, A., & Darling, J. 2005, MNRAS, 364, 99

Walter, F., Carilli, C., & Daddi, E. 2011, ArXiv e-prints

Walterbos, R. A. M., Brinks, E., & Shane, W. W. 1985, A&AS, 61, 451

Walterbos, R. A. M., & Kennicutt, Jr., R. C. 1987, A&AS, 69, 311

Watkins, L. L., Evans, N. W., & An, J. H. 2010, MNRAS, 406, 264

Weaver, H., Williams, D. R. W., Dieter, N. H., & Lum, W. T. 1965, Nature, 208, 29

Weedman, D. W., Hao, L., Higdon, S. J. U., Devost, D., Wu, Y., Charmandaris, V., Brandl, B., Bass, E., & Houck, J. R. 2005, ApJ, 633, 706

Weedman, D. W., & Houck, J. R. 2009, ApJ, 693, 370

Weinreb, S. 1963, Nature, 200, 829

Weinreb, S., Meeks, M. L., & Carter, J. C. 1965, Nature, 208, 440

Weliachew, L. 1971, ApJL, 167, L47+

Werner, M. W., Roellig, T. L., Low, F. J., Rieke, G. H., Rieke, M., Hoffmann, W. F., Young, E., Houck, J. R., Brandl, B., Fazio, G. G., Hora, J. L., Gehrz, R. D., Helou, G., Soifer, B. T., Stauffer, J., Keene, J., Eisenhardt, P., Gallagher, D., Gautier, T. N., Irace, W., Lawrence, C. R., Simmons, L., Van Cleve, J. E., Jura, M., Wright, E. L., & Cruikshank, D. P. 2004, ApJS, 154, 1

Whiteoak, J. B., & Gardner, F. F. 1973, Astrophys. Lett., 15, 211

—. 1976, MNRAS, 176, 25P

Willett, K. W., Darling, J., Spoon, H. W. W., Charmandaris, V., & Armus, L. 2011a, ApJS, 193, 18

—. 2011b, ApJ, 730, 56

Willman, B. 2010, Advances in Astronomy, 2010

Yahil, A., Tammann, G. A., & Sandage, A. 1977, ApJ, 217, 903

Yang, M., Greve, T. R., Dowell, C. D., & Borys, C. 2007, ApJ, 660, 1198

Yates, J. A., Richards, A. M. S., Wright, M. M., Collett, J. L., Gray, M. D., Field, D., & Cohen, R. J. 2000, MNRAS, 317, 28

Yun, M. S., & Carilli, C. L. 2002, ApJ, 568, 88

Zakamska, N. L., Gómez, L., Strauss, M. A., & Krolik, J. H. 2008, AJ, 136, 1607

Appendix A

Glossary

This section defines acronyms and abbreviations used in the thesis.

- **ACS** - Advanced Camera for Surveys (HST)
- **AGN** - active galactic nucleus
- **ALFALFA** - Arecibo Legacy Fast ALFA survey
- **AOT** - Astronomical Observing Template
- **APO** - Apache Point Observatory
- **ASKAP** - Australian SKA Pathfinder
- **BCD** - basic calibrated data
- **BGS** - Bright Galaxy Sample (IRAS)
- **CLUMPY** - radiative transfer code
- **COSMOS** - Cosmic Evolution Survey
- **DCS** - double-correlated sampling
- **DEEP2** - DEIMOS/DEEP redshift survey
- **DUSTY** - radiative transfer code

- **EVLA** - Expanded Very Large Array
- **EW** - equivalent width
- **FF** - FSC-FIRST
- **FIRST** - Faint Images of the Radio Sky at Twenty cm
- **FIR** - far-infrared
- **FSC** - Faint Source Catalog (IRAS)
- **FWHM** - full-width half-maximum
- **GBT** - Green Bank Telescope
- **GBTIDL** - Green Bank Telescope Interactive Data Language
- **GMRT** - Giant Metre-wave Radio Telescope
- **GTO** - guaranteed time observation
- **HAC** - hydrogenated amorphous carbon
- **HR** - high resolution (IRS modules)
- **HSA** - High Sensitivity Array
- **HST** - Hubble Space Telescope
- **HyLIRG** - hyper-luminous infrared galaxy
- **IDL** - Interactive Data Language
- **IR** - infrared
- **IRAF** - Image Reduction and Analysis Facility
- **IRAS** - Infrared Astronomical Satellite

- **IRS** - Infared Spectograph
- **ISM** - interstellar medium
- **ISO** - Infrared Space Observatory
- **JWST** - James Webb Space Telescope
- **K-S** - Kolmogorov-Smirnov
- L_{bol} - total bolometric luminosity
- L_{FIR} - far-infrared bolometric luminosity
- L_{IR} - infrared bolometric luminosity
- L_{OH} - integrated OH isotropic line luminosity
- **LCR** - line-to-continuum ratio
- **LE08** - Lockett & Elitzur (2008)
- **LF** - luminosity function
- **LG** - Local Group
- **LH** - long-high IRS module
- **LH** - Lockman Hole
- **LINER** - low-ionization nuclear emission region
- **LIRG** - luminous infrared galaxy
- **LL1, LL2, LL3** - long-low IRS modules 1, 2, and 3
- **LR** - low resolution (IRS modules)
- **LSRK** - Local Standard of Rest (Kinematic)

- **LTE** - local thermodynamic equilibrium
- **M31** - Andromeda galaxy
- **mas; μas** - milliarcseconds; microarcseconds
- **MS** - measurement set
- **NRQZ** - National Radio Quiet Zone
- **OHM, OHMM** - OH megamaser
- **PAHFIT** - IDL package for decomposition of low-resolution IRS spectra
- **PAH** - polycyclic aromatic hydrocarbon
- **PSCz** - IRAS Point Source Catalog redshift survey
- **PDR** - photo-dissociated region
- **PF1** - Prime Focus 1 (GBT receiver)
- **PF2** - Prime Focus 2 (GBT receiver)
- **PG** - Palomar-Green (quasar)
- **PU** - peakup (IRS module)
- **QSO** - quasi-stellar object
- **RFI** - radio frequency interference
- **RG** - radio galaxy
- **SED** - spectral energy distribution
- **SFR** - star formation rate
- **SH** - short-high (IRS modules)

- **SINGS** - SIRTF Nearby Galaxy Survey
- **SKA** - Square Kilometre Array
- **SL1, SL2, SL3** - short-low IRS modules 1, 2, and 3
- **SMART** - Spectroscopic Modeling Analysis and Reduction Tool
- **SMM, sub-mm** - sub-millimeter
- S/N - signal-to-noise ratio
- **SOFIA** - Stratospheric Observatory for Infrared Astronomy
- **SPICE** - Spitzer IRS Custom Extractor
- *Spitzer* - Spitzer Space Telescope
- **SPOT** - Spitzer Planning Observations Tool
- **SSC** - Spitzer Science Center
- **SUR** - sample-up-the-ramp
- **ULIRG** - ultraluminous infrared galaxy
- **VLA** - Very Large Array
- **VLBA** - Very Long Baseline Array
- **VLBI** - Very Long Baseline Interferometry
- **WFC3** - Wide-Field Camera 3 (HST)
- **WISE** - Wide-Field Infrared Survey Explorer
- **WMAP5** - Five-Year Wilkinson Microwave Anisotropy Probe data
- **XDR** - X-ray dominated region

Appendix B

IRS supplementary data

B.1 High-resolution data with background sky subtraction

As discussed in Chapter 2, the reduction process for galaxies in the IRS sample is slightly different for some archival targets that did not have separate IRS sky backgrounds in the high-resolution modules. Since much of the subsequent analysis (Chapter 3) depends on statistical comparisons between the two samples, I chose to minimize possible systematic errors and reduced all galaxies in a uniform manner **without** high-resolution (HR) sky subtraction. These data are, however, likely to be a more reliable indicator of the absolute flux levels due to subtraction of the zodiacal background. This section presents atomic and molecular line fluxes for galaxies with blank sky subtracted from the HR modules.

Table B.1. Hi-res line fluxes for common atomic emission lines with HR sky subtraction

Object	[S IV] 10.511 μm	[Ne II] 12.814 μm	[Ne III] 15.555 μm	[S III] 18.713 μm
IRAS 01562+2528	–	–	–	0.65
IRAS 02524+2046	–	–	–	0.47
IRAS 04121+0223	–	–	–	0.67
IRAS 04454−4838	0.42	1.95	0.43	–
IRAS 06487+2208	–	–	–	5.01
IRAS 07163+0817	–	–	–	1.34
IRAS 08201+2801	–	–	–	0.41
IRAS 08449+2332	–	–	–	1.60
IRAS 08474+1813	–	–	–	0.14
IRAS 10035+2740	–	–	–	0.35
IRAS 10039−3338	0.98	17.22	4.20	8.08
IRAS 10339+1548	–	–	–	0.97
IRAS 11180+1623	–	–	–	0.40
IRAS 11524+1058	–	–	–	0.27
IRAS 12540+5708	–	19.47	–	–
IRAS 14059+2000	–	–	–	0.59
IRAS 14553+1245	–	–	–	1.58
IRAS 15327+2340	–	59.39	6.73	7.54
IRAS 16255+2801	–	–	–	1.54
IRAS 18368+3549	–	–	–	1.01
IRAS 18588+3517	–	–	–	2.89
IRAS 20286+1846	–	–	–	0.48
IRAS 21077+3358	–	–	–	0.74
IRAS 21272+2514	–	2.22	0.33	0.40
IRAS 22055+3024	–	–	–	1.16
IRAS 22116+0437	–	–	–	0.90
IRAS 00163−1039	2.64	87.43	14.30	32.10
IRAS 05083+7936	–	49.95	7.63	19.60
IRAS 06538+4628	0.84	47.34	5.90	20.49
IRAS 09437+0317	–	8.72	1.22	3.58
IRAS 23394−0353	–	46.45	7.60	18.50

Table B.1 (cont'd)

Object	[S IV] 10.511 μm	[Ne II] 12.814 μm	[Ne III] 15.555 μm	[S III] 18.713 μm

Note. — Fluxes are in 10^{-21} W cm^{-2}. No data is given for the 26 galaxies in Spitzer program 30407 for lines with $\lambda_{rest} \lesssim 16$ μm since there is no SH sky subtraction available for these objects.

Table B.2. Hi-res line fluxes for rarer atomic emission lines with HR sky subtraction

Object λ_{rest} [μm]	H I 7-6 12.368	[Ne V] 14.322	[Cl II] 14.369	[Fe II] 17.936	[Ne V] 24.318	[O IV] 25.890	[Fe II] 25.988	[S III] 33.481	[Si II] 34.815
IRAS 04454−4838	–	–	–	–	–	1.12	–	0.90	–
IRAS 06487+2208	–	–	–	–	–	1.12	–	–	–
IRAS 07163+0817	–	–	–	0.73	–	–	–	–	–
IRAS 10339+1548	–	–	–	–	0.84	2.55	–	–	–
IRAS 11524+1058	–	–	–	0.35	–	0.59	–	–	–
IRAS 14553+1245	–	–	–	0.41	–	–	–	–	–
IRAS 16255+2801	–	–	–	–	–	0.46	–	–	–
IRAS 18368+3549	–	–	–	0.51	–	–	–	–	–
IRAS 21272+2514	0.20	0.10	–	–	–	–	–	–	–
IRAS 00163−1039	0.64	–	–	–	–	1.56	2.46	32.18	74.28
IRAS 05083+7936	–	0.58	0.43	–	–	1.53	1.97	29.34	43.28
IRAS 06538+4628	–	1.08	–	1.06	–	–	2.15	37.21	48.72
IRAS 09437+0317	–	–	–	–	–	0.47	0.68	9.60	22.74
IRAS 23394−0353	0.59	–	–	–	–	1.49	2.53	42.37	53.56

Note. — Fluxes are in 10^{-21} W cm^{-2}. No data is given for the 26 galaxies in Spitzer program 30407 for lines with $\lambda_{rest} \lesssim 16$ μm since there is no SH sky subtraction available for these objects.

Table B.3. Hi-res line fluxes and upper limits for H_2 transitions with HR sky subtraction

Object λ_{rest} [μm]	H_2 S(3) 9.67	H_2 S(2) 12.28	H_2 S(1) 17.04	H_2 S(0) 28.22
IRAS 01562+2528	–	–	0.78	–
IRAS 02524+2046	–	–	0.72	–
IRAS 04454−4838	1.05	1.21	3.03	0.76
IRAS 06487+2208	–	–	2.03	–
IRAS 08201+2801	–	–	0.51	–
IRAS 08449+2332	–	–	1.40	–
IRAS 08474+1813	–	–	0.27	–
IRAS 10035+2740	–	–	1.16	–
IRAS 10039−3338	3.39	1.79	3.85	–
IRAS 10339+1548	–	–	0.46	–
IRAS 11180+1623	–	–	0.89	–
IRAS 11524+1058	–	–	0.81	–
IRAS 12540+5708	2.42	4.22	–	–
IRAS 14059+2000	–	–	2.55	–
IRAS 15327+2340	–	7.36	15.42	14.55
IRAS 16255+2801	–	–	0.55	–
IRAS 21077+3358	–	–	1.17	–
IRAS 21272+2514	0.26	0.35	0.68	–
IRAS 22116+0437	–	–	1.35	–
IRAS 23028+0725	–	–	1.11	–
IRAS 00163−1039	2.18	2.82	6.01	–
IRAS 05083+7936	2.34	2.64	5.11	–
IRAS 06538+4628	–	3.33	8.70	2.99
IRAS 09437+0317	–	–	2.67	1.78
IRAS 23394−0353	3.40	2.25	4.99	1.38

Note. — Fluxes are in 10^{-21} W cm^{-2}. No data is given for the 26 galaxies in Spitzer program 30407 for the S(2) or S(3) lines since there is no SH sky subtraction available for these objects.

B.2 Full IRS spectra of the OHMs and confirmed non-masing galaxies

This section presents the full *Spitzer* IRS spectra for the 51 OHMs and 15 non-masing galaxies in Chapters 2 and 3. The low-resolution ($R \sim 57 - 127$) plots (Figures B.1–B.17) are stitched from the SL1, SL2, LL1, and LL2 modules following the procedure described in Chapter 2.3.1. All detected features that are spectrally broad (PAH emission and absorption from water ice and amorphous silicates) and that are considered valid detections are marked on the low-resolution plots.

Figures B.18–B.34 and B.35–B.51 show the high spectral resolution ($R \sim 600$) short high (SH) and long high (LH) modules, respectively. Neither high-resolution module is scaled in flux to independent photometric measurements; the discontinuity in flux near $\lambda_{obs} = 18$ μm is a result of the different slit sizes for the two modules. All features that are spectrally narrow (atomic and molecular emission) and that are considered valid detections are marked on the high-resolution plots.

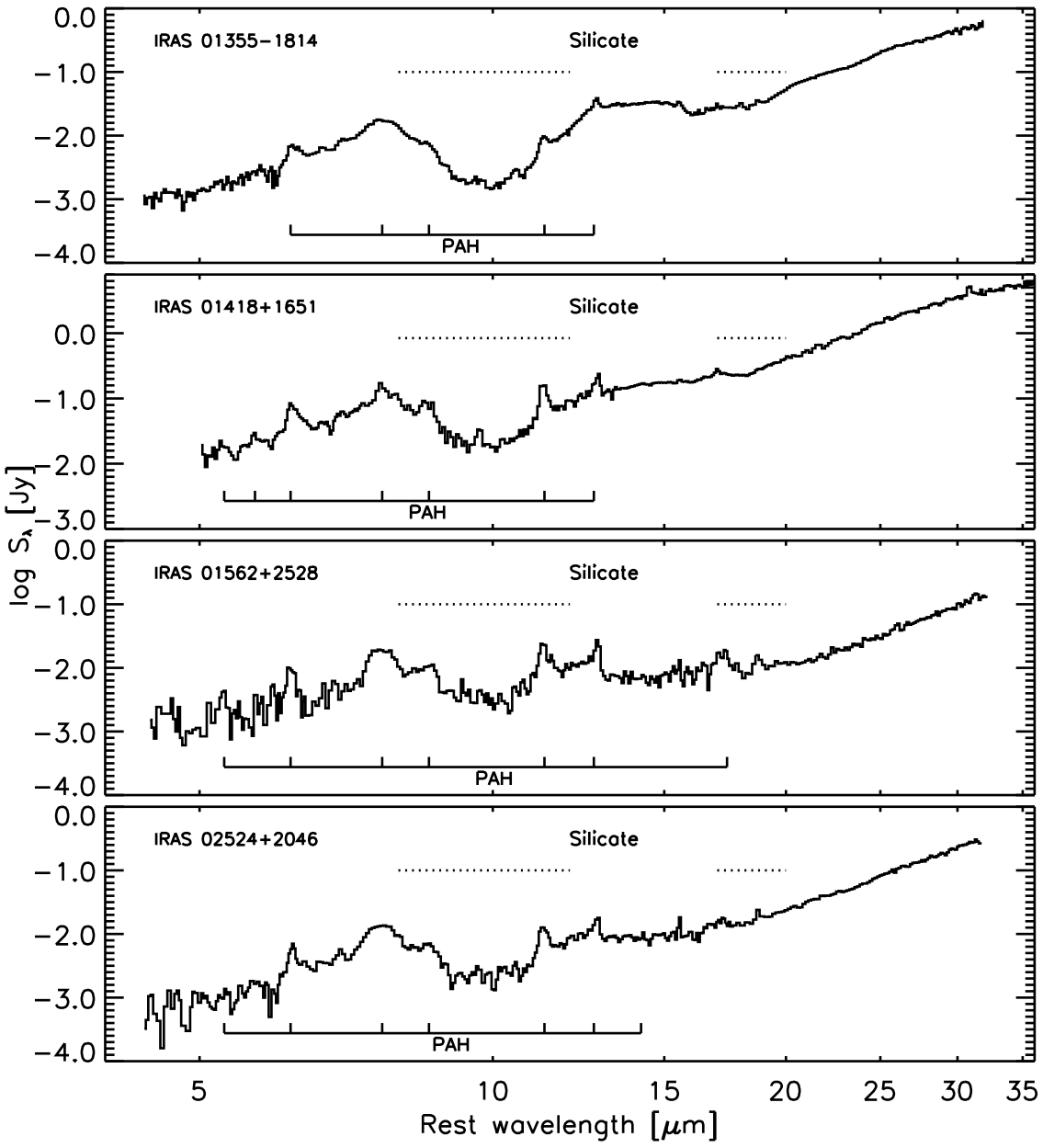

Figure B.1 Full low-resolution (LR) spectra for the OHMs observed with the *Spitzer* IRS. Locations of PAH emission and absorption features from water ices and silicates are marked.

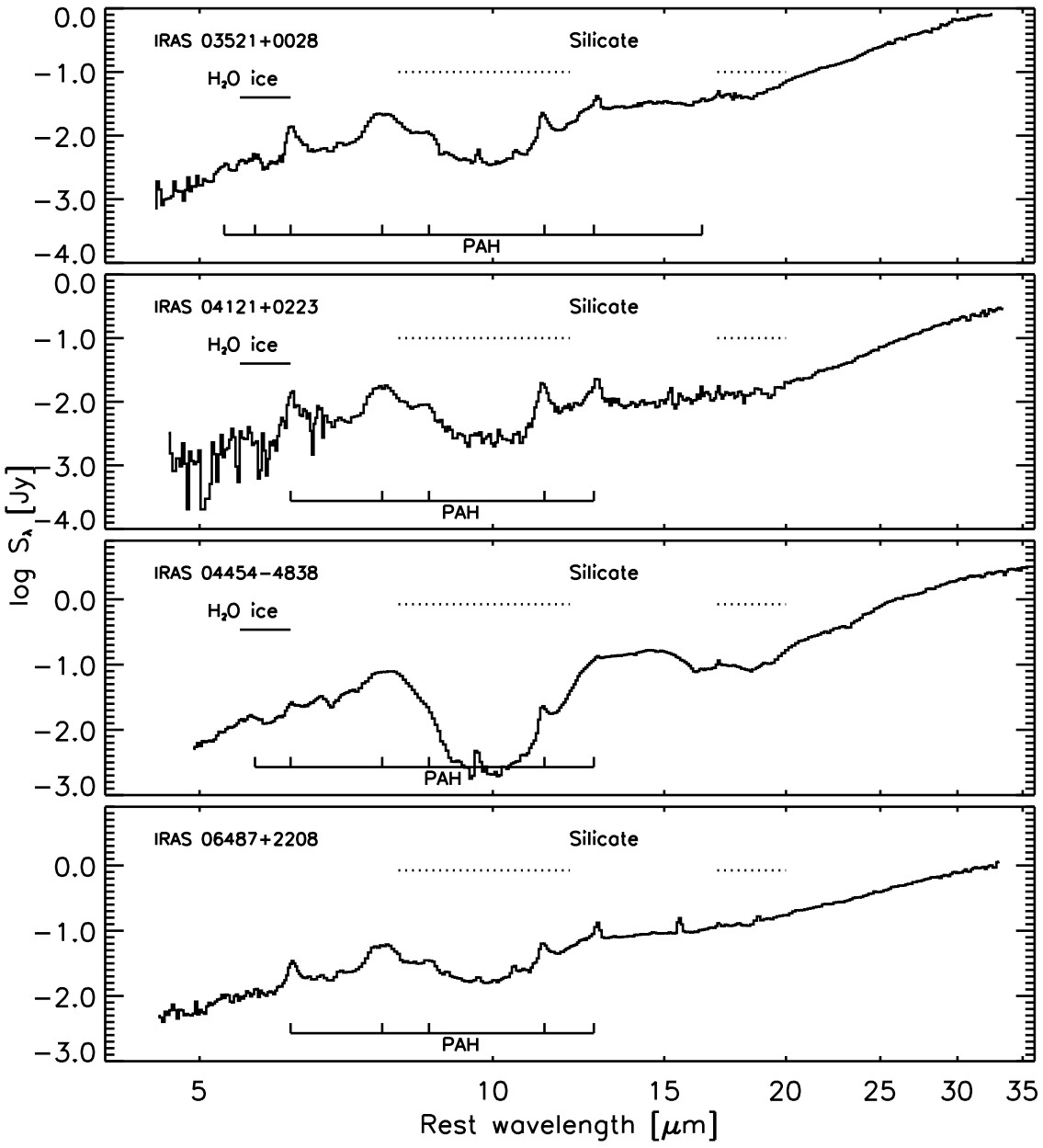

Figure B.2 Full low-resolution (LR) spectra for the OHMs observed with the *Spitzer* IRS. Locations of PAH emission and absorption features from water ices and silicates are marked.

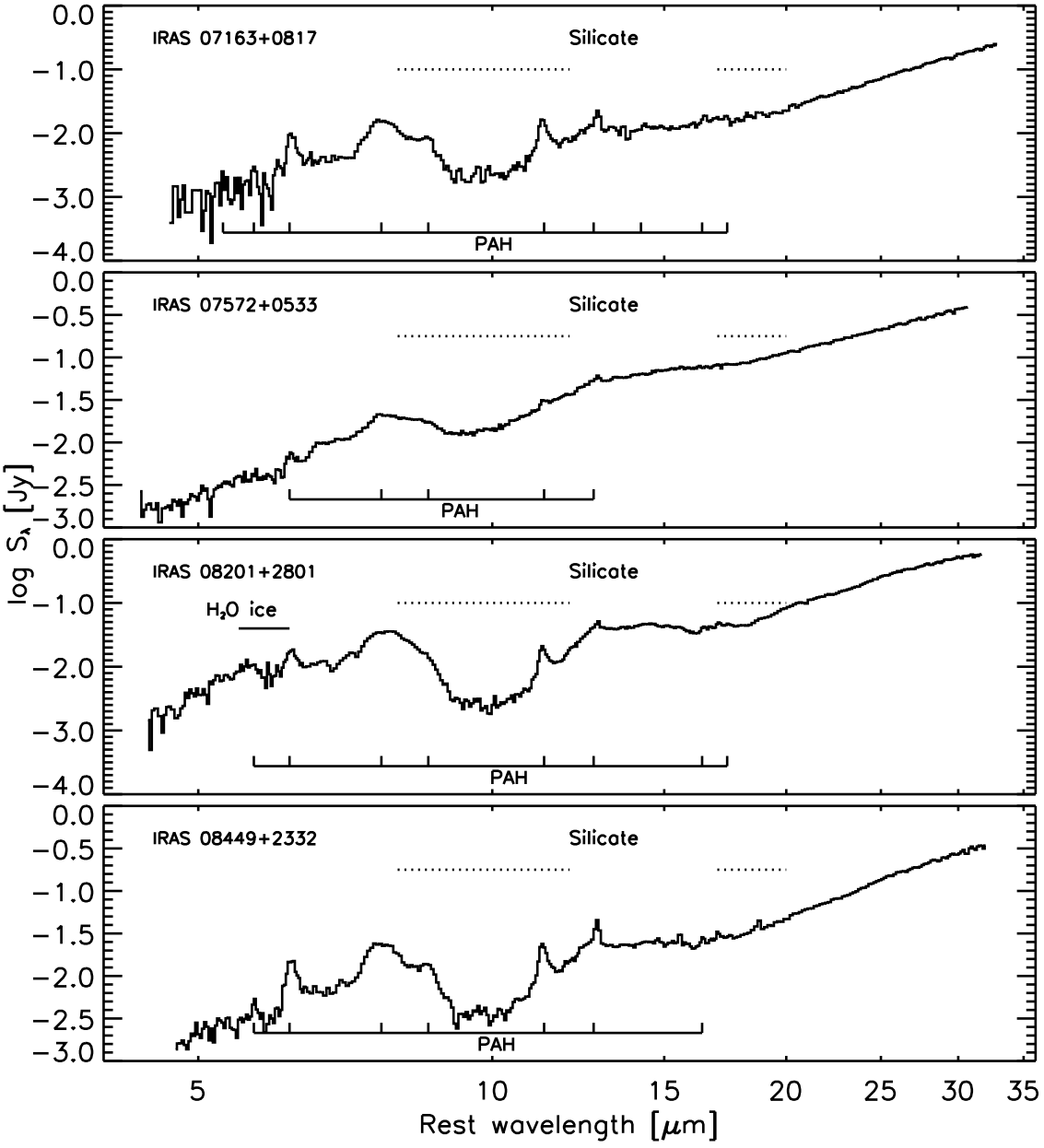

Figure B.3 Full low-resolution (LR) spectra for the OHMs observed with the *Spitzer* IRS. Locations of PAH emission and absorption features from water ices and silicates are marked.

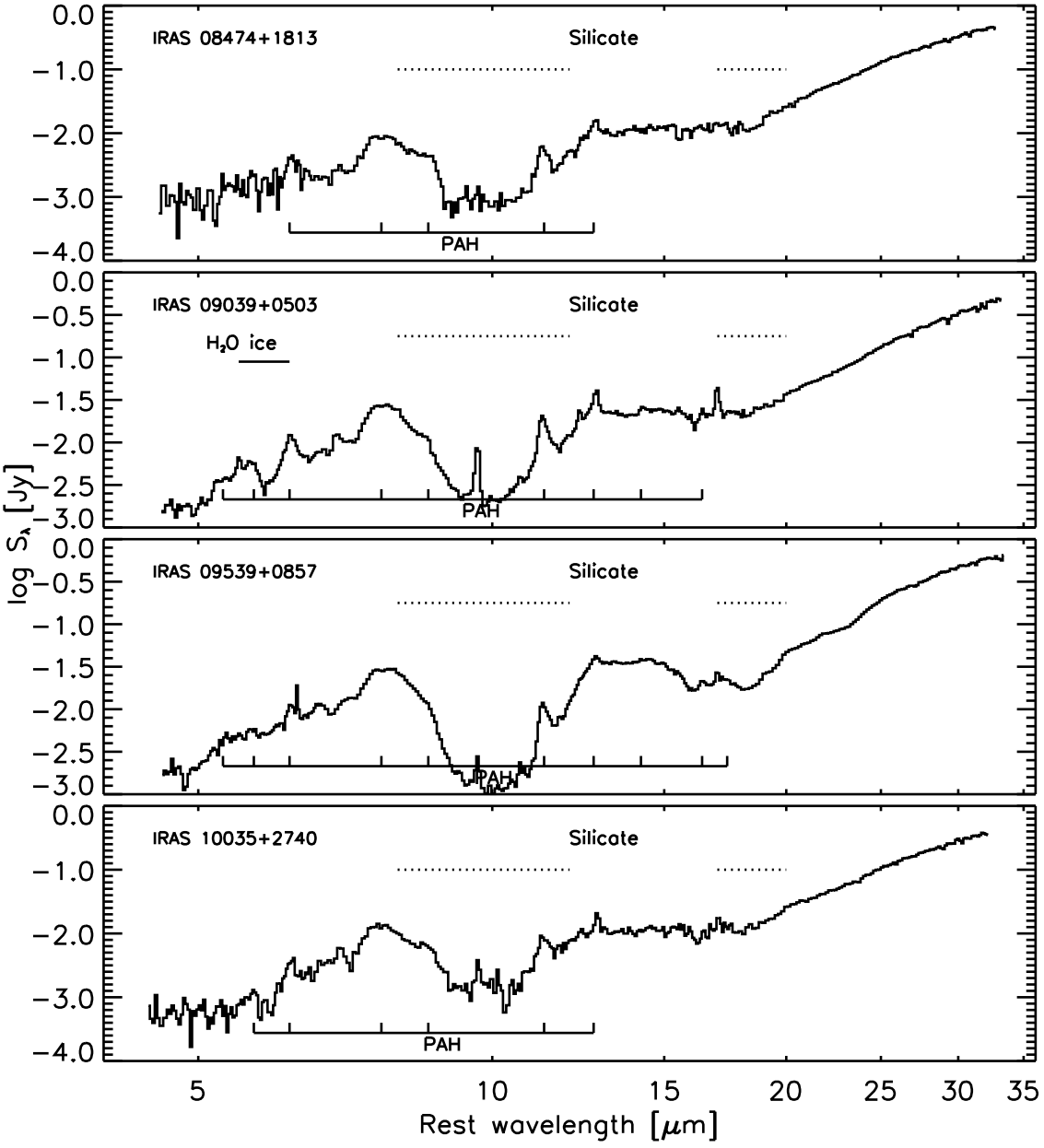

Figure B.4 Full low-resolution (LR) spectra for the OHMs observed with the *Spitzer* IRS. Locations of PAH emission and absorption features from water ices and silicates are marked.

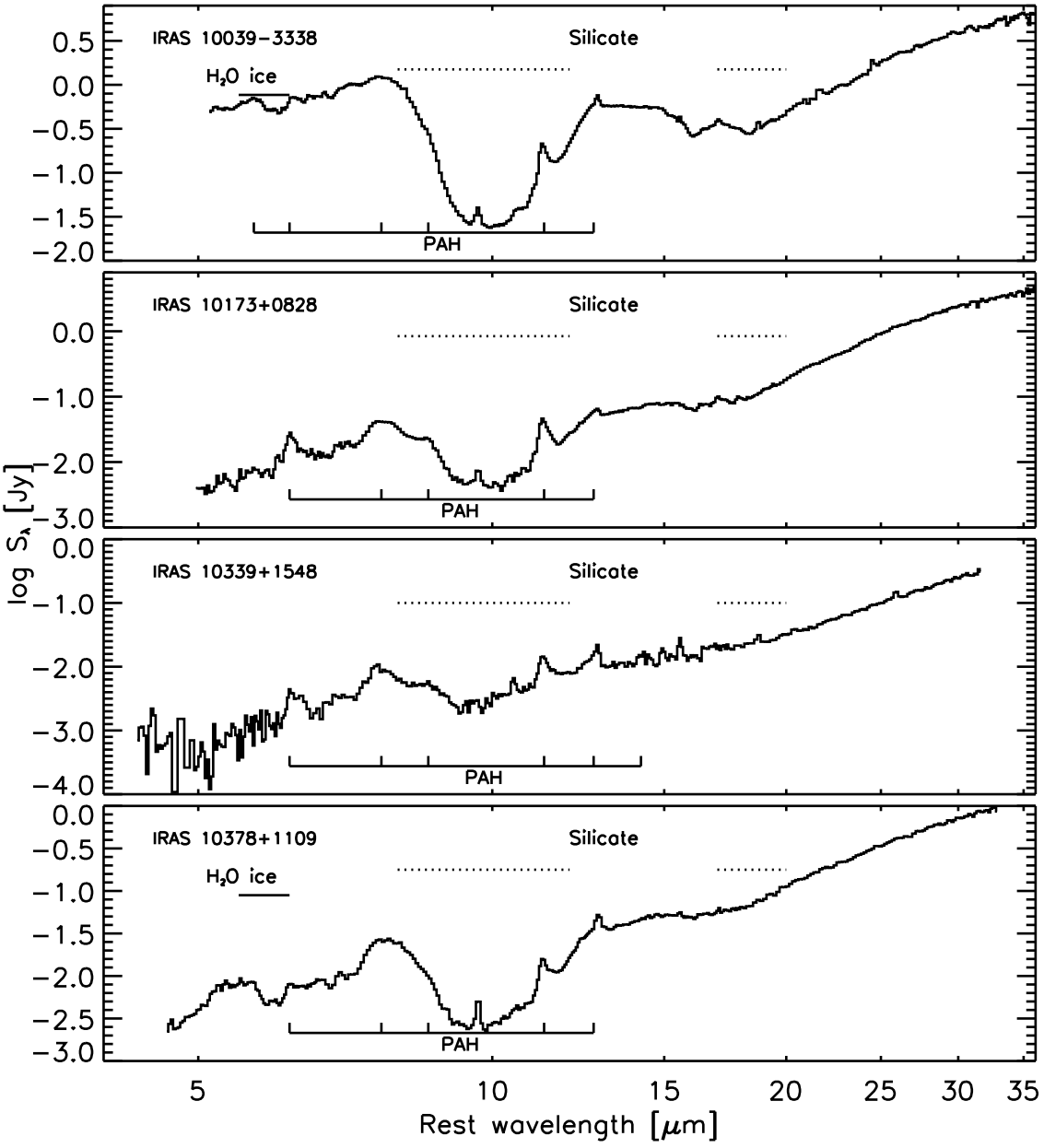

Figure B.5 Full low-resolution (LR) spectra for the OHMs observed with the *Spitzer* IRS. Locations of PAH emission and absorption features from water ices and silicates are marked.

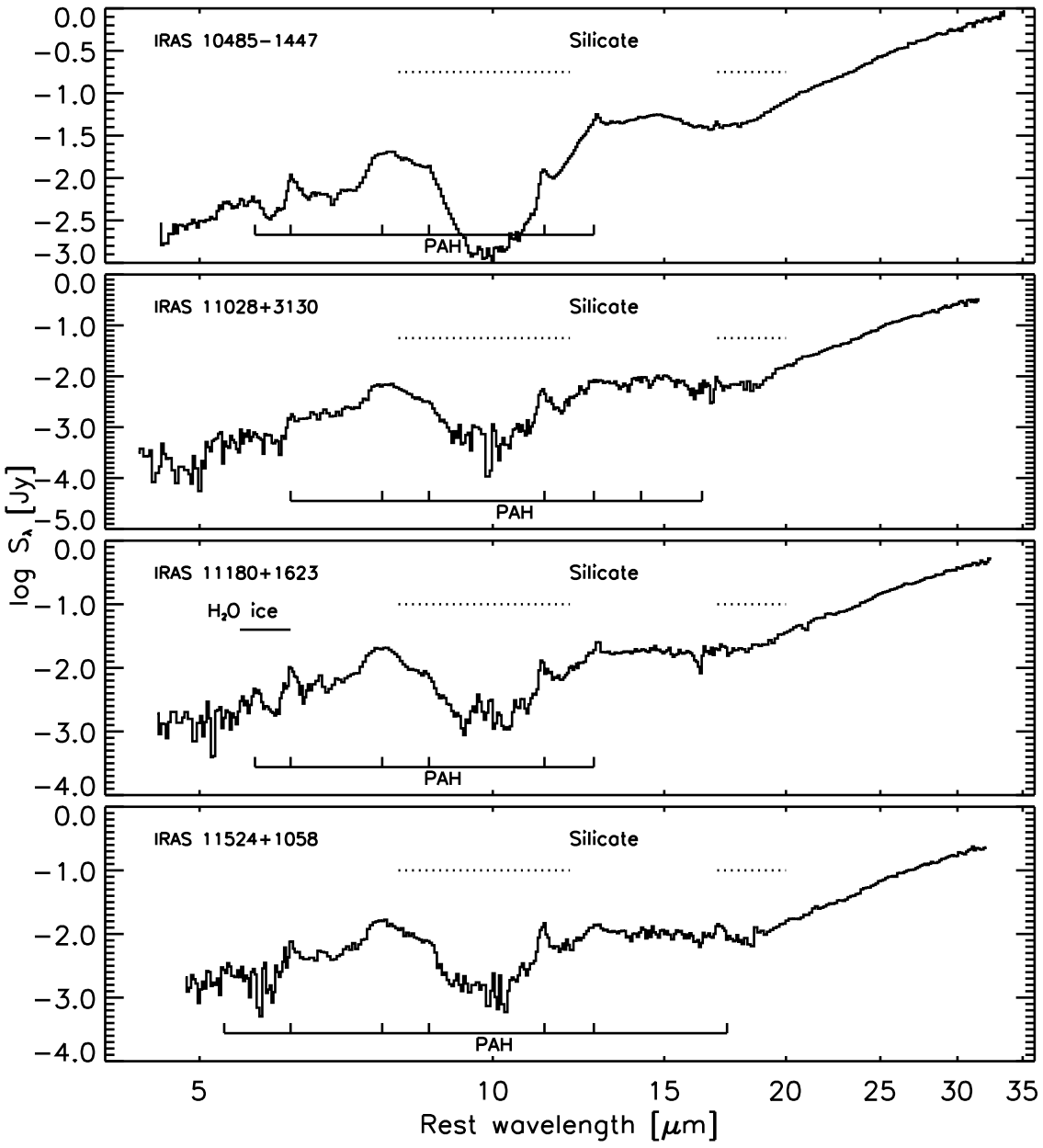

Figure B.6 Full low-resolution (LR) spectra for the OHMs observed with the *Spitzer* IRS. Locations of PAH emission and absorption features from water ices and silicates are marked.

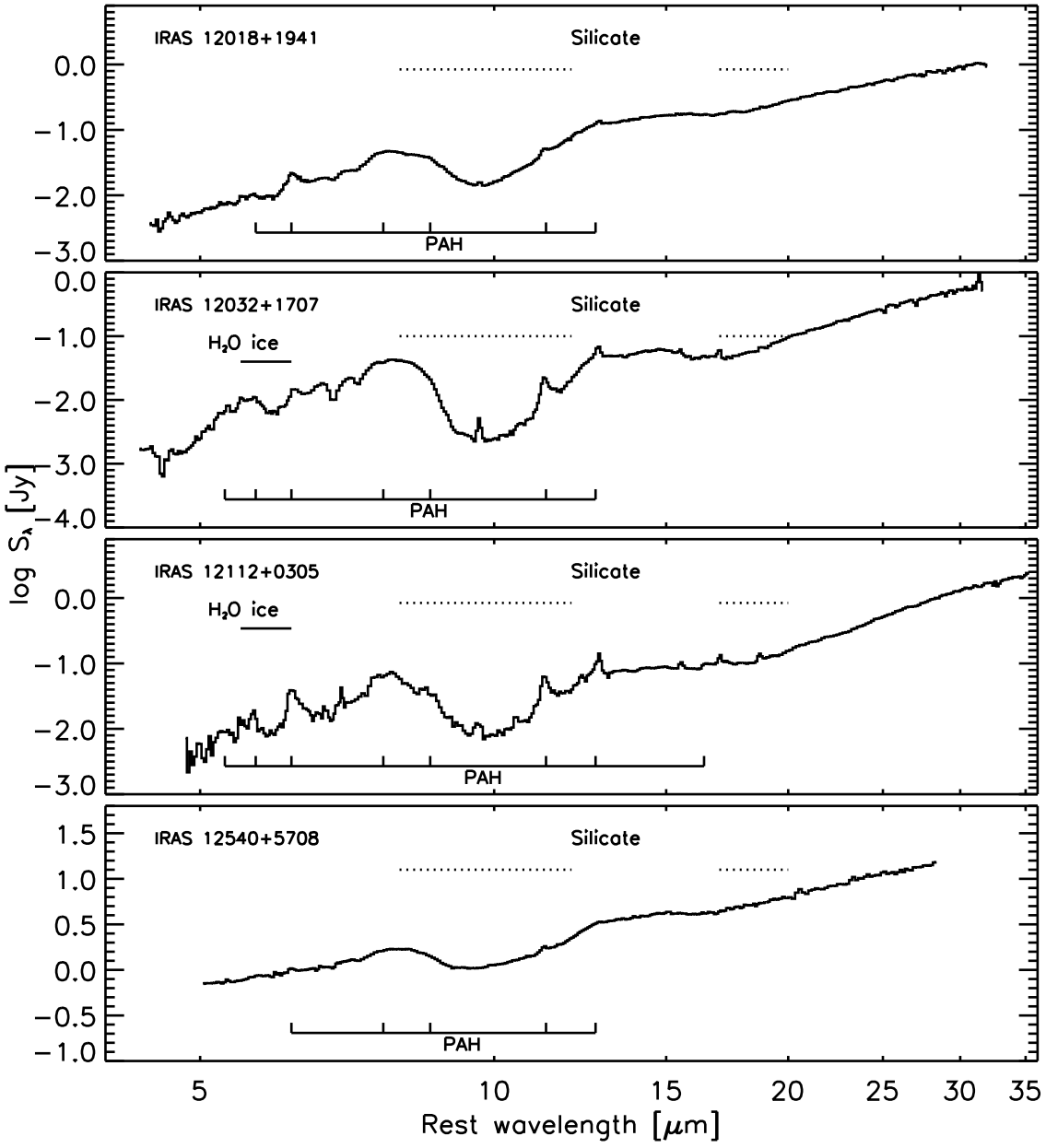

Figure B.7 Full low-resolution (LR) spectra for the OHMs observed with the *Spitzer* IRS. Locations of PAH emission and absorption features from water ices and silicates are marked.

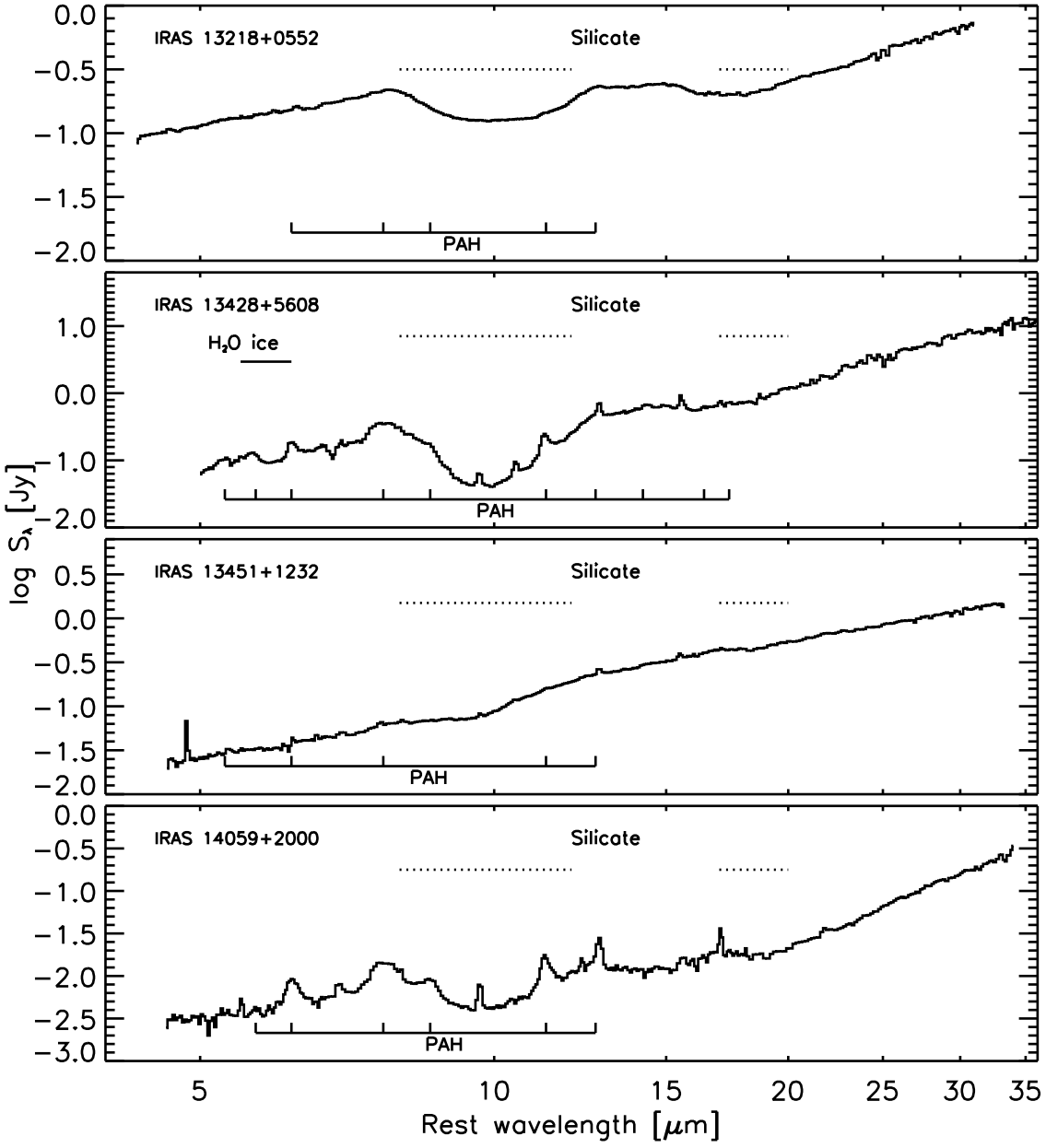

Figure B.8 Full low-resolution (LR) spectra for the OHMs observed with the *Spitzer* IRS. Locations of PAH emission and absorption features from water ices and silicates are marked.

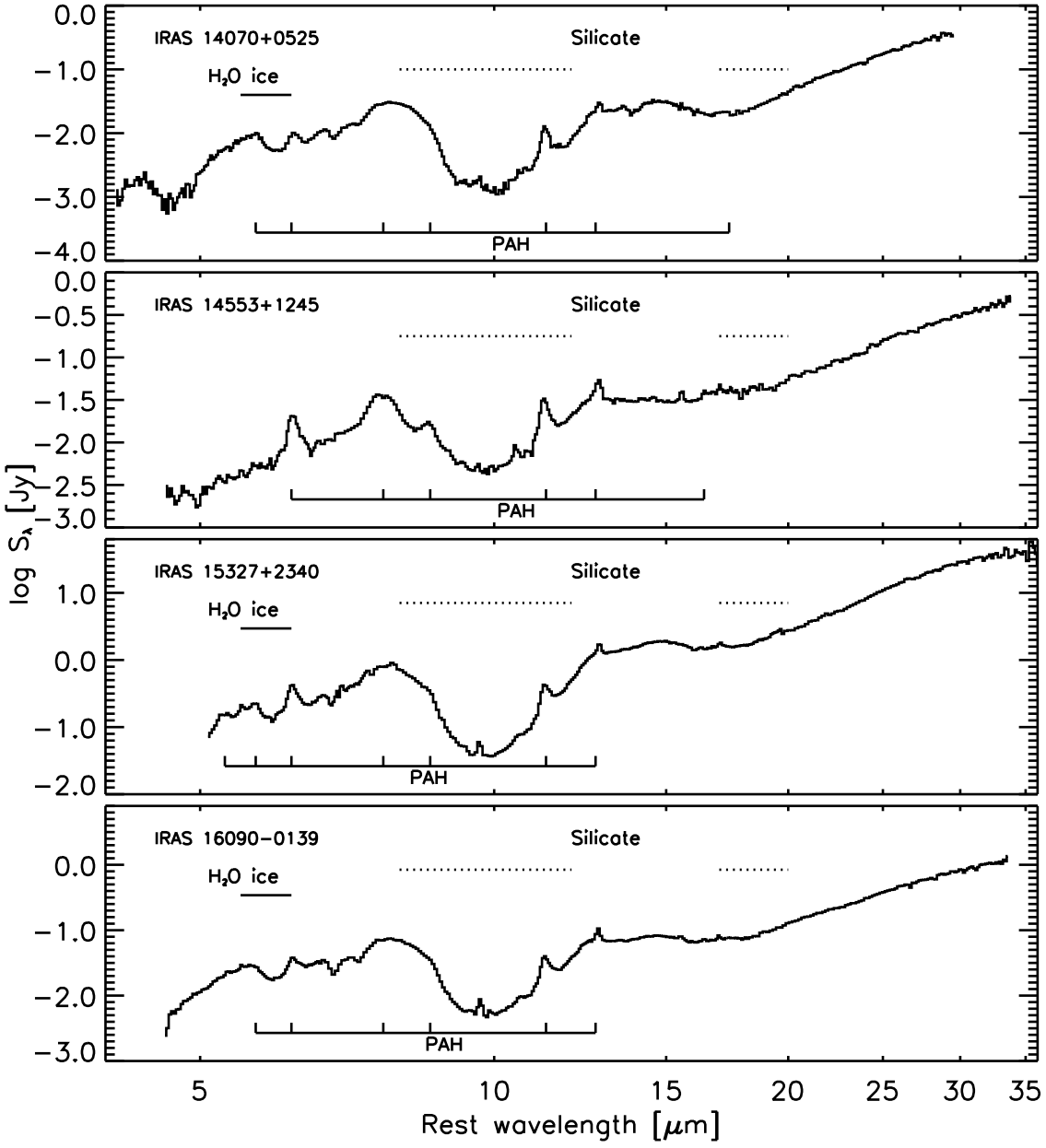

Figure B.9 Full low-resolution (LR) spectra for the OHMs observed with the *Spitzer* IRS. Locations of PAH emission and absorption features from water ices and silicates are marked.

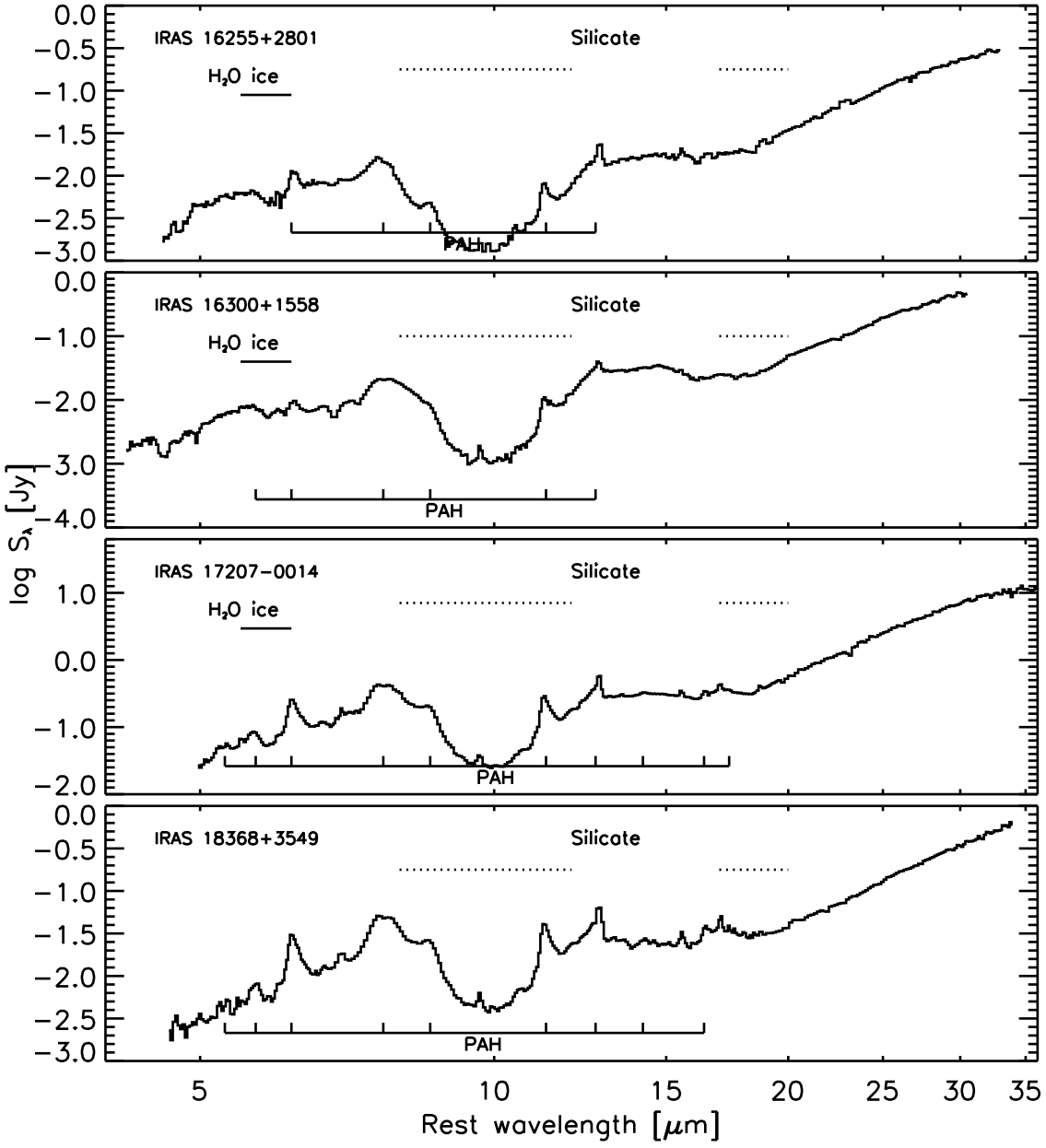

Figure B.10 Full low-resolution (LR) spectra for the OHMs observed with the *Spitzer* IRS. Locations of PAH emission and absorption features from water ices and silicates are marked.

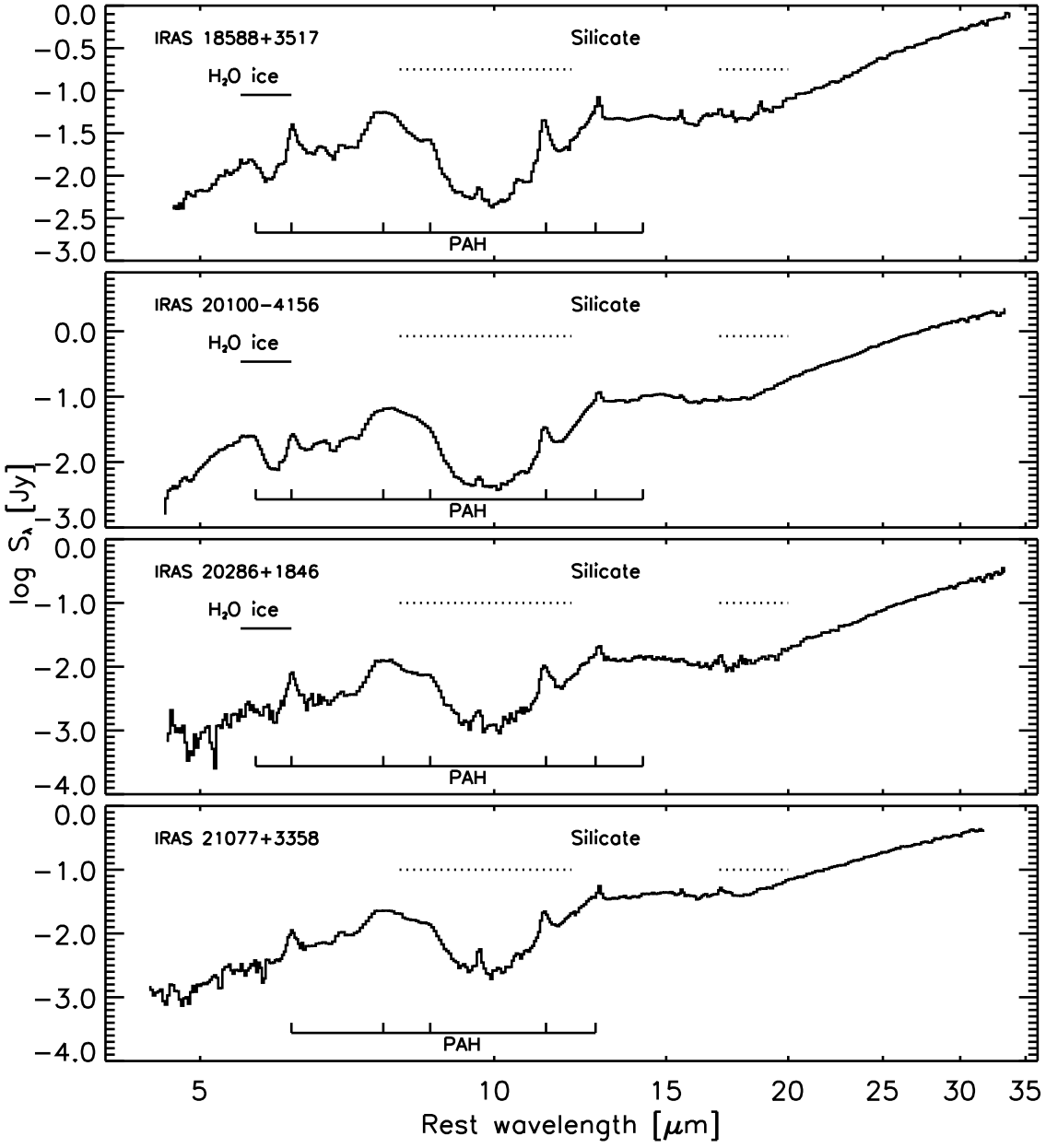

Figure B.11 Full low-resolution (LR) spectra for the OHMs observed with the *Spitzer* IRS. Locations of PAH emission and absorption features from water ices and silicates are marked.

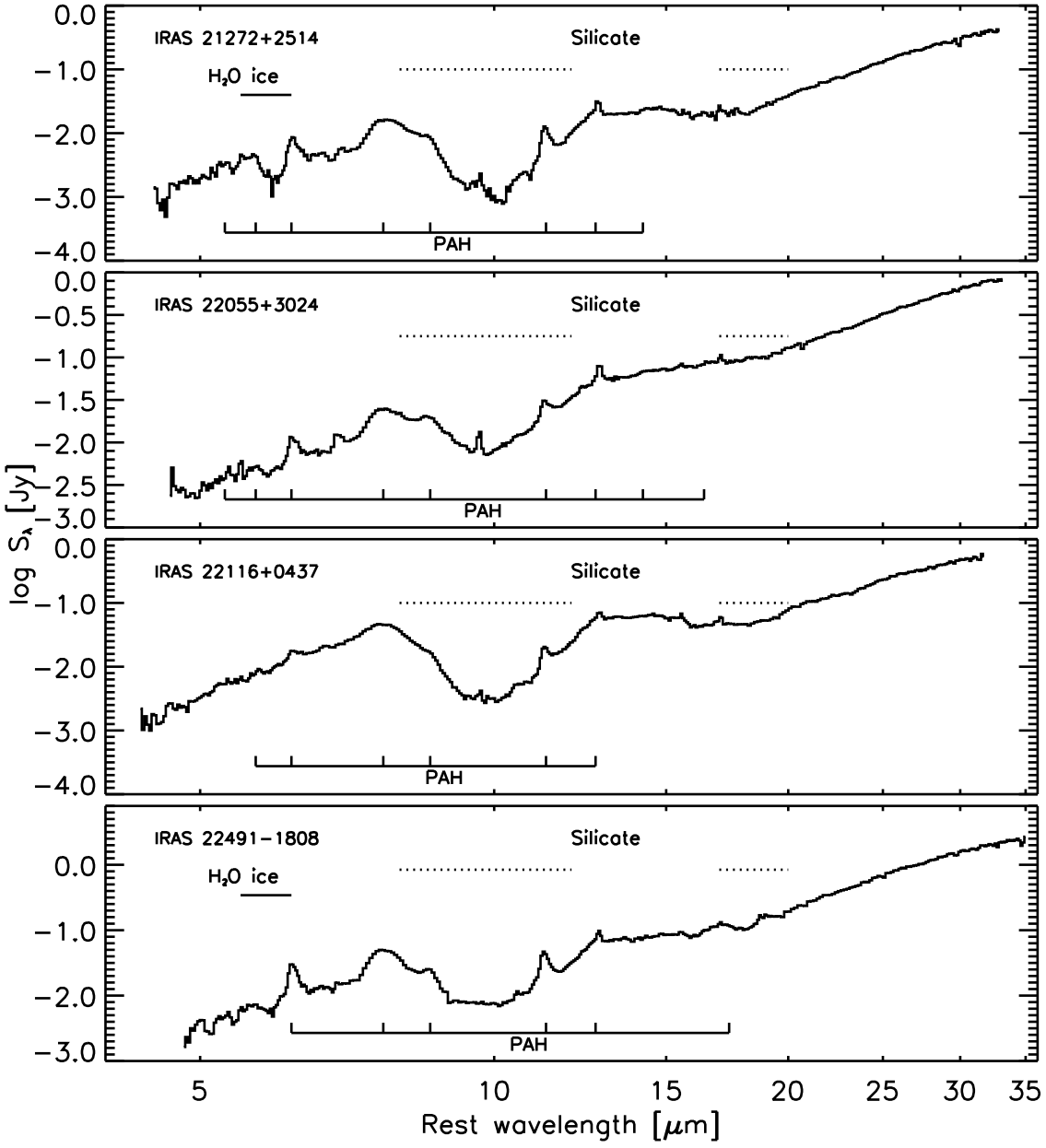

Figure B.12 Full low-resolution (LR) spectra for the OHMs observed with the *Spitzer* IRS. Locations of PAH emission and absorption features from water ices and silicates are marked.

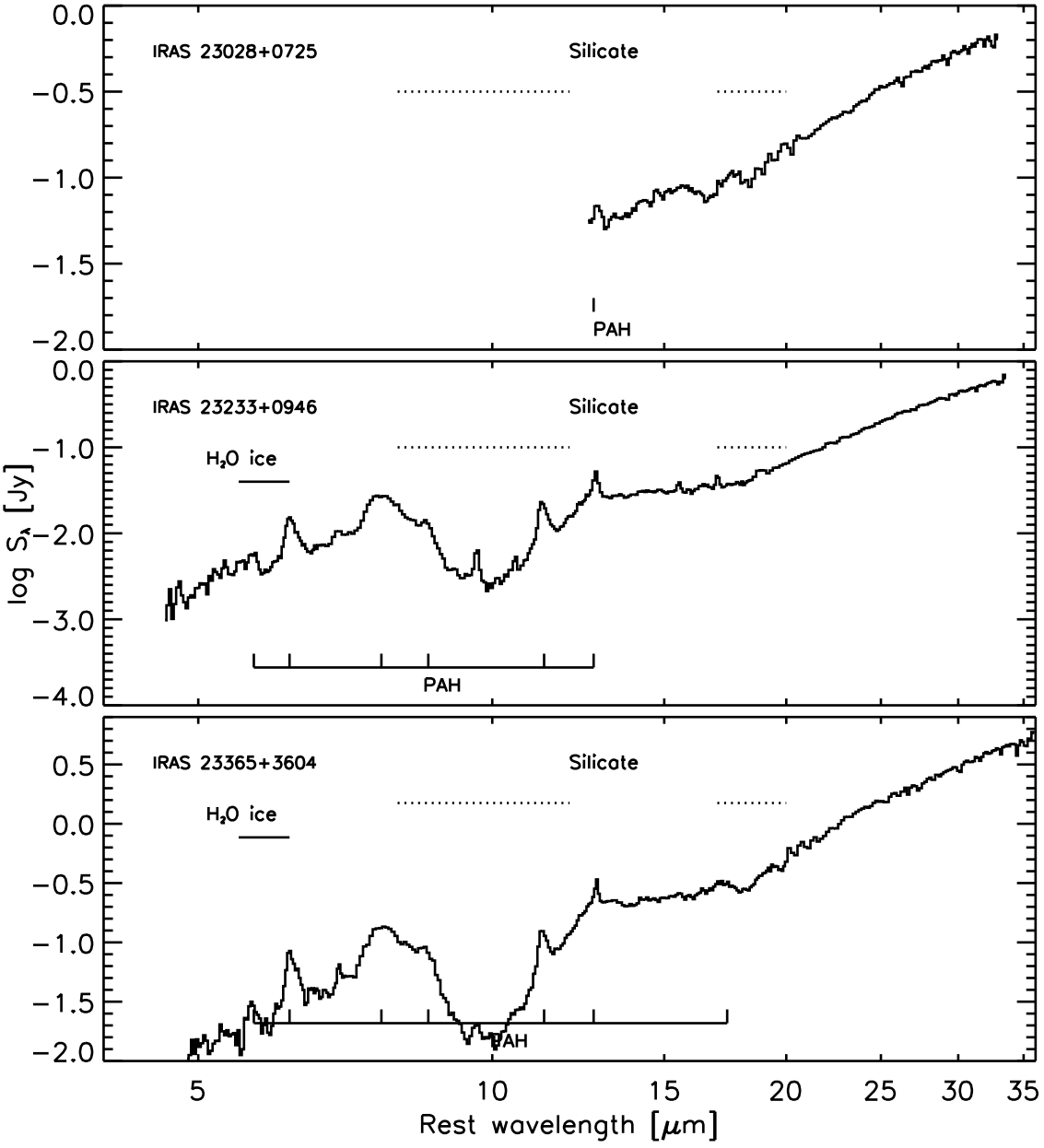

Figure B.13 Full low-resolution (LR) spectra for the OHMs observed with the *Spitzer* IRS. Locations of PAH emission and absorption features from water ices and silicates are marked.

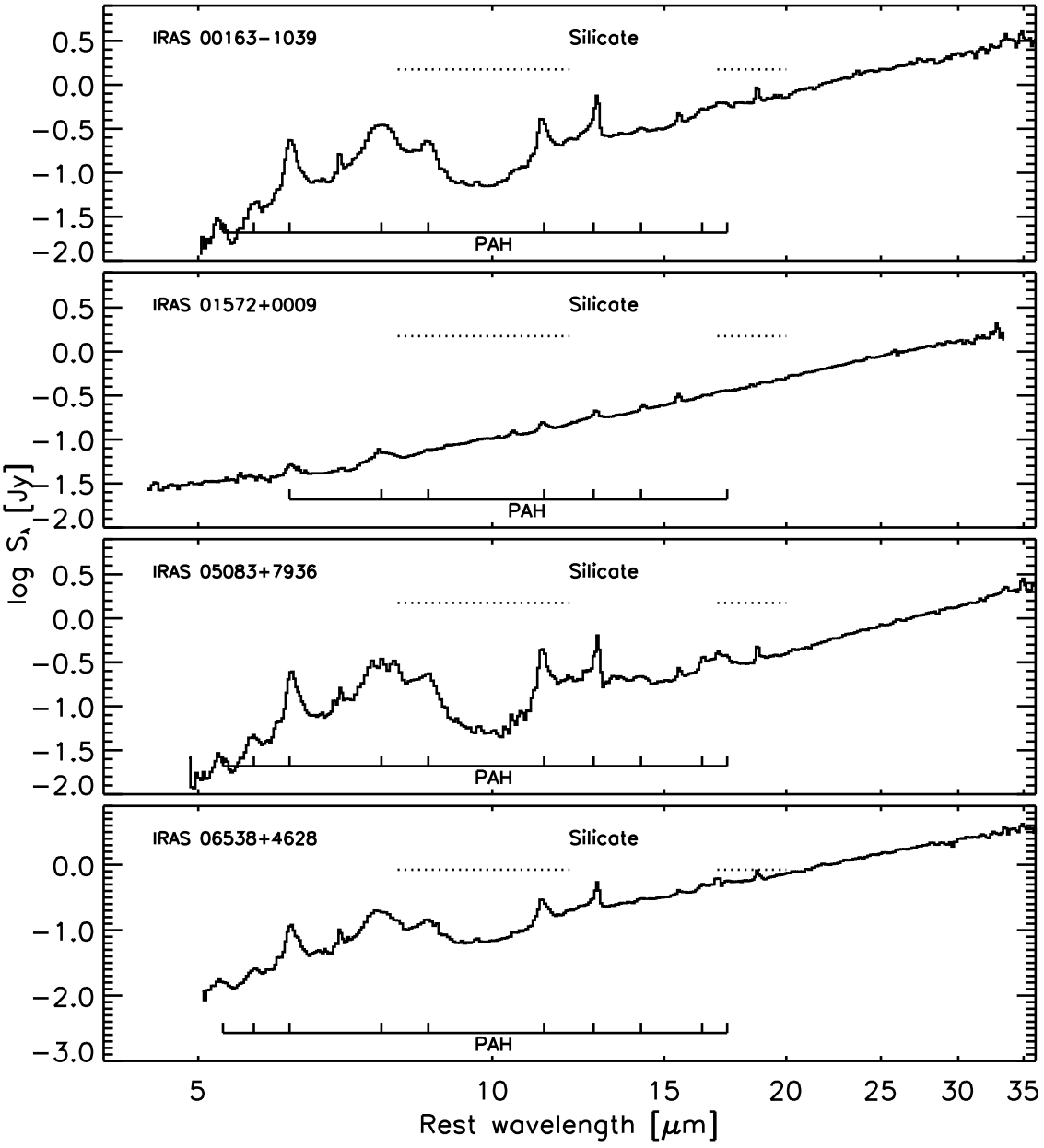

Figure B.14 Full low-resolution (LR) spectra for the non-masing galaxies observed with the *Spitzer* IRS. Locations of PAH emission and absorption features from water ices and silicates are marked.

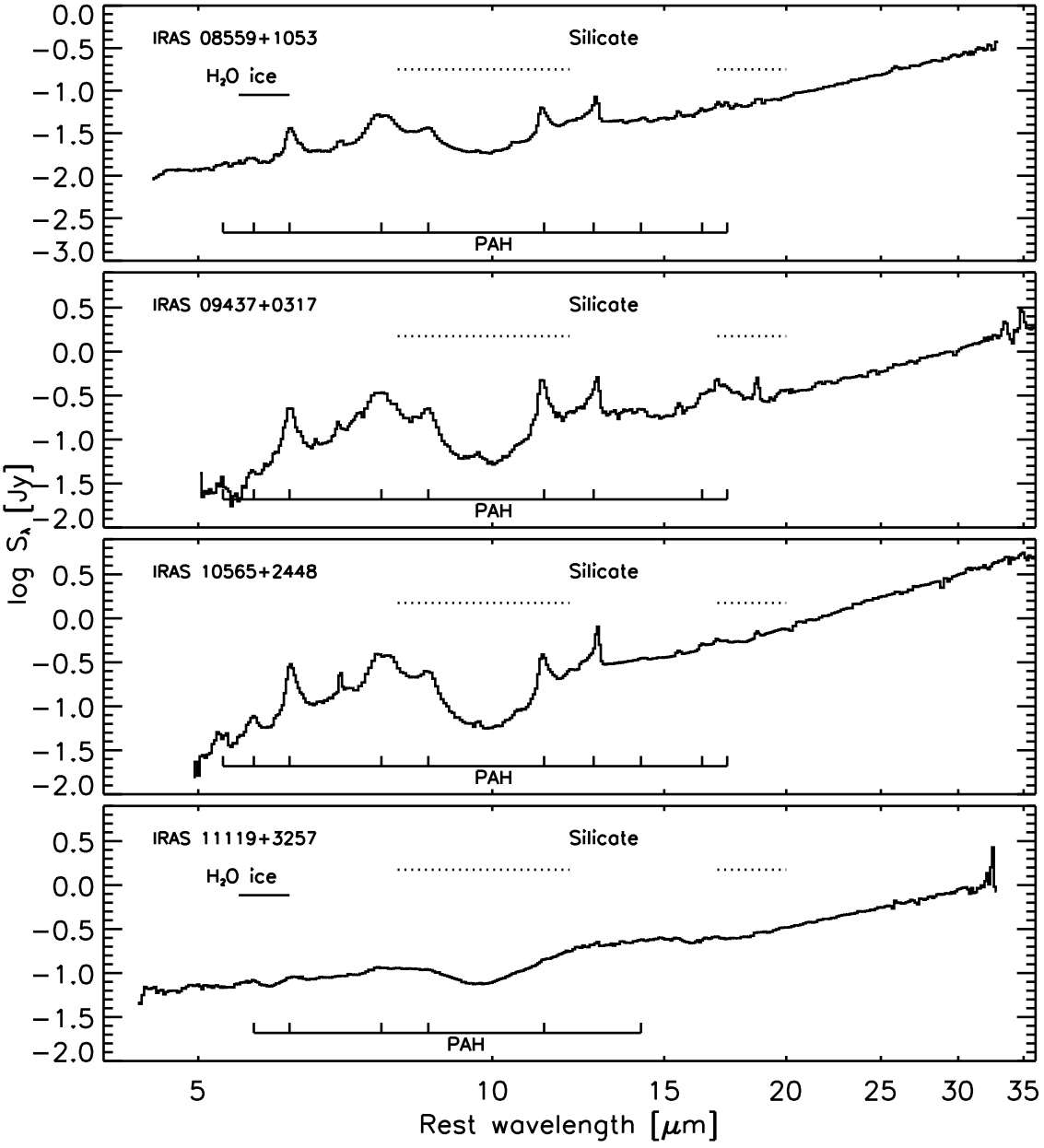

Figure B.15 Full low-resolution (LR) spectra for the non-masing galaxies observed with the *Spitzer* IRS. Locations of PAH emission and absorption features from water ices and silicates are marked.

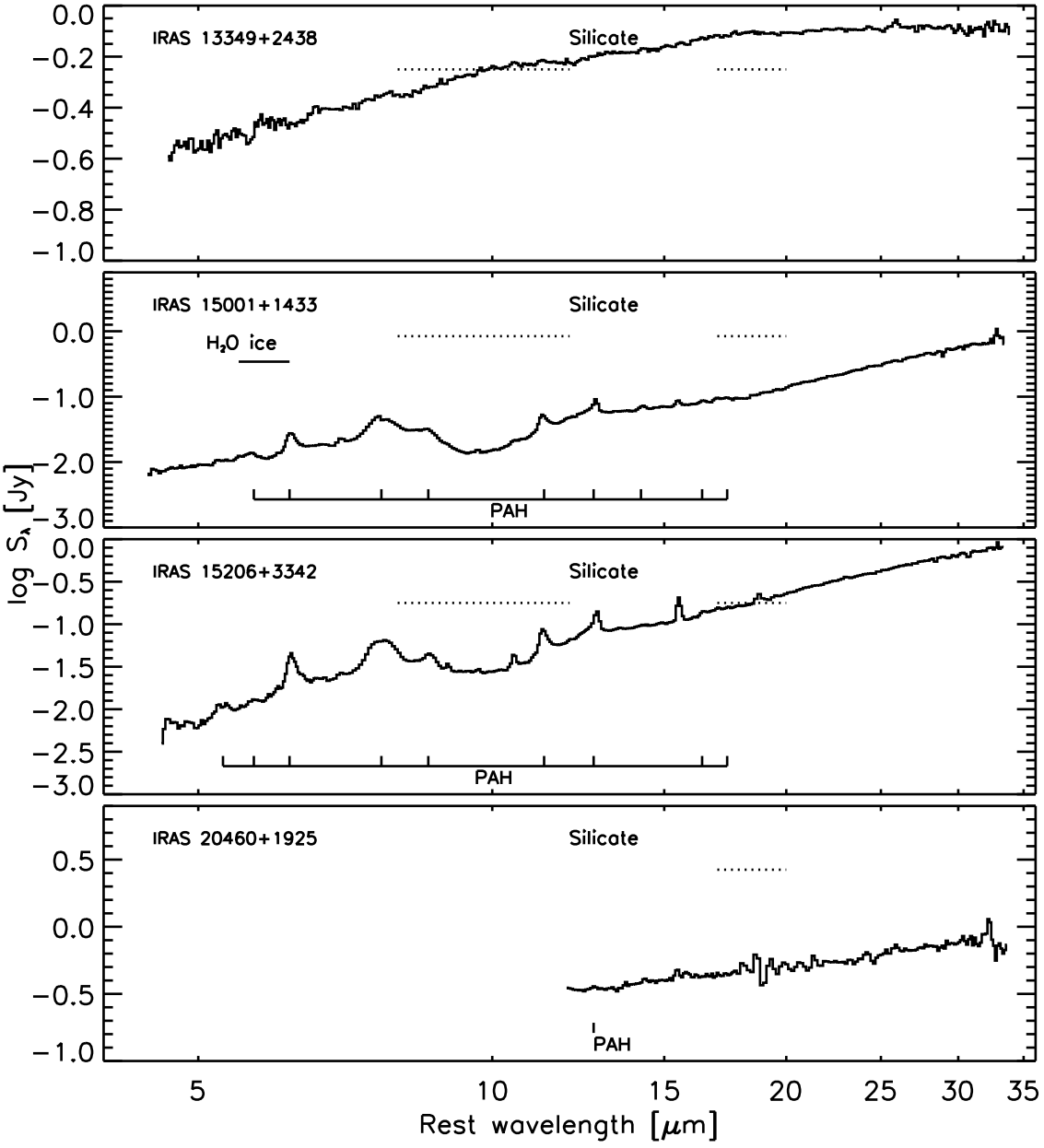

Figure B.16 Full low-resolution (LR) spectra for the non-masing galaxies observed with the *Spitzer* IRS. Locations of PAH emission and absorption features from water ices and silicates are marked.

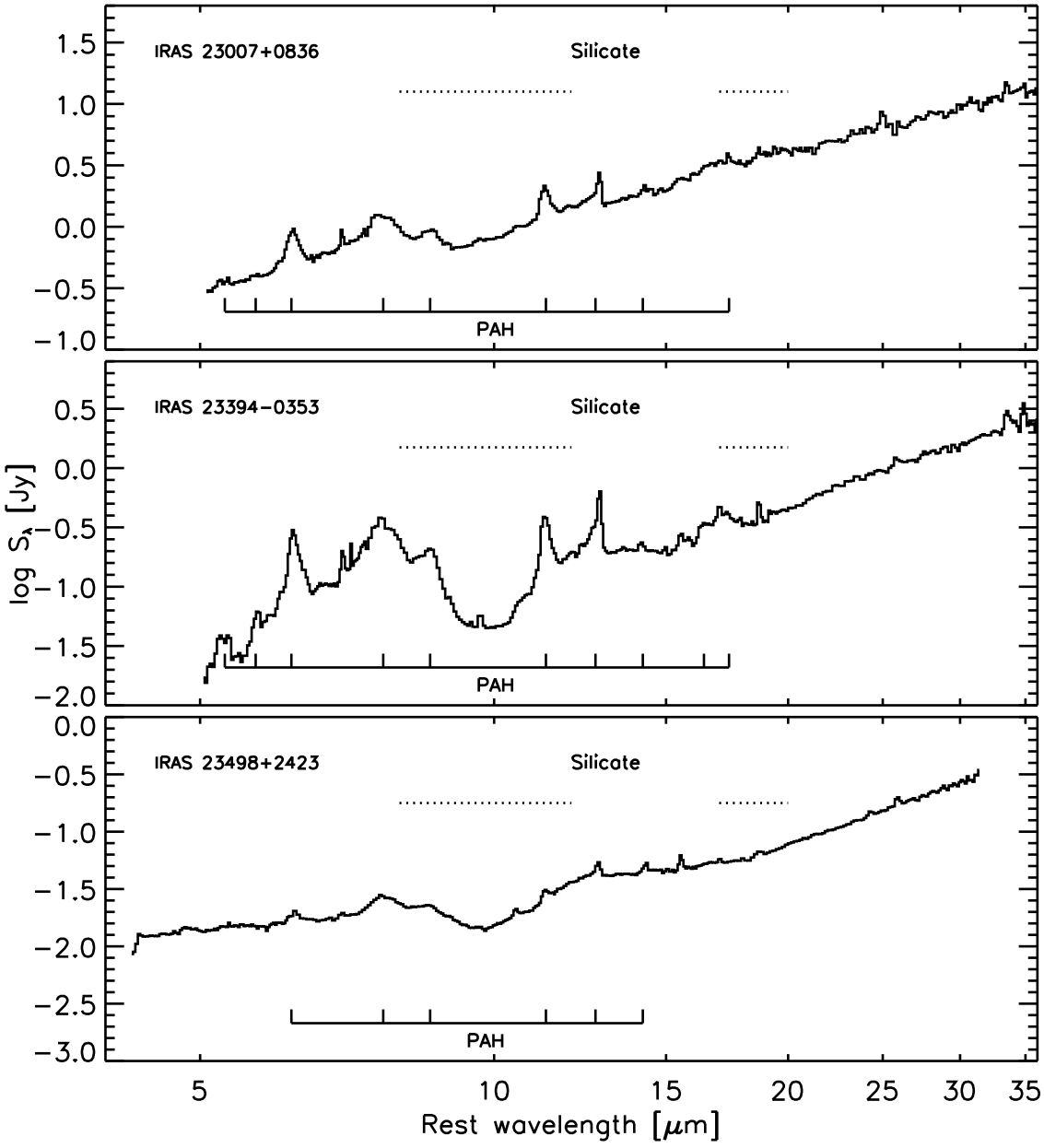

Figure B.17 Full low-resolution (LR) spectra for the non-masing galaxies observed with the *Spitzer* IRS. Locations of PAH emission and absorption features from water ices and silicates are marked.

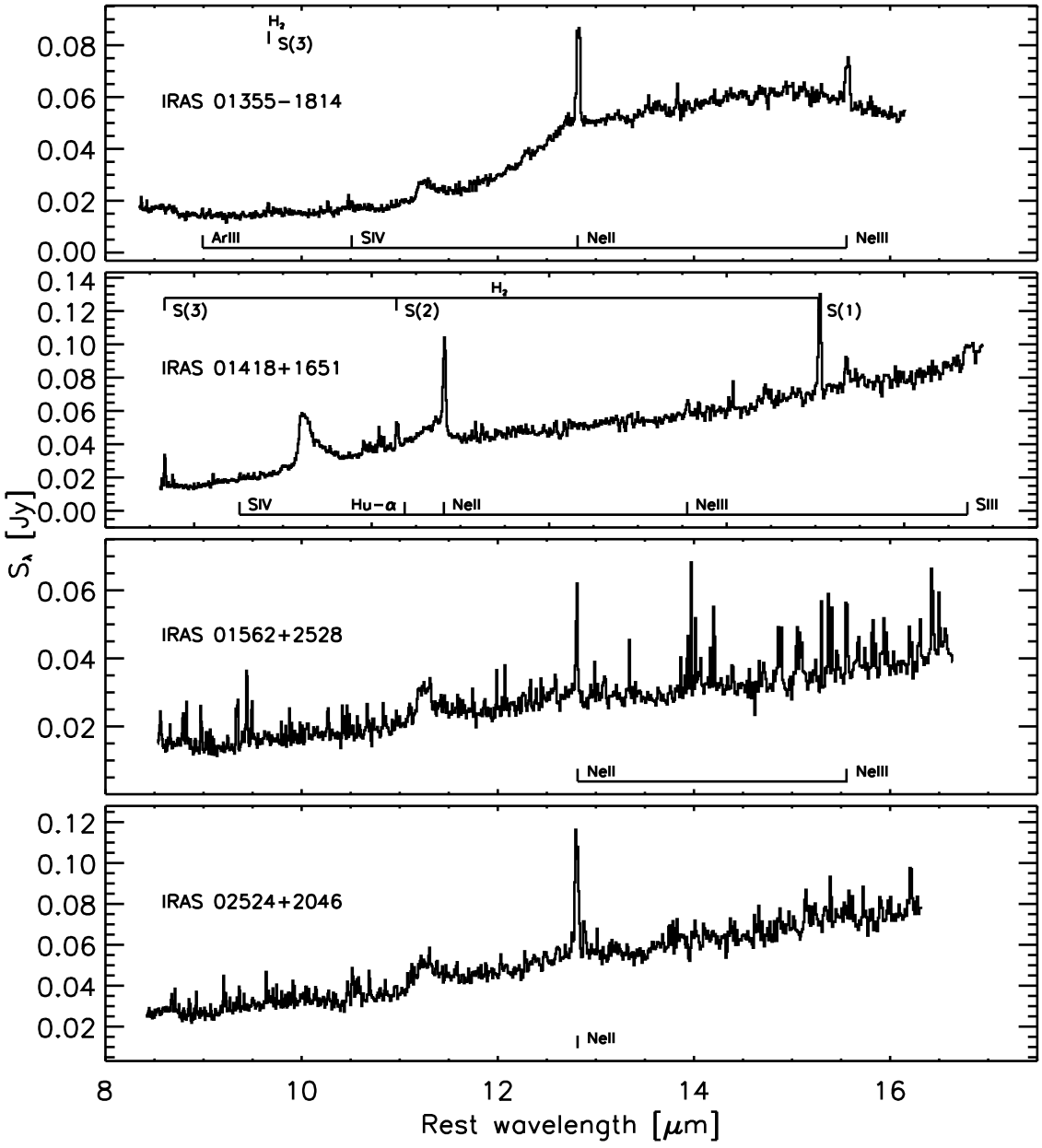

Figure B.18 Short-high (SH) module spectra for the OHMs observed with the *Spitzer* IRS. Detected atomic and molecular emission features in each spectra are marked.

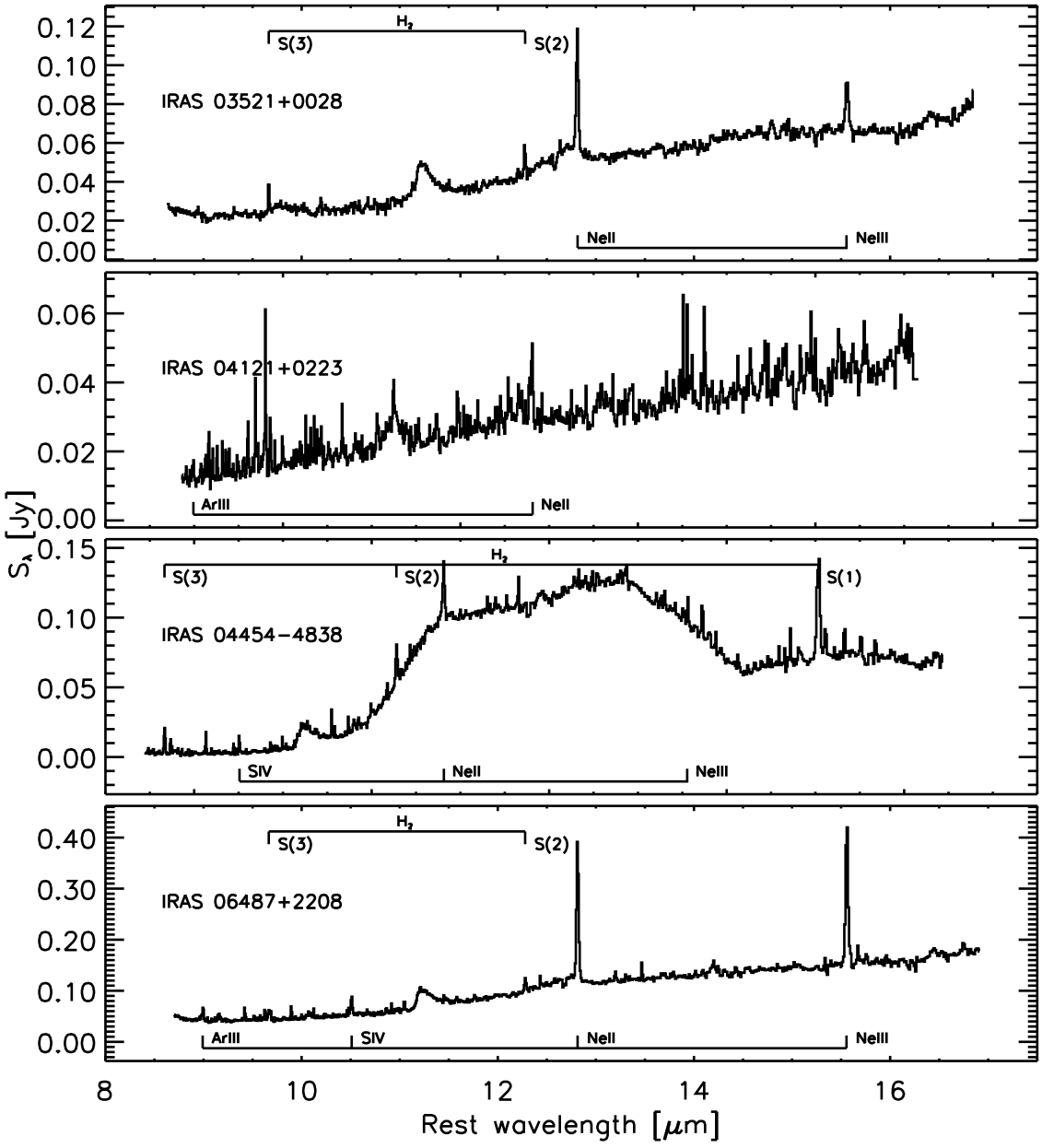

Figure B.19 Short-high (SH) module spectra for the OHMs observed with the *Spitzer* IRS. Detected atomic and molecular emission features in each spectra are marked.

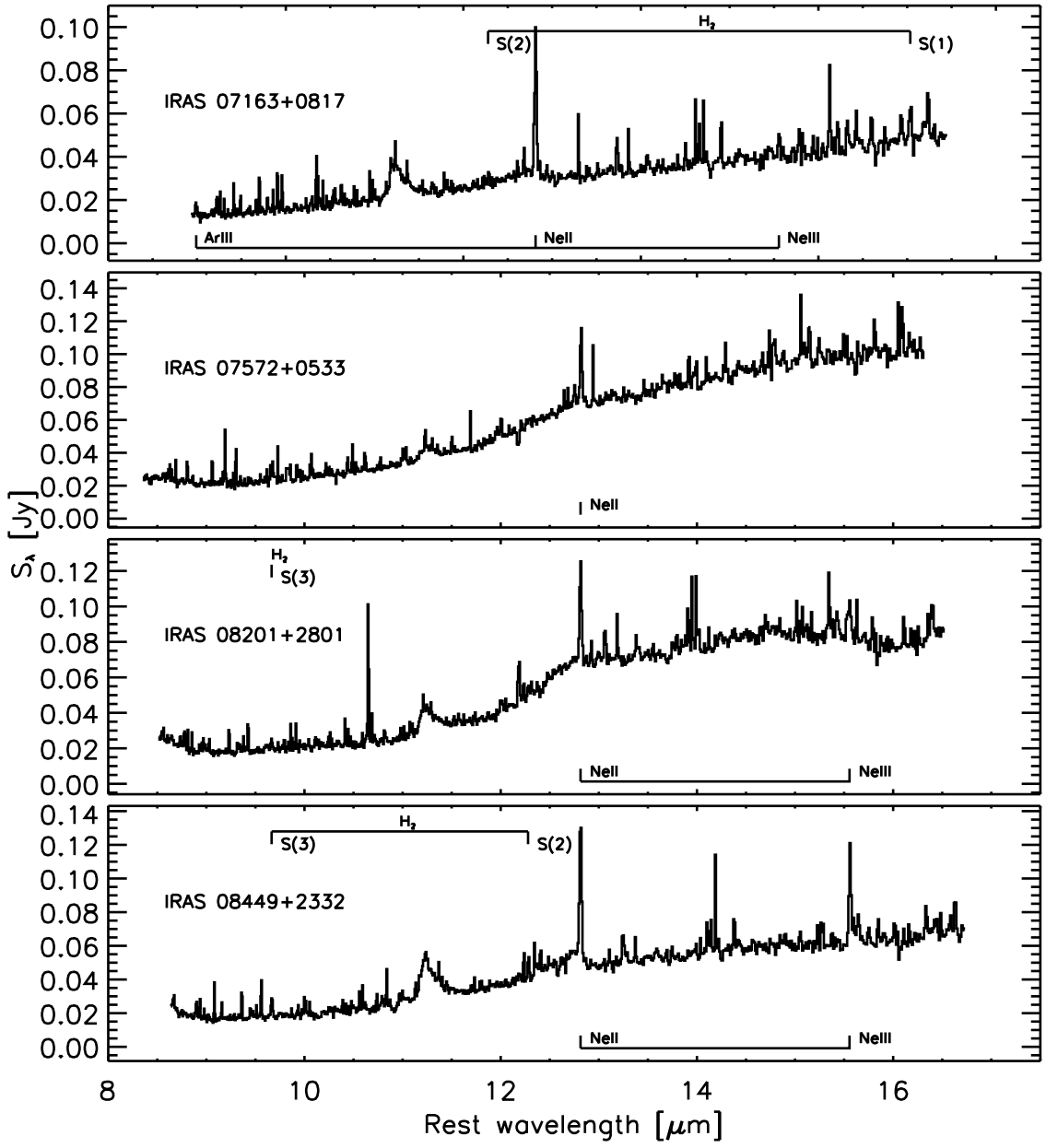

Figure B.20 Short-high (SH) module spectra for the OHMs observed with the *Spitzer* IRS. Detected atomic and molecular emission features in each spectra are marked.

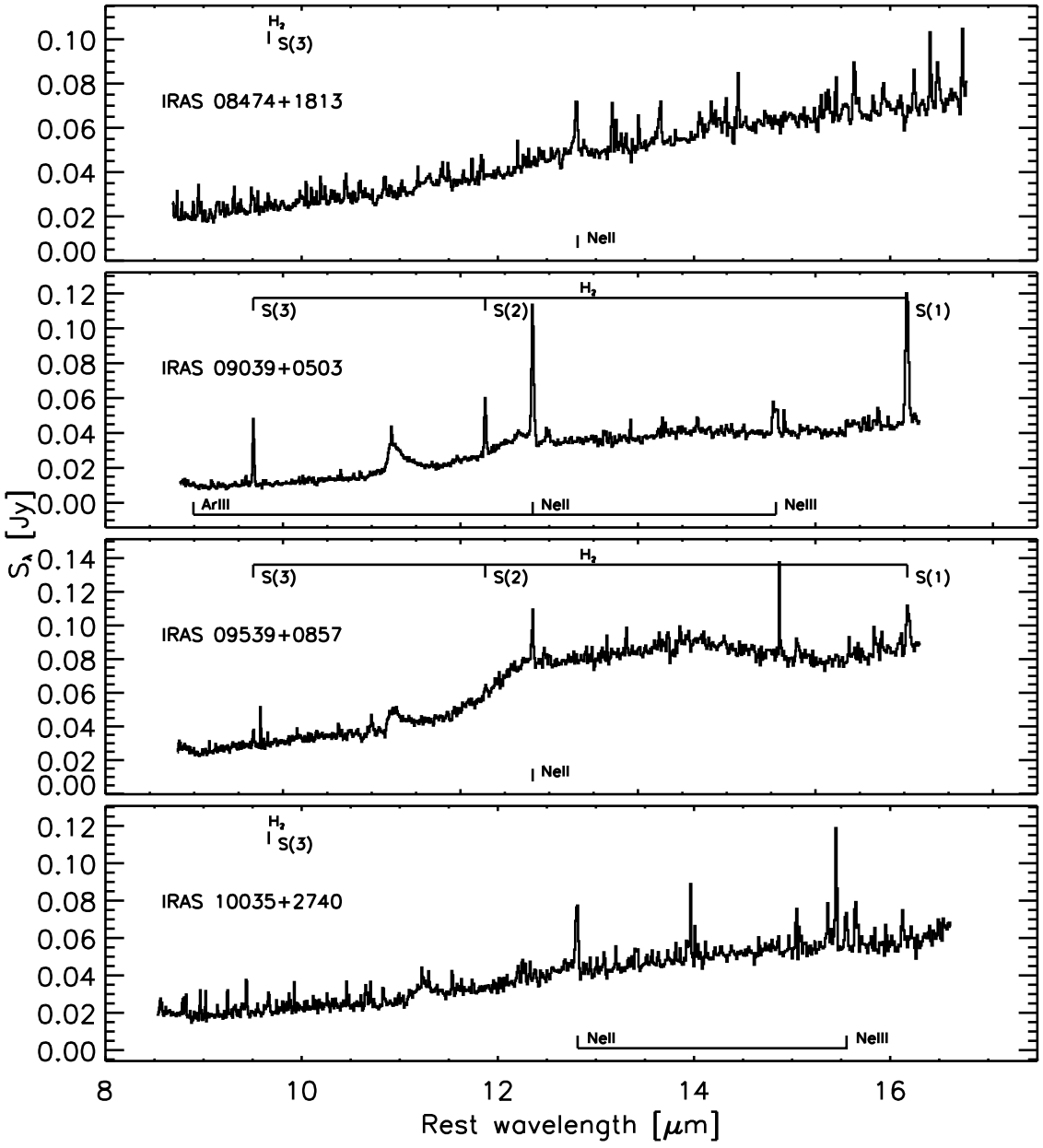

Figure B.21 Short-high (SH) module spectra for the OHMs observed with the *Spitzer* IRS. Detected atomic and molecular emission features in each spectra are marked.

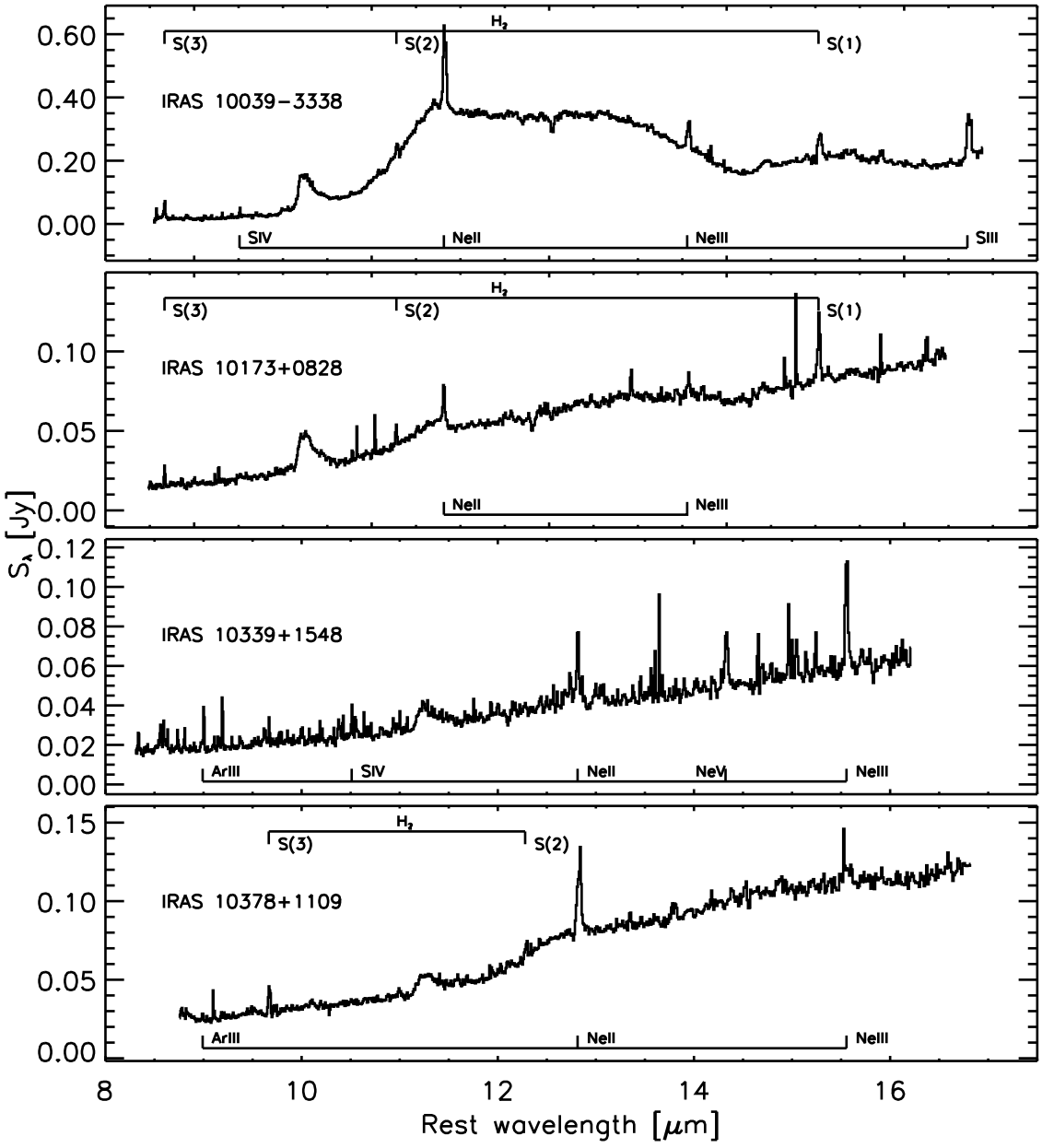

Figure B.22 Short-high (SH) module spectra for the OHMs observed with the *Spitzer* IRS. Detected atomic and molecular emission features in each spectra are marked.

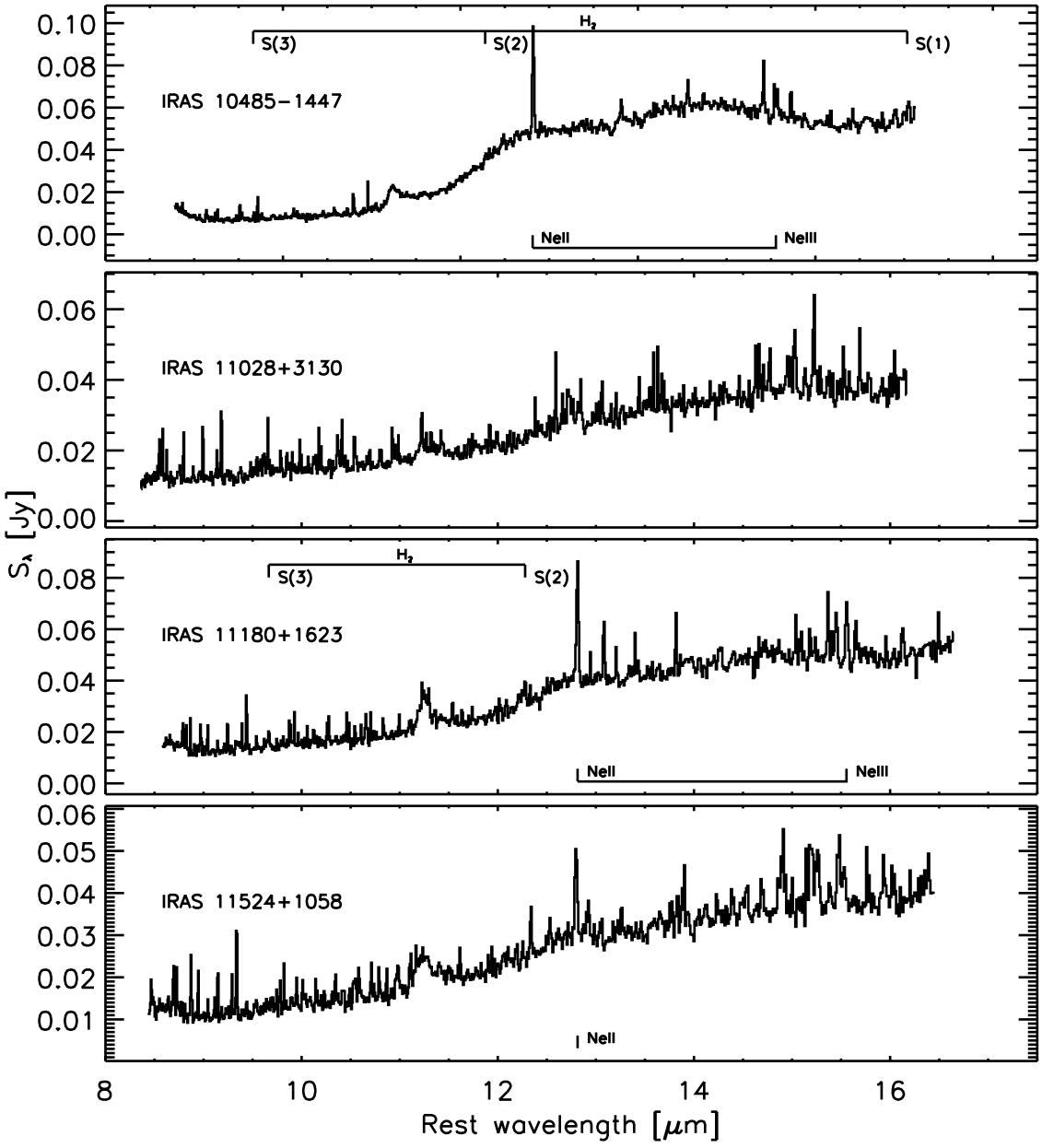

Figure B.23 Short-high (SH) module spectra for the OHMs observed with the *Spitzer* IRS. Detected atomic and molecular emission features in each spectra are marked.

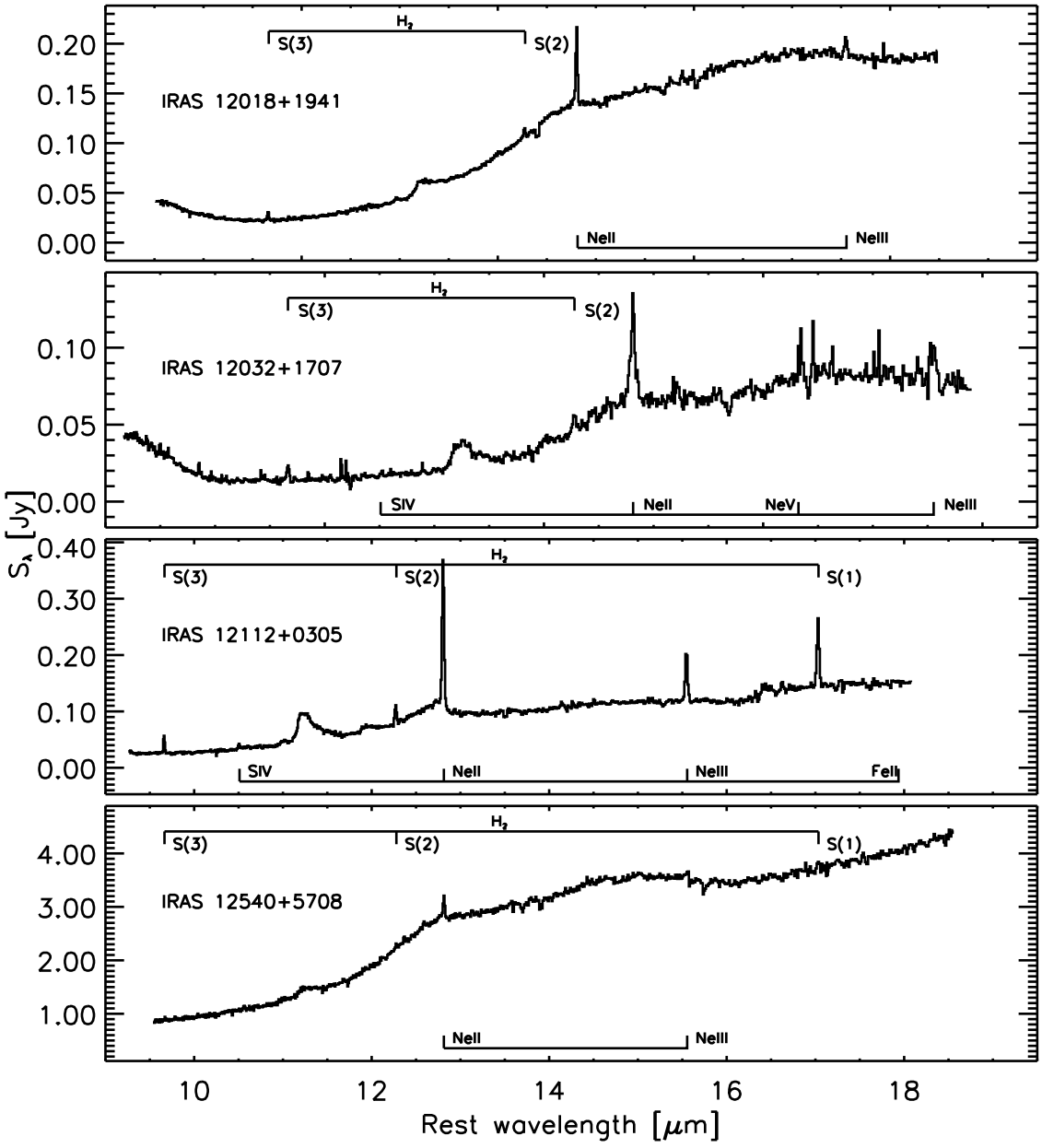

Figure B.24 Short-high (SH) module spectra for the OHMs observed with the *Spitzer* IRS. Detected atomic and molecular emission features in each spectra are marked.

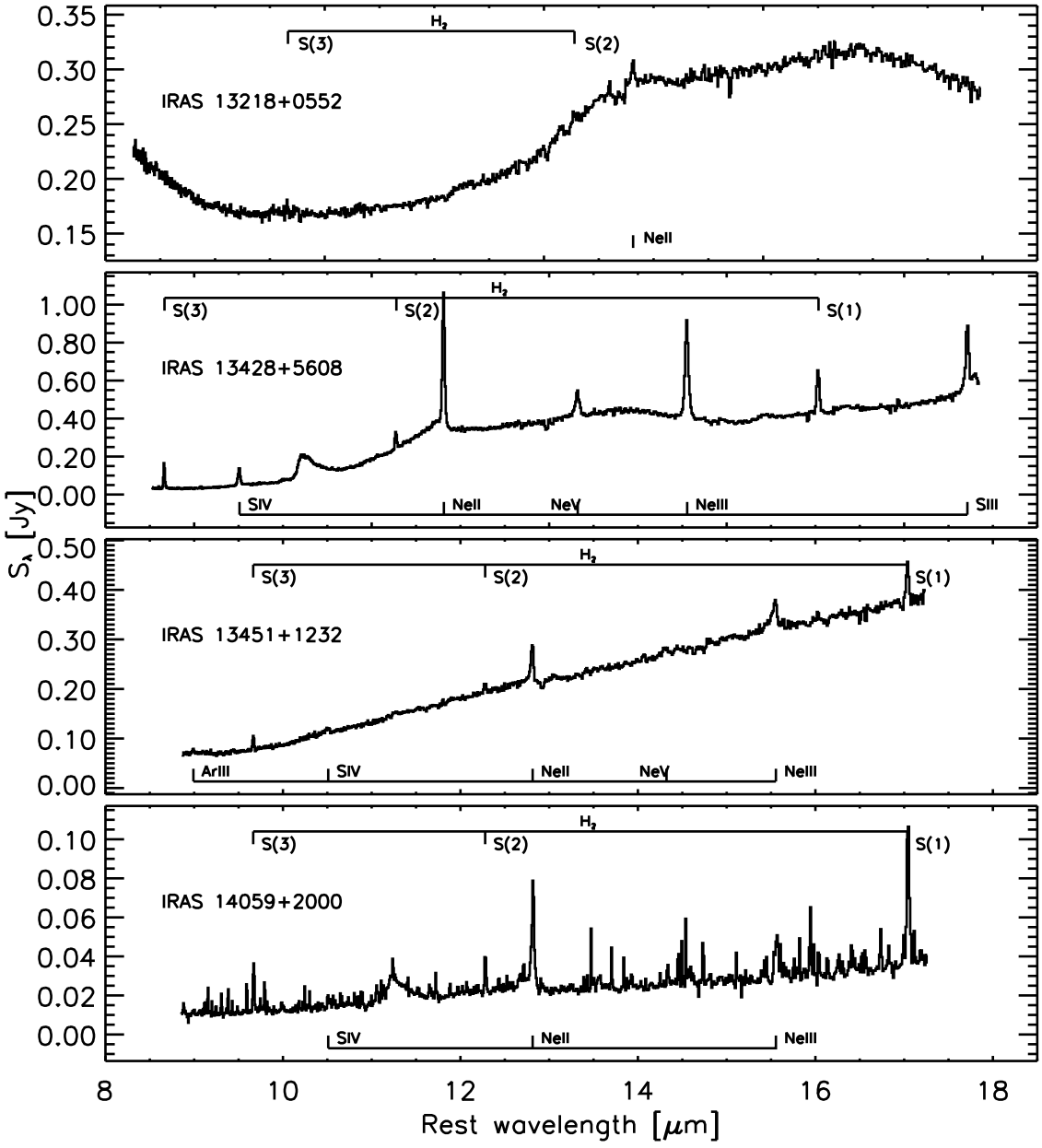

Figure B.25 Short-high (SH) module spectra for the OHMs observed with the *Spitzer* IRS. Detected atomic and molecular emission features in each spectra are marked.

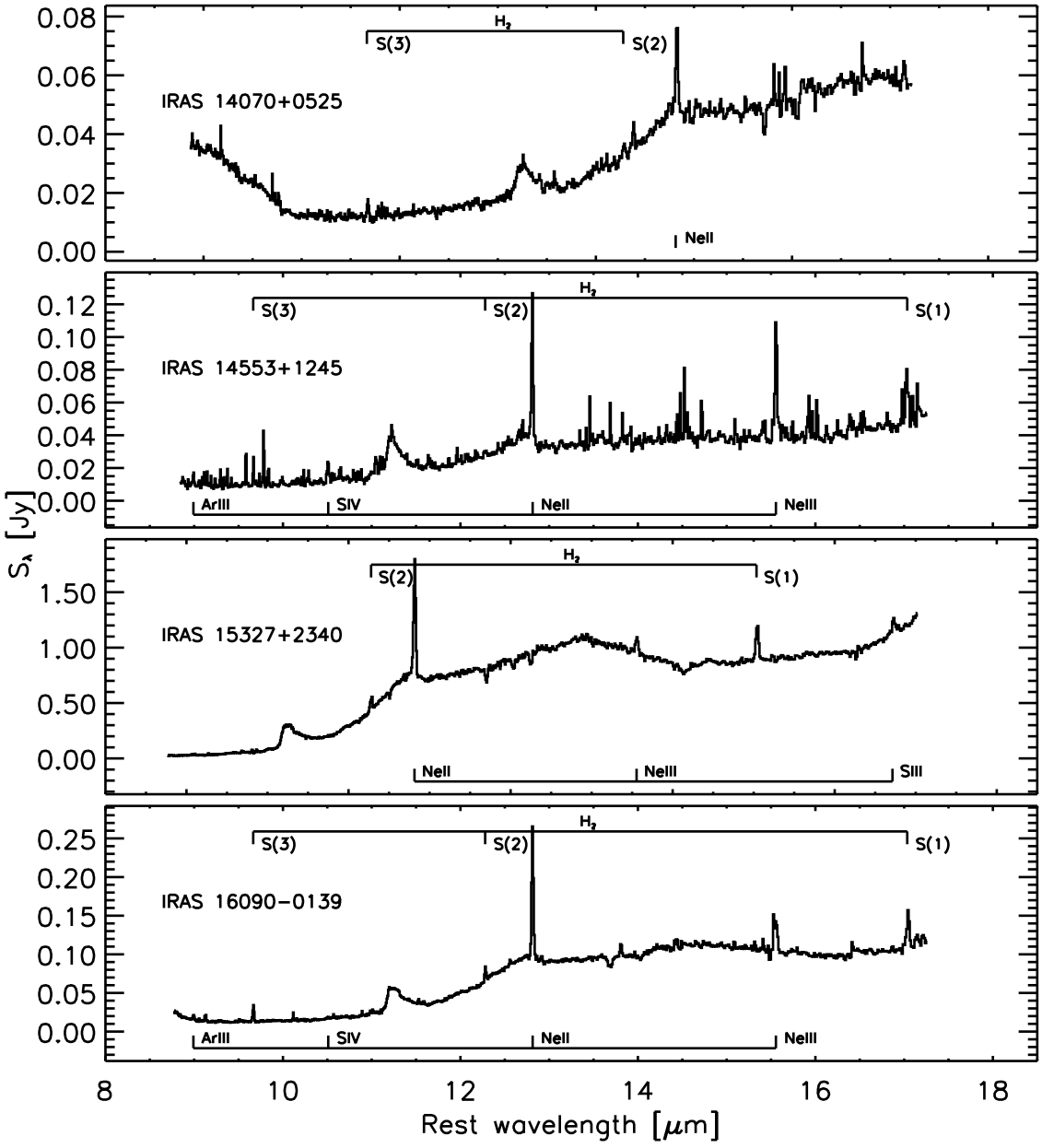

Figure B.26 Short-high (SH) module spectra for the OHMs observed with the *Spitzer* IRS. Detected atomic and molecular emission features in each spectra are marked.

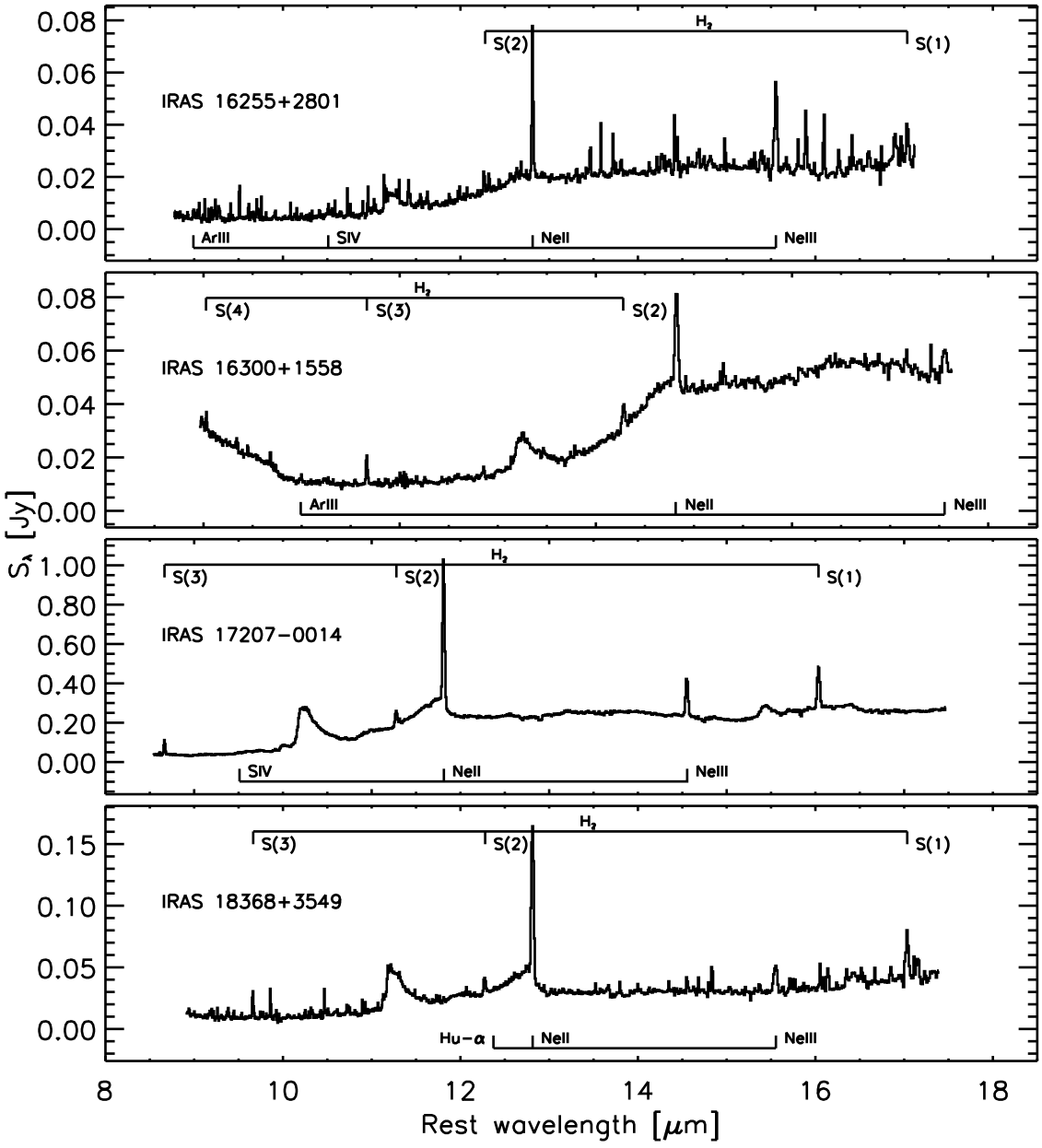

Figure B.27 Short-high (SH) module spectra for the OHMs observed with the *Spitzer* IRS. Detected atomic and molecular emission features in each spectra are marked.

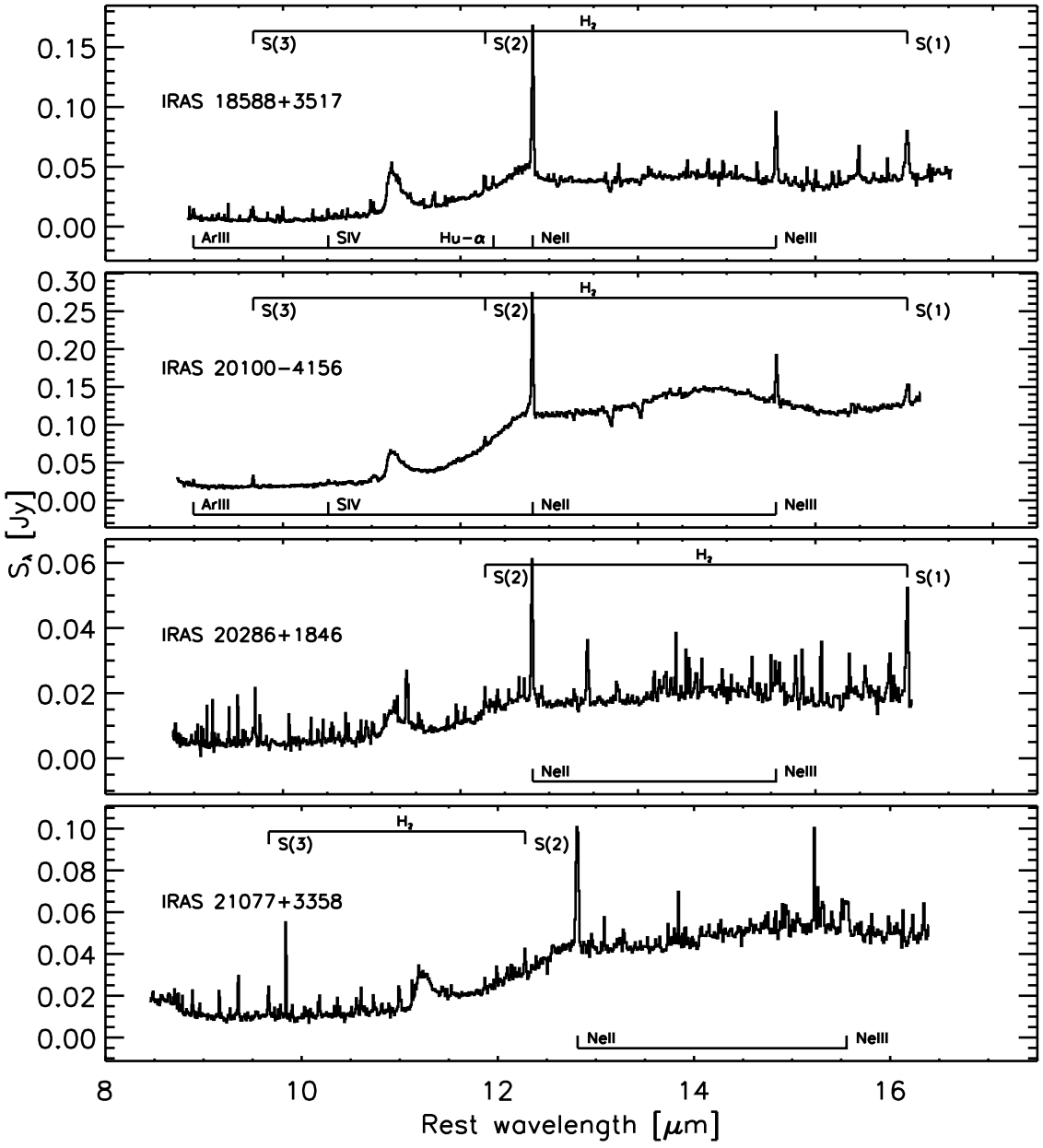

Figure B.28 Short-high (SH) module spectra for the OHMs observed with the *Spitzer* IRS. Detected atomic and molecular emission features in each spectra are marked.

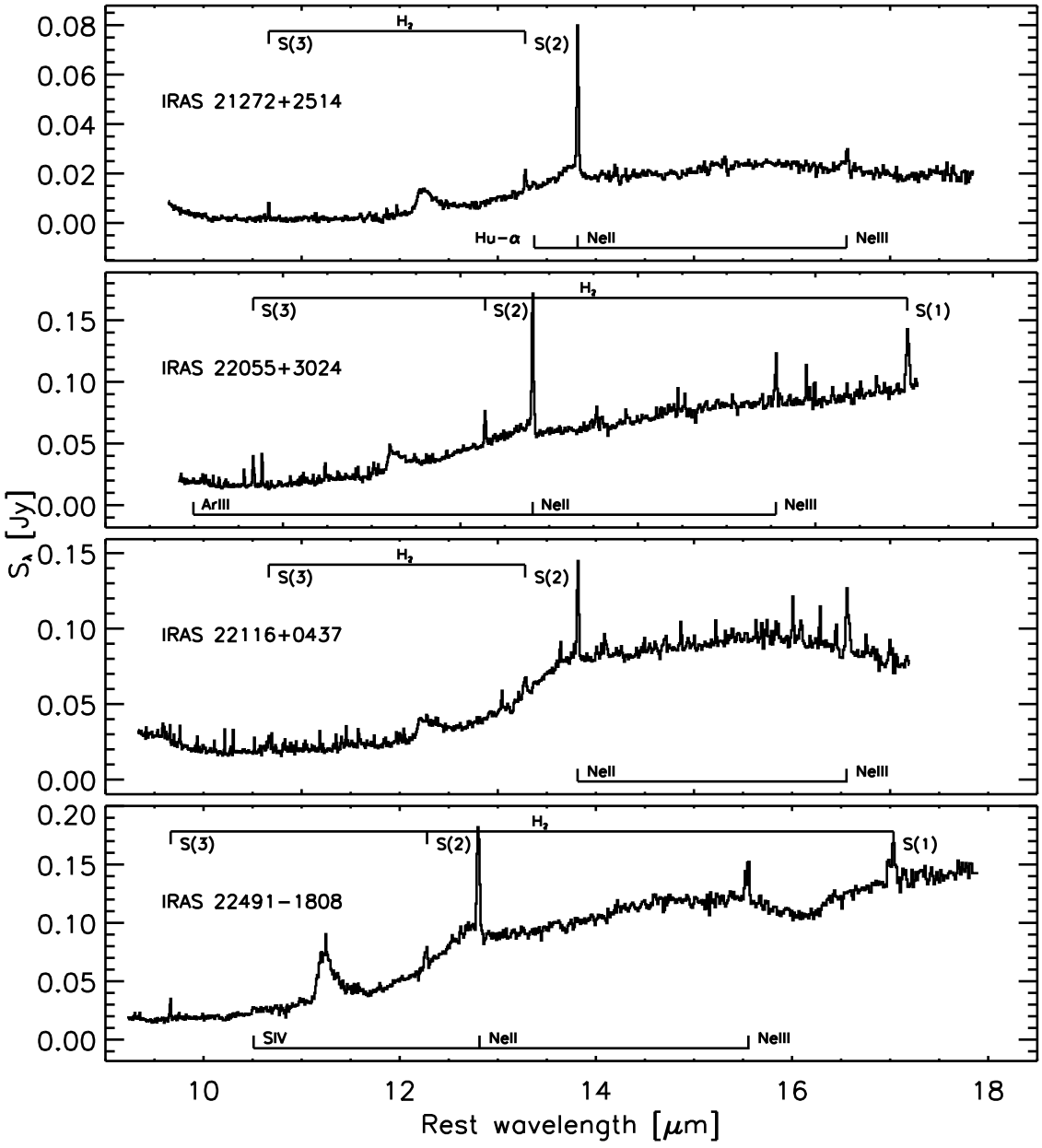

Figure B.29 Short-high (SH) module spectra for the OHMs observed with the *Spitzer* IRS. Detected atomic and molecular emission features in each spectra are marked.

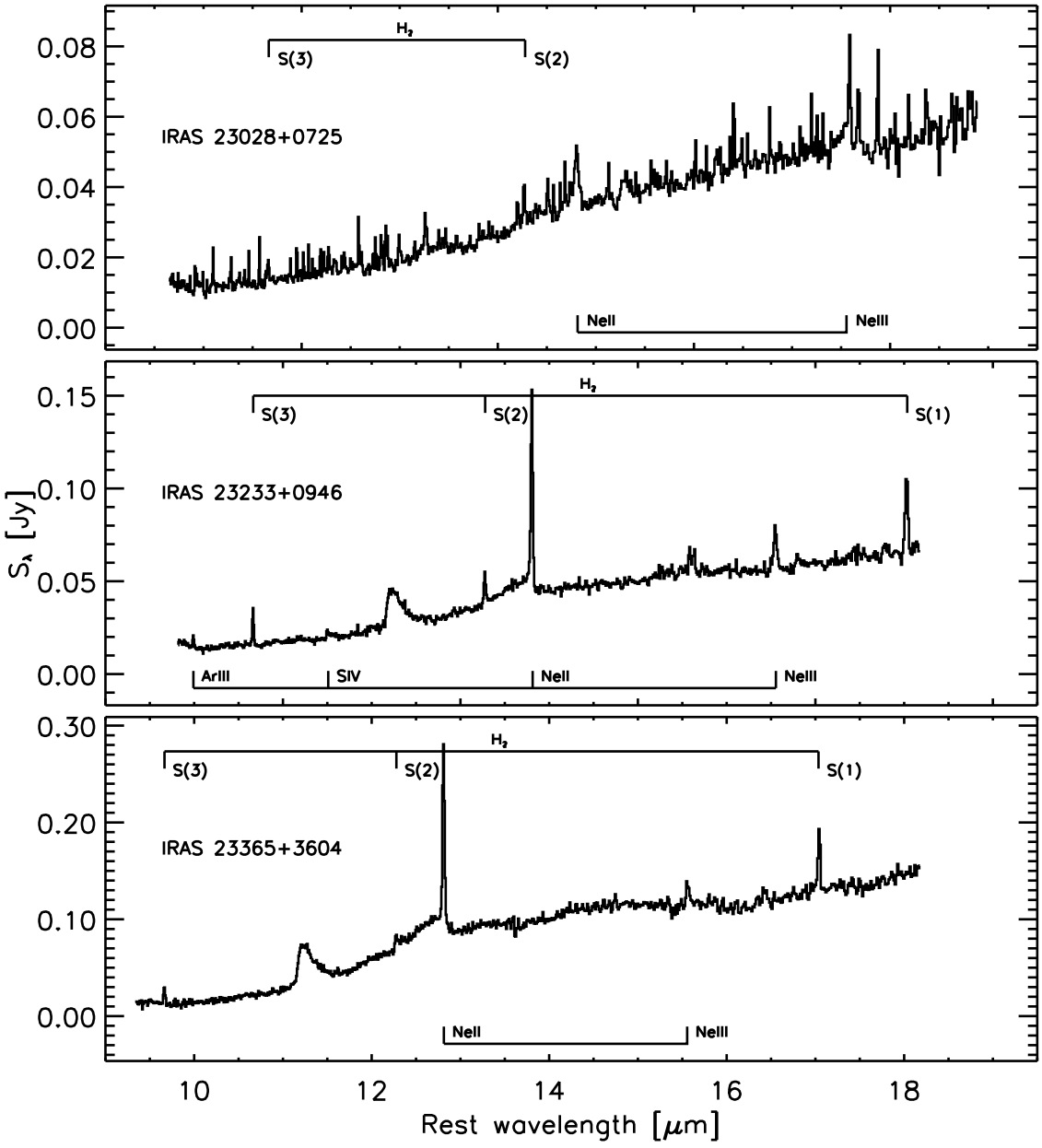

Figure B.30 Short-high (SH) module spectra for the OHMs observed with the *Spitzer* IRS. Detected atomic and molecular emission features in each spectra are marked.

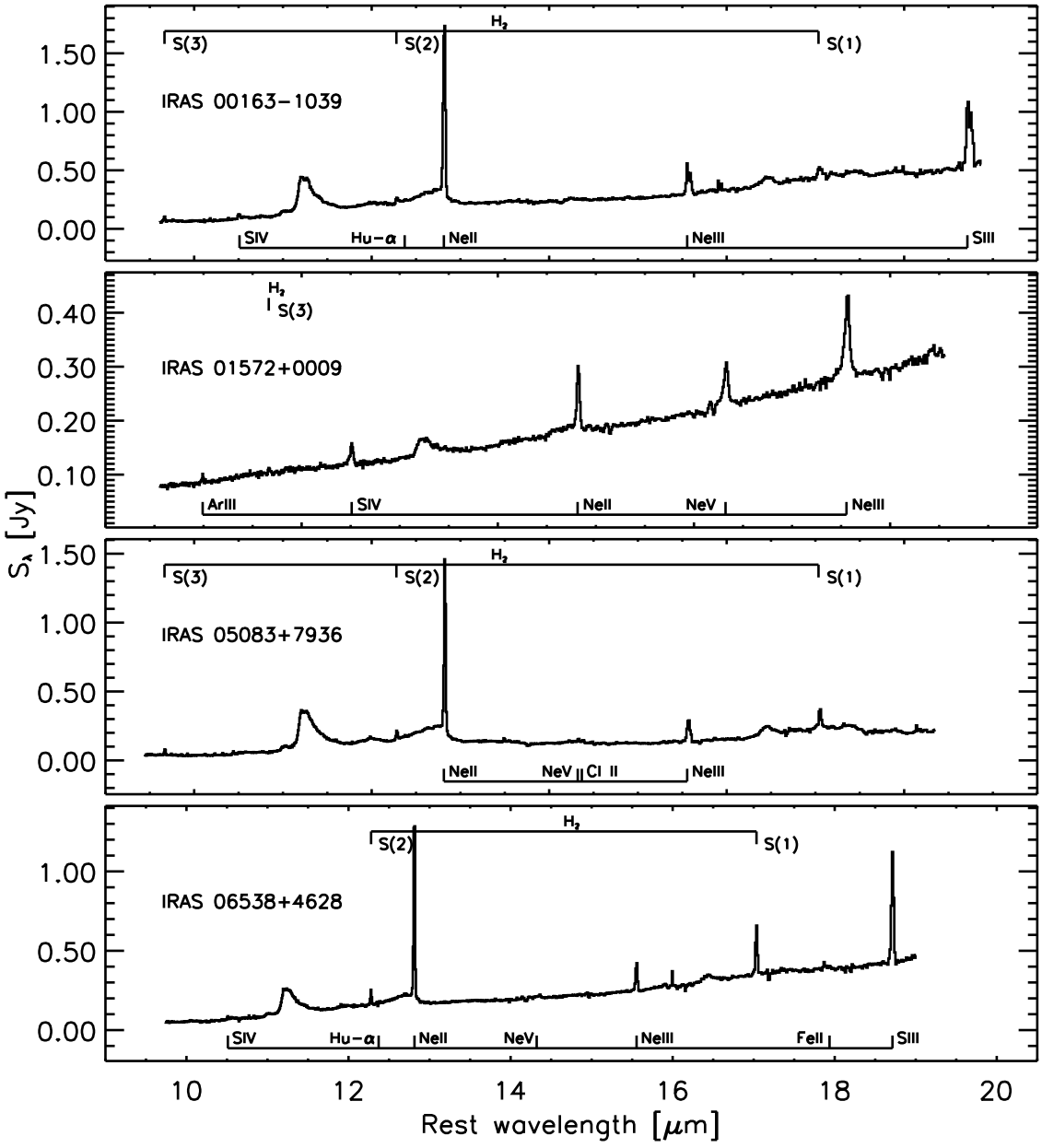

Figure B.31 Short-high (SH) module spectra for the non-masing galaxies observed with the *Spitzer* IRS. Detected atomic and molecular emission features in each spectra are marked.

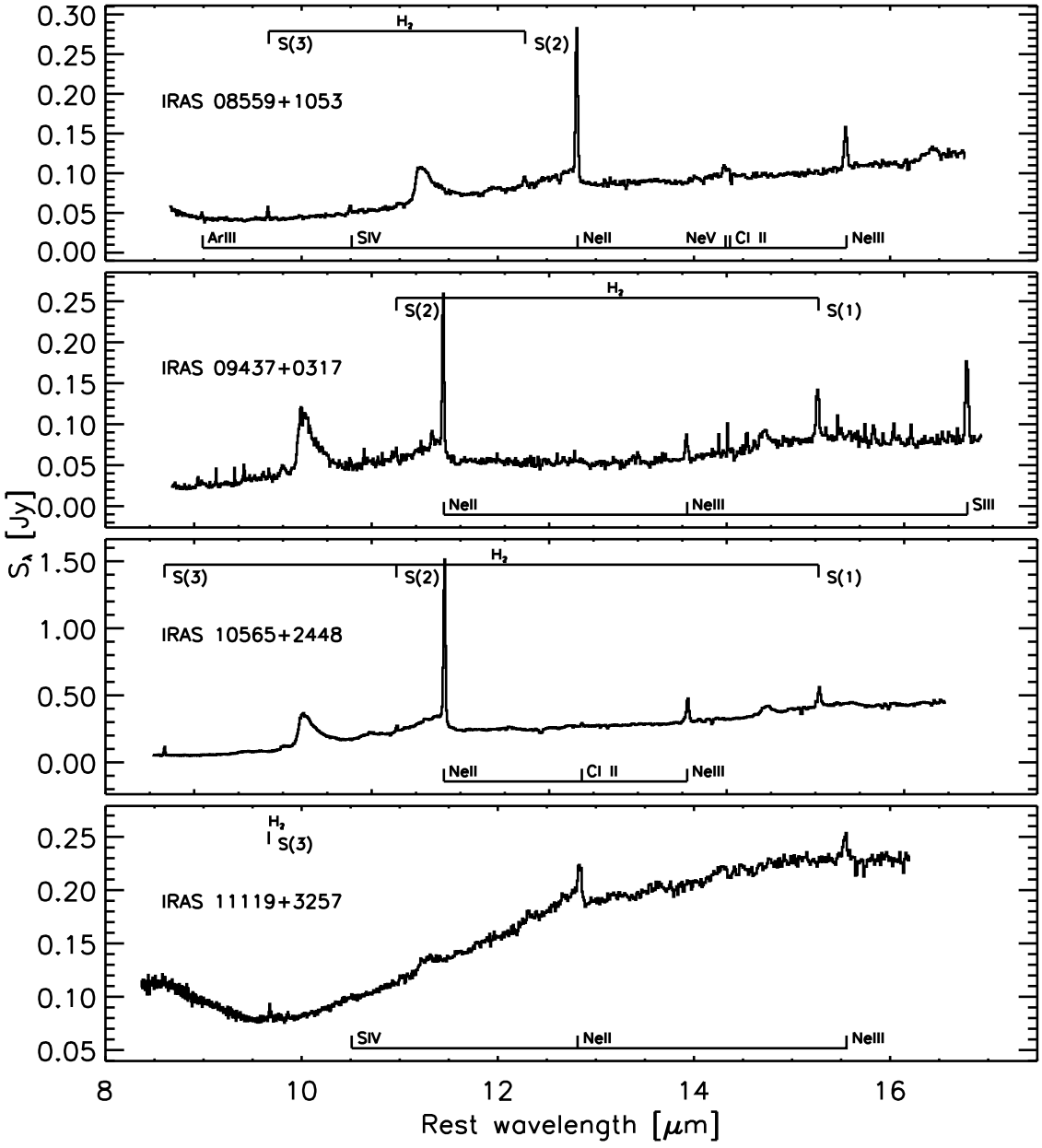

Figure B.32 Short-high (SH) module spectra for the non-masing galaxies observed with the *Spitzer* IRS. Detected atomic and molecular emission features in each spectra are marked.

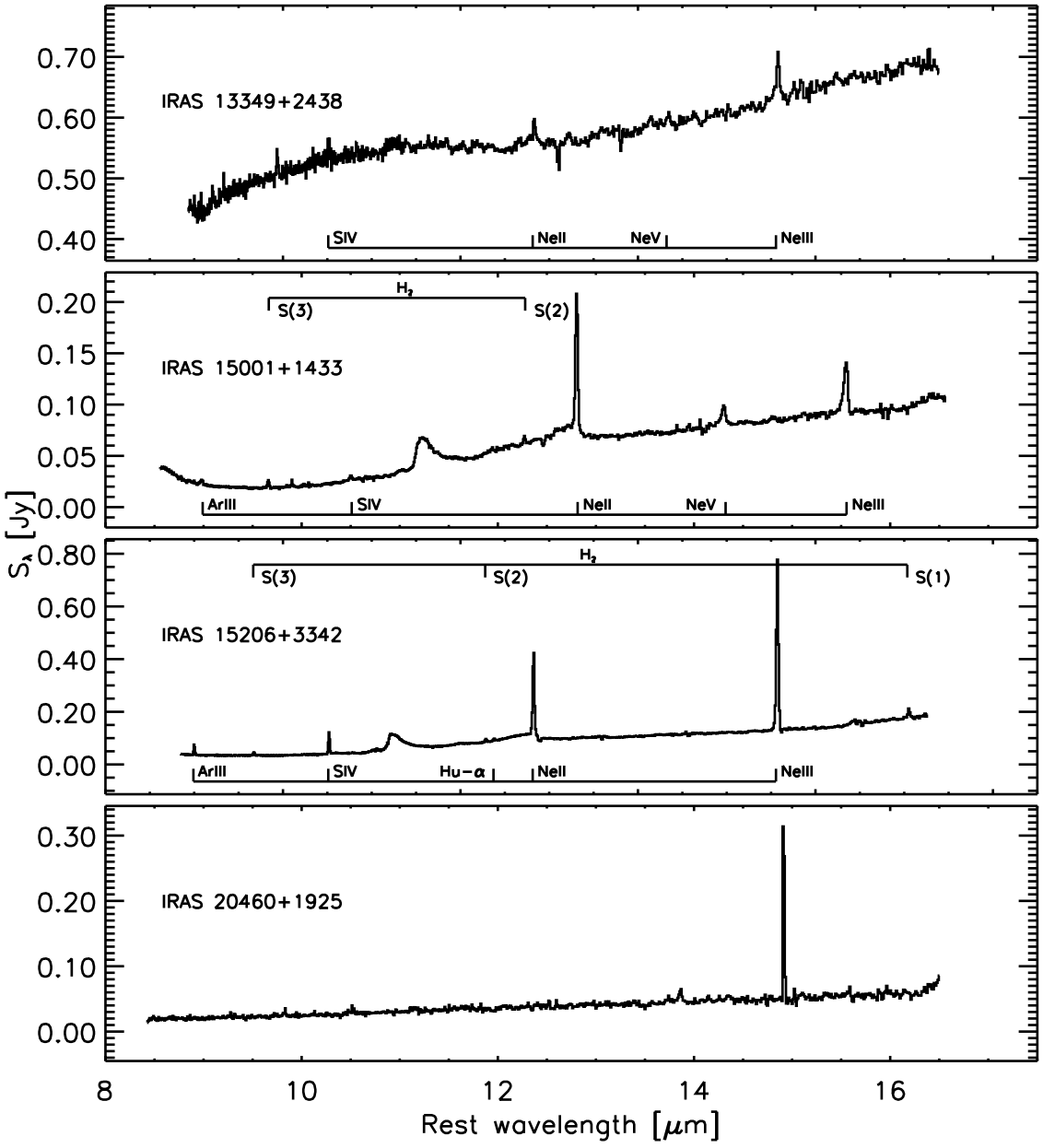

Figure B.33 Short-high (SH) module spectra for the non-masing galaxies observed with the *Spitzer* IRS. Detected atomic and molecular emission features in each spectra are marked.

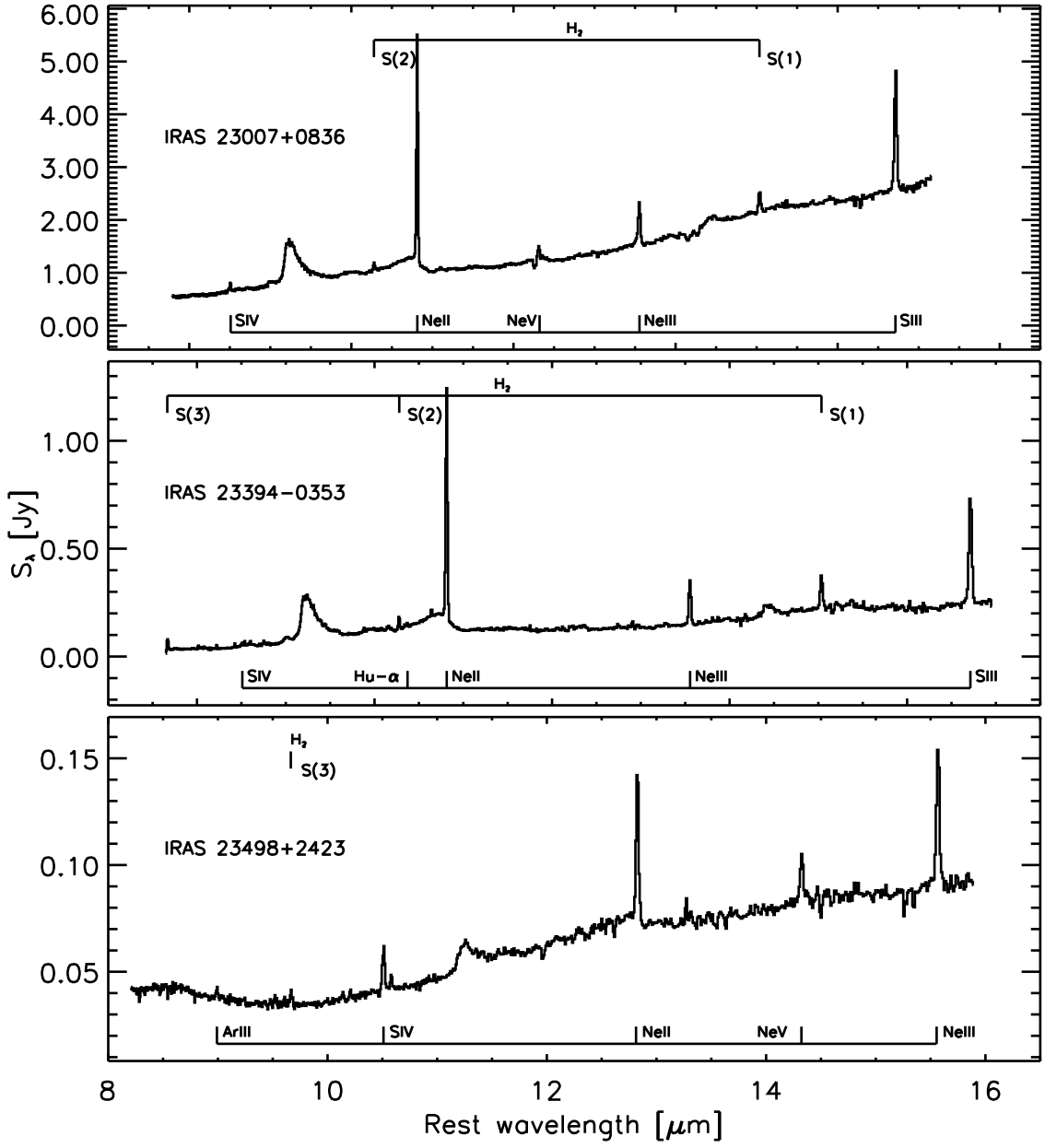

Figure B.34 Short-high (SH) module spectra for the non-masing galaxies observed with the *Spitzer* IRS. Detected atomic and molecular emission features in each spectra are marked.

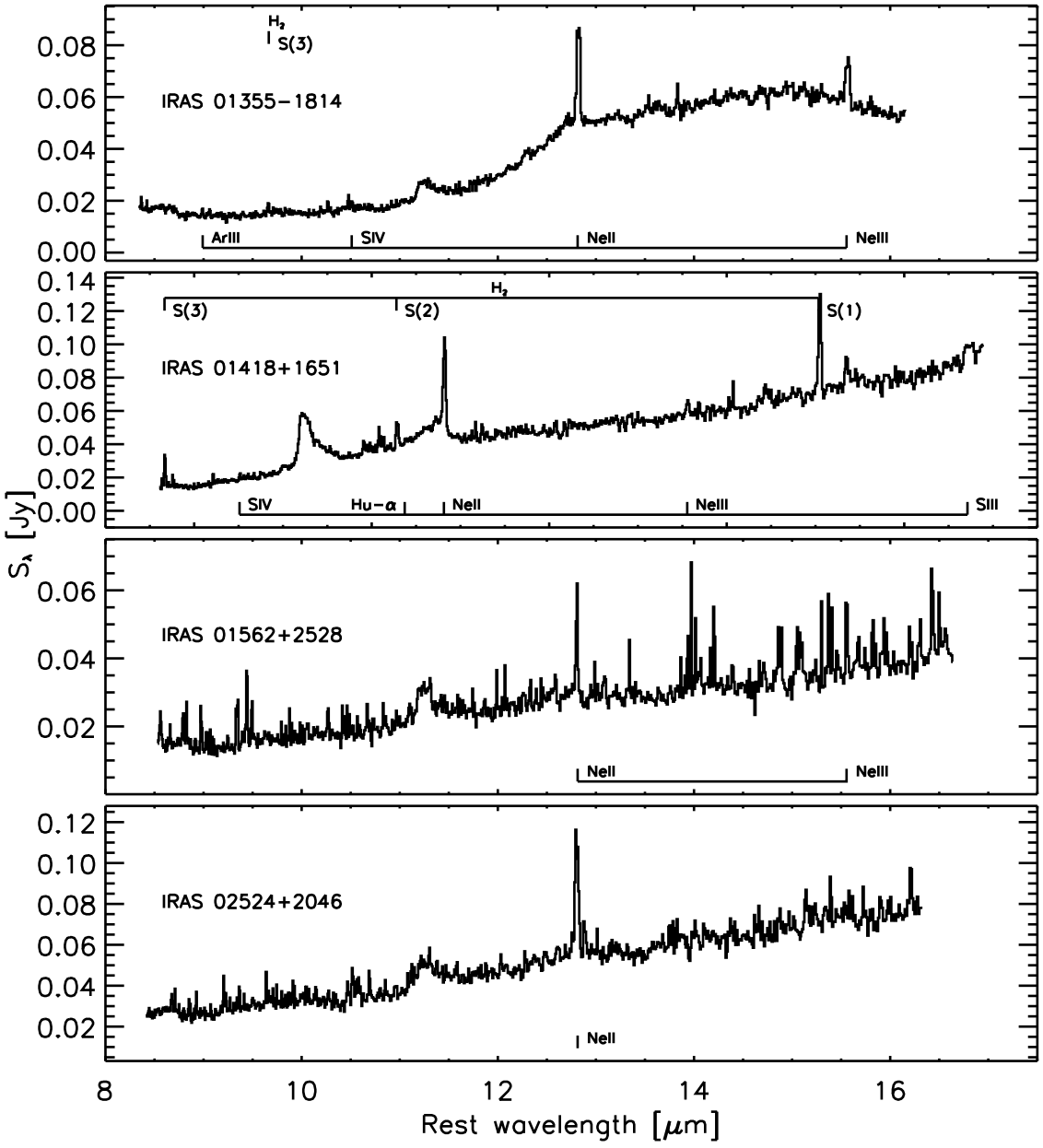

Figure B.35 Long-high (LH) module spectra for the OHMs observed with the *Spitzer* IRS. Detected atomic and molecular emission features in each spectra are marked.

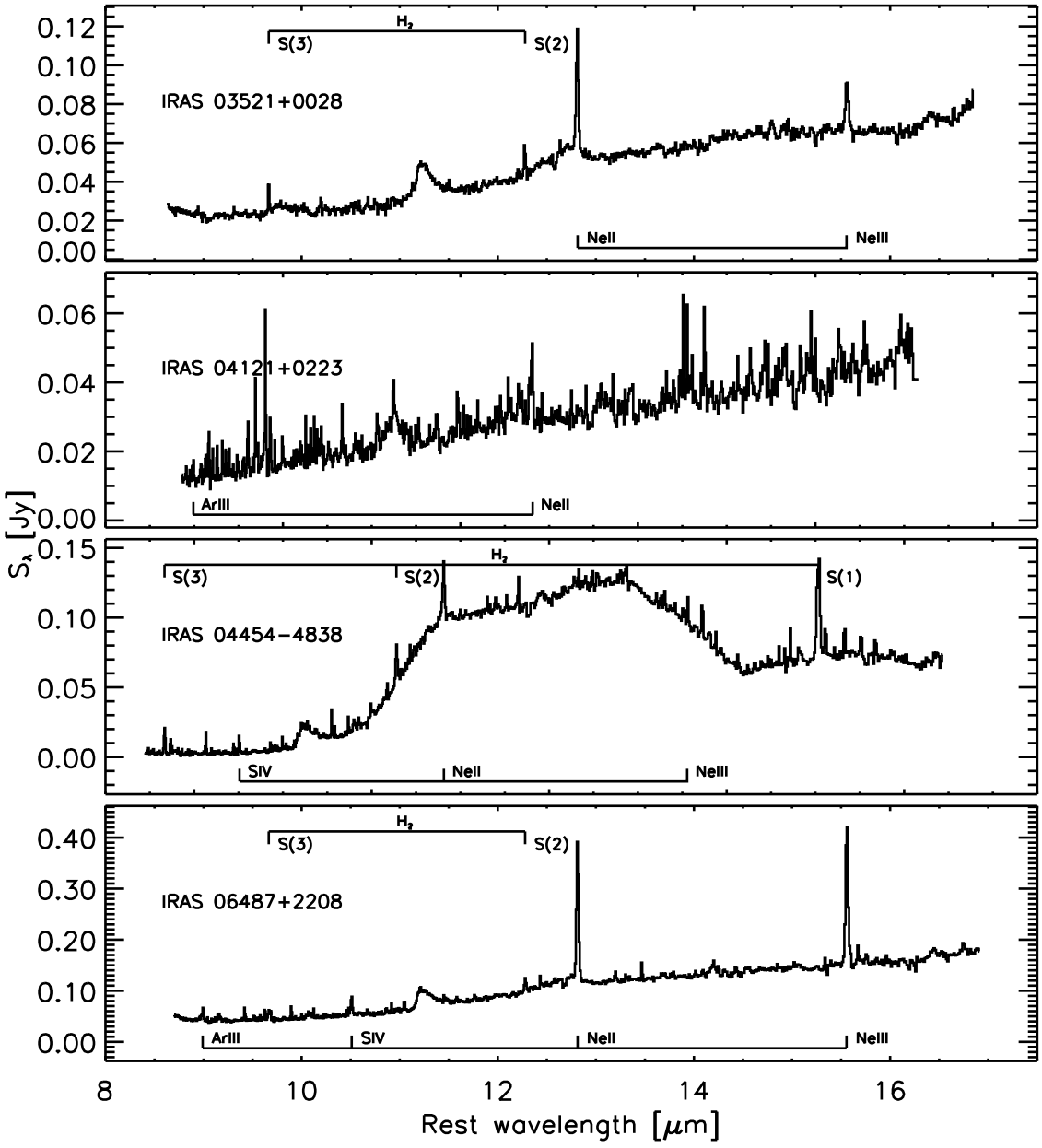

Figure B.36 Long-high (LH) module spectra for the OHMs observed with the *Spitzer* IRS. Detected atomic and molecular emission features in each spectra are marked.

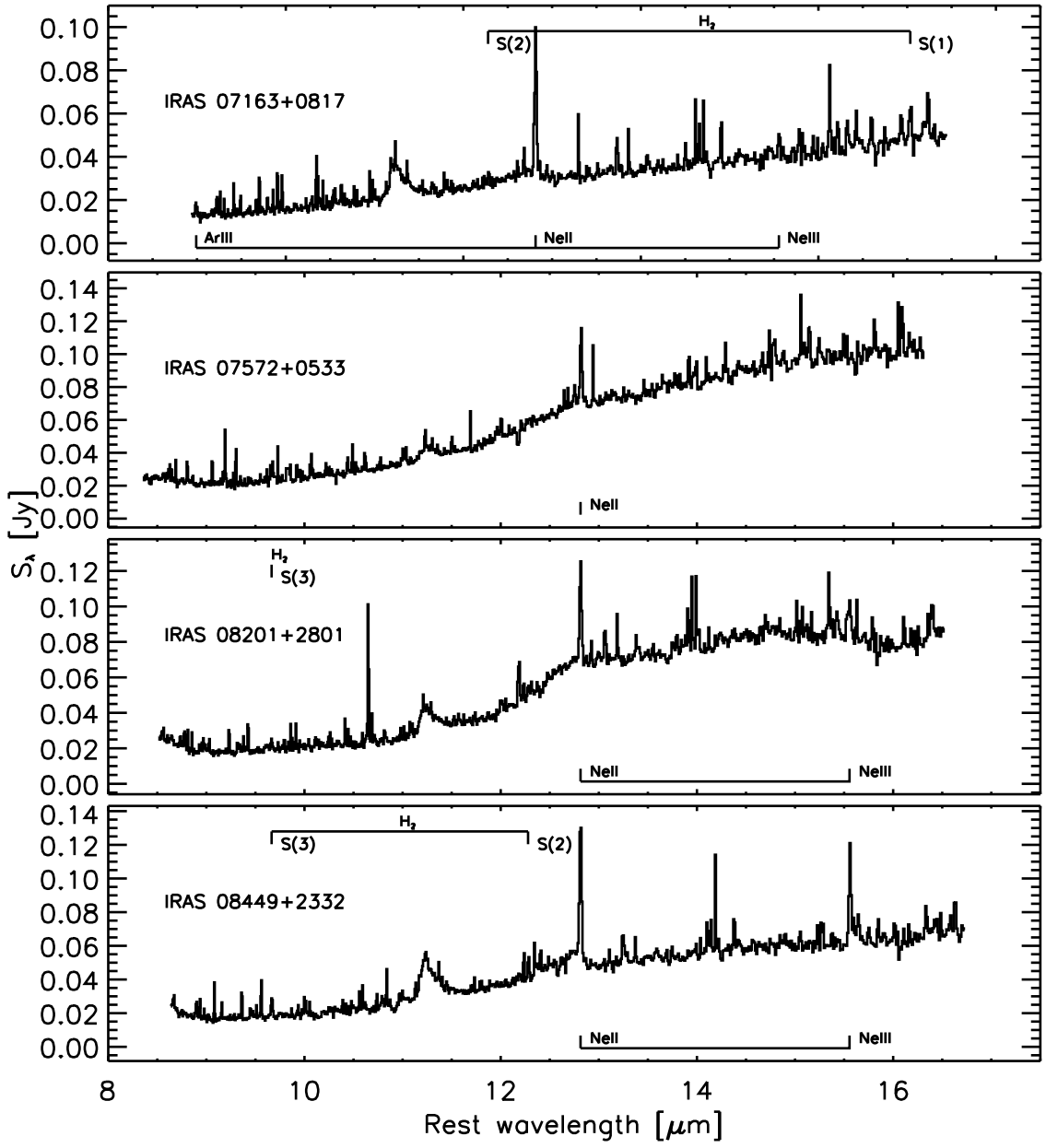

Figure B.37 Long-high (LH) module spectra for the OHMs observed with the *Spitzer* IRS. Detected atomic and molecular emission features in each spectra are marked.

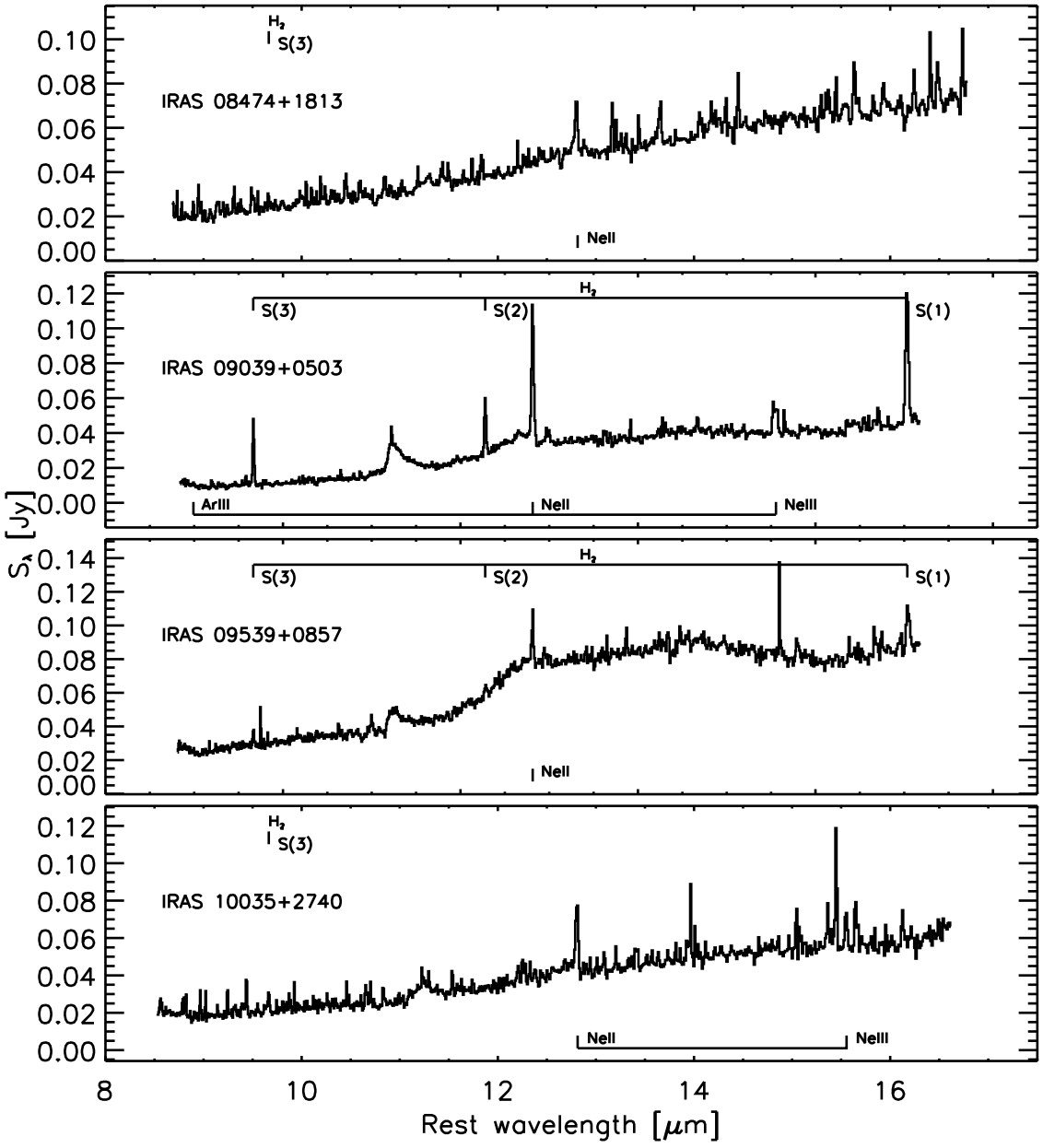

Figure B.38 Long-high (LH) module spectra for the OHMs observed with the *Spitzer* IRS. Detected atomic and molecular emission features in each spectra are marked.

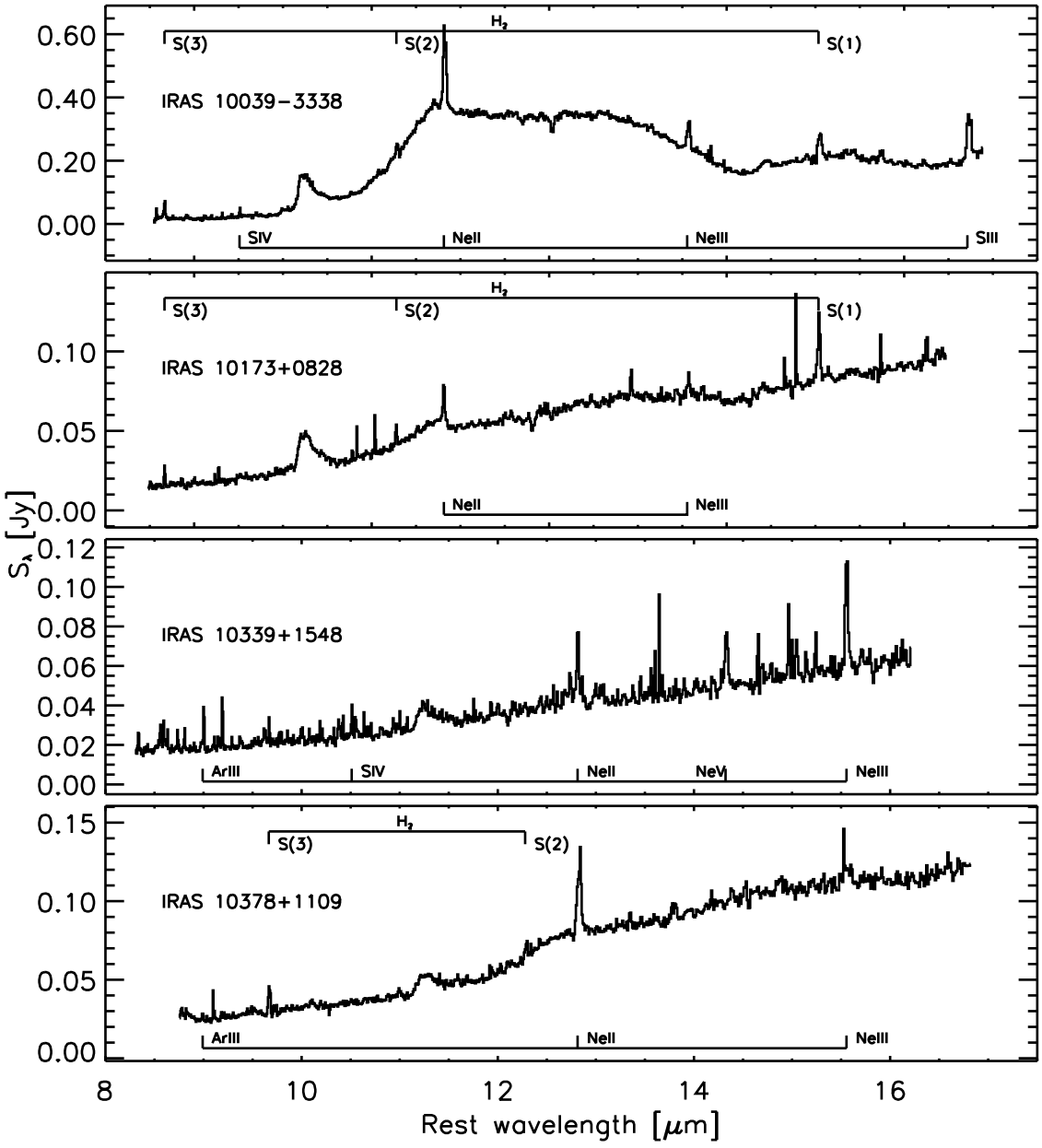

Figure B.39 Long-high (LH) module spectra for the OHMs observed with the *Spitzer* IRS. Detected atomic and molecular emission features in each spectra are marked.

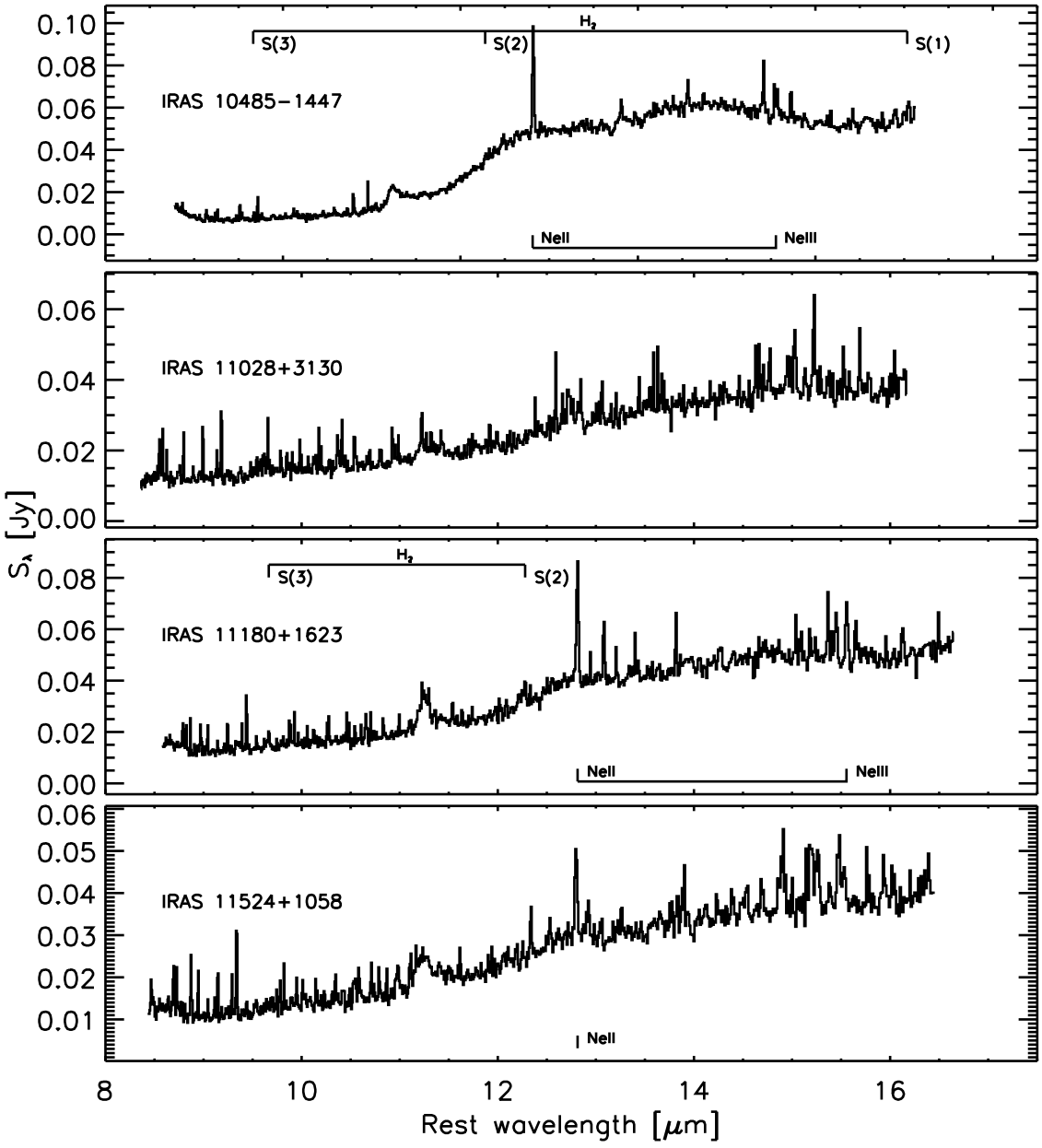

Figure B.40 Long-high (LH) module spectra for the OHMs observed with the *Spitzer* IRS. Detected atomic and molecular emission features in each spectra are marked.

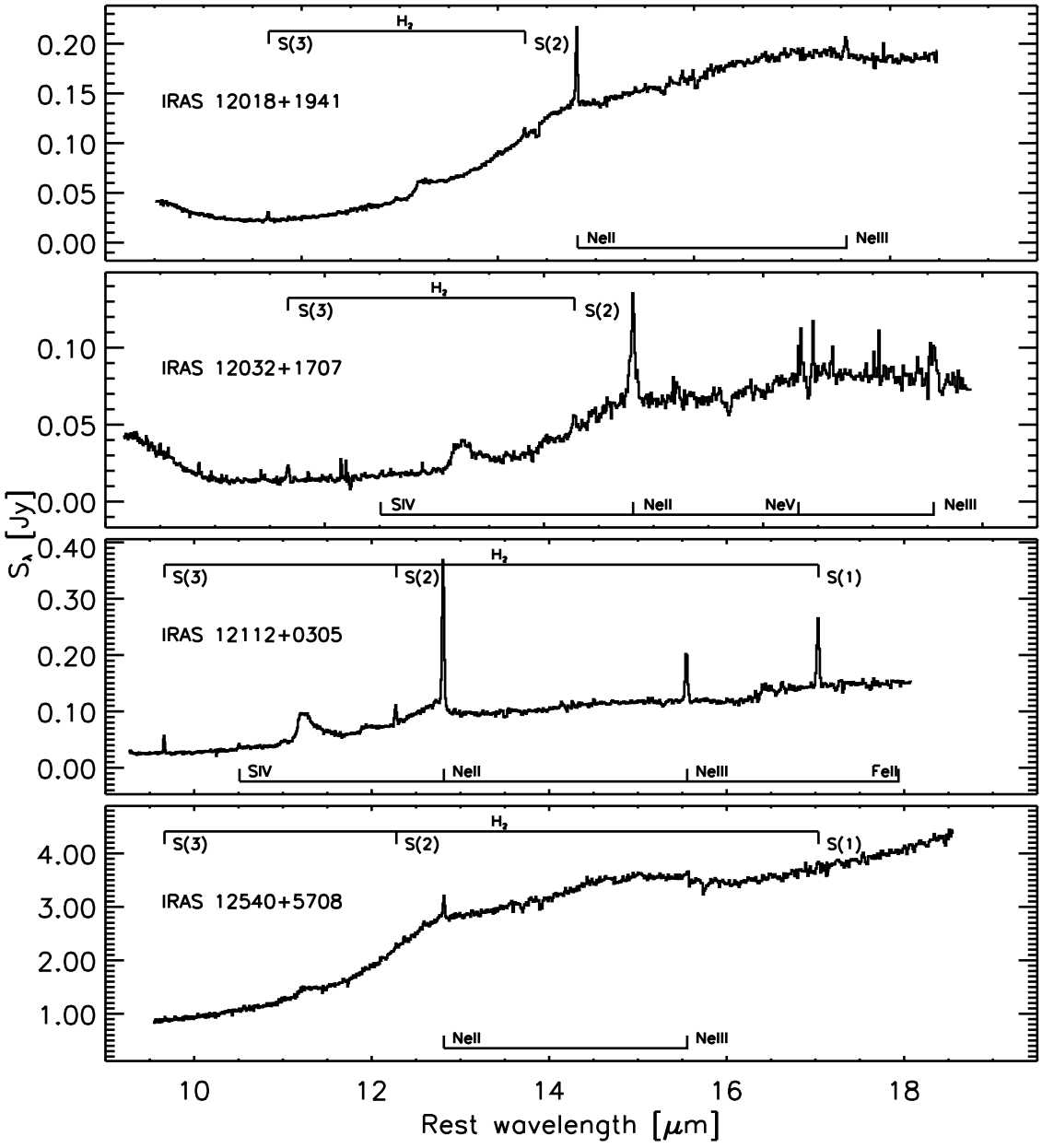

Figure B.41 Long-high (LH) module spectra for the OHMs observed with the *Spitzer* IRS. Detected atomic and molecular emission features in each spectra are marked.

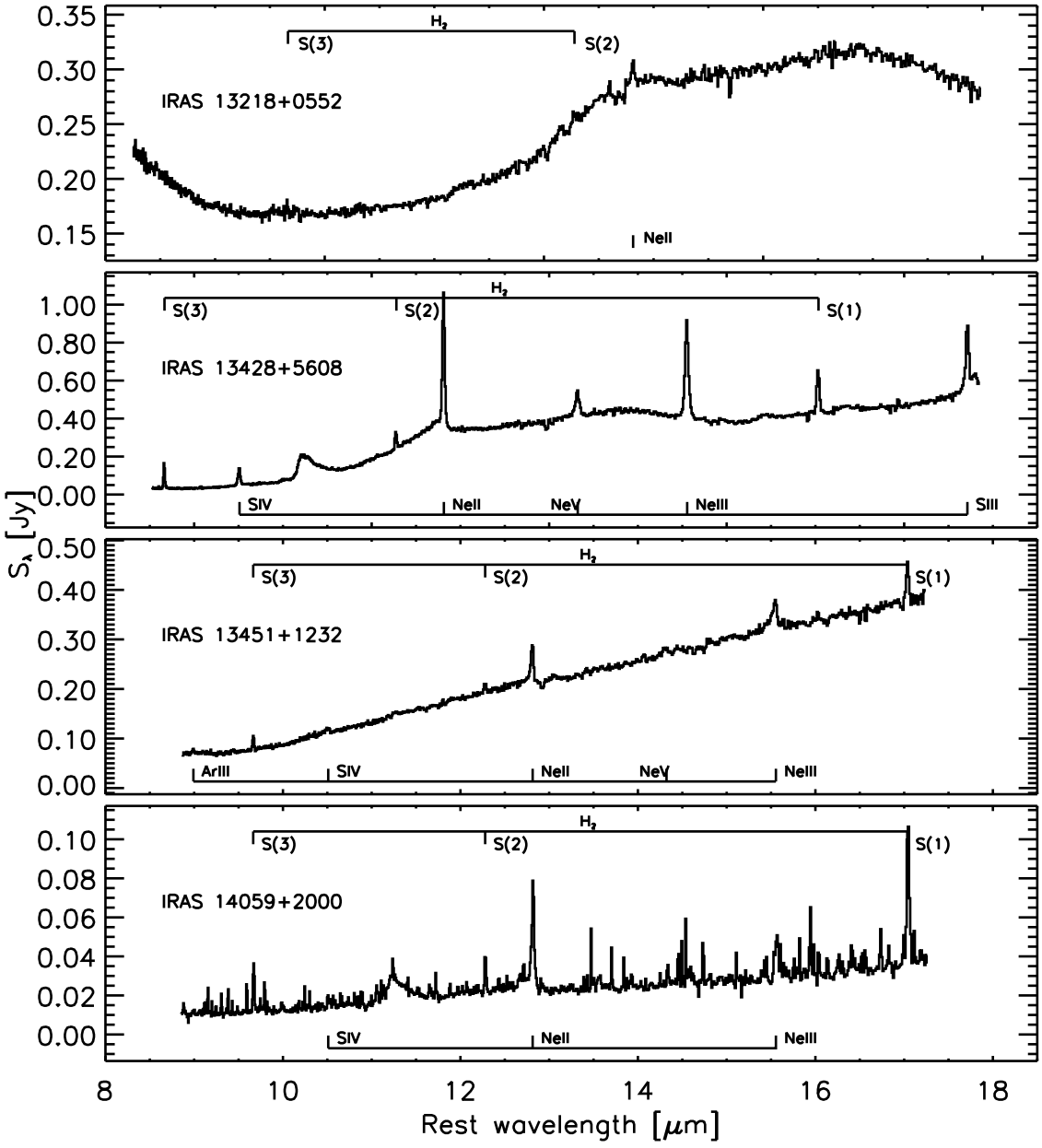

Figure B.42 Long-high (LH) module spectra for the OHMs observed with the *Spitzer* IRS. Detected atomic and molecular emission features in each spectra are marked.

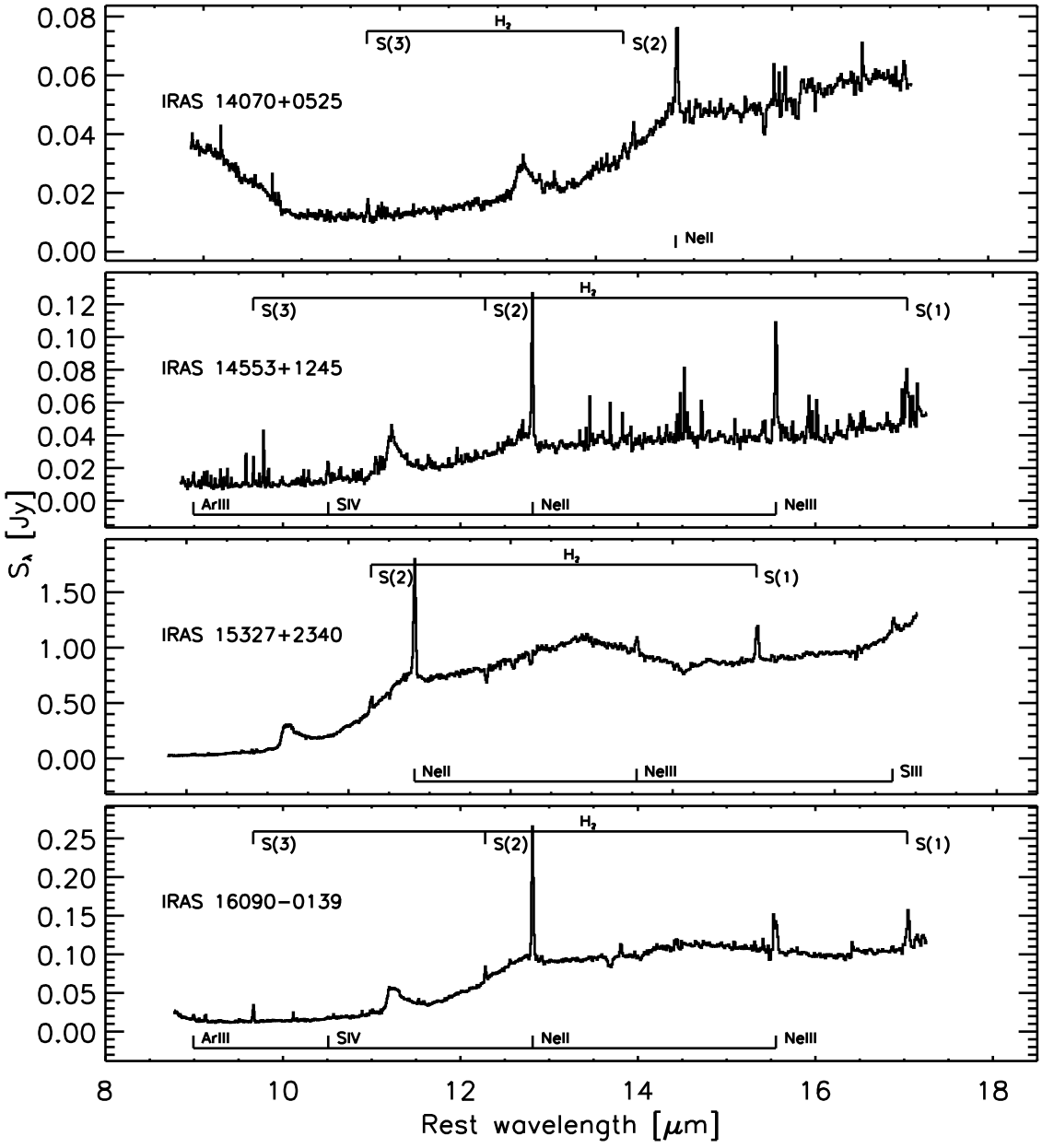

Figure B.43 Long-high (LH) module spectra for the OHMs observed with the *Spitzer* IRS. Detected atomic and molecular emission features in each spectra are marked.

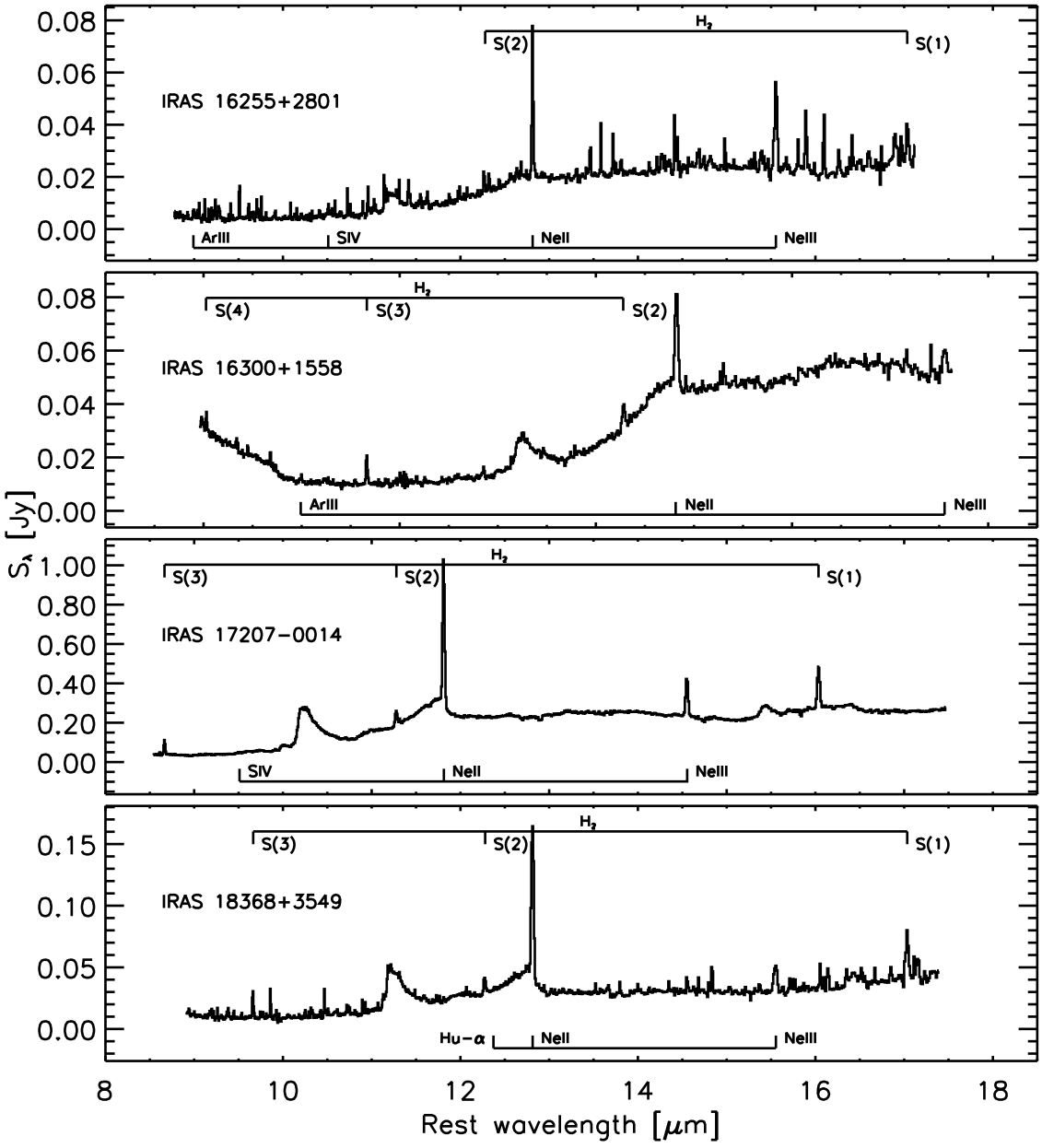

Figure B.44 Long-high (LH) module spectra for the OHMs observed with the *Spitzer* IRS. Detected atomic and molecular emission features in each spectra are marked.

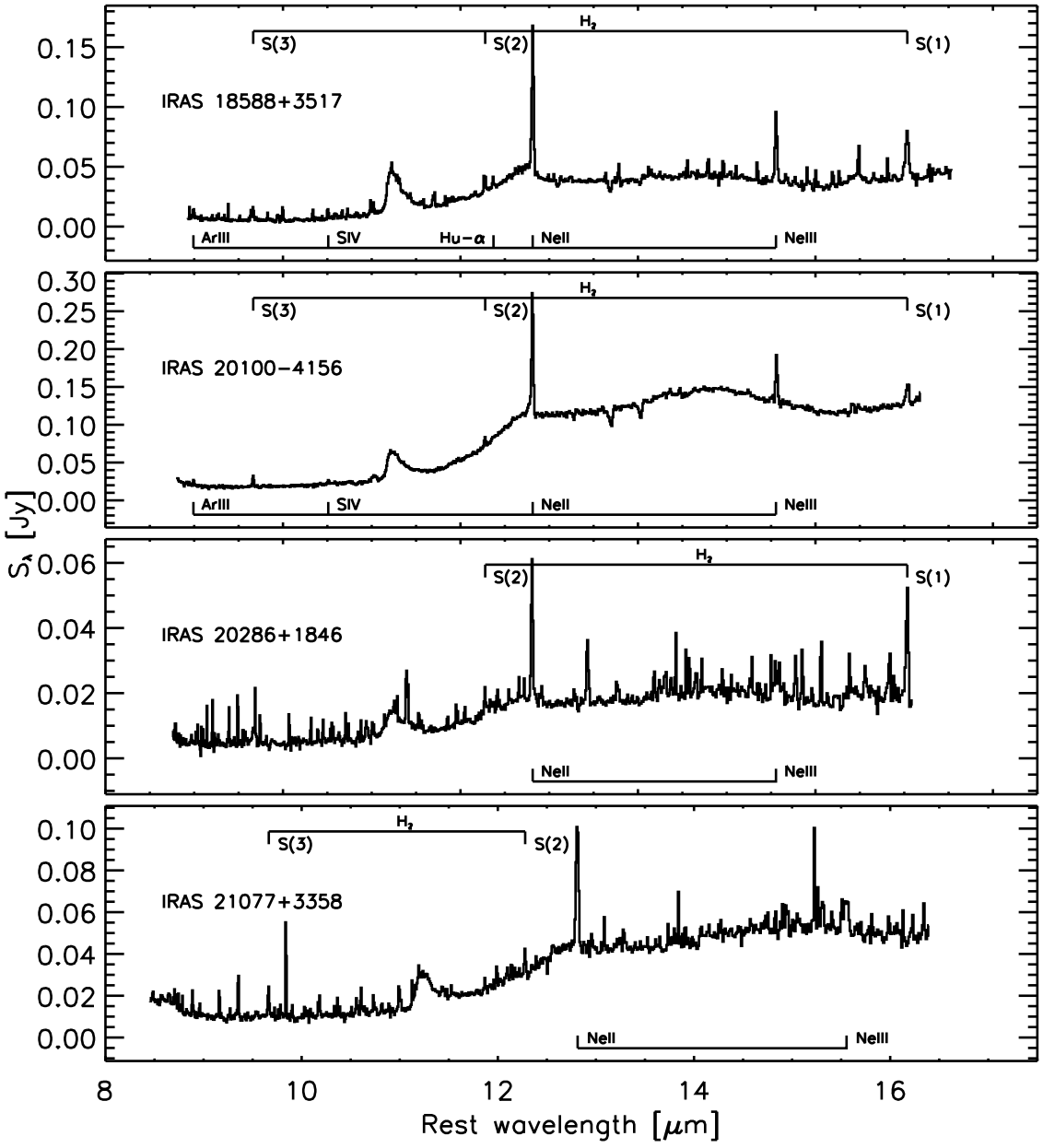

Figure B.45 Long-high (LH) module spectra for the OHMs observed with the *Spitzer* IRS. Detected atomic and molecular emission features in each spectra are marked.

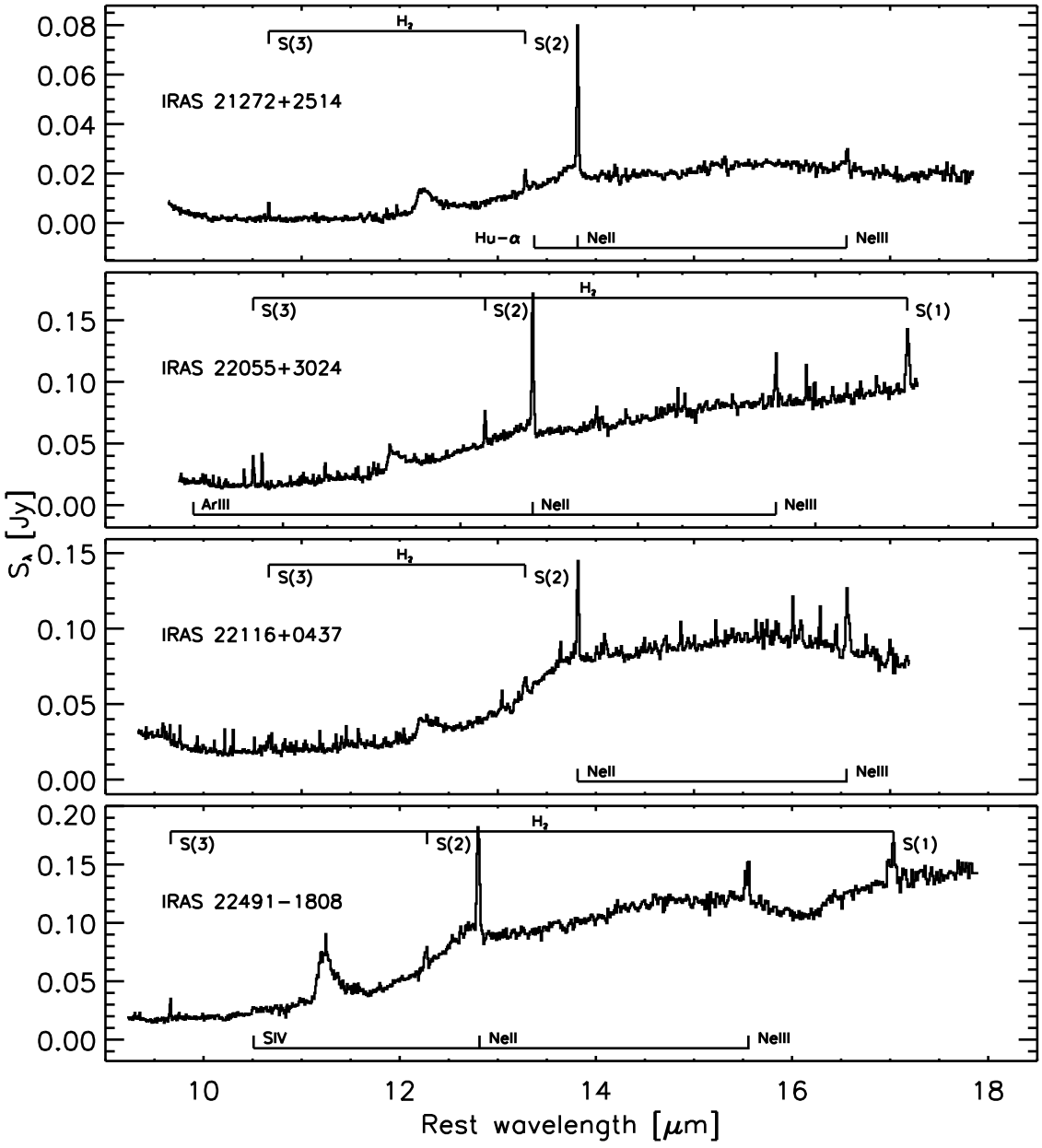

Figure B.46 Long-high (LH) module spectra for the OHMs observed with the *Spitzer* IRS. Detected atomic and molecular emission features in each spectra are marked.

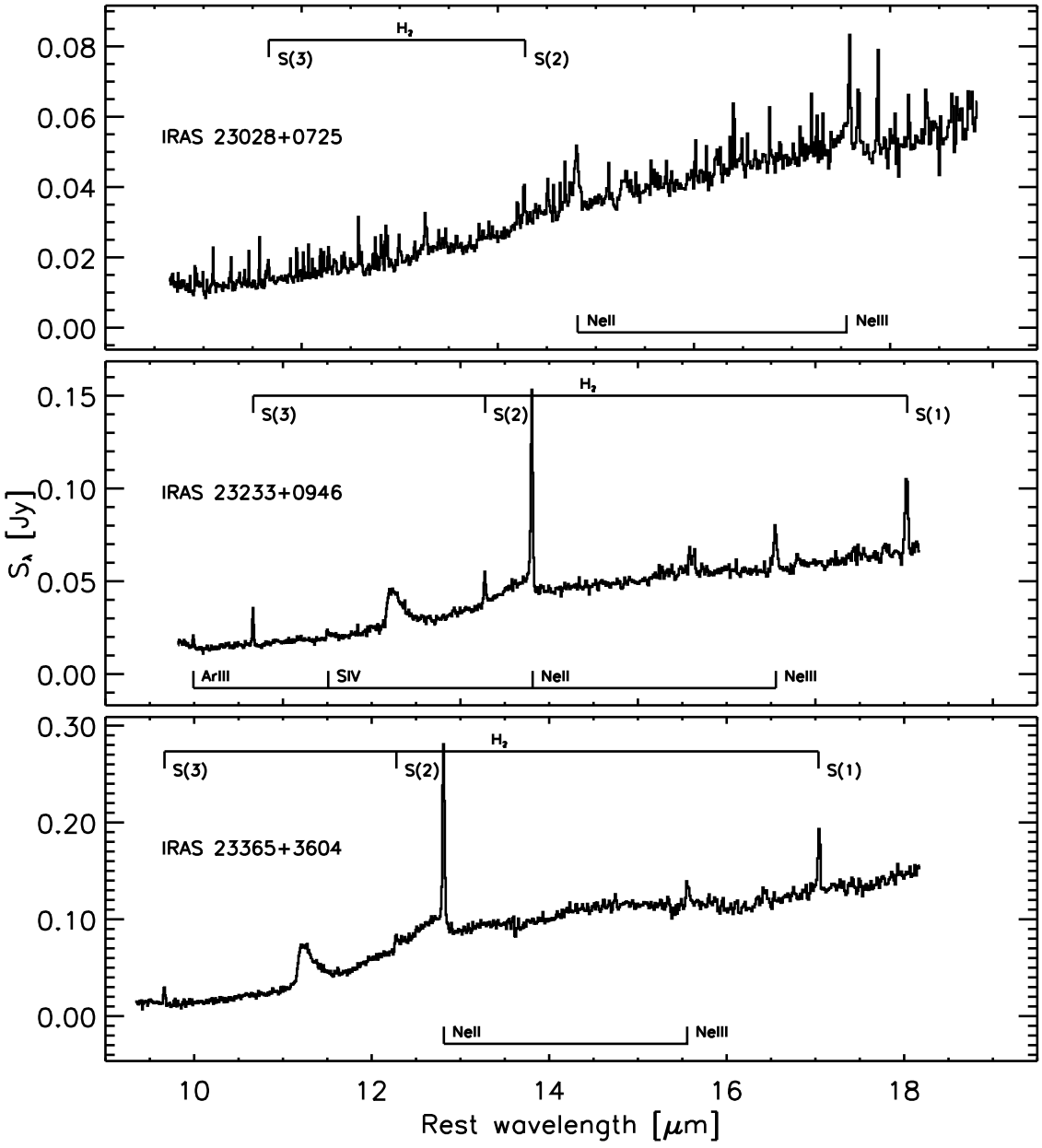

Figure B.47 Long-high (LH) module spectra for the OHMs observed with the *Spitzer* IRS. Detected atomic and molecular emission features in each spectra are marked.

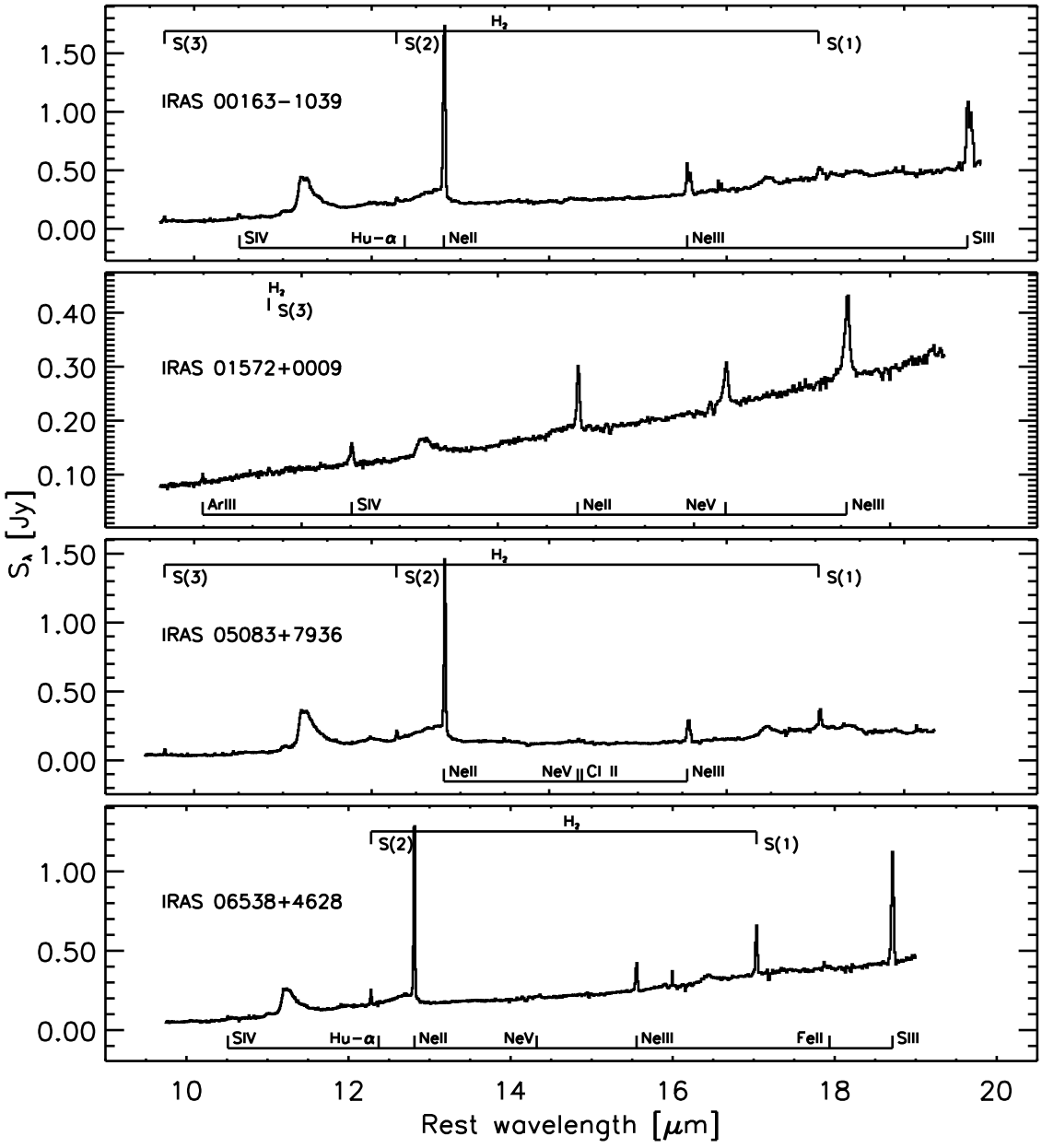

Figure B.48 Long-high (LH) module spectra for the non-masing galaxies observed with the *Spitzer* IRS. Detected atomic and molecular emission features in each spectra are marked.

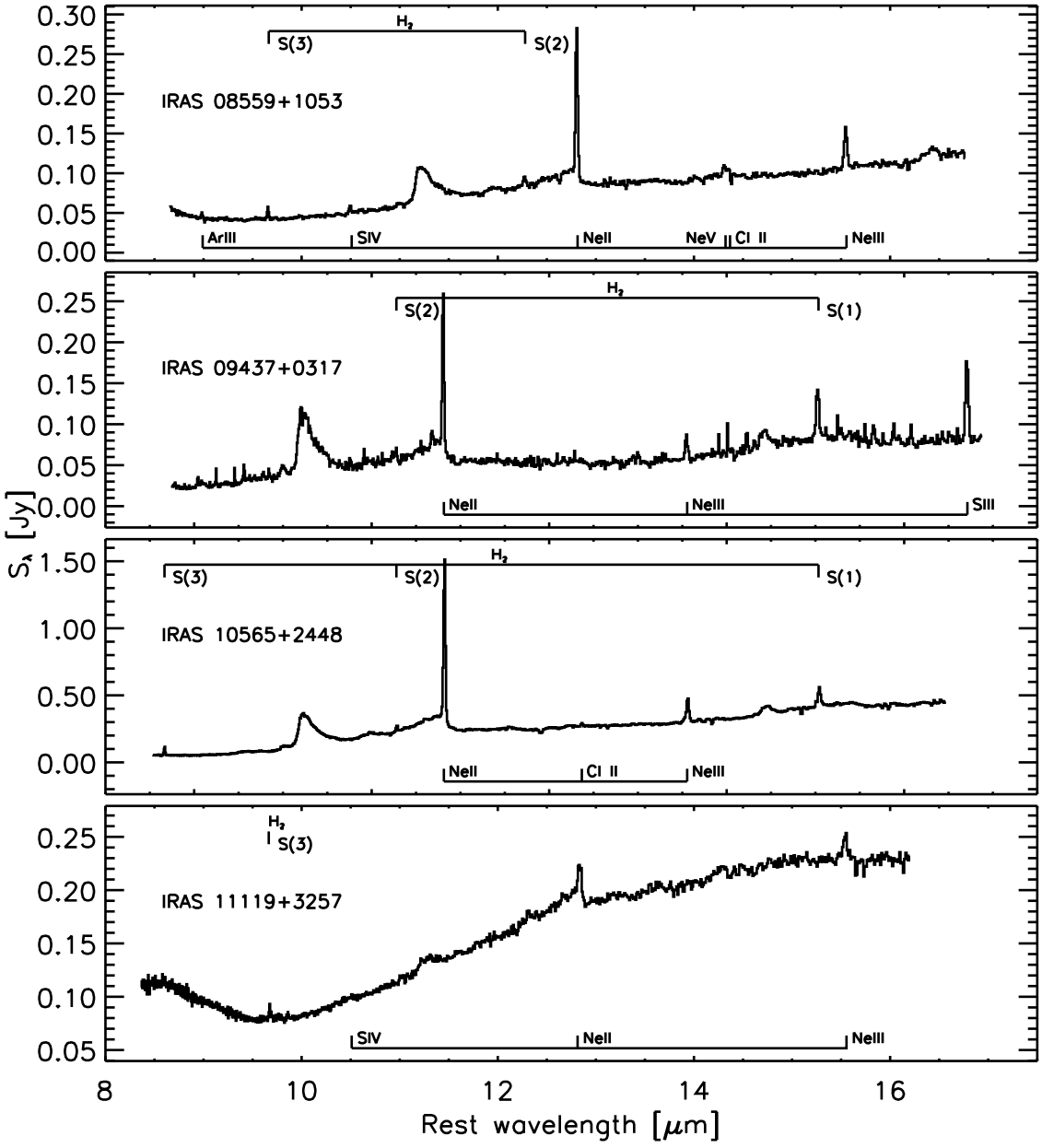

Figure B.49 Long-high (LH) module spectra for the non-masing galaxies observed with the *Spitzer* IRS. Detected atomic and molecular emission features in each spectra are marked.

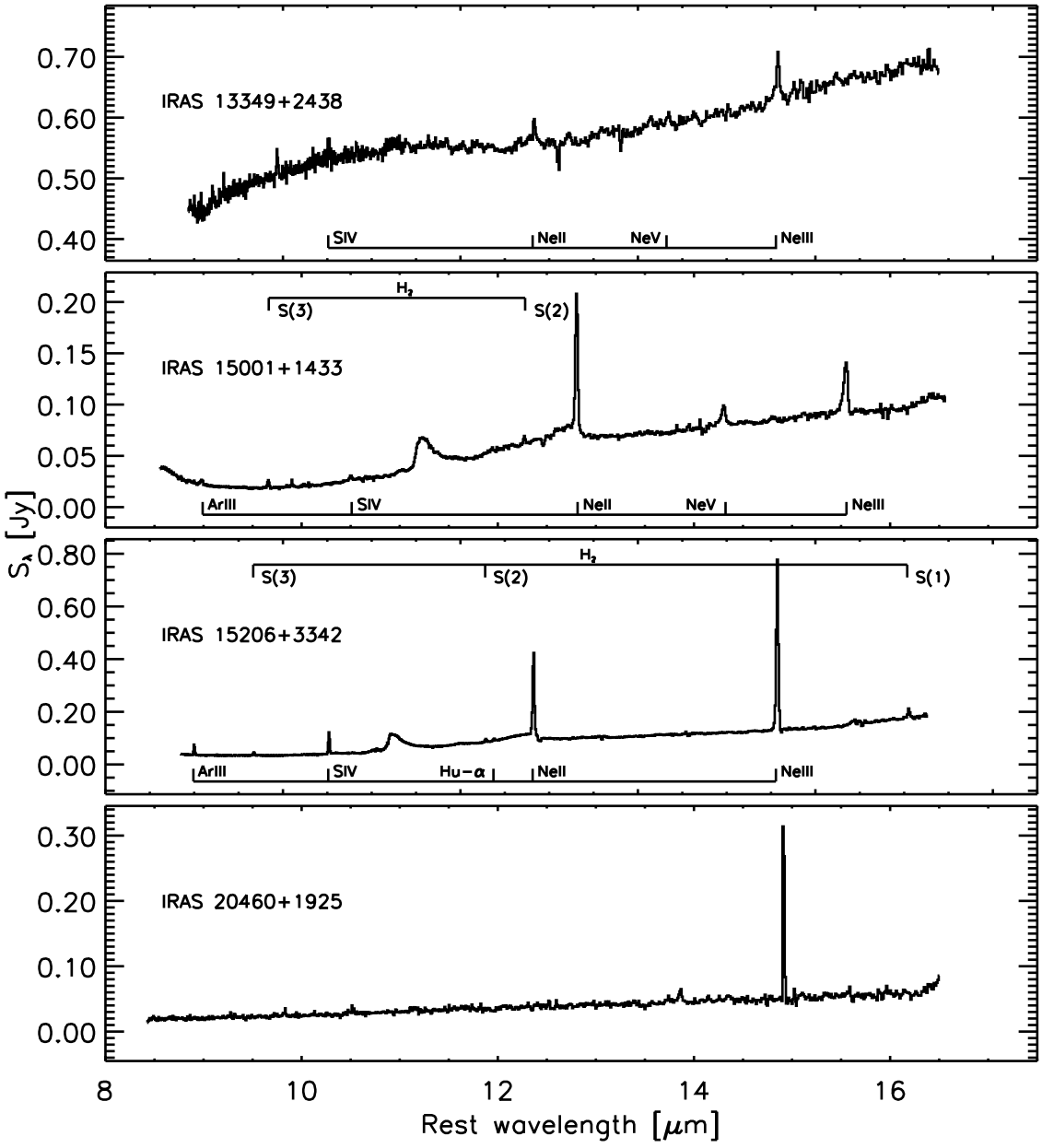

Figure B.50 Long-high (LH) module spectra for the non-masing galaxies observed with the *Spitzer* IRS. Detected atomic and molecular emission features in each spectra are marked.

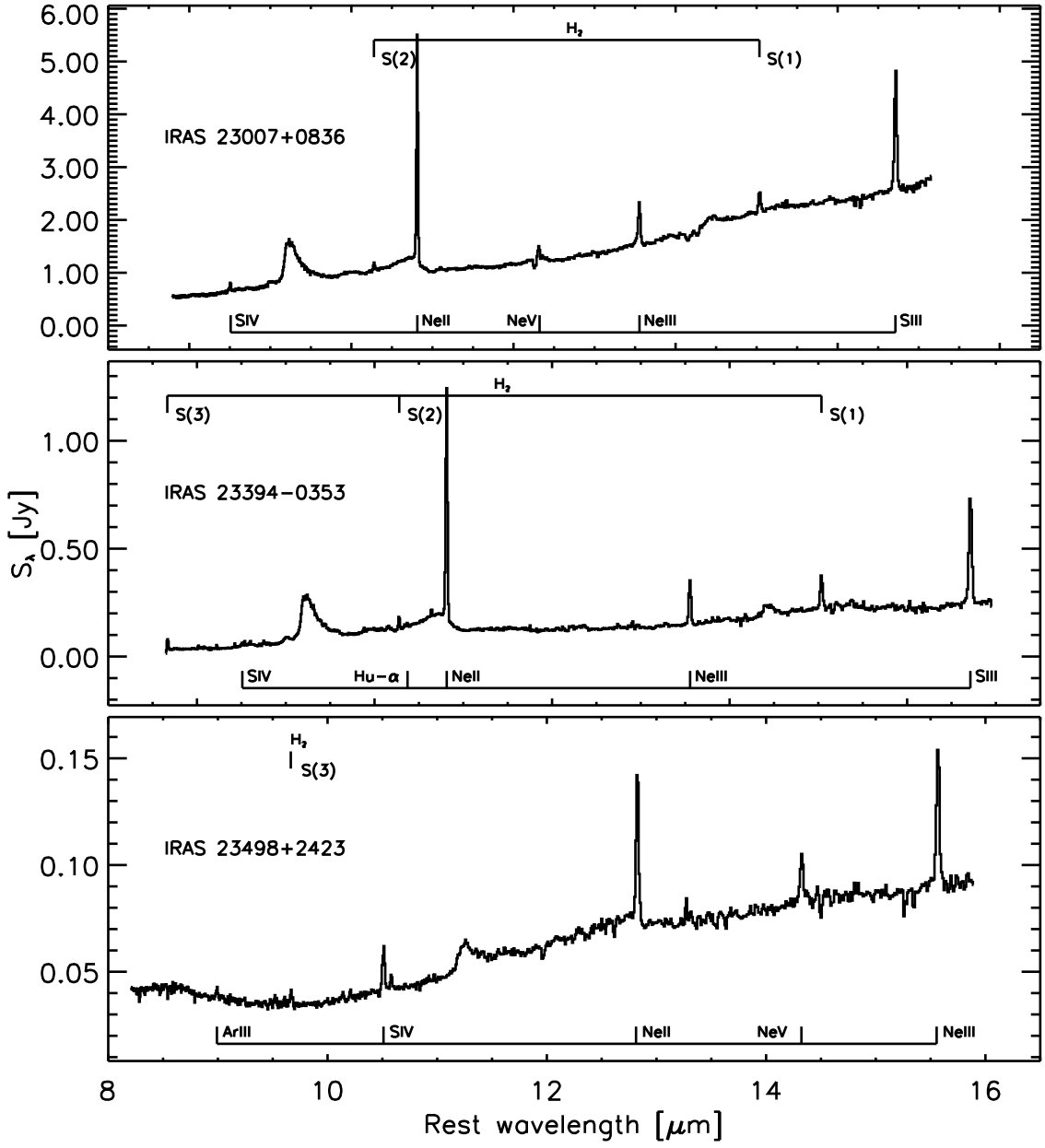

Figure B.51 Long-high (LH) module spectra for the non-masing galaxies observed with the *Spitzer* IRS. Detected atomic and molecular emission features in each spectra are marked.

Appendix C

Non-detections of high-z OHM candidates

This appendix presents the full GBT 18-cm spectra for the 77 galaxies with no OHM detections described in Chapter 4. The data have been flagged for RFI, baseline subtracted, and smoothed to three different velocity resolutions in the rest frame of 18-cm emission: 10, 50, and 150 km s^{-1}. Spectra for the three velocity resolutions have been vertically offset from each other for comparison. The expected locations of the 1667 and 1665 MHz lines (based on the optical redshift of the galaxy) is also shown on each spectrum; the location of the 1667 MHz line is always on the right. In some of the spectra, RFI has been masked from the data.

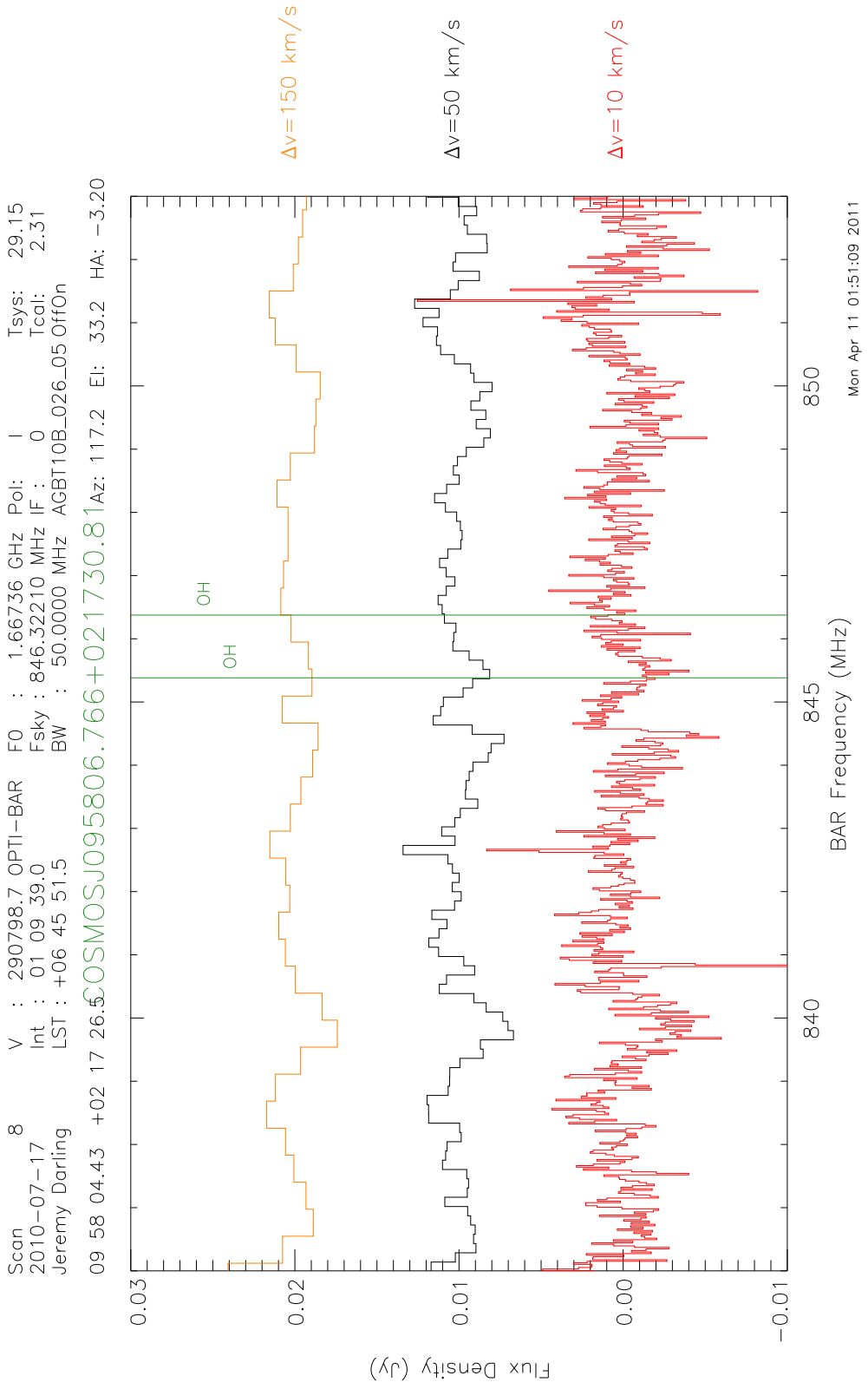

Figure C.1 18-cm spectrum of the galaxy COSMOS J095806.766+021730.81.

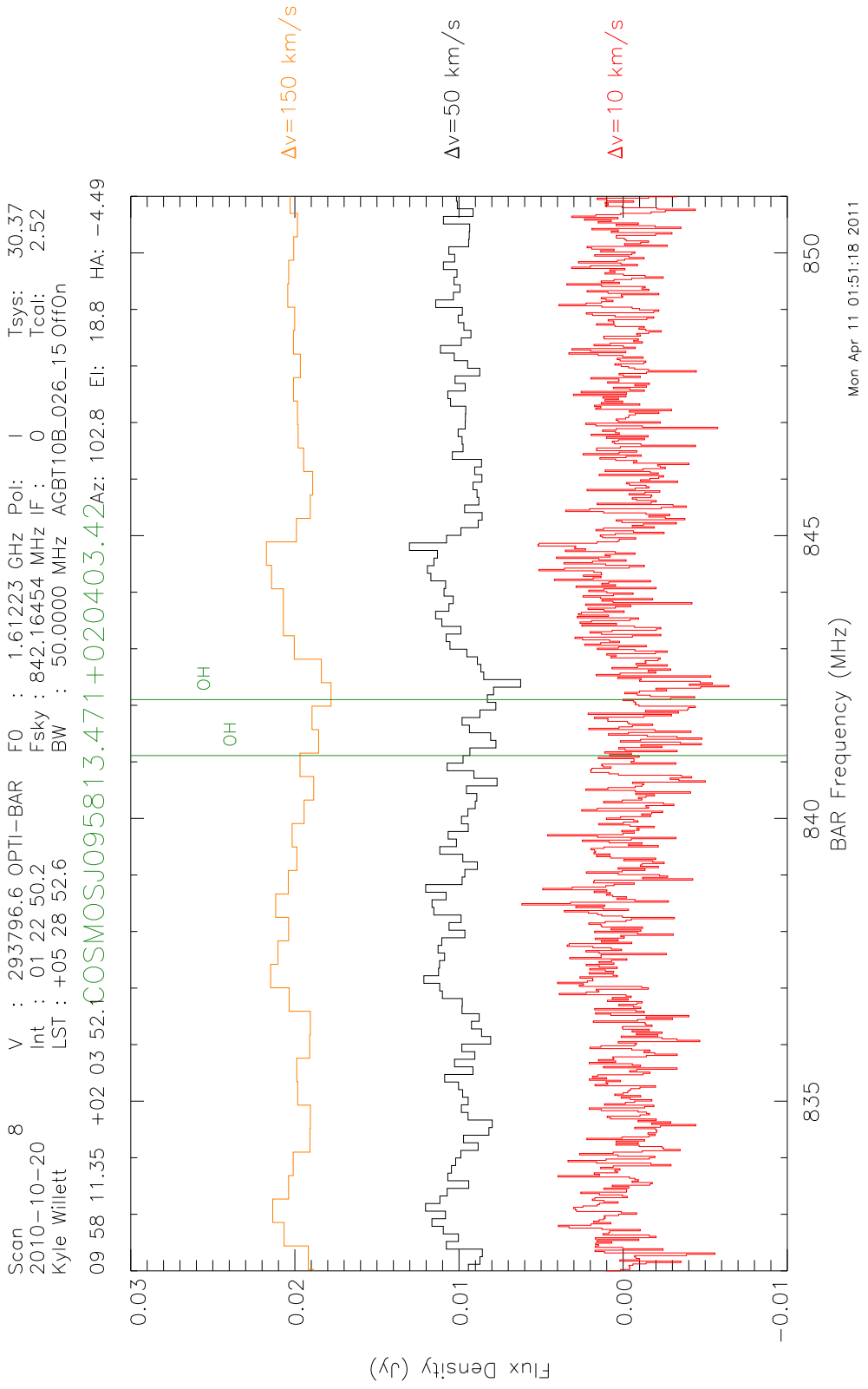

Figure C.2 18-cm spectrum of the galaxy COSMOS J095813.471+020403.42.

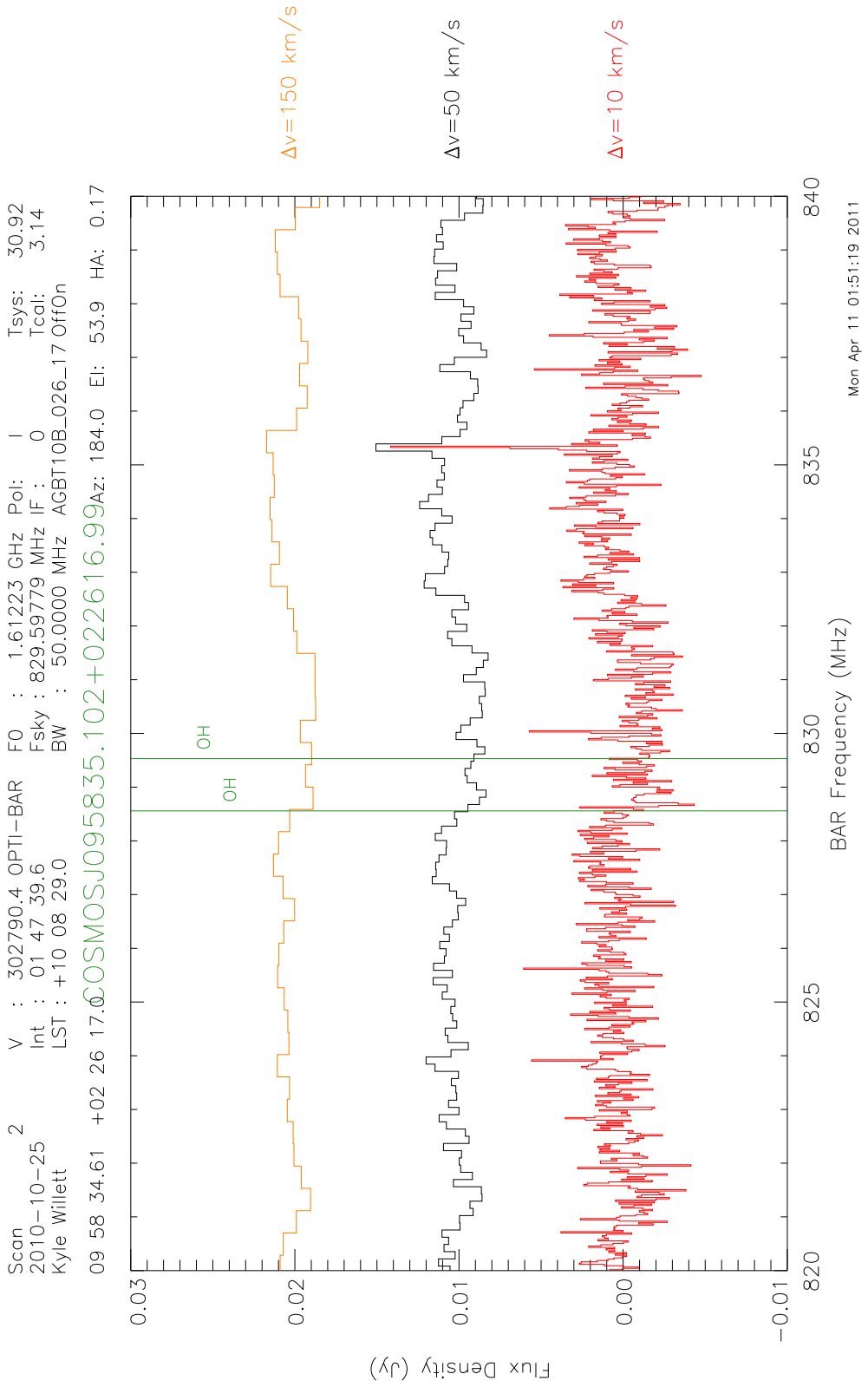

Figure C.3 18-cm spectrum of the galaxy COSMOS J095835.102+022616.99.

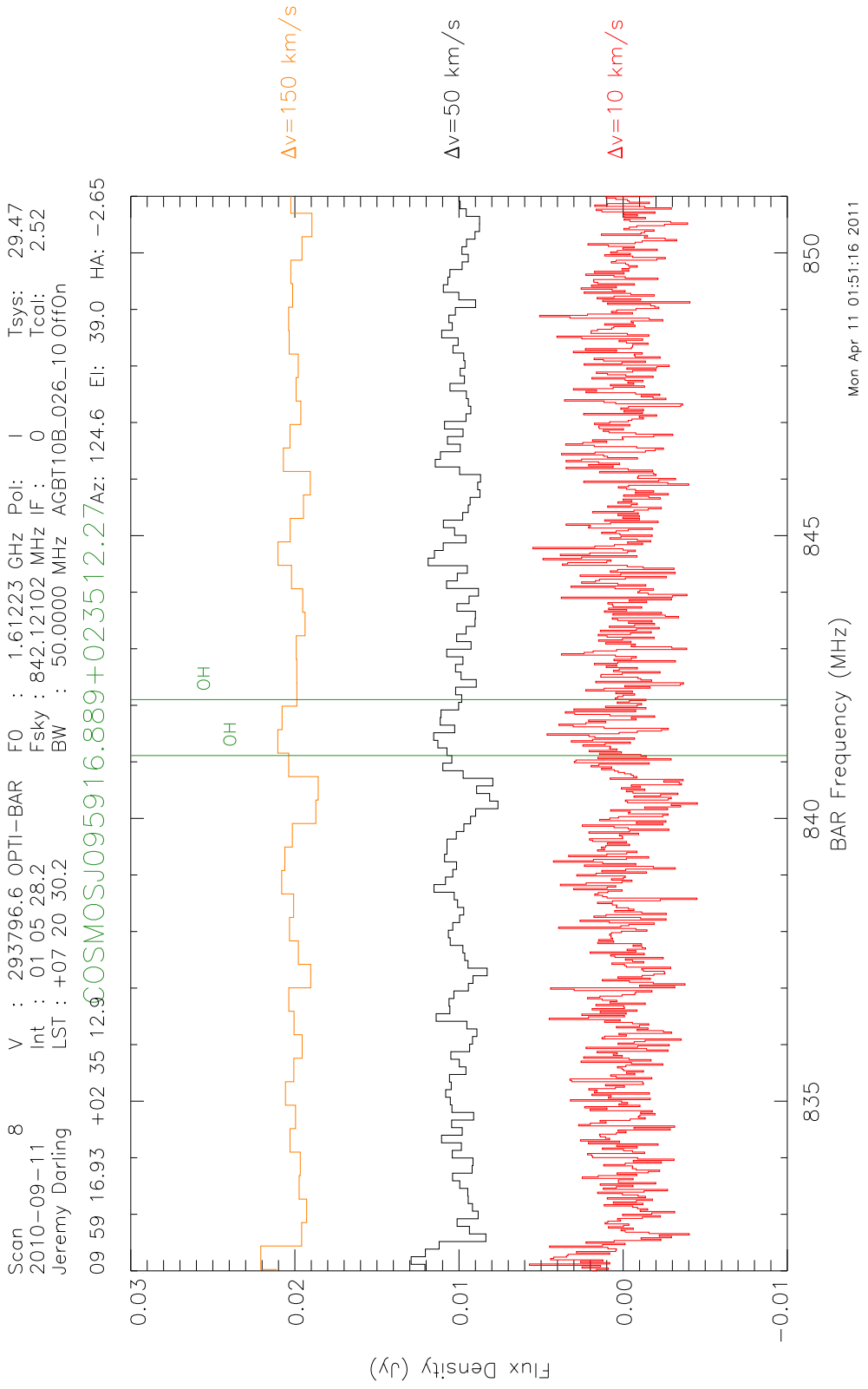

Figure C.4 18-cm spectrum of the galaxy COSMOS J095916.889+023512.27.

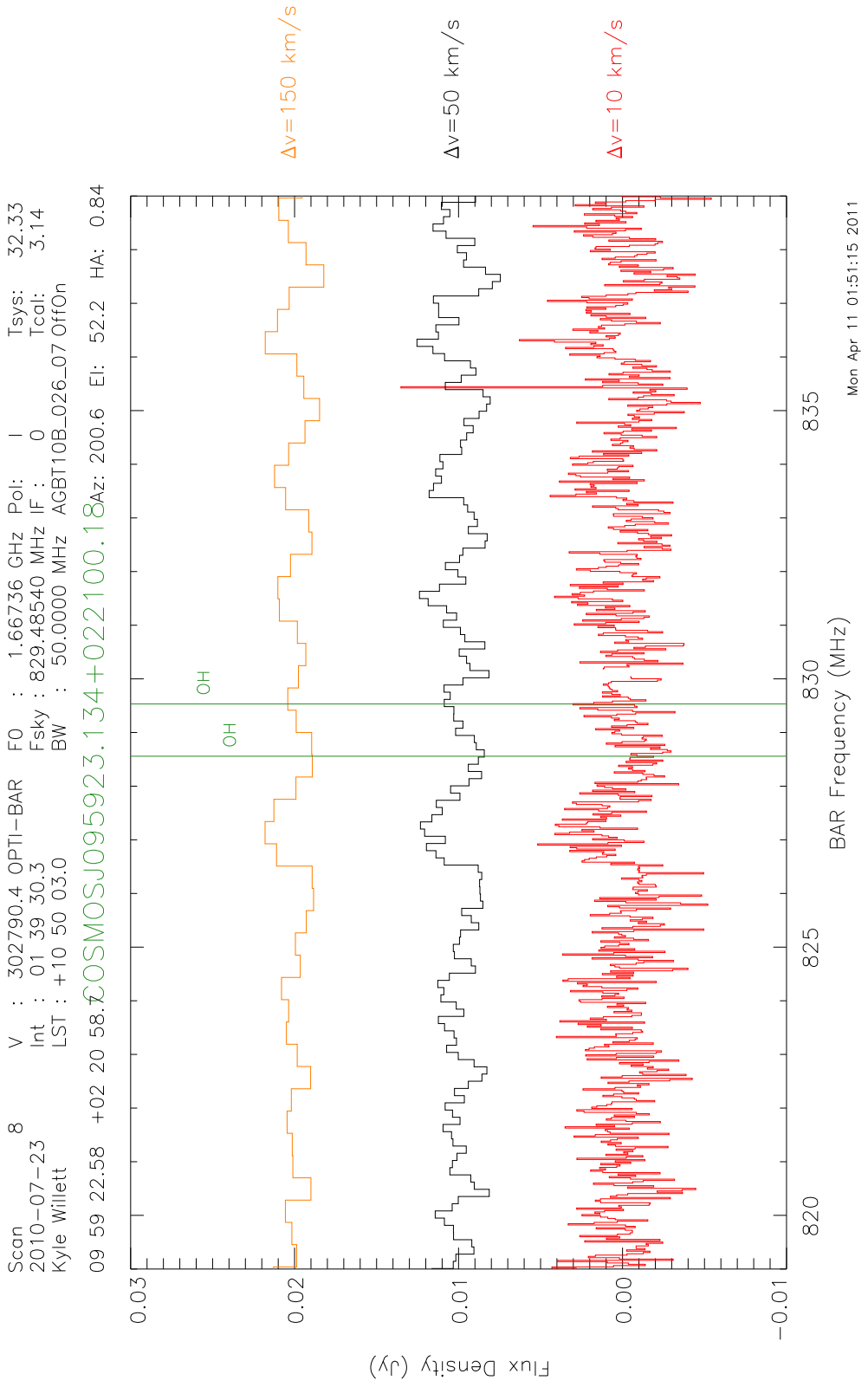

Figure C.5 18-cm spectrum of the galaxy COSMOS J095923.134+022100.18.

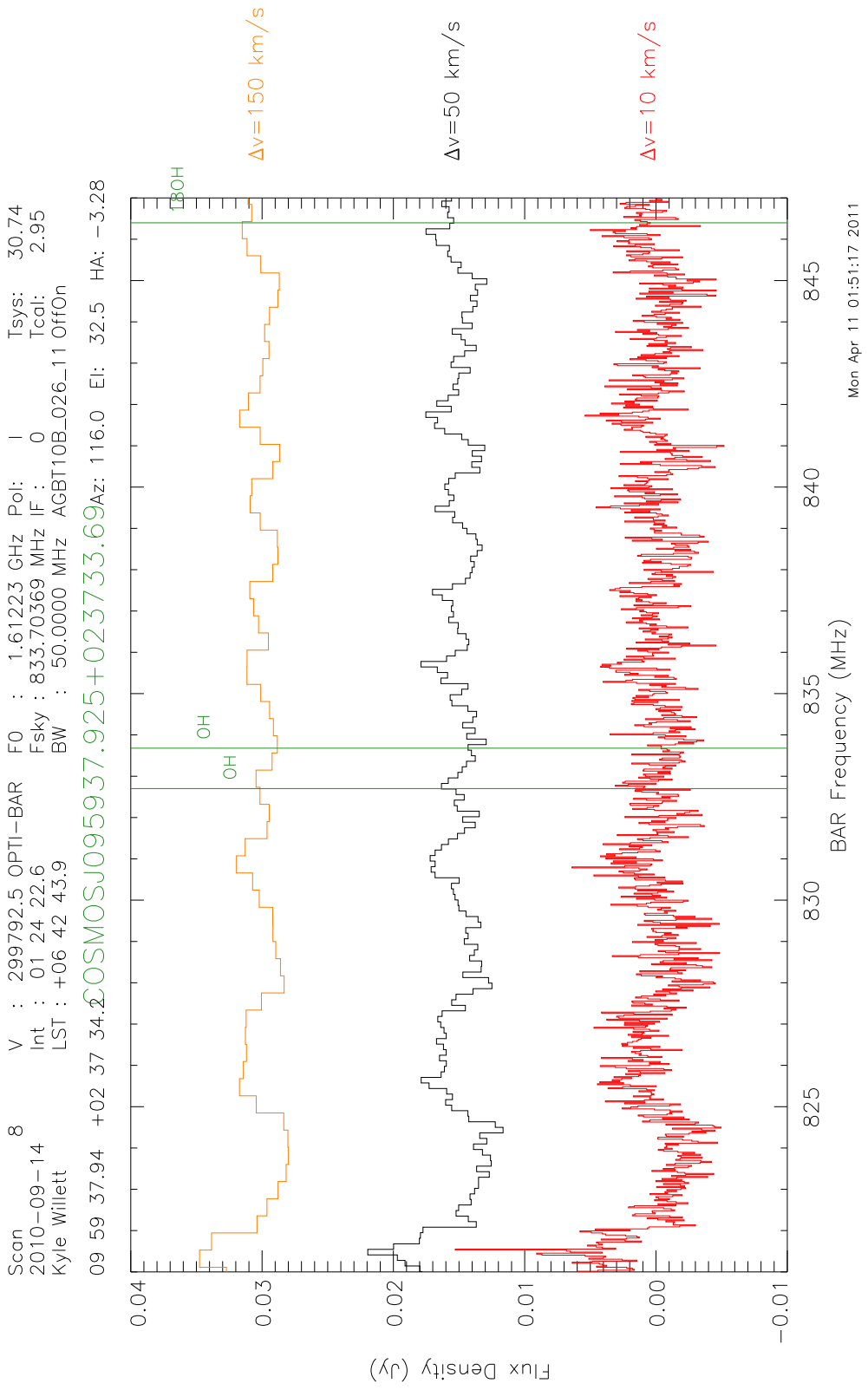

Figure C.6 18-cm spectrum of the galaxy COSMOS J095937.925+023733.69.

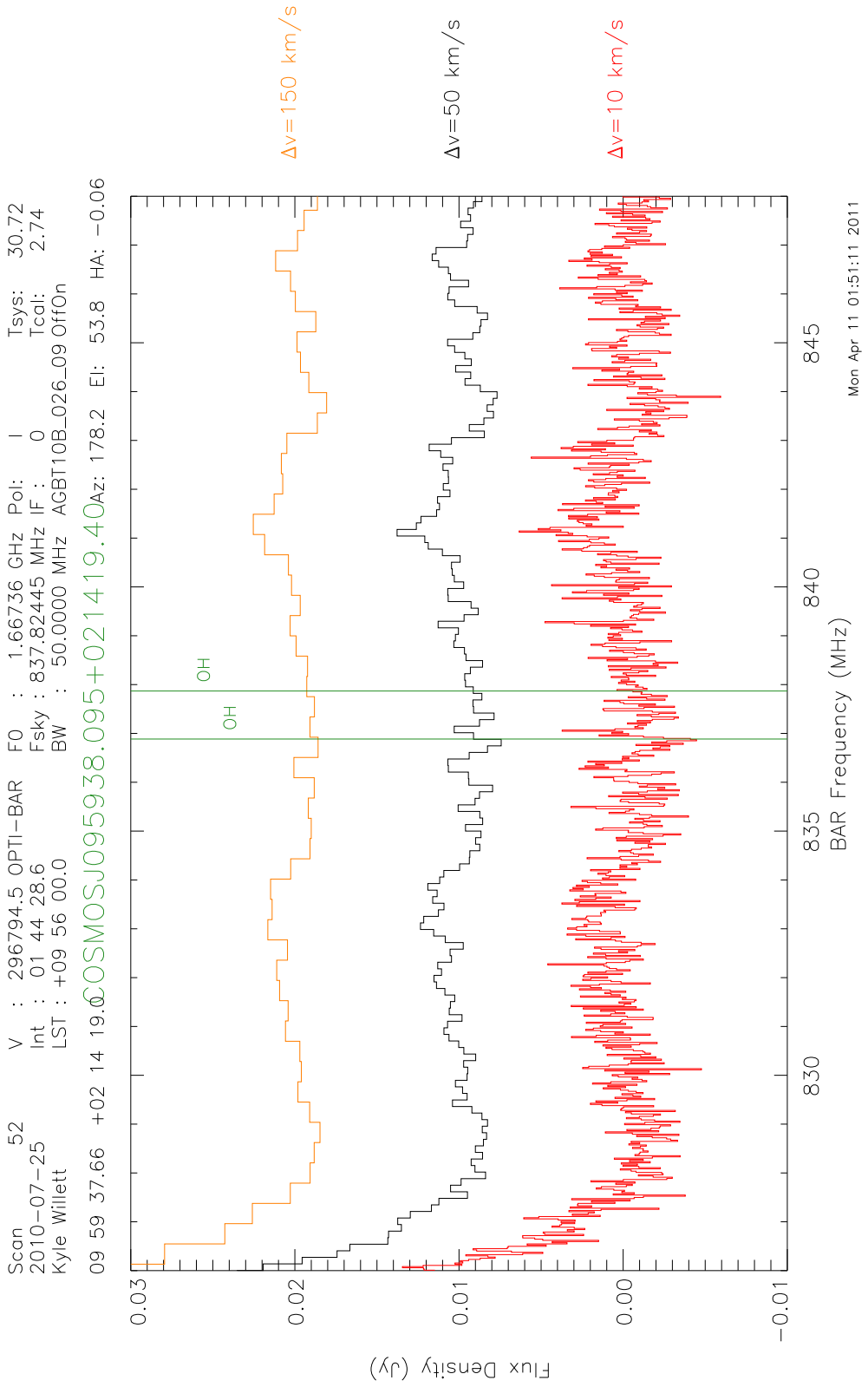

Figure C.7 18-cm spectrum of the galaxy COSMOS J095938.095+021419.40.

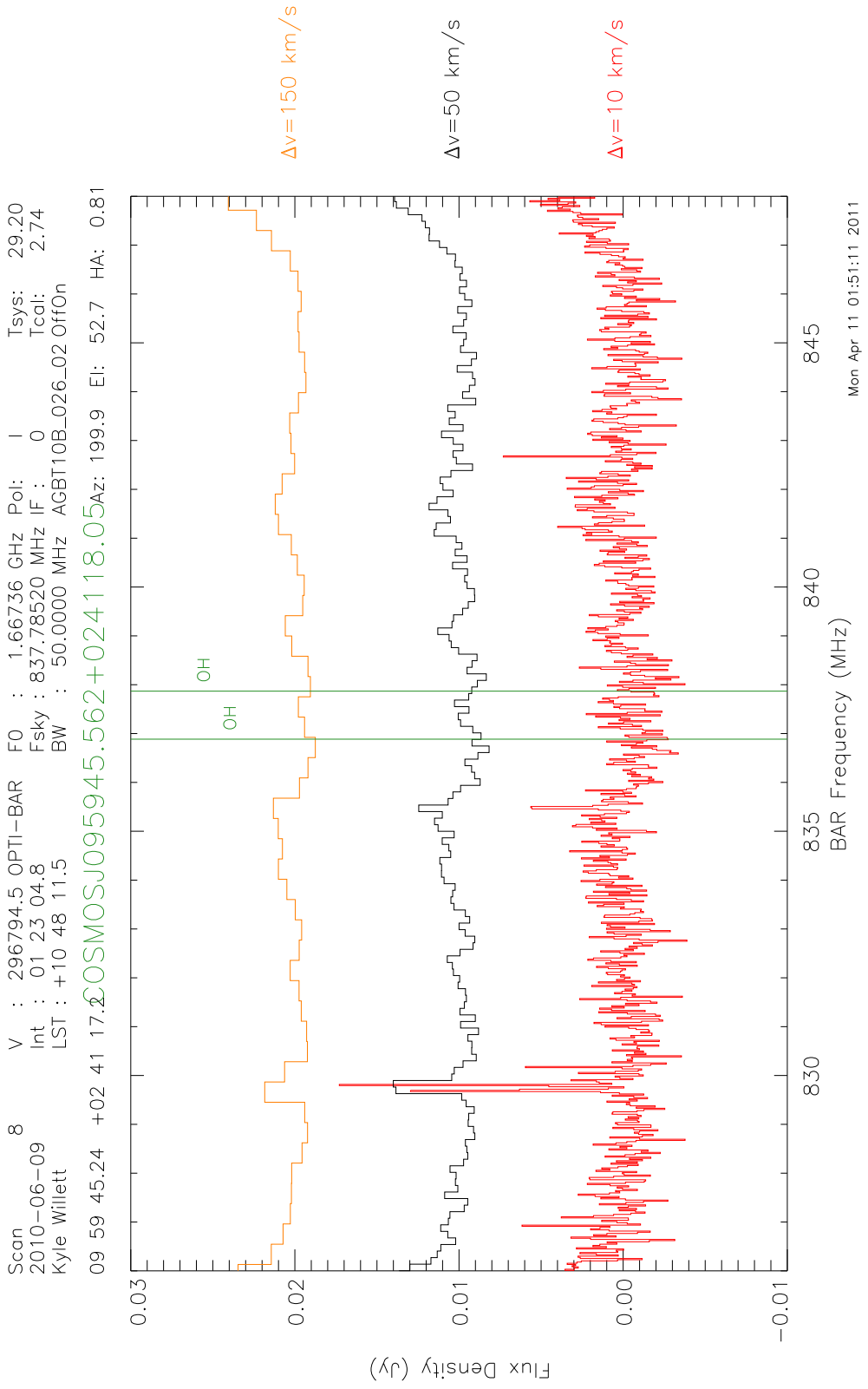

Figure C.8 18-cm spectrum of the galaxy COSMOS J095945.562+024118.05.

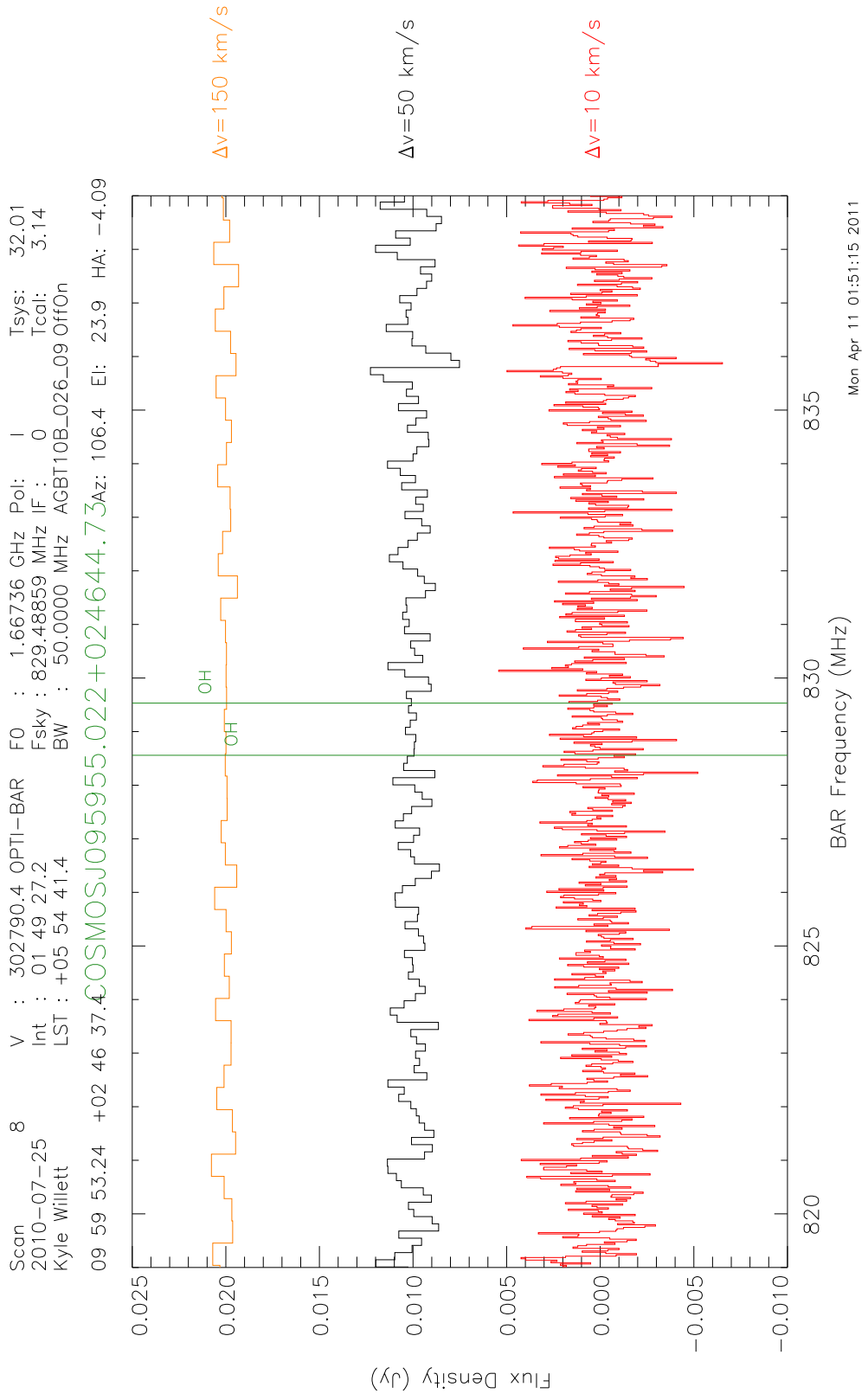

Figure C.9 18-cm spectrum of the galaxy COSMOS J095955.022+024644.73.

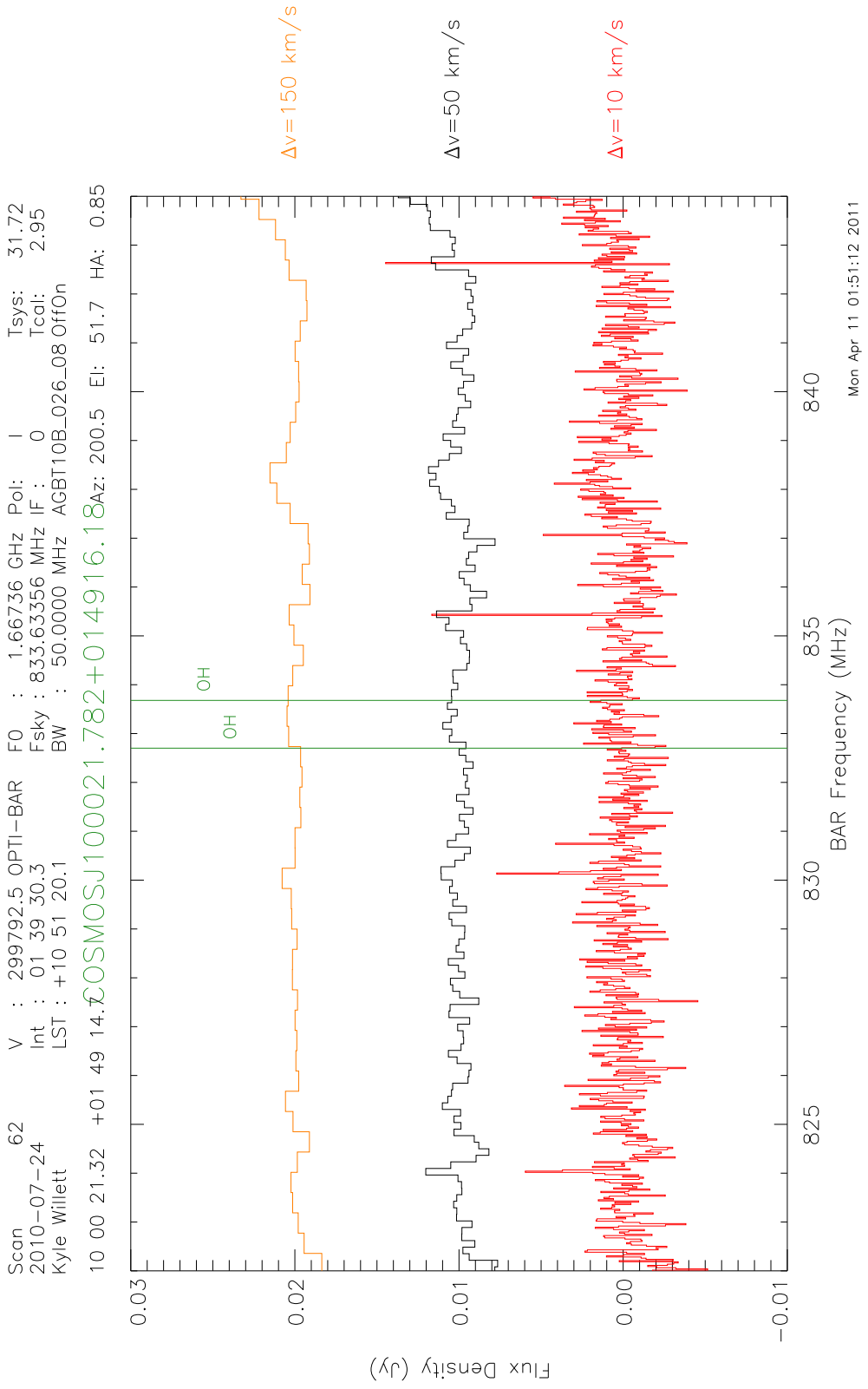

Figure C.10 18-cm spectrum of the galaxy COSMOS J100021.782+014916.18.

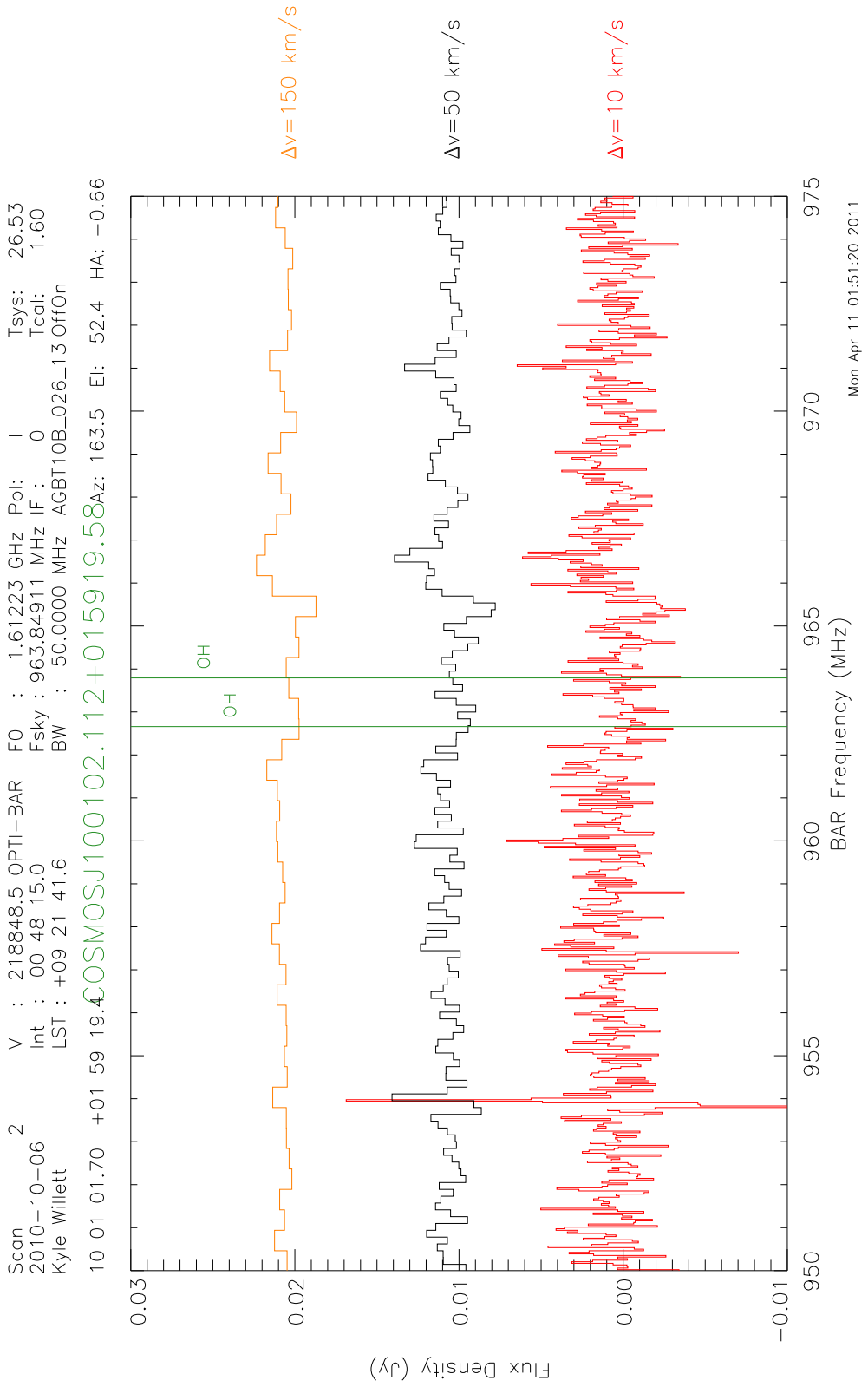

Figure C.11 18-cm spectrum of the galaxy COSMOS J100102.112+015919.58.

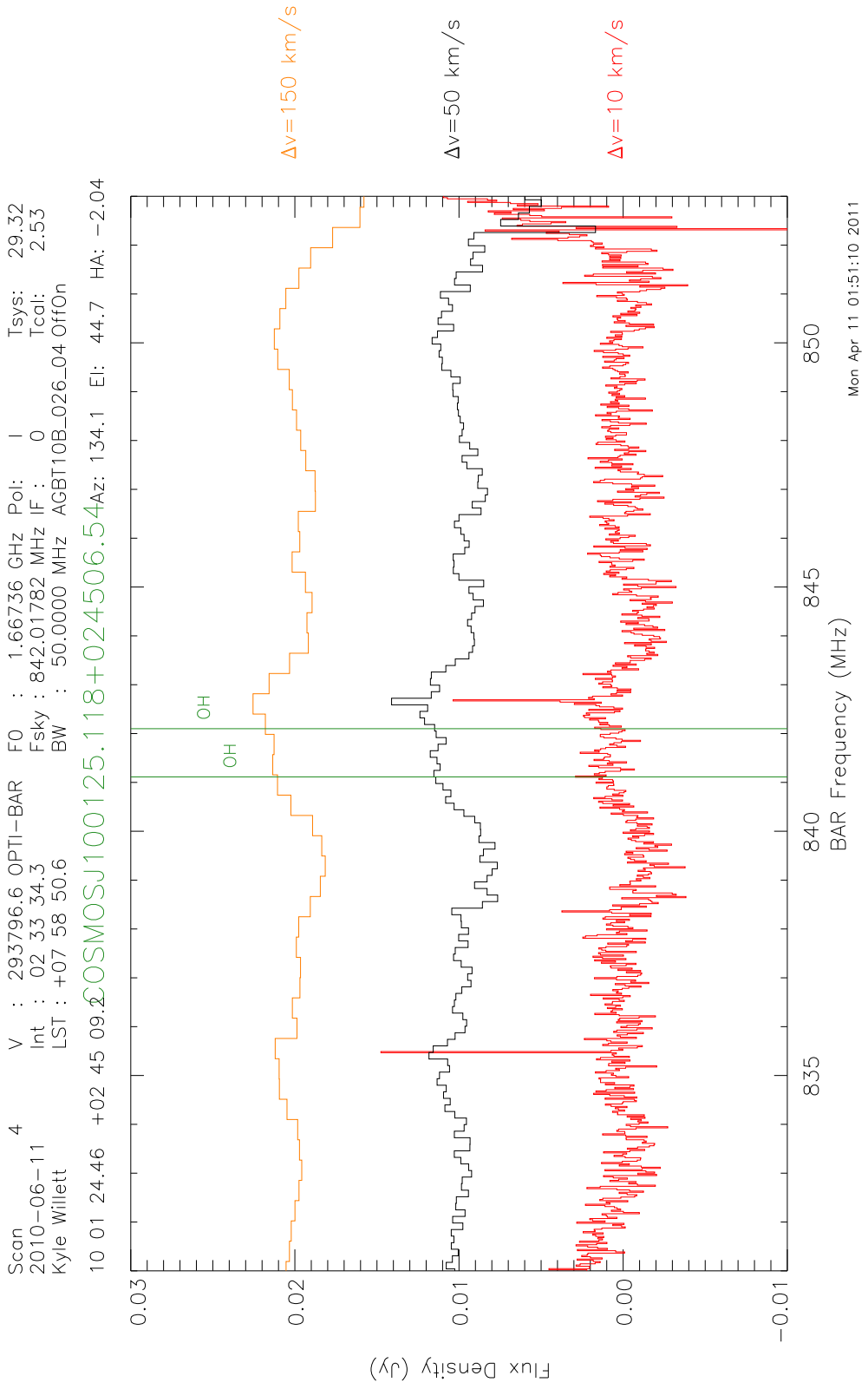

Figure C.12 18-cm spectrum of the galaxy COSMOS J100125.118+024506.54.

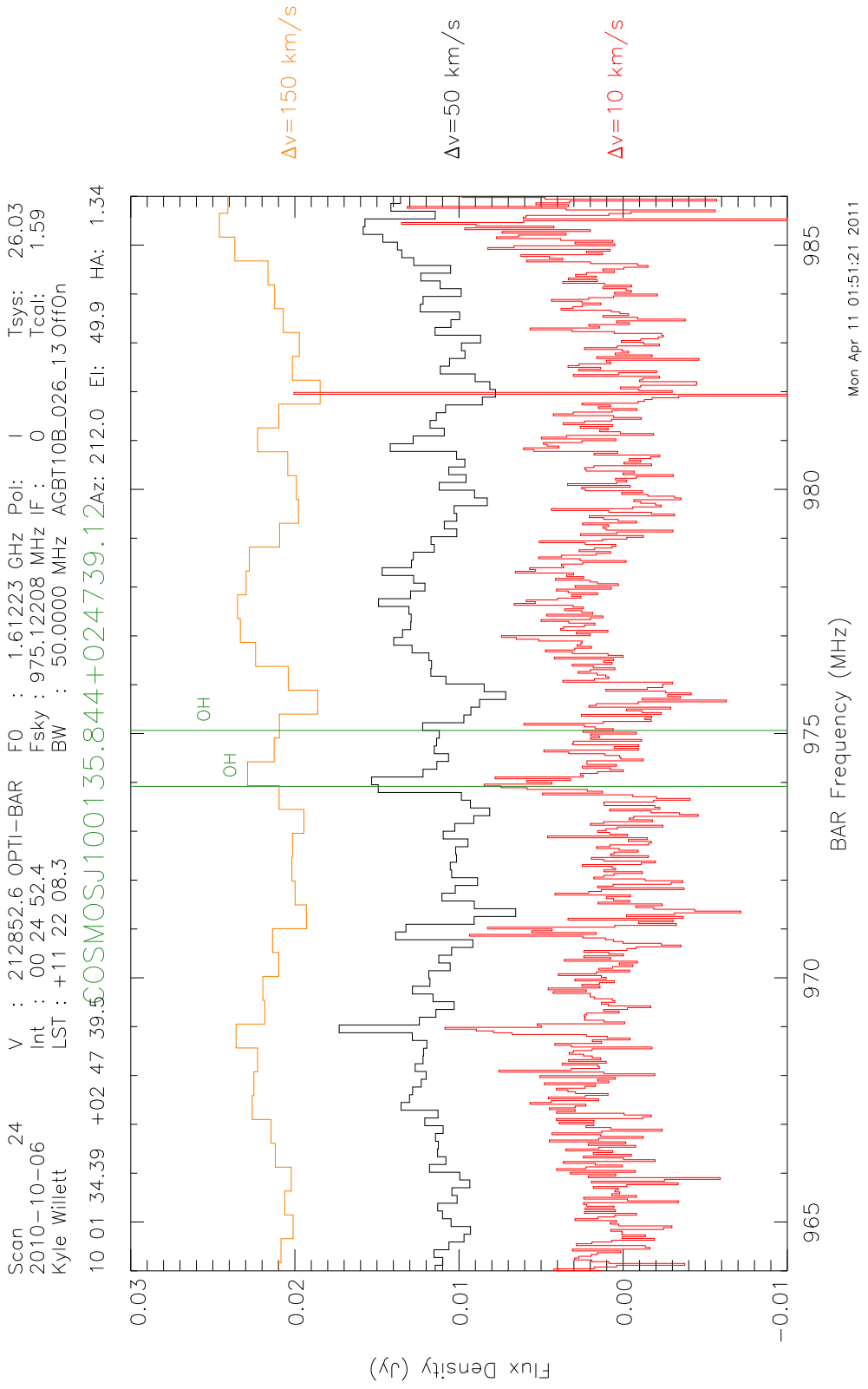

Figure C.13 18-cm spectrum of the galaxy COSMOS J100135.844+024739.12.

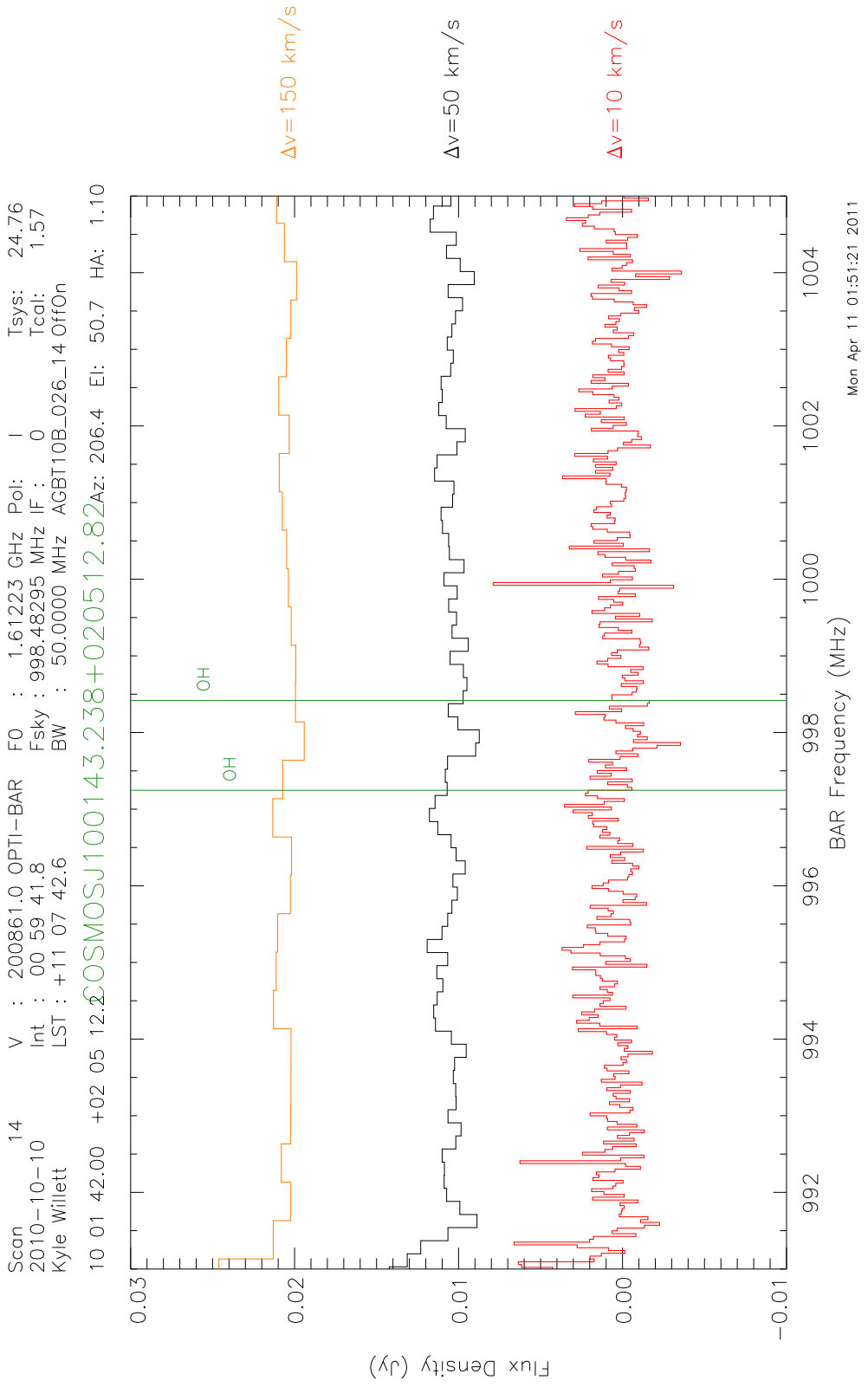

Figure C.14 18-cm spectrum of the galaxy COSMOS J100143.238+020512.82.

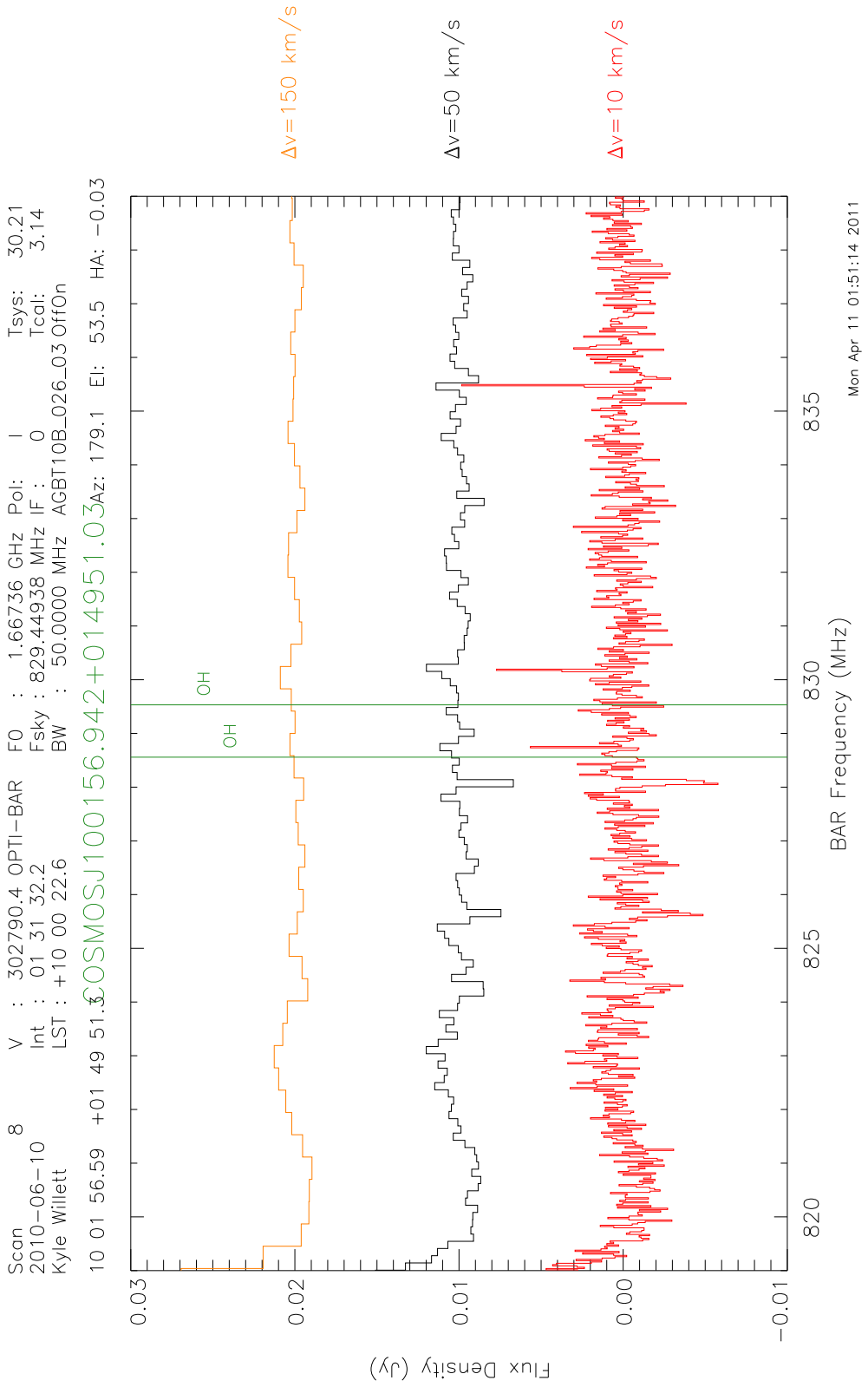

Figure C.15 18-cm spectrum of the galaxy COSMOS J100156.942+014951.03.

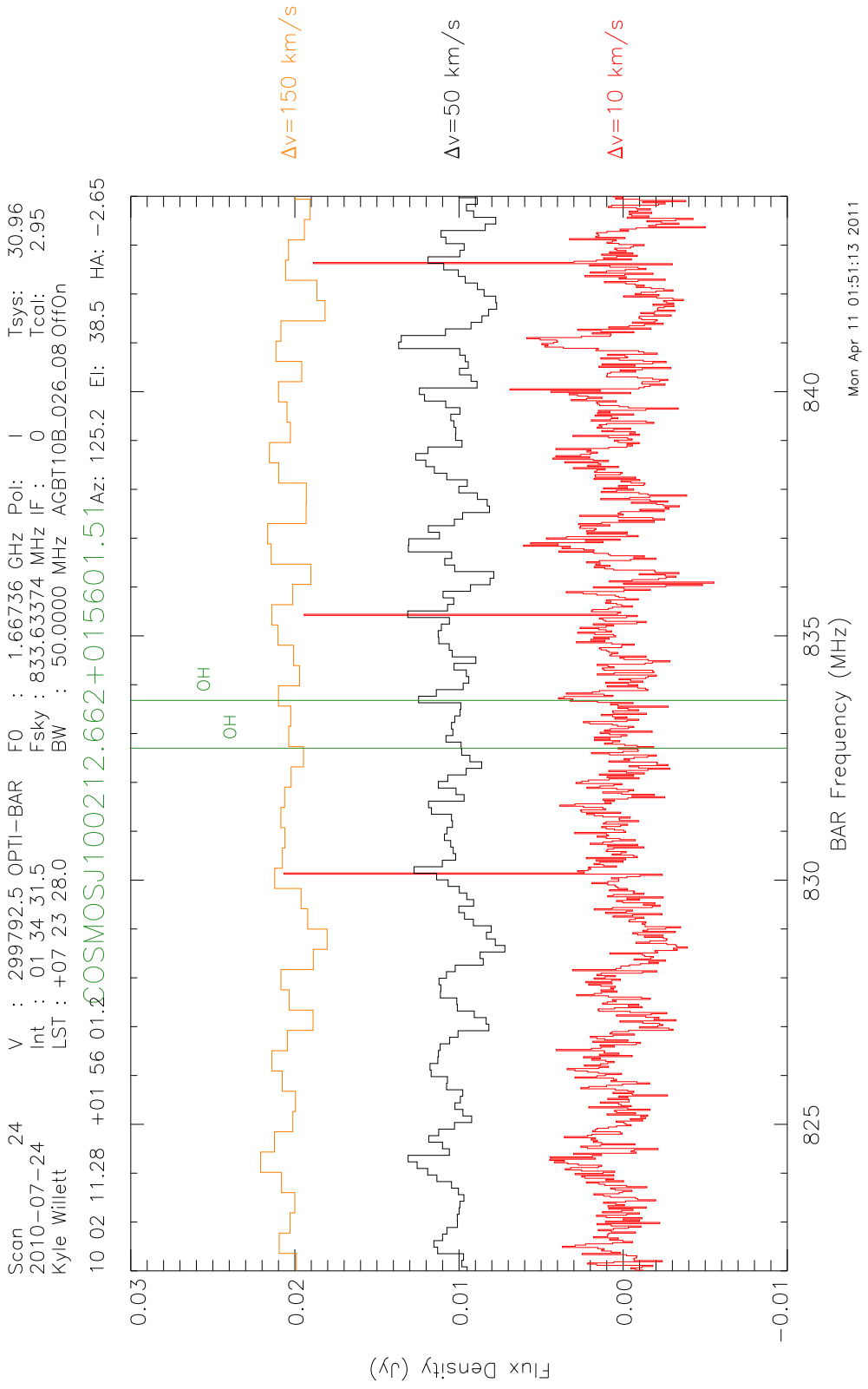

Figure C.16 18-cm spectrum of the galaxy COSMOS J100212.662+015601.51.

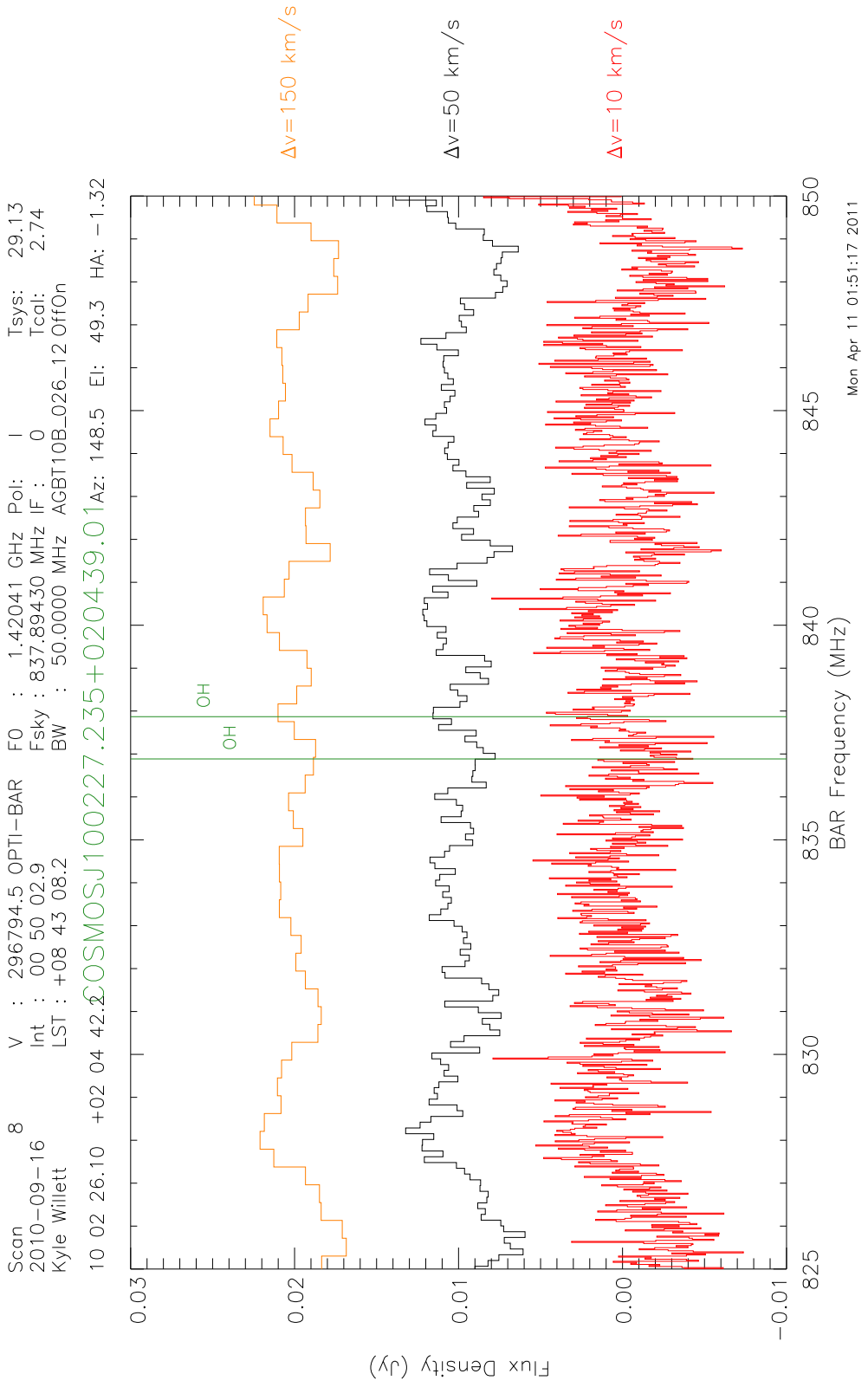

Figure C.17 18-cm spectrum of the galaxy COSMOS J100227.235+020439.01.

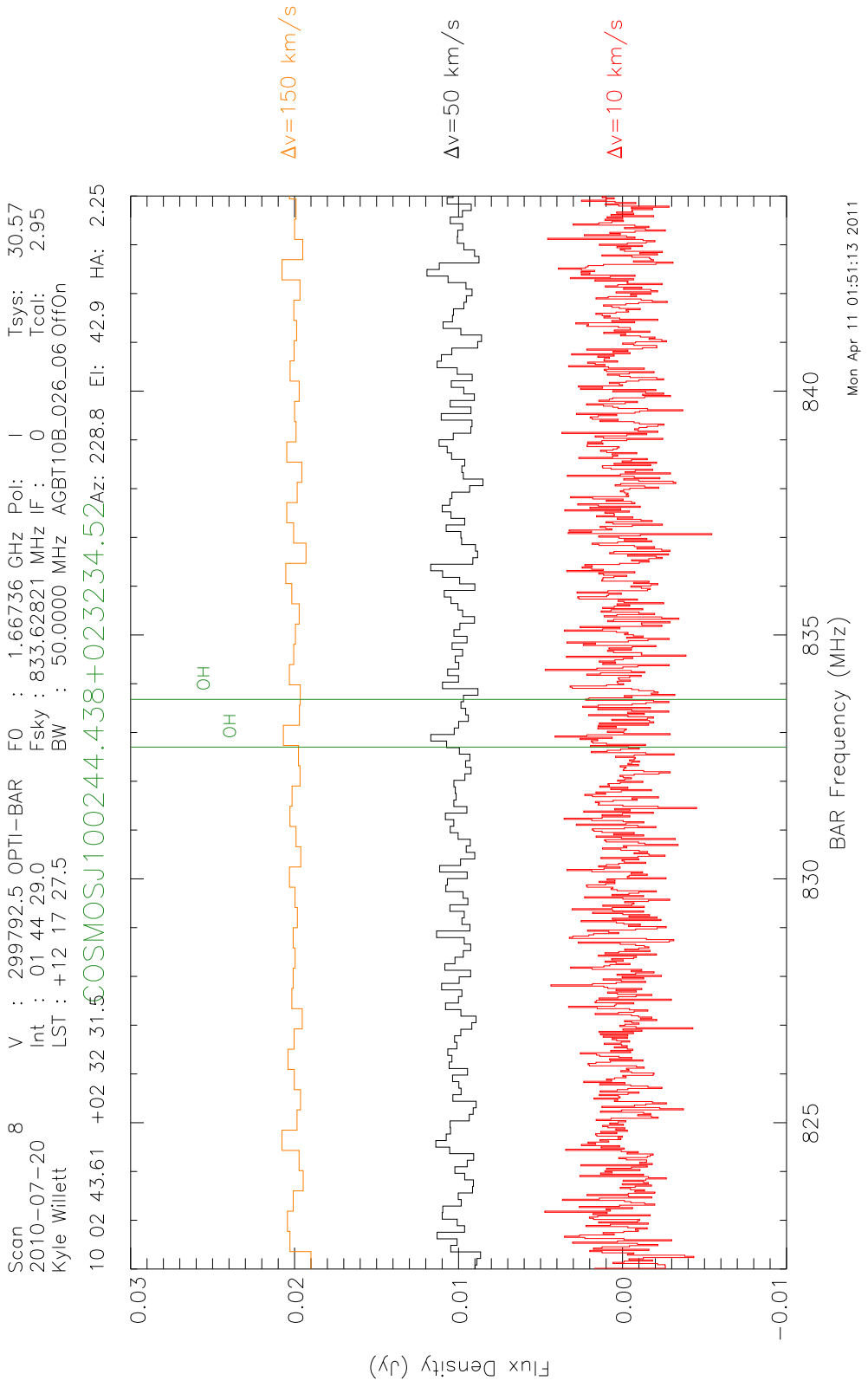

Figure C.18 18-cm spectrum of the galaxy COSMOS J100244.438+023234.52.

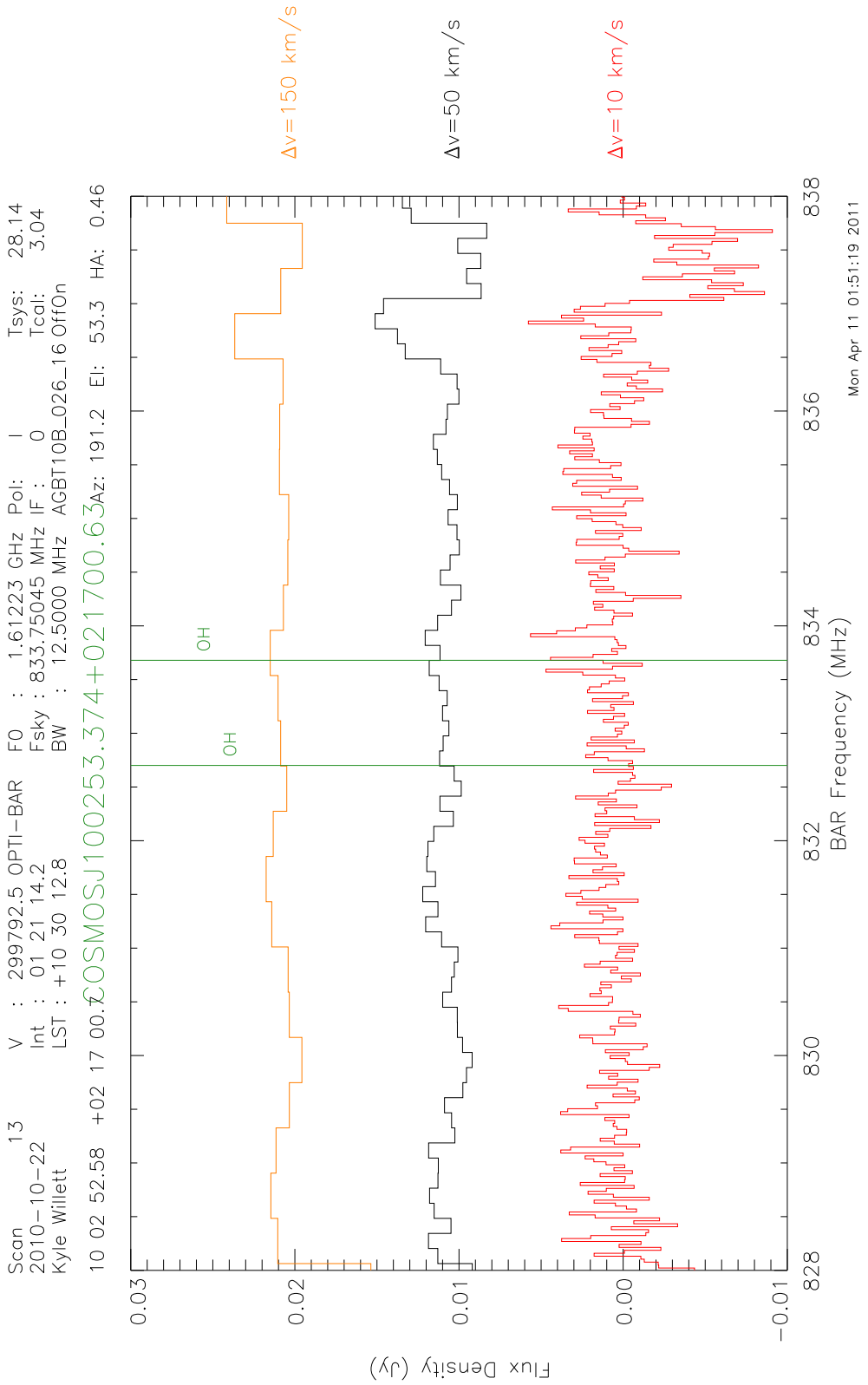

Figure C.19 18-cm spectrum of the galaxy COSMOS J100253.374+021700.63.

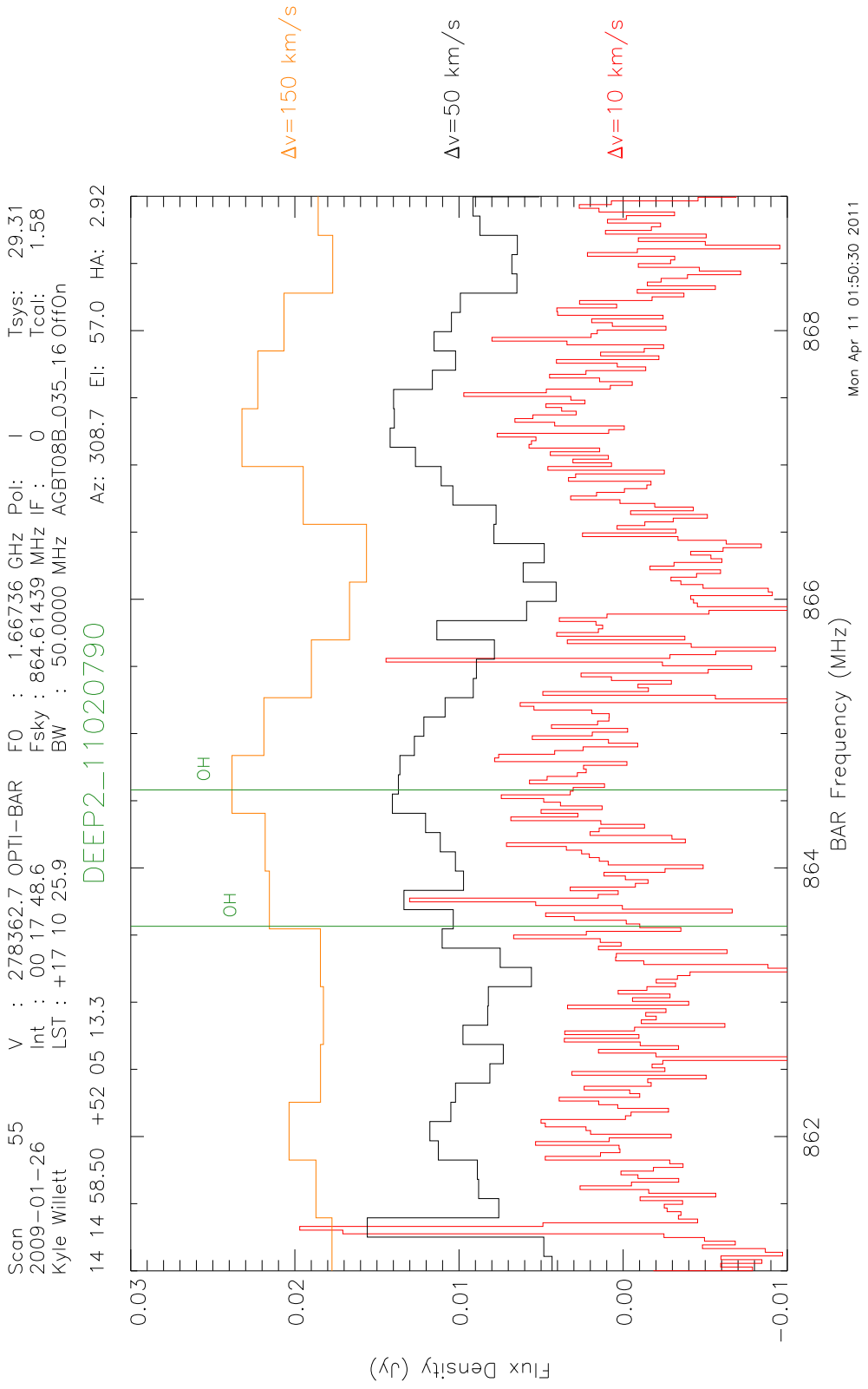

Figure C.20 18-cm spectrum of the galaxy DEEP2 11020790.

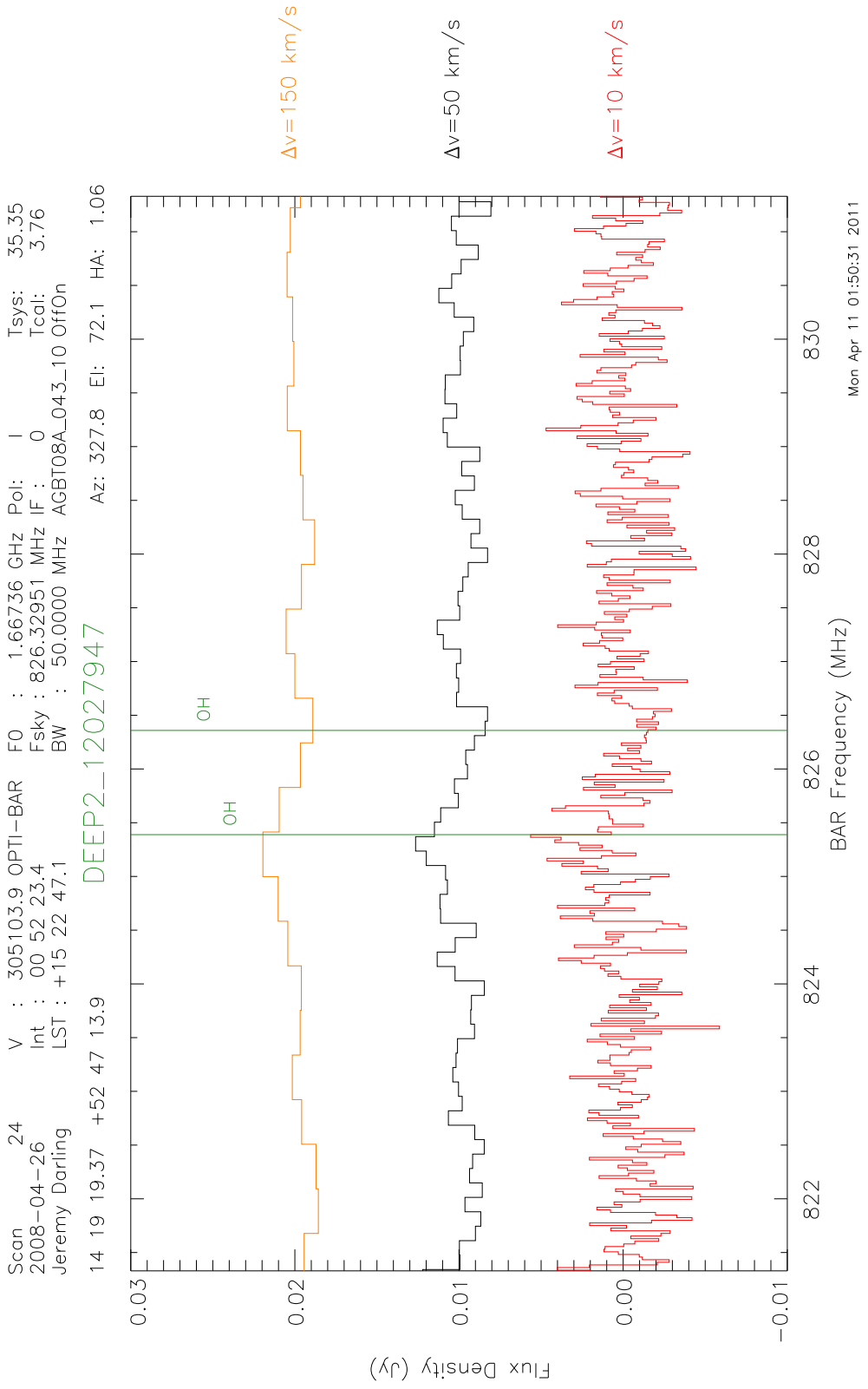

Figure C.21 18-cm spectrum of the galaxy DEEP2 12027947.

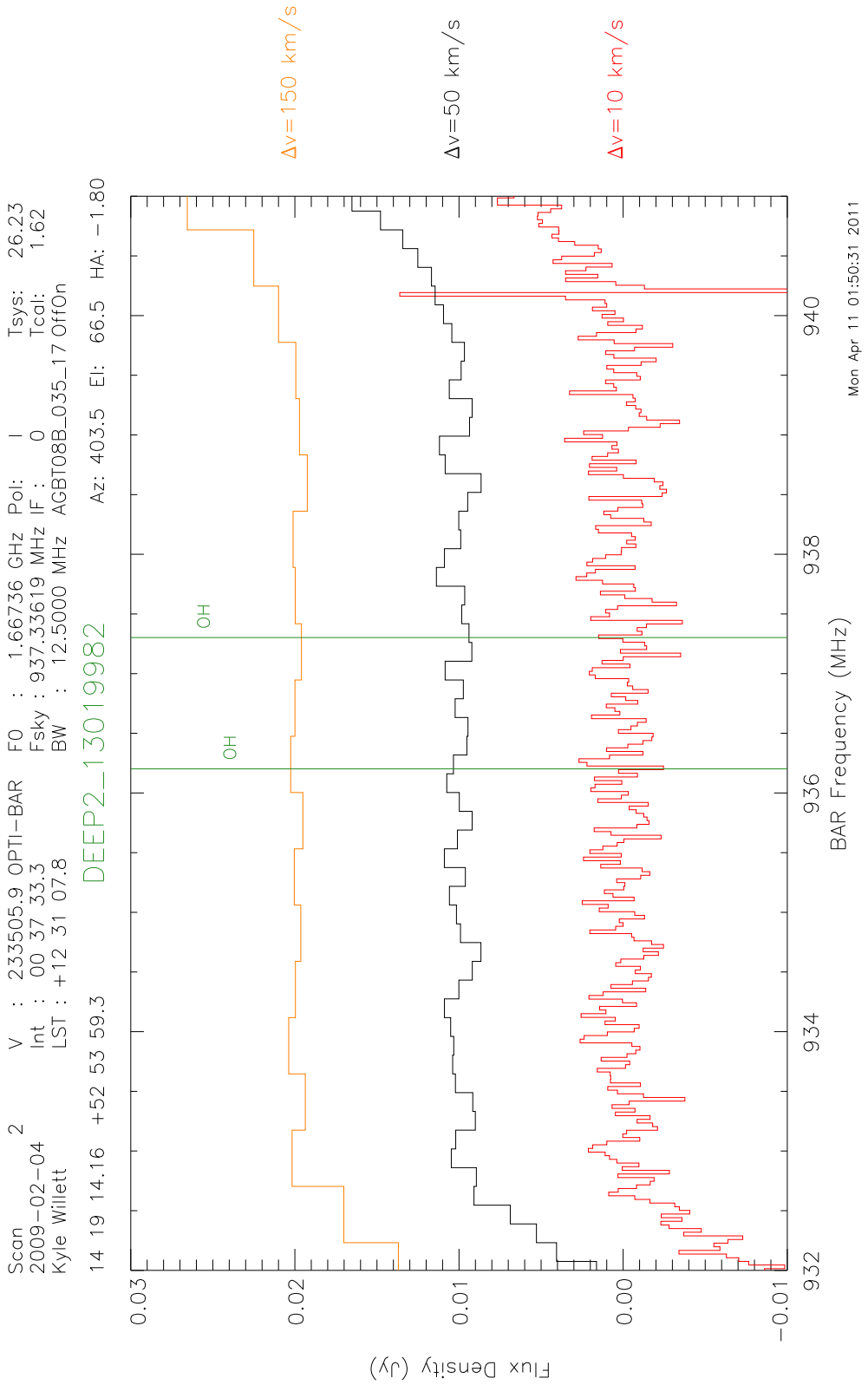

Figure C.22 18-cm spectrum of the galaxy DEEP2 13019982.

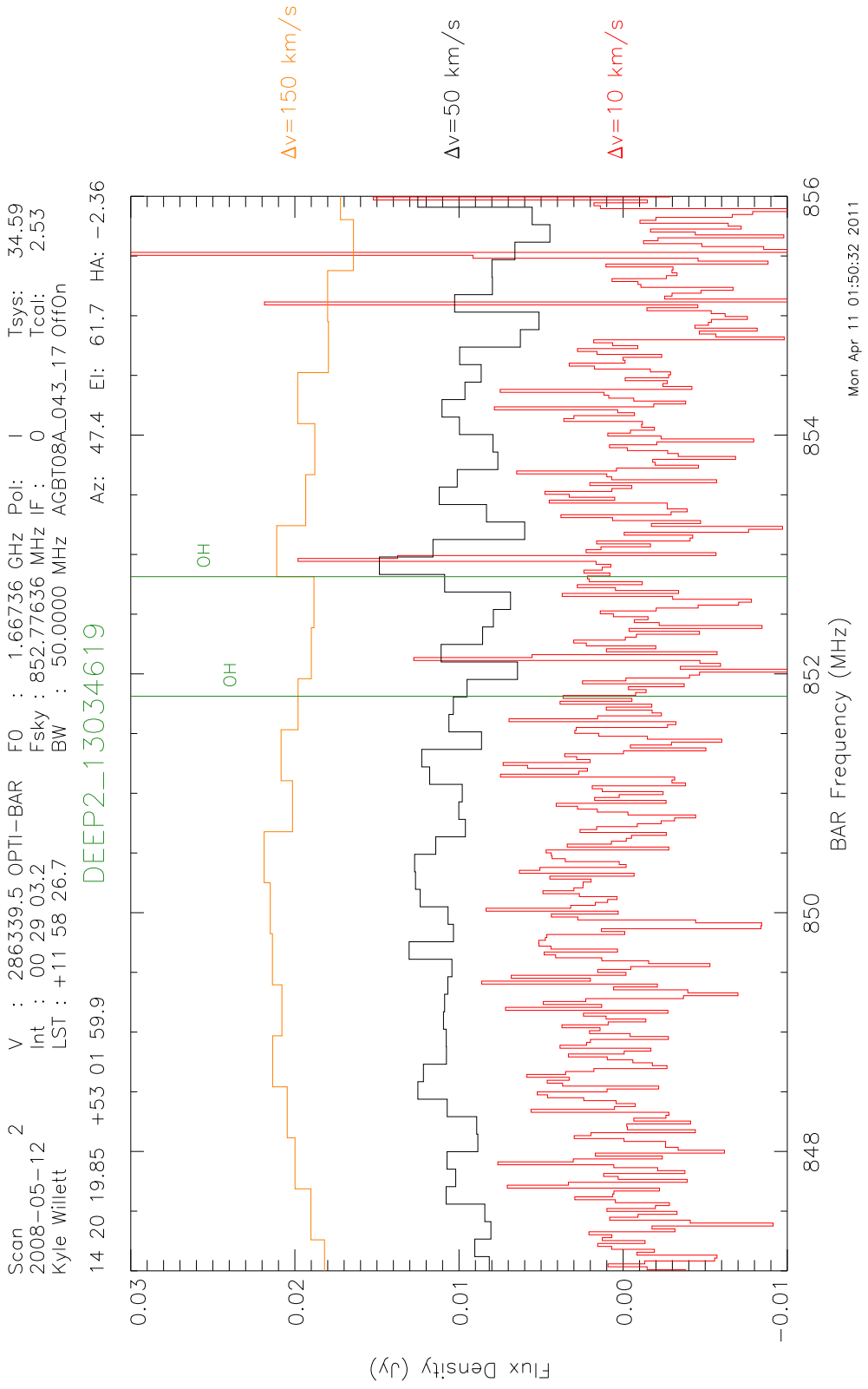

Figure C.23 18-cm spectrum of the galaxy DEEP2 13034619.

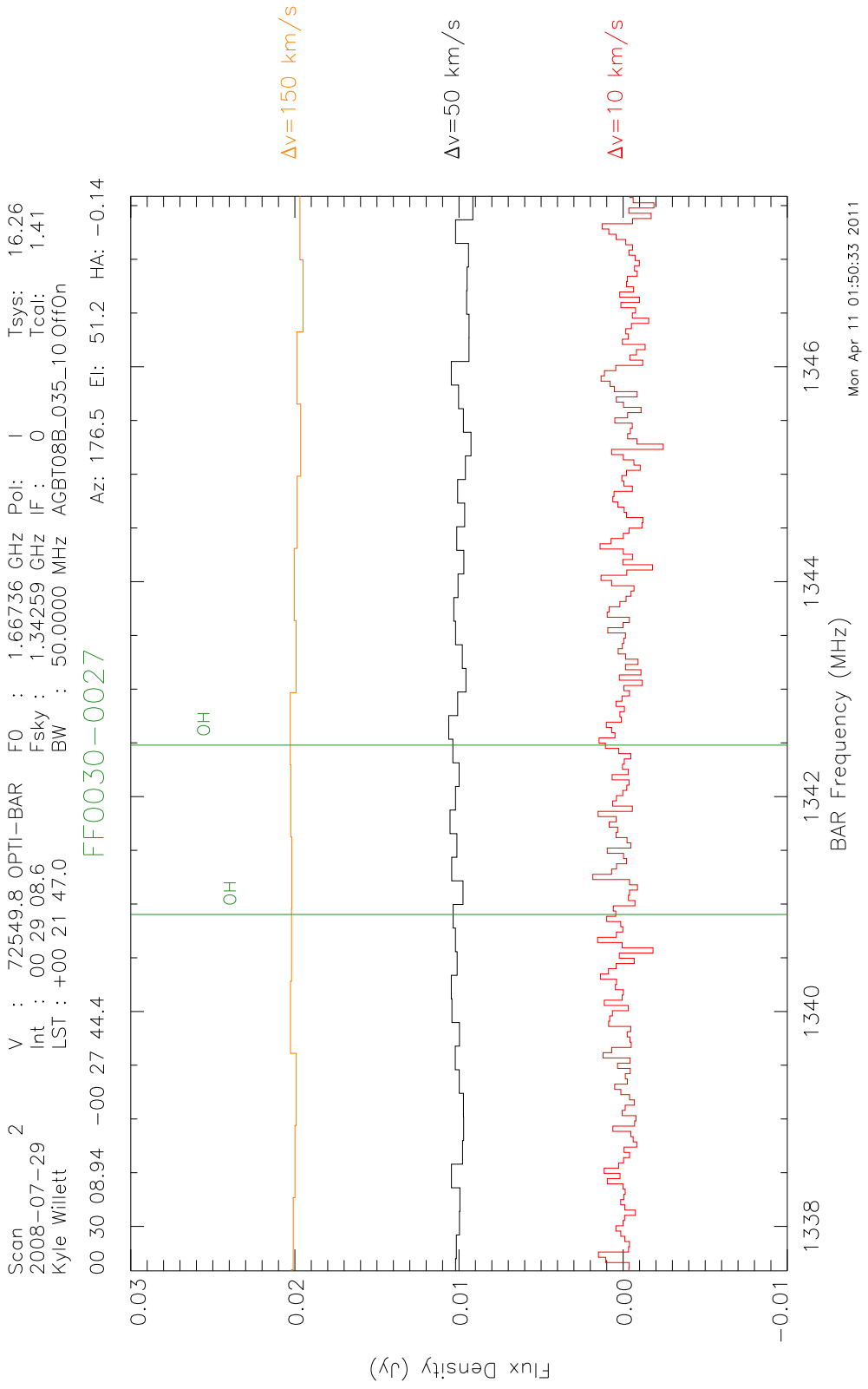

Figure C.24 18-cm spectrum of the galaxy FF 0030−0027.

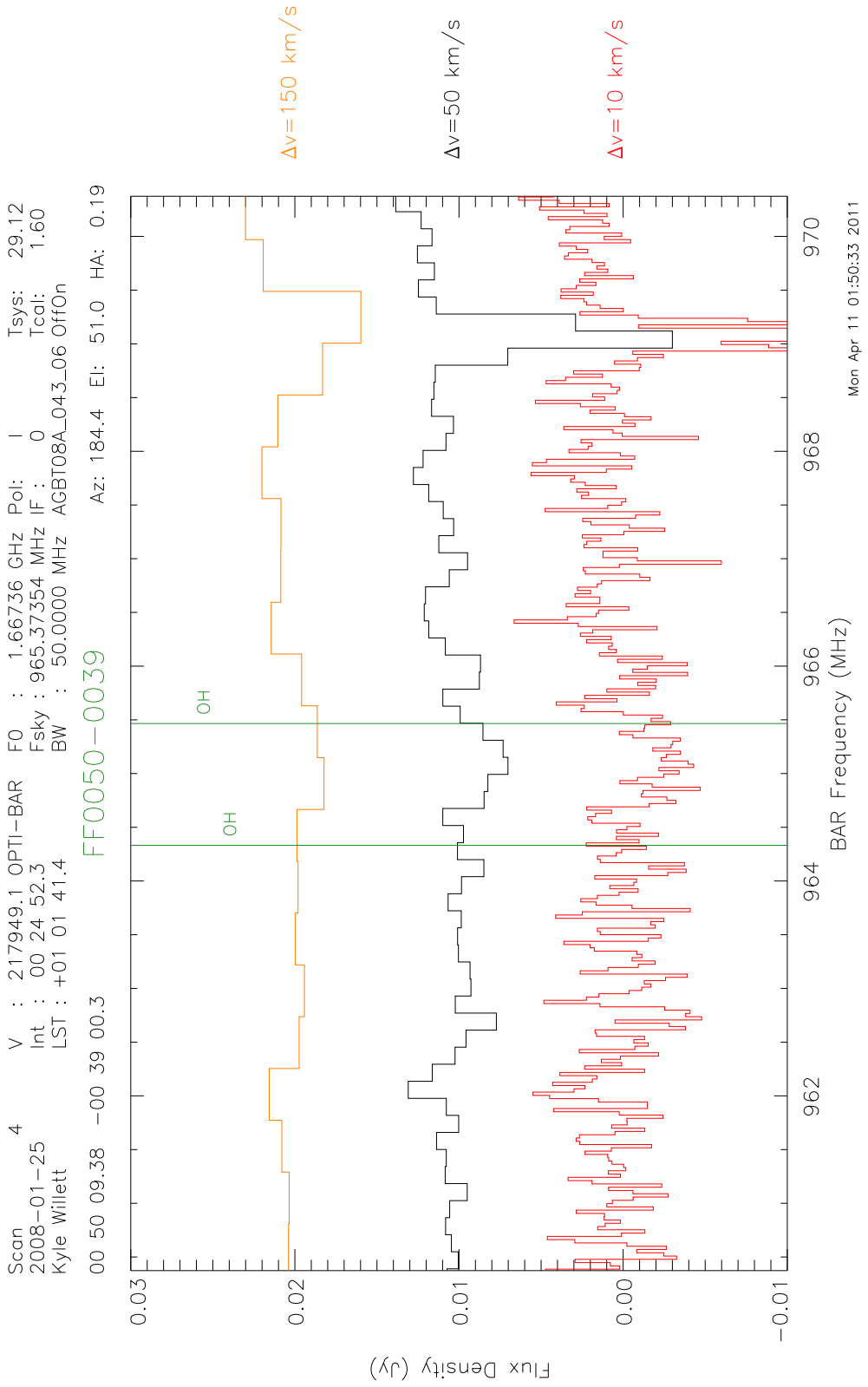

Figure C.25 18-cm spectrum of the galaxy FF 0050−0039.

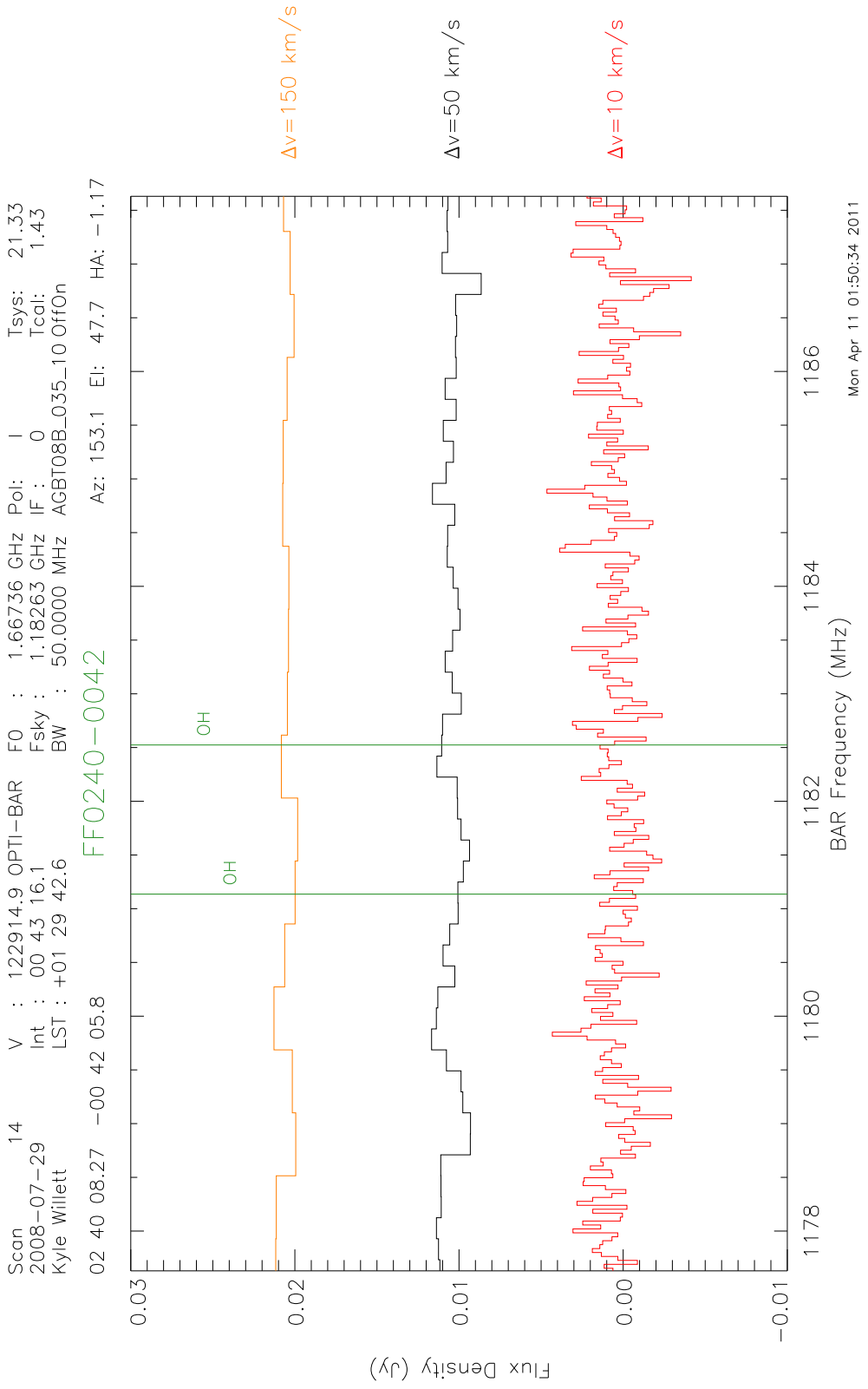

Figure C.26 18-cm spectrum of the galaxy FF 0240−0042.

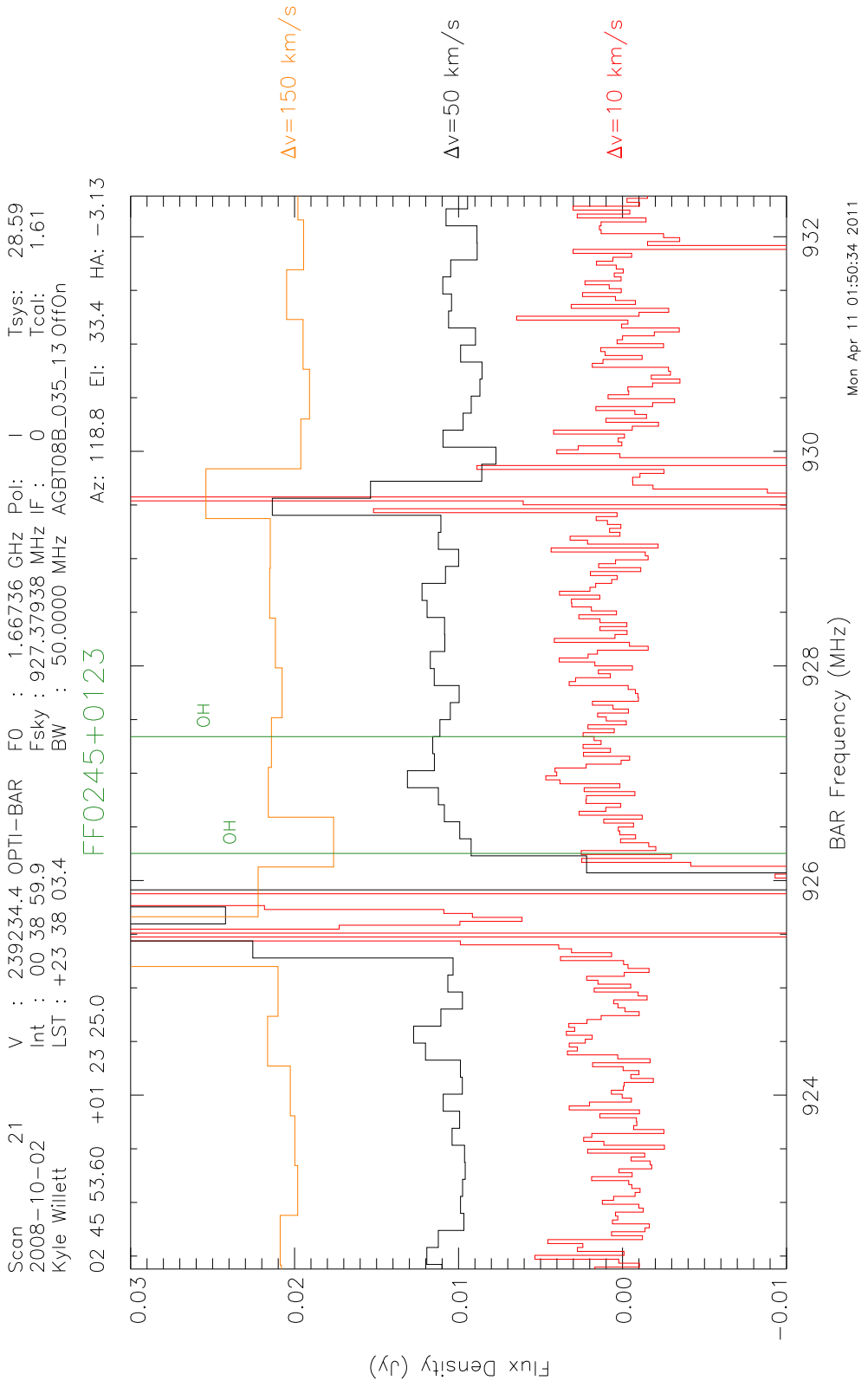

Figure C.27 18-cm spectrum of the galaxy FF 0245+0123.

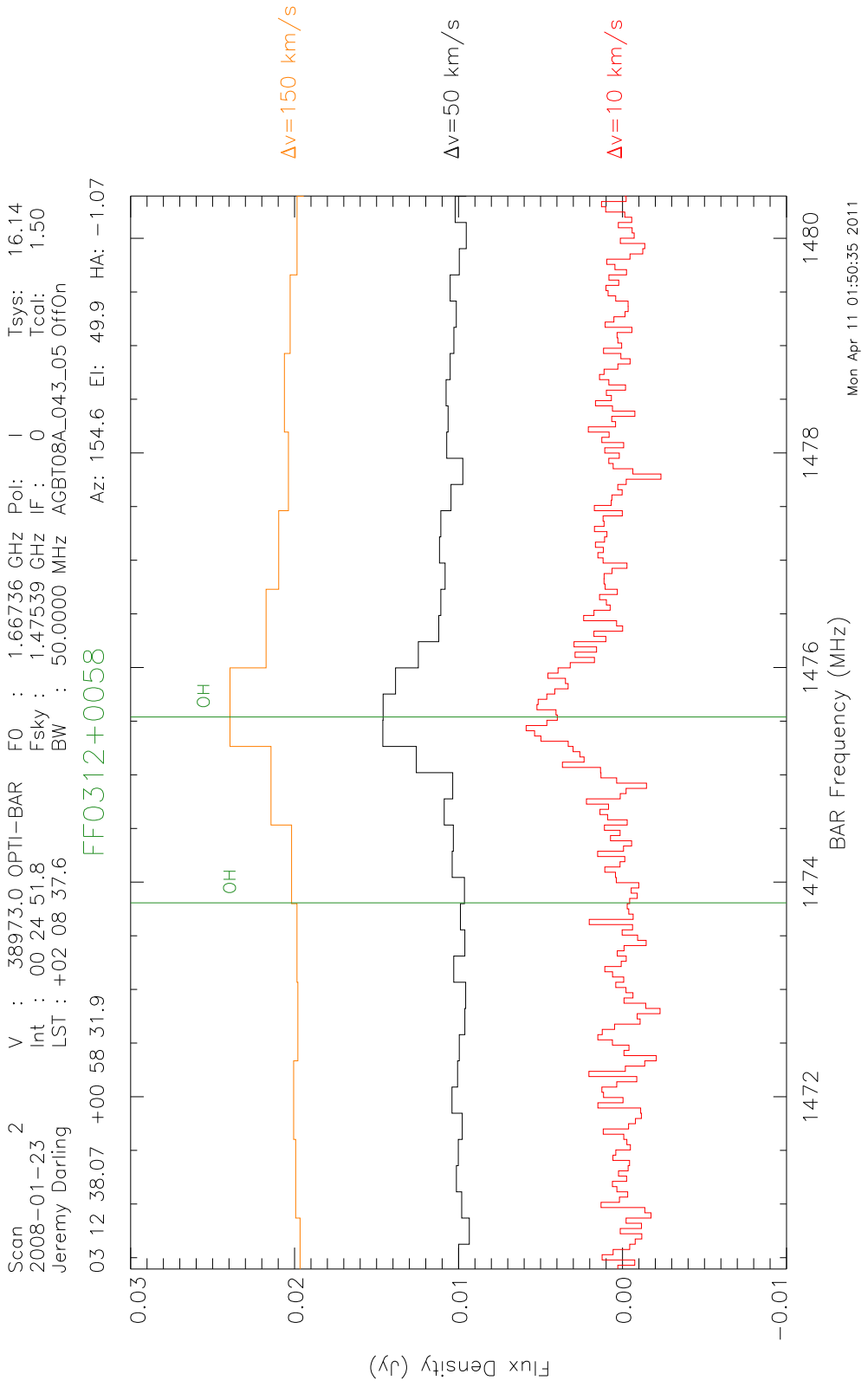

Figure C.28 18-cm spectrum of the galaxy FF 0312+0058.

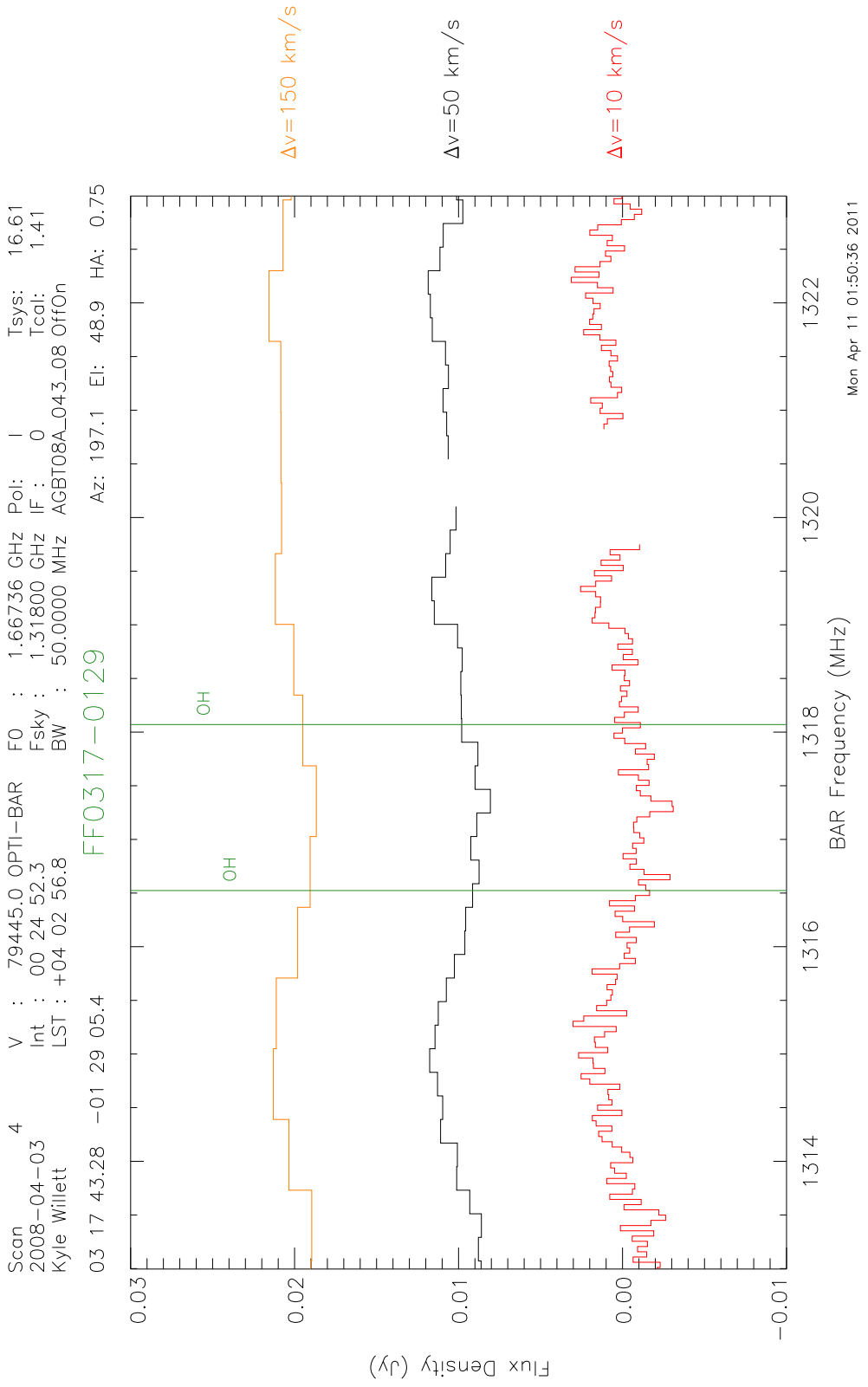

Figure C.29 18-cm spectrum of the galaxy FF 0317−0129.

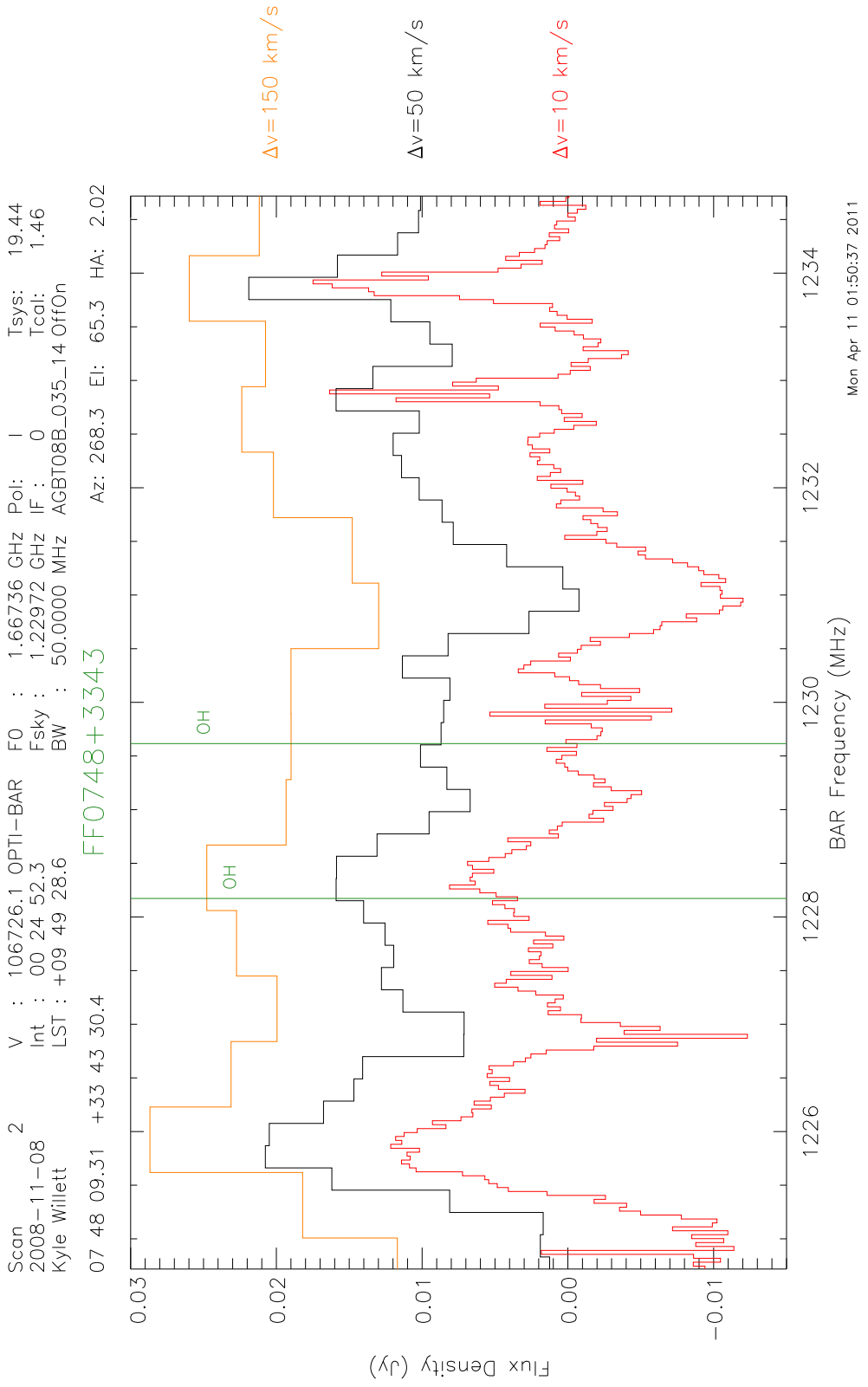

Figure C.30 18-cm spectrum of the galaxy FF 0748+3343.

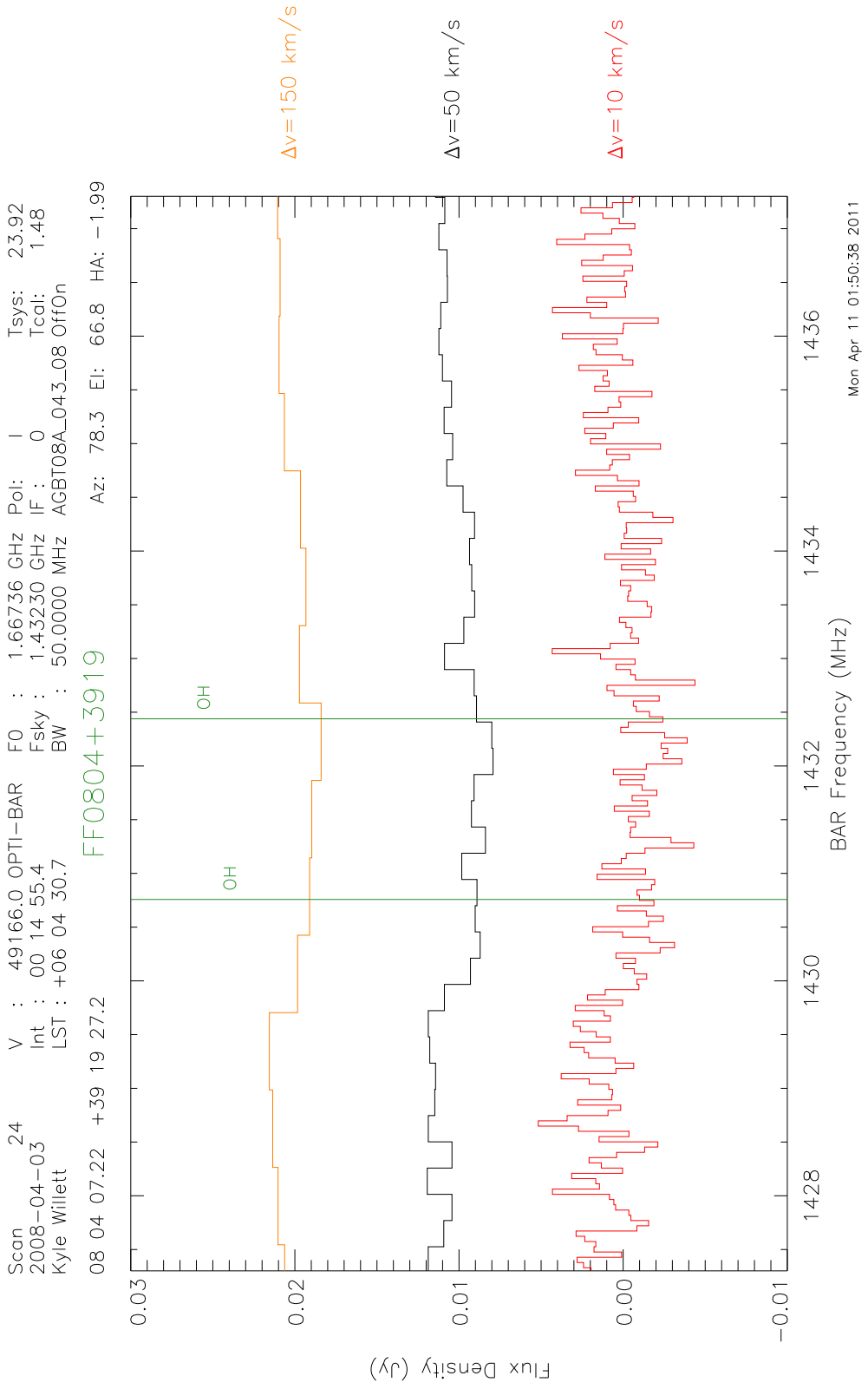

Figure C.31 18-cm spectrum of the galaxy FF 0804+3919.

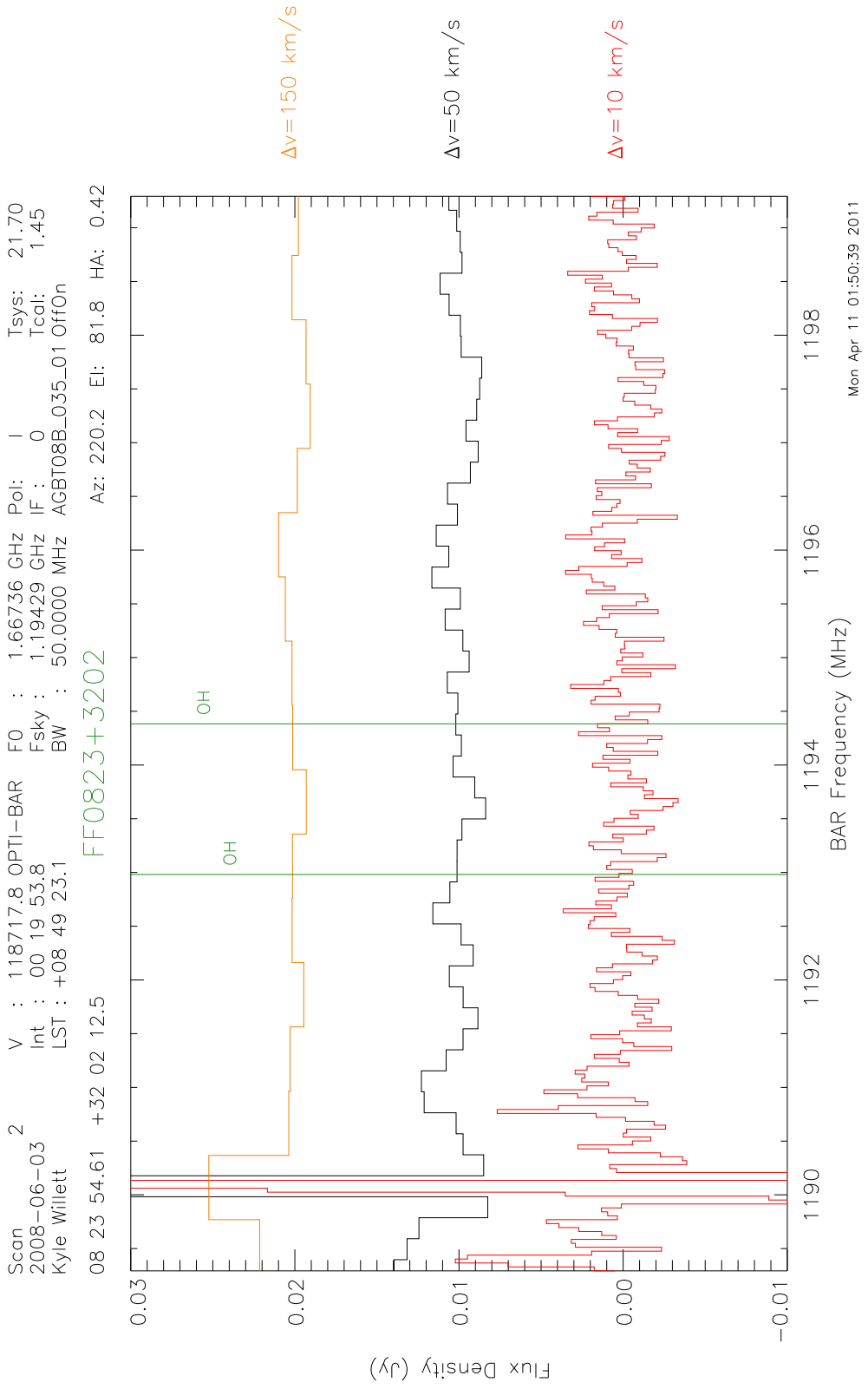

Figure C.32 18-cm spectrum of the galaxy FF 0823+3202.

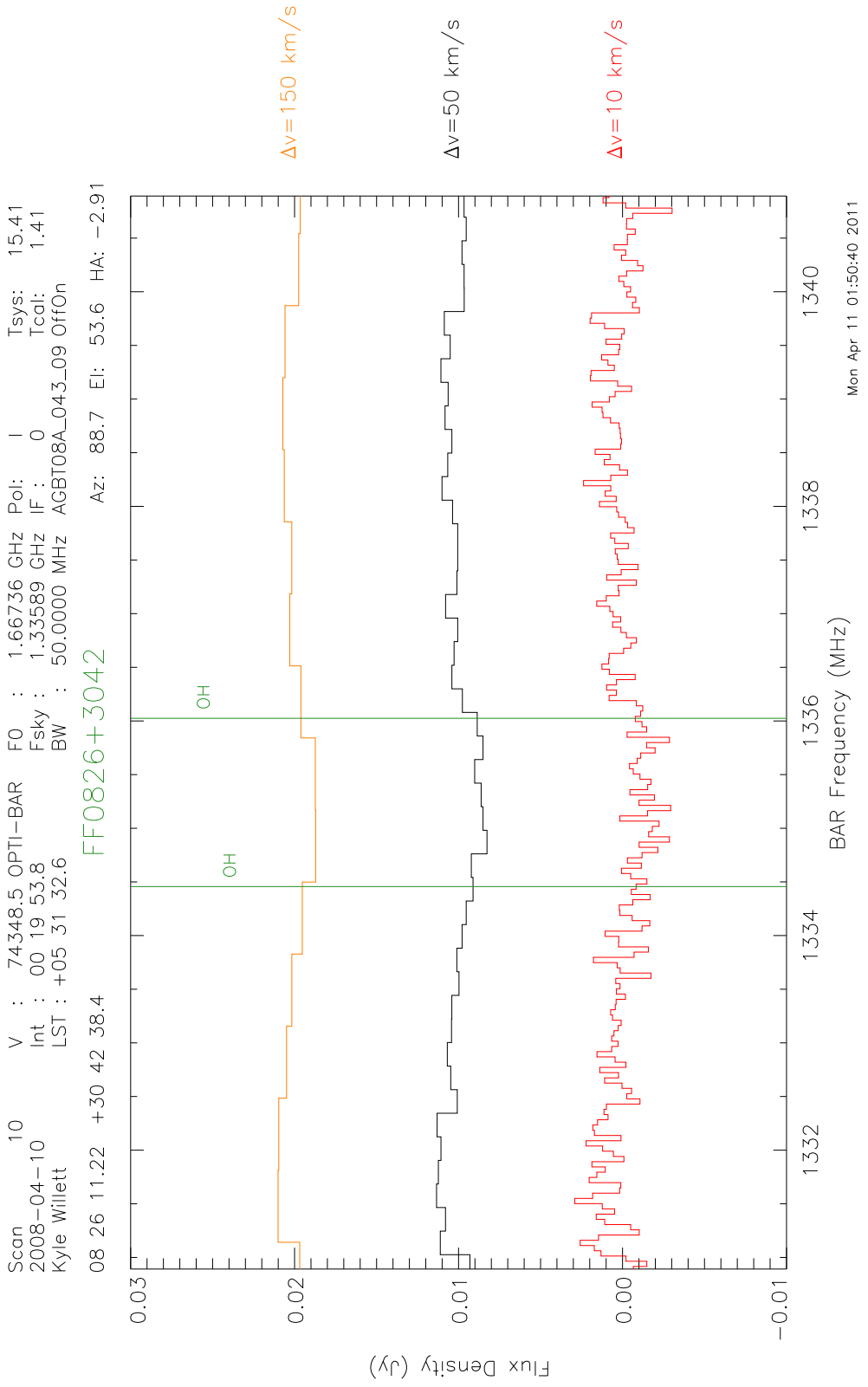

Figure C.33 18-cm spectrum of the galaxy FF 0826+3042.

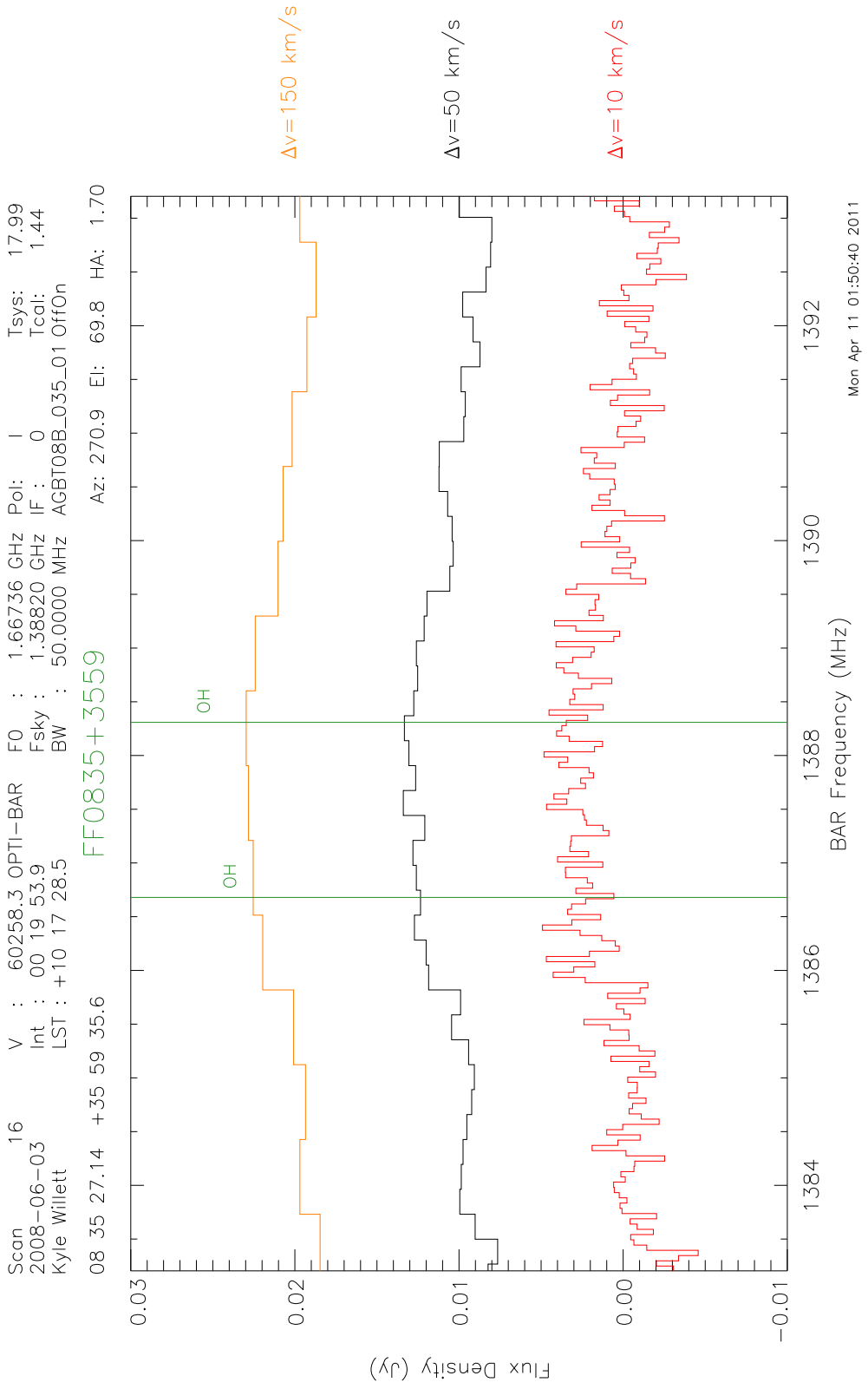

Figure C.34 18-cm spectrum of the galaxy FF 0835+3559.

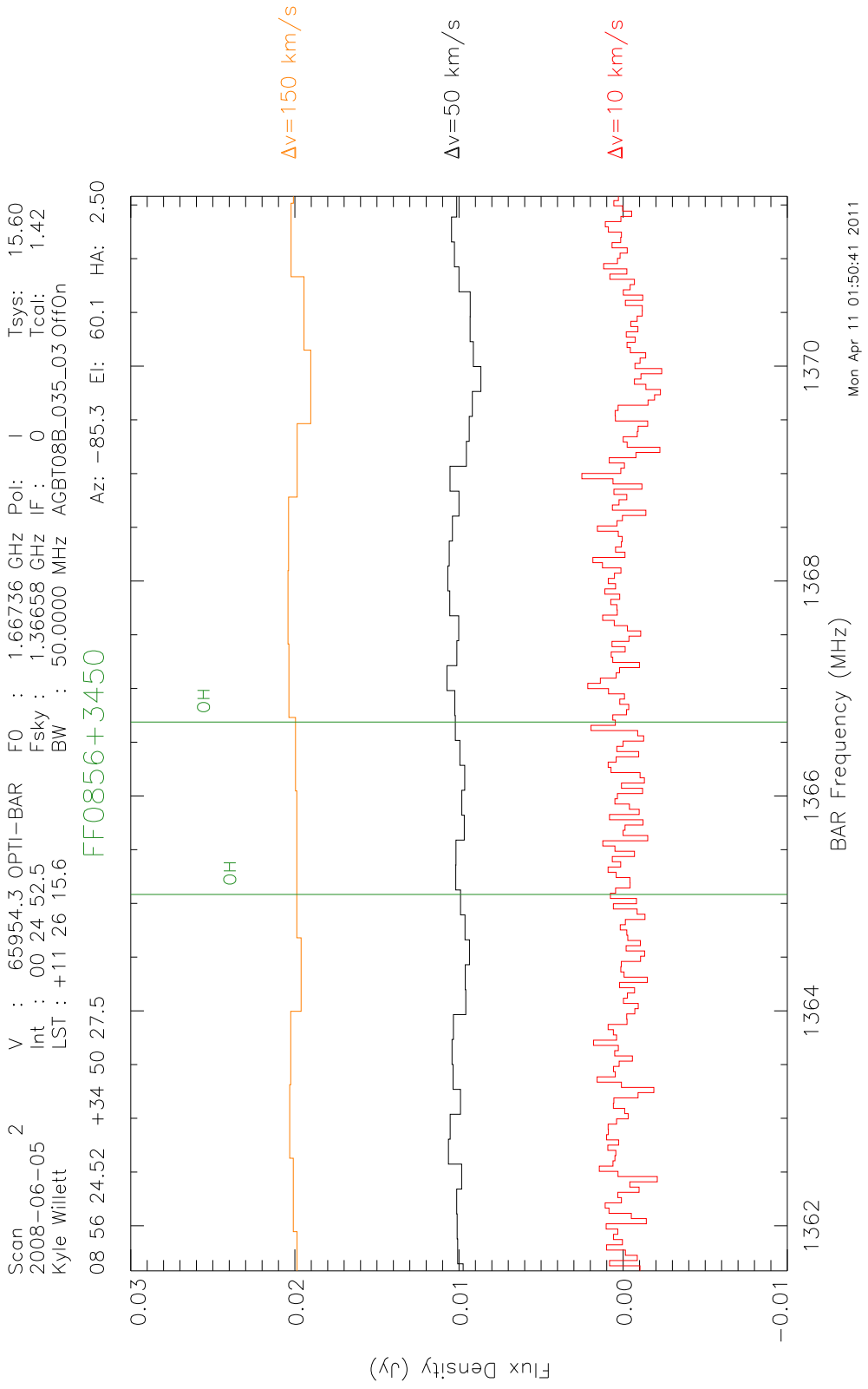

Figure C.35 18-cm spectrum of the galaxy FF 0856+3450.

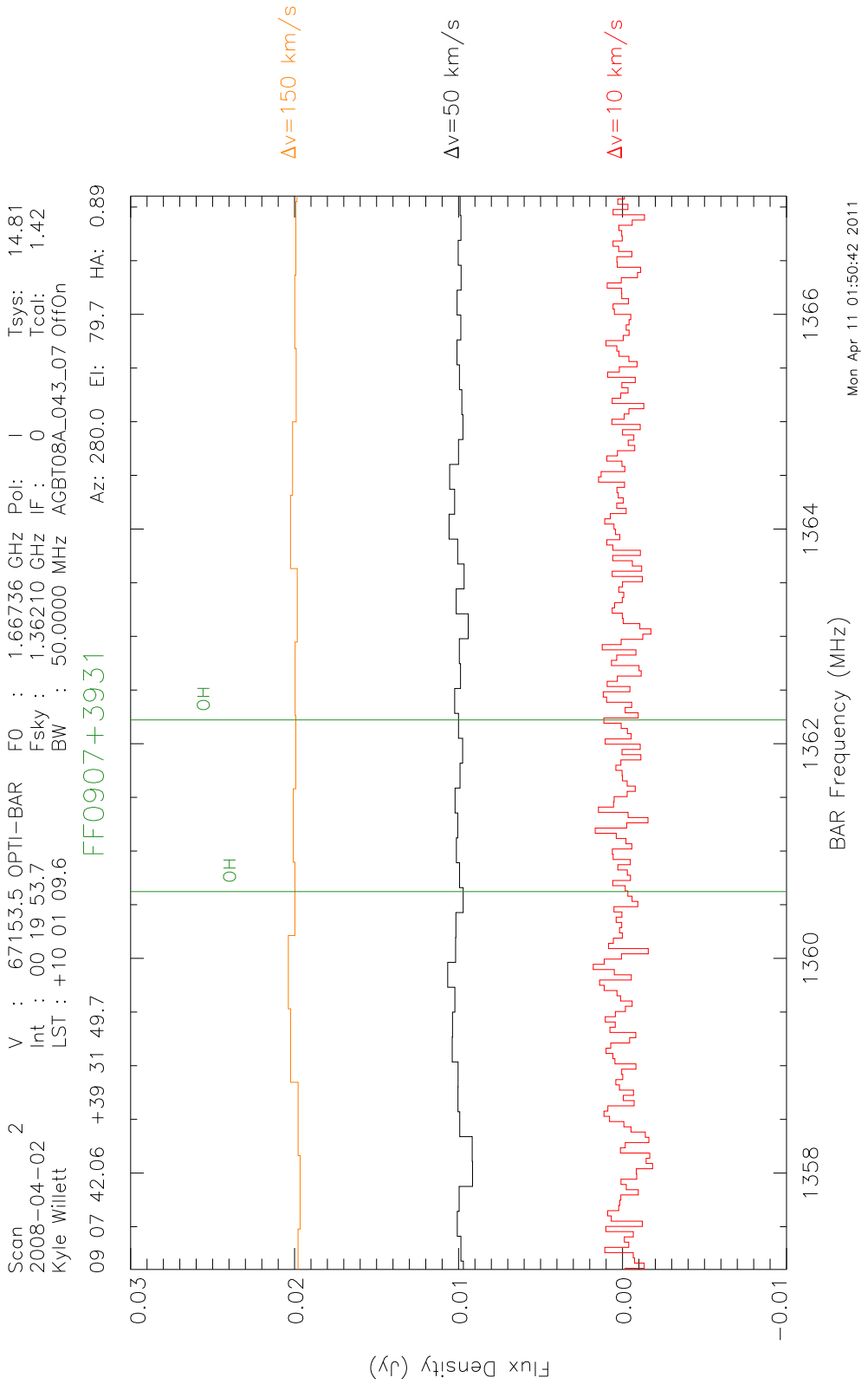

Figure C.36 18-cm spectrum of the galaxy FF 0907+3931.

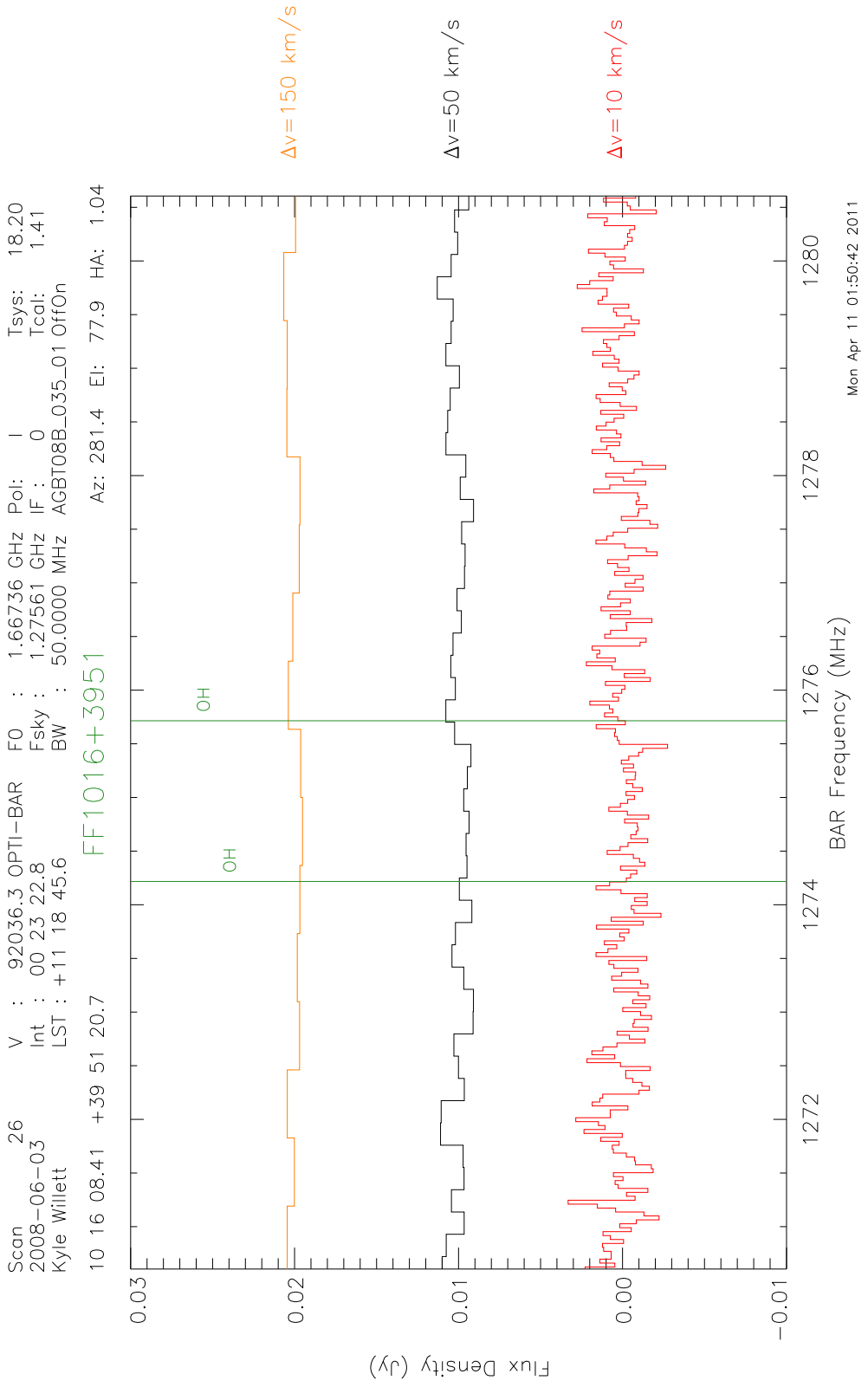

Figure C.37 18-cm spectrum of the galaxy FF 1016+3951.

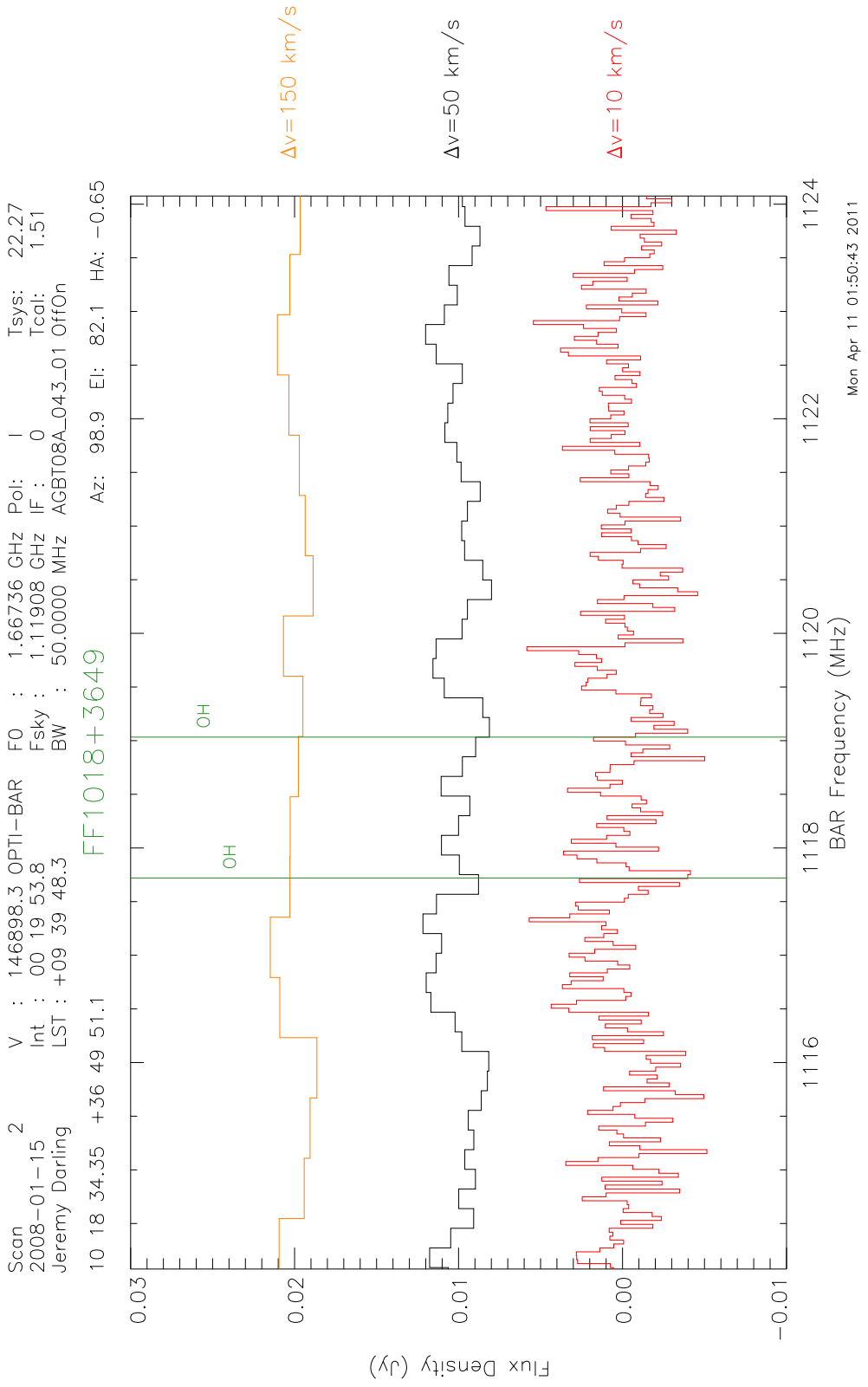

Figure C.38 18-cm spectrum of the galaxy FF 1018+3649.

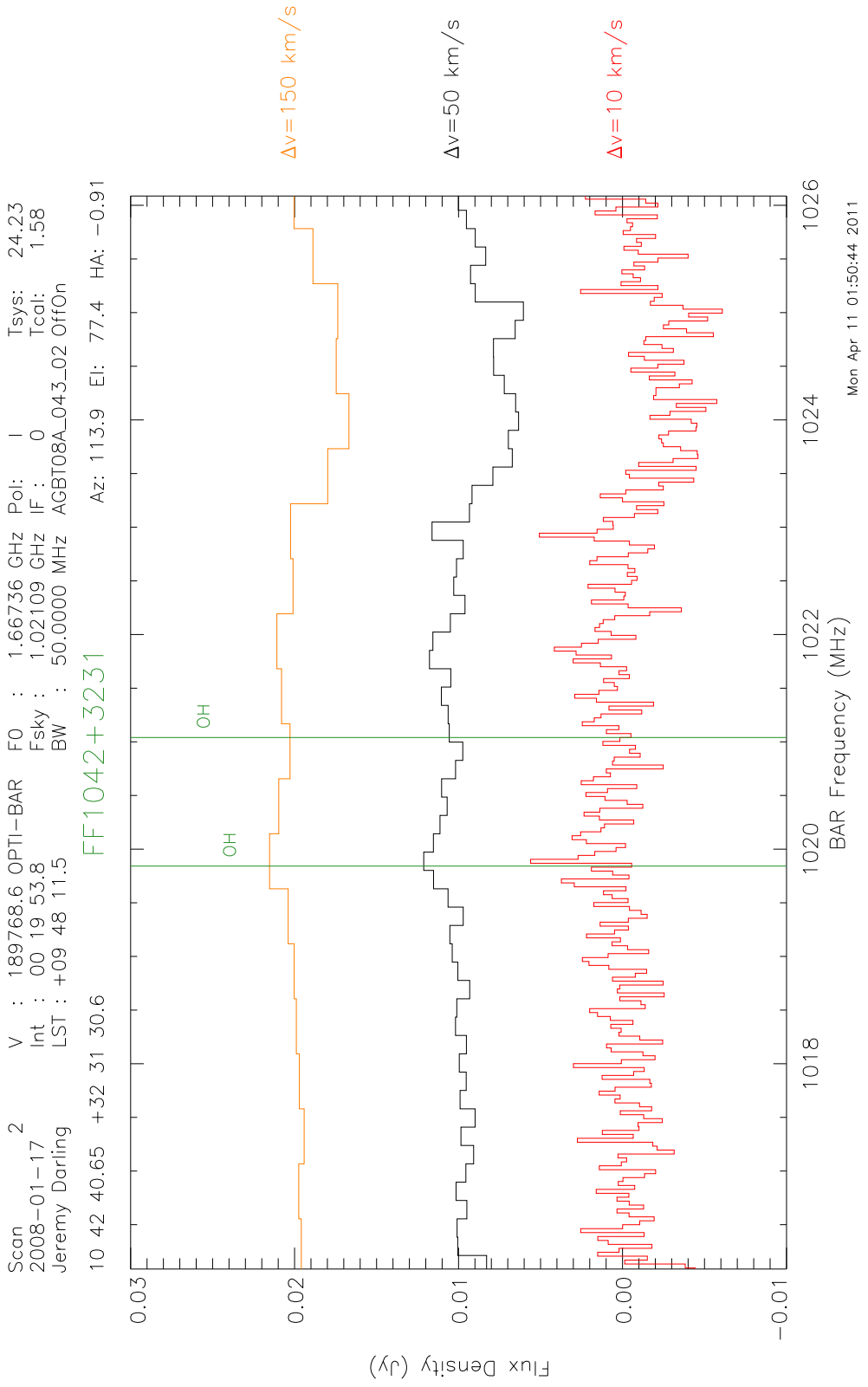

Figure C.39 18-cm spectrum of the galaxy FF 1042+3231.

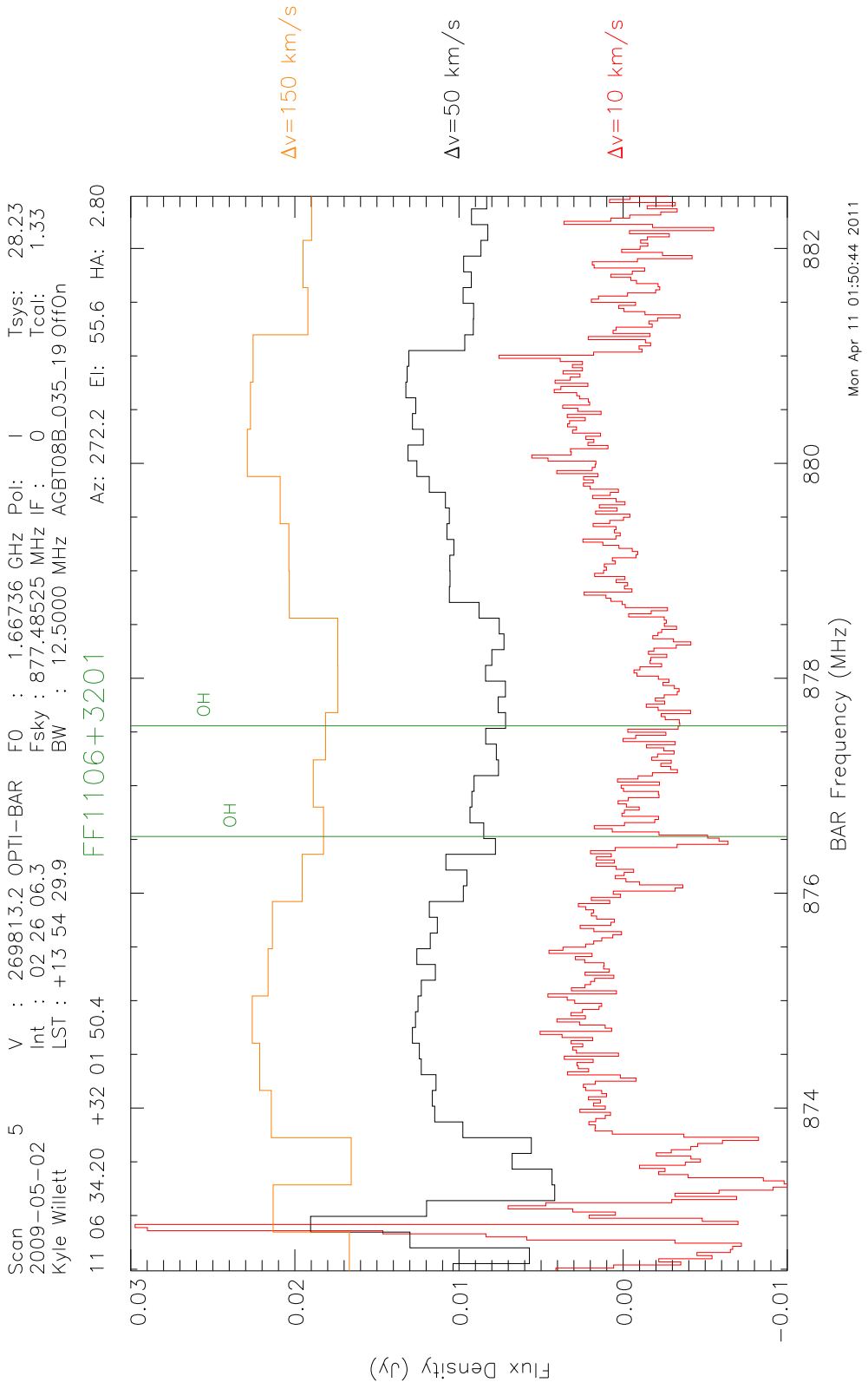

Figure C.40 18-cm spectrum of the galaxy FF 1106+3201.

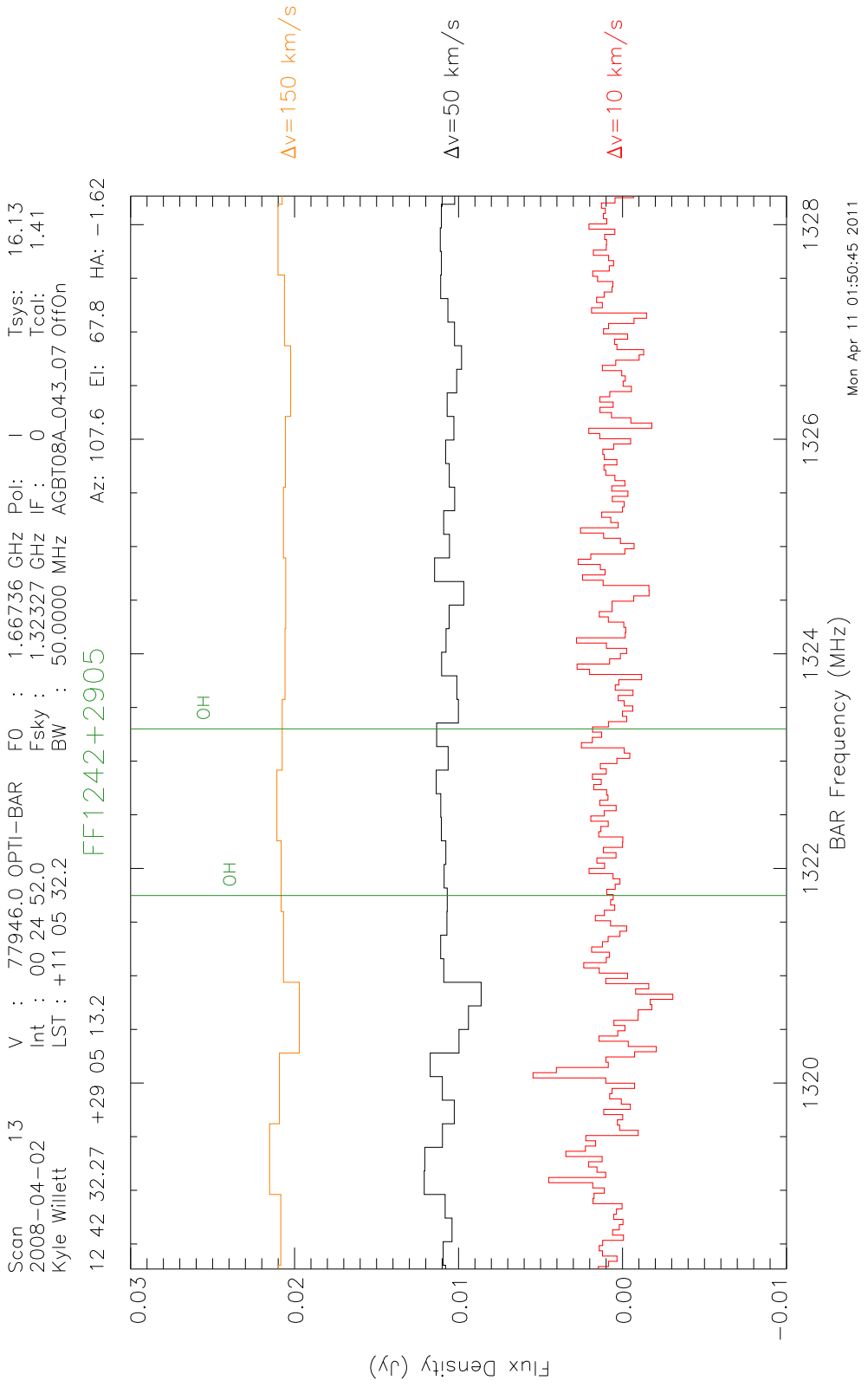

Figure C.41 18-cm spectrum of the galaxy FF 1242+2905.

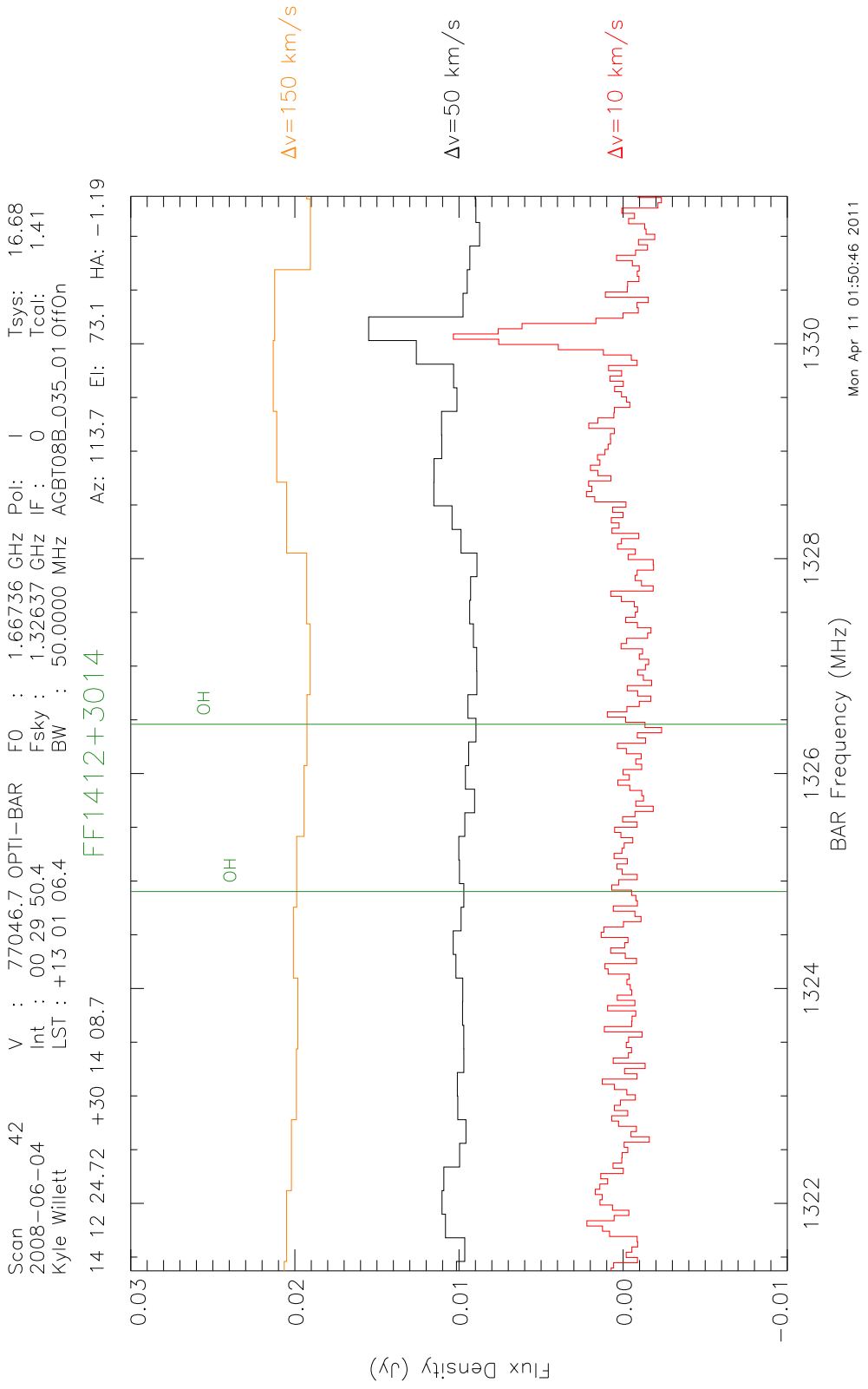

Figure C.42 18-cm spectrum of the galaxy FF 1412+3014.

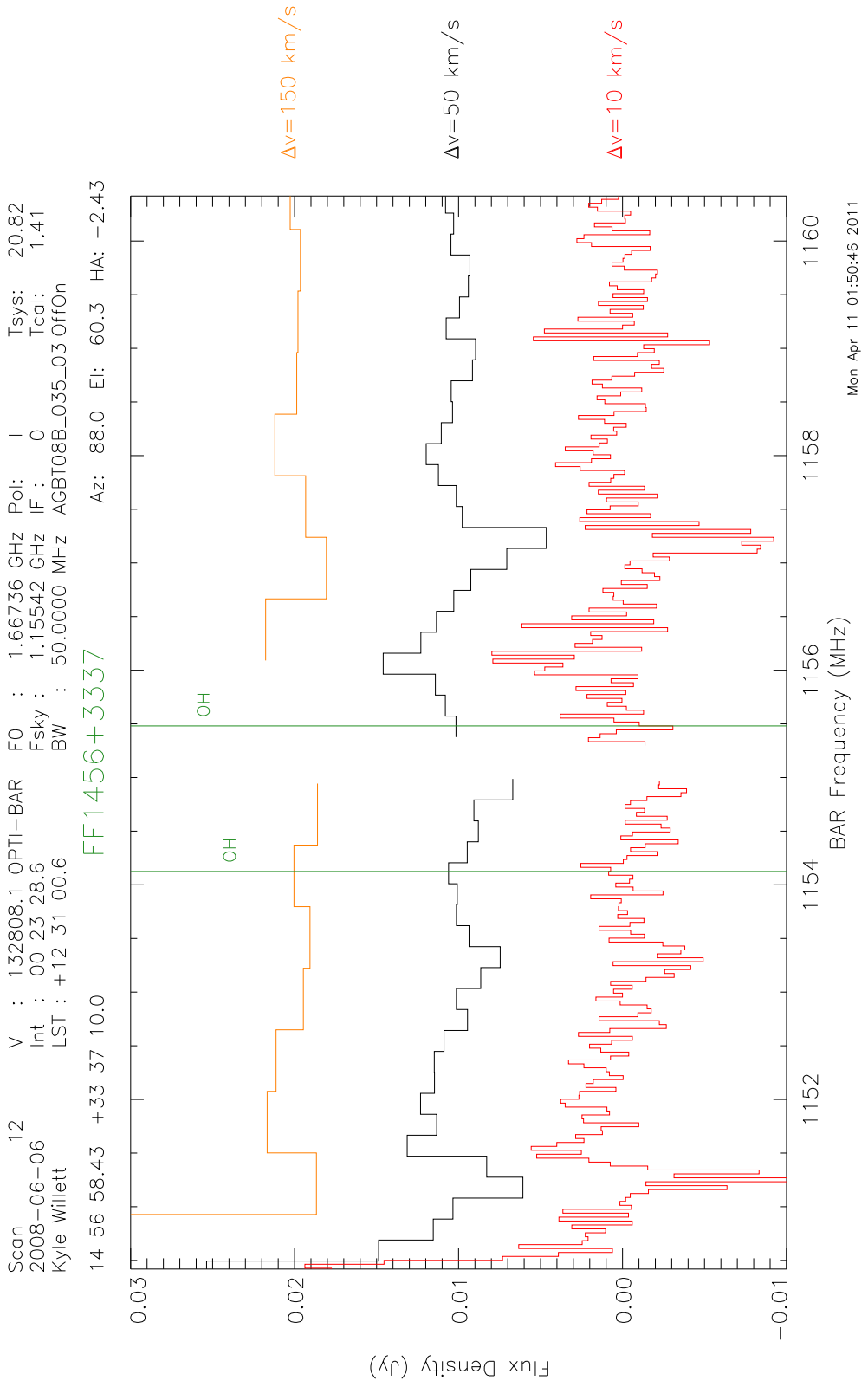

Figure C.43 18-cm spectrum of the galaxy FF 1456+3337.

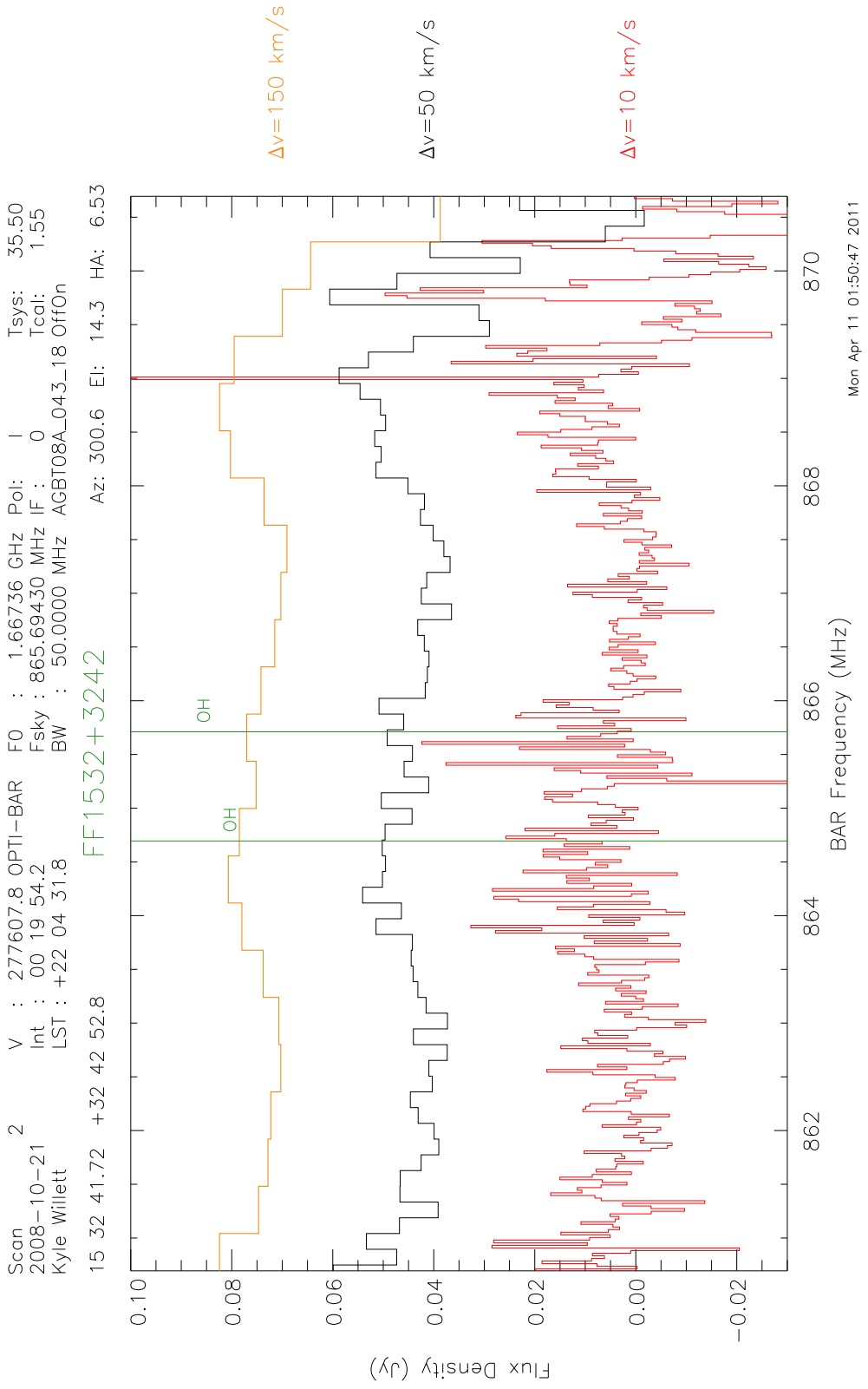

Figure C.44 18-cm spectrum of the galaxy FF 1532+3242.

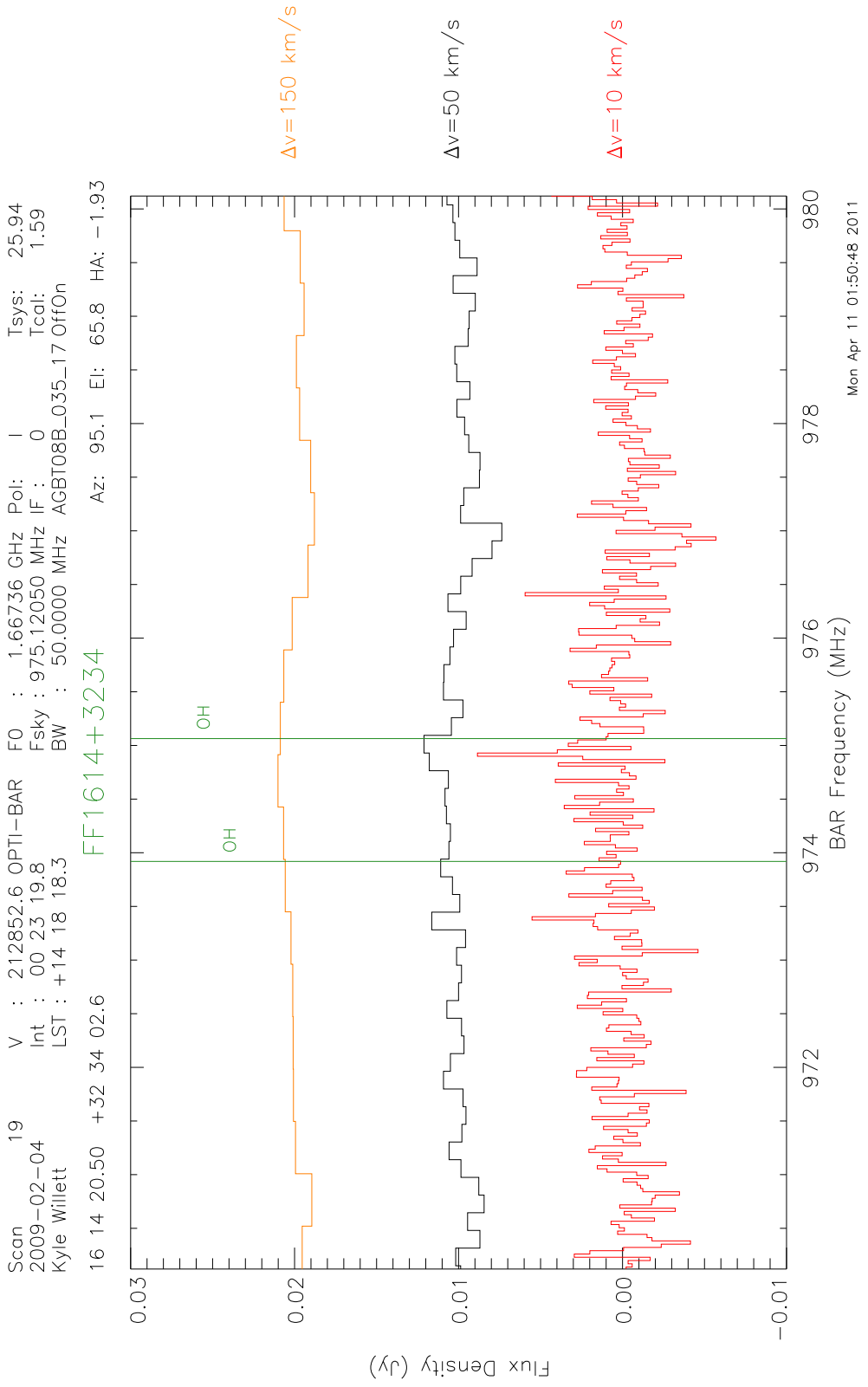

Figure C.45 18-cm spectrum of the galaxy FF 1614+3234.

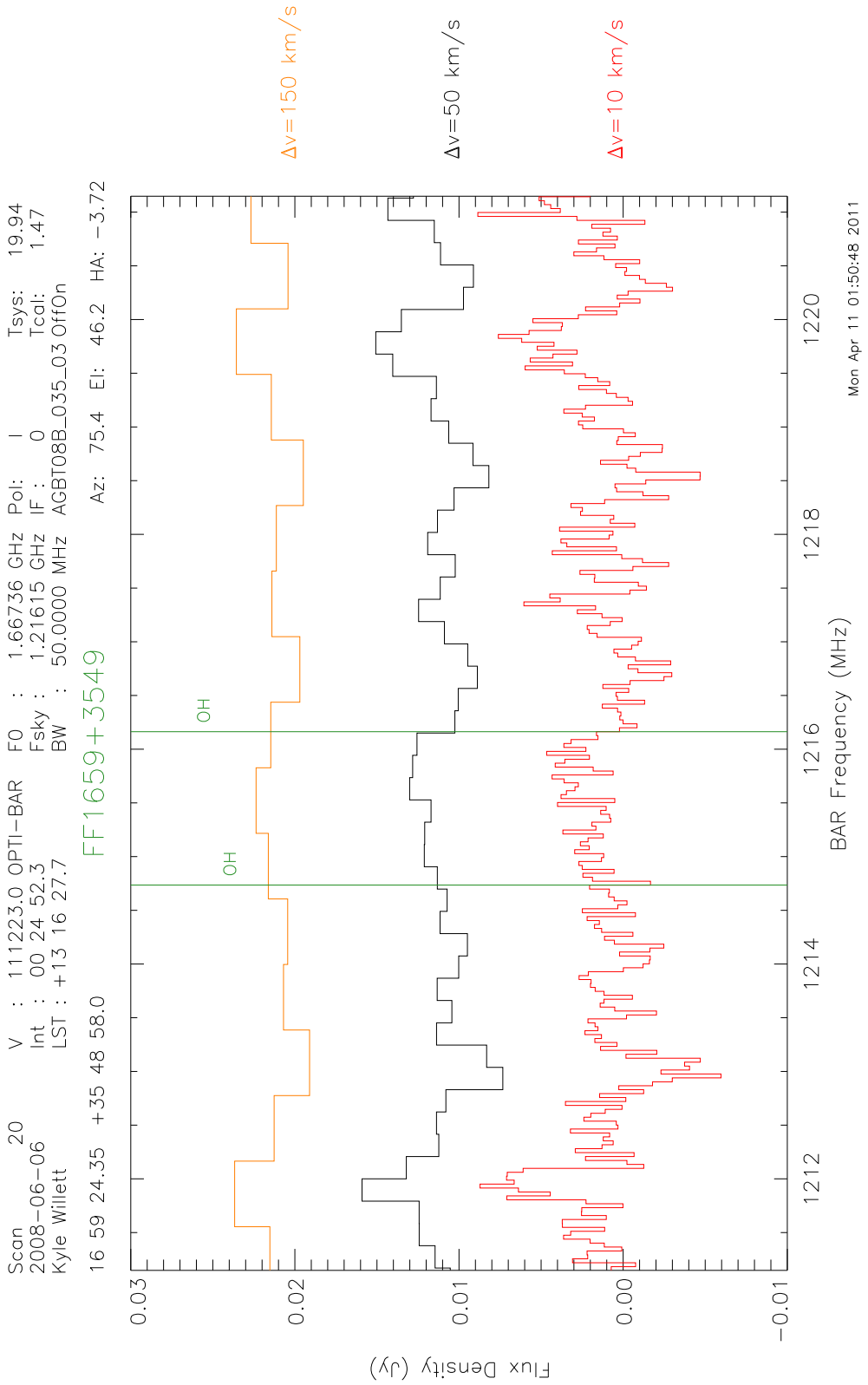

Figure C.46 18-cm spectrum of the galaxy FF 1659+3549.

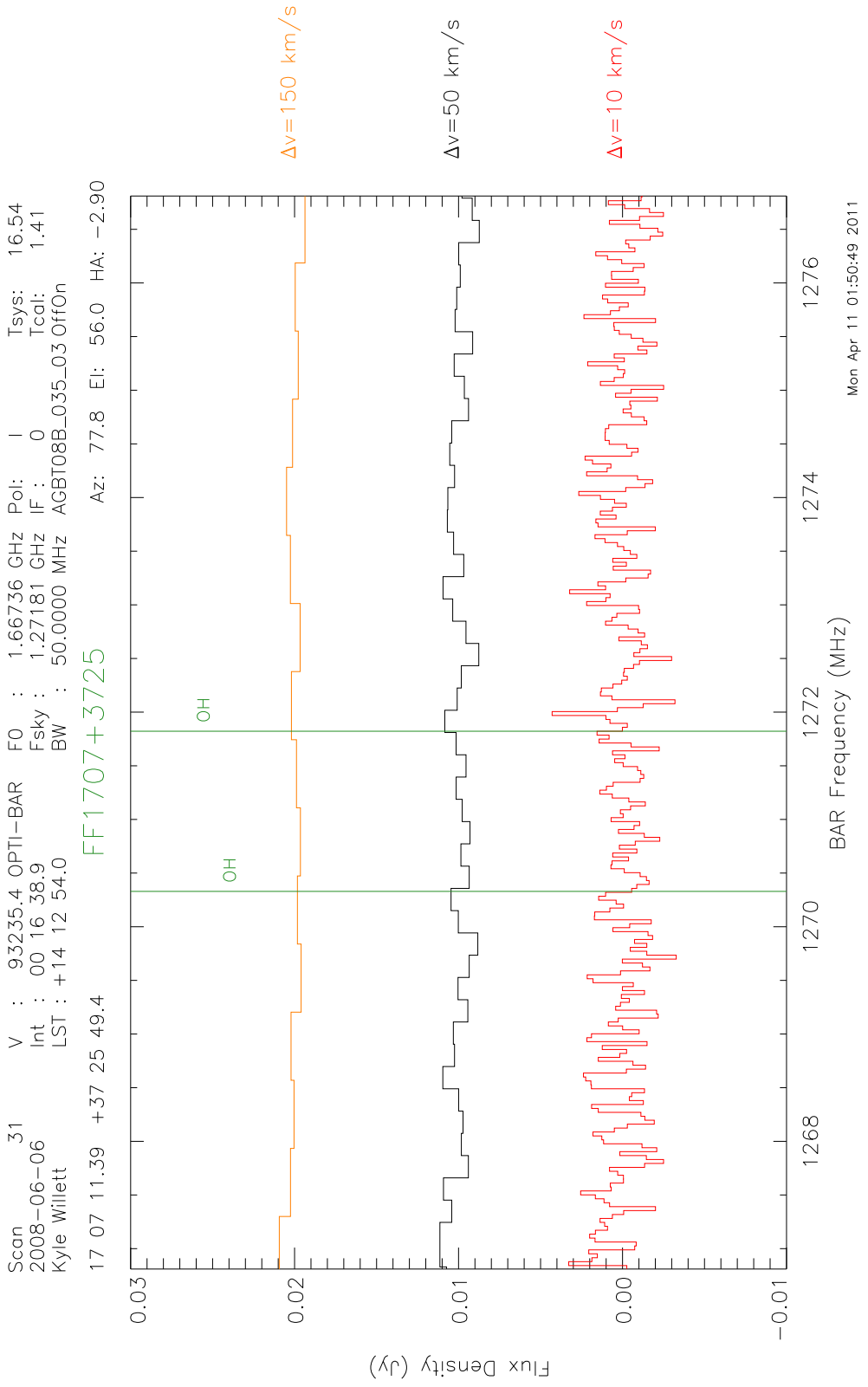

Figure C.47 18-cm spectrum of the galaxy FF 1707+3725.

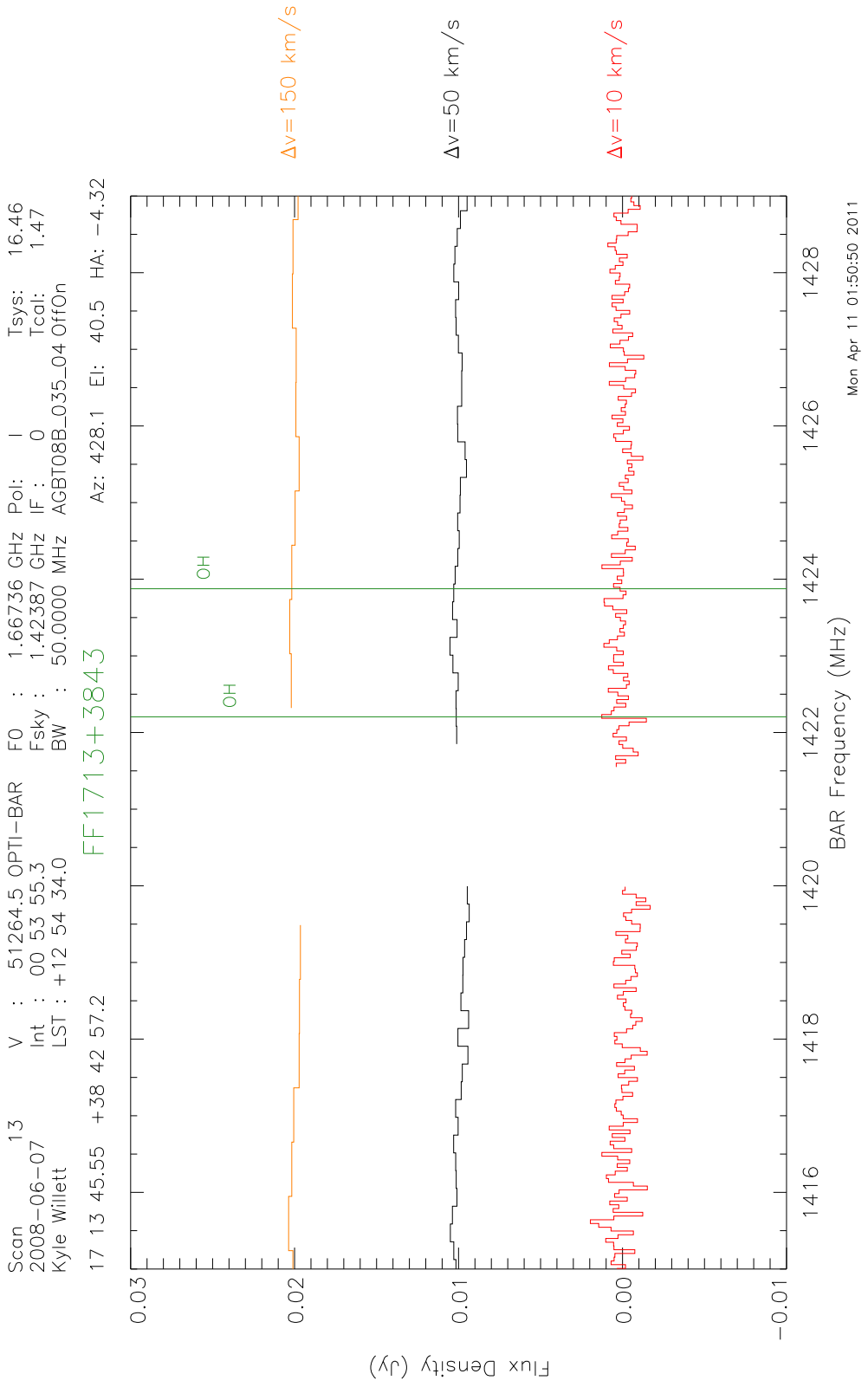

Figure C.48 18-cm spectrum of the galaxy FF 1713+3843.

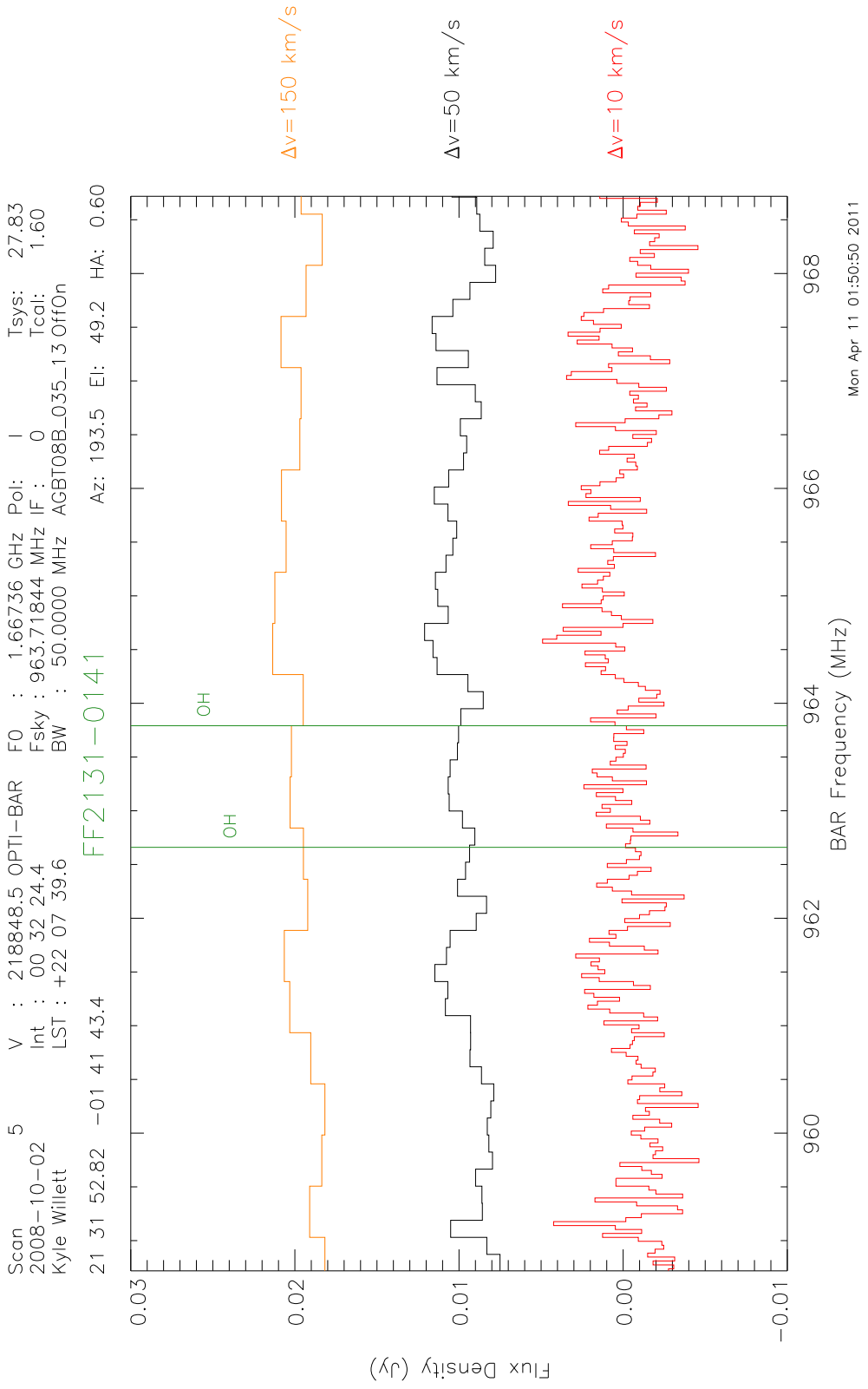

Figure C.49 18-cm spectrum of the galaxy FF 2131−0141.

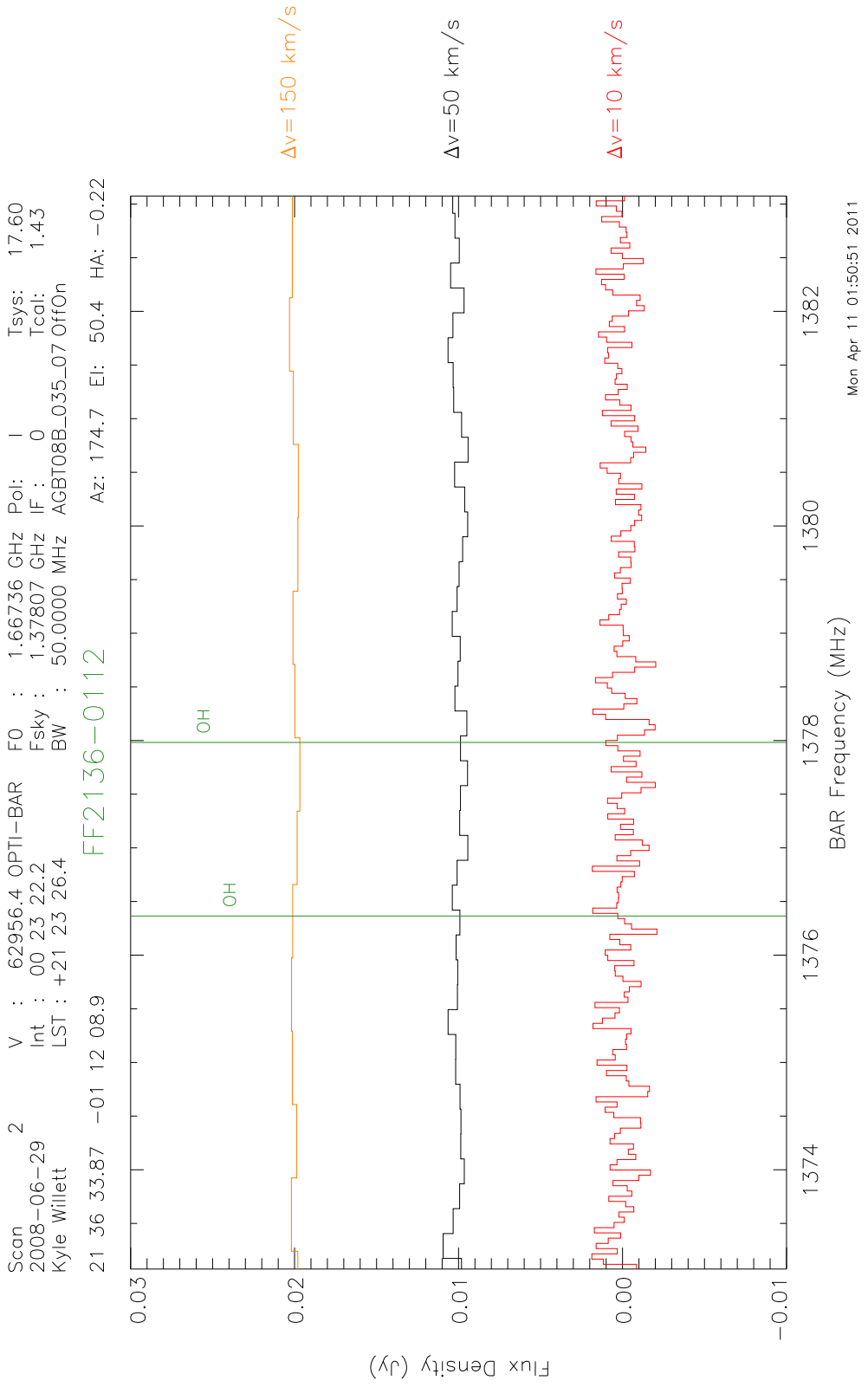

Figure C.50 18-cm spectrum of the galaxy FF 2136−0012.

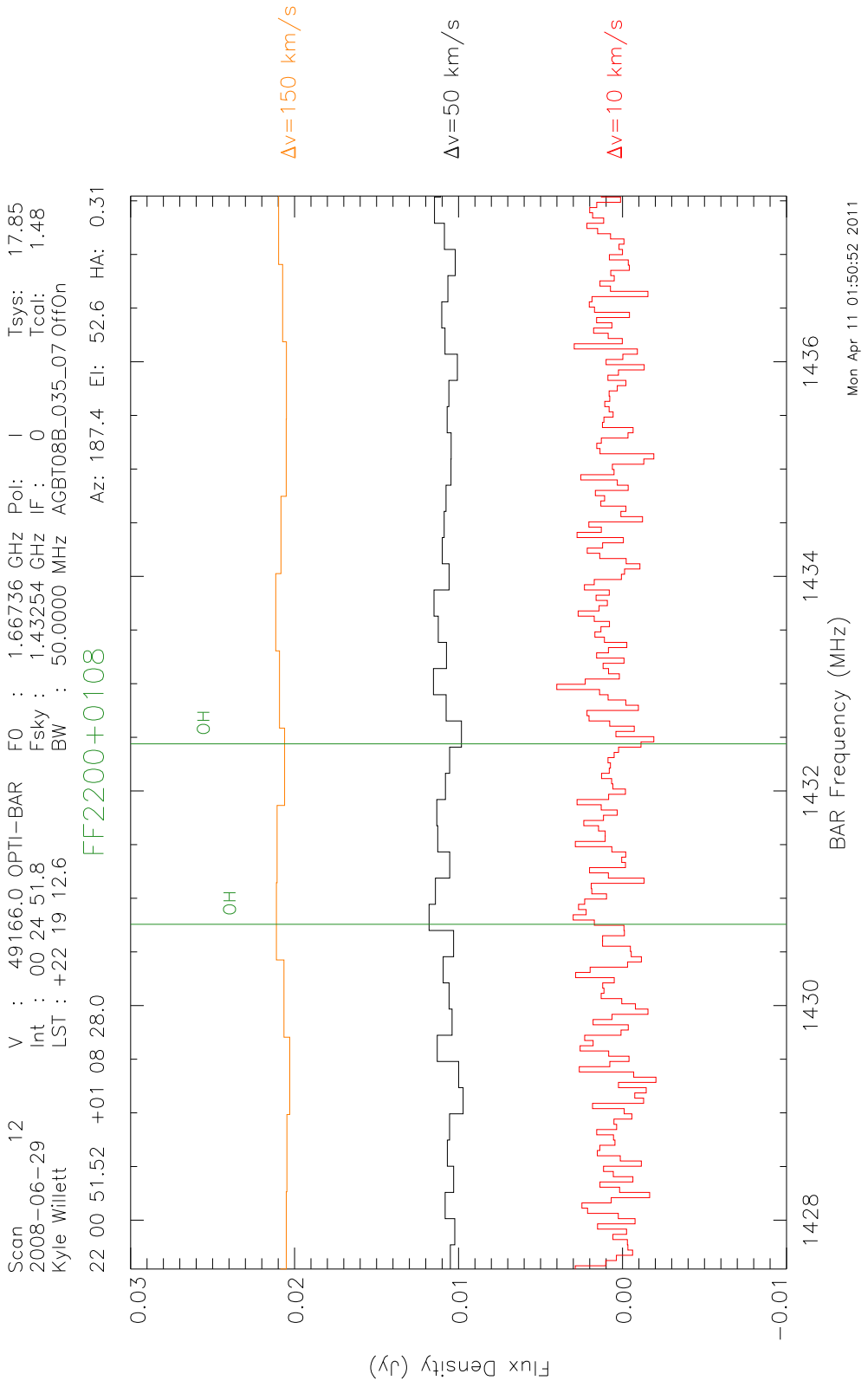

Figure C.51 18-cm spectrum of the galaxy FF 2200+0108.

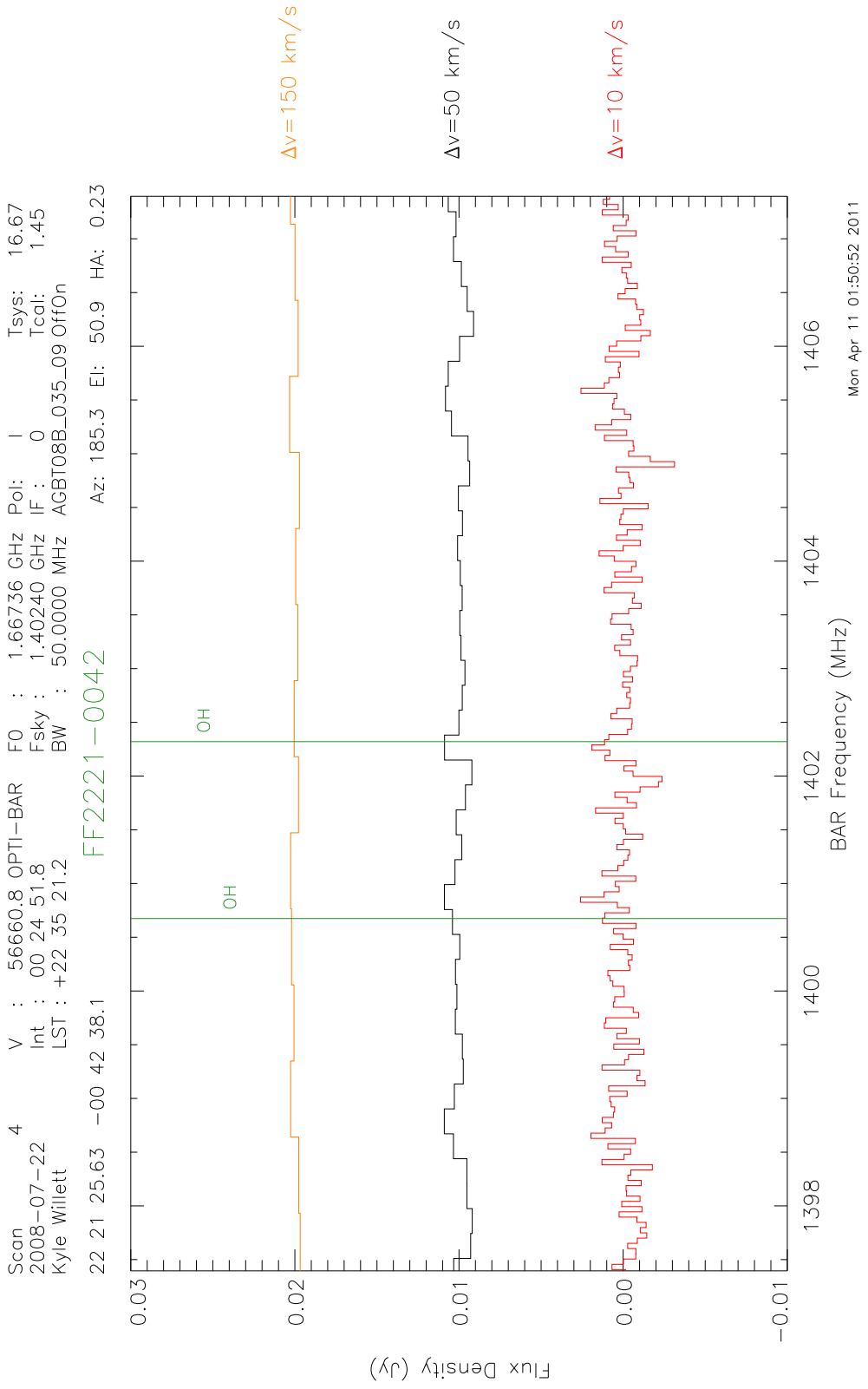

Figure C.52 18-cm spectrum of the galaxy FF 2221−0042.

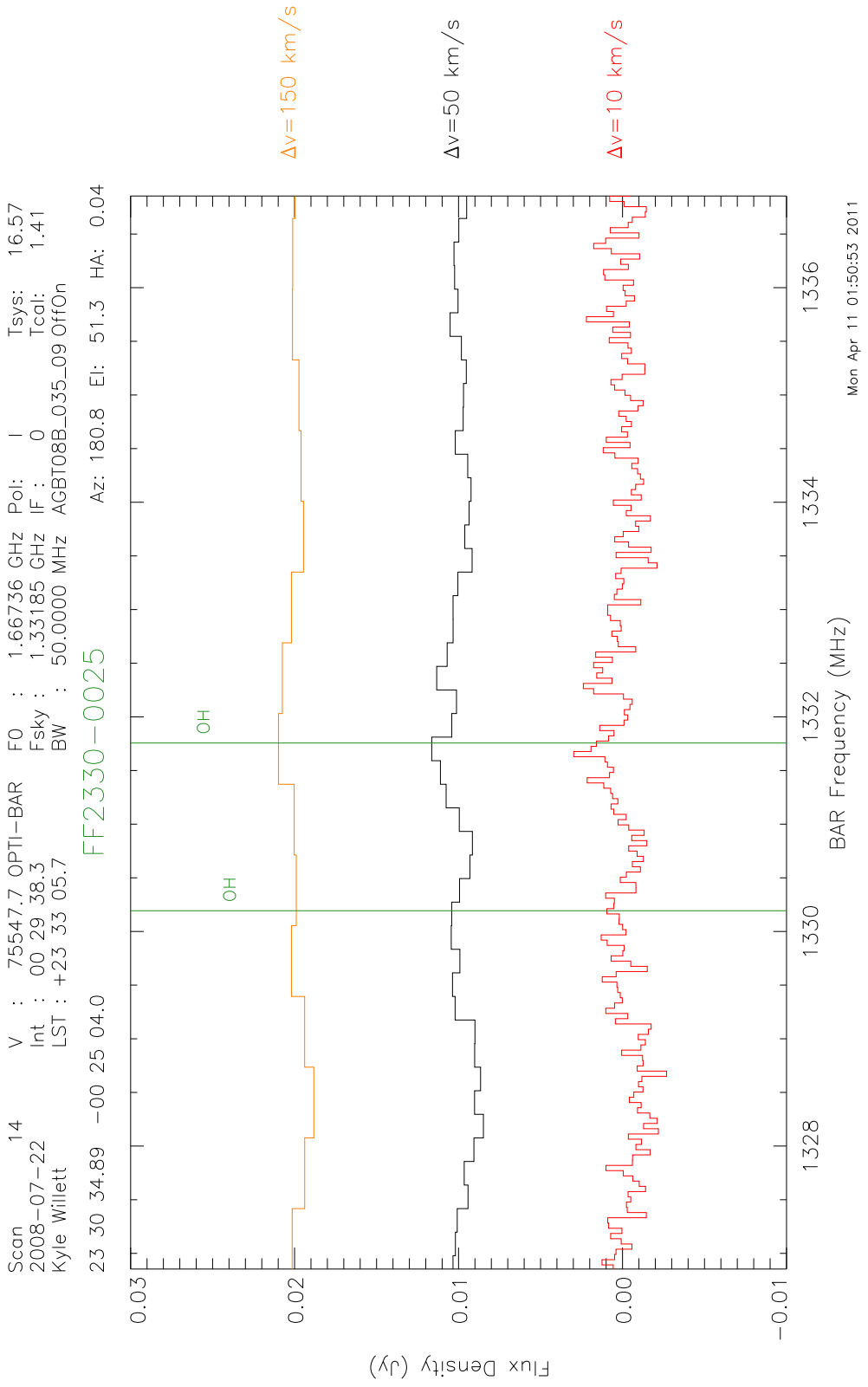

Figure C.53 18-cm spectrum of the galaxy FF 2330−0025.

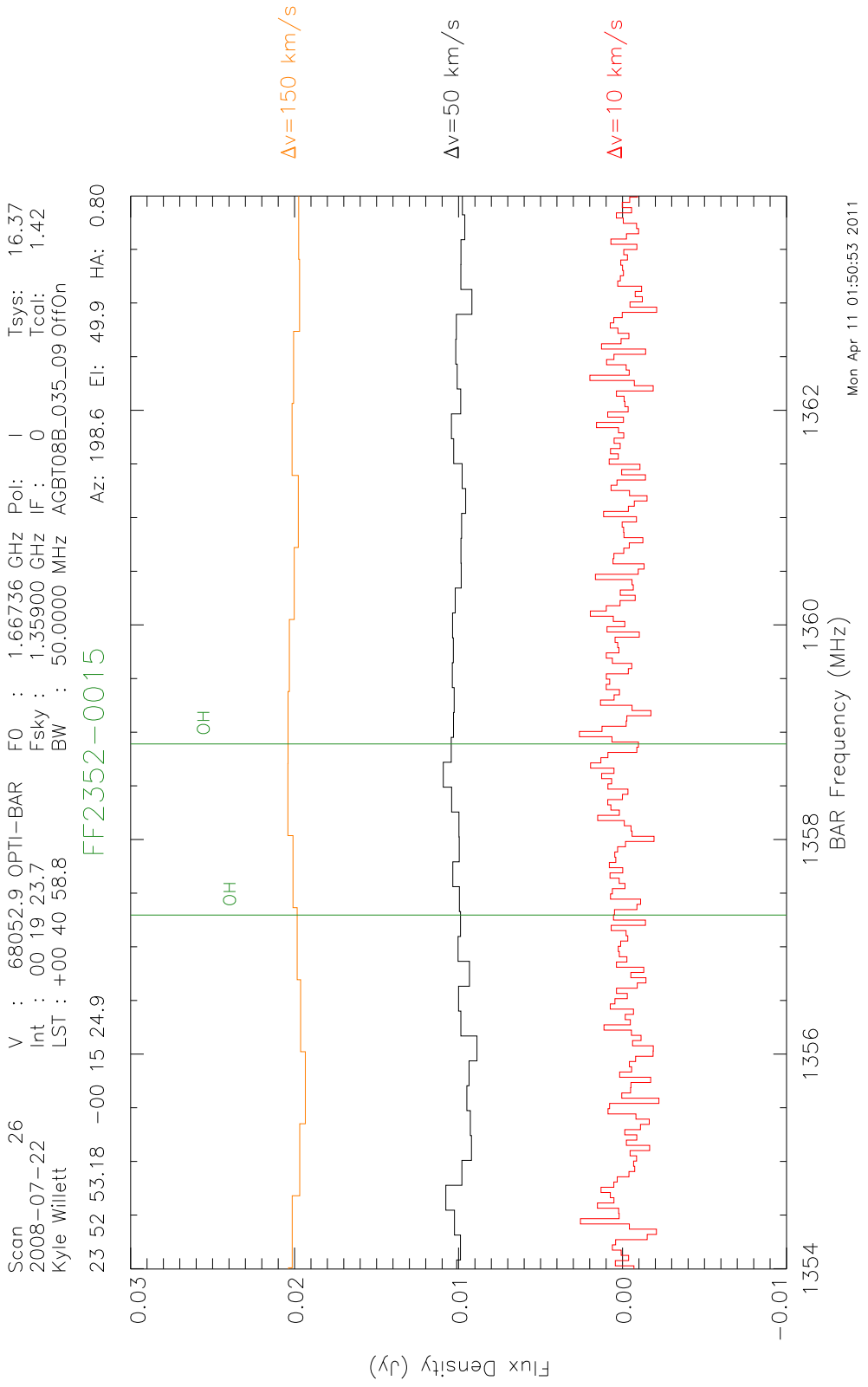

Figure C.54 18-cm spectrum of the galaxy FF 2352−0015.

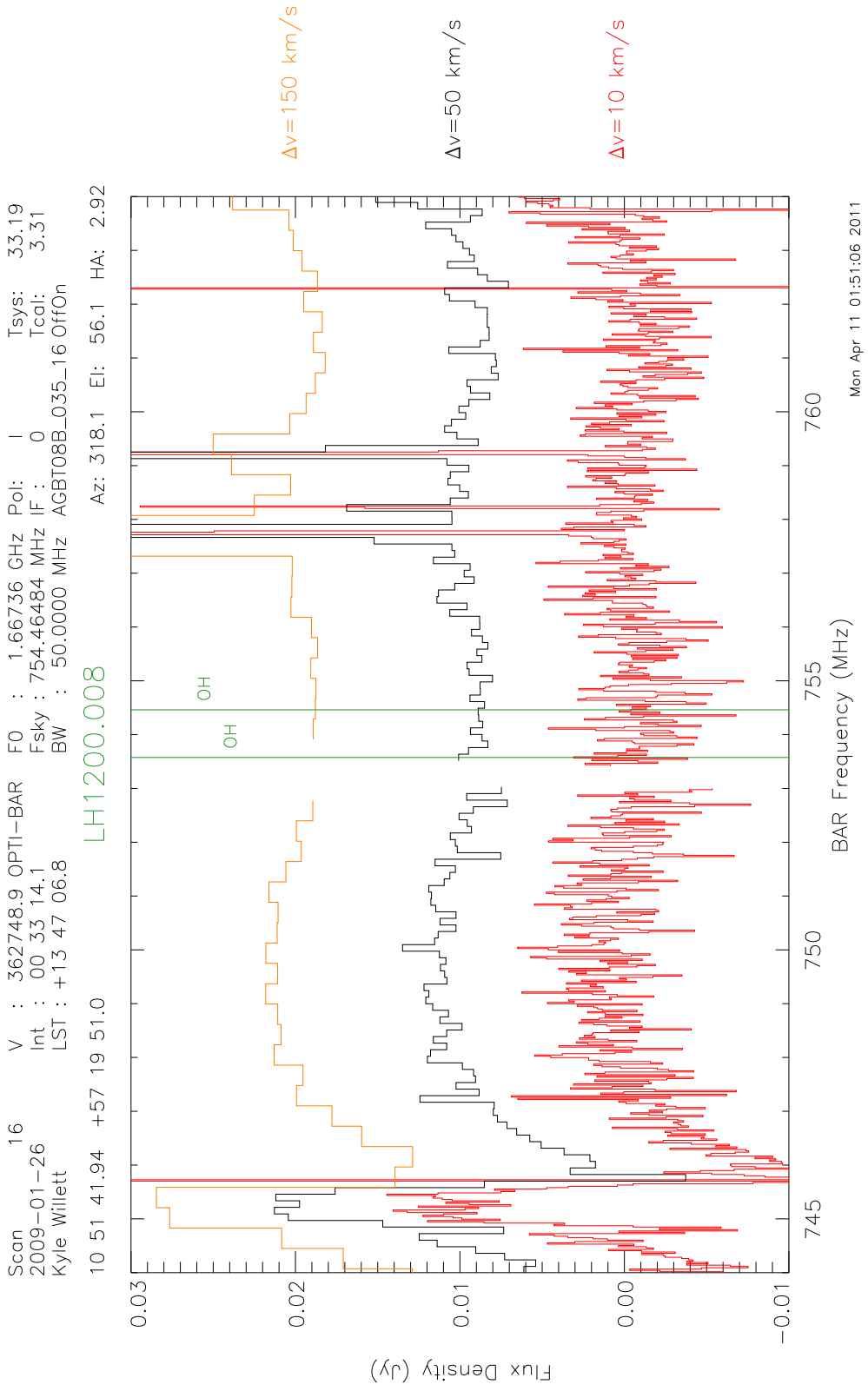

Figure C.55 18-cm spectrum of the galaxy LH1200.008.

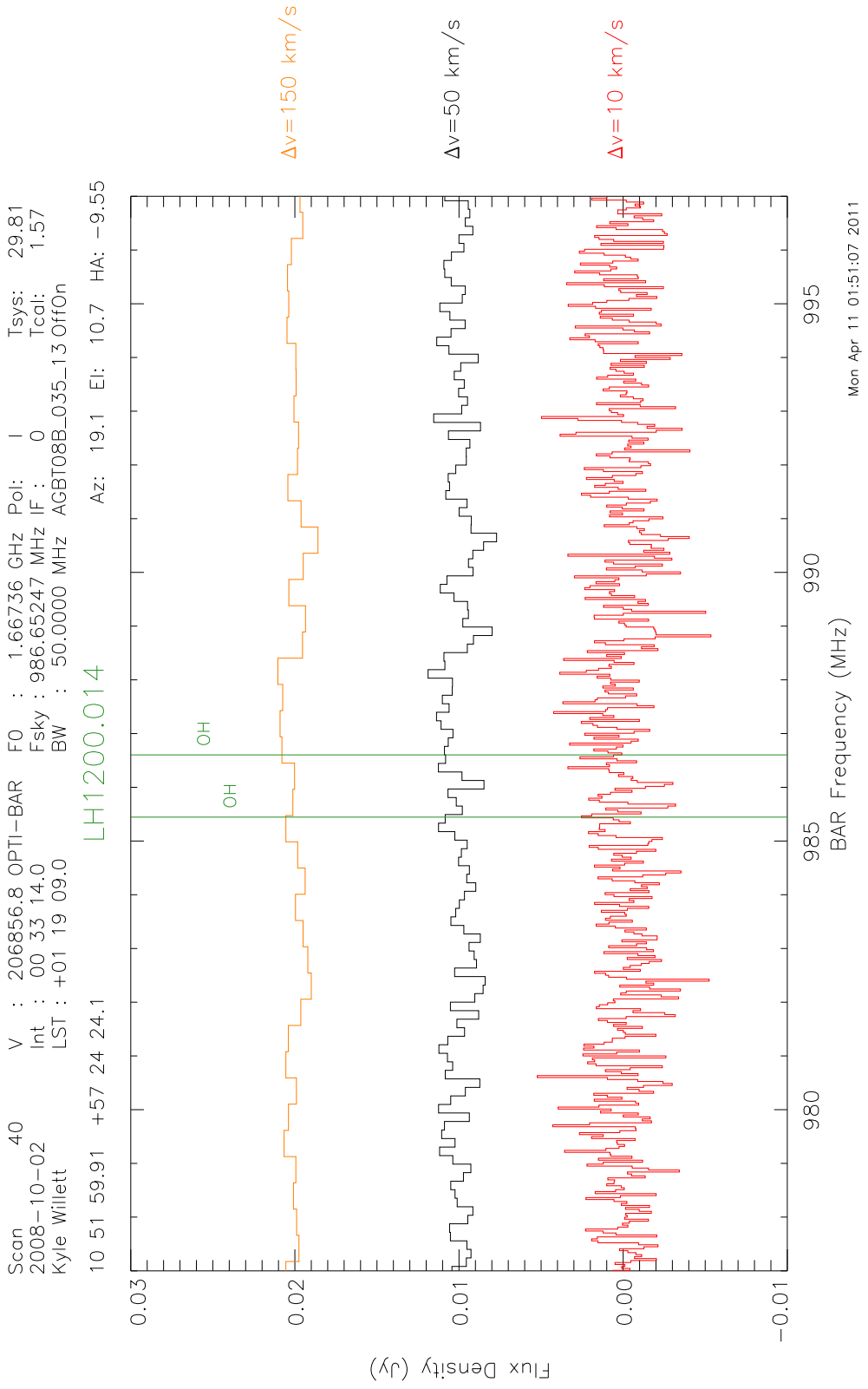

Figure C.56 18-cm spectrum of the galaxy LH1200.014.

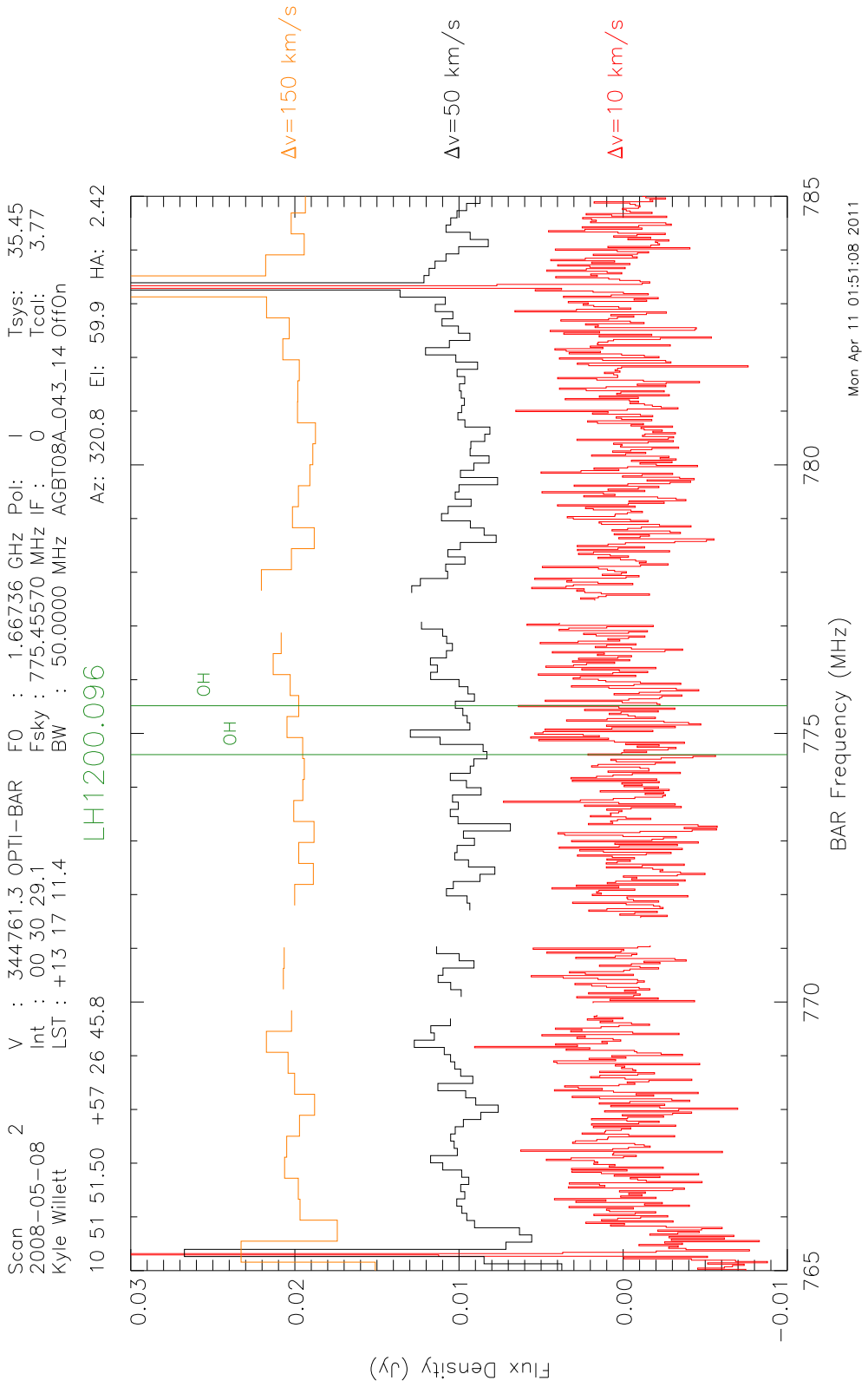

Figure C.57 18-cm spectrum of the galaxy LH1200.096.

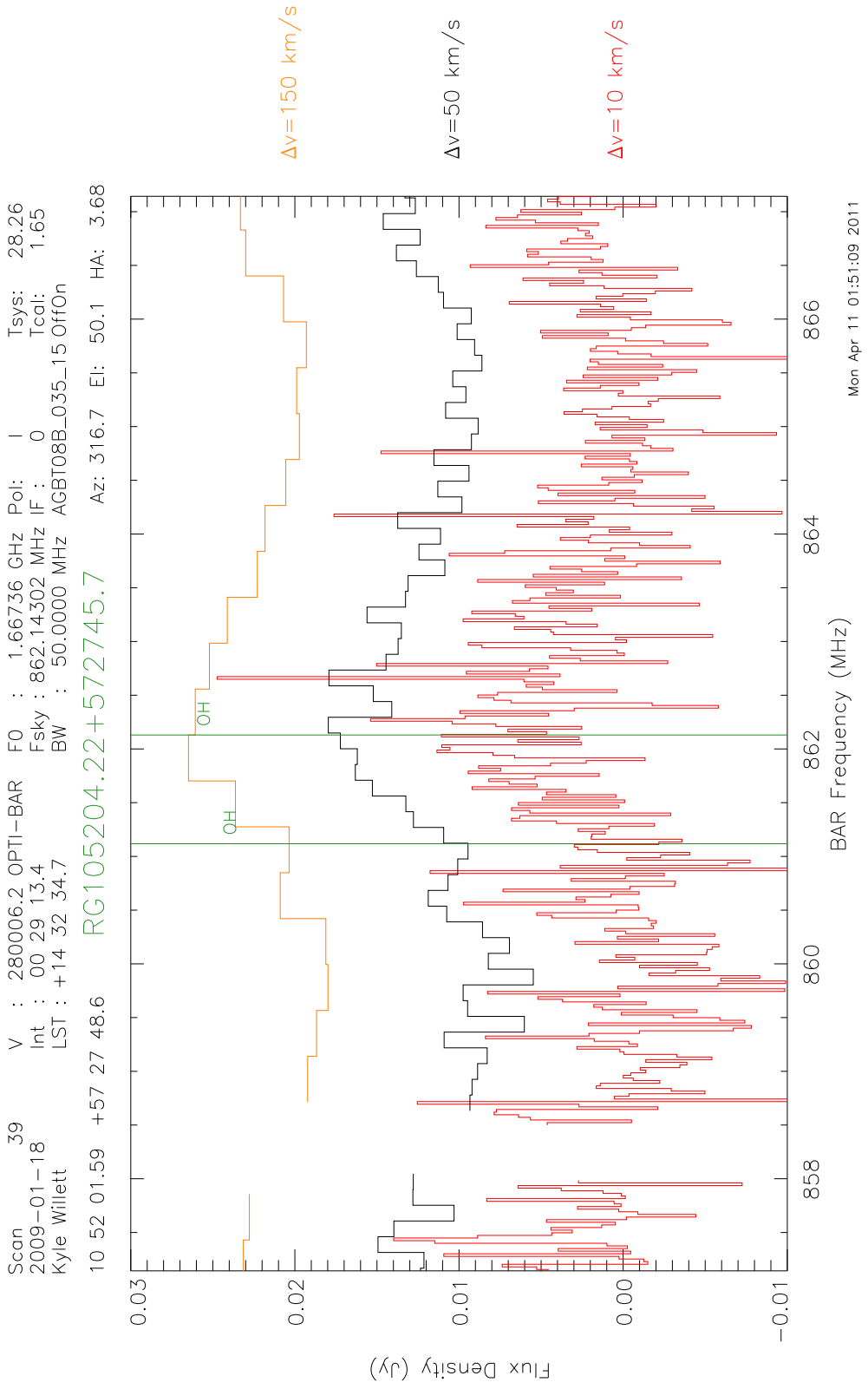

Figure C.58 18-cm spectrum of the galaxy RG 105204.22+572715.7.

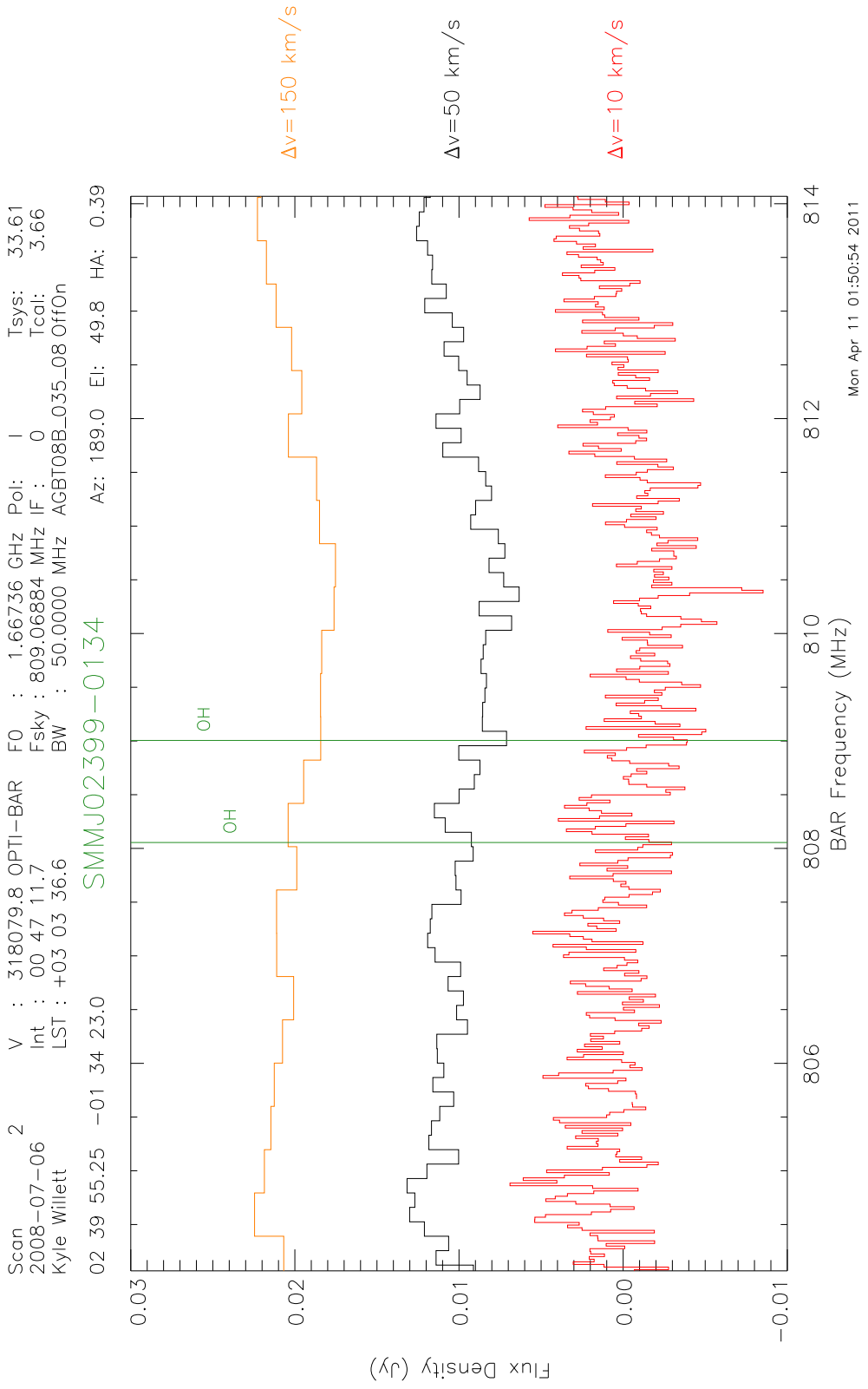

Figure C.59 18-cm spectrum of the galaxy SMM J02399-0134.

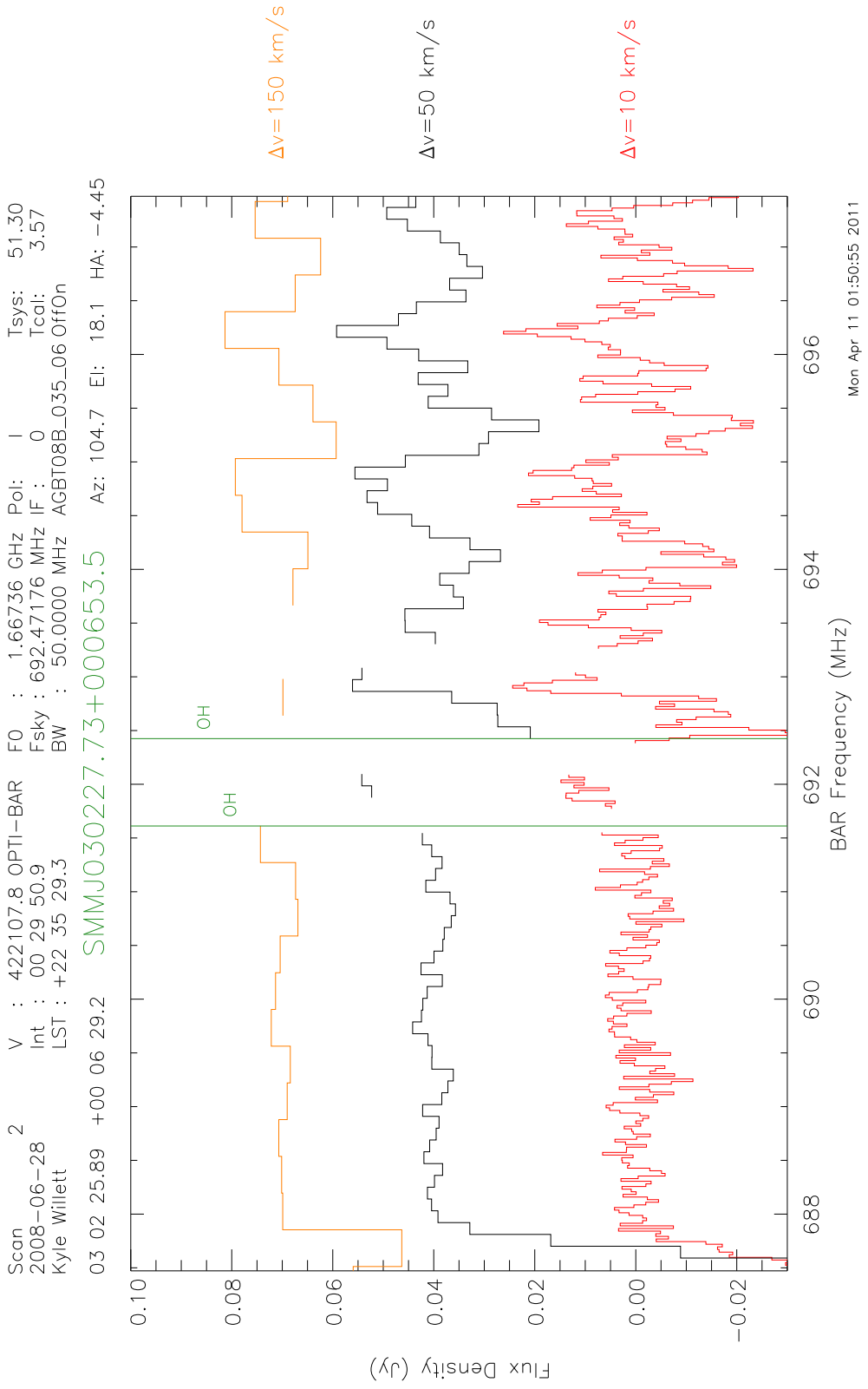

Figure C.60 18-cm spectrum of the galaxy SMM J030227.73+000653.5.

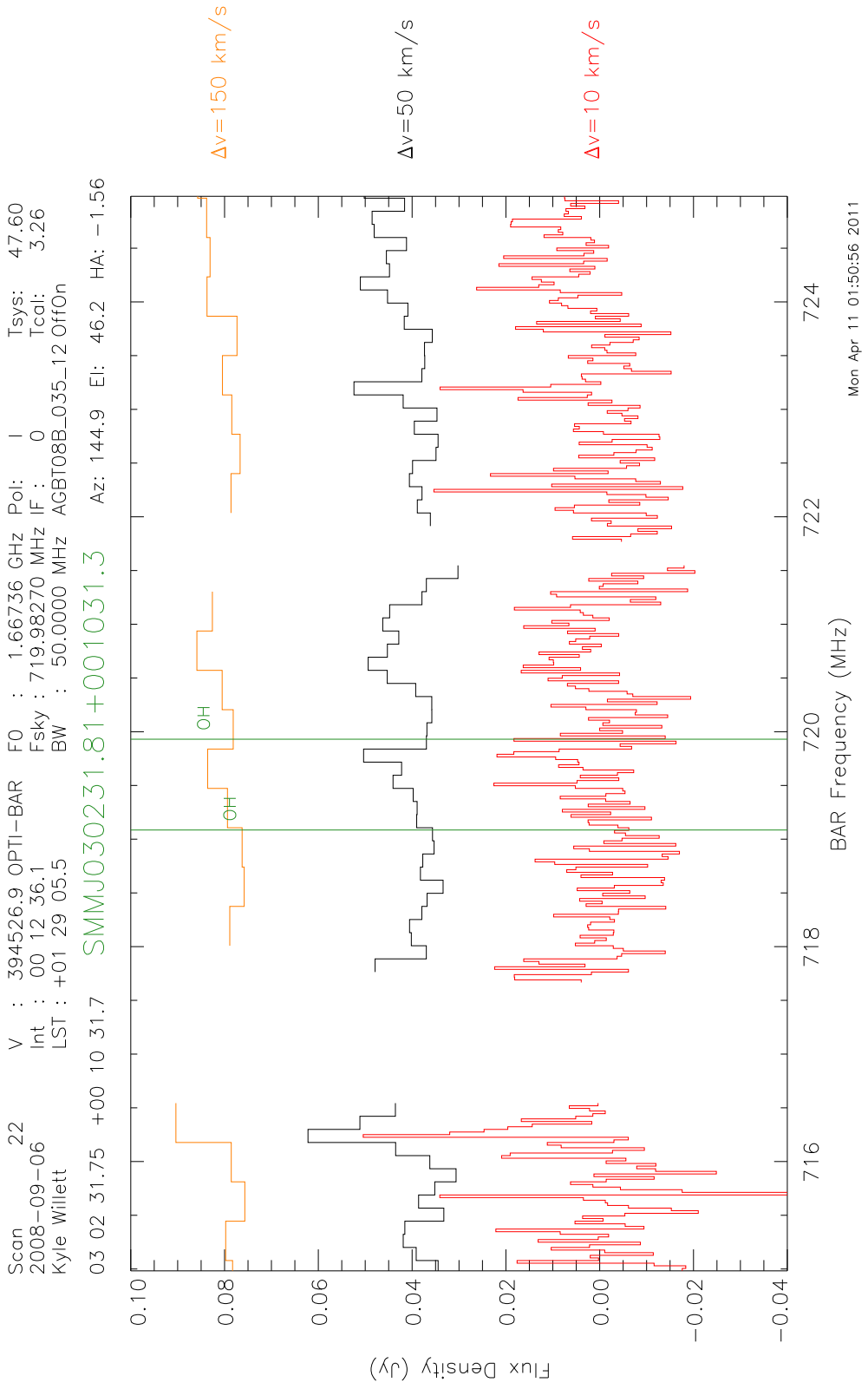

Figure C.61 18-cm spectrum of the galaxy SMM J030231.81+001031.3.

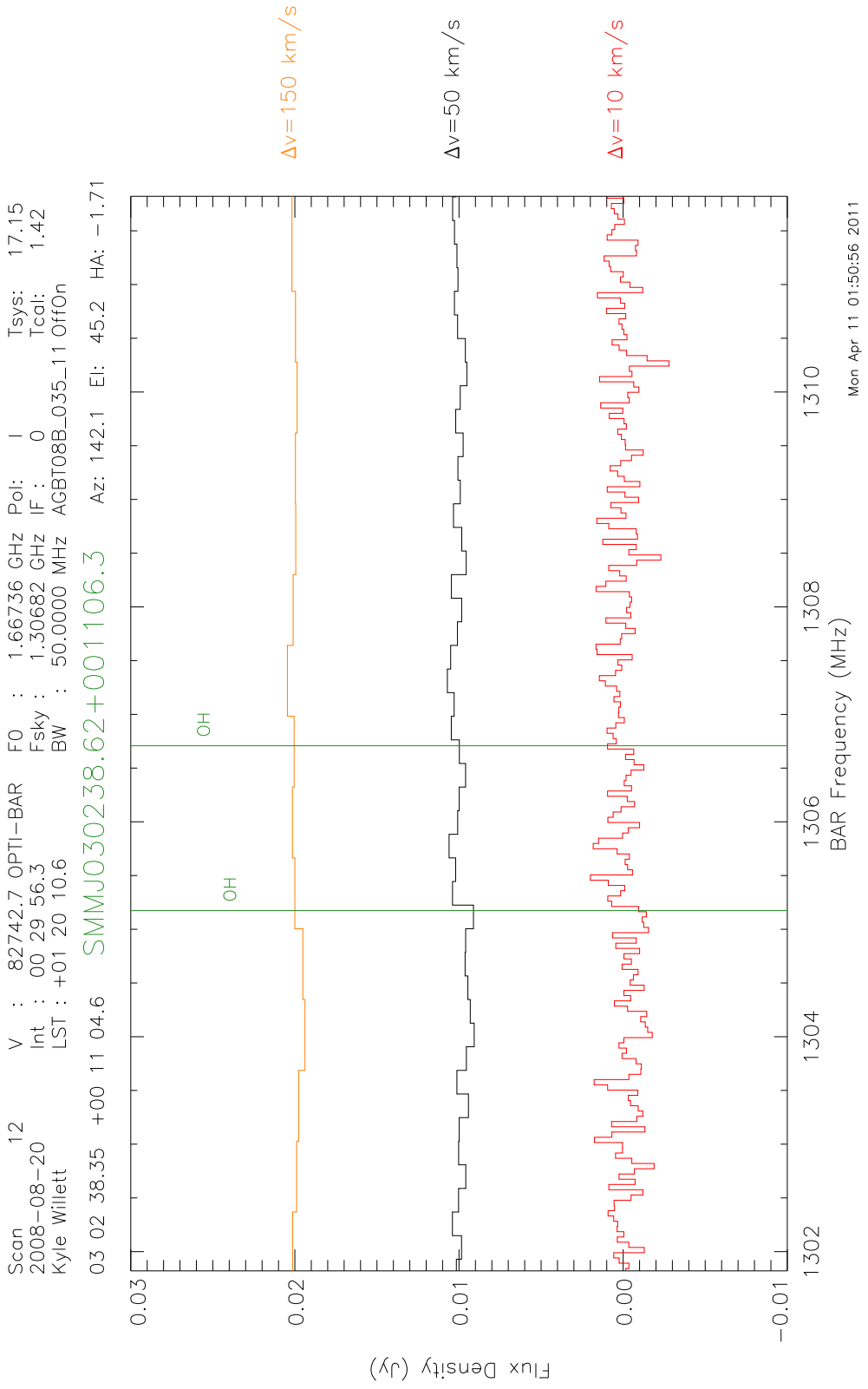

Figure C.62 18-cm spectrum of the galaxy SMM J030238.62+001106.3.

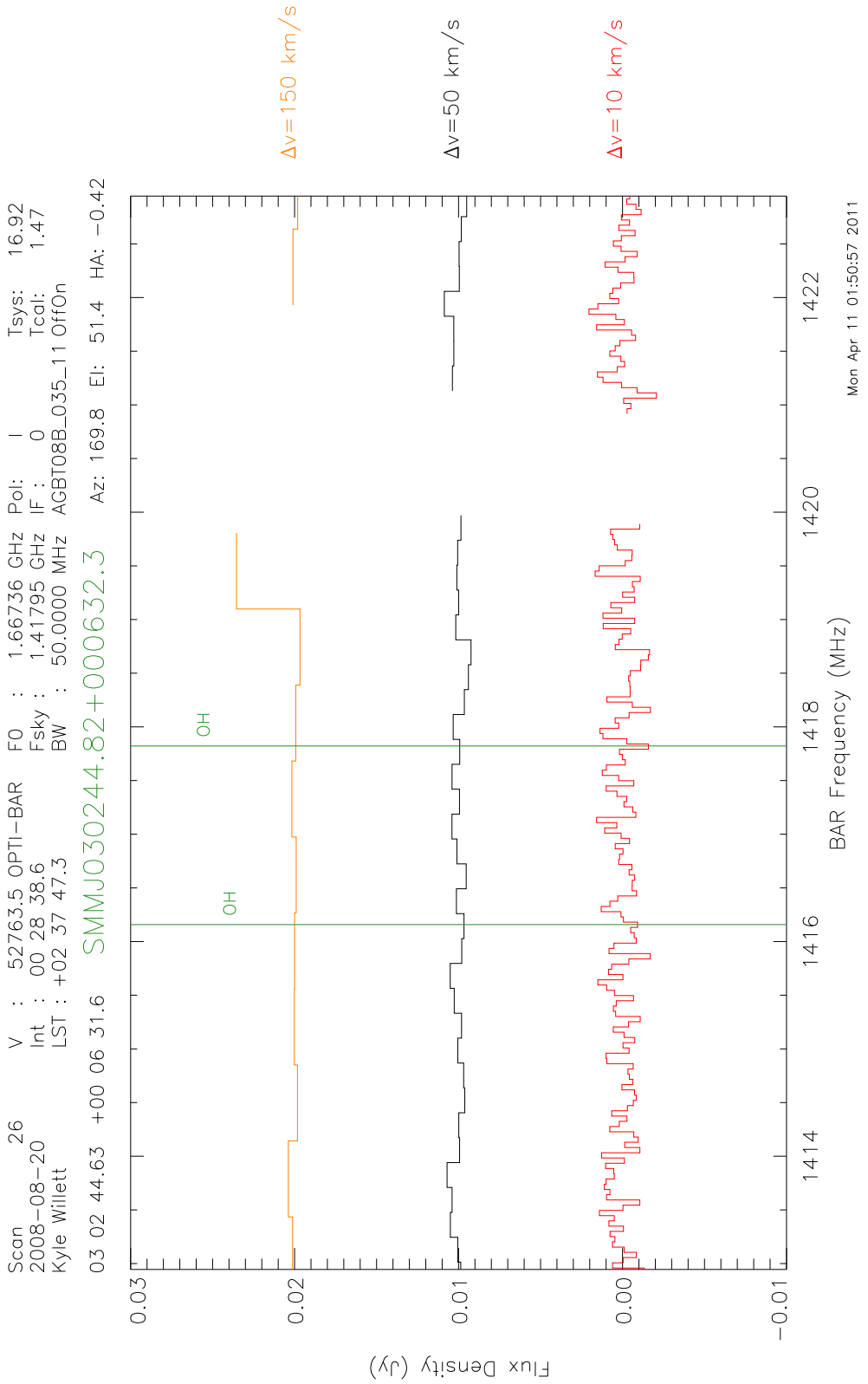

Figure C.63 18-cm spectrum of the galaxy SMM J030244.82+000632.3.

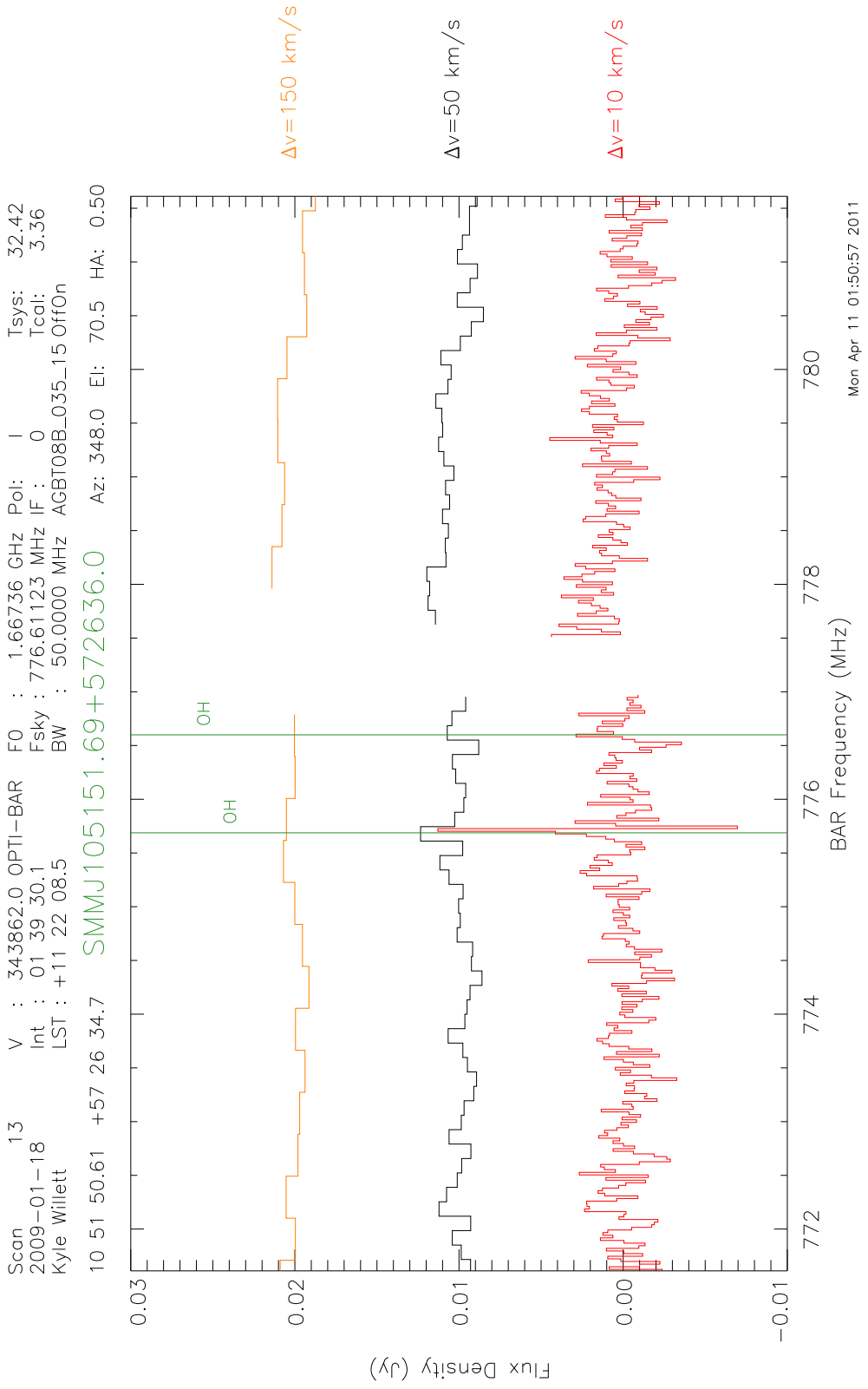

Figure C.64 18-cm spectrum of the galaxy SMM J105151.69+575636.0.

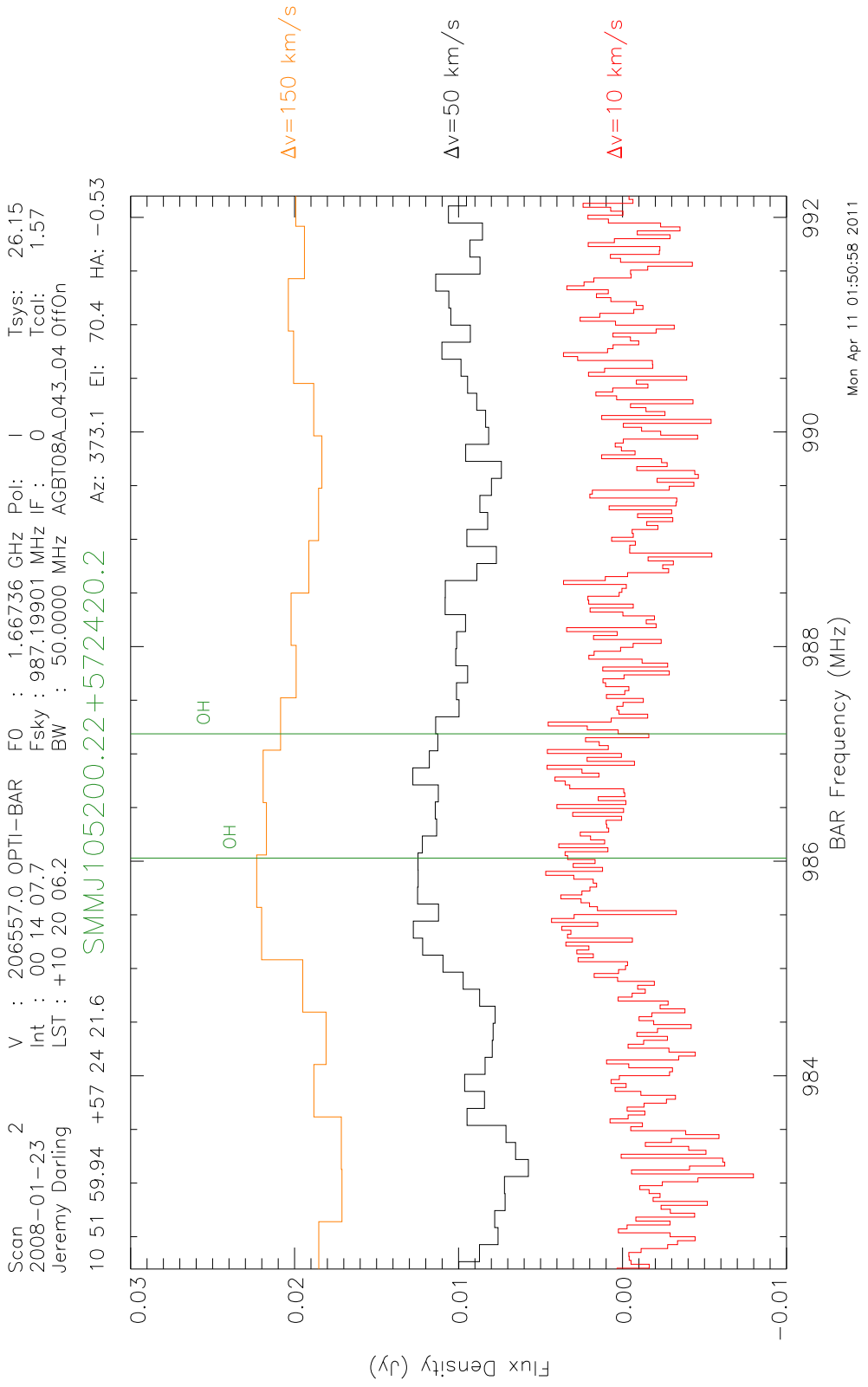

Figure C.65 18-cm spectrum of the galaxy SMM J105200.22+572420.2.

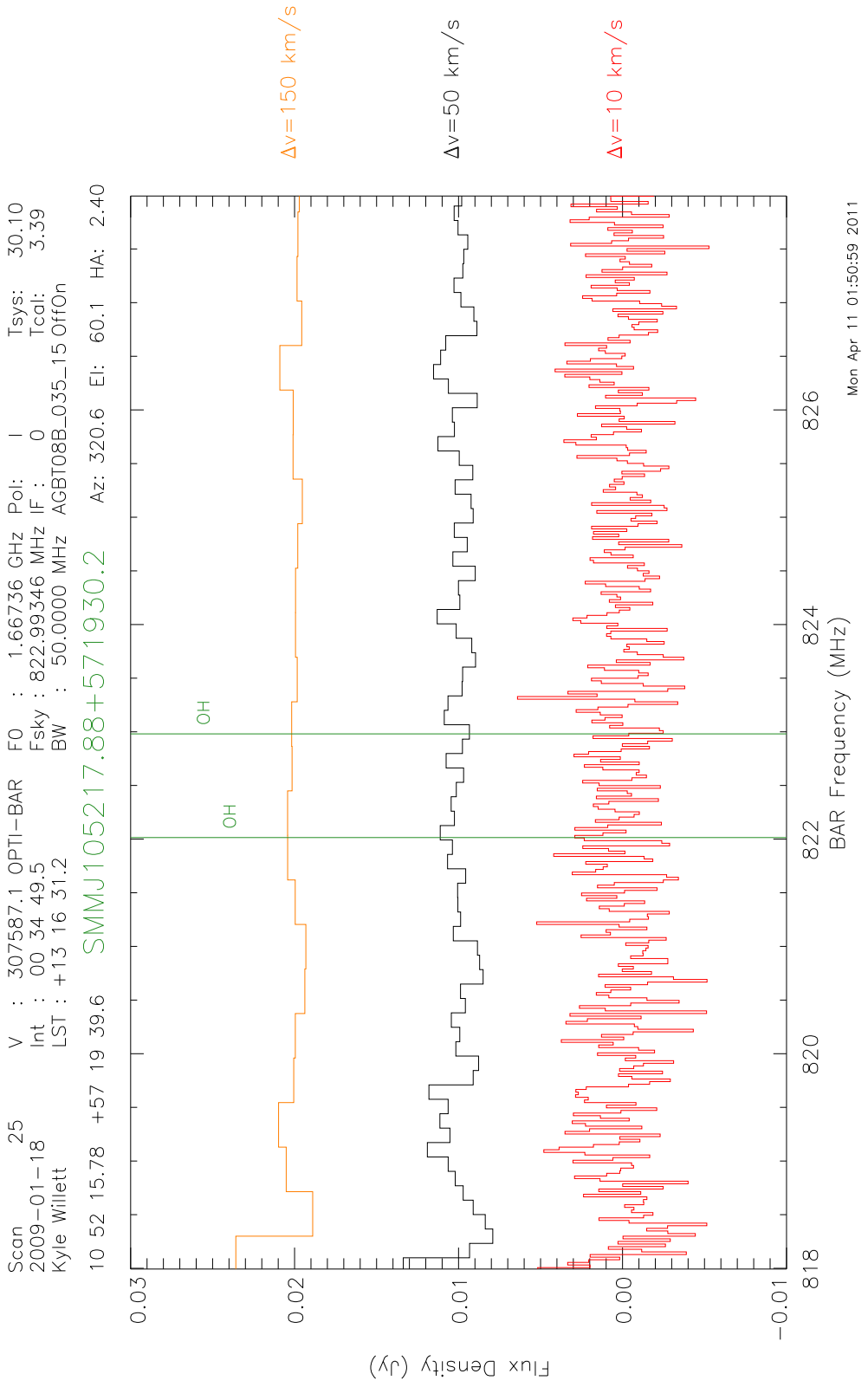

Figure C.66 18-cm spectrum of the galaxy SMM J105217.88+571930.2.

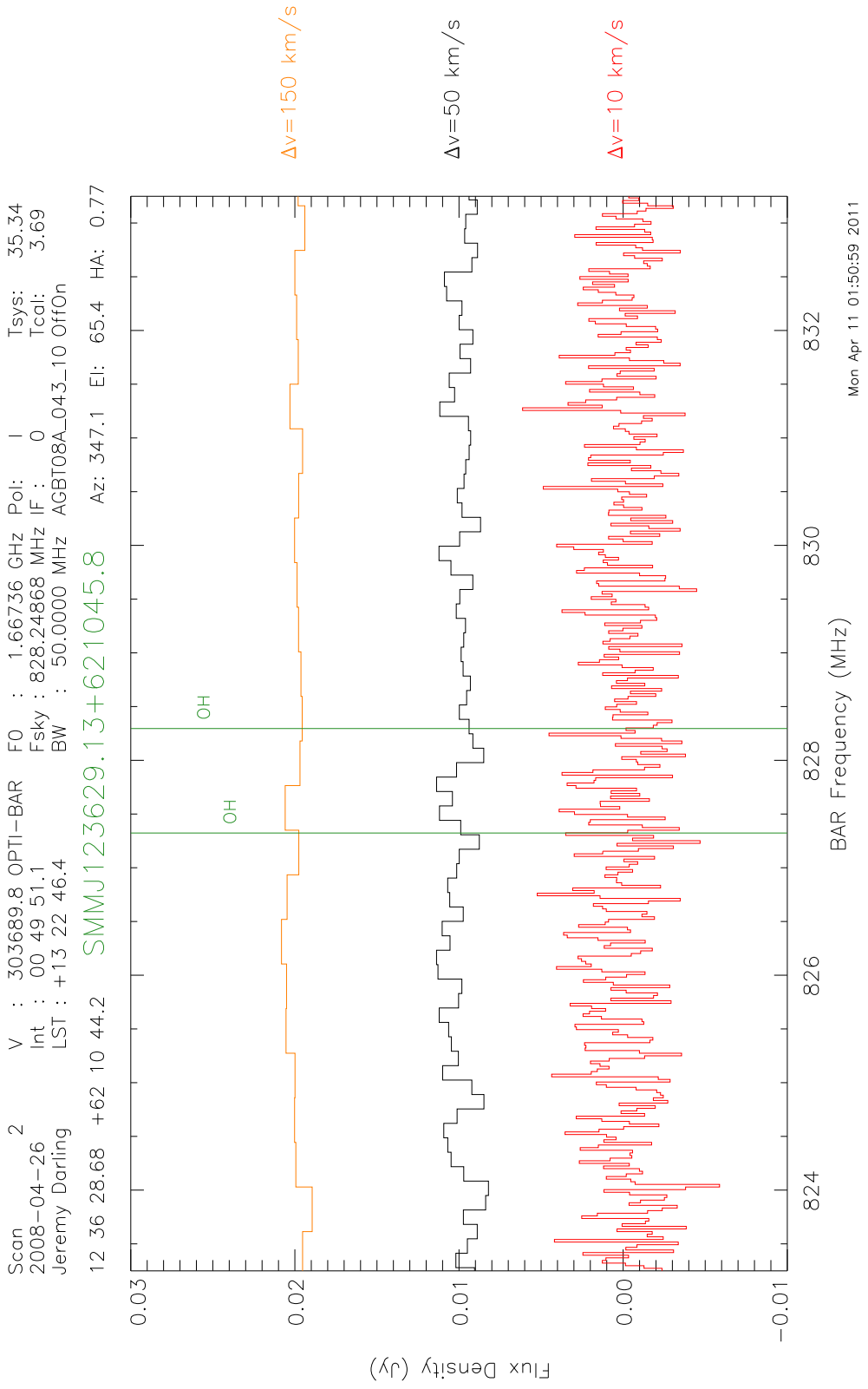

Figure C.67 18-cm spectrum of the galaxy SMM J123629.13+621045.8.

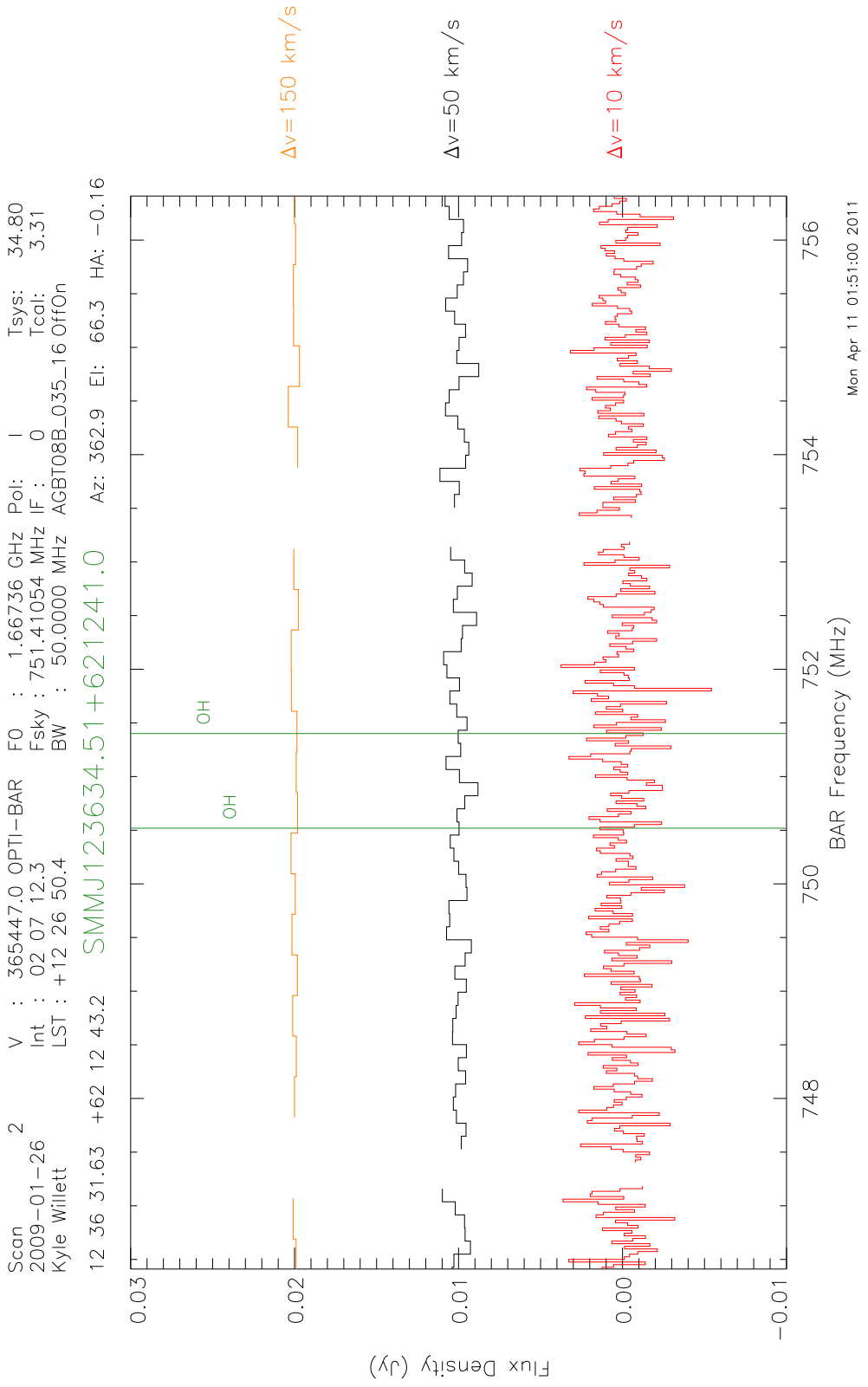

Figure C.68 18-cm spectrum of the galaxy SMM J123634.51+621241.0.

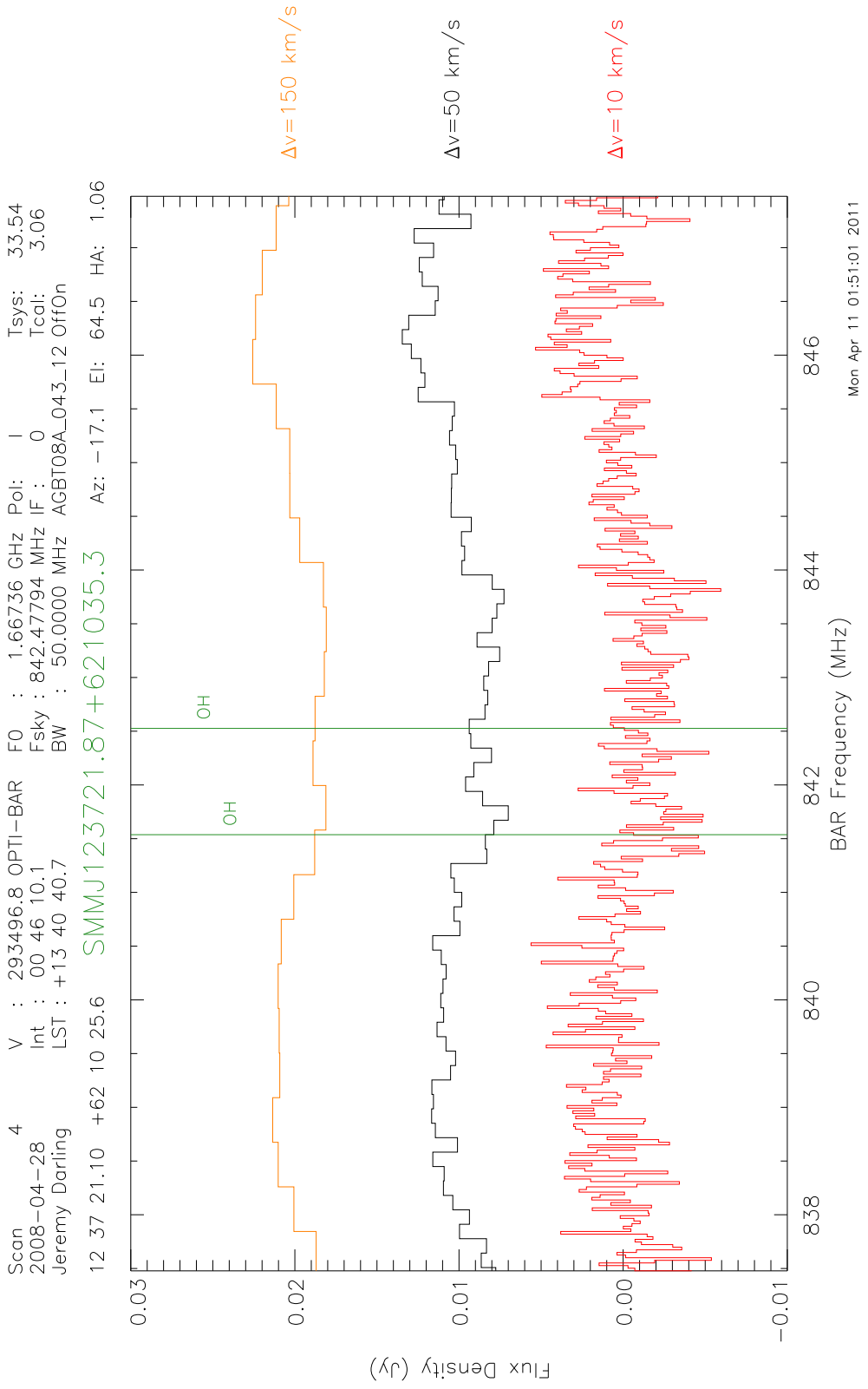

Figure C.69 18-cm spectrum of the galaxy SMM J123721.87+621035.3.

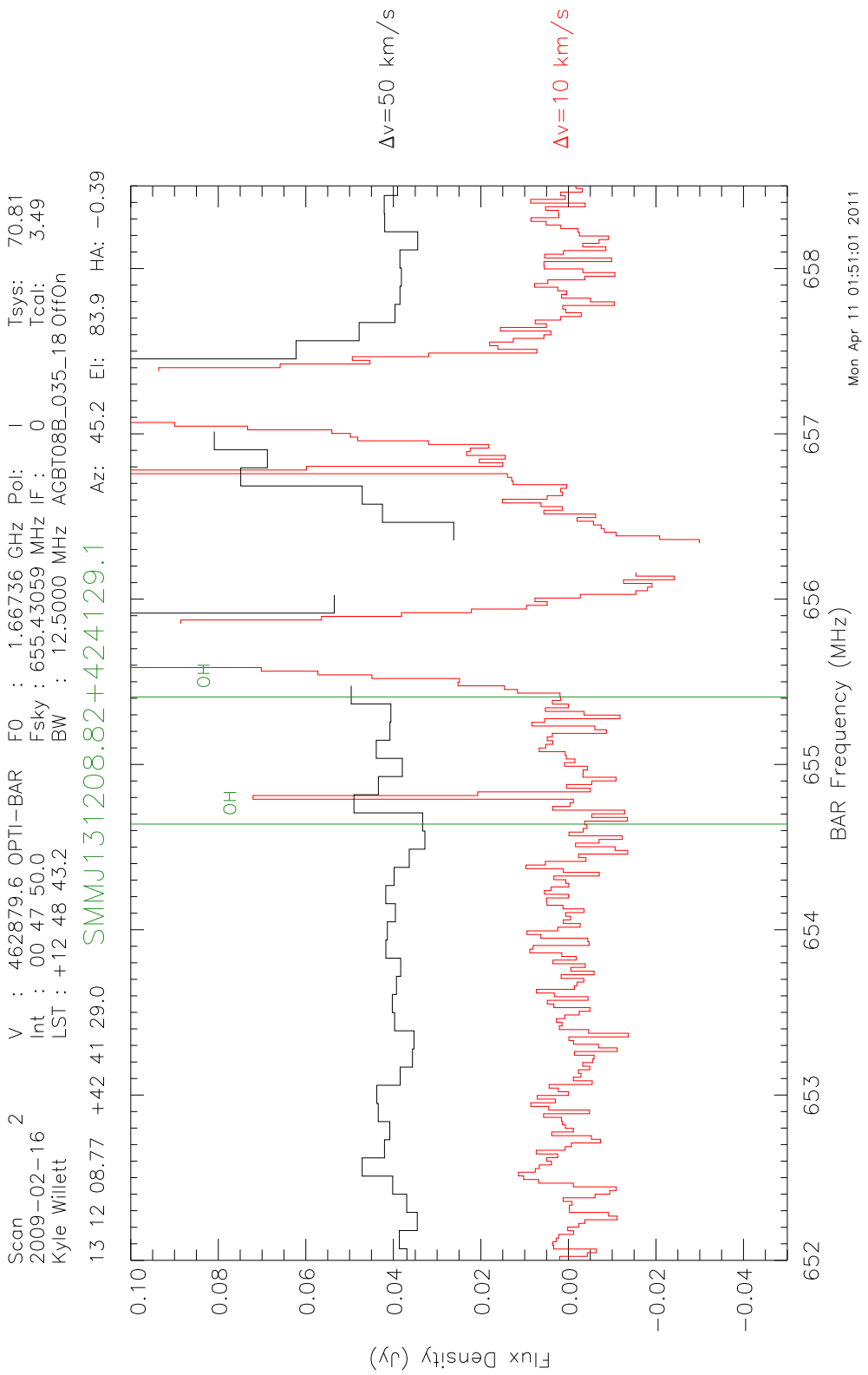

Figure C.70 18-cm spectrum of the galaxy SMM J131208.82+424129.1.

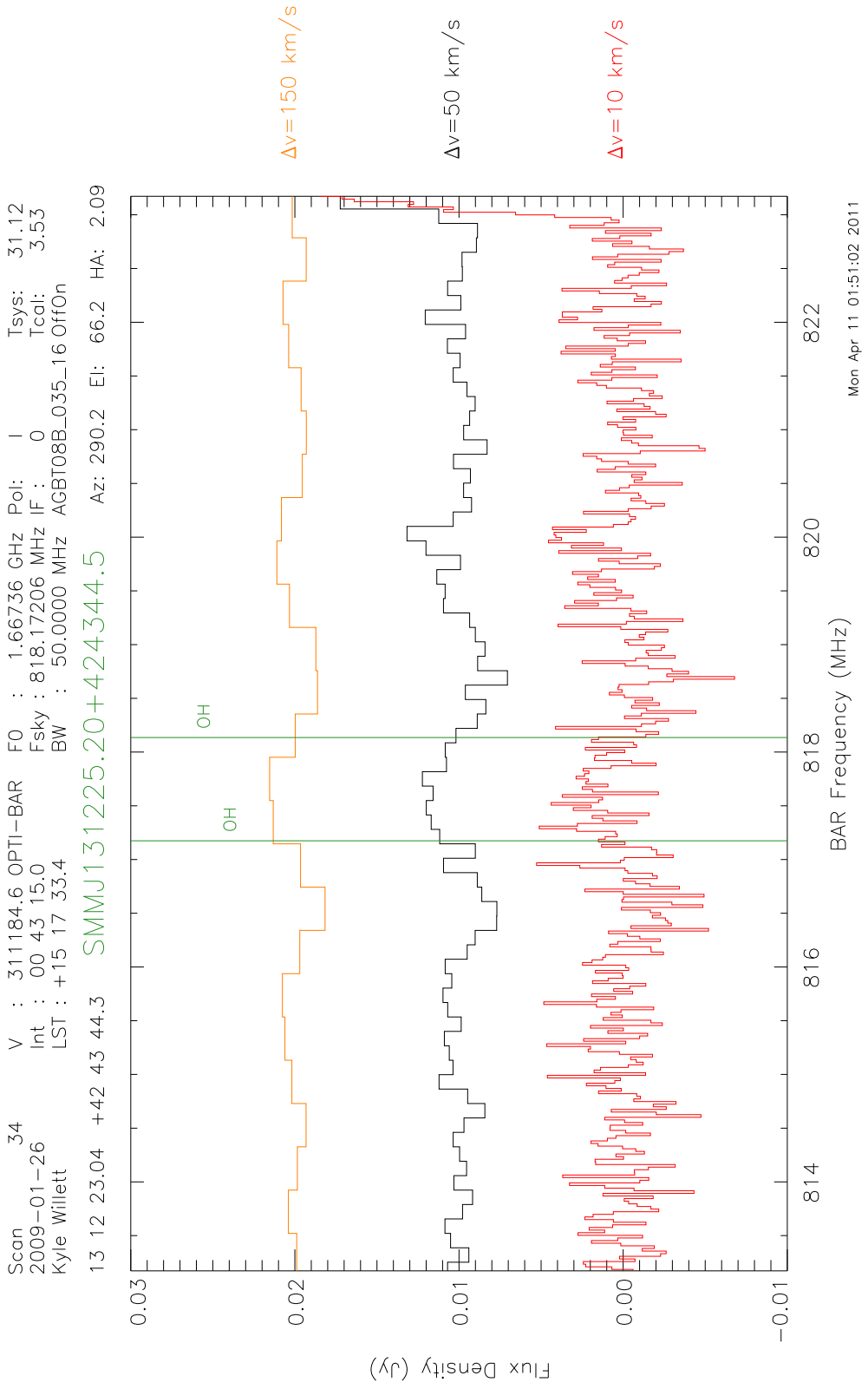

Figure C.71 18-cm spectrum of the galaxy SMM J131225.20+424344.5.

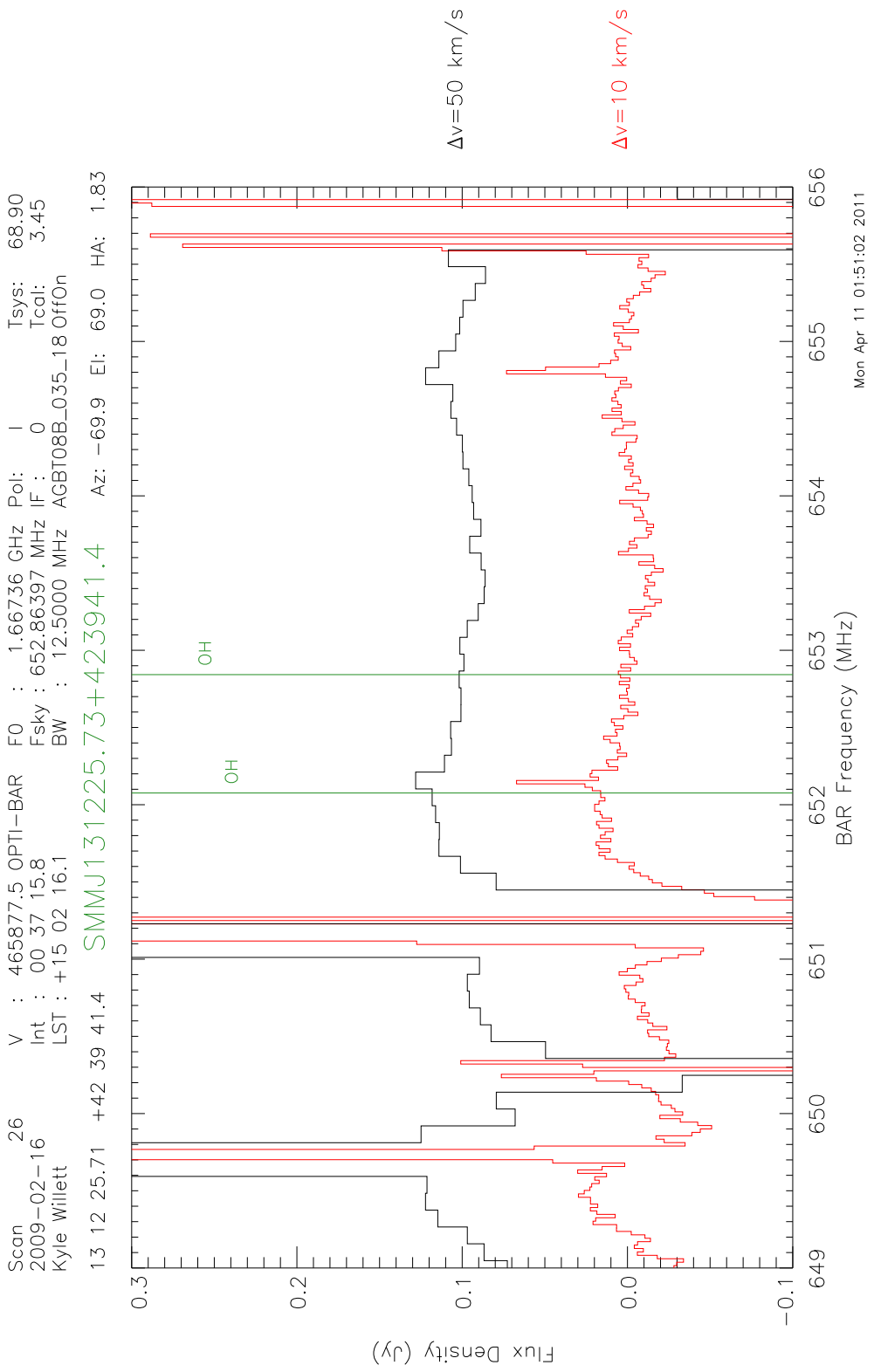

Figure C.72 18-cm spectrum of the galaxy SMM J131225.73+423941.4.

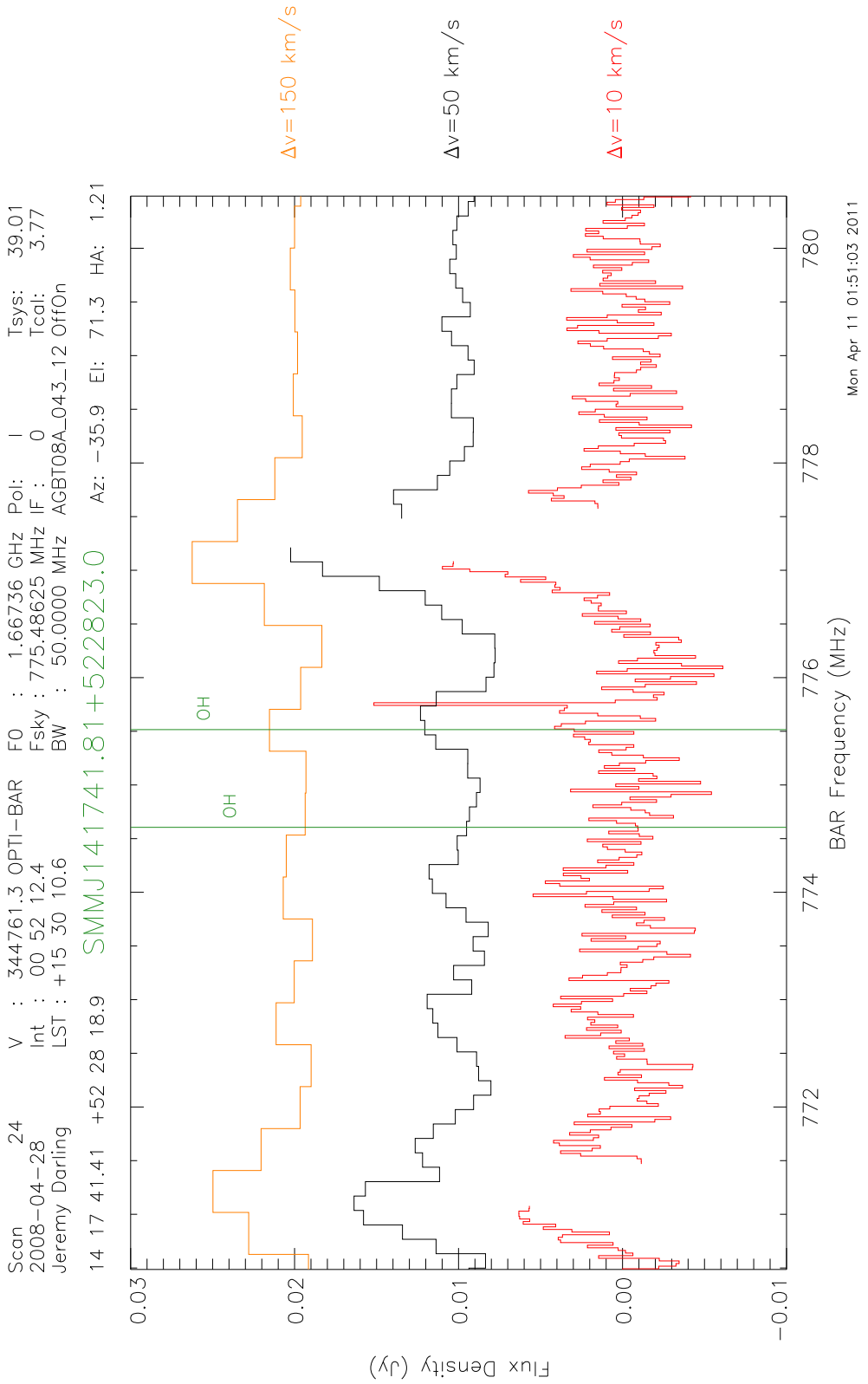

Figure C.73 18-cm spectrum of the galaxy SMM J141741.81+522823.0.

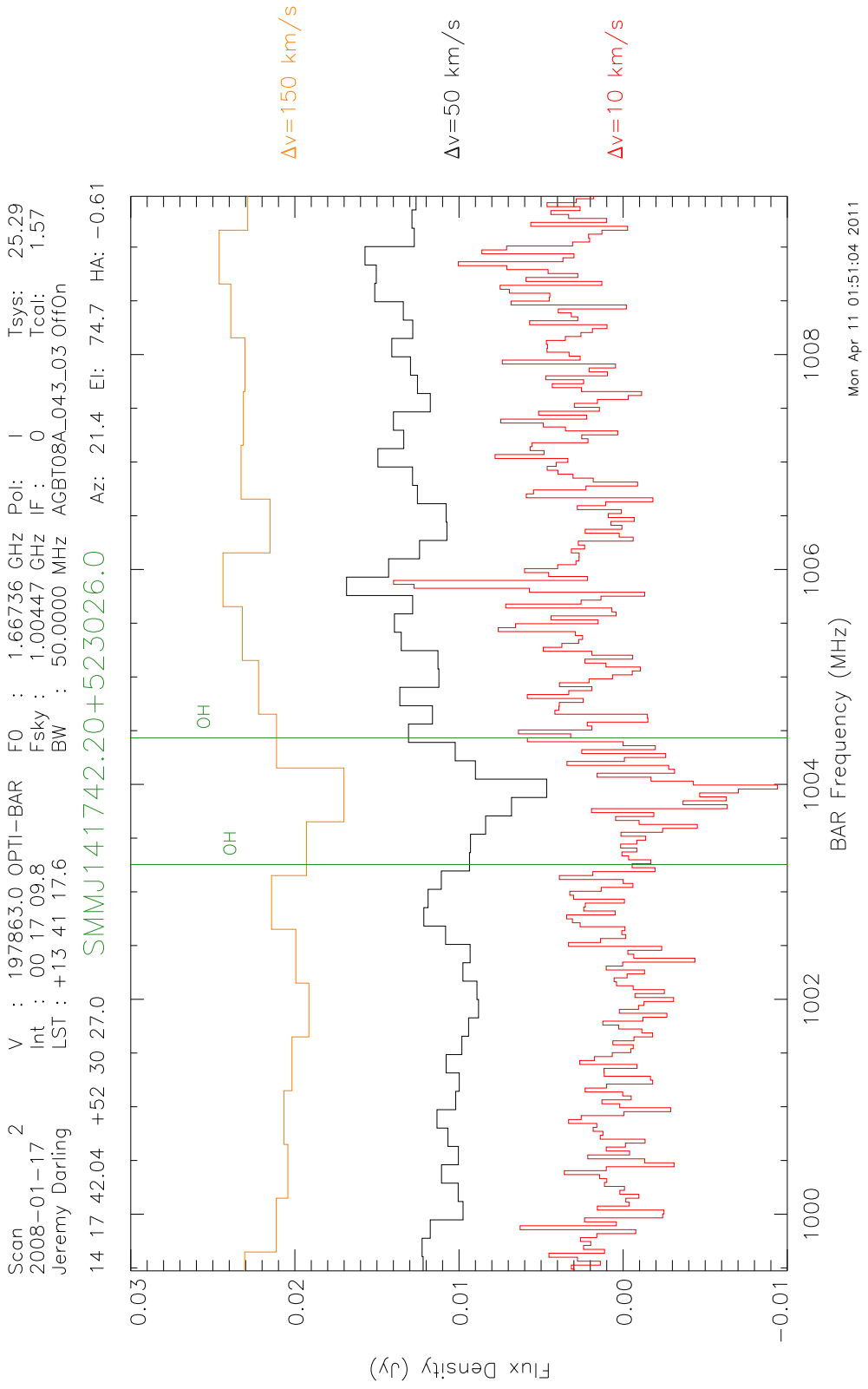

Figure C.74 18-cm spectrum of the galaxy SMM J141742.04+523025.7.

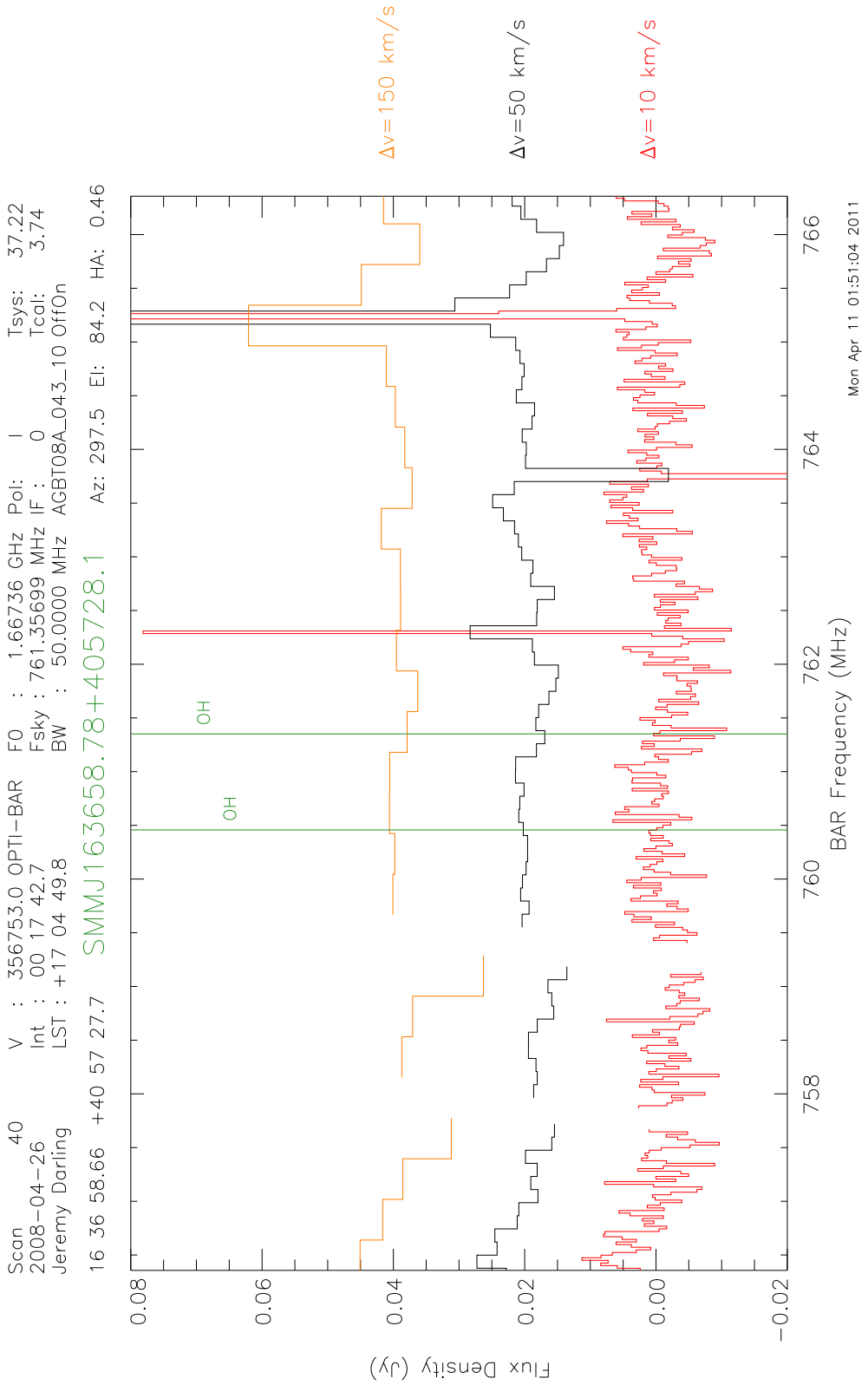

Figure C.75 18-cm spectrum of the galaxy SMM J163658.78+405728.1.

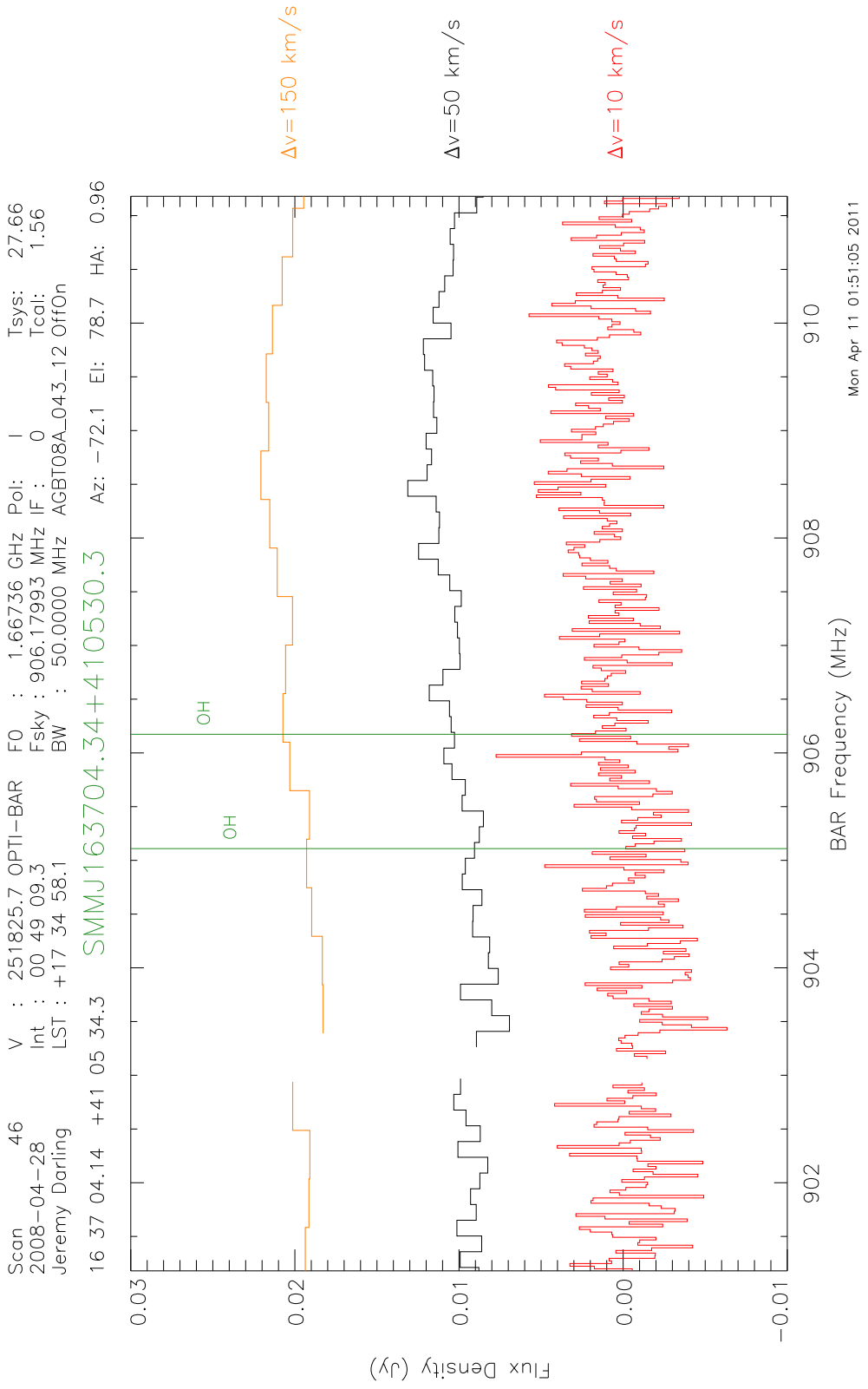

Figure C.76 18-cm spectrum of the galaxy SMM J163704.34+410530.3.

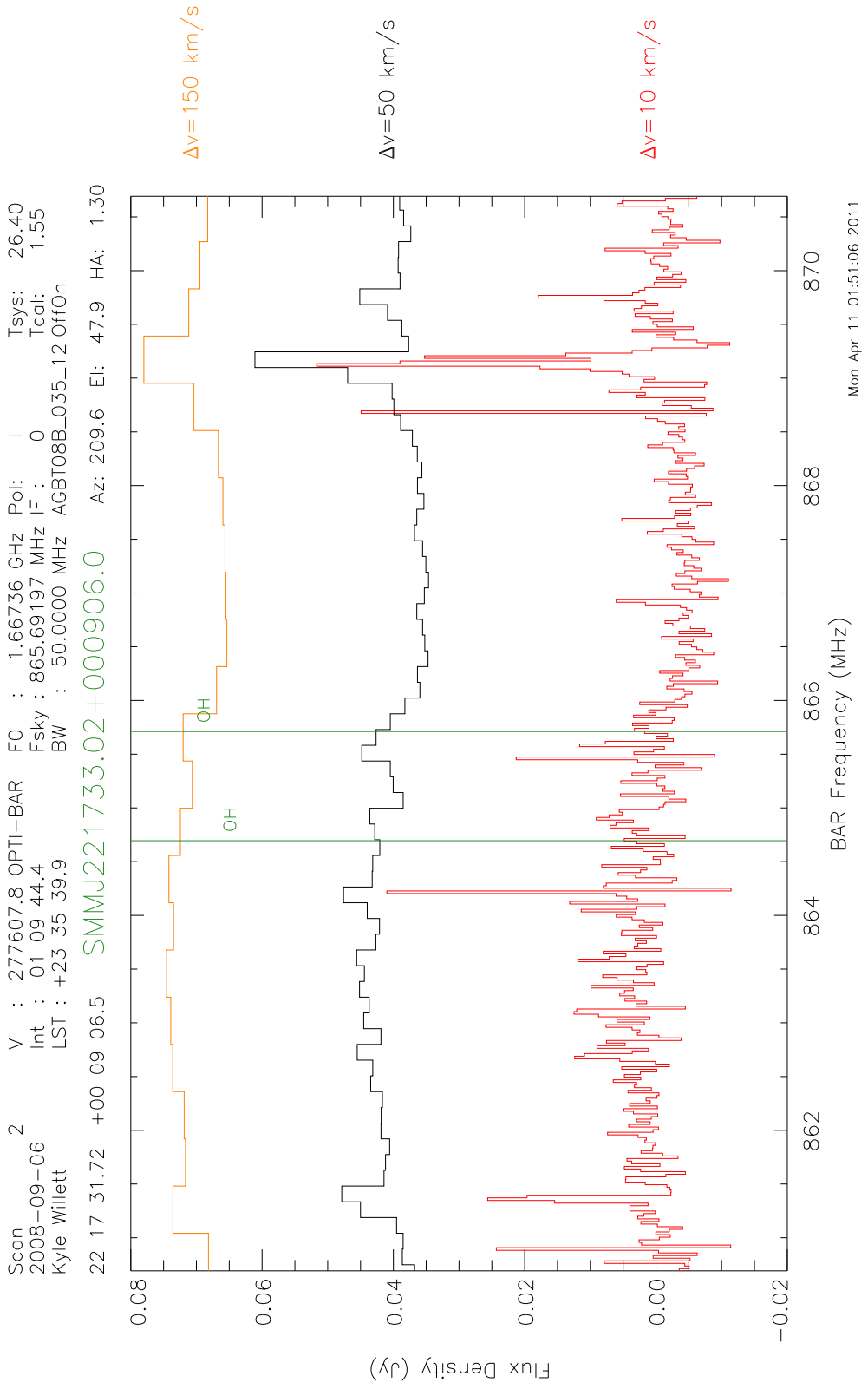

Figure C.77 18-cm spectrum of the galaxy SMM J221733.02+000906.0.